INSTITUTE OF SPACE TECHNOLOGY

Sixth International Conference on

# AEROSPACE SCIENCE & ENGINEERING

*In collaboration with*

Belt and Road Aerospace Innovation Alliance (BRAIA)

November 12-14, 2019

Islamabad, Pakistan

## PROCEEDINGS

# PROCEEDINGS

## Sixth International Conference on Aerospace Science and Engineering

*In collaboration with*

Belt and Road Aerospace Innovation Alliance (BRAIA)

November 12 – 14, 2019

Institute of Space Technology

Islamabad, Pakistan

## Editorial Board





Institute of Space Technology (IST), Islamabad, Pakistan.

# Preface

Institute of Space Technology - one of the premier institutes in Pakistan - is a federally chartered, degree awarding Institute offering graduate and baccalaureate programs in Aerospace, Avionics, Electrical, Mechanical, Materials Science & Engineering, Space Science, Remote Sensing & GISc, Astronomy & Astrophysics, Global Navigation Satellite Systems (GNSS) and Applied Mathematics & Statistics. IST has been ranked amongst the top four engineering universities of Pakistan. The academic and allied research facilities, comprising of state-of-the-art high-tech equipment, are compatible with international standards. IST aims at fostering intellectual and economic vitality through teaching, research and outreach in the field of space science and technology, International Conference on Aerospace Science and Engineering (ICASE) is one effort in this pursuit.

International Conference on Aerospace Science and Engineering is a regular biennial event of Institute of Space Technology (IST) since 2009. The focus of this conference is to provide an international forum wherein scientists, researchers, engineers, academicians, private and public industry professionals, entrepreneurs, and students from all across the globe interact and share the latest themes and trends related to Aerospace Science and Engineering along with their allied Applications. It provides a platform to share experiences, foster academia-industry collaborations, and to evaluate emerging technologies and latest developments in the spacious domains of Space Science and Technology.

Sixth International Conference on Aerospace Science and Engineering (ICASE 2019) encompassed a diverse blend of thematic areas including Aeronautics and Astronautics, Satellite Technology & Applications, Mechanical Engineering for Aerospace Applications, Aerospace Materials Design and Engineering, Guidance, Navigation & Controls and GNSS, Astronomy, Astrophysics and Astrobiology, Remote Sensing, GIS & Space Applications, Mathematical & Statistical Modeling for Space Applications, Space Policy, Law & Management and Space Technology Education & Popularization.

ICASE 2019 featured 62 sessions comprising of 23 Technical Sessions, 12 Workshops, 9 Panel Discussions, 7 Plenary Sessions, 3 Webinars, 4 Forum-360, Poster Session, Science at Glance and Meet the Scientist Sessions. A total of 85 research papers were presented in the conference in consort with 11 poster presentations. The best 32 peer reviewed research papers have been published in IEEE Xplore. A spectrum of over 40 National and International invited speakers shared their research accomplishments with the academicians, researchers and students.

We are thankful to our conference partners namely the National Space Agency of Pakistan SUPARCO, Belt & Road Aerospace Innovation Alliance (BRAIA), Inter-Islamic Network on Space Sciences & Technology (ISNET), Commission on Science and Technology for Sustainable Development in the South (COMSATS), Pakistan Science Foundation (PSF), KRL, IEEE and AIAA (IST Chapter) for their valuable support. Finally, we would like to express our sincere appreciation to all the participants, keynote speakers, financial sponsors, exhibitors, supporting organizations and all the committee members who have put their efforts to make ICASE 2019 successful.

Conference Secretary

*April 2020*

# Table of Contents

# Conference Organizing Committee

| Name | Designation | Conference Role |
|---|---|---|
| Maj. Gen. Aamer Nadeem, H.I (M) | Chairman SUPARCO | Patron – in – Chief |
| Dr. Syed Wilayat Husain | Professor, IST | General Chair |
| Dr. Najam Abbas Naqvi | Assoc. Professor, IST | Secretary |
| Dr. Iqbal Rasool Memon | Dean, IST | Technical Chair |
| Mr. Mirza Kashif Begg | CFO, IST | Treasurer |
| Engr. Ishaat Saboor | Registrar, IST | Sponsorship Chair |
| Engr. Amer Azam Qazi | Director Administration, IST | Administration Chair |
| Mr. Raza Butt | Deputy Director, IST | Publicity and Publication Chair |

# Technical Sessions Chairs

| Name | Designation | Technical Session |
|---|---|---|
| Dr. Abdul Munem Khan | Head of Department<br>Aeronautics and Astronautics, IST | Aeronautics and Astronautics |
| Dr. Khurram Khursheed | Head of Department<br>Electrical Engineering, IST | Satellite Technology & Applications |
| Dr. Asif Israr | Head of Department<br>Mechanical Engineering, IST | Mechanical Engineering for Aerospace Applications |
| Dr. Ibrahim Qazi | Head of Department<br>Material Science and Engineering, IST | Aerospace Materials Design and Engineering |
| Dr. Maj Gen. ® Jamshed Riaz | Professor<br>Aeronautics and Astronautics, IST | Guidance Navigation and Control & GNSS |
| Dr. Hamid Saleem | Professor<br>Space Science, IST | Astronomy, Astrophysics & Astrobiology |
| Dr. Zahir Ali | Head of Department<br>National Center for Remote Sensing & Geo Informatics, IST | Remote Sensing, GIS & Space Applications |
| Dr. Salman Ahmad | Head of Department<br>Applied Mathematics and Statistics, IST | Mathematical & Statistical Modeling for Space Applications |
| Dr. Qamar ul Islam | Head of Department<br>Space Sciences, IST | Space Policy, Law and Management |
| Dr. Najam Abbas Naqvi | Associate Professor<br>Aeronautics and Astronautics, IST | Space Technology Education and Popularization |

# International Scientific Committee

| Name | Designation | Affiliation |
|---|---|---|
| Mr. Mansoor Ahmed | Emeritus | Emeritus; Goddard Space Flight Center, NASA, USA |
| Dr. Vladimir Jazarevic | CEO | Mechatronic Unmanned Systems & Technology Solutions – MUST Solutions |
| Dr. Hongyi Xu | Professor | Fudan University, Shangai, China |
| Dr. Abid Ali Khan | Professor | Military Technological College, Muscat, Oman |
| Dr. Alim Rustem Aslan | Professor | Istanbul Technical University (ITU), Turkey |
| Dr. Jaan Praks | Assistant Professor | Aalto University, Greater Helsinki, Finland |
| Dr. Aquib Moin | Assistant Professor | United Arab Emirates University (UAEU), Al-Ain, UAE |
| Dr. Cun-liang Liu | Professor | Northwestern Polytechnical University (NPU), China |
| Dr. Faiz Ahmad | Professor | Universiti Teknologi PETRONAS, Malaysia |
| Dr. Huiqing Fan | Professor | Northwestern Polytechnical University (NPU), China |
| Dr. Cheng-Xin Li | Professor | Xi’an Jiatong University (XJTU), Xi’an, China |
| Dr. Christine, Marie, Eugenie Amory | Professor | International Centre for Theoretical Physics, Italy<br>UNOOSA |
| Dr. Chen Jie | Associate Professor | Northwestern Polytechnical University (NPU), China |
| Dr. Xiaoliang Wang | Researcher | Shangai Jiaotong University, China |

| | | |
|---|---|---|
| Dr. Sarah Ann Bird | Researcher | National Astronomical Observatories of China,<br>Chinese Academy of Sciences, China |
| Dr. Ali Nouh Ali Ma'bdeh | Professor | Al - Bayt University, Jordan |
| Dr. Dahanayakage Don Gihan Lakmal Dahanayaka | Senior Lecturer | The Open University of Sri Lanka, Sri Lanka |
| Mr. M. E. Elmardi | Researcher | National Centre for Research, Sudan |
| Dr. Liu Nairui | Associate Professor | Northwestern Polytechnical University (NPU), China |
| Dr. Gustavo Alonso Rodrigo | Professor | Polytechnic University of Madrid, Spain |
| Ms. Maruška Strah | Executive Director | World Space Week Association |
| Dr. HAN Zhen | Assistant Professor | Northwestern Polytechnical University, China |
| Dr. ZHAO Dawei | Associate Professor | Northwestern Polytechnical University, China |
| Mr. Saurav Paudel | Researcher | ORION Space (Pvt) Limited, Nepal |

# National Scientific Committee

| Name | Designation | Affiliation |
|---|---|---|
| Dr. Adnan Maqsood | Associate Professor | National University of Sciences and Technology, Islamabad, Pakistan |
| Dr. Ali Javed Hashmi | Assistant Professor | Air University, Islamabad, Pakistan |
| Dr. Arslan Ahmed | Assistant Professor | Sukkur IBA University, Sukkur, Pakistan |
| Dr. Ghulam Jaffer | Assistant Professor | University of the Punjab (PU), Lahore, Pakistan |
| Dr. Muhammad Jawed Iqbal | Professor | University of Karachi, Karachi, Pakistan |
| Dr. Zahir Ali | Associate Professor | National Center for Remote Sensing and Geo Informatics, Institute of Space Technology (IST), Karachi |
| Dr. Aftab Ahmed Khan | Assistant Professor | Karakoram International University, Gilgit |
| Dr. Amjad Sohail | Division Head | Space and Upper Atmosphere Research Commission, Pakistan |
| Dr. Muhammad Fiaz | Associate Professor | University of Engineering and Technology, Lahore, Pakistan |
| Dr. Amir Ikram | Assistant Professor | University of Engineering and Technology, Lahore, Pakistan |

# Scientific Committee - Institute of Space Technology

| Name | Designation | Department |
|---|---|---|
| Dr. Iqbal Rasool | Dean | Institute of Space Technology |
| Dr. Abdul Munem Khan | HoD / Professor | Aeronautics & Astronautics |
| Dr. Khalid Parvez | Professor | Aeronautics & Astronautics |
| Maj. Gen. ® Dr. Jamshed Riaz | Professor | Aeronautics & Astronautics |
| Dr. Ihtzaz Qamar | Professor | Aeronautics & Astronautics |
| Dr. Muhammad Naeem | Professor | Aeronautics & Astronautics |
| Dr. Syed Hossein Raza Hamdani | Professor | Aeronautics & Astronautics |
| Dr. Najam Abbas Naqvi | Associate Professor | Aeronautics & Astronautics |
| Dr. Abdul Waheed | Associate Professor | Aeronautics & Astronautics |
| Dr. Hayat M. Khan | Assistant Professor | Aeronautics & Astronautics |
| Mr. Muhammad Anwar | Assistant Professor | Aeronautics & Astronautics |
| Mr. Sardar Ahmad | Assistant Professor | Aeronautics & Astronautics |
| Dr. Muhammad Farooq Haydar | Assistant Professor | Aeronautics & Astronautics |
| Dr. Munawar Shah | Assistant Professor | Aeronautics & Astronautics |
| Dr. Raees Fida Swati | Assistant Professor | Aeronautics & Astronautics |
| Dr. Umar Iqbal Bhatti | Associate Professor | Aeronautics & Astronautics |
| Dr. Muhammad Ushaq | Associate Professor | Aeronautics & Astronautics |
| Dr. Khurram Khursheed | HoD / Professor | Electrical Engineering |
| Dr. Rehan Mehmood | Assistant Professor | Electrical Engineering |
| Dr. Farrukh Aziz Bhatti | Assistant Professor | Electrical Engineering |
| Dr. Abdur Rahman Mohammad Maud | Assistant Professor | Electrical Engineering |
| Dr. Amena Ejaz Aziz | Assistant Professor | Electrical Engineering |
| Dr. Sadia Shakil | Assistant Professor | Electrical Engineering |
| Dr. Asif Israr | HoD / Professor | Mechanical Engineering |
| Dr. Muhammad Zubair Khan | Professor | Mechanical Engineering |

| | | |
|---|---|---|
| Dr. Owais Ur Rehman Shah | Assistant Professor | Mechanical Engineering |
| Dr. Mariyam Sattar | Assistant Professor | Mechanical Engineering |
| Mr. Muhammad Shaban | Assistant Professor | Mechanical Engineering |
| Dr. Ibrahim Qazi | HoD / Professor | Material Sciences and Engineering |
| Dr. Syed Wilayat Husain | Professor | Material Sciences and Engineering |
| Dr. Anjum Tauqir | Professor | Material Sciences and Engineering |
| Dr. Muhammad Yasir | Assistant Professor | Material Sciences and Engineering |
| Dr. Salman Ahmad | HoD / Associate Professor | Applied Mathematics & Statistics |
| Dr. Maryiam Javed | Associate Professor | Applied Mathematics & Statistics |
| Dr. Muhammad Nawaz | Associate Professor | Applied Mathematics & Statistics |
| Dr. Ayesha Rafiq | Assistant Professor | Applied Mathematics & Statistics |
| Dr. Qamar ul Islam | HoD / Professor | Space Sciences |
| Dr. Hamid Saleem | Professor | Space Sciences |
| Dr. Hammad Gillani | Assistant Professor | Space Sciences |
| Dr. Saleem Ullah | Assistant Professor | Space Sciences |
| Dr. Waqas Ahmed Qazi | Assistant Professor | Space Sciences |
| Dr. Muhmmad Shakir | Assistant Professor | Space Sciences |
| Dr. Mujtaba Hassan | Assistant Professor | Space Sciences |
| Dr. M. Shahid Iqbal | Assistant Professor | Space Sciences |
| Dr. Saeeda Sajjad | Assistant Professor | Space Sciences |
| Dr. Zahir Ali | HoD / Associate Professor | National Center for Remote Sensing and Geo Informatics |
| Dr. Muhammad Ateeq Qureshi | Assistant Professor | National Center for Remote Sensing and Geo Informatics |
| Dr. Uzma Shaukat | Assistant Professor | Bio Technology |

# Conference Secretariat

| Name | Role |
|---|---|
| Dr. Najam Abbas Naqvi | Conference Secretary |
| Mr. Raza Butt | Media & Publicity |
| Mr. Nasir Ali | Protocol & Liaison |
| Ms. Rabia Ali | Sessions Coordination |
| Mr. Faaiz Ahmed Jeelani | Protocol & Hospitality |
| Mr. Usama Ahmed | Technical Program Development |
| Mr. Waqas Jilani Joiya | Logistics & Operations |
| Mr. Muhammad Adeel | Graphics & Creative Designing |
| Mr. Waqas Ramzan | Data & Record Management |
| Mr. Faran Ali | Hospitality & Lodging |
| Mr. Ahsan Abdul Rauf | Technical Sessions |

# List of Papers Published in IEEE Xplore

ISBN: 978-1-7281-1955-7

*https://ieeexplore.ieee.org/servlet/opac?punumber=9043179*

| S. No. | Author Name & Affiliation | Research Title |
|---|---|---|
| 1 | Muhammad Jamil<br>*National University of Sciences and Technology, Pakistan* | Influence of Dimple Design on Aerodynamic Drag of Golf Balls |
| 2 | Maaze Tariq<br>*Institute of Space Technology, Pakistan* | Design and Analysis of High Pressure Ratio Transonic Fan Stage |
| 3 | Daniyal Ahmed Khan<br>*Center of Excellence in Science and Applied Technologies, Pakistan* | Design of Hypersonic Scramjet Engine Operating between Mach 5 to Mach 9 |
| 4 | Muhammad Ihtisham Babar<br>*National University of Sciences and Technology, Pakistan* | Experimental Flutter Analysis of the Wing in Pitch and Plunge Mode |
| 5 | Syed Baleegh Hussain<br>*National University of Sciences and Technology, Pakistan* | Aerodynamic Design Considerations for a Soccer Ball |
| 6 | Mishma Akhtar<br>*National University of Sciences and Technology, Pakistan* | Two Dimensional Insect Flight Trajectory Tracking and Analysis |
| 7 | Maha Batool<br>*Institute of Space Technology, Pakistan* | Geometric Sensitivity of Static Equivalent Modeling Techniques for Honeycomb Cores |
| 8 | Mansoor Tariq<br>*University of the Punjab, Pakistan* | Use of LiDAR and RADAR Technologies for Watershed Analysis in Feather River near California |
| 9 | Imran Aziz<br>*National University of Sciences and Technology, Pakistan* | Comprehensive Review of Pulse Repetitions Interval (PRI) Classification Schemes |
| 10 | Malik Ahmed Hassan<br>*Institute of Space Technology, Pakistan* | Vibration Response of Human Arm in Machine Operation |
| 11 | Amjid Khan<br>*National University of Sciences and Technology, Pakistan* | Performance Variation of Transonic Centrifugal Compressor at Different Tip Clearances Using Numerical Simulations |

| | | |
|---|---|---|
| 12 | Nouman Nazir<br>*National University of Sciences and Technology, Pakistan* | Comparison of 1kW Horizontal Axis Wind Turbine Rotor Blade Performance Using Numerical Simulation |
| 13 | Zunair Masroor<br>*Institute of Space Technology, Pakistan* | Crack Repairing of Aluminum Alloy 2024 by Reinforcement of Al2O3 and B4C Particles using Friction Stir Processing |
| 14 | Zamurad Khan<br>*National University of Sciences and Technology, Pakistan* | Effect of Moisture / Liquid Absorption on Mechanical Properties of Composites |
| 15 | Muhammad Ali Asghar<br>*Institute of Space Technology, Pakistan* | Rheokinetic Analysis of HTPB-TDI Based Polyurethane Binder System |
| 16 | Muhammad Saleem<br>*Institute of Space Technology, Pakistan* | Use of Global Navigation Satellite System (GNSS) Software Defined Receiver (SDR) for Determining the 3D Real Time Position Variation in Dense Urban Areas by Averaging Method |
| 17 | Arif Hussain<br>*Sukkur IBA University, Pakistan* | Real-Time Monitoring and Logging of Ionospheric Scintillation and Total Electron Content |
| 18 | Arif Hussain<br>*Sukkur IBA University, Pakistan* | Investigation of Ionospheric Scintillations and Total Electron Content (TEC) over Mid-latitudinal Region (Pakistan) |
| 19 | Maria Mehmood<br>*National University of Sciences and Technology, Pakistan* | GPS Total Electron Content (TEC) Estimation using Single Station Measurements |
| 20 | Adnan Ashraf<br>*Institute of Space Technology, Pakistan* | Ambiguity Resolution in Carrier Phase Based Positioning Using Lambda Method |
| 21 | Rafia Sarwar<br>*Institute of Space Technology, Pakistan* | Event Rates of EMRIs and IMRIs in Milky Way Galaxy |
| 22 | Khola Anees<br>*Institute of Space Technology, Pakistan* | Photometry Result of an Eclipsing Binary Star V798Her in the Globular Cluster NGC 6341 |
| 23 | Khusharah Aslam<br>*Institute of Space Technology, Pakistan* | Modeling Coral Reef Susceptibility Using GIS Multi-Criteria Analysis |
| 24 | Fahim Irshad<br>*Institute of Space Technology, Pakistan* | Wet Snow Mapping using SAR C-Band through Google Earth Engine |

| | | |
|---|---|---|
| 25 | Saqib Mehdi<br>*Institute of Space Technology, Pakistan* | Atmospheric Anomalies Associated with 2011 M_w9.1 Japan Earthquake from Remote Sensing |
| 26 | Zahida Najmi<br>*University of the Punjab, Pakistan* | Forest Inventory Parameters from LIDAR RADAR and Optical Data: Case Study Lubrecht Experimental Forest in California |
| 27 | Abdul Basit<br>*Institute of Space Technology, Pakistan* | Estimation of Ground Level PM2.5 by using MODIS Satellite data |
| 28 | Syeda Saleha Fatim Ali<br>*Institute of Space Technology, Pakistan* | River Runoff Modelling Through Geospatial Techniques-A Case Study Of Snow And Glacier Fed Astore River Basin, Northern Pakistan |
| 29 | Dr. Liu Nairui<br>*Northwestern Polytechnic University, China* | NOx Emission Prediction Analysis and Comparison in Gas Turbine Combustor Utilizing CFD and CRN Combined Approach |
| 30 | Muhammad Amjad Sohail<br>*Space and Upper Atmosphere Research Commission, Pakistan* | Enhancement of Solution Resolutions by Mesh Generation and Adaptively Tools |
| 31 | Sheikh Imran Nasir<br>*National University of Sciences and Technology, Pakistan* | Nascent Space Powers: Some Policy Issues |
| 32 | Muhammad Zakaria<br>*National Defence University, Pakistan* | National Space Policy: Updates, Changes and Potential in Light of a New Age |

# List of Posters

| S. No. | Author Name & Affiliation | Research Title |
|---|---|---|
| 1 | Farrukh Iqbal<br>*National University of Sciences and Technology, Pakistan* | Sloshing Analysis of a Supersonic Fuel Tank of an Aircraft |
| 2 | Umar Khalid<br>*Institute of Space Technology, Pakistan* | Design Modification of Rolling Airframe Projectile by Increasing Number of Tail Stabilizing Fins |
| 3 | Hamood Ur Rahman<br>*National University of Sciences and Technology, Pakistan* | Numerical Study on Effect of High Lift Devices on Dynamic Stability Characteristics of a Generic Airfoil |
| 4 | Azhar Abbas<br>*National University of Sciences and Technology, Pakistan* | Active Flow Control Using Dielectric Barrier Plasma Actuators |
| 5 | Shafiq Ur Rehman<br>*Sir Syed University of Engineering and Technology, Pakistan* | The Pakistan Hybrid Earthquake Extrapolation Structure for the World Expanding Hybrid Energy |
| 6 | Sadaf Sadiq<br>*Institute of Space Technology, Pakistan* | Additional Rain Gauge Site Appropriation for Monitoring Precipitation in Sindh, Pakistan Using Geospatial Techniques & Multi-Criteria Decision Making |
| 7 | Penha Zaki<br>*Institute of Space Technology, Pakistan* | Estimating Watershed Characteristics and Calculating AEP, Case Study Jhal Magsi, Balochistan |
| 8 | Kanwal Javid<br>*University of The Punjab, Pakistan* | Monitoring the transformation of Lahore's Urban Form using Geomatics Techniques |
| 9 | Rumana Siddiqui<br>*University of The Punjab, Pakistan* | Physiographic Study and Monitoring Climatic Impacts on Cold Desert Satpana, Skardu, Pakistan |
| 10 | Usman Iqbal Ahmed<br>*National University of Sciences and Technology, Pakistan* | An Astro-Imaging Module for Identification of LEO Satellites |
| 11 | Rida Batool<br>*Lahore Grammar School, Pakistan* | Evaluating Spatial Patterns of Urban Green Spaces in Karachi, Pakistan Through Satellite Remote Sensing Techniques |

# Research Papers

# Comparative Study of Parametrization Techniques for Low Reynolds Number Airfoils

Hamza Fiaz
*Department of Aerospace Engineering*
*National Univeristy of Sciences and Technology*
Islamabad, Pakistan
hamzafiaz@aerospace.pk

Taimur Ali Shams
*Department of Aerospace Engineering*
*National Univeristy of Sciences and Technology*
Islamabad, Pakistan
taimur.shams@cae.nust.edu.pk

Syed Irtiza Ali Shah
*Department of Aerospace Engineering*
*National Univeristy of Sciences and Technology*
Islamabad, Pakistan
irtiza.shah@gatech.edu

Nadeem Hussain
*Department of Aerospace Engineering*
*National Univeristy of Sciences and Technology*
Islamabad, Pakistan
nadeemhussain65@gmail.com

***Abstract*— Three techniques of parameterization were used to parametrize various airfoils. These techniques were Bezier-PARSEC, Class Shape Transformation-CST and Improved Geometric Parameter-IGP. Airfoils from different design classes were parametrized for comparative study and those were NACA-0012 (symmetrical), RAE-2822 (transonic) and $SC_2$-0714 (super critical). Instead of IGP method that uses zero trailing edge gap assumption, modified IGP method was used for more accuracy. Comparative study of techniques revealed that CST and modified IGP worked within accepted error for symmetrical, transonic and super-critical airfoils however, they cease to perform efficiently for low Reynold number airfoils because of less controllability factor. Low Reynolds Number is specified to vary from 50,000 to 100,000 since all low Reynolds number related phenomenon like laminar separation bubble formation, movement to upstream locations upon inclination angle, bursting and stalling occur in this range. SD-7003 and SD-7080 have been studied in this research since most of micro aerial vehicle use these airfoil as they give large values of L/D at trim angle of attack. These airfoils have unique geometrical feature at leading edge which posed multitude of problems in correct parametrization. The research concluded that Bezier-PARSEC exactly matched leading edge of low Reynolds number airfoils (SD-7003 and SD-7080) with minimum error while remaining methods failed to capture either leading edge or trailing edge of airfoils. Bezier-PARSEC appeared to be the best method for high as well as low Reynold number airfoils due to its controllability, intuitiveness, use of less geometrical variables (13) and maximum Sobieczky accuracy.***

***Keywords*— *Parametrization, Class-Shape Transformation (CST), Bezier-PARSEC, Improved Geometric Parameter (IGP), Low Reynolds Airfoils***

## I. INTRODUCTION

Parametrization relates the curves and the surfaces of geometry to the analytical modeling in such a way that coefficient of the model acts as design parameter for that particular geometry. Most airfoils are given in the form of vectors. These vectors represent the coordinates of upper and lower surface [1]. Optimization is vital to aircraft design. It helps us to find the main objective function efficiently and effectively in the design space of multiple variables and constraints [2]. Effective parametrization technique helps to represent the aircraft by using a minimum required design variable, so that optimization work load can be minimized. Three main objectives are usually considered in developing parameterization. First is use of less design parameters hence less degree of freedom. Second is intuitive behavior of design parameters. Third is proposed parameterization technique should result in effective and computationally efficient technique so that ultimate goal of optimization in less time is achieved [3]. Airfoil is an important source of lift generation in the whole aircraft design. While designing aerial vehicles, it is required either to evolve a new airfoil or use existing airfoil for optimization of mission segments. This is because airfoil required for takeoff and landing missions might be significantly different from that required in cruise or climbing performance. Since airfoil and hence wing cannot be replaced during aircraft flight therefore a need of optimization is felt which optimizes various airfoils into single airfoil suitable for all mission segments. Parametrization eased out optimization process by requiring less design parameters to describe an airfoil. Therefore, parameterized airfoil uses less time for optimization process with no compromise on accuracy of results. Earlier airfoil was represented by the coordinates. Each point acted as a design variable, therefore it was very difficult to use coordinates as a design variable. The geometry representation method can affect the efficiency of the selected optimization process. The use of discrete coordinates as design variables may not be suitable with the optimization process [4]. In other words, accurately parametrized airfoil coupled with optimization techniques helps to find the desired shape of airfoil so that the efficiency of design can be increased.

Micro Air Vehicles operate in low Reynolds number regime. They are small in size and move slowly in fluidic medium. Airfoils used in such vehicles have unique slope and curvature. The lower and upper surface curvature at leading edge is discontinuous. Further their thickness is very small. This is due to the fact that flow properties below $Re < 10^5$ are different from higher regime and traditional airfoils cannot be used for efficient flight [5]. Aerodynamic coefficients of traditional airfoils show constant behavior with Reynold number. But as Reynold number is decreased below $10^5$ these coefficients are affected by Reynold number variation as shown in Fig. 1. The non-linearity is due to the influence of viscous forces in low Reynold number regime. Due to

increase in viscous effects, the extended separation bubble along airfoil chord increases the thickness of turbulent boundary layer and as a result parasite drag increases and lifts decreases. This phenomenon is very common in conventional airfoils working below $10^5$. In order to get rid of this nonlinear behavior, thin airfoils are used as they form thin separation bubble decreasing parasite drag and as a result lift is not decreased [6]. Many parametrization techniques have been formulated and compared for transonic airfoils, super critical airfoils and symmetrical airfoils but for low speed airfoils no accurate mathematical method is proposed. This work is related to effective and efficient parametrization of low Reynold number airfoils. The error in the parametric and actual airfoil should be less than $10^{-4}$ [7].

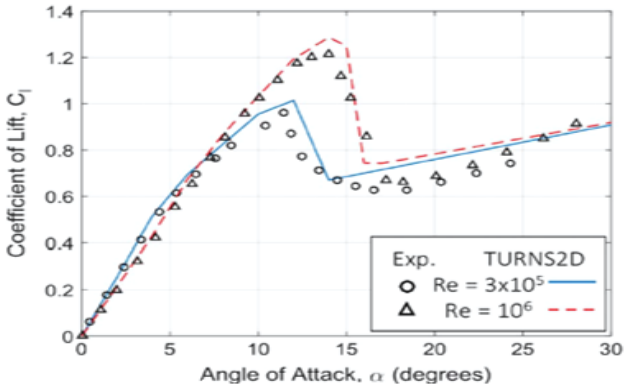


Fig. 1. Variation of (Cl) of NACA 0012 at high and low Re [6]

## II. Methodology

The problem stated in the previous section can only be taken care off if an adequate amount of knowledge is sought on the said topic. The field of micro air vehicles is comparatively new to the society yet it is the most interesting, rising and useful for serving the benefits in large segments of research area around the world. Two different low Reynold number airfoils are selected (SD-7003 and SD-7080). From literature review, it is concluded that CST, Bezier-PARSEC and IGP method are the most suitable methods. In order to check the effectiveness of these methods, three airfoils from different design families will be parameterized: Symmetrical airfoil (NACA-0012), Super critical airfoil ($SC_2$-0714) and Transonic airfoil (RAE-2822). In CST method, Bernstein coefficients will be calculated by using curve-fitting method. Furthermore, it is concluded from literature review that $5^{th}$ order Bernstein polynomial is effective and efficient. In Bezier-PARSEC method, airfoil is divided into four cubic polynomial segments and total 13 control points will be used. From geometric characteristics of an airfoil, each control point is calculated using the formulae given in literature [8].

For more accurate results, degree of Bernstein polynomial in CST and Bezier-PARSEC method can be increased respectively. It will increase the accuracy of the solution but with additional number of design variables. Consequently, computational cost will increase reducing the efficiency of the optimization process. For IGP method, eight design parameters will be calculated from the geometrical characteristics of the airfoil. In IGP method, assumption was used that airfoil has no trailing edge gap [9] but in this work, trailing edge gap will also be included in order to increase the accuracy of the method. In order to check the accuracy of modified IGP method (trailing edge gap included), NASA SC-0010 will be parametrized. In last section of present work, best curve fit method among CST, Bezier-PARSEC and modified IGP method will be used to parametrize low speed airfoils (SD-7003 and SD-7080). Parametric and original airfoil curve will be compared both geometrically and aerodynamically by using Fluent® as analysis tool. The error in the parametric and actual airfoil should be less than $10^{-4}$ according to Sobieczky.

## III. Results & Discussion

Symmetrical airfoil (NACA-0012), Super critical airfoil ($SC_2$-0714) and Transonic airfoil RAE-2822 are parametrized by using CST method. Bernstein coefficients are calculated by using curve fitting technique. Shape function of original airfoil is curve fitted and then by iterated method, error is minimized. Equations used are as follows:

$$\frac{z}{c}\left(\frac{x}{c}\right) = C\left(\frac{x}{c}\right) S\left(\frac{x}{c}\right) + \frac{x}{c}\left(\frac{\Delta z}{c}\right) \quad (1)$$

Where C(x/c) represents the class function, S(x/c) represents the shape function and Δz(x/c) function represents the trailing edge thickness of the airfoil.

$$C\left(\frac{x}{c}\right) = \left(\frac{x}{c}\right)^{N_1}\left(1-\frac{x}{c}\right)^{N_2} \quad (2)$$

$$\left(\frac{x}{c}\right) = \sum_{i=0}^{n} A_i \left(\frac{x}{c}\right)^i, \qquad 0 \le i \le n \quad (3)$$

For airfoil, value of $N_1$ and $N_2$ is 0.5 and 1 respectively. 'n' represents the order of Bernstein polynomial used. The value of $A_i$ i.e. defines the perturbations in the shape function. Following figures show the CST comparison between original and parametric airfoils. NACA-0012 and RAE-2822 shows acceptable results but error is analyzed in $SC_2$-0714 as in Fig. 3.

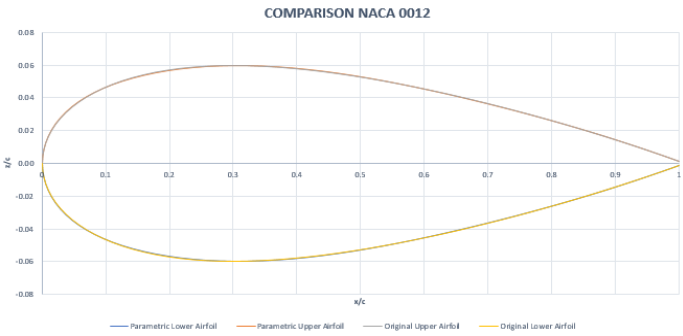

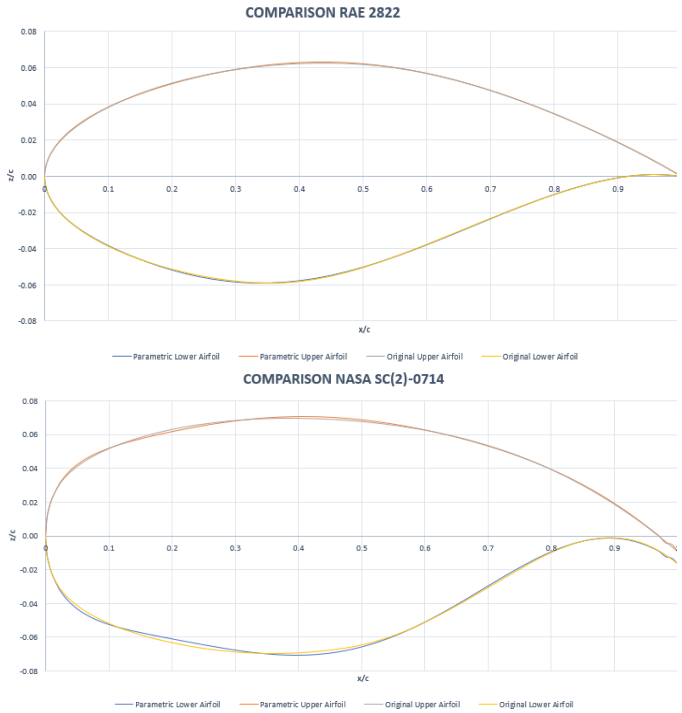


Fig. 2. CST Parametric and Original NACA 0012, RAE2822 and $SC_2$-0714 airfoils

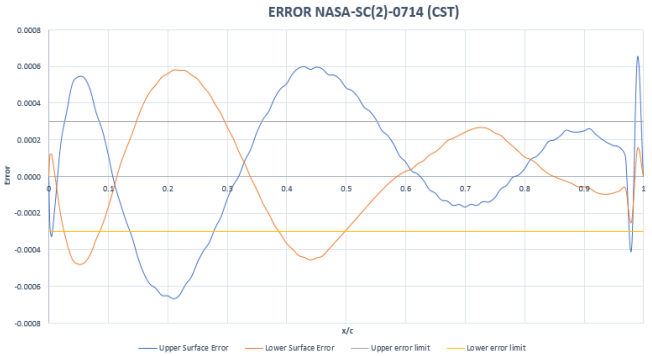


Fig. 3. Error comparison of original and parametric airfoil

After CST parameterization, Bezier-PARSEC method was used for the same airfoils. In this method, both upper and lower surfaces of airfoil were divided into two curves. Third order Bezier curve was used. Total number of control points (CPs) required were 13. These control points were obtained by using geometrical properties of an airfoil and formulae given in literature [10]. Following Fig. showed the baseline used to define each airfoil for parametrization:

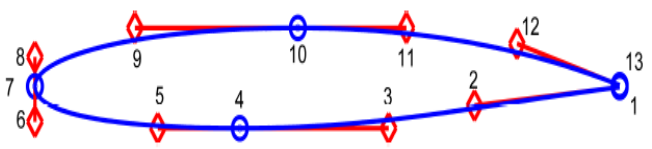


Fig. 4. Bezier-PARSEC airfoil CPs numbering and location [10]

The table below considered as standard for the control points numbering and layout. Alphabets (a, b, c) shown in the table are constant values obtained from the geometric characteristics of an airfoil. Equation used is as follows:

$$Z(t) = (1-t)^3 P_0 + 3t(1-t)^2 P_1 + 3t^2(1-t)P_2 + P_3(t^3) \quad (4)$$

TABLE 1. CONTROL POINTS VALUES [10]

| Points No. | X | Y |
|---|---|---|
| 1 | 1 | a |
| 2 | $x_2$ | $y_2$ |
| 3 | $x_3$ | b |
| 4 | $x_4$ | b |
| 5 | $x_5$ | b |
| 6 | 0 | $y_6$ |
| 7 | 0 | 0 |
| 8 | 0 | $y_8$ |
| 9 | $x_9$ | c |
| 10 | $x_{10}$ | c |
| 11 | $x_{11}$ | c |
| 12 | $x_{12}$ | $y_{12}$ |
| 13 | 1 | -a |

Fig. 4 shows Bezier-PARSEC comparison between original and parametric airfoils and the error was found to be within Sobieczky accuracy limit.

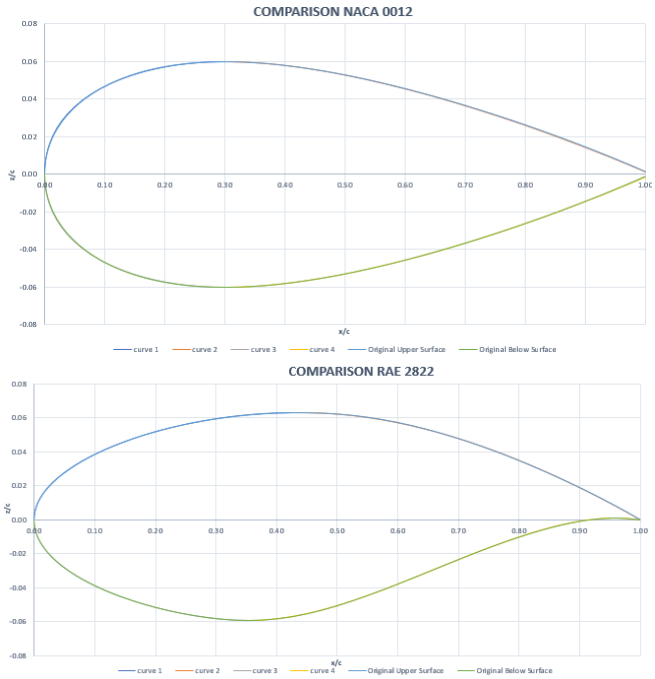

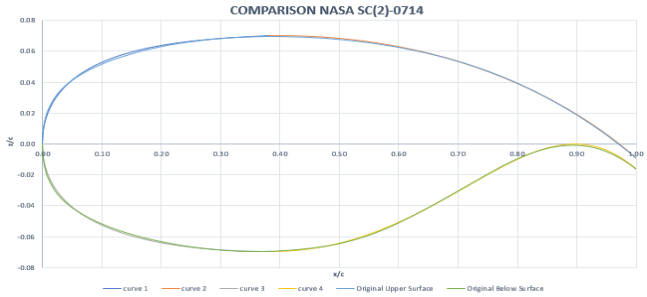


Fig. 5. Bezier-PARSEC Parametric and Original NACA-0012, RAE-2822 and $SC_2$-0714 airfoils

Last method which was selected for parameterization was Improved Geometric Parameter (IGP) technique. It was the latest among all but it can only be applicable for the geometrical study of such airfoils that follow thin airfoil theory. In this method camber and thickness curve were decoupled in order to reduce the design variables for efficient optimization [9]. This method used 8 simultaneous equations (4 for camber curve and 4 for thickness curve) to find 8 unknowns which were used as control parameters for the camber and thickness curve. Lu Xiaoqiang, Huang Jun, Song Lei and Li Jing in their IGP method had used an assumption that trailing edge gap is zero in order to reduce the cost of optimization but with loss of accuracy.

In this work, no such assumption was used and trailing edge gap was treated as a design value. In order to verify the accuracy of proposed method, NASA SC-0010 was first parameterized using IGP and modified IGP method both. The modified IGP method was then utilized for parameterization of NACA-0012, RAE-2822 and $SC_2$-0714 airfoils. Equations used in this method were:

$$x_c = 3c_1k(1-k)^2 + 3c_2k^2(1-k) + k^3 \quad (5)$$

$$y_c = 3c_3k(1-k)^2 + 3c_4k^2(1-k) \quad (6)$$

$$t = t_1(x)^{0.5} + t_2x + t_3x^2 + t_4x^3 + t_5x^4 \quad (7)$$

$c_1, c_2, c_3$ and $c_4$ were design parameters of camber curve. $t_1$ , $t_2$, $t_3$ and $t_4$ were design parameters of thickness curve and can be calculated by using geometrical properties of an airfoil. Final airfoil was parametrized by using following equations:

$$x_u = x_c \; and \; x_l = x_c \quad (8)$$

$$y_u = y_c + 0.5t(x_c) \quad (9)$$

$$y_l = y_c - 0.5t(x_c) \quad (10)$$

Fig. 6 showed comparison when parameterized by IGP and modified IGP method. It was concluded that modified IGP method was more accurate as compared to the IGP method given by Lu Xiaoqiang, Huang Jun, Song Lei and Li Jing.

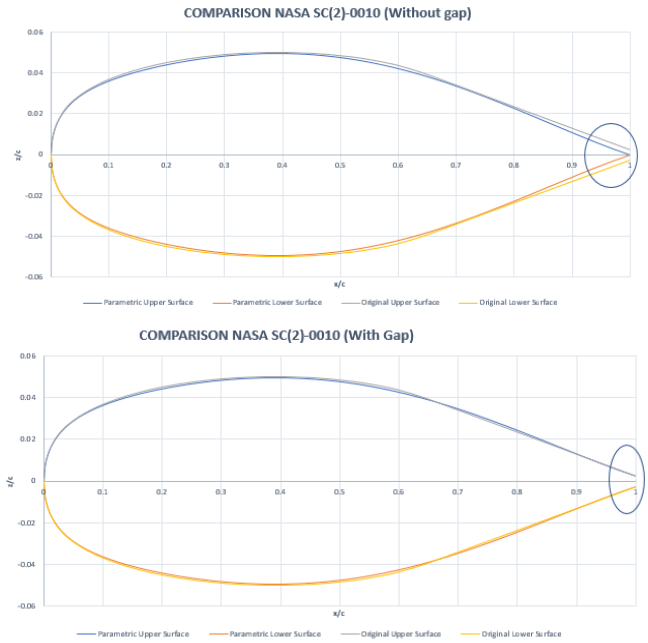


Fig. 6. IGP Method and Modified IGP Method for NASA $SC_2$-0010

Modified IGP was used to parameterized NACA-0012, RAE-2822 and $SC_2$-0714 airfoils. Despite the fact that NACA-0012 and RAE-2822 were parameterized efficiently but $SC_2$-0714 could not be parameterized and therefore modified IGP method gave degenerated results as reflected in Fig. 7

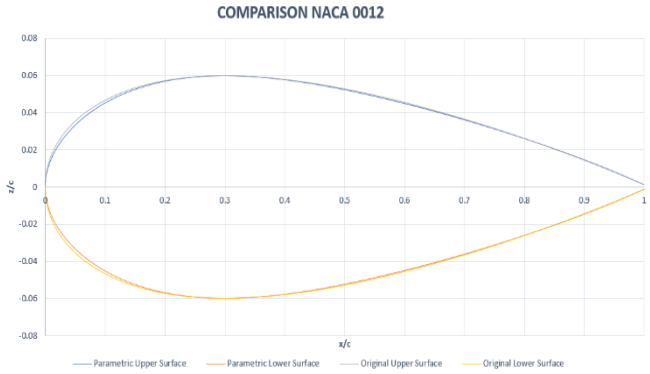

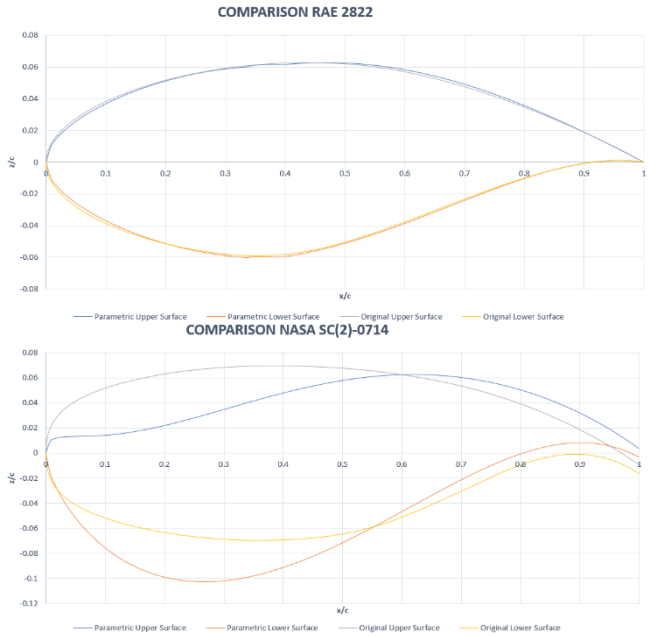


Fig. 7. Modified IGP model for NACA 0012, RAE-2822 and $SC_2$-0714

It was found that though modified IGP method used less number of design parameters (eight) but it could not be used to parametrize airfoils with maximum camber location greater than 70 % of chord, like in the case of super critical airfoils. It would degenerate the shape as shown in Fig. 7. Furthermore, airfoils with discontinuous slope at leading edge cannot be parametrized using modified IGP method. Therefore, modified IGP method could not be used for parameterizing low Reynold airfoils. CST and Bezier-PARSEC were found to be a good candidate but CST gave less accuracy as shown in Fig. 3. This is due to the fact that polynomial used in CST had less control over the airfoil surface as compared to Bezier-PARSEC method. In Bezier-PARSEC method, airfoil was divided into four curves and each curve used geometrical properties of an airfoil directly. Consequently, it gave more intuitiveness and control as compared to CST. Higher order Bernstein polynomials could be used in CST for increased accuracy and control but with the higher cost of computational power. Therefore, Bezier-PARSEC method was finally selected for the parameterization of low Reynold number airfoils. In next section, this technique is described to parameterize low Reynold number airfoils. In this research paper two such airfoils are selected, namely SD-7003 and SD-7080. Reasons for the selection of Bezier-PARSEC method are as follows:

- It defines both upper and lower surface of airfoil separately therefore discontinuity at leading edge can be captured.
- Airfoil is divided into four curves; therefore, airfoils with maximum camber location above 70% of chord can also be parametrized without degeneration.
- Functions used in this method are single-valued functions which reduces the chance of degeneration.
- Thin airfoils (low Reynold number airfoils) can easily be parameterized without intersection.

## IV. Proposed Model

Leading and trailing edges treatment was found to be easy for Bezier -PARSEC method; therefore, it was selected for low Reynold number airfoil parameterization. Results are show in the fig. 7.

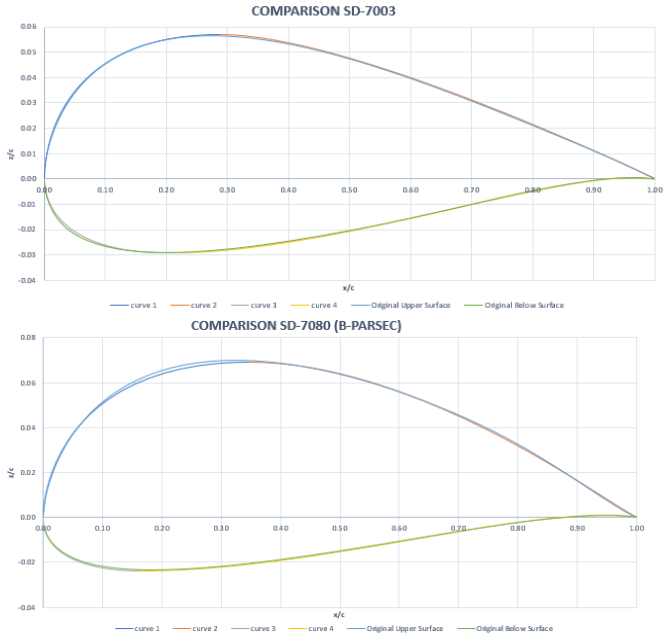


Fig. 8. Bezier-PARSEC parametric and original airfoil

Error estimation for SD-7003 and SD-7080 airfoil is presented in Fig. 8. Since the order of magnitude is to fourth decimal place, it was deduced that Bezier -PARSEC method captured curvature of airfoils perfectly. Maximum error is faced on 15% of camber where curve had maximum gradient and again on trailing edge where again curve had maximum negative gradient. Both these errors have magnitude of 0.0001 which satisfied criterion as set out by Sobieczky.


Fig. 9. Error comparison of parametric and original airfoils

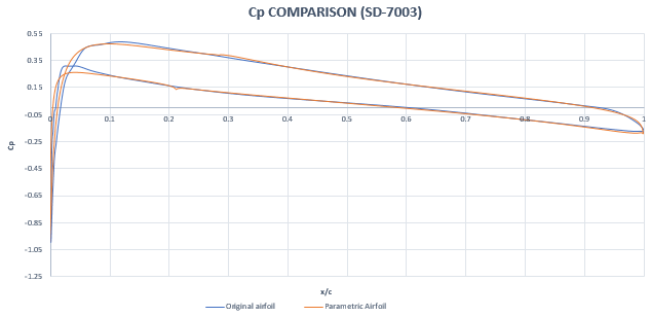


Fig. 10. Aerodynamic Comparison of SD-7003

## V. CONCLUSIONS

In this paper, Improved Geometric Parameter method was modified by the addition of trailing edge gap in thickness curve equation. Accuracy of modified IGP method was verified by parametrizing SC (2)-0010 airfoil and comparing result with IGP method given in literature. Comparative study of three methods (CST, Bezier-PARSEC and modified IGP) was carried out for three airfoils from different design families (Symmetrical NACA 0012, SC (2)-0714 and RAE-2822). After analyzing results, Bezier-PARSEC method was selected for low Reynold number airfoil parameterization and following conclusions were obtained:

- Many aerodynamic properties of an airfoil depend upon the trailing edge gap. IGP method assumes that trailing edge gap is zero and consequently gives inaccurate results at trailing edge. Modified IGP method gives more accurate results without changing parsimonious property of IGP method.
- Modified IGP method uses camber and thickness curve to define an airfoil. The camber curve is controlled by only two points which results in less controllability and can give ill-behaved shapes. Therefore, airfoils with maximum camber location >70% of chord cannot be parameterized.
- Low Reynold number airfoils which are characterized by low t/c value, sharp trailing edge, discontinuous leading edge and highly curved upper and lower surface cannot be parameterized accurately using CST and modified IGP method.
- Low Reynold number airfoils have large discontinuity in the slope at leading edge and have very thin trailing edge therefore Bezier-PARSEC is the best curve fit method. In Bezier-PARSEC method upper and lower surface of an airfoil is parameterized using more control points (10) as compared to modified IGP method that has only two control points.
- Two Low Reynold number airfoils (SD-7003 and SD-7080) were used to check the accuracy of Bezier-PARSEC method. Sobieczky criteria was selected for its accuracy check. Both geometric and aerodynamic results were compared and finally it was observed that Bezier-PARSEC method was the most precise and accurate for low Reynold number airfoils giving intuitive and continuous curve fit results.

## REFERENCES

[1] V. Sripawadkul, "Geometrical representations for efficient aircraft conceptual design and optimization," 2012.

[2] K. M. Selvan, "On the effect of shape parametrization on aerofoil shape optimization," *IJRET*, vol. 04, no. 02, pp. 123-133, 2015.

[3] R. &. T.Rogalsky, "Optimum aerofoil parameterization for aerodynamic design," in *Computer Aided Optimum Design in Engineering XI* , WIT press, 2009, pp. 197-206.

[4] M. P. M. G. V. Sripawadkul, "A Comparison of Airfoil Shape Parameterization Techniques for Early Design Optimization," in *American Institute of Aeronautics and Astronautics* , 2010.

[5] A. P. &. T. J. Mueller, "Low Reynolds Number Aerodynamics of Low-Aspect-Ratio, Thin/Flat/Cambered-Plate Wings," *JOURNAL OF AIRCRAFT*, Vols. 37, NO. 5, pp. 825-832, 2000.

[6] H. O. B. G. a. I. C. Justin Winslow, "Basic Understanding of Airfoil Characteristics at Low Reynolds Numbers," *JOURNAL OF AIRCRAFT*, Vols. 55, NO. 3, pp. 1050-1061, 2018.

[7] A. S. a. A. I. J. Forrester, Aircraft Aerodynamic Design (Geometry and Optimization), John Wiley & Sons, 2015.

[8] W. S. &. A. J. Keane, "A Study of Shape Parameterisation Methods for Airfoil Optimisation," in *American Institute of Aeronautics and Astronautics*, 2004.

[9] H. J. S. L. L. J. Lu Xiaoqiang, "An improved geometric parameter airfoil parameterizationmethod," *Aerospace Science and Technology*, vol. 78, pp. 241-247, 2018.

[10] T. Melin, An Aerodynamic and Geometric Comparison Between Parametrized and Point Cloud Airfoils, Linkoping: Linkoping University, Sweden, 2013.

# Transient Analysis of Lateral-Directional Dynamic Modes of A Jet Aircraft at Different External Store Configurations Using DATCOM

Jalal Uddin Muhammad
Aerospace Dept. College of Aeronautical Engineering
National University of Sciences and Technology
Islamabad, Pakistan
Jalalmuhammad99@gmail.com

Ali Javed
Aerospace Dept. College of Aeronautical Engineering
National University of Sciences and Technology
Islamabad, Pakistan
ali.javed@cae.nust.edu.pk

Nadeem Hussain
Aerospace Dept. College of Aeronautical Engineering
National University of Sciences and Technology
Islamabad, Pakistan
Nadeemhussain65@gmail.com

***Abstract*—This paper focuses on analyzing the effect of external stores on static and dynamic stability of a jet aircraft. The problem is modeled in DATCOM environment which employs empirical relations to calculate stability of newer aircraft by comparing its data with existing aircraft. Test cases are modeled with and without external store configurations. Static and dynamic stability derivatives are calculated using empirical and theoretical relations. Digital DATCOM lacks the ability of modeling twin ventral fins. These were modeled through USAF Stability and Control DATCOM and effect of twin ventral fins on the aircraft stability was also analyzed. The parameters obtained are then used to carry out an in depth stability analysis of the aircraft. Static stability analysis is conducted about the lateral and directional axes. Subsequently, dutch roll, spiral and roll modes are evaluated by solving state space equations of lateral-directional stability derivatives. The solution of these equations gives four Eigen values out of which two correspond to the oscillatory (Dutch Roll) mode and the other two correspond to spiral and roll mode each. Damping ratio, time period and frequency of these modes are then evaluated from their Eigen values. Results show the clean aircraft unstable in Dutch roll behavior whereas stable in Roll and Spiral modes. External stores effect was calculated using the equations present in the printed USAF DATCOM. Nature of stability does not change after application of external stores, however, time period, frequency and damping ratio do change.**

***Keywords—Dynamic Stability; Lateral Stability; Directional Stability; Dutch Roll; jet aircraft.***

## I. INTRODUCTION

An airplane is described differently by the different personnel associated with it. An engineer describes it based on the performance parameters which influence the mission profile. A Pilot on the other hand describes an airplane on its flying qualities which are none other than the stability and control characteristics which determine how easily and safely the aircraft can be maneuvered to complete the mission. To achieve good flying qualities, the aircraft must possess the required amount of stability and control characteristics. It is not desirous to gain the highest value of stability or control characteristics as it makes the pilot unable to perform certain maneuvers. So, when the optimum hallmark is achieved by the designer, flying qualities increase the ability of the pilot to perform a certain mission.

Before moving towards static stability, it is essential to understand the coordinate axis system of an aircraft. Axes system of an aircraft may be taken as per the understanding. Conventionally, the origin is taken at the center of the aircraft. X axis is positive in the direction of the nose and Y axis in the direction of right wing. Obviously then, Z axis takes the positive direction downward. An aircraft has six degrees of freedom, namely:

1. Forward velocity in direction of positive x-axis, u
2. Sideways velocity in direction of positive z-axis, v
3. Downward velocity in direction of positive y-axis, w
4. Rolling moment, p
5. Pitching moment, q
6. Yawing moment, r.

## II. STABILITY

### A. Static Stability

Aircraft is a dynamic system. This means it is moving because of certain forces and moments applied on it. The aircraft is said to be in equilibrium if the net sum of forces and moments cancel each other. An aircraft is said to be statically stable if, by disturbing from equilibrium condition, it has a tendency to return back to the previous (i.e. equilibrium) state. Along the three axis of an aircraft, the static stabilities are defined as:

1. Longitudinal static stability along y-axis(pitch axis)
2. Directional static stability along z-axis(directional axis)
3. Lateral static stability along x-axis(lateral axis)

### B. Dynamic Stability

Dynamic stability of an aircraft may be defined as the tendency to eventually attain the equilibrium condition from which the aircraft was disturbed. The disturbance may be

because of a Pilot's input or any external perturbation. An aircraft has 6 degrees of freedom of motion excited by forces along the three axes and moments about the three axes. Study of dynamic stability includes the change in these forces and moments due to change in angle of attack, side slip angle, linear velocity or angular velocity. Yaw and roll moments of an aircraft are coupled i.e. an excitement of either of the two moments will excite the other simultaneously. Therefore, for simplicity dynamic derivatives are classified into two types, each of them having their specific modes of motion. Important characteristics of these modes are frequency (or time period) and damping ratio. Frequency determines how quick the motion is taking place. It is measured in "cycles per second". Damping ratio determines how quick the motion vanishes. An aircraft with low damping ratio in a mode will be active towards the Pilot's input. On the other hand, an aircraft with higher damping ratio will have a sluggish response towards the Pilot's input. Two classes of dynamic derivatives are:

1. Longitudinal derivatives
2. Directional/lateral derivatives.

5 dynamic modes of an aircraft are classified as follows:

a. Longitudinal modes ( degrees of freedom : u,w,q) :
   1. Phugoid mode
   2. Short period mode

b. Lateral/directional modes ( degrees of freedom : v,p,r) :
   1. Spiral mode
   2. Roll mode
   3. Dutch roll mode

Static and dynamic stabilities determine the response of an aircraft towards any disturbance. A general transport aircraft requires least perturbations from a steady flight for safe flight of passengers. This is why they are designed in the most stable manner. The stable aircraft is resistive to any changes in angle of attack, side slip or bank angle without any input by the pilot. Fighter aircraft generally prefer maneuverability within the flying qualities. For this reason they tend to be lesser stable than transport aircraft, so that the Pilot can perform any required turn with least effort and within least distance covered.

The free response of an airplane towards any external perturbation or pilot's initial input is of two types. If, after an initial disturbance, the control stick is set free, the response is known as stick free response. Control surfaces will continuously be deflecting to align themselves with angle of the incoming air. In the other type of response, known as stick-fixed response, the control surfaces are fixed at 0 degree deflections so that they act like rest of the aircraft body. Forced response of an airplane towards instability modes can also be determined with a little effort after the dynamic derivatives are known. That is a field where designers of auto-pilot control systems are greatly interested. In this paper, only stick fixed response will be studied after the dynamic derivatives are calculated.

## III. Equations of Lateral-Directional modes

Dynamic stability modes are evaluated by starting with rigid body equations of motion. These are nothing but Newton's second law of motion in linear and angular form. Six equations are introduced, each corresponding to motion in each degree of freedom.

$$F_x = \frac{d}{dt}(mu) \qquad F_y = \frac{d}{dt}(mv) \qquad F_z = \frac{d}{dt}(mw)$$

$$L = \frac{d}{dt}(H_x) \qquad M = \frac{d}{dt}(H_y) \qquad N = \frac{d}{dt}(H_z)$$

After reasonable substitutions into the equations, they take the following form:

$$X - mgS_\theta = m(\dot{u} + qw - rv)$$
$$Y + mgC_\theta S_\emptyset = m(\dot{v} + ru - pw)$$
$$Z + mgC_\theta C_\emptyset = m(\dot{w} + pv\text{-qu})$$

$$L = I_x\dot{p} - I_{xz}\dot{r} + qr(I_z - I_y) - I_{xz}pq$$
$$M = I_y\dot{q} + I_{xz}(p^2 - r^2) + qr(I_x - I_z)$$
$$N = -I_{xz}\dot{p} + I_z\dot{r} + pq(I_y - I_x) + I_{xz}qr$$

These six equations are then linearized using small disturbance theory. This theory assumes that the motion of aircraft consists of small changes from steady flight condition. Although this theory yields sufficiently accurate results for many practical engineering purposes, it cannot be applied to motions in which larger amplitude changes are expected like spin or stalled flight. Thus, the equations are now in the below form:

**Longitudinal Equations**

$$(\frac{d}{dt} - X_u)\Delta u - X_w\Delta w + (g\cos\vartheta_0)\Delta\theta = X_{\delta e}\Delta\delta_e + X_{\delta T}\Delta\delta_T$$

$$-Z_u u\Delta u + \left((1 - Z_{\dot{w}})\frac{d}{dt} - Z_w\right)\Delta w - \left((u_0 + Z_q)\frac{d}{dt} - g\sin\theta_0\right)\Delta\theta = Z_{\delta e}\Delta_{\delta e} + Z_{\delta T}\Delta\delta_T$$

$$-M_u\Delta u - \left(M\dot{w}\frac{d}{dt} + M_w\right)\Delta w + \left(\frac{d^2}{dt^2} - M_q\frac{d}{dt}\right)\Delta\theta = M_{\delta e}\Delta\delta_e + M_{\delta T}\Delta\delta_T$$

**Lateral Equations**

$$\left(\frac{d}{dt} - Y_v\right)\Delta v - Y_p\Delta p + (u_0 - Y_r)\Delta r - (gcos\theta_0)\Delta\emptyset = Y_{\delta r}\Delta\delta_r$$

$$-L_v\Delta v + \left(\frac{d}{dt} - L_p\right)\Delta p - \left(\frac{I_{xz}}{I_x}\frac{d}{dt} + L_r\right) \quad \Delta r = L_{\delta a}\Delta\delta_a + L_{\delta r}\Delta\delta_r$$

$$-N_v\Delta v-\left(\frac{I_{xz}}{I_z}\frac{d}{dt}+N_p\right)\Delta p+(\frac{d}{dt}-N_r)\Delta r = N_{\delta a}\Delta\delta_a+N_{\delta r}\Delta\delta_r$$

The above are simple, ordinary linear differential equations with constant coefficients. The coefficients are made up of stability derivatives and mass and inertia characteristics of the aircraft. These equations can be written as first order differential equations. They are called the state space or state variable equations and are represented as:

$$\dot{x}=Ax+B\eta$$

where x is the state space vector, A is the stability derivatives matrix, B is the control derivatives matrix and $\eta$ is the control vector. Following are the representations of both the sets of equations in state variable form:

**Longitudinal Equations of motion in state variable form**

$$\begin{bmatrix}\Delta\dot{u}\\ \Delta\dot{w}\\ \Delta\dot{q}\\ \Delta\dot{\theta}\end{bmatrix}=\begin{bmatrix}X_u & X_w & 0 & -g\\ Z_u & Z_w & u_0 & 0\\ M_u+M_{\dot{w}}Z_u & M_w+M_{\dot{w}}Z_w & M_q+M_{\dot{w}}u_0 & 0\\ 0 & 0 & 1 & 0\end{bmatrix}\begin{bmatrix}\Delta u\\ \Delta w\\ \Delta q\\ \Delta\theta\end{bmatrix}+\begin{bmatrix}X_\delta & X_{\delta T}\\ Z_\delta & Z_{\delta T}\\ M_\delta+M_{\dot{w}}Z_\delta & M_{\delta T}+M_{\dot{w}}Z_{\delta T}\\ 0 & 0\end{bmatrix}\begin{bmatrix}\Delta\delta\\ \Delta\delta_T\end{bmatrix}$$

**Lateral-directional Equations of motion in state variable form**

$$\begin{bmatrix}\Delta\dot{\beta}\\ \Delta\dot{p}\\ \Delta\dot{r}\\ \Delta\dot{\phi}\end{bmatrix}=\begin{bmatrix}\frac{Y_\beta}{u_0} & \frac{Y_p}{u_0} & -(1-\frac{Y_r}{u_0}) & \frac{g\cos\theta_0}{u_0}\\ L_\beta & L_p & L_r & 0\\ N_\beta & N_p & N_r & 0\\ 0 & 1 & 0 & 0\end{bmatrix}\begin{bmatrix}\Delta\beta\\ \Delta p\\ \Delta r\\ \Delta\phi\end{bmatrix}+\begin{bmatrix}0 & \frac{Y_{\delta r}}{u_0}\\ L_{\delta a} & L_{\delta r}\\ N_{\delta a} & N_{\delta r}\\ 0 & 0\end{bmatrix}\begin{bmatrix}\Delta\delta_a\\ \Delta\delta_r\end{bmatrix}$$

The above form was taken by lateral-directional equations after assuming the product of inertia $I_{xz} = 0$. At this point an important step has to be taken. Since, we are concerned with free response of stick-fixed behavior of our aircraft, the control vector and control derivatives matrix need to be ignored. Thus we are left with the following form:

$$\begin{bmatrix}\Delta\dot{\beta}\\ \Delta\dot{p}\\ \Delta\dot{r}\\ \Delta\dot{\phi}\end{bmatrix}=\begin{bmatrix}\frac{Y_\beta}{u_0} & \frac{Y_p}{u_0} & -(1-\frac{Y_r}{u_0}) & \frac{g\cos\theta_0}{u_0}\\ L_\beta & L_p & L_r & 0\\ N_\beta & N_p & N_r & 0\\ 0 & 1 & 0 & 0\end{bmatrix}\begin{bmatrix}\Delta\beta\\ \Delta p\\ \Delta r\\ \Delta\phi\end{bmatrix}$$

$$\dot{x}=Ax$$

Now, the Eigen values can be determined by finding the Eigen values of matrix A. The resultant will yield four roots corresponding to the three modes of motion in lateral-directional form.

These unknowns are enough to evaluate complete lateral dynamic stability modes of an aircraft that include the Dutch Roll mode, the spiral mode and the Roll mode. In other words, after inserting these unknowns in the state space matrix of lateral-directional stability given above, time period (or frequency) and damping constant of all the three modes of lateral dynamic instabilities can be calculated.

## IV. METHODOLOGY

DATCOM is a huge data compendium of stability parameters of different aircraft that have been compiled over the years to calculate stability of newer aircraft by comparing its data with existing aircraft. Aircraft geometric data has to be entered first in the DATCOM input file. The most convenient way to extract geometric data of an aircraft is from its 3D CAD model. CATIA model of the aircraft was digitized to extract geometric data which was fed into the DATCOM+ input interface. The output included a clean geometric model of the aircraft and both dynamic as well as static stability curves. A few aerodynamic and static stability derivatives were benchmarked with wind tunnel data of the aircraft for validation. The dynamic stability derivatives were input to the linearized state space matrix of lateral-directional stability as mentioned above. The solution gave the respective Eigen values of all the three modes of lateral-directional stability. Application of external store is not possible in the DATCOM program. Therefore, the USAF Stability and Control DATCOM was consulted which includes a large scope of external store effects by solving thorough equations requiring data of the stores. These equations provide the increment in dynamic derivatives due to application of an external store. These increments were added to the original dynamic derivatives to compute dynamic derivatives of the new configuration. Eigen values were then calculated. Perimeters of dynamic behavior such as frequency, damping ratio etc. were then derived from the Eigen values of both configurations for analysis.

### *A. DATCOM*

DATCOM is commonly used to refer to the Digital Datcom program. Actually, it is the paper version of United States Air Force Data Compendium comprising of 3000+ pages. The fundamental purpose of the USAF Stability and Control DATCOM is to provide a systematic summary of methods for

estimating stability and control characteristics of a given aircraft configuration at given flight conditions. Since, acquiring each derivative separately from the book for an aircraft was a tedious task, a program was written to do this task digitally. Consequently, days of extra effort was reduced to hours. This program is explained in the next paragraph.

The Digital Datcom program, written by engineers at Wright-Patterson Air Force Base, started in the late 1960's, and improved upon up through the mid 1990's. The development of the Digital Datcom computer program is an approach to provide rapid and economical estimation of aerodynamic stability and control characteristics. In preliminary design phase, rapid computation of stability and control derivatives for different configurations is desirous. This was the primary reason DIGDAT was introduced.
User interface of DIGDAT is highly unfavourable. The program requires aircraft configuration in the form of a code which is highly syntax-oriented. A number of name lists are included for each type of input. For example wing and horizontal tail planforms are input using the WGPLNF and HTPLNF namelists. These namelists include all the input data required for the complete description of the wing or horizontal tail. Below is an example of a wing planform namelist. The $ sign indicates the start and end of a namelist. Figure IV-a is a snapshot of wing planform input through the WGPLNF namelist. Table IV-a is a list of the namelists available in DATCOM.

```
$WGPLNF CHRDTP=2.91, SSPNOP=8.69, SSPNE=11.13, SSPN=13.94
CHRDBP=11.45,CHRDR=26.145, SAVSI=70.183, SAVSO=43.446,
        CHSTAT=0.0, SWAFP=0.0, TWISTA=0.0, SSPNDD=0.0,
        DHDADI=0.0, TYPE=2.0$
```

Figure IV-a: Sample namelist from DATCOM describing wing planform

Table IV-a: Namelists included in Digital DATCOM

| | |
|---|---|
| BODY | Fuselage coordinates at 20 stations |
| FLTCON | Flight Conditions |
| SYNTHS | Aircraft configuration |
| OPTINS | Options |
| WGSCHR | Wing airfoil |
| HTSCHR | Horizontal tail airfoil |
| VTSCHR | Vertical tail airfoil |
| VFSCHR | Dorsal fin airfoil |
| WGPLNF | Wing planform |
| HTPLNF | Horizontal tail Planform |
| VFPLNF | Dorsal fin Planform |
| VTPLNF | Vertical tail planform |
| EXPR | Experimental(Wind tunnel) data input |
| SYMFLP | Symmetrical flap (control surface) input |
| ASYFLP | Asymmetrical flap (aileron) input |
| CONTAB | Trim tabs |
| PROPWR | Propeller engine input |
| JETPWR | Jet engine input |
| TVTPAN | Twin vertical tail input |

Once, the complete aircraft is synthesized in the input file and run in the program, an output file is generated in the same folder. This output file contains all the data. This file is in notepad form which must be imported to MATLAB to convert its data into readable format. Two programs have been written in MATLAB in order to extract data from the DATCOM format. The "DrawDatcomAircraft.m" displays three views of the aircraft and the airfoils. The "Datcomimport.m" displays all the stability and control derivatives which can then be plotted in MATLAB.

This is an updated DIGDAT program, scripts, and associated programs, bundled together in a convenient package. This program has a better user interface than the previous version. The origins of this package were started in 1996. Moreover, the coding has been made easy by addition of comments lines. Therefore, an input file of the DIGDAT runs over DATCOM+ but the vice versa is not always possible. The Datcom+ package has been used worldwide by thousands of students and aerospace professionals, and has helped in many research and thesis papers over the years. Datcom+ was the predecessor to the Datcom+ Pro package. The Datcom+ package is no longer updated to correct any errors. Difference between the DATCOM+ and the DIGDAT user interface will be made clear later in the report.

In late 2010, a professional edition was created, which added features to the basic DIGDAT program, compiled the tools better, and included better user to program interaction, to allow a student and professional both to use the tools quickly, rather than the previous slow learning process. A number of additions have been added to this program in order to improve the visualization and execution of the code. The code includes additional namelists that embodies the features of the newer generations of aircraft. Moreover, there are also changes in the interface.

## V. Geometric Modelling

DATCOM program has plenty of namelists, as mentioned above, to model different components of the aircraft. Namelists usage depends upon the user's requirement. There are always numerous ways to input your aircraft. Remember that the requirement of this paper was to study stick fixed stability. Therefore we do not need to model control surfaces separately. The control surfaces are modeled rigid like rest of the aircraft with no hinge.

### *A. Wing Modelling*

Wing modeling starts with specification of location of leading edge root chord in x and z directions. Then incidence angle is given. This data is given in the SYNTHS namelist and a consistent axis is chosen which is to be used throughout the modeling process. Wing airfoil is input in the WGSCHR namelist. DATCOM has this limitation of modeling of a single airfoil throughout the wing i.e. aerodynamic twist cannot be introduced but since the existing aircraft does not have any aerodynamic twist so this problem did not arise. Airfoil was extracted from CATIA model by defining the spline at 43 different locations (50 locations is the limit in

DATCOM). X and Y coordinates of 43 locations were entered in the WGSCHR namelist. Following are the snapshots of the actual airfoil extracted from the 3d model and the one generated by DATCOM+ Pro after entering the coordinates. Figures V-a to V-h show a comparison of the actual airfoil and the DATCOM+ generated.

One limitation of the DATCOM program is that wing strake cannot be modeled separately. This problem was overcome as described in the next section. Rest of the inputs were defined in the WGPLNF namelist. These included the tip chord, semi span of outboard panel, semi span of exposed panel, semi span, chord at break point, root chord, sweep of inboard panel, sweep of outboard panel, dihedral angle and twist angle. These parameters were easily picked up from CATIA model of the jet aircraft using the constraint and measure functions.

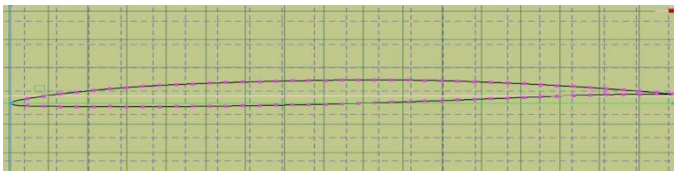

Figure V-a: Wing airfoil extracted from CATIA model

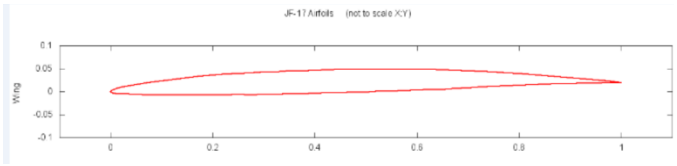


Figure V-b: Wing airfoil output from DATCOM

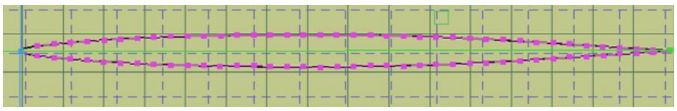

Figure V-c: Horizontal tail airfoil extracted from CATIA model

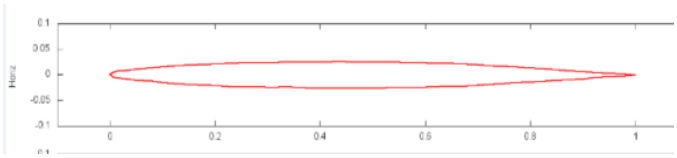


Figure V-d: Horizontal tail airfoil output from DATCOM

### B. *Horizontal Tail Modelling*

Horizontal tail definition is similar to wing definition. Specification of location of leading edge root chord in x and z directions and incidence angle is done in the SYNTHS namelist. Airfoil was extracted from CATIA model by defining the spline at 42 different locations (50 locations is the limit in DATCOM). X and Y coordinates of 42 locations were entered in the HTSCHR namelist.

Rest of the inputs were the same as WGPLNF entered in the HTPLNF namelist.

### C. *Vertical Tail Modelling*

Vertical tail is defined in the same way as wing and horizontal tail. Specification of location of leading edge root chord in x and z directions is done in the SYNTHS namelist. Airfoil was extracted from CATIA model by defining the spline at 41 different locations (50 locations is the limit in DATCOM). X and Y coordinates of 41 locations were entered in the VTSCHR namelist.

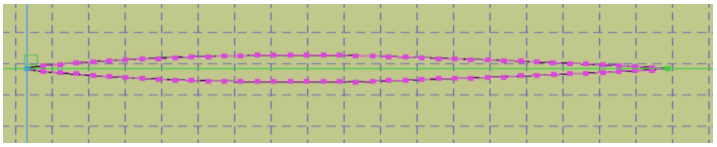

Figure V-e: Vertical tail airfoil extracted from CATIA model

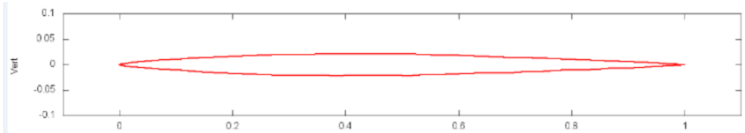


Figure V-f: Vertical tail airfoil output from DATCOM

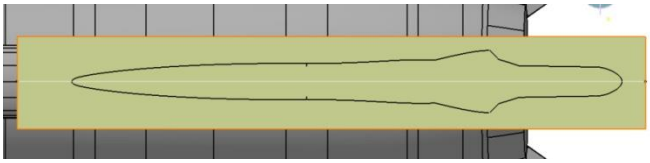

Figure V-g: Dorsal fin airfoil extracted from CATIA model

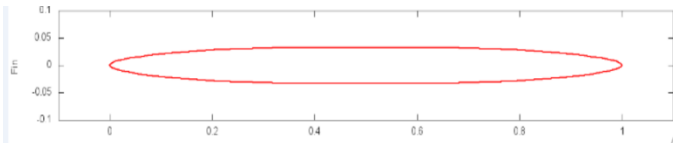


Figure V-h: Dorsal fin airfoil output from DATCOM

Rest of the inputs were the same as WGPLNF entered in the VTPLNF namelist.

### D. *Dorsal Fin Modelling*

Dorsal fin is defined in the same way as wing, vertical tail and horizontal tail. Specification of location of leading edge root chord in x and z directions is done in the SYNTHS namelist. Airfoil was extracted from CATIA model by defining the spline at 26 different locations (50 locations is the limit in DATCOM). X and Y coordinates of 26 locations were entered in the VTSCHR namelist.

Rest of the inputs were the same as WGPLNF entered in the VFPLNF namelist.

### *E. Fuselage Modeling*

Fuselage entering was a tedious and time-consuming task. 20 sections along the fuselage center-line were taken at appropriate distances (where maximum change occurs). 5 required inputs were entered at each cross-section. These inputs were perimeter and surface area of the cross section, upper and lower surface coordinate along x-axis of the cross section and widest coordinate (radius) of the cross section along y-axis. Perimeter and surface area data were collected by slicing the CAD model of the aircraft using CATIA. Coordinates of the required data were taken after digitizing the aircraft using image Digitizer. Figures V-i and V-j will elaborate the work done.

### *F. Aircraft characteristics:*

Although there are computational methods available to compute values of these parameters but, generally, these methods use approximation. That is why this data was acquired from the concerned aircraft manual. This data is reliable because the aircraft manual contains data entered by the designers. Following is the list of data that was acquired:

- Location of moment reference along x axis (xcg)
- Location of moment reference along y axis (ycg)
- Location of moment reference along z axis (zcg)
- Weight of the aircraft

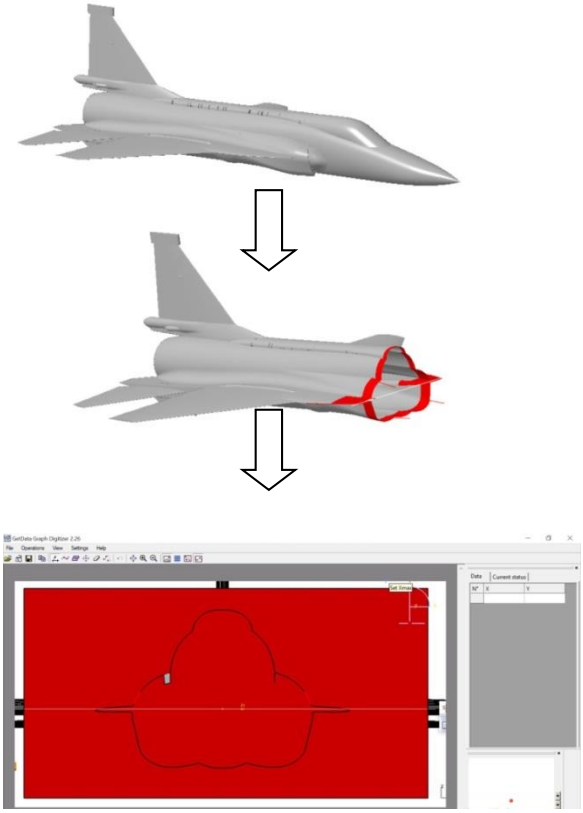

Figure V-i: Process of extracting cross section perimeter and surface area from CATIA model

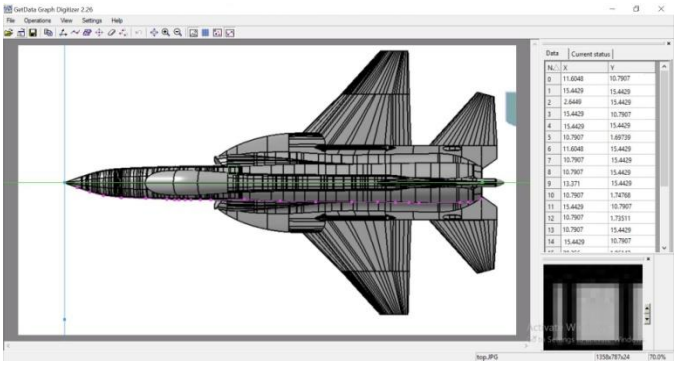

Figure V-j: Extraction of coordinates from digitized model of jet aircraft

## VI. CHALLENGES IN MODELLING

There is no specified option in DATCOM+ that models a wing strake. This problem has been addressed by THE USAF STABILITY AND CONTROL DATCOM Volume I, User's Manual by McDonnell Douglas Astronautics Company St. Louis Division St Louis, Missouri 6316. The alternative suggested in this reference was that wing strake can be modeled along with wing planform as double delta planform. This idea is also used by Bilal Siddique[20]. Table VI-a is a comparison of the jet aircraft wing along with the wing strake versus the approximated double delta wing.

Ventral fin input is not present in DATCOM program, although it is present in USAF Stability and Control DATCOM. May be, the next versions of DATCOM program

include ventral fin through any namelist. The jet aircraft has twin ventral fins. Due to the limitations of DATCOM, these ventral fins could not be modeled. This problem was solved by using the equations present in USAF Stability and Control DATCOM

Modeling of external bodies (except external engines) like fuel tanks, missiles and bomb kits is a limitation of DATCOM+. In this research, the problem was solved using the equations given in USAF Stability and Control DATCOM.

Table VI-a: Comparison of equivalent double delta planform with actual wing.

| **Parameters** | **Difference with actual wing parameter** |
|---|---|
| $S_{ref}$ | -4.77 $ft^2$ |
| Root chord | 1.18 ft |
| Tip chord | 0 ft |
| Outboard angle | $0^0$ |
| Inboard angle | $0^0$ |
| Span | 0.42 ft |
| Mean Aerodynamic Chord | 0.22 ft |
| Aerodynamic centre | 0.0 ft |

## VII. OUTPUT

### *A. The resulting model*

Figures VII-a to VII-d show different views of the aircraft model generated by DATCOM+

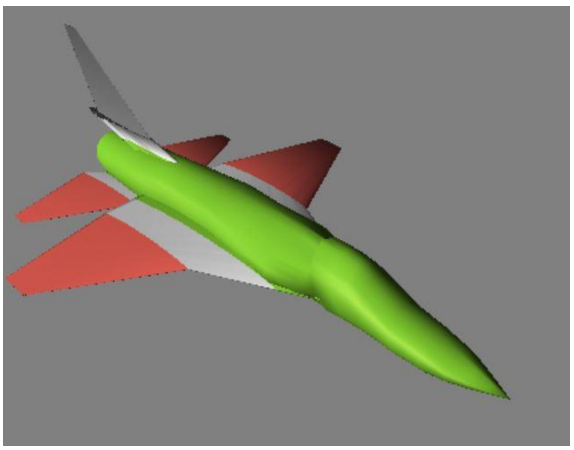

Figure VII-a: Isometric view of DATCOM+ jet aircraft

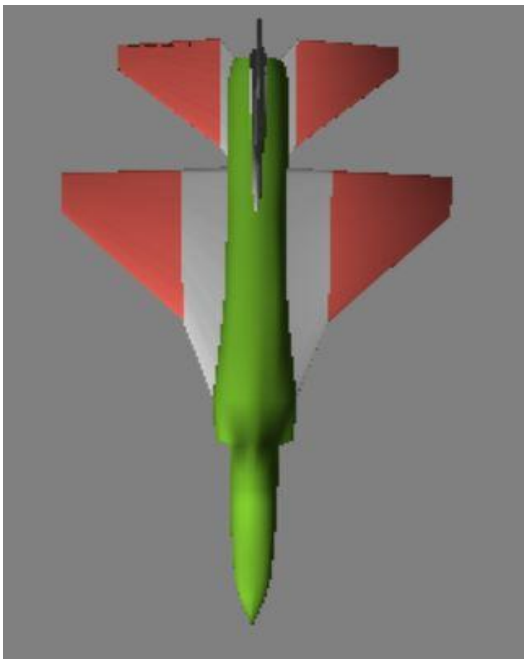

Figure VII-b: Top view of DATCOM+ jet aircraft

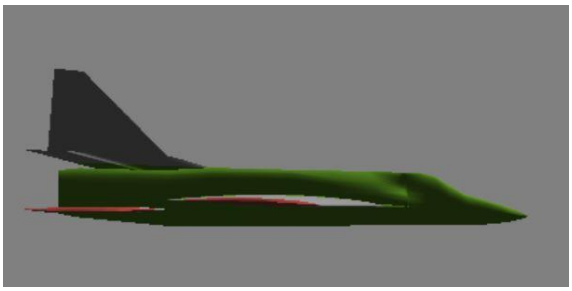

Figure VII-c: Side view of DATCOM+ jet aircraft

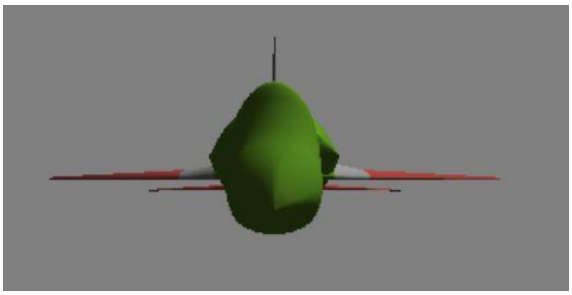

Figure VII-d: Front view of DATCOM+ jet aircraft

### *B. Stability derivatives*

The program generates a curve for each stability (dynamic and static) derivative. Flight conditions of cruise for the aircraft were used. Figures VII-e to VII-h are four of slopes of the derivatives required to calculate complete lateral stability of an aircraft. Cyr is not readily given as output like rest of the derivatives. The reason is that in USAFSCD no method exists to calculate value of Cyr in wing-body combination. This may be input by calculating it experimentally or using approximation. Method for calculation of Cyr due to wing-body-tail combination does

exist. This method comprises of an equation that includes the term wing-body derivative but as mentioned in USAFSCD that the wing-body derivative is negligible as compared to the wing-body-tail derivative, thus the value of Cyr was calculated.

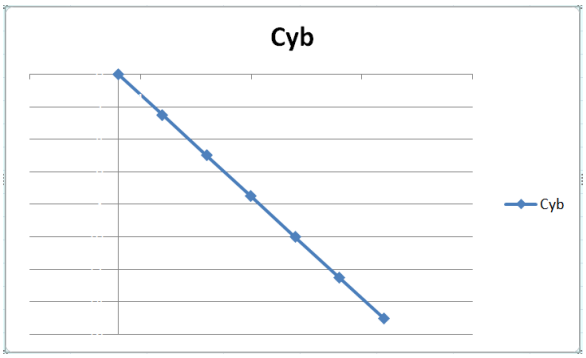


Figure VII-e: Change in side force with sideslip

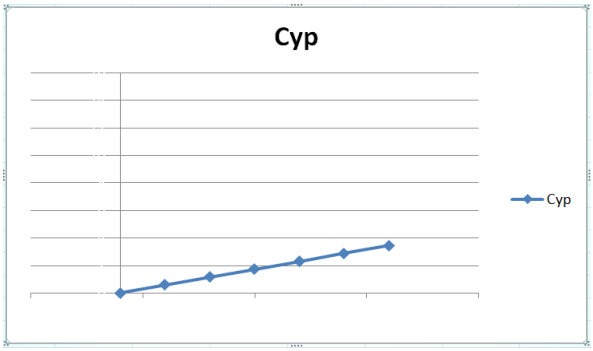


Figure VII-f: Change in side force with roll rate

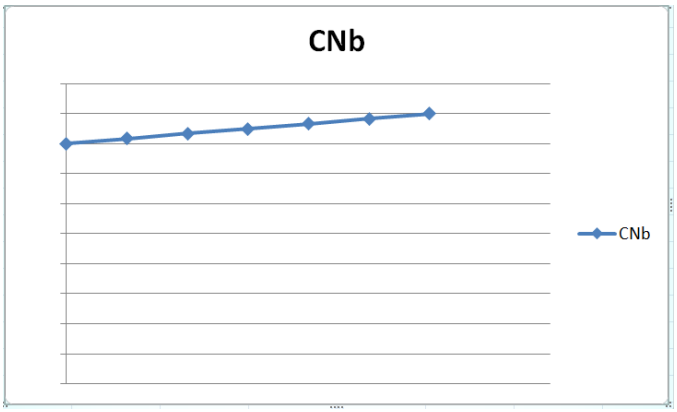


Figure VII-g: Change in Yawing moment with sideslip

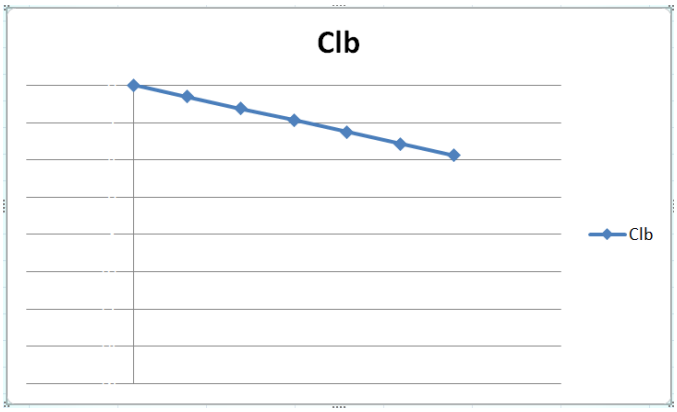


Figure VII-h: Change in roll rate with side slip

*C. Validation*

DATCOM has been proved to be a reliable source of aerodynamic and stability parameters prediction through the years. Although, termed as the predictor for the preliminary phase of design, DATCOM results have shown close agreement with the final design of the aircraft too. A number of papers are present that show the validity of this software by comparing the results with other methods. A few aerodynamic parameters were compared to the wind tunnel data of the aircraft which showed satisfactory agreement with error not greater than 8% in any of them. Results are generated upto angle of attack of 12 degrees as DATCOM error increases at higher angles of attack. Figures VII-i to VII-k is a comparison of DATCOM+ result with wind tunnel data.

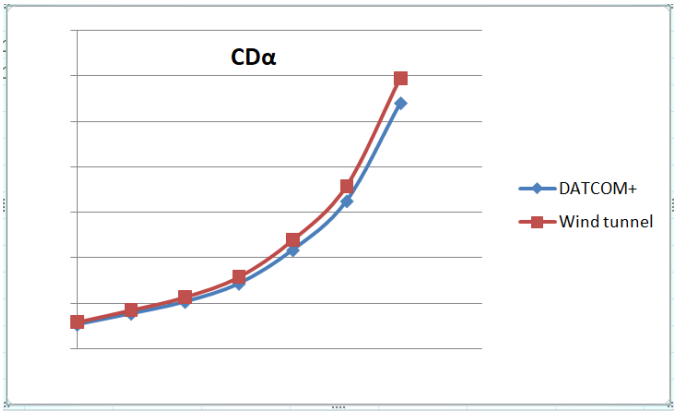


Figure VII-i: Comparison of Drag coefficient vs angle of attack

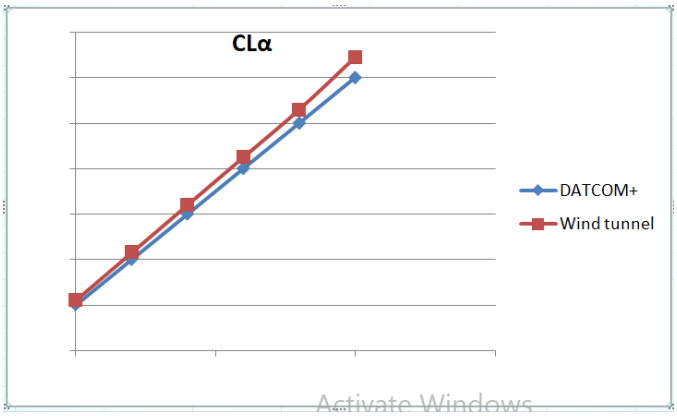


Figure VII-j: Comparison of lift coefficient vs. angle of attack

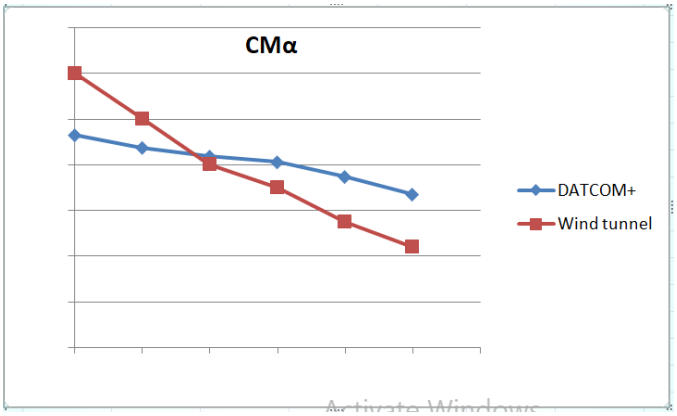


Figure VII-k: Comparison of coefficient of pitching moment with angle of attack

### *D. Limitations*

USAF Stability and Control DATCOM has been written for almost all types of aircraft configurations. DATCOM+ program which is based on the equations inside the USAF Stability and Control DATCOM does not include all the features of it (for example twin ventral fins or external stores etc.). The reason may be because most of the aircraft fall in the simple configuration domain which does not require these complex equations to be included in the program. The jet aircraft has twin ventral fins that could not be included in the input file. For this reason, the effect of twin ventral fins was calculated from the original source and added in the existing derivatives. The dynamic derivatives were corrected in the similar way. The determination of change in side force due to change in sideslip is a tedious task. Once it is calculated, rest of the parameters use the same value in some form or the other. Table VII-a pertains to the changes in derivatives after ventral fin is installed on the aircraft.

### *E. Calculations*

Moments of inertia around all the three axes of the aircraft were acquired from the concerned aircraft manual. At this stage, all the inputs of dynamic modes were done with. These values were inserted in lateral directional equations of motion in state variable form and the Eigen values were generated. From these Eigen values, time period, frequency, damping ratio, time to half the amplitude etc. can be readily calculated. MATLAB script is a good idea to calculate Eigen values as the program has to be used again for different configurations. Figure VII-i is a plot of the Eigen values generated for the clean jet aircraft.

Table VII-a: Comparison of values with and without twin ventral fins

| | **Change due to twin ventral fins (per radian)** |
|---|---|
| **Cyb** | -0.01144 |
| **Cyp** | Negligible change |
| **Cyr** | 0.009306 |
| **Clb** | 0.0008961 |
| **Clp** | Negligible change |
| **Clr** | -0.0002761 |
| **Cnb** | 0.004653 |
| **Cnp** | Negligible change |
| **Cnr** | -0.003784 |

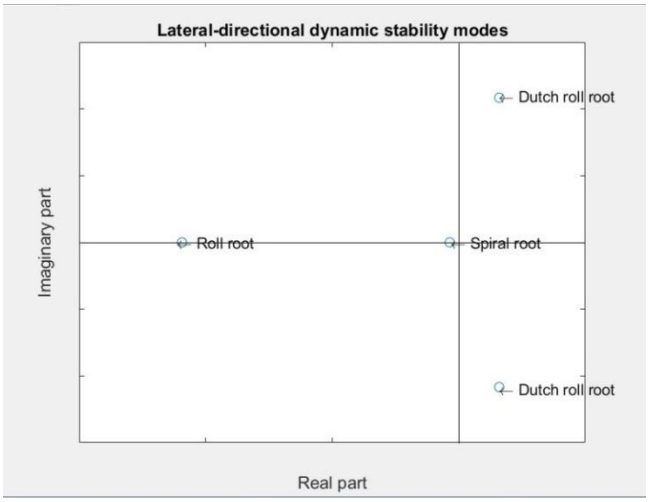


Figure VII-l: Eigen values of the jet aircraft plotted on a complex plane

Eigen value = $\eta + \omega\iota$

- Damped frequency = $\omega$
- $\theta = \tan^{-1}\frac{\omega}{\eta}$
- Damping ratio = $\xi = cos\,\vartheta$
- Natural frequency = $\frac{\omega}{\sqrt{1-\xi^2}}$
- Time period required to double or halve amplitude = $\frac{0.69}{|\eta|}$
- Period = $\frac{2\pi}{\omega}$
- Number of cycles required to halve amplitude = $0.110\frac{\omega}{|\eta|}$

Observations: Results generated show the aircraft stable in roll mode and spiral mode and unstable in Dutch roll mode.

## VIII. Application of Supersonic Fuel Tank at Centreline

The above calculations are concerned with clean configuration of the aircraft. Section 3 of USAF Stability and Control DATCOM[21] named "Effect of external stores" is completely concerned with missile combinations, bomb kit or fuel tank stores. Concerning data regarding fuel tank was taken from the aircraft manual Equations in this section require $CD_0$ of the tank in uninstalled configuration. This could have been done by wind tunnel testing or CFD. In this case DATCOM+ was used to model and analyze the tank parameters as shown in figure VIII-b. Table VIII-a is a list from USAF stability and control DATCOM that shows the possibilities of external store configurations DATCOM can handle. The current configuration is fuselage pylon mounted single store with single carriage mode as shown in figure VIII-a.

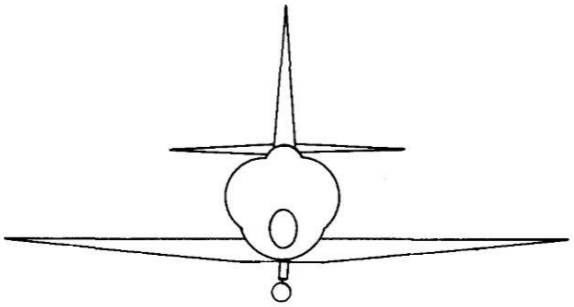

Figure VIII-a: Configuration of fuselage pylon mounted single store

### *A. DATCOM Model of Indigenous Supersonic fuel tank*

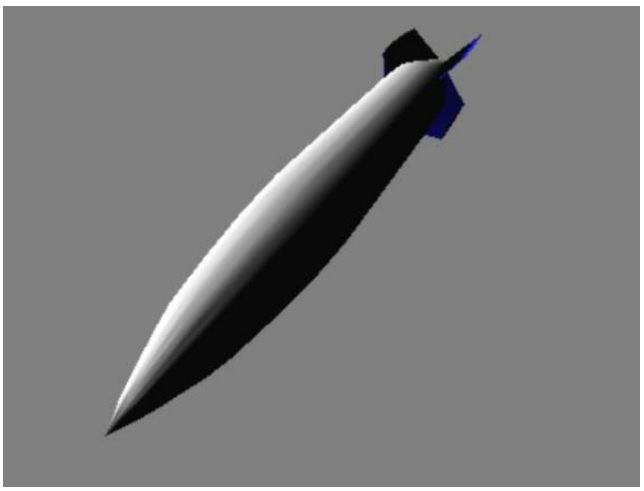

Figure VIII-b: Isometric view of DATCOM+ generated supersonic tank model

Table VIII-a: Aircraft characteristics change with fuel tank

| | **Increment after applying fuel tank at fuselage centre line (per radian)** |
|---|---|
| **X c.g** | 3.291 cm |
| **Y c.g** | 0.0 cm |
| **Z c.g** | -10.414 cm |
| **Ixx** | 793 kg $m^2$ |
| **Iyy** | 1496 kg $m^2$ |
| **Izz** | 111 kg $m^2$ |

Table VIII-b: Limitations of external store configuration and Mach number in USAF stability and Control DATCOM

| Mounting location | Carriage mode | Mount/Loading type | Mach number range |
|---|---|---|---|
| Wing | Single | Pylon-Empty | 0.6-2.0 |
| | | Pylon- Single store | |
| | Multiple | Pylon-Empty MER | 0.6-1.6 |
| | | Pylon-Fully loaded MER | |
| | | Pylon-Partially loaded MER | |
| | | Pylon-Empty TER | |
| | | Pylon-Fully loaded TER | |
| | | Pylon-Partially loaded TER | |
| Fuselage | Single | Tangent-One store | 0.6-1.6 |
| | | Tangent-Two or more stores | 0.6-0.9 |
| | | Pylon-Empty | 0.6-2.0 |
| | | Pylon-One Store | 0.6-1.6 |
| | | Pylon-Two or more Stores | 0.6-0.9 |
| | Multiple | Tangent-Two or more Stores | 0.6-1.6 |
| | | Pylon-One Store installation | |
| Wing or fuselage | | Adjacent Store Installation | 0.6-1.2 |
| | | Additional drag due to lift | 0.6-1.6 |

**Calculations**

New values of moment reference point and moment of inertias were calculated analytically as location and mass of tank were known. The values are given in table VIII-b. Stability derivatives were given by DATCOM+ shown in table VIII-c

Table VIII-c: Stability derivatives comparison after applying fuel tank

| | **Increment after applying fuel tank at fuselage centre line (per radian)** |
|---|---|
| **$CD_0$** | 0.003057 |
| **Cla** | -0.001657 |
| **Cyb** | -0.007705 |
| **Cnb** | -0.01896 |
| **Clb** | -0.0128 |
| **Clp** | - 0.0002 |
| **Cyp** | -0.0019 |
| **Cnp** | 0.00102 |
| **Cnr** | 0.0023 |
| **Clr** | 0.0069 |

**Results and comparison**

Parameters due to installation of Indigenous Supersonic Tank were modified in the existing program and results were generated for dynamic derivatives and Eigen values. Table VIII-d is a comparison of dynamic parameters with and without supersonic tank.

Table VIII-d: Change in Aircraft lateral-directional stability modes after applying fuel tank at centreline

| | **Increment** |
|---|---|
| **Natural frequency of Dutch Roll** | -0.1571 $s^{-1}$ |
| **Damped frequency of Dutch Roll** | -0.0737 $s^{-1}$ |
| **Damping ratio of Dutch Roll** | 0.0105 |
| **Time period to double amplitude of Dutch Roll** | -0.3674s |
| **Period of Dutch Roll** | 0.0992s |
| **Number of cycles to half amplitude of Dutch Roll** | 0.001 |
| **Time period to half amplitude of Roll mode** | 0.002 s |
| **Time period to half amplitude of spiral mode** | -1.436 s |

## IX. Application of Supersonic Fuel Tanks under both the Wing Planforms

Fuel tank used for this analysis was the same. Pylon location at the wing was mentioned in the aircraft manual. Configuration was wing pylon mounted single store with single carriage mode as shown in figure IX-a. Required inputs were entered in concerning equations of Section 3 of USAF Stability and Control DATCOM. It gives increment in Cyb, Cnb, $C_L$ and $C_{D,}$ due to external stores, readily. To calculate rest of the derivatives, the EXPR namelist of DATCOM was used to enter the new value of $C_{L\alpha}$ and new location of centre of gravity. The changes in stability derivatives are shown in table IX-b. Changes in aircraft characteristics are shown in table IX-a while changes in dynamic parameters are shown in table IX-c. Figure IX-b shows the shift in Eigen values due to installation of wing pylon mounted fuel tanks.

**Calculations**

Table IX-a: Aircaft characteristics change with wing fuel tanks

| | **Increment after applying fuel tanks under wing planform (per radian)** |
|---|---|
| **X c.g** | 7.437 cm |
| **Y c.g** | 0.0 cm |
| **Z c.g** | -23.78 cm |
| **Ixx** | 6384 kg $m^2$ |
| **Iyy** | 3301 kg $m^2$ |
| **Izz** | 42228 kg $m^2$ |

Table IX-b: Stability derivatives comparison after applying wing fuel tanks

| | **Increment after applying fuel tank at fuselage centre line (per radian)** |
|---|---|
| **Cyb** | -0.004246 |
| **Cnb** | -0.0106 |
| **Clb** | -0.0283 |
| **Clp** | - 0.0003 |
| **Cyp** | -0.0042 |
| **Cnp** | 0.0027 |
| **Cnr** | 0.0055 |
| **Clr** | 0.0098 |

Table IX-c: Change in Aircraft lateral-directional stability modes after applying wing fuel tanks

| | **Increment** |
|---|---|
| **Natural frequency of Dutch Roll** | -0.1919 $s^{-1}$ |
| **Damped frequency of Dutch Roll** | -0.0861 $s^{-1}$ |
| **Damping ratio of Dutch Roll** | 0.0155 |
| **Time period to double amplitude of Dutch Roll** | -1.9139s |

| | |
|---|---|
| **Period of Dutch Roll** | 0.116s |
| **Number of cycles to half amplitude of Dutch Roll** | 0.0028 |
| **Time period to half amplitude of Roll mode** | 0.1963 s |
| **Time period to half amplitude of spiral mode** | -0.369 s |

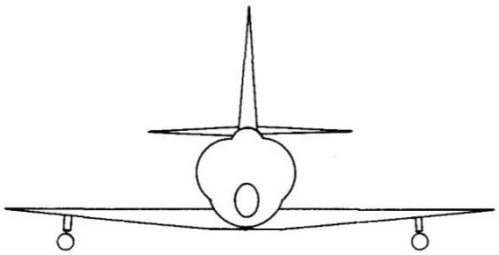

Figure IX-a: Configuration of wing pylon mounted single store

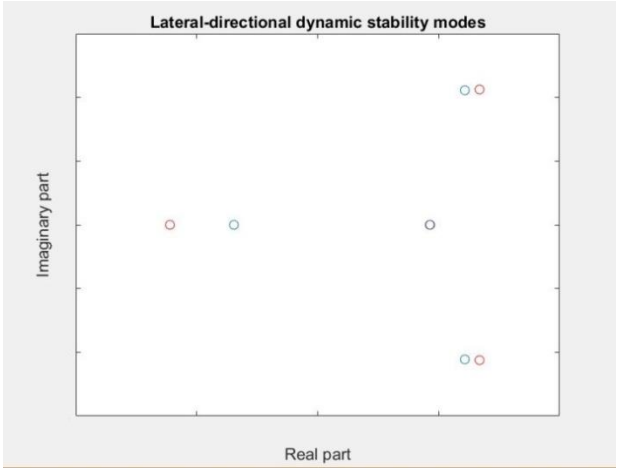


Figure IX-b: Shift in Eigen values after installation of wing fuel tanks. The blue circle indicates the later configuration.

## X. CONCLUSION

Though parameters of dynamic stability change with installation of fuel tanks, nature of stability remains the same whether or not the tanks are installed in any configuration. Effect of twin ventral fins on stability of the jet aircraft in subsonic speed is shown to be under 5%. Ventral fins, therefore, do not play an important role in stability of an aircraft at subsonic speeds. Dutch roll has been shown to be unstable by a very small margin whereas roll and spiral modes are stable in stick fixed condition After application of a single fuel tank at the centerline, the nature of Dutch Roll stability remains the same with a slight change in frequency and damping ratio. The frequency decreases because of increase in moment of inertia $I_{zz}$ of the aircraft due to addition of weight of the tank. The aircraft, now, has a sluggish behavior to disturbances. The increased wet area of the new configuration allows the damping ratio to increase. Increase in damping ratio may also be attributed to the decrease in $Cn_{\beta}$ and increase in $Cn_r$. The decrease in yawing moment with sideslip will reduce the yaw that was earlier generated, thus, reducing the damping factor as well. $Cn_r$, here, acts as a yaw rate damper. Increasing the yaw rate damping is analogous to increasing damping in a spring mass damper system. Another effect seen was the extension of time to damp the roll mode. This was mainly due to the increase in moment of inertia $I_{xx}$ around the lateral axis which is in agreement with law of conservation of angular momentum. The same effect was seen at larger amplitude when the side tanks were deployed. This calls for automation of the control surfaces of the jet aircraft that increases the damping ratio of the Dutch roll. Obviously, that will have an effect on the other two modes as well. So new Eigen values will be generated after the system is installed, now with the control vector accounted.

## REFERENCES

[1] Stefan Goetz and David R. McDaniel, United States Air Force Academy, "Towards an Efficient Aircraft Stability and Control Analysis Capability using High-Fidelity CFD", 2007.

[2] R. D. Kimberlin, "*Flight Testing of Fixed-Wing Aircraft*," AIAA Educational Series, 2003

[3] Lawrence L. Green, Angela M. Spence, "Computational methods for dynamic stability and control derivatives", 2004.

[4] Green, Lawrence L., and Spence, Applications of Computational Methods for Dynamic Stability and Control Derivatives", 2004.

[5] Tom Wagner and John Valasek, "Comparison of Computational Methods for Stability and Control Analysis" , 2004

[6] Tom Wagner and John Valasek, "Comparison of Computational Methods for Stability and Control Analysis", 2004

[7] J. Jensin Joshua, P. Azhaguraja, P. Banumathi, P. Abirami, "Lateral and Longitudinal Stability Analysis of UAV Using XFLR5", 2014

[8] Dr. Robert C Nelson, "Flight stability and Automatic Control", 1989

[9] XFLR5 and Stability Analysis, 2010

[10] V., Murphy, P. C., Curry, T. J., and Brandon, J. M., NASA/TM-97-206276, "Analysis of Wind Tunnel Longitudinal Static and Oscillatory Data of the F16XL Aircraft Klein"

[11] D. Raymer, "Aircraft Design – A conceptual approach", 1992

[12] Simon, J. M., AIAA paper "Dynamic Derivative Data for High - Angle-of-Attack Simulation", Aug. 1992.

[13] Sangho Kim, "Stability Analysis of Full Geometry Aircraft through CFD and Response Surface Method"

[14] M. Sareez, M. G. Goman and N. Abramov, "Impact of Ground Effect on Airplane Lateral Directional Stability during Take-Off and Landing," in Scientific Research Publishing Inc. , Leicester, UK, 2018.

[15] UgurOzdemir., et al, "Calculation of the Longitudinal Stability Derivatives of a Transport Aircraft and Analysis of Longitudinal Modes", Proceedings of the 9th WSEAS International Conference, Istanbul,Turkey, May,2007.

[16] Yechout, T.R., Morris S.L., Bossert D.E. and Hallgreen W.F., "Introduction to aircraft flight mechanics: performance, static stability, dynamic stability, and classic feedback control", AIAA, 2003.

[17] Alan Pope, "Low-speed Wind Tunnel Testing",1966

[18] Edward C.Polhamus and Joseph M. Hallisy "Effect of Airplane configuration on static stability at subsonic and transonic speeds", 1958

[19] Jesse L. Mitchell, "The static and dynamic longitudinal stability characteristics of some supersonic aircraft configurations"

[20] Bilal Siddique, Atif Khushnood, "Improving USAF DATCOM Predictions of Aircraft Nonlinear Aerodynamics**",** May 2009

[21] McDonnell Douglas Corporation, "USAF Stability and Control DATCOM', April 1978.

[22] William B Blake, "Prediction of Fighter Aircraft Dynamic Derivatives Using Digital Datcom", 1985

[23] Ansar Rauf , Muhammad Aamir Zafar , Aerodynamic modeling and state-space model extraction of a UAV using DATCOM and Simulink, March 2011.

[24] Aamir Naveed, Ali Javed, “Effects of variation in flow field on store separation”, 2018

# Mobile Software Platform for Aircraft Maintenance Engineering Industry

Muhammad Shahrukh Khan
*Institute of Aviation Studies*
*University of Management and Technology*
Lahore, Pakistan
ameshahrukh.khan97@gmail.com

Muhammad Mehmood Ashraf
*Institute of Aviation Studies*
*University of Management and Technology*
Lahore, Pakistan
mehmoodashraf15@gmail.com

Lazib Jamil
*Institute of Aviation Studies*
*University of Management and Technology*
Lahore, Pakistan
lazib.jamil@gmail.com

Ahmad Aizaz
*Institute of Aviation Studies*
*University of Management and Technology*
*Lahore, Pakistan*
ahmad.aizaz@umt.edu.pk

Arslan Asim
*Institute of Aviation Studies*
*University of Management and Technology*
Lahore, Pakistan
arslan.asim@umt.edu.pk

***Abstract*—Aircraft maintenance engineers constitute a very valuable part of the aviation safety and security. No major aircraft operator can function properly without having a strong aircraft maintenance engineering setup. Most of the aircraft maintenance industries are following the conventional paper-based system, which requires a lot of shelf space, consumes more time and is not eco-friendly. E-Maintenance is a new concept being developed and utilized by very few organizations worldwide. The paper includes a discussion on the various traditional as well as latest methods being used by the contemporary aircraft maintenance industries. The pros and cons of the various methods will also be brought to light. Ideas similar to the one under progress include 'One Powerful Solution' developed by the Boeing Company, 'Maintenance Mobility' launched by the Airbus and Honeywell's Go-Direct solution. The purpose of this paper is to discuss the prospects of replacing the paper-based maintenance activity by a more systematic electronic maintenance management system, whilst proposing a specimen software application using the Android operating system. For this purpose, a survey was conducted among the senior engineering management of the flying clubs at the Walton Airport in Lahore, Pakistan. Their opinions, recommendations and reservations were documented with the intention to develop the application in conformity with their suggestions. The idea was greeted with a lot of alacrity from the professionals. In this paper, the data collected through the survey will also be presented in a succinct form with the objective of highlighting the dire need for the proposed solution in the paper. This paper will also present a prototype of the application. For the application development, Android Studio is being used which implies that the final product will be readily available for use on most Android based devices. Also, the Android operating system is fundamentally an open source operating system which tremendously improves the chances of providing a widespread solution to the paper based system. For the development of the graphical user interface, the Adobe Photoshop CC 2014 was used and a rudimentary design was prepared to be implemented on the Android Studio.***

***Keywords— Android Operating System, E-Maintenance, Aircraft Maintenance Engineering.***

## I. INTRODUCTION

With the growing number of people who travel through aircraft, the number of aircraft is also expected to increase in a decade or two. The increasing number of aircraft and the ageing fleet and keeping up with the work pressure demands timely and correct maintenance so that the operator's operations can run smoothly. The projected forecast shows that MROs are expected to increase by 3.4% worldwide annually to meet the needs of the aircraft operators. The number of aircraft is expected to increase 9000 within a decade. These problems can be answered by using an electronic and digital maintenance operations platform that will increase efficiency, save time resulting in less delays and save money.

### *A. Problem Statement*

Maintenance is carried out on the aircraft by approved aircraft maintenance engineers. Maintenance is carried out on the aircraft by using conventional methods in most of the industries. Safety is the top-notch priority in aviation. Most of the accidents happening in aviation are a result of human error. These conventional methods present a great hazard and can cause a human error which can result in disaster. Also as a result of expected growth in this sector and to keeping up with work pressure and timely

completion of work, these conventional methods are not suitable and are the result of delays and cause loss to the operator of millions of dollars. As it is said that the aircraft is only earning when it is flying.

As the world is modernizing, technology is the only solution is such problems. The android application for aircraft maintenance engineers can answer many such problems and it also meets the needs of today's MROs.

It can reduce delays and save the operator's millions by cutting downtime. It also ensures safety by reducing the chances of human errors. The application will include the e-manuals, e-checklists, e logbook and ATA chapters of the aircraft, that will be needed while doing its maintenance. It also has many other advantages over the conventional systems. [1].

## II. Conventional Methods

The current system is not inauthentic but is very time consuming and annually costs airlines a lot. The two methods being used are listed.

- Paper based system
- Verbal communication system

In Aviation the thumb rule followed is "TIME IS MONEY", which means the less time spend on maintenance the more revenue that aircraft would generate because aircraft would only be earning if it's in air. In current practice when an Engineer has to perform maintenance, he first has to carry heavy manuals. Then he has to find a feasible location to place them and to search for a particular chapter for particular maintenance. All these are very much time consuming and due to age factor and a lot of experience the personnel don't bother to look for manuals which could miss an important step and could lead to improper procedures being performed, which would make a chain of small incidents that in the end could lead to a disaster. Further, the maintenance personnel have to go or call someone from inventory store to get tool/spare parts, by filling demand form to inventory store to have that tool/part. For all these, there is a lot of paperwork that has to be completed and copies of different forms have to be sent in different departments, which consumes a lot of time. In aerospace industries, there are people from different cultures and backgrounds so communication can also be a major problem.

**Disadvantages;**

- Requires a lot of shelf space.
- There are many channels involved in completion of work ultimately increasing time factor and man power.
- Due to many people involved there are high chances of human error.
- Nearly 4 billion trees worldwide are cut down each year for paper, representing about 35 percent of all harvested trees.
- As people have different backgrounds and cultures, misunderstandings and complacencies arise more often that can also be hazardous [2].

## III. Modern Methods

### *A. The Connected Engineer*

It is being used by Virgin Atlantic which is an airline whose headquarters are located in Crawley, United Kingdom. They have integrated all of their paper-based maintenance and engineering work in an application and they have achieved significant results. They have named it The Connected Engineer. The application consists of the following features: [3]

- **Electronic Logbook**

This feature replaces all the electronic logbooks to improve efficiency. The application has been uniquely designed to include interfaces for flight crew client, cabin client, maintenance client and electronic logbook data control that further enhances the productivity.

- **Maintenance Turn Time**

This feature greatly reduces delays and cancellations by enhancing the ability to quickly identify and resolve defects that are unscheduled. It assists in troubleshooting and provides quick access to aircraft maintenance history. It also facilitates for photo and 3D image documentation.

- **Airplane health management**

This feature includes real-time fault management, custom analytics and performance monitoring, the airline has achieved analytical decision-making power.

- **Toolbox Mobile Library**

This feature supports the maintenance turn time with a library of documentation which does not require the internet. It also includes maintenance manual, fault isolation manual and schematics manual and other manuals as well. With the help of this application, the airline achieved 20% reduction in delays, 15% reduction in defects, 24% man hours saved, 2 hours per day saved, the turnaround time of 20 to 30 minutes saved per day shift as can be seen in the **Figure 1.**

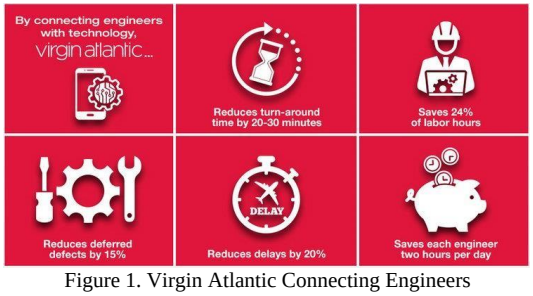


Figure 1. Virgin Atlantic Connecting Engineers

### *B. E-MRO*

The introduction of E MRO has the purpose of bringing e enabled systems to industry to control maintenance and engineering operations and also for maintaining the

efficiency of work. The international civil aviation organization predicts that the number of aircraft is going to double in the region and even tripling in some areas within a decade as a result of the pace with which the industry is growing. This demands the MRO to efficiently complete the operations so that the operator can smoothly run operations as can be seen in **Figure 2.**

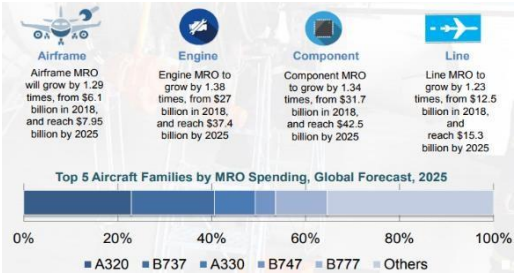


Figure 2.MRO Growth Rate

The application's development is based on rapid application development principle. It uses mathematical algorithms to generate inspection requirements and task checks for aircraft.

The supervisors have their own interface to assign a task to the mechanic. The mechanic will be able to access the job after the supervisor has assigned it and save it after its completion. The system also allows a job to be assigned to a workgroup instead of an individual. The system will authorize all the mechanics in the workgroup to access the job. Utilization of this system has enabled improved visibility of an MRO task and allows advance scheduling operations. It allows a more proactive approach to MRO requirement and enables advanced sourcing and monitoring of supplies. [4].

### *C. Go Direct by Honeywell*

Cathay Pacific is an airline that implemented the e maintenance solution called Go Direct by Honeywell. This system was implemented on their whole fleet of Airbus A330. It helps in predictive maintenance by predicting the condition and upcoming maintenance of mechanical parts by combining the aircraft's connectivity with in-depth knowledge and data analytics.

During the trial, it showed it that reduced inoperative systems up to 35%. It reduces operating and maintenance costs and reduces aircraft downtime. It also reduced flight and APU related delays by 51% and also reduced cancellations by making the flying safer, efficient and cost effective. It saved airline a lot of money and reactive maintenance costs per aircraft.

According to Honeywell, the system can not only enhance customer experience but also makes an aircraft comprehensive and makes it an agile platform that makes flying even safe and efficient. Without this system, it becomes very difficult for the airline to manage unscheduled maintenance. It helps in predictive maintenance and highlights the most critical faults to repair and also gives the recommendations.

Its predictive fault analyses have a false positive rate of less than 1%. The fault analysis monitors the trends of failures and compares them with the previous readings and shares critical faults and also shares recommendations to deal with it. It helps the maintenance personnel and flight crew in predicting and planning one time ahead and also allows replacement of parts on the right time. [5].

### *D. Flight docs*

Flight docs help in daily operations and particularly scheduled maintenance and it is fully integrated with the maintenance department and it connects the maintenance and crew by developing relations and connecting technology and tools. They are providing services to aircraft operators, air medical providers, air charters and flight departments. It evolves with the needs of its customers and addresses the needs of many other departments as well.

Some of its maintenance related features are work orders which help in managing the planning, record the performed maintenance, update and sign it. Another feature is the inclusion of electronic logbooks which includes digital entries, reduces errors and saves time. It also addresses non-routine, unscheduled maintenance. This reports and tracks and gives solutions for the unscheduled tasks. It eliminates paper write-ups and increases reliability. It includes the feature of electronic signatures to speed up the compliance procedures, helps easy editing and ensures accuracy. It also includes any other features like component tracking, manuals, inventory control, maintenance management, service bulletins, purchase orders and hours tracking. [6].

### *E. Maintenance Mobility*

Airbus is a leading aircraft manufacturer based in the Netherlands that has launched maintenance mobility. It is an e maintenance solution for aircraft maintenance engineers providing updated critical information including work packages and documentation. It also optimizes line and base maintenance by utilizing the full advantage of technology. It also includes:

- Specific interface for supervisor for real time awareness of maintenance procedures and also anticipates corrective procedures.
- Interface for mechanics featuring real time awareness of ongoing maintenance activities, ease of interaction with maintenance control center. It also includes e signature features to sign the performed task.

With this solution, they optimize turnaround time and reduce flight delays and cancellations, improve overall productivity and also making troubleshooting more effective [7].

## IV. PROTOTYPE

The figure below is the GUI layout of the application designed in adobe Photoshop CC 2014.

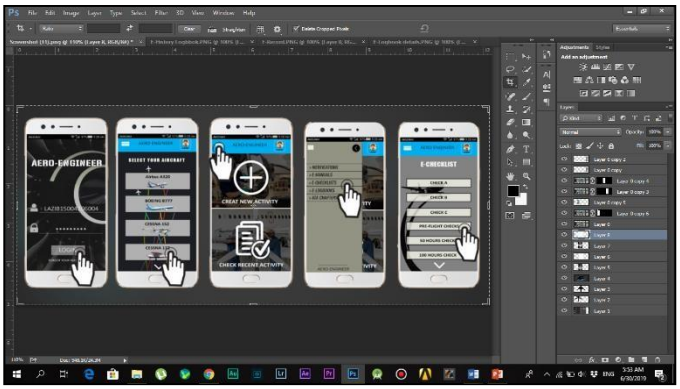

Figure 3: GUI designing in Photoshop

A prototype layout of the actual android application for the arcraft maintenance engineer can be seen in the figuer above. It contains some of the key layouts of the application for example the login layer and the aircraft selection layer, which are incorporated in the actual working app and were designed using these design layouts in application development softwares (Android Studio).
These layers were designed using some basic tools and techniques available in the adobe Photoshop. These tools and techniques included:

- Quick selection tool
- Rectantular tool
- Crop tool
- Adding layer styles
- Using photoshop filters
- Text tool and many other

Images such as background image, aircraft images, user profile picture etc all were outsourced and imported into the photoshop for giving an asthetic look to graphical user interface. There images can be seen stacked upon each other in layer panel.

## V. PLATFORM

The platform used for developing the application is Android Studio. Android Studio is the official IDE (Integrated development environment) for Google's Android operating systems, making it the number one choice for the majority of Android app developers around the globe who are looking to make basic apps or even get started and get familiar with android developing tools. Android studio helps developers make apps with Google's basic material design guidelines and access to all advance features and tools of this platform [8].
There are few major factors contributing to why android studio is being selected. Some of them are listed below:

- Open source development.
- Extensible build tools.
- Powerful code editing.
- Smoother and richer GUI.
- Google services. [9]

## VI. WORK STAGES

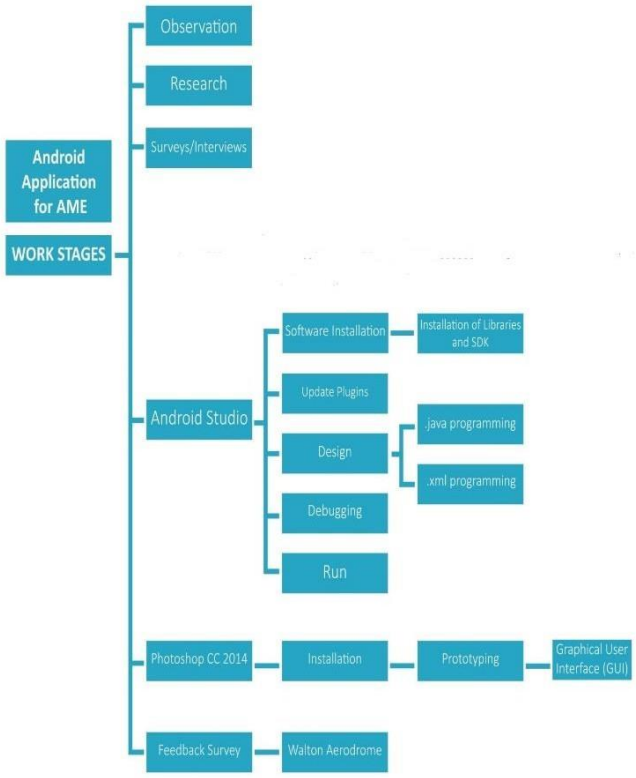


Figure 4: Work stages

## VII. FLOW CHART OF APPLICATION WORK STAGES

Following is the pseudo code of the application.

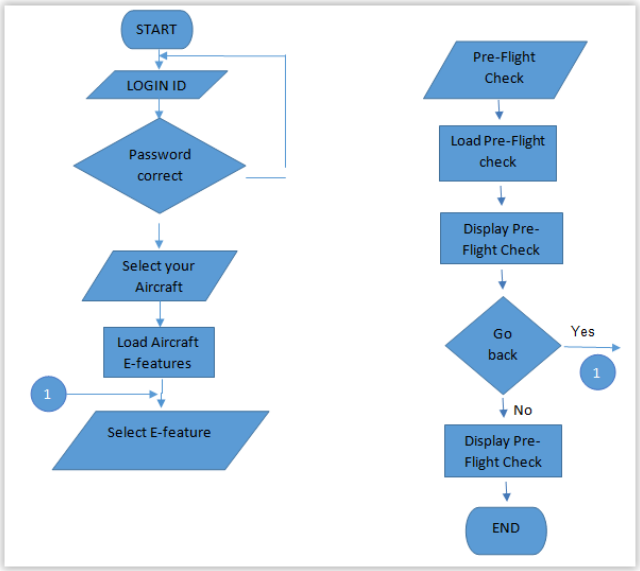


Figure 5. Flow Chart of Application

Following are the layers of application that were design and developed in Android Studio using the .xml and the .java file.


Figure 6. Login Page

Login Page is the first layer of the application. It consists of a user ID, password and a login button. There are 5 attempts of logging in at one time in case of continuous unsuccessful attempts. This feature ensures security. Every user in the industry has been assigned his own User ID and password and has his own profile and interface. The login layer allows the engineer and the mechanic to access their own respective interfaces and also ensures the security of the user's profile and important data. Upon a successful login, the 2nd layer shows up which allows the user to select particular aircraft

.

## REFERENCES

[1] Tom, "Modernizing MRO," 2018. [Online]. Available: https://aerospaceamerica.aiaa.org/departments/modern izing-mro/.

[2] S. Martin, "Paper chase," 2011. [Online]. Available: http://www.ecology.com/2011/09/10/paper-chase/. [Accessed 28 October 2018].

[3] Connect, "The Connected Engineer Drives Efficiency, Value for Virgin Atlantic," 2016. [Online]. Available: http://newsletters.jeppesen.com/connectnews/posts/20 16/12/12/virgin-Atlantic-connected-engineers.

[4] S. Naseri, "The development of e-enabled MRO- maintenance, repair and operations in the global air transport industry for optimizing airplane utilization through minimizing downtime," 2006.

[5] A. Xu-blog, "honeywell's connected aircraft maintenance reduces delays And cancellations for cathay Pacific," 2017. [Online]. Available: https://aerospace.honeywell.com/en/press-release-listing/2017/june/honeywell-s-connected-aircraft- maintenance-reduces-delays-and-cancellations-for- Cathay-pacific.

[6] F. Docs, "Maintenance Tracking," 2019. [Online]. Available: https://www.flightdocs.com/maintenance-tracking/.

[7] Airbus, "Airbus," 2018. [Online]. Available: https://services.airbus.com/en/aircraft-availability.html/e-solutions/airbus-smarter-fleetandreg/maintenance-mobility.

[8] A. Sinicki, "Best Android developer tools," 18 June 2018. [Online]. Available: https://www.androidauthority.com/best-android- developer-tools-671650/. [Accessed 5 November 2018].

[9] T. N. K. C. Xavier Ducrohet, "Android Studio: An IDE built for Android," 2013. [Online]. Available: https://android-developers.googleblog.com/2013/05/android-studio- ide-built-for-android.html. [Accessed 5 NOVEMBER 2018].

# Design of a Gas-Liquid Injection System for a Staged Combustion Main Chamber

Muhammad Rehan Ahmad
*Institute of Space Technology*
*Islamabad, Pakistan*
rehan256666@gmail.com

Fatima tuz Zehra
*Institute of Space Technology*
*Islamabad, Pakistan*
zehrafatima734@gmail.com

***Abstract*— A Liquid Centered Gas Liquid Swirl Coaxial injection system is being developed for the Staged Combustion Main Chamber of the Liquid Propellant Rocket Engine (LPRE) with LOx and methane being the propellant pair. The swirling liquid flow coming out from the center of the injector is impinged upon by the coaxial gaseous sheet, resulting in the atomization and mixing of the propellants. The designing of the injector is carried out in MATLAB. The coefficient of discharge for gaseous propellant is calculated through iterative process, depending upon the injector assembly parameters' ratios. A combustion chamber is also designed and prototyped to be used for the testing purposes, including both cold testing and hot testing. The velocity mismatching in injector is verified through CFD performed in ANSYS. The future work of this project includes testing of the prototyped injector and verification of calculations. Moreover, the procedures and techniques adopted for designing of this injector can be extended to a bigger scale whereby testing can be performed by prototyping an injector head containing more than one such injectors, and an up scaled version of prototyped combustion chamber.**

**Keywords— Gas-Liquid Injector; Staged Combustion; Combustion Chamber; Liquid Propellant Rocket Engine; Coefficient of Discharge.**

## I. INTRODUCTION

The efficiency of the combustion chamber of a liquid propellant rocket engine depends on the mixing and atomization of the propellants and the injector is responsible for that, making it an integral and important part of the combustion engine [1].

The use of injectors is not only confined to the aerospace industry rather it has been employed in other industries like medicine and agriculture with great success but aerospace industry is where the injectors have found extensive applications because of its importance in the combustion process as mentioned earlier [1].

Injectors can be bi-propellant or monopropellant and their further type and position determines the grade of atomization and mixing of the propellants [1].

A lot of work has been done in the past on coaxial injectors which have been successfully employed in different systems whereas the swirl injector has found extensive applications in the monopropellant systems. Now the research is focused towards the development of swirl coaxial injectors which combines the atomization and mixing properties of the swirl and the coaxial injectors. Swirl coaxial injectors have been developed for liquid-liquid combination but the recent research is focused on the development of swirl coaxial injectors for gas-liquid systems. The inspiration of developing a swirl coaxial injector for a gas-liquid system stems from the fact that they have not been employed or developed in Pakistan before.

The designing of the combustion chamber depends on some factors like choosing the shape of the chamber, the type of nozzle and the ease of manufacturing. Volume of chamber is an important parameter to ensure its good performance. Greater the volume, better is the atomization, mixing, evaporation and complete combustion of propellants [2].

The designing of a liquid centered swirl coaxial injector and a combustion chamber is described in this work.

## II. SCOPE

The scope of this project includes the technology development in Pakistan, since, as mentioned before, there has been no swirl coaxial injector for Gas-Liquid propellant combination developed in Pakistan before. The project aims at establishing a preliminary design followed by prototype development which then will be subjected to cold and hot testing. Additionally, a combustion chamber is also designed and the injector designed is subjected to CFD analysis for verification.

## III. DESIGNING OF INJECTOR

### A. Methodology

The designing of the injector can be separated into two phases; the design of swirl chamber and the design of outer chamber. The selection of the type of injector depends on the system in which it is to be used and the mixing and atomization requirements of that system [1].

### B. Design Requirements

The propellant pair was Liquid Oxygen as an oxidizer with a mass flow rate of 0.04 kg/s and Gaseous Methane as a fuel with the mass flow rate of 0.01 kg/s. The pressure drop for the swirl chamber and gas/outer chamber is 15 bars and 10 bars respectively.

### C. Design

The design of Swirl coaxial injector is carried out in two parts; the design of swirl chamber and the gas/outer chamber.

The mechanism that follows is that the liquid oxygen is to swirl through the inner chamber while the gas sheet impinges upon it from the outer chamber. The important parameters for both chambers' design include area, coefficient of discharge and velocity.

#### 1) Swirl Chamber

The swirl chamber makes the liquid oxygen swirl through it. The main design parameters, along with those mentioned before, include the recess length. The coefficient of discharge for the inner chamber is 0.5 [2]. The velocity of flow through the inner chamber is calculated using following formula:

$$v = \left(\sqrt{\frac{2*\Delta P}{\rho}}\right)*C_d \quad (1)$$

For the purpose of area of chamber calculation, following equation was referred to:

$$A = \pi \frac{D^2}{4} \quad (2)$$

Whereas the discharge area is calculated through the following equation

$$A_o = m_f / \rho * v \quad (3)$$

The recess length of swirl chamber is 1.5mm.

*2) Outer Chamber*

The main design parameters for outer chamber include the coefficient of discharge, the area of outer chamber, and velocity of flow through the outer chamber as well as the tangential ports specifications.

*a) Tangential Ports Specifications*

Length of tangential ports is 7 mm with 1.5 mm diameter. The area of tangential ports is calculated as

$$A_p = (2\pi r_p l_p) + (2\pi r_p^2) \quad (4)$$

*b) Coefficient of Discharge*

The lack of numerical scheme to determine the coefficient of discharge makes it difficult to determine a fair value but some ratios and numerous empirical equations have been developed which can be used to get a fair value of $C_d$.

For the purpose of determining the $C_d$; equations (11), (12) and (13) can be used which were developed by Carlisle, Risk and Lefevbre and Jones respectively and are mentioned by Pedro Teixeira [3].

The important ratios include $D_s$ / $D_o$, where $D_o$ is the discharge diameter and $D_s$ is the diameter of outer chamber. The acceptable range for this ratio is 1.41 to 8.13, $A_p$/ $D_sD_o$, where $A_p$ is the area of tangential ports, should vary from 0.19 to 1.21, $L_s$/ $D_s$, where $L_s$ is the length of outer chamber. $L_s$ / $D_s$ should be kept lower since its large value brings with it the frictional effects that are not to our advantage, hence should vary from 0.5 – 1 [4]. The last important ratio is $L_p$/ $D_p$, where $L_p$ is the length of tangential ports and $D_p$ is the diameter of tangential ports. $L_p$ / $D_p$ should be greater than 1.3 because otherwise the spray may get unstable [5]. The discharge diameter is selected and other parameters are obtained through the above mentioned ratios. The equations used for evaluation of coefficient of discharge are:

$$C_{di} = \frac{\dot{m}}{A\sqrt{2\Delta P.\rho}} \quad (5)$$

$$C_d = \left(0.0616 \frac{D_s}{D_o} \frac{A_p}{D_s D_o}\right) \quad [6] \quad (6)$$

$$C_d = 0.35 \left(\frac{D_s}{D_o}\right)^{0.5} \left(\frac{A_p}{D_s D_o}\right)^{0.25} \quad [7] \quad (7)$$

$$C_d = 0.45 \left(\frac{D_o.\rho.v}{\mu}\right)^{-0.02} \left(\frac{L_o}{D_o}\right)^{-0.03} \left(\frac{L_s}{D_s}\right)^{0.05} \left(\frac{A_p}{DsDo}\right)^{0.52} \left(\frac{D_s}{D_o}\right)^{0.23} \quad [8] \quad (8)$$

The procedure adopted for calculation of $C_d$ is that an initial value of mass flow rate is used for determination of an ideal velocity and area of chamber i.e. the values without $C_d$ and hence not incorporating the frictional effects. From these ideal values, an initial $C_d$ is evaluated and compared with those evaluated from the above mentioned set of equations and the one closest to the initial value is chosen.

*c) Area of Chamber and Velocity*

Since outer chamber is hollow from inside so two diameters are used for calculation of its area; inner is the outer diameter of the swirl chamber while outer being the inner diameter of the gas chamber. The formula used for area calculation is

$$A = \pi ((r_o)^2 - (r_i)^2) \quad (9)$$

The velocity is calculated through the same procedure as that for the swirl chamber.

The summarized design parameters for both swirl chamber and outer chamber are given in table 1.

## IV. Modelling of Injector

The assembled model for inner chamber and outer chamber is shown in Fig.1. The 3D Modelling of injector is carried out in the software CATIA V5R20 and is proceeded part by part.

The parts include Swirler; through which liquid oxygen was to be swirled, Inner Chamber; comprising of Swirler, Tangential ports; for injection of propellants, Outer chamber; for flow of gaseous methane, perforation disk and caps, which are then assembled.

## V. CFD Analysis of Injector

The CFD Analysis of injector is carried out to verify the velocity mismatching. The RSM model was employed to solve the complex swirling flows inside the injector. RSM solves additional six transport equations for the Reynolds stresses in addition to the Reynolds-Averaged Navier Stokes (RANS) equations. RSM is used to compute the complex flows because it accounts for swirl, streamline curvature, rotation and high strain rates. The RSM equation is given next:

$$\frac{\partial}{\partial t}\left(\rho\overline{u_i'u_j'}\right) + \frac{\partial}{\partial x_k}\left(\rho u_k \overline{u_i'u_j'}\right) = -\frac{\partial}{\partial x_k}\left[\rho\overline{u_i'u_j'u_k'} + \overline{p\left(\delta_{kj}u_i' + \delta_{ik}u_j'\right)}\right] + \frac{\partial}{\partial x_k}\left[\mu\frac{\partial}{\partial x_k}\left(\overline{u_i'u_j'}\right)\right] - \rho\left(\overline{u_i'u_k'}\frac{\partial u_j}{\partial x_k} + \overline{u_j'u_k'}\frac{\partial u_i}{\partial x_k}\right) - \rho\beta\left(g_i\overline{u_j'\theta} + g_j\overline{u_i'\theta}\right) + p\left(\frac{\partial u_i'}{\partial x_j} + \frac{\partial u_j'}{\partial x_i}\right) - 2\mu\overline{\frac{\partial u_i'}{\partial x_k}\frac{\partial u_j'}{\partial x_k}} - 2\rho\Omega_k\left(\overline{u_j'u_m'}\epsilon_{ikm} + \overline{u_i'u_m'}\epsilon_{jkm}\right) + S_{user}$$

*Results*

The results obtained from the CFD analysis of the injector confirmed the calculations done in the designing of the

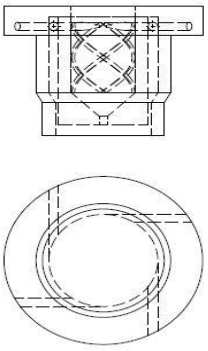

**Figure 1. Injector**

**Table 1 DESIGN PARAMETERS OF INJECTOR**

| Sr.no | | Parameter | | Value |
|---|---|---|---|---|
| 1 | Inner Chamber | Pressure | | 15 bars |
| 2 | | $C_d$ | | 0.5 |
| 3 | | Velocity | | 25.6 $ms^{-1}$ |
| 4 | | Area | Chamber | 78.5 $mm^2$ |
| | | | Discharge | 1.2 $mm^2$ |
| 5 | | Diameter | Chamber | 10 mm |
| | | | Discharge | 1.3 mm |
| 6 | | Recess Length | | 1.5 mm |
| 7 | Outer Chamber | Pressure | | 10 bars |
| 8 | | $C_d$ | | 0.2564 |
| | | Chamber | $D_o$ | 15 mm |
| 9 | | | $D_s$ | 17 mm |
| | | | Area | 23 $mm^2$ |
| | | Tangential Ports | $L_p$ | 7 mm |
| 10 | | | $D_p$ | 1.5 mm |
| | | | $A_p$ | 36.5 $mm^2$ |
| 11 | | Velocity | | 141 $ms^{-1}$ |

injector as the velocities achieved were nearly the same as the velocities calculated with some error. The velocity contours obtained are shown in Fig.2.

## VI. DESIGNING AND MODELLING OF COMBUSTION CHAMBER

Design of combustion chamber comprises of four phases including the frozen equilibrium calculation, volume of chamber, pressure; temperature and velocities at nozzle throat and exit, and finally the nozzle lengths. The converging diverging nozzle is chosen as per our design requirements.

The Frozen equilibrium is calculated in CPROPEP. The pressure for combustion chamber is 15 bars. The stoichiometric mixing ratio for the selected propellant pair is 4. The important outputs obtained from frozen equilibrium calculation are shown in Table 2.

The volume of chamber is calculated through the following equation:

$$V_c = L^* A_t \quad (10)$$

L* generally varies from 0.8 to 3 m and for this project purpose it is selected as 1.1m. $A_t$ is the area of throat calculated as $A_t = \pi\frac{D^2}{4}$, where the diameter of throat is 13.5 mm. Length of chamber is calculated depending upon the area of chamber. The diameter of the chamber is to be chosen by keeping its effect on cooling requirements and effective combustion, in mind.

$$L_c = \frac{V_c}{A_c} \quad (11)$$

$A_c$ can be calculated the same way as $A_t$ and the area of exit can be calculated through the expansion ratio obtained from the CPROPEP output file.

The pressure, temperature and velocities at the throat and exit of nozzle are obtained from CPROPEP and can also be verified through the basic isentropic relations.

Pressure: $$P_t = P_c \left[\frac{2}{\gamma+1}\right]^{\frac{\gamma}{\gamma-1}} \quad (12)$$

Temperature: $$T_t = T_c \left[\frac{P_t}{P_c}\right]^{\frac{\gamma-1}{\gamma}} \quad (13)$$

Velocity: $$V_t = \sqrt{\frac{2\gamma}{\gamma+1} R T_c} \quad (14)$$

As the converging diverging type of nozzle is selected its respective lengths and contour radius are calculated. The convergent cone angle has a general variation from 20˚ to 45˚ while that of divergent cone angle is 12˚ to 18˚. The convergent angle selected is 30˚ while the divergent cone angle is selected as 15˚. The contour radius for chamber walls is calculated as:

$$R = 0.6^* R_t \quad (15)$$

The convergent, divergent and throat lengths are calculated through the next mentioned equations.

Convergent:

$$L_{convergent} = \frac{R_t\left(\sqrt{\frac{A_c}{A_t}}-1\right)+R_u(\sec(\alpha_{convergent})-1)}{\tan(\alpha_{convergent})} \quad (16)$$

Where $$\frac{A_c}{A_t} = 8\,(D_t)^{-0.6} + 1.25$$

Divergent:

$$L_{divergent} = \frac{R_t\left(\sqrt{\frac{A_e}{A_t}}-1\right)+R_u(\sec(\alpha_{divergent})-1)}{\tan(\alpha_{divergent})} \quad (17)$$

Throat:

$$L_{throat} = R_u * (\sin(\alpha_{divergent})) \quad (18)$$

The designed parameters of the combustion chamber are summarized in Table 2.

The modelled combustion chamber is shown in Fig 3.

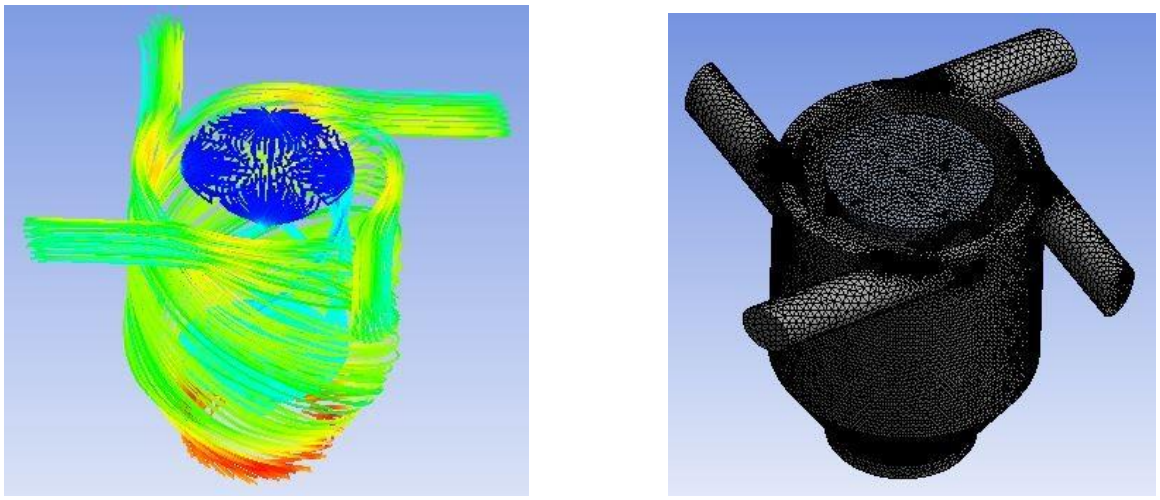

**Figure 2. CFD Results of Injector**

**Table 2 DESIGN PARAMETERS OF COMBUSTION CHAMBER**

| Sr.no | Parameter | | | Value |
|---|---|---|---|---|
| 1 | Frozen Equilibrium | Pressure | | 15 bars |
| 2 | | O/F (stoichiometric) | | 4 |
| 3 | | Temperature | Chamber | 3360 K |
| 4 | | | Throat | 3050 K |
| 5 | | | Exit | 2100 K |
| 6 | | Gamma | | 1.20143 |
| 7 | | C* | | 1713 m/s |
| 8 | | $C_f$ | | 1.35 |
| 9 | | $I_s$ | | 235 s |
| 10 | | Expansion ratio | | 2.9 |
| 11 | Volume of Chamber | $D_t$ | | 13.5 mm |
| 12 | | $A_t$ | | 143 $mm^2$ |
| 13 | | L* | | 1.1 m |
| 14 | | $V_c$ | | $1.5745*10^5$ $mm^3$ |
| 15 | | $L_c$ | | 125 mm |
| 16 | | $D_c$ | | 40 mm |
| 17 | | $A_c$ | | $1.2566*10^3$ $mm^2$ |
| 18 | | $A_e$ | | 415 $mm^2$ |
| 19 | | $D_e$ | | 23 mm |
| 20 | Nozzle Parameters | Throat | Pressure | 8 bars |
| 21 | | | Temperature | 3050 K |
| 22 | | | Velocity | 797 m/s |
| 23 | | Exit | Pressure | 1.01325 bars |
| 24 | | | Temperature | 2100 K |
| 25 | | | Velocity | 1589 m/s |
| 26 | Nozzle Lengths | Convergent angle | | 30˚ |
| 27 | | Divergent angle | | 15˚ |
| 28 | | Contour radius | | 4 mm |
| 29 | | Convergent length | | 22 mm |
| 30 | | Divergent length | | 18 mm |
| 31 | | Throat length | | 1 mm |

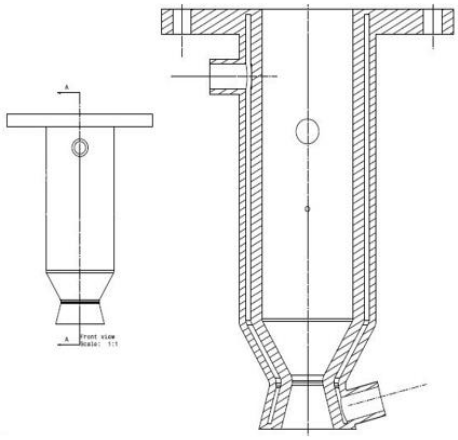

**Figure 3 Combustion Chamber**

## VII. FUTURE WORK

As par the breakdown of project planning, the prototyped injector is to be subjected to testing and analyzed. The injector will be subjected to both the cold testing and the hot testing. Cold testing will be performed using water while hot testing will be done in the combustion chamber using the propellant pair. Flow patterns will be analyzed and an atomized cone of propellants at the outlet will be received, verifying the calculations done prior to designing. Towards the completion of project, a swirl coaxial injector will be obtained for a gas-liquid propellant combination. This lab level work can be expanded to higher level. This project focuses on the development of one injector, however, at a higher level a number of injectors can be developed following the same procedure and can be employed in bigger systems. This work will kick off the development of swirl coaxial injectors in Pakistan which will help improve the research work.

## ACKNOWLEDEGMENT

This work was supported by PEARL Lab and supervised by Dr. Ihtzaz Qamar.

## REFERENCES

[1] Rodrigo Monteiro Eliott, Pedro Teixeira Lacava. “Development of a Gas-Liquid Injector for Liquid Rocket Engine”

[2] George P. Sutton and Oscar Biblarz. Rocket Propulsion Elements. John Wiley and Sons, INC., 2001...

[3] Pedro Teixeira Lacava, Demetrio Bastos-Netto, Amilcar Porto Pimenta. “Design Procedure and Experimental Evaluation of Pressure Swirl Atomizers”. 24th International Congress of the Aeronautical Sciences, 2004.

[4] Elkotb M M, Rafat N M and Hanna M A. “The Influence of Swirl Atomizer Geometry on the Atomization Performance”. Proceedings of the 1st International Conference on Liquid Atomization and Spray Systems, Tokyo, pp. 109 – 115, 1978

[5] Tipler W and Wilson A W. “Combustion in Gas Turbines”. Proceedings of the Congress International des Machines a Combustion (CIMAC), Paris, pp. 897 – 927, 1959

[6] Carlisle D R. “Communication on the Performance of a Type of Swirl Atomizer”, by A. Radcliffe. Proc. Inst. Mech. Eng., Vol. 169, p.101, 1955

[7] Risk N K and Lefebvre A H. “Internal Flow Characteristics of Simplex Swirl Atomizers”. Journal of Propulsion Power, Vol. 1, No. 3, pp.193– 199, 1985

[8] Jones A.R. “Design Optimization of a large pressure jet atomizer for Power Plant”. Proceedings of Second International Conference on liquid Atomization and spray systems, Madison, Wis., pp 181-185, 1982

# A Survey of Research Advancement on Unstart Flow Mechanism of The Air-Breathing Hypersonic Inlet

Naeem Haider
*Department of Aerospace Engineering. CAE*
*National University of Sciences and Technology*
Islamabad, Pakistan
nhaider@cae.nust.edu.pk

Dr. Ali Sarosh
*Department of Aerospace Engineering. CAE*
*National University of Sciences and Technology*
Islamabad, Pakistan
alisarosh@cae.nust.edu.pk

***Abstract*—For the air-breathing hypersonic vehicle's propulsion system, the air flow, and compression ratio depending upon the inlet shape. The inlet start is defined as the desired operating mode of the engine inlet. Inlet unstart is defined as the ejection of the shock system from the inlet of the scramjet/ramjet engine. The inlet unstart decreases the mass capture coefficient and total pressure recovery coefficient. The thermal loads and aerodynamic drag increases because of unstart. In recent flight tests for the scramjet, engine failure occurred because of the unstart phenomenon. Therefore, it is very important to understand the reason and controlling method of unstart. In this paper, a summary of the detection and control methods of unstart has been presented. The different reasons for unstart have been presented. The effect of the back pressure rise, heat release rise, change in Mach number and change in Contraction Ratio has been discussed. The prediction and detection of the unstart using different algorithm are also presented. The comparison of the algorithm for the start or unstart detection is presented. The available methods for preventing or delaying unstart are discussed. The effect of flow control and feedback control on unstart has been presented. Lastly, the future recommendations for further analysis of the unstart phenomenon are discussed.**

***Keywords— Unstart flow Mechanism; Shock train Leading Edge; Inlet controls; Unstart Detection and Control***

## I. INTRODUCTION

The compression ratio of the hypersonic system is totally depending upon the inlet of machinery. There is no rotating machinery in the hypersonic system [1]. The compression and capture of air in the hypersonic air-breathing system are done by the inlet of the system. This compressed air burns with the fuel in the combustion chamber with an extensive range of conditions at which it can operate. The main function of the inlet is to get the optimum compression ratio with minimum geometry weight [2,3]. Start can be defined as the desired operating mode for the inlet. The inlet start condition is established by mounting an oblique shock wave on the lip of the wall of the inlet. This relative stable oblique shock wave system generates a stable operating condition for the inlet [4]. For the operating mode conditions, started mode should provide a high compression ratio, uniform flow for the combustion process and low drag. The operating condition in which the flow capture properties for the internal flow does not change is termed as the inlet start. The Second criterion can employ only for the start condition [5,6]. The unstart condition is defined as the condition where the start condition does not exist. This condition for both the supersonic and hypersonic depends upon the different factors. Unstart mainly depends upon the angle of attack, Internal contraction ratio (ICR), Mach number, time-dependent properties and recovery coefficient of total pressure [1]. The change in these properties cause the unstart phenomena for example when the ICR is oversized the chokes condition at the inlet throat exits [7,8]. Oversize ICR causes the excessive heat release, extra fuel mass addition and downstream choking due to the back pressure [9]. In inlet unstart, the total pressure recovery coefficient and air mass capture very low [3]. Due to this condition, the thermal loads and the aerodynamic drag increases [10]. Because of these losses, the operating condition for the hypersonic air-breathing system should be started. In the hypersonic air-breathing propulsion system, the unstart condition developed unavoidably because of the several reasons like inadequate Computational Fluid Dynamics (CFD) simulation, imperfect design method, etc. [11,12]. In many previously conducted flight tests, the flight failed because of the unstart mechanism. Some of the flight test failures due to the unstart is the NASA/CIAM Mach 6.5 [10] and HyCAUSE [13]. The main reason for the failure of X51A during both flight test in 2010 and 2011 is the unstart [14, 15]. In air-breathing propulsion for the hypersonic system, inlet unstart is a very critical problem. A typical example of the flow stations for the scramjet inlet is shown in Figure 1. The control of the unstart is done by using different techniques like controlling the boundary layer interaction or the shock wave [16, 17]. To understand this phenomenon, a lot of studies has been made in recent years. The characteristics expressed by the flow in hypersonic are hysteresis and nonlinear in nature [5] which make the detection and control of the unstart difficult and complex [18, 19]. Therefore, for the detection and control of the unstart, a lot of advanced techniques and method has been developed. In this paper, previous studies on the unstart mechanism and different control method have been summarized.

## II. UNSTART MECHANISM AND TYPES FOR HYPERSONIC INLET

Unstart can cause by many factors. The factors like the internal contraction ratio, heat release, Mach number, and back pressure can trigger the unstart. The failure in the recent flight test is because of the unstart caused by the improper control of the backpressure [11]. Therefore, it is very important to study the reason for the unstart. The main reasons for the unstart can be divided into following four categories.

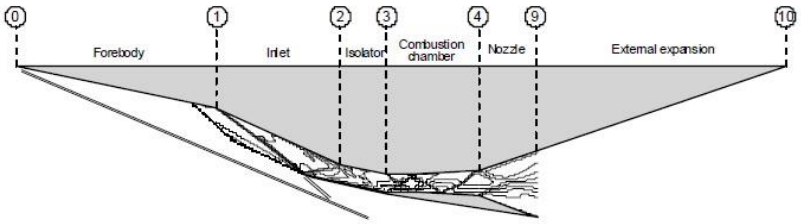


Figure 1 Typical flow stations for the scramjets. [20].

### A. *Unstart because of the Internal Contraction Ratio*

The state of the inlet with fixed geometry for which flow state transfer to start from the unstart is known as self-start. The ability of a fixed geometry inlet of self-start can be measured as its ability to restart when the unstart flow condition is removed [21,22]. Inlet start state can be developed by using different suction devices or variable geometry feature features for the geometry with less self-start ability [1]. For the hypersonic inlet, the inlet start depends upon the Internal contraction ration (ICR) and local Mach number [4]. The start mode for the fixed geometry inlet has a certain region for the ICR with specified freestream conditions [23]. But for the variable geometry inlet, ICR is adjustable during the operating mode at any time. For variable geometry, the inlet is started at an ICR with small and safe value than with the increase in speed the ICR is increased to maintain the Start Mode.

Kantrowitz limit is one of the classical methods to find the safe value of ICR for he self-starts [4]. The assumption for the Kantrowitz limit is the velocity of freestream is normal to plane at entry, no spillage of flow at the ICR region, Fully closed. the occurrence of Normal Shock at start of IC, 1-D (One dimensional) flow, Isentropic flows and at the throat, flow is sonic [4]. Kantrowitz limit in terms of the area ratio (Kantrowitz area at the sonic throat to the start of the contraction area) is given by equation 1. In equation 1 the value of the specific heat ratio γ is taken 1.36 because of the high-temperature effect for the hypersonic flight (value of γ for normal temperature is 1.4) [24].

$$\frac{A_0}{A_{t_{Kantrowitz}}} = \sqrt{\frac{\gamma+1}{2+(\gamma-1)M_\infty^2}}\, M_\infty^{\frac{\gamma+1}{\gamma-1}} \left(\frac{2\gamma}{\gamma+1} M_\infty^2 - \frac{\gamma-1}{\gamma+1}\right)^{\frac{1}{1-\gamma}} \quad (1)$$

For the Prandtl Meyer inlet or Hybrid Contraction inlet, the Kantrowitz limit can be used [25]. The isentropic limit can be found by supposing that stream is isotopically compressed from start or front of the inlet to throat. Equation 2 gives the $A_{i,\ Isentropic}$ for the sonic flow at the throat.

$$\frac{A_0}{A_{i_{Isentropic}}} = \frac{1}{M_\infty}\left(\frac{2}{\gamma+1} + \frac{\gamma-1}{\gamma+1} M_\infty^2\right)^{\frac{\gamma+1}{2(\gamma-1)}} \quad (2)$$

The Co-efficient of Start Ability S can be calculated by equation 3. First ICR is found by Kantrowitz limit than ICR for isentropic is calculated using the external contraction ratio [26]. Equation 3 is used to find the S as follow

$$S = \frac{\frac{A_t}{A_0} - \frac{A_{i_{isentropic}}}{A_0}}{\frac{A_{t_{Kantrowitz}}}{A_0} - \frac{A_{i_{isentropic}}}{A_0}} = \frac{\frac{1}{CR} - \frac{A_{i_{isentropic}}}{A_0}}{\frac{A_{t_{Kantrowitz}}}{A_0} - \frac{A_{i_{isentropic}}}{A_0}} \quad (3)$$

The typical value of S for Prandtl Meyer inlet is 0.6. Inlet Start mode exit only for S greater than 0.6.

Another limit for supersonic inlet which can be used is Mashoney Limit. In Mashoney Limit, it is assumed that the Mach no. for the throat is half of $M_\infty$ i.e. the flow at throat can be supersonic. This limit can found by using equation 4 [23].

$$\frac{A_0}{A_{t_{Mashoney}}} = \frac{\frac{1}{M_\infty}\left(\frac{2}{\gamma+1} + \frac{\gamma-1}{\gamma+1} M_\infty^2\right)^{\frac{\gamma+1}{2(\gamma-1)}}}{\frac{1}{M_t}\left(\frac{2}{\gamma+1} + \frac{\gamma-1}{\gamma+1} M_\infty^2\right)^{\frac{\gamma+1}{2(\gamma-1)}}} \quad (4)$$

For the hypersonic inlet, if the upstream Mach number is lower than incident shock wave acts outside of the inlet lip. The Capture Area $A_c$ is less than the geometric area $A_0$. So, the effective contraction ratio is defined as equation 5 [24].

$$CR_{effective} = CR \times \frac{A_c}{A_0} \quad (5)$$

The ability of inlet start can be increased by using the large internal contraction ratio. Therefore, a lot of studies have been carried out for the inlet design for the high ICR. The ability of inlet start can also be increased by changing the ratio of exit area to entry area with a possible increase in freestream Mach as shown in Figure 1. Use of flexible geometry is one of the examples [26]. For the fixed geometry inlet, intakes are not fully closed and external compression section wall's one side is removed for possible spillage [27, 28]. All these techniques can be used for increasing the spillage area at the starting process. These methods also are known as Overboard-spillage Techniques. Kantrowitz limit is only applicable to the internal part only. It is not applicable to the whole inlet for the start ability. For the Kantrowitz limit, start ability is displayed as Kantrowitz line like a 2 shock intake. The 2nd shock in this is a strong shock. In this model, it is assumed that the second shock occurs at the throat and there is overboard spillage aided starting [29]. Figure 2 shows the summary of both maximum contraction ratio and

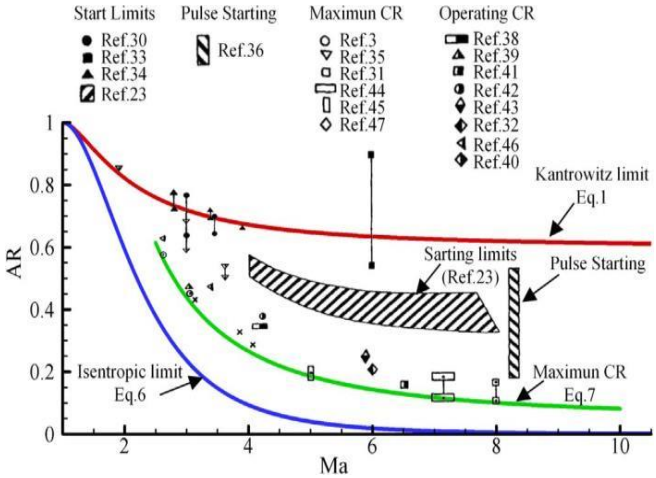


Figure 2. ICR and Mach number Limits. [1]

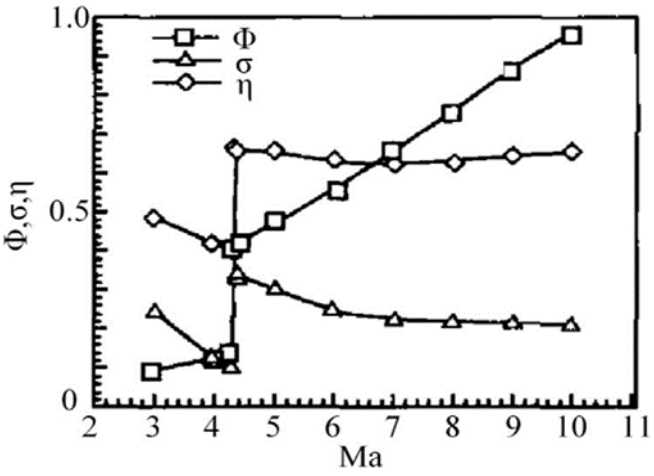


Figure 3. Curve of performance coefficient for the unstart due to Lower Ma. [1]

inlet starting. For the increased Mach, Maximum and allowable CR can be improved. For supersonic, the maximum CR is different than operating CR. For the Hypersonic inlet, there is a significant difference between the theoretical and experimental data curves as shown in Figure 2 [1]. The difference is because of the difference in the temperature ratio of wall to stream and inlet geometry. For these cases, higher ICR is used than the Kantrowitz limit. This because of the reason that the shock in hypersonic has high pressure-recovery. This error is because of the single normal shock assumption.

### *B. Unstart because of the Mach Number*

Inlet unstart can be occurred because of the Mach number. The effect of the ICR and Mach number on the Unstart mode is already discussed in the previous section [6]. For the hypersonic inlet, the Mach increase with the passage of time. In start, the Mach number is beneath the operating design value but with time, the Mach number becomes higher than the design value [44,45]. Therefore, unstart because of the Mach number can be divided into two classes as because of the lower Mach number and higher Mach number.

ICR value is fixed for the fixed geometric inlet. The fixed geometry inlet is only designed for the range of Mach number. This range is the double-solution region in between isentropic limit and Kantrowitz limit. The left side limit for the isentropic is single-solution region [1]. For the operating value of Mach, if the value is under the region of single-solution for the isentropic process limit than theoretically, flow is subsonic at throat and unstart at the inlet will happen. But in practical conditions, this value is greater than the isentropic limit because of the viscous and shear loses and shock waves [1]. Figure 3 shows the performance coefficients for the inlets. The unstart occurs at a value of 4.4 for the Mach number when the Mach number is decreased. The change in performance parameters can is seen in figure 3.

For the inlet of hypersonic system, a broad range for the operating Mach number is available. Therefore, the design value of the Mach number is select at the central value. In hypersonic flight, the Mach is higher than designed value and both the shock reflection and impingement occurs. The shock wave developed at fore-body impinges at a point downstream to lip and then reflect [44,45]. This shock wave's configuration is named as Mach reflection (MR) and regular reflection (RR) [46]. This phenomenon was observed in scramjet inlet by the Mahapatra [47]. He found that the shock detached from the cowl's lip because of the Mach reflection. Jiao also studied this phenomenon which is known as "local unstart" [20]. The local unstart has bow shock earlier than cowl lip and at the cowl has a subsonic region. Figure 4 shows the condition for local Unstart. Shock Reflection under the inviscid condition has been studied by lots of researchers [48-53]. The transition between the MR and RR is really important. Von-Neumann and detachment criterion can be used to find out the MR-RR transition. The dual solution region with hysteresis phenomenon formed between the MR and RR [53-57].

In the hypersonic inlet, the boundary layer separation bubble occurs at the impingement point of the shock wave on the lip side because of high Mach number. In upstream of this bubble, an interaction between the shock wave and induced shock (because of separation) take place. In downstream, reattachment of the Boundary Layer took place and caused a recompression shock.

### *C. Unstart because of Heat Release*

The heat release is one of the main reason for the unstart which increases the downstream pressure and pushed the shock outside of the inlet. Hieser Curran and Pratt showed that isolator part of the engine might cause the unstart [58]. The excessive heat release in the isolator cause the thermal choking which leads to the unstart. In 2001, Mashio found that thermal choking is one of the reason for unstart [59]. The flow blockage was studied by the Mc Daniel and Edward [60]. They found that the main reason for the blockage was the thermal choking which caused the excessive heat release in an isolator. This also caused the disturbance of a large scale because of the high pressure. This disturbance propagates towards the downstream.

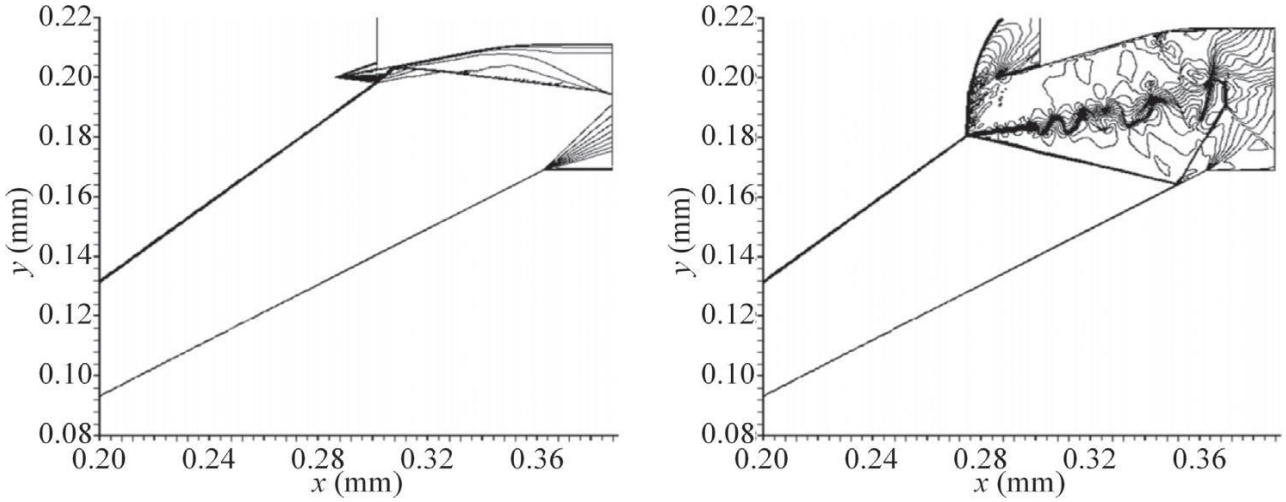


Figure 4. Mach Contour (a) left side with θc=10 deg .(b) right side with θc=15 deg. [20].

The investigation under the more realistic conditions, many researches have been tried to investigate the unstart for the hypersonic under the high enthalpy conditions. In 2000, O'Byrne investigate the relations between flow fluctuation and thermal choking [61]. He was not able to produce a good explanation for the unstart because of the less understanding. In 2013, Laurence studied the different behavior of fluid combustion [63]. He investigates the quasi-steady and transient properties of the flame flow. his study was mainly concern flame flow dynamics.

The influence of the concentrated combustion was studied by the Huang [64]. He found that the intensive combustion increase the shock wave's separation intensity and recirculation zone was produced inflow [65, 66]. He also investigates the combustion under cold flow conditions. The shock train remains at its position under the ignition conditions [67].

### *D. Unstart because of the Back Pressure*

The reasons for the unstart can be found by analyzing the low enthalpy condition of the flow properties. The unstart caused by the back pressure is because of rises in pressure in downstream. The choking of supersonic flow is caused by this back pressure [68, 69]. The hypersonic engine with multiple modes also has unstart problem. In this type of engine,

downstream pressure rises in one module cause the unstart in other modules by interacting the flow spillage [70]. A shock system is introduced and propagate towards the upstream due to pressure rise in downstream. The leading edge of this shock train interacts with the pressure gradients. Because of this pressure gradient, the shock system moves towards the upstream continuous [69]. If the pressure gradient is less than the pressure rise in downstream than this unstart shock system moves toward the upstream. With the rise of this back pressure, the unstart shock system moves towards the inlet and cause the unstart [71, 72]. In 2009, a very comprehensive study on the quasi-steady and transient propagation of shock system was studied by Wagner [69, 71]. He also measured the effect of oscillations caused by the unstart and measure the pressure on the wall surface. In 2012, Chang also published a study on this oscillation and pressures [73].

## III. Detection of Unstart for Hypersonic Inlet

In air-breathing hypersonic propulsion systems, one of the main reason for failure in recent tests is unstart. In the CIAM/NASA scramjet engine test in 1998, the unstart occurred because of the larger boundary layer separation than anticipated and pressure increase than the design value [10, 107]. The restart is initiated by decreasing the flow of hydrogen fuel. The scramjet engine's control system still senses the unstart even after the restart. This is because of an inadequate detection system for unstart. Another test for efficient and low-cost scramjet engine was carried out by the HyCAUSE. They investigate the unstart phenomenon for the engine [12]. They found that inlets unstart and start happen many times as shown by the pressure data [13]. During the flight test of X-51A, the unstart is detected by the control system and system took measurement to restart the inlet [74].

For hypersonic aircraft, an inlet unstart protection system is used to avoid the unstart. The unstart protection system consists of three parts, Unstart Detection, Identification of patterns of inlet unstart, Unstart Margin establishment and Control measurement for the Unstart.

Failure of any part of the protection system leads to the unstart of the engine. Therefore, unstart protection helps to find out the problems and has been widely studied. In scramjet, inlet unstart ejected the shock train from the inlet [75]. This unstart happens because of the large increase in the back pressure with the change in the angle of attack [76]. The effects of the unstart on the initial flow field can be described in two aspects [77]. Steady and transient characteristics. In steady characteristics, shock train affects the flow structure as well as the pressure. The back pressure produced to create the bubbles because of boundary layer separation. This phenomenon is seen in the CIAM flight test. In transient characteristics, intense oscillation produced because of

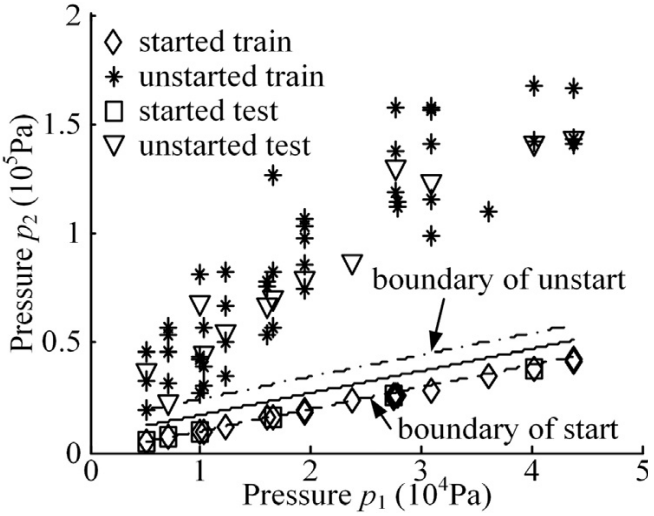


Figure 5. Test and Trains for the Hypersonic inlet's Start or unstart [81].

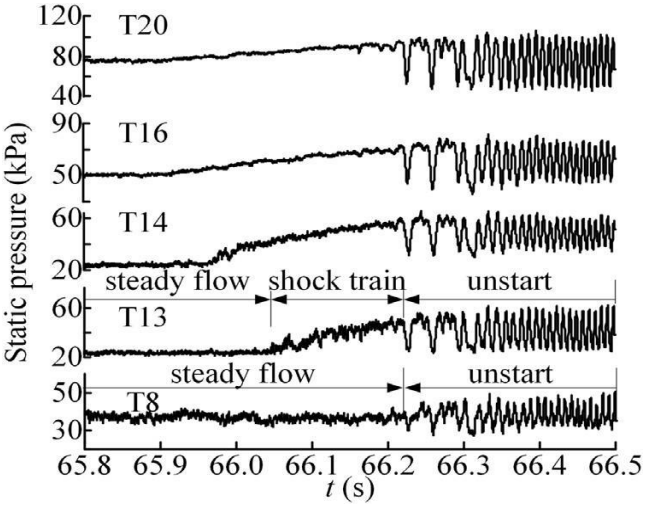


Figure 6. Comparison of the results of frequency analysis for the start and unstart flow [85].

unstart. The flow is affected by the separated shock movement to upstream. This also changes the oscillation characteristics. Based upon these aspects, unstart detection method divided into two types. One steady state pattern classification and second the instantaneous analysis of the information of the parameters.

### *A. Detection of Unstart based upon the steady state information*

The structure of flow for both condition start and unstart are dissimilar. The operating conditions for the freestream with fixed properties can be found at fixed points. But, operating condition for freestream with the variable properties like the angle of attack, Mach number, etc. is very difficult to find at selected monitoring sites. With this high data variation like the inlet surface pressure distribution, the classification of the pattern is quite difficult.

The unstart detection is quite difficult and can be done by classifying the inlet as the unstart/start with the help of artificial intelligence. In artificial intelligence, the selection of the criterions of classification and algorithm is important. The action on the raw input data is based upon the pattern category. This pattern category classified the pattern as the start or unstart condition at the inlet [78]. A transducer is used to sense the classifying object. First, the signals from the transducer are preprocessed than the signal data information is extracted and the classification of the signal is produced [79]. Vapnik proposed an algorithm known as Support-vector Machine Recursive Feature elimination (SVM-RFE) [79]. Fisher also proposed an algorithm linear discriminant analysis (FLD analysis) for the classification of start and unstart [80]. This algorithm was further investigated by Chang.

The classification of the start/unstart was done by using artificial intelligence via different algorithms and feature selection criteria. Figure 5 shows the start and unstart teste samples with the boundary train classification. To obtain the optimal classification, linear discrimination is done by using the FLD analysis for the two classes in multidimensional space [79, 81].

### *B. Detection of Unstart based upon the steady state information*

The detection of the unstart depends upon the sample data and the pattern of the sample data in the pattern classification method. There are other better ways to detect the unstart. Fast response transducers are used to analyze the instantaneous information to detect the unstart. This is a universal method to detect inlet unstart. The prediction of the inlet unstart in this method is based upon the detection of the shock train before reaching the inlet. This detection is done by using some precursors. The detection of the unsteady properties of flow is another way to detect the operating mode of the unstart. Figure 6 shows the typical signal plot [85]. As the pressure is measured at the transducer T-20 at t=65.913s, T-16 at t-65.962s and T-14 at t=66.044s, the pressure increases the downstream to upstream with shock train moving towards upstream. The flow follows the three pattern, steady, shock train and unstart from T-20 to T-14 and flow transform at the T-13 from start to unstart mode. In Figure 6, a phase of big energy level is corresponding to the big buzz (high oscillations). This phenomenon of the high energy level exists for several hundred microseconds. This energy concentration is belonging to the frequency range of 30-150 Hz. The shock train energy is lower than the unstart flow energy and there is an overlap between the frequency range for both cases. The utilization of frequency difference for the detection of the flow pattern is completely possible.

*1) GLR algorithm:*

This Generalized likelihood ratio Algorithm detects the unstart by using a parameter θ. In this method, θ is to be detected. The threshold value is set to be at h=400, which gives the alarm at the t=5.825s [86] as shown in figure 7. In this figure, there are two peaks. One is for the starting of divergence of the buzz frequency and the other is corresponding to the strong buzz oscillations. The GLR

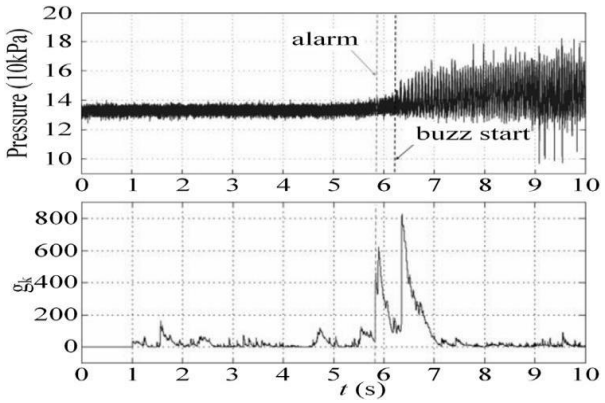


Figure 7. Using the bleeding and GLR algorithm at Ma=2, the detection of big buzz [86].

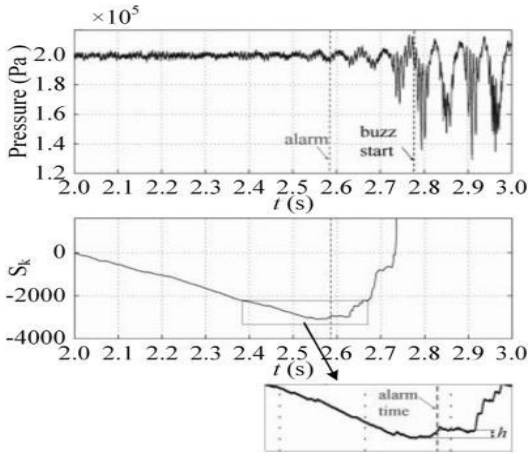


Figure 8. CUSUM algorithm detection of signal [86].

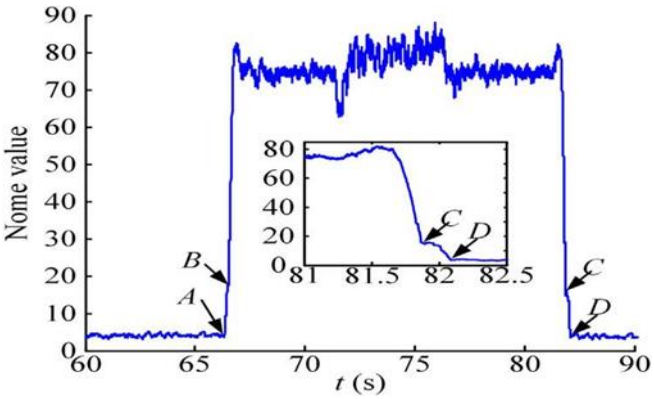


Figure 9. At T-14, the pressure signal using Recursive Fourier Transform [85].

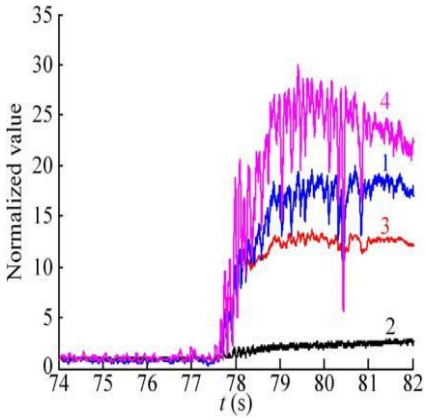


Figure 10. The comparison of the four techniques of the detection of the unstart [87].

algorithm detects the buzz onset 1/10 seconds before starting. The GLR algorithm is very simple, one parameter threshold and general algorithm for use. But the calculation time and memory are much high.

*2) Cumulative Sum Algorithm:*

The cumulative sum (CUSUM) algorithm detection is based on the change in analyzing the signal's probability density [86]. Figure 8 shows the analyzed signal. The CUSUM algorithm is based on two parameters gk and alarm time. The threshold value is set to be h=100 with ta= 2.38s alarm time. This algorithm alarmed at t=0.2 s because he irreversible buzz started when the first normal shock approaches the compression ramp of upstream for the present case [86]. The probability density function's exact value depends upon the changing condition of the signal and quite impossible to find.

*3) Recursive Fourier transform:*

The detection and the prediction of the unstart can be done by using the recursive Fourier transform introduced by Chang [85]. The detection of the unstart for this method based upon the value of the norm value. Norm value for the start mode is lower than the value for unstart mode. Algorithm's threshold value is selected as it detects the only single unstart. Until the shock train reaches the T-14, the start mode's norm value remains stable as shown in Figure 9. An energy level increases rapidly for the big buzz with a range of frequency as discussed in the previous section. The shock train energy level is higher and stronger than the steady flow energy which leads to high norm value. The restarting process caused a small decrease in this high norm value.

The four basic detection techniques, the standard deviation based techniques (STD), the spectrum power based techniques (SPD), derivative-based technique and pressure magnitude based techniques are studied by the Chang [87]. Figure 10 shows the unstart and start mode amplified by the pressure magnitude is feeblest. STD detection is stronger than pressure based detection. The derivative based is stronger than the STD based and the SPD based is strongest among them [87]. The threshold value mainly depends upon the amplification factor. The SPD and STD techniques only detect a few milliseconds before the derivative based technique.

## IV. Control of Unstart for Hypersonic Inlet

Many flight tests resulted in failure because of the unstart. Only the detection of unstart is not sufficient to avoid failure. The only detached unstart can be prevented like in the flight test of X-51A a detached unstart at the inlet was detected. In order to prevent the failure, a restart of the inlet is necessary by suppressing of the unstart. The stable operating mode can

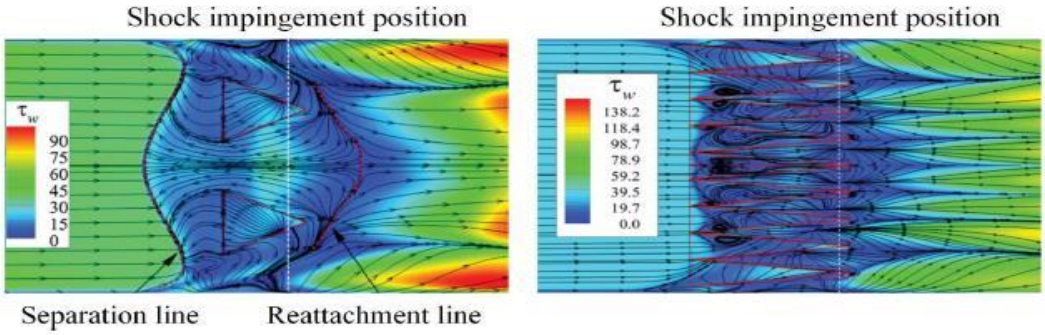


Figure 11. Numerical Simulations results for the plate and micro ramp's shear stress line [91].

be obtained by keeping or pushing the shock train back to the inlet. The unstart can be stopped or delayed by suppressing the boundary separation which slows down the motion of the shock train. If the boundary layer separation's suppression does not affect the shock train motion than the unstart can be delayed by reducing the fuel. Two methods are available for protecting the inlet from unstart, flow control, and feedback control.

*A. Unstart control using Flow Control*

The inlet unstart can be prevented from controlling the flow field. The flow field can be controlled by changing the back pressure. If the backpressure increases, then the shock train shows the resistance which delayed or prevented the unstart at the inlet. There are two ways available for controlling the flow field, vortex generators and bleeding.

*1) Using Vortex Generators:*

Vortex generators can be used to prevent the shock train from exiting the inlet. Vortex generator (VG) creates the vortices in freestream flow which interacts with the boundary layer's low-momentum wall flow. This allows the increase in pressure in the boundary layer without boundary layer separation. The separation induced by the shock can be suppressed by using low-profile VG [88]. These low-profile VG also improve the characteristics of the shock's downstream boundary layer. The increase in back pressure increases the resistance of the shock train which expands the unstart limit [89]. The performance of the ramp was investigated by Lin [89]. The traditional micro ramps were investigated by the Tan. He discovered that these ramps cannot effectively suppress the separation. This is because of the generation of swirling, 3 dimensional and complex flow structure [90].

The computational analysis of the traditional micro ramps shows That a largescale flow separation with the spindle shape exists as shown in Figure 11. By comparing the wall shear lines of the traditional micro ramp with micro-ramp with highly swept configuration close to the side wall, the wall shear lines of the ramp with swept configuration suppressed the flow region significantly and divide the large region of flow separations into small regions. Highly swept configuration micro ramps very effectively controlled the interaction of the shock-boundary layer.

Valdivia studied the wheeler doublets and found that the lower backpressure (7.5% of the mean) unstart delayed [91, 92]. The vortex generators jet causes the unstart because of the blockage from the bow shock of the jet in cross-flow. The inlet isolator prevents the unstart by using the combination of the wheeler doublets and the vortex generators jets. This isolator bounded the pressure disturbance but once the unstart begins it can be reversed with activation of vortex generators jets and wheeler doublets.

*2) By Using Bleeding:*

Another way to control the flow filed is by removing the low momentum flow. this removal causes the weaker interaction between the boundary layer and delayed the bubble separation. This reduction in the boundary layer-shock wave interaction causes the pressure to increase. This pressure rise delayed or prevent the unstart. In German aerospace center (DLR), different studies show that the inlet unstart can be controlled by using bleeding with mass discharge 5.5 % at Ma 6. The bleeding decreases the slope of the pressure rise and wall pressure of upstream for interaction region [93]. The effect of the suction ratio change at the inlet was studied by the Yuan and Liang [94]. They found that when the suction ration approach 10 % than the Mach number for self-start decrease to 3.4 from 4.2 for the hypersonic inlet. The other factor on which the bleeding depends is rate, angle, and position of the bleeding [94-97]. Detection and prediction of the inlet buzz for supersonic were done by the Trapier and Hirschen [98]. They tried to predict using the transient-signal analysis. Trapier and Hirschen established that by using the bleeding device, little oscillation (buzz) can be minimized.

In the hypersonic inlet, the unstart flow's oscillating dominant frequency is less. For the low Mach number inlet, the performance parameters are improved whereas for the high Mach inlet they decrease slightly [118]. The averaged performance parameters are improved for the hypersonic inlet because of the weaker interaction of shock-boundary layer [99]. A new method of controlling the flow field was developed by the Zhan [100]. He used the movable slot-plate to control the mass flow chocking in downstream. The mass flow rate changed by the opening of the movable slot plate.

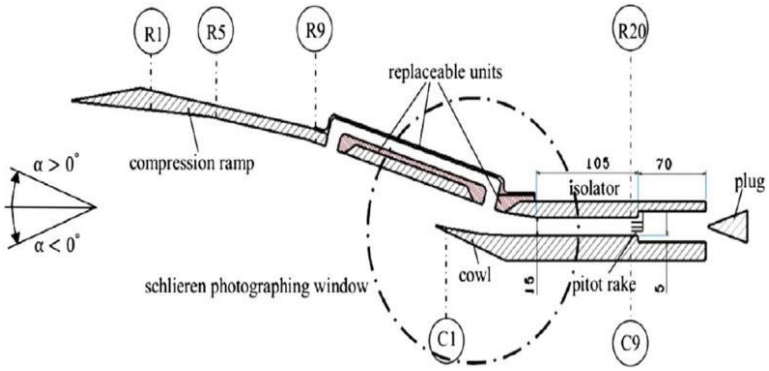


Figure 12. Test Model's Sketch [102].

Another new method proposed by the Tan was the use of the controlled isolators [101]. The shock train leading edge (STLE) oscillates in such a way that it does not almost change the leading shock's position. This oscillating process is suppressed effectively. For the hypersonic inlets, Fluidic control method was introduced by the Wang to increase the self-start ability [102]. The flow separation is well controlled by using Wang's method for the backflow duct as shown in figure 12. Wang found that for the α=4 the Mach number for self-start decreases to the 4.3 from 5. The main purpose of the implementation of the bleeding is to control the flow separation and prevent the unstart by controlling the flow field.

## V. CONCLUSION

Inlet unstart is an important issue faced by the air-breathing propulsion for the hypersonic system. In recent flight tests, unstart occurred frequently and was one of the main sources of failure. Unstart decreases the coefficient of mass capture and total pressure recovery. But the aerodynamic drag and thermal loads increases. The understanding of the unstart is important to control these losses.

In this paper, a summary of different reasons of the unstart, different detection method and the different controlling methods for the unstart are presented which have been studied in recent years. Different methods for pattern classification are also presented. It has been found that the recursive Fourier transform algorithm gives the good detection of unstart but has a high computational cost. Whereas, other algorithms are easy to use but do not give prediction or detection for the unstart. Different suppression and control method has been discussed. The inlet unstart can be prevented or delayed by using the combination of flow techniques like combination of bleeding and vortex generators.

The available methods are not sufficient for the control of the unstart and the is still a large room available for the further studies. For the future work, an experiment can be carried out for the high enthalpy condition with flow combustion coupling with the flow instabilities.

## REFERENCES

[1] Van Wie, David M. "Scramjet inlets." Scramjet propulsion 189 (2000): 447-511.
[2] Xu, Kejing, Juntao Chang, Weixing Zhou, and Daren Yu. "Mechanism of shock train rapid motion induced by variation of attack angle." Acta Astronautica 140 (2017): 18-26.
[3] Holland, Scott D. "Wind-tunnel blockage and actuation systems test of a two-dimensional scramjet inlet unstart model at Mach 6." (1994).Van Wie, D., F. Kwok, and R. Walsh. "Starting characteristics of supersonic inlets." In 32nd Joint Propulsion Conference and Exhibit, p. 2914. 1996.
[4] Im, Seong-kyun, and Hyungrok Do. "Unstart phenomena induced by flow choking in scramjet inlet-isolators." Progress in Aerospace Sciences (2018).
[5] Van Wie, D., F. Kwok, and R. Walsh. "Starting characteristics of supersonic inlets." In 32nd Joint Propulsion Conference and Exhibit, p. 2914. 1996.
[6] Tan, Hui-jun, Shu Sun, and Zhi-Long Yin. "Oscillatory flows of rectangular hypersonic inlet unstart caused by downstream mass-flow choking." Journal of Propulsion and Power 25, no. 1 (2009): 138-147.
[7] S. Im, D. Baccarella, Unstart phenomena induced by mass addition and heat release in a model scramjet, J. Fluid Mech. 797 (2016) 604–629.
[8] C.R.McClinton, J.L.Hunt, Airbreathing hypersonictechnology vision vehicles and development dreams, AIAA Paper 1999–4987
[9] H.J. Tan, R.W. Guo, Experimental study of the unstable unstarted condition of a hypersonic inlet at Mach 6, J. Propuls. Power 23 (4) (2007) 783–788.
[10] E.T. Curran, S.N.B. Murthy, Scramjet propulsion, Prog. Astronaut. Aeronaut. 189 (2001) 462–466.
[11] C.G. Rodriguez, Computational fluid dynamics analysis of the central institute of aviation motors/NASA scramjet, J. Propuls. Power 19 (4) (2003) 547–555.
[12] S.H.Walker, F.C.Rodgers, A.L.Esposita, The Hypersonic Collaborative Australia United States Experiment (HyCAUSE), AIAA Paper 2005–3254
[13] S.H.Walker, F.C.Rodgers, A.Paull, D.M.Van Wie, HyCAUSE FlightTest Program, AIAA Paper 2008–2580
[14] M. Lewis, X-51 scrams into the future, Aerosp. Am. 48 (9) (2010) 27–31.
[15] Dora Musielak. High-speed air-breathing propulsion, AEROSPACE AMERICA, 2011-49.
[16] Xie, Wen-Zhong, Zhong-Ming Wu, An-Yuan Yu, and Shengmin Guo. "Control of Severe Shock-Wave/Boundary-Layer Interactions in Hypersonic Inlets." Journal of Propulsion and Power 34, no. 3 (2017): 614-623.
[17] Leonov, Sergey B., Campbell D. Carter, Brock E. Hedlund, Alec W. Houpt, Timothy Ombrello, and Alexander A. Firsov. "Control of Amplitude and Position of Reflected Shock Wave by Stripwise Plasma." In 2018 AIAA Aerospace Sciences Meeting, p. 0683. 2018.
[18] J.T. Chang, L. Wang, W. Bao, Q.C. Yang, J. Qin, Experimental investigation of hysteresis phenomenon for scramjet engine, AIAA J. 52 (2) (2014) 447–451.
[19] T. Cui, Z. Lv, D.R. Yu, Multistability and complex routes of supersonic inlet start/unstart, J. Propuls. Power 27 (6) (2011) 1204–1217.
[20] X.L. Jiao, J.T. Chang, Z.Q. Wang, D.R. Yu, Mechanism study on local unstart of hypersonic inlet at high Mach number, AIAA J. 53 (10) (2015) 3102–3112..
[21] M.K. Smart, C.A. Trexler, Mach 4 performance of hypersonic inlet with rectangular-to-elliptical shape transition, J. Propuls. Power 20 (2) (2004) 288–293.

[22] B. Sun, K.Y. Zhang, Empirical equation for self-starting limit of supersonic inlets, J. Propuls. Power 26 (4) (2010) 874–875.
[23] M.K. Smart, Experimental testing of a hypersonic inlet with rectangular-toelliptical shape transition, J. Propuls. Power 17 (2) (2001) 276–283.
[24] W.H. Heiser, D.T. Pratt, D.H. Daley, U.B. Mehta, Hypersonic Airbreathing Propulsion, AIAA Education Series, AIAA, Washington, DC, 1994.
[25] S.Molder, E.V.Timofeev, R.B.Tahir, Flow Stating in High Compression Hypersonic Air Inlets by Mass Spillage, AIAA Paper 2004–4130
[26] C.A.Trexler, Inlet Starting Predictions for Sidewall Compression Scramjet Inlets, AIAA Paper 1988–3257.
[27] Zhang, Yue, Hui-Jun Tan, Hao Chen, Wan-Ning Gao, and He-Xia Huang. "Shock Control Method for Hypersonic Inlets Based on Forebody Secondary Flow Recirculation." AIAA Journal 56, no. 6 (2018): 2124-2130.
[28] J.J. Mahoney, Inlets for supersonic missiles, Am. Inst. Aeronaut. (1990).
[29] T.F.O'Brien, Viscous Performance Map of a Blunt Streamline-Traced Busemann Inlet, AIAA Paper 2011–2255.
[30] M.K. Smart, M.K. Trexler, Mach 4 performance of hyper Sonic inlet with rectangular-to-elliptical shape transition, J. Propuls. Power 20 (2) (2004) 288–293.
[31] K. Tani, T. Kanda, K. Kudo, D. Akihisa, Effect of sides-spillage from airframe on scramjet engine performance, J. Propuls. Power 17 (1) (2001) 139–145.
[32] X. Veillard, R. Tahir, E. Timofeev, S. Molder, Limiting contractions for starting simple ramp-type scramjet intakes with overboard spillage, J. Propuls. Power 24 (5) (2008) 1042–1049.
[33] E.H.Andrews, C.R.McClinton, S.Z.Pinckney, Flowfield Starting Characteristics of an Axisymmetric Mixed-Compression Inlet, NASA TM-X-2072, 1971.
[34] A.I.Karanian, C.E.Kepler, Experimental Hypersonic Inlet Investigation with Application to Dual Mode Scramjet, AIAA Paper 1965-588.
[35] D.M. Van Wie, D.A. Ault, Internal flowfield characteristics of a two-dimensional inlet at Mach 10, J. Propuls. Power 12 (1) (1996) 158–164.
[36] T.J.Goldberg, J.N.Hefner, Starting Phenomena for Hypersonic Inlets with Thick Boundary Layers at Mach 6, NASA TN-D6280, 1971.
[37] V.G. Gurylev, Yu.A. Mamet'yev, Effect of cooling of the central body on start-Up separation of the flow at the intake and the throttling characteristics of air scoops at supersonic and hypervelocity velocities, Fluid Mech. Res. 7 (3) (1978).
[38] J.W. Cnossen, R.L. Obrien, Investigation of the diffusion characteristics of supersonic streams composed mainly of boundary layers, J. Aircr. 2 (6) (1965) 485–492.
[39] R.J. McGregor, S. Molder, T.W. Paisley, Hypersonic inlet flow starting in the Ryerson/University of Toronto gun tunnel, Investig. Fluid Dyn. Scramjet Inlets (1992) 1–50.
[40] E.C.Watson, An Experimental Investigation at Mach Numbers from 2.1 to 3.0 of Circular Internal Compression Inlets Having Translatable Centerbodies and Provisions for Boundary Layer Removal, NASA TM-X-156, 1960.
[41] W.A.Vahl, W.I.Oehman, Internal Flow Characteristics of a Fixed-Geometry Induction System Having AxialSymmetry at Mach Numbers from 3.8 to 4.2, NASA TM-X-759, 1963.
[42] K.Sakata, R.Yanagi, A.Murakami, S.Shindo, S.Honami, T.Shizaua, K.Sakamoto, K. Shiraisha, J.Omi, An Experimental Study of Supersonic Air-Intake with 5-Shock System at Mach 3, AIAA Paper 1993–2305.
[43] C.A.Trexler, S.W.Souders, Design and Performance at a Local Mach number of 6 of an Inlet for an Integrated Scramjet Concept, NASA TN-D-7944, 1975.
[44] M.N. Shneider, S.O. Macheret, Modeling of plasma virtual shape control of ram/scramjet inlet and isolator, J. Propuls. Power 22 (2) (2006) 447–454.
[45] M.N.Shneider, S.O.Macheret, R.B.Miles, Nonequilibrium MagnetohydrodynamicControl of Turbojet and Ram/Scramjet Inlets, AIAA Paper 2002-2251.
[46] H.C. Yuan, D.W. Liang, Analysis of characteristics of restart performance for a hypersonic inlet, J. Propuls. Technol. 27 (5) (2016) 390–398.
[47] G. Ben-Dor, Shock Wave Reflection Phenomena, Springer, New York, 2007.
[48] D. Mahapatra, G. Jagadeesh, Studies on unsteady shock interactions near a generic scramjet inlet, AIAA J. 47 (9) (2009) 2223–2232.
[49] N.Bachchan, R.Hillier, Hypersonic Inlet FlowAnalysis at off-design Conditions, AIAA Paper 2004-5380.
[50] S.Boon, R.Hillier, Hypersonic Inlet FlowAnalysis at Mach 5, 6 and 7, AIAA Paper 2006-0012.
[51] S.Boon, R.Hillier, Mach 6 Hypersonic Inlet FlowAnalysis at Incidence, AIAA Paper 2006-3036.
[52] R. Hillier, Shock-wave/expansion-wave interactions and the transition between regular and Mach reflection, J. Fluid Mech. 575 (2007) 399–424.
[53] J.V. Neumann, Oblique Reflection of Shock, Explosive Research Report 12, Navy Deptartment, Bureau of Ordinance, Washington, DC, 1943.
[54] J.V.Neumann, Refraction, Intersection and Reflection of Shock Waves, NAVORD Report 203–245, Navy Deptartment, Bureau of Ordinance, Washington, DC, 1945.
[55] A. Chpoun, D. Passerel, J.C. Lengrand, H. Li, G. Ben-Dor, Mise en évidence expérimentale et numérique d'un phénomène d'hystérésis lors de la transition réflexion de Mach-réflexion régulière, C.R. l' Acad. Des. Sci. Paris 319 (2) (1994) 1447–1453.
[56] A. Chpoun, D. Passerel, H. Li, G. Ben-Dor, Reconsideration of oblique shock wave reflection in steady flows-Part 1. Experimental investigation, J. Fluid Mech. 30 (1995) 19–35.
[57] J. Vuillon, D. Zeitoun, G. Ben-Dor, Reconsideration of oblique shock wave reflection in steady flows-Part 2. Numerical investigation, J. Fluid Mech. 301 (1995) 37–50.
[58] E.T. Curran, W.H. Heiser, D.T. PRATT, Fluid phenomena in scramjet combustion systems, Annu. Rev. Fluid Mech. 28 (1) (1996) 323–360.
[59] S.Mashio, K.Kurashina, T.Bamba, S.Okimoto, S.Kaji, Unstart Phenomenon due to Thermal Choke in Scramjet Module, AIAA Paper 2001-1887.
[60] K.S.Mcdaniel, J.R.Edwards, Three-Dimensional Simulation of Thermal Choking in a Model Scramjet Combustor, AIAA Paper 2001-0382.
[61] M. Doolan, S.R. Olsen, A.F.P. Houwing, Analysis of transient thermal choking processes in a model scramjet engine, J. Propuls. Power 16 (5) (2012) 808–814.
[62] S.J. Laurence, S. Karl, J.M. Schramm, K. Hannemann, Transient fluid-combustion phenomena in a model scramjet, J. Fluid Mech. 722 (2013) 85–120.
[63] S.J. Laurence, D. Lieber, J.M. Schramm, K. Hannemann, J. Larsson, Incipient thermal choking and stable shock-train formation in the heat-release region of a scramjet combustor. Part I: shock-tunnel experiments, Combust. Flame 162 (4) (2015) 921–931.
[64] W. Huang, L. Yan, Numerical investigation on the ram–scram transition mechanism in A strut-based dual-mode scramjet combustor, Int. J. Hydrog. Energy 41 (8) (2016) 4799–4807.
[65] W. Huang, L. Yan, J.G. Tan, Survey on the mode transition technique in combined cycle propulsion systems, Aerosp. Sci. Technol. 39 (2014) 685–691.
[66] W. Huang, L. Jin, L. Yan, J.G. Tan, Influence of jet-to-crossflow pressure ratio on nonreacting and reacting processes in A scramjet combustor with backward-facing steps, Int. J. Hydrog. Energy 39 (36) (2014) 21242–21250.
[67] W. Huang, L. Ma, M. Pourkashanian, D.B. Ingham, S.B. Luo, J. Liu, Z. Wang, Flow-field analysis of a typical hydrogen-fueled dual-mode scramjet combustor, J. Aerosp. Eng. 25 (3) (2011) 336–346.
[68] W. Huang, Z. Wang, S.B. Li, W.D. Liu, Influences of H2O mass fraction and chemical kinetics mechanism on the turbulent diffusion combustion of H2–O2 in supersonic flows, Acta Astronaut. 76 (2012) 51–59.
[69] H. Do, S. Im, M.G. Mungal, M.A. Cappelli, The influence of boundary layers on supersonic inlet flow unstart induced by mass injection, Exp. Fluids 51 (3) (2011) 679–691.
[49] H. Do, S. Im, M.G. Mungal, M.A. Cappelli, Visualizing supersonic inlet duct unstart using planar laser Rayleigh scattering, Exp. Fluids 50 (6) (2011) 1651–1657.
[70] J. Hu, J. Chang, L. Wang, S. Cao, W. Bao, Unstart Coupling MechanismAnalysis of Multiple-Modules Hypersonic Inlet, Sci. World J., 2013-254376.
[71] J.L. Wagner, A. Valdivia, N.T. Clemens, Experimental investigation of unstart in an inlet/isolator or model in Mach 5 flow, AIAA J. 47 (6) (2009) 1528–1542.

[72] W. Huang, Z. Wang, M. Pourkashanian, L. Ma, D.B. Ingham, S.B. Luo, J. Lei, J. Liu, Numerical investigation on the shock wave transition in a three-dimensional scramjet isolator, Acta Astronaut. 68 (11) (2011) 1669–1675.
[73] J.T. Chang, L. Wang, W. Bao, J. Qin, J. Niu, W. Xue, Novel oscillatory patterns of hypersonic inlet buzz, J. Propuls. Power 28 (6) (2012) 1214–1221.
[74] R.Mutzman, S.Murphy, X-51 Development: A Chief Engineer'sPerspective, AIAA Paper, 2011-0846
[75] C.Cox, C.Lewis, R.Pap, C.Glover, K.Priddy, J.Edwards, D.McCarty, Prediction of Unstart Phenomena in Hypersonic Aircraft, AIAA Paper, 1995-6018
[76] J.T. Chang, Y. Fan, W. Bao, D.R. Yu, Y. Shen, Unstart margin control of hypersonic inlets, Acta Astronaut. 66 (1) (2010) 78–87.
[77] S.R. Kulkarni, G. Lugosi, S.S. Venkatesh, Learning pattern classification-a survey, IEEE Trans. Inf. Theory 44 (6) (1998) 2178–2206
[78] R.T.Voland, A.H.Auslender, M.K.Smart, CIAM/NASA Mach 6.5 Scramjet flight and ground test program: analysis results, in: Proceedings of the 35th JANNAF Combustion Subcommittee/Propulsion Systems Hazards Subcommittee/ & Airbreathing Propulsion Subcommittee Joint Meeting. Tucson, AZ.Dec. 7-11 1998
[79] S.R. Kulkarni, G. Lugosi, S.S. Venkatesh, Learning pattern classification-a survey, IEEE Trans. Inf. Theory 44 (6) (1998) 2178–2206.
[81] I.Guyon, N.Matic, V.Vapnik, Discovering Informative Patterns and Data Cleaning, AAAI Paper, 1994-03
[82] D.R. Yu, J.T. Chang, W. Bao, Z. Xie, Optimal classification criterions of hypersonic inlet start/unstart, J. Propuls. Power 23 (2) (2007) 310–316.
[83] R.A. Fisher, The use of multiple measurements in taxonomic problems, Ann. Eugen. 7 (2) (1936) 179–188.
[84] J.T. Chang, R.S. Zheng, D.R. Yu, W. Bao, F. Chen, W. Jiang, R.H. Zheng, Minimization of classification samples for supercritical and subcritical patterns of supersonic inlet, J. Therm. Sci. 23 (4) (2014) 375–380.
[85] J.T. Chang, L. Wang, B. Qin, W. Bao, D.R. Yu, Real-time unstart prediction and detection of hypersonic inlet based on recursive Fourier transform, Proc. Inst. Mech. Eng. G: J. Aerosp. Eng. 229 (4) (2015) 772–778.
[86] S. Trapier, S. Deck, P. Duveau, Time-frequency analysis and detection of supersonic inlet buzz, AIAA J. 45 (9) (2007) 2273–2284.
[87] J.T. Chang, R.S. Zheng, L. Wang, W. Bao, D.R. Yu, Backpressure unstart detection for a scramjet inlet based on information fusion, Acta Astronaut. 95 (2014) 1–14.
[88] D.C. McCormick, Shock/boundary-layer interaction control with vortex generators and passive cavity, AIAA J. 31 (1) (1993) 91–96.
[89] K.C.Lin, C.J.Tam, K.Jackson, P.Kennedy, R.Behdadnia, Experimental Investigations on Simple Variable Geometry for Improving Scramjet Isolator Performance, AIAA Paper 2007-5378
[90] Y. Zhang, H.J. Tan, M. Du, D.P. Wang, Control of shock/boundary-layer interaction for hypersonic inlets by highly swept microramps, J. Propuls. Power 31 (1) (2014) 133–143.
[91] A.Valdivia, K.B.Yuceil, J.L.Wagner, N.T.Clemens, D.S.Dolling, Active Control of Supersonic Inlet Unstart UsingVortex GeneratorJets, AIAA Paper 2009-4002
[92] A. Valdivia, K.B. Yuceil, J.L. Wagner, N.T. Clemens, D.S. Dolling, Control of supersonic inlet-isolator unstart using active and passive vortex generators, AIAA J. 52 (6) (2014) 1207–1218.
[93] S.A.Skebe, Experimental Investigation of Two-DimensionalShock Boundary Layer Interactions, AIAA Paper 1983-0135
[94] H. Yuan, D. Liang, Effect of suction on starting of hypersonic inlet, J. Propuls. Technol. 27 (6) (2006) 525 (in Chinese).
[95] W.X. Wang, H.C. Yuan, G. Huang, D.W. Liang, Impact of suction position on starting of hypersonic inlet, J. Aerosp. Power 4 (2009) 034.
[96] W.J. Chyu, M.J. Rimlinger, T.P. Shih, Control of shock-wave/boundary-layer interactions by bleed, AIAA J. 33 (7) (1995) 1239–1247.
[97] S. Ghosh, J.I. Choi, J.R. Edwards, Simulation of shock/boundary-layer interaction with bleed using immersed-boundary methods, J. Propuls. Power 26 (2) (2010) 203–214.
[98] A. Weiss, H. Olivier, Behavior of a shock train under the influence of boundarylayer suction by a normal slot, Exp. Fluids 52 (2) (2012) 273–287.
[99] C.M. Hirschen, D. Herrmann, A. Gülhan, Experimental investigations of the performance and unsteady behavior of a supersonic intake, J. Propuls. Power 23 (3) (2007) 566–574.
[100] J.T. Chang, D.R. Yu, W. Bao, Y. Fan, Y. Shen, Effects of boundary-layers bleeding on unstart/restart characteristics of hypersonic inlets, Aeronaut. J. 113 (1143) (2009) 319–327.
[101] H.X.Huang, H.J.Tan, S.Sun, L.Ning, A Fluidic Control Method of Shock Train in Hypersonic Inlet/Isolator, AIAA Paper 2014-3846
[102] J.Y. Wang, L.R. Xie, H. Zhao, Y.L. Teng, G.F. Ma, Fluidic control method for improving the self-starting ability of hypersonic inlets, J. Propuls. Power 32 (1) (2015) 153–160.

# Design And Analysis Of Rocket Assisted Take-off High-Speed UAV

Mahrukh M. Hussain
*Engineering Sciences*
*NUST-PNEC*
*Karachi, Pakistan*
mahrukh.mhussain@gmail.com

Dr. Bilal A. Siddiqui, FRAeS,
*MIMechE, CEng*
*Aviation Design Institute*
*Pakistan Aeronautical Complex,*
*Kamra,* Pakistan
air.bilal@gmail.com

Dr. Ataullah Memon
*Electrical Power Engineering*
*NUST-PNEC*
*Karachi, Pakistan*
attaullah@pnec.nust.edu.pk

**Abstract - This paper presents design analysis of a high speed unmanned aerial vehicle (HS-UAV) which is unconventionally launched using hybrid rocket boosters. This allows the UAV to reach the target altitude and velocity rapidly, and then transition to a conventional jet-powered for completion of its mission. Mission statement specified a drone capable of 0.6 Mach flight, range of 30km and endurance of 30 minutes, with various mission payloads such as IR flares, corner reflectors, Luneburg lend etc. Initial sizing was carried out using fixed engine approach after selection of appropriate power plant. Aircraft was designed for Class IV (highly maneuverable aircraft) Level 1 and 2 flying qualities during critical flight phases. Static and dynamic stability analysis was performed using CFD, USAF Stability and Control Datcom as well as Vortex Lattice Methods (VLM). Hybrid rocket propulsion technology is a relatively new but environmentally safe and economically viable. Rocket engine was designed following an iterative process for propellant selection and engine sizing under stringent geometric and weight constraints. Finally, detailed six degree of freedom simulations were performed to verify aircraft performance, especially in the launch phase.**

**Keywords—aircraft design, hybrid rocket engine, rocket assisted takeoff (RATO), target drone, high subsonic**

## I. INTRODUCTION

Unmanned Aerial Vehicles (UAVs) also known as drones, robot-planes, pilotless aircraft, remotely piloted vehicles or aircrafts (RPVs or RPAs) are growing and diversifying their application in various civilian and military avenues. They are available in spectrum of classes, ranging from difference in functionality, areas and mode of operations, lift mechanisms and performance characteristics. Fixed wing UAVs can be boosted in the launch phase relieving the need for a runway and enabling a quick take-off. This is done by means of catapults (steam, gas or electromagnetic) or rocket assisted take-off systems (RATO). In this paper, we present preliminary co-design of a high-speed rocket assisted aerial target vehicle.

Contrary to conventional solid and liquid rocket engines, the cutting-edge technology of "Hybrid Rocket Engine" employs the use of solid fuel and liquid / gaseous oxidizer to produce high amount of thrust in a green or environment-friendly manner. It is being actively pursued by majority of reputable universities such as Stanford University and Technical University of Munich, and organizations like NASA, Space X and Virgin Galactic.

UAVs and Hybrid Rocket Engines have taken the world's attention and extensive research is being carried out globally in these two areas. This HS-UAV study is utilizing the successful characteristics / application of UAVs and hybrid rockets together. It will aid in the development of similar local technologies and can greatly augment the drive towards self-reliance in the field of UAV and booster rocket design. It can greatly augment the drive towards self-reliance in the field of UAV design and manufacturing. The use of such UAVs shall not be limited to monitoring and surveillance activities, but rather more high-tech applications as mentioned in the areas of application. Moreover, rockets assisted launch is an enabling technology for the Pakistan Navy for runway-free, ship-based UAV launch system.

## II. UNMANNED AERIAL VEHICLE DESIGN

### A. Mission Profile

The objective is to design a high speed and light weight fixed-wing UAV to be used for high cruising velocities and high-altitude missions. Following design specifications are selected for the case study of HS-UAV:

| | |
|---|---|
| Altitude | > 5,000 m (15,000 ft) |
| Speed | 100 -200 m/s (290-485 knots) |
| Endurance | > 30 min |
| Range | 30-50 km (16-27 nautical mile) |
| Payload | Chaff, flare, IR towed target |
| Other requirements | Night flying capability, composite airframe, multiple object tracking, telemetry |

### B. Review of Existing HS-UAVs

There are not many existing HS-UAVs with similar performance criteria. A review of available data establishes the following characteristics common to all of them:

a) Launched by either:
   a. Pneumatic catapult
   b. Rocket boosters (RATO / JATO)
b) Recovered by parachute
c) Powered with turbojet engines

Table 1 depicts some data related to existing HS-UAVs. It lends some insights, despite the varying capabilities and configurations of systems cited:

a) Thrust to weight ratio (T/W) of all systems lies in range of 0.54-0.68, with an average of 0.6.
b) Wing loading (W/S) of all systems lies in range of 45-65 lb/ft2, with an average of 55 lb/ft2.
c) Wing aspect ratios (A) lie in the range of 3-6, with an average of around 4.5.
d) Rate of climb of most HS-UAVs is about 5,000 ft/min.

Besides these similarities aircraft configurations and geometries varied greatly.

TABLE 1 REVIEW OF EXISTING HS-UAVS

| HS System | L (ft) | Wing Span (ft) | Weight (lb) | Turbojet Engine | Max V. (kt) | Alt. (ft) |
|---|---|---|---|---|---|---|
| Ryan Firebee (USA) | 22.0 | 13.0 | 2,500 | 1,700 lbf x 1 | 600 | 60 |
| Raytheon MQM-107 (USA) | 18.0 | 10.0 | 1,465 | 830 lbf x 1 | 516 | 40 |
| Northrop Chukar (USA) | 15.0 | 7.0 | 595 | 240 lbf x 1 | 540 | 40 |
| Nord CT20 (France) | 18.0 | 10.3 | 1,455 | 880 lbf x 1 | 485 | 40 |
| QinetiQ Banshee 110 (UK) | 10.0 | 8.2 | 210 | 120 lbf x 2 | 390 | 26 |
| QinetiQ Banshee 80 (UK) | 10.0 | 8.2 | 205 | 88 lbf x 2 | 350 | 26 |
| Mirach 100/5 (Italy) | 13.0 | 7.5 | 725 | 350 lbf x 2 | 530 | 40 |
| Mirach 40 (Italy) | 8.0 | 5.0 | 150 | (unknown) x 1 | 390 | 26 |
| TAI Şimşek (Turkey) | 11.0 | 5.0 | 165 | 90 lbf x 1 | 350 | 30 |
| Denel Skua (South Africa) | 19.5 | 11.7 | unknown | (unknown) x 1 | 570 | 36 |
| HAL Lakshya (India) | 7.8 | 16.4 | 1,554 | 840 lbf x 1 | 470 | 30 |

### *C. Engine Selection*

The primary factor driving the design of HS-UAV is selecting a powerful turbojet engine which is both available and efficient. After enquiring with vendors, the CYS-40WP is selected. This single stage axial compressor and turbine combination has following specifications:

TABLE 2 CYS-40WP ENGINE SPECIFICATIONS

| S. No. | Property | Value |
|---|---|---|
| 1 | Engine Diameter (in) | 6.06 |
| 2 | Engine Length (in) | 16.50 |
| 4 | Weight (lb) | 15.50 |
| 6 | Thrust (lb) | 90.00 |

### *D. Preliminary Sizing*

Preliminary sizing is done using Raymer's approach[1], based on fixed engine above. Weight estimation is summarised as below:

| Weight | Gross Take-Off | Fuel | Empty | Payload |
|---|---|---|---|---|
| | 165 lb | 33 lb | 82 lb | 50 lb |

Guidelines developed from the review were utilized for wing sizing. According to the same data the length of fuselage was calculated using a correction factor of 1.22:

$$L_f = 1.22 \times 0.8 W_0^{0.44} = 10\ ft \quad (1)$$

Using a fineness ratio of 12, the fuselage diameter is found to be:

$$d_f = \frac{1}{11.9} \times L_f \cong 0.85\ ft \quad (2)$$

An ogive nose cone design is used for HS-UAV due to favorable drag characteristics at high speeds involved.

An unconventional arrangement of V-tail is adopted in HS-UAV. This tail configuration utilises the two control surfaces projected by V-form which replaces conventional shaped horizontal and vertical surfaces. The V-tail is therefore, lighter in weight and faces less drag (induced and parasitic) due to lesser wetted surface area. The design process follows the design of horizontal and vertical tail separately as projected by the V-Tail components.

Following conventional tail volume coefficients for a fighter jet[2] are selected:

$\forall_{HT} = 0.35, \qquad \forall_{VT} = 0.06$

Horizontal and vertical tail arm is taken at 33% of fuselage length, at the aft most centre of gravity position:

$$S_{HT} = \frac{\forall_{HT} \bar{c} S}{L_{HT}} = 0.24\ ft^2 \quad (3)$$

$$S_{VT} = \frac{\forall_{VT} b S}{L_{VT}} = 0.33\ ft^2 \quad (4)$$

The total area of the vee tail should be:

$$S_V = S_{HT} + S_{VT} = 0.570\ ft^2 \quad (5)$$

Following are empennage and wing parameters:

TABLE 3 SUMMARY OF EMPENNAGE & WING PARAMETERS

| Parameter | Wing | V Tail (included angle of 80°) |
|---|---|---|
| Airfoil | NACA 2412 | NACA 0012 |
| Aspect ratio (A) | 8.25 | 5.92 |
| Taper ratio (λ) | 0.60 | 0.5 |
| Leading edge sweep (ΛLE) ° | 6.91 | 12 |
| Trailing edge sweep (ΛTE) ° | 0 | 0 |
| Planform area ($ft^2$) | 3.55 | 0.57 |
| Span (ft) | 5.41 | 1.84 |
| Root chord (ft) | 0.82 | 0.79 |
| Tip chord (ft) | 0.50 | 0.39 |
| Position | Mid mounted | Top mounted |

### *E. Control Surfaces*

For the designing of control surfaces, following are considered:

- HS-UAV falls in Class IV (Highly maneuverable aircraft).
- Flight Phases are significant to determine flying quality requirement that are different for distinct phases of missions. Taking off, climbing, cruising, descending, and landing are the minimum manoeuvres necessary for a conventional flight mission[3].
- Highest level of acceptability is targeted in designing of control surfaces for ease of flight and flight safety.

A stepwise procedure is followed for aileron and elevator design [3] to reach the desired roll requirements and pitch control effectiveness. For aileron, it is primarily the time ($t_{req}$) taken by an aircraft to roll between two bank angles and elevator is designed by checking its effectiveness and contribution. The layout and control surface configuration are initially established using data of characteristics of control surfaces for several aircraft, against which handling qualities are calculated and compared with the handling quality design requirements for Class IV / III aircraft in different flight phases. It is an iterative process, and was repeated until the handling requirements were sufficiently met.

TABLE 4 AILERON AND ELEVATOR LAYOUT

| Parameter | | Value | |
|---|---|---|---|
| Half aileron span | $b_a/2$ | 0.628 | ft |
| Location of inner edge of the aileron along the wing span | $b_{ai}/2$ | 0.489 | ft |
| Location of outer edge of the aileron along the wing span | $b_{ao}$ | 1.117 | ft |
| Aileron chord | $c_a$ | 0.165 | ft |
| Aileron planform area | $S_a$ | 0.215 | ft2 |
| Aileron maximum deflection angle | $\delta_{Amax}$ | ±12.00 | degrees |
| Elevator span | 1/2 $b_E$ | 0.393 | ft |
| Elevator chord | $c_E$ | 0.196 | ft |
| Elevator planform area | $S_E$ | 0.152 | ft2 |
| Elevator deflection angle | $\delta_{E\,max}$ | ±20.00 | degrees |

Aileron rolling moment coefficient derivative was calculated as below between $y_0$ to $y_i$:

$$C_{l\,\delta_A} = \frac{2\,C_{L\alpha w}\,\tau c_r}{S.b}\left[\frac{y^2}{2} + \frac{2}{3}\left(\frac{\lambda-1}{b}\right)y^3\right] \quad (6)$$

TABLE 5 AILERON ROLLING MOMENT COEFFICIENT

| | | |
|---|---|---|
| Airfoil lift curve slope | $C_{l\alpha}$ | 6.28 per rad |
| e for wing (tapered, nearly elliptic) | 0.8 | |
| Wing sectional lift curve slope | $C_{L\alpha w}$ | 4.82 per rad |
| Aileron rolling moment coefficient | $C_{l\delta A}$ | 0.087 per rad |

Handling qualities were calculated and checked against level 1 qualities in the following cases:

TABLE 6 LATERAL HANDLING QUALITIES

| Case | Low Speed and Altitude | High Speed |
|---|---|---|
| Velocity, m/s | 69 | 197 |
| Altitude, m | Sea Level | 3000 |
| Total desired bank angle $\Phi_{des}$, degree | 30 | 90 |
| $t_{req}$, seconds | **1.1** | **1.0** |
| $t_{req}$, seconds by Level 1, Class IV Aircraft | **1.1** | **1.1** |

Therefore, the HS UAV holds Level 1 handling qualities in terms of lateral control. Elevator effectiveness is the most important criterion for longitudinal control design. It is a representation of longitudinal control powers and is frequently evaluated through the following 3 non-dimensional:

TABLE 7 ELEVATOR EFFECTIVENESS

| | | | |
|---|---|---|---|
| Aircraft pitching moment control | $C_{m\delta E}$ | $-0.24$ rad$^{-1}$ | |
| Osswald Efficiency factor for tail (tapered, nearly elliptic) | e | 0.8 | |
| Airfoil lift curve slope- Tail | $C_{l\alpha}$ | 6.28 rad$^{-1}$ | |
| Tail h sectional lift curve slope | $C_{L\alpha h}$ | 3.02 rad$^{-1}$ | |
| Elevator effectiveness parameter | $\tau_E$ | 0.52 | |
| Dynamic pressure ratio | $\eta_h$ | 0.9 | |
| ***Contribution to the aircraft lift, $CL_{\delta E}$*** | | | |
| $C_{L\delta E}$ | 0.05 | $\Delta C_L$ | 0.96 |
| ***Contribution of elevator to tail lift*** | | | |
| $C_{Lh\delta E}$ | | | 2.30 |

Hinge moment is generated by a control surface and is used to size servo motors moving the control surfaces. Hinge moments for HS-UAV are as below:

TABLE 8 HS-UAV HINGE MOMENTS

| Case | Low Speed | High Speed |
|---|---|---|
| Aileron Hinge Moment $H_a$, Nm | -0.24 | -0.66 |
| Elevator Hinge Moment $H_e$, Nm | -0.21 | -0.57 |

### *F. Stability Analysis*

Stability analysis of the HS-UAV was done using USAF Digital Datcom (Data Compendium) Software to derive the dynamic and static stability coefficients and derivatives.

#### *a) Static Stability:*

To check longitudinal static stability, following curves were obtain for HS-UAV for pitching moment coefficient and the lift coefficient for the 2 designed Mach Numbers. The resulting slope of the plot indicates the desired characteristic of positive static longitudinal stability.

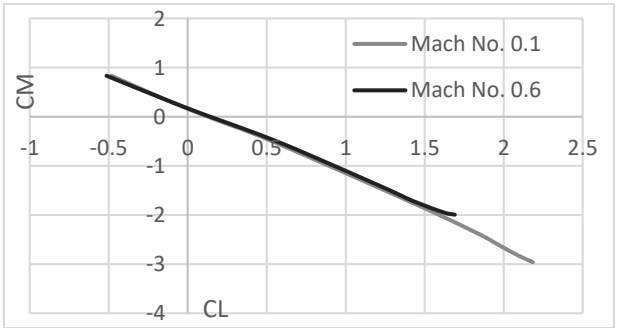


Figure 1 HS-UAV CM vs CL

The static directional stability of an aircraft comprises of accounting of rolling moments due to sideslip. As an aircraft is subjected to positive sideslip angle, static directional stability will be apparent when yawing moment coefficient is positive. This is achieved by the HS UAV case in study as can be seen in Datcom Output values of the coefficient under different flight conditions. Therefore, positive static directional stability is achieved.

#### *b) Dynamic stability*

To check dynamic stability, time period, frequency and damping values of the phugoid and short period mode are calculated as below (Tab. 9) for HS-UAV using stability coefficients and derivatives.

Approximation method is used as provided in Robert Nelson's Flight Stability and Automatic Control. The results for three different cases are as below:

TABLE 10 DYNAMIC STABILITY LEVELS

| Cases | Case 1: Low Speed & Low Altitude | Case 2: High Speed & Low Altitude | Case 3: High Speed & High Altitude |
|---|---|---|---|
| ***Short-period mode, ζsp*** | 0.34 | 0.35 | 0.30 |
| ***Level*** | **2** | **1** | **2** |
| ***Phugoid mode, ζp*** | 0.06 | 0.23 | 0.23 |
| ***Level*** | **1** | **1** | **1** |

The lateral dynamic directional stability analysis was performed for three different cases and the results are provided below:

TABLE 11 LATERAL DYNAMIC DIRECTIONAL STABILITY LEVELS

| Cases | Case 1: Low Speed & Low Altitude | Case 2: High Speed & Low Altitude | Case 3: High Speed & High Altitude |
|---|---|---|---|
| ***Spiral Mode, $t_{1/2}$ (s)*** | 2.81 | 0.26 | 0.38 |
| ***Roll Mode, τ (s)*** | 0.67 | 0.10 | 0.15 |
| ***Level*** | **1** | **1** | **1** |
| ***Dutch Roll, ζ*** | 0.033 | 0.028 | 0.025 |
| ***Dutch Roll, ω*** | 2.24 | 15.9 | 12.9 |
| ***Level*** | **2** | **2** | **2** |

However, it is to be noted that the Spiral mode approximation is often not the most accurate one and should be used with caution. Since the other modes are at the required level, HS UAV is qualifying as directionally stable aircraft.

### *G. 3 Dimensional Views of HS-UAV*

Figure 2 Side View

Figure 3 Top View

Figure 4 Front View

Figure 5 Isometric View

## III. HYBRID ROCKET BOOSTER DESIGN

### *A. Mission Profile*

The objective for the purpose of HS-UAV case-study was to design a booster rocket with a maximum burn-out time of 5 second, to provide zero-length take-off. The UAV shall be positioned on a stand and will be launched, free to fly.

### *B. Impulse / Thrust requirements*

As the launch of UAV will be from an on-ground fixture (stationary), initial velocity is 0. The mass of booster rocket is assumed initially for preliminary design (it is finalised after an iterative process; calculations were made using the assumed mass and the process was reversed for calculating the actual booster rocket mass).

TABLE 12 UAV AND BOOSTER ROCKET MASS

| | | |
|---|---|---|
| **Mass of Hybrid Rocket, $m_r$** | 22 lb | 10 kg |
| **Mass of Rocket & UAV, $m_a$** | 187 lb | 84.83 kg |

Take off velocity is approximated as below:

TABLE 13 TAKE-OFF VELOCITY APPROXIMATION

| | | |
|---|---|---|
| **Stall Velocity** | $Vs = \sqrt{\frac{2gW}{\rho S C_{L_{max}}}}$ (7) | 175 ft/s |
| **Take-off Velocity (est.)** | 1.15 x Vs | 201 ft/s |

Therefore, a take-off velocity of 213 ft/s is selected.

From the two main known design inputs, total mass and velocity required at the burnout, energy requirements and hence the size of the rocket is calculated.

Impulse is given by the equation below:

$$I = m\,(v_1 - v_0) \quad (8)$$

As the launch of UAV will be from an on-ground fixture (stationary), initial velocity is 0.

Using the mass of booster rocket, impulse and thrust required is:

TABLE 14 BOOSTER ROCKET ENERGY REQUIREMENTS

| | | | |
|---|---|---|---|
| **Impulse** | 5514 N.s | 1245 lb.sec | |
| **Time** | T | 5 s | |
| **Thrust** | F | 1103 N | 248 lbf |

The maximum sustainable acceleration for a UAV (and on-board systems) is very significant and is dictated by structural integrity of the frame. The maximum thrust force the UAV can sustain can be calculated by maximum acceleration (a general threshold value) and mass and can be compared with the thrust required to check whether the value is bearable for the UAV or not.

TABLE 15 MAXIMUM FORCE / THRUST

| | | | |
|---|---|---|---|
| **Max. acceleration** | a max | 6gs | |
| **Max. Thrust (Force)** | F max | 5090 N | 1144 lbf |

*C. Rocket Design*

Components of the hybrid rocket booster in study are:

- Pressurized liquid / gaseous oxidiser container
- Solid propellant in combustion chamber
- Separator between them

As the valve opens, the oxidizer is allowed to flow into the combustion chamber followed by vaporization to initiate reaction with the solid propellant. Ignition is provided through appropriate source. Combustion takes place in a boundary layer diffusion flame next to the surface of the solid fuel. Therefore, the high energy exhaust gases generate the required thrust to launch the HS-UAV.

*D. Propellant and Oxidizer Selection*

Owing to the uniqueness of two-phase characteristics of hybrid rocket systems, it is important to comprehensively research propellants.

Since it is a very complex process to cast large sized oxidizer grains, reverse hybrid rocket technology is having less accessibility. Additionally, solid oxidizers are brittle and usually explosive. All benefits of Hybrid Rockets are negated by reverse motors. Therefore, for this study conventional hybrid rocket propellant and oxidizer combinations are considered.

Following table provides an overview on different oxidizers which aids in selecting a feasible one [4]:

TABLE 16 OVERVIEW OF DIFFERENT OXIDIZERS

| S. No. | Oxidizers | | Remarks |
|---|---|---|---|
| 1 | Halogen Oxidizers | $F_2$, $Cl_2$, $BR_2$ | Toxic / Sensitive |
| 2 | Hydrogen Oxides | $H_2O_2$ | Toxic / Sensitive |
| | | H2O | Low Performance |
| 3 | Solid Oxidizers | $CLO_4$, $NO_3$ | Toxic / Sensitive |
| 4 | Oxygen Based | $O_3$ | Toxic / Sensitive |
| | | LOX | Best option |
| | | GOX, Air | Low Performance |
| 5 | Nitric Acid | IRFNA, WFNA | Toxic / Sensitive |
| 6 | Oxides of Nitrogen | NO, $N_2O$, $NO_2$, $N_2O_4$ | Toxic / Sensitive |
| | | N2O | Best option |
| 7 | Other Oxidizers | HAN, $OF_2$, $ClF_3$, $NF_3$ | Toxic / Sensitive |

Comparing the two most common and best [5]:

TABLE 17 LOX VS $N_2O$

| Oxidizers | Liquid Oxygen (LOX) | Nitrous Oxide ($N_2O$) |
|---|---|---|
| ***Density*** | 1.141 g/mL | 1.22 g/mL |
| ***Melting Point*** | -218.8 °C | -90.8 °C |
| ***Boiling Point*** | -182.96 °C | -88.5 °C |
| ***Advantages*** | High Specific Impulse<br>Readily Available<br>2nd Most Common Oxidizer in other hybrid rockets | Most Common Oxidizer in Hybrid Rockets<br>Self-Pressurizing<br>Positive heat of formation<br>Readily Available |
| ***Disadvantages*** | Expensive<br>Not Self Pressurizing<br>Cryogenic | Varying Boil off Pressure<br>Susceptible to Deflagration/Detonation |

Nitrous Oxide has been chosen as oxidizer and is considered a green propellant: it's nontoxic when released to the atmosphere, it contains an adequate oxygen content for a combustion reaction and its positive heat of formation adds to combustion energy [6]. The main advantage of this choice is that Nitrous Oxide is a Self-Pressurizing Propellant. Therefore, it can be injected into a combustion chamber without the aid of turbopumps or other pressurization systems, reducing the weight, cost and complexity of the motor. The required Tank Pressure can be achieved just by heating the tank.

Selection of propellant / fuel involved research of common fuels in terms of their Regression Rate, Density, Specific Impulse, Stability and Availability/Cost. However, the process is not as simple as selecting an oxidizer. The two widely used non-toxic propellants are HTPB and Paraffin wax are compared below [5]:

TABLE 18 PARAFFIN WAX VS HTPB-(R45-M)

| Propellants | Paraffin Wax | HTPB -(R45-M) |
|---|---|---|
| ***Density*** | ~ 900 kg/m3 | ●Density 94.94 kg/m3<br>Mixed with catalysts and curing agents to polymerize<br>Hardener (SUL-4 Resin): lengthen mer chains to make HTPB stiffer, stronger, and harder.<br>Catalyst (Isonate 143-L): Start polymerization process |
| ***Melting Point*** | 50 °C - 70 °C | - |
| ***Boiling Point*** | > 370 °C | - |
| ***Advantages*** | High Regression Rate<br>Sea Wave Effect<br>High Specific Impulse | Inexpensive<br>Chemically stable<br>Readily available<br>Most Common Hybrid Solid Fuel |
| ***Disadvantages*** | Properties can vary drastically<br>Unstable and Soft<br>Premature Melting | Low Regression Rate<br>Complex Curing Ratios |

Paraffin wax are also called alkanes are organic compounds consisting entirely of hydrogen and carbon atoms. The generalised formulation of alkanes is $C_nH_{2n+2}$. They are branched and straight-chained compounds with full saturation. The chemical bonding is through single bonds. Paraffin wax is characteristically grouped into 2 categories, the macrocrystalline and the microcrystalline. Macrocrystalline paraffin waxes are mixtures that consists of mainly of saturated hydrocarbons and smaller amounts of iso-alkanes and cycloalkanes with carbon contents ranging from 18 to 40. Additional to the normal hydrocarbons,

microcrystalline paraffin waxes constitute large quantities of iso-alkanes and naphthenes with long alkyl side-chains. The typical carbon content in microcrystalline paraffin waxes ranges from 40 to 55. Paraffin hydrocarbons are non-toxic, nonhazardous, tasteless, odourless, white in colour, and are in a solid state at room temperature.

The exothermic reaction of nitrous oxide and paraffin wax produces typically unharmful gases such as hydrogen, nitrogen, and carbon dioxide. The reaction products depend significantly on the residence time of the hot gases in the post-combustion chamber. Incomplete combustion reaction produces carbon monoxide and hydrogen, along other minor species, are liberated from the dissociation of the ideal products ($CO_2 + N_2 + H_2O$).

Stanford University in their recent researches has revealed that fuels based on paraffin requires much lesser burning time (3 to 4 times quicker) than rubber fuels. The burning phenomena of these waxes demonstrates formation of a liquid layer as it burns hydro-dynamically unstably, this leads to droplet entrapment into the gas stream. This process enhances the regression rate of paraffin waxes. This high rate of regression property of paraffin waxes decreases the complexities of grain fabrication multiple ports to a single cylindrical port [7].

### *E. Reaction*

Following are the details of combustion:

TABLE 19 COMBUSTION REACTION

| | | | |
|---|---|---|---|
| **Combustion Equation** | $C_nH_{2n+2} + (3n/2 + 1/2)\ NO_2 \rightarrow (n + 1)\ H_2O + n\ CO_2 + (3n/2 + 1/2)/2\ N_2$ | | |
| **N** | 20 | | |
| **OFR** | 4.9751773 | | |
| **No. of Moles** | ***Reactants*** | $C_nH_{2n+2}$ | 1 |
| | | $NO_2$ | 30.5 |
| | ***Products*** | $H_2O$ | 21 |
| | | $CO_2$ | 20 |
| | | $N_2$ | 15.25 |
| **Adiabatic Flame Temperature** | 3431 K | | |

Adiabatic flame temperature is calculated using Cpropep - web online tool that computes rocket motor performance.

### *F. Rocket Calculations*

Calculations of the booster rocket are performed as per George Sutton's book, Rocket Propulsion Elements[8].

| | | |
|---|---|---|
| Exit Velocity | $v_2 = \sqrt{\frac{2k}{k-1} RT_1 \left[1 - \left(\frac{p_2}{p_1}\right)^{\frac{k-1}{k}}\right]}$ (9) | |
| K | 1.2 | - |
| Universal R | 8.314 | kJ/kmol. K |
| R | 180.73913 | J/kg. K |
| $P_1$ | 23 | Bar |
| $P_2$ | 1.01325 | Bar |
| $T_1$ | 3431 | K |
| $v_2$ | 1738 m/s | 5702 ft/s |
| Mass flow of Propellants | $T = m_p \times V$ | |
| Mp | 0.635 kg/s | 1.400 lb/s |
| Throat Area | $\dot{m} = \frac{A_t v_t}{V_t} = A_t p_1 k \frac{\sqrt{\left[\frac{2}{k+1}\right]^{\frac{k+1}{k-1}}}}{\sqrt{kRT_1}}$ (10) | |

| | | |
|---|---|---|
| $A_t$ | 203 mm2 | 0.315 in2 |
| Dia | 16 mm | 0.630 in |
| Exit Area | $\frac{A_t}{A_2} = \left(\frac{k+1}{2}\right)^{\frac{1}{k-1}} \left(\frac{p_2}{p_1}\right)^{\frac{1}{k}} \sqrt{\frac{k+1}{k-1}\left[1 - \left(\frac{p_2}{p_1}\right)^{\frac{k-1}{k}}\right]}$ (11) | |
| $A_2$ | 803 mm2 | 1.245 in2 |
| Dia | 32 mm | 1.260 in |
| Con-di nozzle Area Ratio | $A_2/A_t$ | 4.0 |
| Ratio of Length of the Nozzle to Diameter | 15' conical nozzle | 1.875 |
| L | 30 mm | 1.181 in |
| Specific Impulse | $Isp = \frac{Thrust}{mass\ flow \times g}$ (12) | |
| Isp | 177 kg·m/s | 1280 lb.ft/s |

### *G. Solid Fuel Regression Rate Modelling*

The process of combustion of a hybrid rocket engine fundamentally depends upon the regression rate properties of the propellant. Every combination of propellant has an optimal oxidiser-to-fuel ratio called the stoichiometric ratio. Any changes in the composition of the mixture drastically affects the performance of a hybrid rocket, which requires critical regression rate analysis. There is no universal law governing the regression rate theories. As of now there are a number of theories that have been development for a variety of propellant combinations. Nevertheless, all the theories share strong dependence of solid fuel burning rate on oxidiser flow rate. Following are the most established theories:

- the classical diffusion limited theory by Marxman et al. (1964), and
- the nonclassical liquefying entrainment mass-transfer theory by Karabeyoglu et al. (2002).

This case-study is based on the classical diffusion limited theory which is further simplified into a semi-empirical expression for designing and analysis with practical utility [7].

| | | |
|---|---|---|
| **Semi-empirical Regression Rate** | $\dot{r} = aGox^n$ (13) | |
| **Ballistic Coefficients** | ***a*** | 0.000132 |
| | ***n*** | 0.555 |

The values of ballistic coefficients are selected from the available data of fuel oxidizer combination (Paraffin wax and $N_2O$ – Grosse 2009). Therefore,

| | | |
|---|---|---|
| **Mass flow of propellants** | $m_{ox} + m_f$ (14) | $m_{ox} + (\frac{m_{ox}}{OFR})$ (15) |
| | 0.635 kg/s | |
| **Mass flow of oxidizer** | 0.528 kg/s | |

In order to calculate the mass flux of oxidizer, input port area is required. Therefore, a suitable value of propellant input port area is selected, and further calculations are performed as below:

| **Input Port (propellant)** | | |
|---|---|---|
| $A_p$ | 700 mm2 | 1.085 in2 |
| Dia | 30 mm | 1.18 in |
| Port Length | $L = (\dot{m}_f/N) / (2\pi R_i \rho_f \dot{r}_i)$ (16) | |
| $L_p$ | 275 mm | 10.83 in |

| | | |
|---|---|---|
| Mass flux of oxidizer | $G_{ox,p} = \frac{\dot{m}_{ox,t}}{N_p A_p}$ (17) | |
| $G_{ox}$ | 755 kg / s $m^2$ | 155 lb/s $f^{t2}$ |
| Regression Rate | 5.22 m/s | 0.21 in/s |

Furthermore, injector is calculated for the booster rocket:

| | | |
|---|---|---|
| Injector Area | $A_{inj} = \frac{m_{ox}}{C_d \sqrt{2.\rho_{ox}.p_{ox}.\left[\frac{2}{\gamma_{ox}+1}\right]^{\frac{\gamma_{ox}+1}{\gamma_{ox}-1}}}}$ (18) | |
| Coefficient of discharge of injector holes, $C_d$ | 0.6 | |
| $\rho_{ox,g}$ | 1.98 kg/$m^3$ | 0.061 lb/$ft^3$ |
| Pressure | 2300 KPa | 23 bars |
| $\gamma_{ox}$ | 1.31 | |
| $A_{inj}$ | 500 $mm^2$ | 0.775 $in^2$ |
| $D_{inj.}$ | 25 mm | 0.984 |

### *H. Weight of Propellent*

The "specific impulse" of a propellant is a measure of the amount of impulse that can be produced by burning a unit mass of the propellant. Generally, propellants offer a specific impulse in the range of 180 – 240 lb·s/lb.

$$W_p = \frac{I}{Isp} \quad (19)$$

Division of the impulse required to boost the rocket by specific impulse the propellant can deliver provides an estimation of the total propellant weight that will be used. From required and specific impulse calculated above, weight of the propellant is:

| | | |
|---|---|---|
| **Wp hr** | 31.15 N | 7 lbf |
| **mp hr** | 3 Kg | 6.61 lb |

### *I. Weight of Booster rocket*

For the estimation of the total weight of the booster rocket, following estimation can be done:

Weight of Booster Rocket = 3 x Weight of propellant of booster rocket [9] (20)

Therefore, estimated above the mass of Hybrid Rocket booster is 22 lb (10kg).

### *J. 3 Dimensional Views of Booster Rocket*

Figure 6 HR Booster Side View

Figure 7 Side View - Exploded

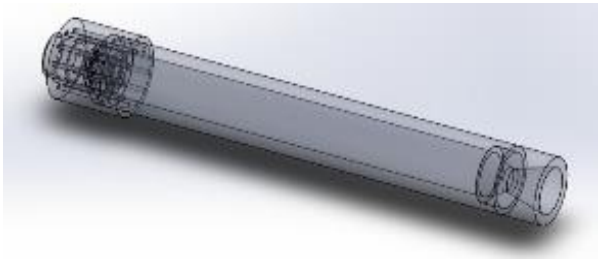

Figure 8 Isometric View

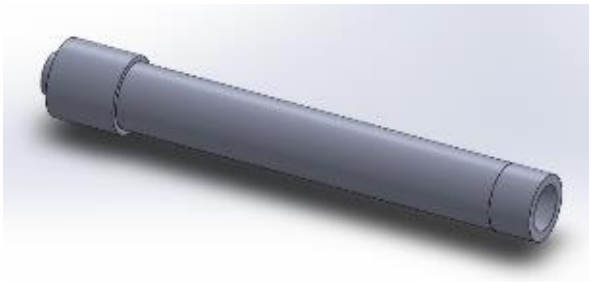

Figure 9 Isometric View

## IV. OTHER SUPPORT EQUIPMENT

To facilitate proper launching of the HS-UAV ground support system can arranged. A fixed-stand or launch-stand should be secured properly on the ground so that it can firmly support the launching of UAV. The stand should further be equipped with a proper holding and realising mechanism may. Positioning of the UAV on the stand is critical, the wings of the UAV must be levelled and with nose at the anticipated elevation angle. The launching-stand can offer different utility options, for example deck-tie-down provisions, and for transportation convenience it may also be retractable. The holding-back releasing mechanism should be equipped to restrain the UAV against high speed winds and the engine thrust at start up and during launching. Furthermore, it also has the provision of automatically releasing the UAV at the instance of RATO unit ignition.

## V. BOOSTER ROCKET ATTACHMENT AND UAV LAUNCH

UAV is to be positioned on the stand with a mounting angle along with a booster rocket attached. At the take-off, ignition of RATO unit initiates the acceleration of the UAV until its own engine takes over the flight. The unit is then released so it does not add to the weight during the rest of the UAV's operation. The size and the number of components needed for the launch makes it logistically easy to use at different locations, even carrying aboard a ship and does not require any significant modifications on the ship deck [10].

The simplest and safest way to attach booster hybrid rocket is rearward of the centre of gravity of HS-UAV. Furthermore, it is critical to ensure that the rocket is angled in such a way that the thrust vector it generates passes through the centre of gravity of the UAV, as displayed below:

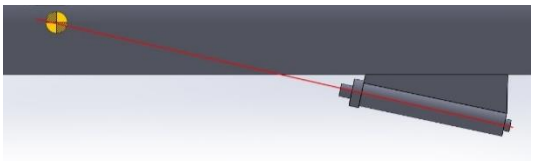

Figure 10 Booster Rocket angled to pass CG of HS-UAV

This will eliminate development of any unwanted moments that may cause divergence of course of the HS-UAV Launch.

In general, UAV launch angle setting is appropriately in the range of 15 to 35 degrees [11]. Therefore, any angle between the range can be utilized for launching the UAV depending on final cruising altitude and payload settings.

## VI. Solid Booster Rocket Case

A case for the use of solid rockets can be compared against hybrid rocket technology to be used for launching HS-UAV. In 'Recent Advances in Hybrid Propulsion' (B. Cantwell, A. Karabeyoglu and D. Altman, 2010), the inherent advantages of the hybrid rocket concept are mentioned as:

- increased safety,
- reduced environmental impact,
- throttlability,
- ability to shut down and be restarted,
- addition of metals or energetic

The concept of Hybrid rocket technology has been available for over 75 years; whereas, it was given spotlight after the 1960s. The main cause of this interest was the nonexplosive nature of the design, which led to safety in both operation and manufacture. The fabrication process of fuel can be set up at any conventional commercial site and even at the launch complex with no danger of explosion. Accordingly, a huge cost savings can be archived both in manufacturing and launching operations. However, for smaller booster rockets the cost saving is not significant but the increase in safety is noteworthy.

Additional advantages of the hybrid over the solid rocket are greatly reduced sensitivity to cracks and debonds in the propellant (manufacturing process impacts), and the ability to thrust terminate/restart on demand.

Furthermore, products of hybrid rocket combustion are environmentally benign compared with conventional solids that generally use perchlorate-based oxidizers. Solid rocket combustion products contain acid-forming gases such as hydrogen chloride. In addition, there are concerns about the effects of low levels of environmental perchlorate, most of which comes from propellant and explosive manufacture [12].

## VII. Conclusion

Throughout the last two decades, momentous developments have been witnessed in UAVs and UAS. The main sponsorship of military in a majority of research and development projects have accelerated the development and deployment UAS in air, sea and ground. Newer designs are being evolved at an exponential rate. Shared purposes and ideas of any such designs are: improved autonomy through innovative sensing and control strategies, enhanced reliability and endurance through fault-tolerant control, advanced materials and high efficiency power plants. This paper provided the initial groundwork for co-design of drone and rocket systems and can be used for further optimization studies to improve performance.

## References


[1] "UAS China Conference & Exhibition 2014", Pakistan Defence, 2019. [Online]. Available: https://defence.pk/pdf/threads/uas-china-conference-exhibition-2014.334256. [Accessed: 14- Apr- 2019].

[2] Raymer, D. P. "Aircraft Design: A Conceptual Approach/Daniel P. Raymer." (1992).]

[3] Sadraey, Mohammad H. Aircraft design: A systems engineering approach. John Wiley & Sons, 2012.

[4] Karabeyoglu, Arif. "Hybrid rocket propulsion for future space launch." Department of Aeronautics and Astronautics, Stanford University, Aero/Astro 50th Year Anniversary (2008).

[5] "Hybrid Propellant Selection 2/13/15", Wsuwp-uploads.s3.amazonaws.com, 2019. [Online]. Available: https://wsuwp-uploads.s3.amazonaws.com/uploads/sites/44/2014/10/14.-Hybrid-Propellant-Selection.pdf. [Accessed: 14- Apr- 2019].

[6] Merrill, Claude. Nitrous oxide explosive hazards. No. AFRL-RZ-ED-TP-2008-184. AIR FORCE RESEARCH LAB EDWARDS AFB CA PROPULSION DIRECTORATE, 2008.

[7] Geneviève, Bernard. "Development of a Hybrid Sounding Rocket Motor." MScEng thesis, Discipline of Mechanical Engineering, University of KwaZulu-Natal, South Africa (2013).

[8] Sutton, George P., and Oscar Biblarz. Rocket propulsion elements. John Wiley & Sons, 2016.

[9] Fahlstrom, Paul, and Thomas Gleason. Introduction to UAV systems. John Wiley & Sons, 2012.

[10] Eriksson, Marcus, and Patrick Ringman. "Launch and recovery systems for unmannedvehicles onboard ships. A study and initialconcepts." (2013).

[11] Wang, Hailong, Jingyu Yang, Zhijie Zhang, Chen Li, Zhihao Zhang, Guangliang Xu, Bowen Zhang, and Gang Wang. "The Design of Lightweight UAV Classification Accelerating Ectromagnetic Launcher." In 2016 International Conference on Modeling, Simulation and Optimization Technologies and Applications (MSOTA2016). Atlantis Press, 2016.

[12] Cantwell, Brian, Arif Karabeyoglu, and David Altman. "Recent advances in hybrid propulsion." International Journal of Energetic Materials and Chemical Propulsion 9, no. 4 (2010).

[13] "Unmanned aircraft systems roadmap 2005-2030", Fas.org, 2019. [Online]. Available: https://fas.org/irp/program/collect/uav_roadmap2005.pdf. [Accessed: 14- Apr- 2019].

# Rim Rotor Rotary Ramjet - Aerodynamic Design and Analysis

Muhammad Zaid Amin
*Institute of Space Technology*
Islamabad, Pakistan
zaidamin22@yahoo.com

Kashif Ahmed
*Institute of Space Technology*
Islamabad, Pakistan
Kashifahmedbutt936@gmail.com

Dr. Khalid Parvez (Co-Author)
HEC Approved Ph.d Supervisor
*Institute of Space Technology*
Islamabad, Paksitan
khalid.pervez@ist.edu.pk

***Abstract*—Rim-rotor rotary ramjet engine (R4E) is a new kind of propulsion system which eliminates the need of compressor and turbines used in the conventional gas turbine and uses a single supersonic circumferential rotor which has ramjet channels integrated on the inner radius of the rim performing compression combustion and expansion inside a single rim-rotor. This approach eliminates the complexity of the system and provides an enhanced power density. This paper is the detailed description of work and procedure carried out for various tasks related to design and analytical calculations and validation of rim-rotor rotary ramjet. Initially quasi-one dimensional model of R4E is designed using inside-out approach and ceramic made rim to generate power of 850KW providing power density of 7.33 KW/kg for a tangential velocity of 884.45 m/s (2.6 Mach) which is almost twice the conventional gas turbines. Analytical analysis addresses shockwave compression, viscous losses, heat transfer effects on the efficiency, inlet and outlet conditions of the ramjet channels and windage losses. CFD Analysis is performed on the ramjet channel to validate the results from analytical calculations. Results confirm the validity and usefulness of this technique in both jet propulsion systems as well as in stationary power generation at least in a limited domain in which combustion and windage losses are not catered completely.**

***Keywords-rim-rotor rotary ramjet engine (R4E); power density; shockwave; windage losses***

## I. INTRODUCTION

Conventional gas turbines works on the Brayton cycle that require a compressor which is driven by the turbine and turbine get energized air from the compressor and combustion chamber for power generation. As the weight of the turbine and compressor will be added to the system so power generation will be too less as compared to the weight of the system. Material temperature limitation also restricts the maximum turbine inlet temperature which directly relates to the power output. The bleed air used for the cooling system of turbine blades further effects the power output of the system. The traditional turbines and compressors also demand maintenance that increases the cost and ultimate life of the system. So to get the overall better efficiency the conventional gas turbines require a complex designs and expensive fabrication.

Here is somewhat different and more appealing approach that uses ramjet channels integrated on the rim of a high speed rotating disk to get power. This will operate by rotating the disk at very high rpm which will accelerate the air particles at tip of the disk to a higher supersonic Mach number in tangential direction. In this technique compression, combustion and expansion is done in a single rotating disk called rotor which will increase the power density and little bit efficiency of the system as overall weight and drag of the system will be reduced. The Power density plays a vital role in the performance of the system applications for small duration and generating more power such as auxiliary power units of aircrafts, jet packs, starter engines for aircrafts, and range extenders for the elastic cars.

To start the system some initial system will be required to rotate the disk initially at higher rpm to get the tangential Mach at the radius of the rotor sufficiently high to get ram air compressed and get positive net thrust by the ramjet channels and after that the system will become self-sustained. So on the basis of its design and principle of working this system is named as Rim-rotor rotary ramjet engine (R4E).

The concept of rotary ramjet system was first introduced in 1950s by the National Advisory Committee for Aeronautics (NACA) which installed the ramjet engines at the tip of the helicopter [1]. In 1998, Ramgen power system introduced a new technique using the ramjet system to get power and thrust. A 1.83-m diameter megawatt-sized rotary engine was developed to burn different fuels, including natural gas, methane, and hydrogen [2].The system was to operate at speed of 500 m/s (1.5 Mach) and it was claimed that efficiency that can compete with the conventional gas turbine would be achieved by this technique. This technique was called Outside-Out technique. No net power output was generated but the reduction of about 43% in the drag was observed in tests. The main reason of failure of this technique was its improper design. First reason was that it contained the metallic rim rotor like other conventional gas turbines which caused loss of heat during combustion and it also could not bear the centrifugal loads which were tensile in nature in this design. As in this outside technique the centrifugal forces forced to high density combustion products outward and less dense products inwards so the good combustion could not be achieved by this design. The Researcher at university of Michigan also introduced a new configuration of Rotary ramjet engines by using R4E approach. In this configuration the ramjet channels are grooved on the inner radius of the rim rotor. Ramjet channels are made up of ceramics roof (stator made up of ceramic) which enable them to withstand to the maximum combustion temperature inside the combustion as well as in the nozzle and also prevents the heat loss during combustion which can hugely contribute in increasing the efficiency of this system [3] but in this design pressure recovery was very low as well as the pressure ratio due to several normal and oblique shockwaves.

The purpose of this paper is to introduce a conceptual design of a rotor assembly which is somewhat more reliable than the previous techniques and then it's validation with analytical calculations.

## II. PROPOSED DESIGN

Somewhat new design of the rotor assembly using Inside-out approach as shown in Fig. 1 is introduced in this paper which will be an more reliable and little efficient than the previous techniques. Normal, bow and oblique shockwaves which were used in the previous approaches have replaced with number of weak oblique shockwaves only a single weak normal shock which will help us to get an impressive total pressure recovery after the diffuser which ultimately will contribute positively in the overall efficiency of the system. Rim rotor assemble is made up of ceramic material which will resist the heat loss during the combustion and combustion efficiency will be enhanced. The ramjet channels are all ceramic made which will allow them to withstand to high temperatures in the combustion chamber and high centrifugal loads due to its high compressive strength. Rotor assembly is trapped in a compartment filled with lighter gas i.e. Helium gas which will reduce drag on the rotor and will reduce the windage losses. Although windage losses will be less in the inside approach but system will face little power loss.

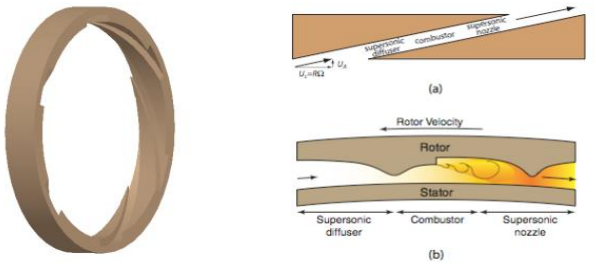


Fig. 1 Rim Rotor Assembly and helical Ramjet Channels of R4E [4]

### A. Design Parameters

Table 1 Design Parameters

| | |
|---|---|
| No of Ramjet Channels | 04 |
| Inlet Mach number | 2.6 |
| Combustion Outlet Temperature | 1850 K |
| Mass flow rate | 2.325 kg/s |
| Rotor Rpm | 23700 Rpm |

## III. ANALYTICAL DEVELOPMENT

Analytical analysis is developed by considering the system as the Quasi-one-dimensional system and assumed that the basic flow parameters and properties are function of one directional only and the change of the properties in other vertical directions is negligible. These assumptions are mainly used in the aerospace propulsion analysis because it gives a clear view of the performance behavior of any kind of propulsion system under the analysis with simplicity. Although, these results cannot be considered as ideal but these can be validated by multi-dimensional analysis and experimentation after the initial validation of theories. On the same note the objective of this paper is to predict the performance and behavior of different parameters of rim rotor rotary ramjet by considering the mass flow rate, indicated power, areas of ramjet channels, pressure recoveries and the length of the ramjet channels. This model is not intended to design the exact prototype model but it gives a wide and logical trend of behavior of operations in different conditions. For further development the studies will have to shift towards the multi-dimensional analysis. The performance parameters are calculated by designing the model according to the theories and principles and the actual validation is proved from the experimental results in the literature.

### A. Model Description

Ramjet channel flow is modeled as a steady flow in a rotating frame of reference. Air fuel mixture is assumed as an ideal gas the reactants chemical composition is assumed as constant during the combustion process. Quasi one dimensional approach is used in modeling the flow from the ramjet. The reactant flow stream enters the diffuser and gets encountered with infinite oblique shockwaves which helps the flow to deaccelerate and get compressed at the expenditure of total pressure. After the combustion the flow is expanded by the nozzle at the atmospheric pressure with area variations. Power indicated is calculated by the difference of momentum between the upstream and downstream of the ramjet channels. Actual shaft power is calculated by considering the different losses during the operation including windage losses. An overall weight of the engine is estimated for the evaluation of rim rotor rotary ramjet engine power density and then compared it to the other conventional gas turbines.

### B. Inlet Model

For inlet we have to select some design conditions i.e. inlet Mach, total and static temperatures and pressures. By considering the inlet Mach of 2.6 the flow will be compressed with weak oblique shockwaves in the inlet of the converging diverging diffuser and will become sonic at throat (Choked). This choking is established with the help of oblique shockwaves instead of area change to get the maximum compression ratio and pressure recovery at the end of the diffuser section.

After considering all the factors required to get the required result the ramjet jet channel is designed with the multiple oblique shock in the diffuser part as shown in Fig. 2.

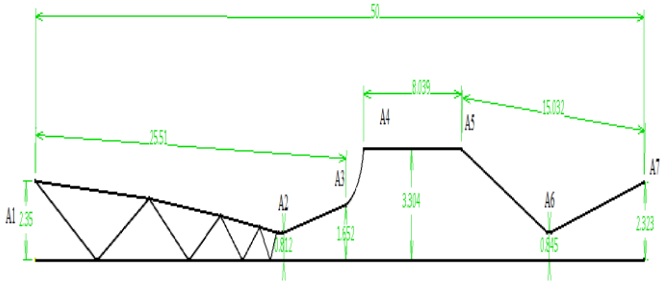


Fig. 2 Ramjet channel designed with reflected oblique shockwaves

In our design we select exit Mach number at which combustion will be easy so, we set exit Mach to be 0.3 and all other properties are calculated through it. At the end of complete inlet design we get following results:

$$\frac{P_{exit}}{P_{inlet}} = 18.28$$

$$\frac{T_{exit}}{T_{inlet}} = 2.309$$

$$\frac{P_{oexit}}{P_{oinlet}} = 0.9753$$

So, we have pressure recovery of 97.53% and exit velocity of 155.33 m/s with an impressive pressure ratio of above 18.

### C. Mach number variation inside the channel

Flow Mach number varies inside the channel depending on several factors including area change, friction, heat addition, heat transfer and local Mach can be calculated by the relation mentioned below.

$$dM = \frac{M}{2}\left[C_1\frac{dA}{A} + C_2\frac{(dh+dQ)}{c_pT} + C_3\frac{4f}{D_h}dl - C_4\frac{d\widetilde{M}}{\widetilde{M}} - \frac{d\gamma}{\gamma}\right] \quad (1)$$

In which,

$$C_1 = -\frac{2\left(1+\frac{\gamma-1}{2}M^2\right)}{1-M^2}$$

$$C_2 = C_4 = \frac{1+\gamma M^2}{1-M^2}$$

$$C_3 = \frac{\gamma M^2\left(1+\frac{\gamma-1}{2}M^2\right)}{1-M^2}$$

Where $c_p$ is the constant-pressure specific heat, $\widetilde{M}$ is the average molar mass, $f$ is the Fanning friction factor, $dh$ is the heat of reaction, $D_h$ is the hydraulic diameter, $dQ$ is the heat transfer and $dl$ is the cell length. [5]

Here we will now discuss each factor except heat addition because combustion modeling is not in our scope of study and further work has to be done on this area.

#### 1) Area Change

The area of each section of the model is defined according to the Mach required at that section and defined by its height and the width.

#### 2) Friction

Friction is a factor that can decrease the Mach and mass flow. It observed that there are not much effect in the R4E system because here the characteristic lengths are very larger than the actual length so there will be no severe effects on the Mach and flow rate .The model assumes an average and reasonable friction factor of 0.003 which is Fanning friction factor f in the above equation. Even immense change in the friction factor does not greatly affect the indicated power which is maximum 4% reduction of power [5] so this precision is acceptable for early conceptual study.

#### 3) Heat transfer

Heat transfer coefficient can be computed using Colburn equation but as in our case the channels are ceramic made which resist the heat transfer so we can neglect the heat transfer for early stages.

### D. Outlet Model

To get the optimum conditions the flow should be expanded to the atmospheric pressure i.e. the nozzle exit pressure should be equalized to the atmospheric pressure for this we could use over-expanded nozzle where there would be the oblique shocks which would be beneficial to change the direction of the flow to get more tangential velocity but in this case there is the risk of formation of normal shock inside the nozzle which can cause pressure loss. Nozzle design condition is set to about 17% under expanded to overcome this risk and the flow is expanded to the atmospheric pressure. But for analytical model the nozzle is assumed as perfectly expanded which will simplify the calculations. In actual cases there would be the combine effect of outlet angle variation, oblique shocks and the expansion fan which will affect the nozzle power ratio which is the ratio of indicated power to the power produced by the perfectly expanded nozzle.

Indicated power of the R4E can be calculated by the expression mentioned below.

$$\dot{W}_i = \dot{m}\omega\Delta(rv_t) \quad (2)$$

Where $\omega$ is the angular velocity, $\dot{m}$ is the mass flow rate, $v_t$ is the tangential velocity in inertial reference frame, $\dot{W}_i$ is the power and $r$ is the mean radius.

### E. Windage losses

The windage losses are induced due to high tangential velocity inside the rotary ramjet channel. To predict the windage losses, a disk model is applied for the rear and front portion of the engine and the cylinder model is used for the radial surface of the rotor. To calculate the drag coefficient by considering the rim rotor as a flat plate the empirical formula of the drag is written below. By considering the rotor assembly trapped inside the compartment filled with helium gas as

$$\mathrm{C_D} = \frac{0.455}{(\log \mathrm{Re_L})^{2.58}} \quad (3)$$

Where $Re_L$ is the Reynolds number in which the characteristic dimension is the unwrapped rim-rotor length and $C_D$ is the drag co-efficient.

Power losses due to drag are calculated by

$$P_{cylinder} = [0.455\rho L\pi R^4]\frac{\omega^3}{\left[\log\left(\frac{2\pi R^2\omega}{\nu}\right)\right]^{2.58}} \quad (4)$$

Where $\nu$ is the kinematic viscosity, $L$ is the width, $\omega$ is the angular velocity, $\rho$ is the surrounding gas constant and $R$ is the radius.

The rear and front portion of the engine cause the windage losses which are model as a disk model by neglecting the inlet and outlet opening of the ramjet on the rim rotor and calculated by

$$P_{disk} = \frac{1}{2}C_m\rho R^5\omega^3 \quad (5)$$

Where $\omega$ is the angular velocity, $\rho$ is the surrounding gas constant, $R$ is the radius and $C_m$ is the moment coefficient. This moment coefficient can be expressed by following empirical relation:

$$Re_R < 7\times10^6 \;\rightarrow\; C_m = \frac{0.073}{Re_R^{0.2}} \quad (6)$$

$$Re_R > 7\times10^6 \;\rightarrow\; C_m = \frac{0.491}{(\log(Re_R))^{2.58}} \quad (7)$$

These relations are based on the Reynolds number (based on the radius of disk). [5]

The surface roughness is also a major cause of windage losses and we have to cater these losses also.[6] Windage losses are predicted by these analytical methods are about 17% (Including roughness) which are well lesser then the previous techniques.

### F. Complete Engine weight estimation

As the major objective of the proposed design was to improve the power density of the system compared to the other conventional gas turbines, the total weight of the proposed rotor assembly along with the accessories including gearbox and structure of the engine is estimated. Rotor weight is estimated by referring to a 3D model of a 65mm diameter prototype [5] in the literature and taken as the initial approximation because in the real case the rotor will be made

up of ceramics or other light materials with different levels of strength so the weight can be remodeled but this approximation will give a good initial weight estimation. Weight of housing is typically taken as thrice of the rotor weight. The weight of accessories is taken 80 g/KW based on the typical gas turbines wright distribution.

## IV. ANALYTICAL RESULTS

To evaluate the potential of the proposed design, quasi-one-dimensional model is used to show the significant analytical proof of the improved power density of the R4E system. Different properties of the gas moving at high speed in the ramjet channels of rim–rotor are evaluated at different sections and then presented to predict the effects caused by the flow physics.

### *A. R4E DESIGN*

The model is design to produce 850 KW power as presented in the Table 3. Hydrogen gas is used as the fuel because it is light weight and give a stable and high flame velocity other gas can also be used for the fuel. The Tangential velocity is limited to the 1500 m/s which can be achieved by using the cooled ceramic materials. The ceramic material (Silicon Nitride) is used which can bear high temperature up to 1850 K without any cooling and can bear up to 1950 with a slight cooling system. Windage losses are estimated to be 17% almost half as of the previous techniques. Helium gas is used in the surrounding of the rotor to reduce the drag to more than 50 % as it is in the atmospheric conditions. [5]

### *B. Properties along the Ramjet*

The variation of the properties along the ramjet as the function of the area change for an inlet Mach 2.6 are shown in the plots shown in Fig. 4-8.

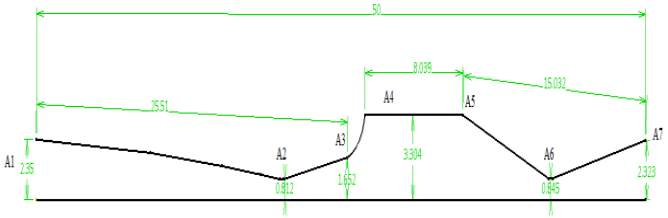


Fig. 3 Ramjet channel length

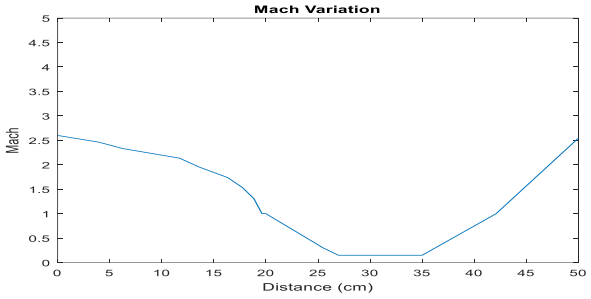


Fig. 4 Mach number variation in the ramjet channel along the rotor length

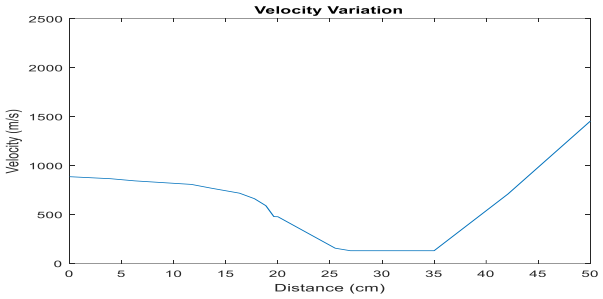


Fig. 5 Velocity variation in the ramjet channel along the rotor length

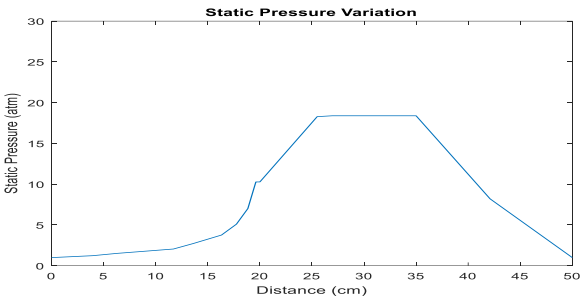


Fig. 6 Static pressure variation in the ramjet channel along the rotor length

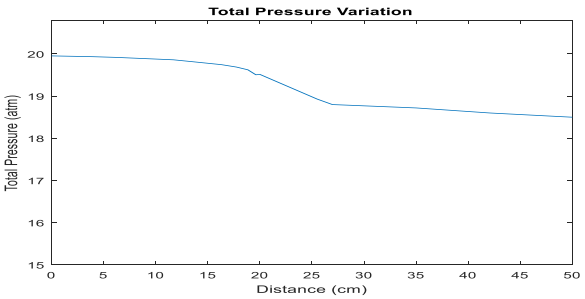


Fig. 7 Total pressure variation in the ramjet channel along the rotor length

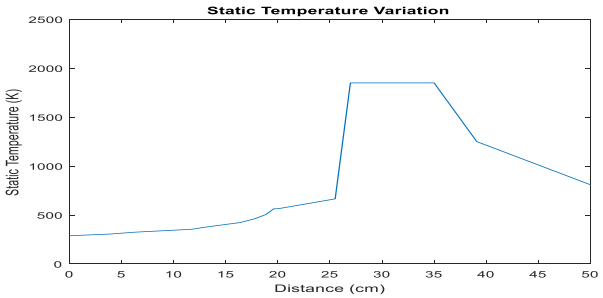


Fig. 8 Static temperature variation in the ramjet channel along the rotor length

### *C. Efficiency Prediction*

The efficiency and power output of the R4E will be less as it is estimated by the expression mentioned above in Equation A and B. there will be some losses due to some factors including heat addition which causes total pressure loss and changes the properties of gas flowing in the channels. Kinetic energy remained in the exited flow is also a major loss in the reaction turbines. Friction is also a major factor which causes the losses. There also losses due to shockwaves in the path of the flow as we want to slow down the flow to Mach 1 at the first throat then there will be significant losses along the shockwaves. Heat transfer is also a factor which causes losses

but it is not of a big concern. The major and most significant factor which causes drastic losses are windage effects which are due to drag so windage losses haves to be minimized to reduce drag and optimizing efficiency.

Windage has also a major effect in the output power density as shown in the Fig. 9. R4E power density can be achieved almost 7.5 if we minimize the windage losses and maximize the structural limits.

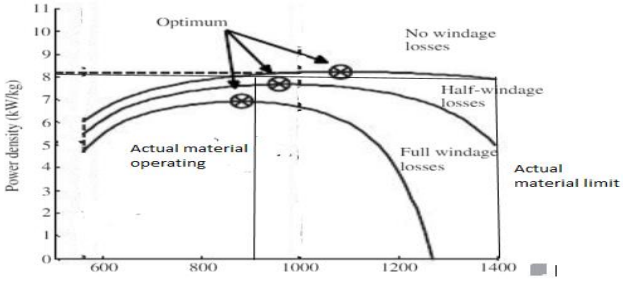


Fig. 9 Power density of R4E at different tangential velocities for different range of windage losses [5]

The losses in the efficiency occurred due to all the factor mentioned above are shown in the Fig. 10 as

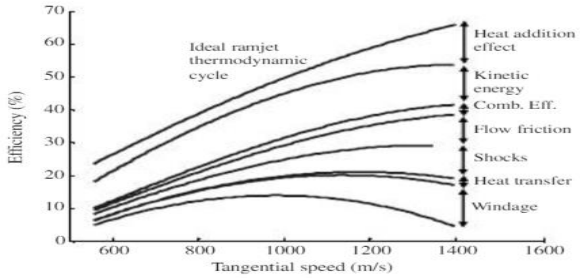


Fig. 10 Loss in the efficiency of R4E system due to multiple factors [5]

After all the optimizations in are resources we can get efficiency of above 25% which is good enough comparatively to the other techniques.

To validate the performance of the R4E design it is compared with two other conventional gas turbines on the basis of the power density and it is clear depicted in the Table. 2, that R4E system gives more than double power density as compared to the other systems.

Table 2 Comparison of Power density of R4E with other engines

| Engine | Power density (without gearbox and accessories) KW/Kg | Power density (with gearbox and accessories) |
|---|---|---|
| R4E | 16.35 | 7.33 |
| Pratt PT6A-66 | 4.4 | 3.1 [7] |
| Rolls-Royce RR500 | 4.7 | 3.3 [8] |

*D. Final Design of R4E*

Table 3 Final design and performance predictions of proposed R4E design

| Parameters | Values |
|---|---|
| Mean inlet diameter | 32.5 cm |
| Rim-Rotor outside diameter | 35cm |
| Length | 20cm |
| Rotor weight | 13 kg |
| Chassis weight | 39 kg |
| Gearbox and accessories weight | 64 kg |
| Indicated power | 1031 KW |
| Windage losses | 17 % |
| Actual power | 850KW |
| Efficiency | 25% |

*E. 3D CAD Model*

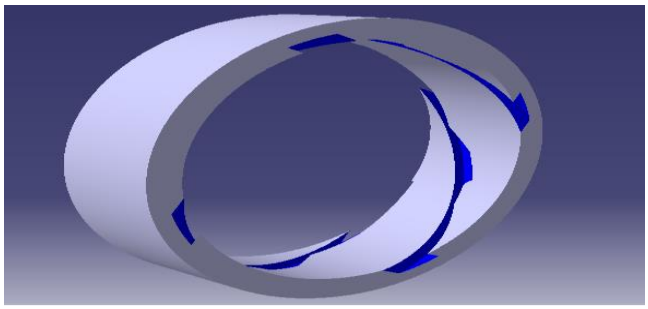

Fig. 11 3D view of rotor of rim-rotor rotary ramjet engine

## V. CFD ANALYSIS

Result gained from the analytical model of ramjet channel are validated through CFD Analysis by using ANSYS Workbench. Mesh is generated of high quality and then flow inside the ramjet channel is simulated in Fluent. The ambient condition are set to be at sea level with incoming Mach number as 2.6.

*A. Inlet*

At inlet boundary conditions are set at the inlet and outlet portion of the diffuser and air is considered to be the ideal gas. The variations of Mach number, velocity, pressure and temperature are computed.

### 1. *Mach Variation*

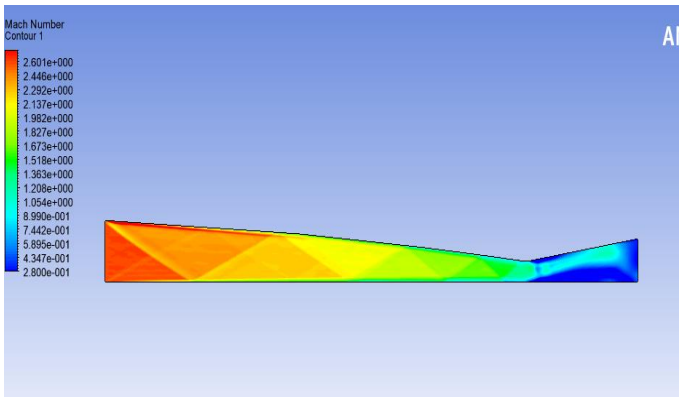


Fig. 12 Mach variation inside the Diffuser by CFD Analysis

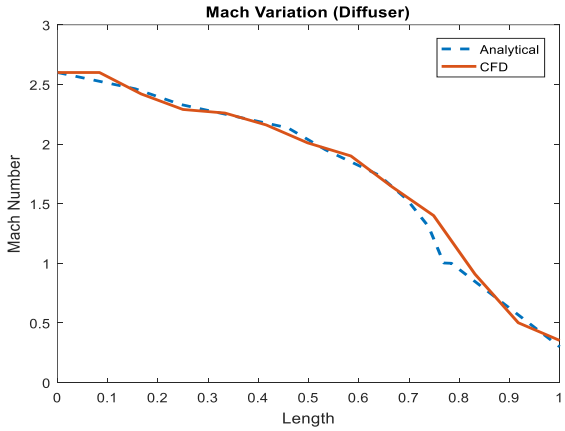


Fig. 13 Mach variation inside the Diffuser

Mach number variation inside the ramjet channel is shown in the figure. Mach number is continuously decreasing due to weak oblique shockwaves and at the end of the throat there is a weak normal shock at the end of the diffuser and we get 0.3 at the diffuser exit. Mach which was required according to the analytical model. There is no significant difference between trends in analytical and CFD results.

### 2. *Velocity Variation*

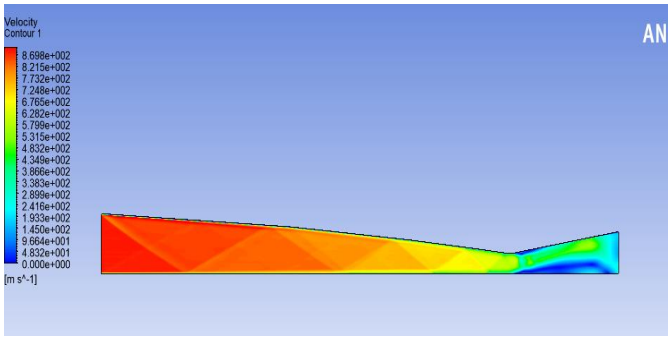


Fig. 14 Velocity variation inside the Diffuser by CFD Analysis

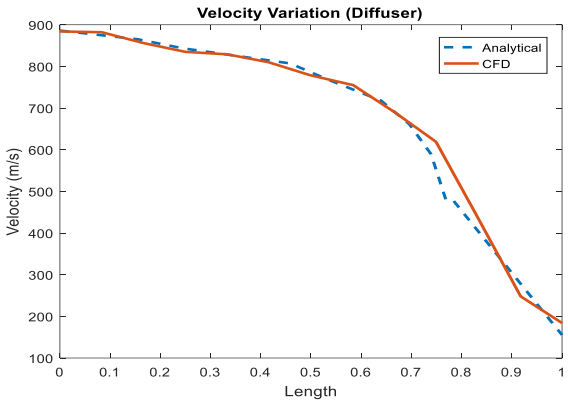


Fig. 15 Velocity variation plot inside the Diffuser

Velocity variation is shown in the figure. Variation of velocity inside the ramjet channel is same as of the Mach number. Velocity is continuously decreasing due to shockwaves and at the end of the diffuser we get velocity of about 70 m/s. There is no significant difference between trends in analytical and CFD results.

### 3. *Pressure Variation*

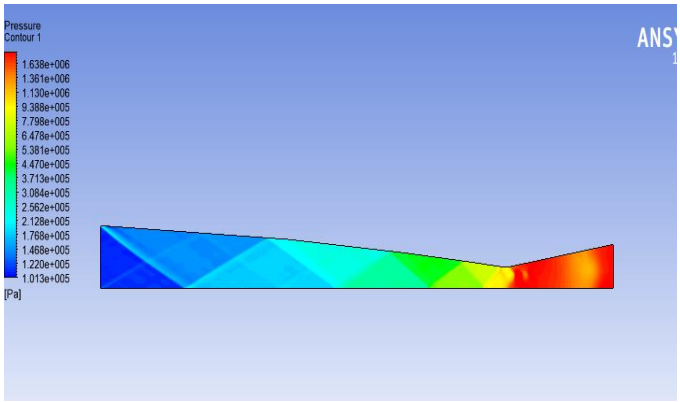


Fig. 16 Pressure (Static) variation inside the Diffuser by CFD Analysis

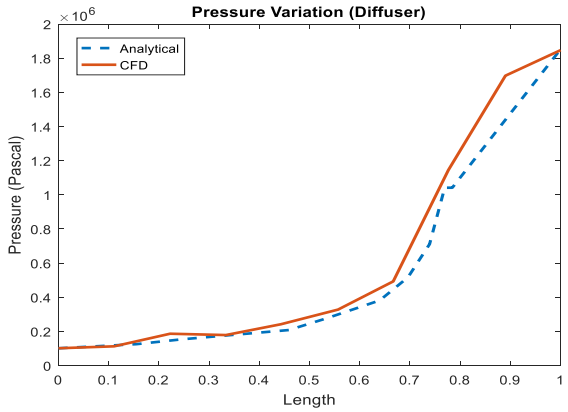


Fig. 17 Pressure (Static) variation plot inside the Diffuser

Static pressure variation is shown in the figure. Static pressure is increasing continuously inside the channel due to shockwaves before the throat and after throat is increases due to area variation. At the end of diffuser we get pressure ratio

of about 18.4. There is no significant difference between trends in analytical and CFD results.

*4. Temperature Variation*

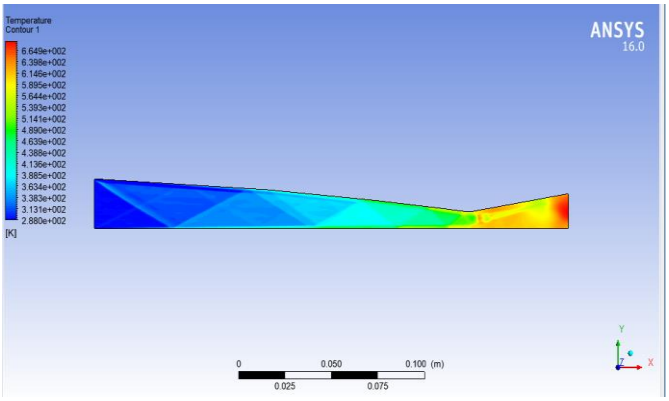


Fig. 18 Temperature variation inside the Diffuser by CFD Analysis

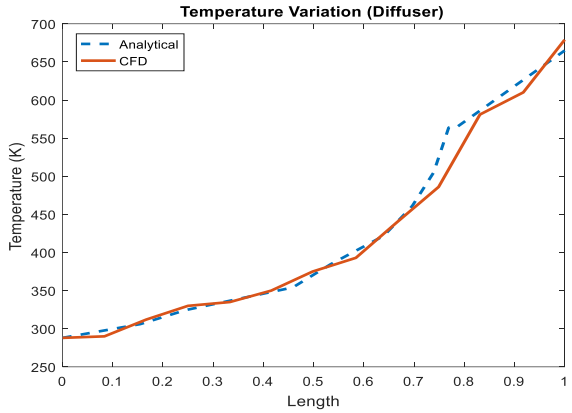


Fig. 19 Temperature variation plot inside the Diffuser

Temperature variation inside the diffuser is shown in the figure. Temperature is continuously increasing due to shockwaves and compression and at the end of diffuser we get about 670. There is no significant difference between trends in analytical and CFD results.

*B. Outlet*

The outlet conditions of the diffuser are given to the inlet of combustion chamber and heat is added of 1208 W/m2 is added to raise the temperature inside the combustion chamber to 1850K. Temperature inside the combustion chamber is considered as constant as combustion is not modelled analytically. Variation of Mach, velocity, pressure and temperature is computed inside the combustion chamber and nozzle.

*1. Mach Variation*

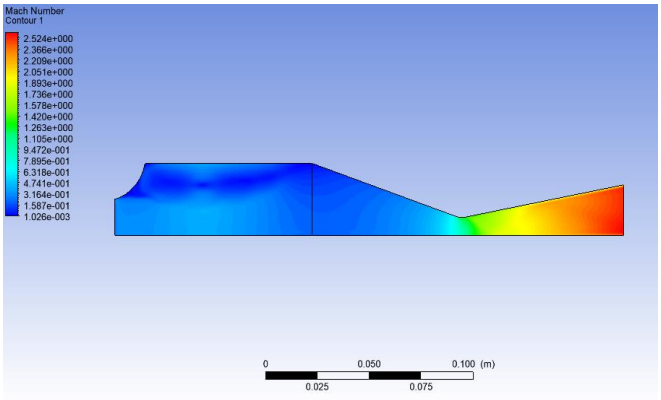


Fig. 20 Mach variation inside the CB and Nozzle by CFD Analysis

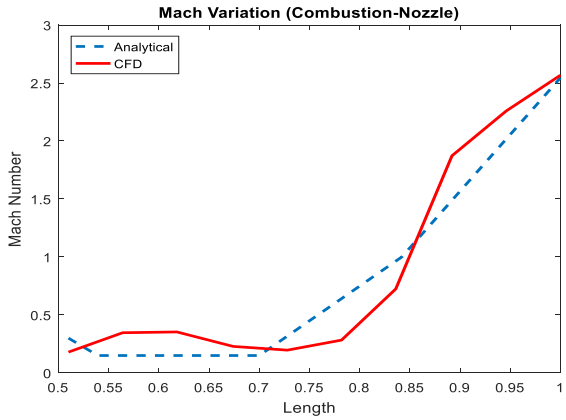


Fig. 21 Mach variation plot inside the CB and Nozzle

Mach number variation inside the combustion chamber and nozzle is shown in the figure. Mach number decreases slightly inside the combustion chamber due to some heat addition affects but it increases continuously in the nozzle section and reaches to 2.52 Mach. There is no significant difference between trends in analytical and CFD results.

*2. Velocity Variation*

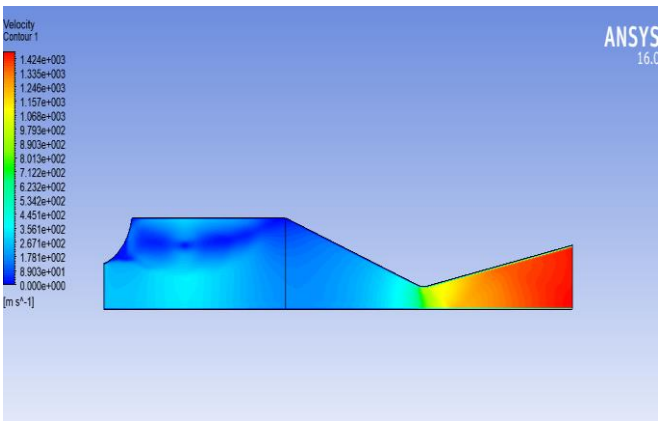


Fig. 22 Velocity variation inside the CB and Nozzle by CFD Analysis

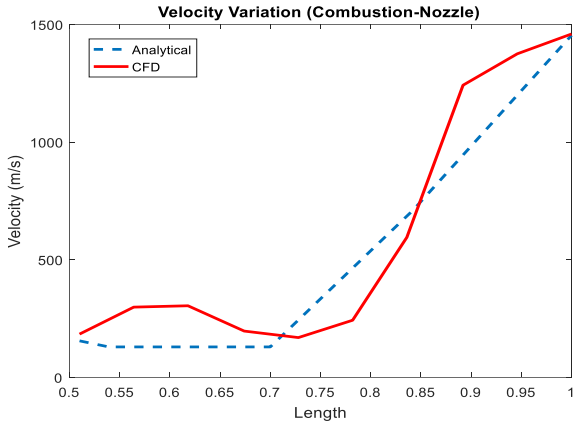


Fig. 23 Velocity variation plot inside the CB and Nozzle

Velocity variation is shown in the figure. Variation of velocity inside the ramjet channel is same as of the Mach number. Velocity at the nozzle exit is around 1440 m/s which is considerably high as compared to the incoming air velocity. There is no significant difference between trends analytical and CFD results.

### 3. *Pressure Variation*

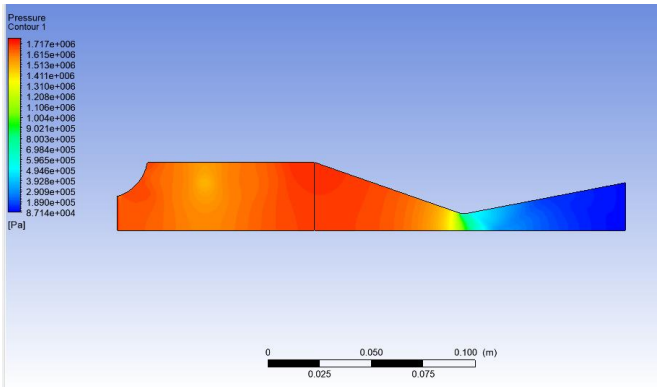


Fig. 24 Pressure (Static) variation inside the CB and Nozzle by CFD Analysis

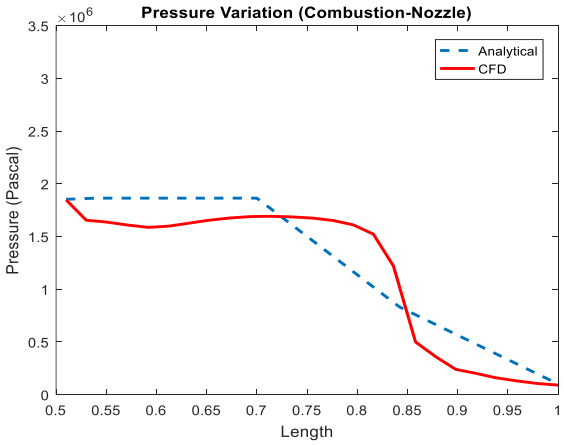


Fig. 25 Pressure (Static) variation plot inside the CB and Nozzle

Static pressure variation is shown in the figure. Static pressure is almost constant inside the combustion chamber but it decreases gradually to the ambient conditions. There is no significant difference between trends in analytical and CFD results.

### 4. *Temperature Variation*

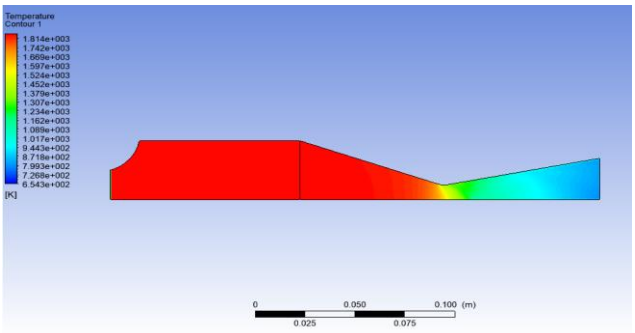


Fig. 26 Temperature variation inside the CB and Nozzle by CFD Analysis

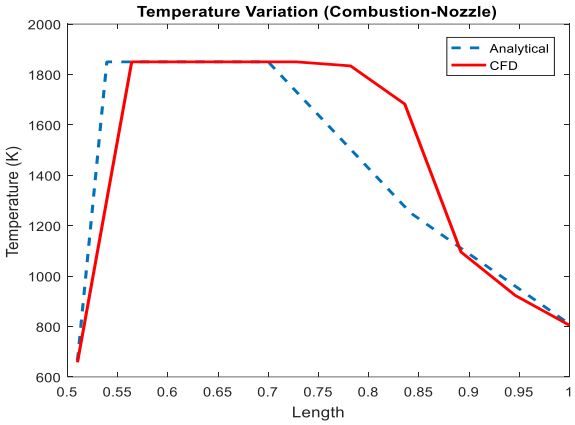


Fig. 27 Temperature variation plot inside the CB and Nozzle

Temperature variation inside the combustion chamber and nozzle is shown in the figure. Temperature increases to its maximum value at inlet of combustion chamber and then it remains constant in the combustion chamber while temperature decreases gradually in the nozzle section due to expansion and becomes around 800K from 1850k.

The results gained from the CFD Analysis are almost identical to the analytical results with some discrepancies due to some boundary layer effects which are not catered completely in analytical calculations. So we can conclude that our design is acceptable and feasible practically.

## VI. CONCLUSION

Quasi-one dimensional aerothermodynamics model is used to model an 850 KW R4E engine by considering all the physics of the system including the variation of different gas properties inside the ramjet channels integrated on the inner radius of the rim-rotor, power losses due to shockwaves, viscous effects, friction, heat transfer and windage losses. It is observed that most of the losses are due to windage losses and the shockwaves followed by the friction and heat transfer which are not significant.

The power density of 7.33 KW/kg is predicted by the model with inlet Mach number of 2.6 with tangential velocity of 886 m/s and the combustion temperature of 1850 K which is far

more than the power density of conventional gas turbines. The indicated power of 1031 KW was calculated by the theoretical formulas and then the actual power output of 850 is estimated after including the power losses of about 20% due to shockwaves and windage losses. In practical model these losses can be more than estimated but these can be minimized up to a limit with proper precautions and measures. Further, the design is validated by Computational Fluid Dynamic (CFD) Analysis of the ramjet channel which showed almost identical trends of each property as it was calculated by analytical calculations.

The R4E design is found to be a good alternative of the conventional old gas turbines to get more power with less cost and weight. In present case the R4E modeled to generate the power in the form of shaft power which can be used in any mechanical application or generating electricity but R4E can also be developed for propulsive applications to produce thrust.

## ACKNOWLEDGMENT

The authors are thankful to Institute of Space Technology, Islamabad, for providing them with best suited conditions and labs to work out the simulations, as well supporting the authors in this project. Authors thank Dr. Khalid Parvez, a senior Ph.D HEC approved Supervisor (Also the co-author) from the department of Aeronautics & Astronautics, (Institute of Space Technology), to enlighten them with his vast experience and knowledge in the field of Turbo machinery. Authors are also thankful to Syed Hossein Raza Hamdani from the department of Aeronautics & Astronautics, (Institute of Space Technology), for sharing their knowledge about CFD.

## REFERENCES

[1] Carpenter, P. J., and Radin, E. J., "Investigation of a Ramjet-Powered Helicopter Rotor on the Langley Helicopter Test Tower," NACA RM-L53D02, 1953.

[2] Ramgen Power System, "Development and Testing of a Pre-Prototype Mach 2 Ramgen Engine Final Report," DOE Award No. DE-FC26-00NT40915, Department of Energy, Washington, DC, 2001.

[3] Dahm, W. J. A., Lapsa, A. P., and Hamlington, P. E., "Inside-Out Rotary Ramjet Turbogenerator," International Energy Conversion Engineering Conference, Vol. 2, AIAA, San Diego, CA, 2006, pp. 1221–1235.

[4] Dahm, W. J., "Rotary Ramjet Turbo-Generator," U.S. Patent US 7,685,824, Jan. 2006.

[5] Picard, M., Rancourt, D., Plante, J., and Brouillette, M., "A HighPower-Density Rim-Rotor Rotary Ramjet Engine, Part 2: One Dimensional Aerothermodynamic Flow Design and Experimental Validation," Journal of Propulsion and Power 2012.

[6] Bruckner, R. J., "Windage Power Loss in Gas Foil Bearings and the Rotor–Stator Clearance of High Speed Generators Operating in High Pressure Environments," NASA TM-2009-215826, 2009

[7] U.S. Department of Transportation Federal Aviation Administration, "Certification Data Sheet EN26NE," 2007.

[8] Rolls-Royce, "RR500 turboshaft specifications," 2009.

# Critical Analysis of Gurney Flaps for Increase of Aerodynamic Performance in Airfoils

Muhammad Khizer Ali Khan
*Department of Aerospace Engineering,*
*College of Aeronautical Engineering (CAE-NUST),*
Risalpur, Pakistan
khizer.khan@cae.nust.edu.pk

Dr. Syed Irtiza Ali Shah
*Department of Aerospace Engineering,*
*College of Aeronautical Engineering (CAE-NUST),*
Risalpur, Pakistan
irtiza_shah@gatech.edu

***Abstract*—The design and safety of any airplane configuration greatly depends upon its aerodynamics characteristics at low speed. A very common and an effective method for lift enhancement is to add a Gurney flap (GF). It is simply a flat plate, placed at the trailing edge on the pressure side of airfoil, in perpendicular direction. Generally, GF tends to increase the maximum lift coefficient, in some cases nearly by 30%. It also decreases zero-lift angle of attack for certain air foils. The original GF was employed by Dan Gurney in his racing car, which helped increase the downward force and hence the traction control. Previous wind tunnel testing has shown that GF increases the lift and aerodynamic characteristics. Further testing showed GF increased the effective camber of airfoil. Trailing edge flap (TEF) employed along with gurney flaps prove to be a better off-design high-lift device as compared to a simple TEF alone design. This papers aims to examine different applications and methods to generate gurney flap effect on diverse range of airfoils. Application may include changing the length of GF with respect to the chord, or deflecting at different angles. In this work, it is aimed to summarize the result of various approaches that are adopted. Some approaches involve solving 2D, steady RANS equation to study the effects of a GF. The impact of GF of different height on the wake and aerodynamic characteristics of various airfoils is also investigated experimentally. Simulations of different case and their subsequent results have shown to be in line with the experimental results. We can appreciate a drastic increase in performance of airfoils with the application of GF. GF has attracted attention due to its diverse application on helicopters horizontal stabilizer, racing cars, wing turbines, rotor blades and short take-off and landing (STOL) aircraft. Hence it remains a valuable topic of research.**

***Keywords— Aerodynamics, Experimentation, Gurney flap, Lift coefficient, Performance***

## I. INTRODUCTION

The gurney flap mechanical device which is used to enhance the overall performance of airfoils. It has a basic construction of a flat plate placed at the trailing edge on pressure side of an airfoil, in perpendicular direction. Benefits of such a device include low cost, allows substantial control by improving the airfoil camber, and requires very less input energy. Flap can be employed in either the upper (suction) or the pressure (lower) side of an airfoil, which as required either alleviates the lift or deteriorates it respectively. The flow field around a gurney flap is greatly altered by the presence of a gurney flap. Despite the simplicity of its design and its small size, the lift characteristics is greatly enhanced by the presence of gurney flap, with only a small penalty of drag. The $C_{L,max}$ increment comes from the effective increase of the camber. Due to the addition of gurney flap, the TE of the airfoil shifts downwards. This causes an increase in the effective angle of attack as compared to a clean airfoil, and hence the lift. Airfoils lift increases with the increase of angle of attack, up to a certain angle after which the airfoil tends to stall by virtue of flow separation on the suction side. With addition of gurney flap at the trailing edge, the flow that separates form the suction side creates a low-pressure wake that interacts with the counter rotating wakes at the pressure side. This improves flow suction at the trailing edge, which mitigates the effect of high-pressure gradient and reattaches the flow. Hence the $C_{L\alpha, max}$ is increased.

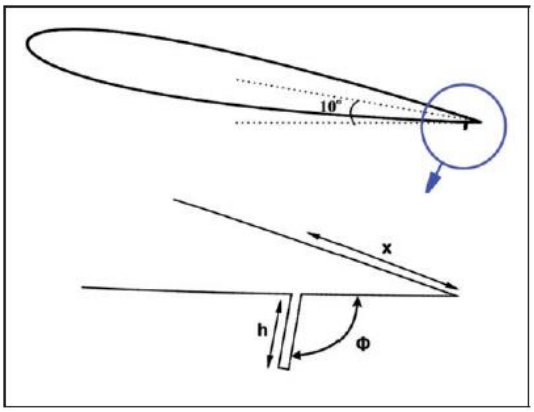


Fig. 1. The geometric parameters of a conventional gurney flap [15]

Danial Gurney is the pioneer of gurney flaps, who first used it on his team racing cars. His drivers reported better control and stability allowing them to turn at higher speeds, which resulted in better lap times. Being unaware of the technicalities of his design, he shared his ideas with Robert H. Liebeck of Douglas Aircraft Company in 1976. Hence Liebeck became the first researcher of gurney flap. He published the results of his experiments his paper [1], where he performance wind tunnel testing of Newman symmetric airfoil with and without gurney flap, yielding surprisingly positive results in increment of lift with were little penalty of drag. The discovery of his simple design triggered the chain of researches with modified versions of the gurney flap being attached at different angle at the trailing edge, of varying heights at different locations of the airfoil [2][7]. Tang et al [4] studied the effect of an oscillating GF at TE. Lee et al. [5] used the gurney flaps

along with trailing edge to investigate the combined effect of both the high lift devices. He used Particle image velocimetry to view the vortex generated at the tips. Gurney flap was the first discovery which was made in the motorsport field and adopted in the aerodynamic industry. Not only fixed wing, but gurney flaps were also studied for their possible use in blades of helicopter rotors, wind turbine etc. Pastrikakis et al [3] investigated the effect of gurney flaps on the rotor blade in forward flight. Researcher have also attempted to use alternate ways of producing the gurney effect on airfoil. Some have resolved to using jets at the trailing edge, while others have chosen to opt for DBD at the trailing edge, that has proven to give some benefits over a conventional gurney flap. Fernandez-Gamis et al. [8] studied the effects of passive devices such as vortex generator on the gurney flaps.

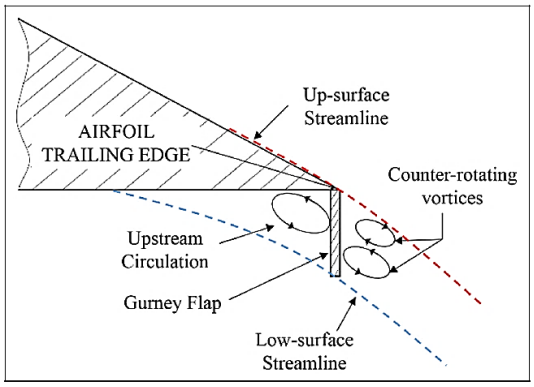


Fig. 2. Schematic shows oppositely rotating vortices being formed downstream of flap. [9]

## II. Analysis of Approaches

### A. *Sensitivity to L-tab chord-wise length*

Saha et al. [10] in their study on NACA 2412 airfoil investigated the effect of gurney flap at trailing edge perpendicular to the chord, with heights ranging from 2%-5% of the chord length. Lift and drag forces were calculated from 0-32 degrees angle of attack using computational fluid dynamics [10]. Flow over complete airfoil was assumed to be an incompressible, viscous, ideal air. Two equation turbulence model namely the K-ε was used for numerical analysis. Based on their investigation, they conclude that gurney flap with 2% of the chord length gave the best performance in contrast to 3,4, and 5% chord length.

They also proposed that the ideal size of the gurney flap should be kept less than the boundary layer thickness which exists at TE as it assists in increasing the lift to drag ratio. The reason for this is that as it can be interpreted from the figure below, the lift curve is linear up to 17 deg angle of attack for all heights of gurney flap. But it's important to see that the lift starts to drop steeply as angle of attack is increase beyond 17 deg, which is the stall angle of attack for the selected airfoil. However, we can see that the stall angle of attack increases with increase in flap height. From this result only, we could conclude that bigger the flap height, the better. However, as we move on to the drag curve, we will realize the drastic drag penalty in all heights of gurney flap except 2%. So if we finally calculate the L/D ratio, it will be most for 2% flap height, as compared to airfoil with no gurney flap or flaps of heights greater than 2% C (Figure 3).

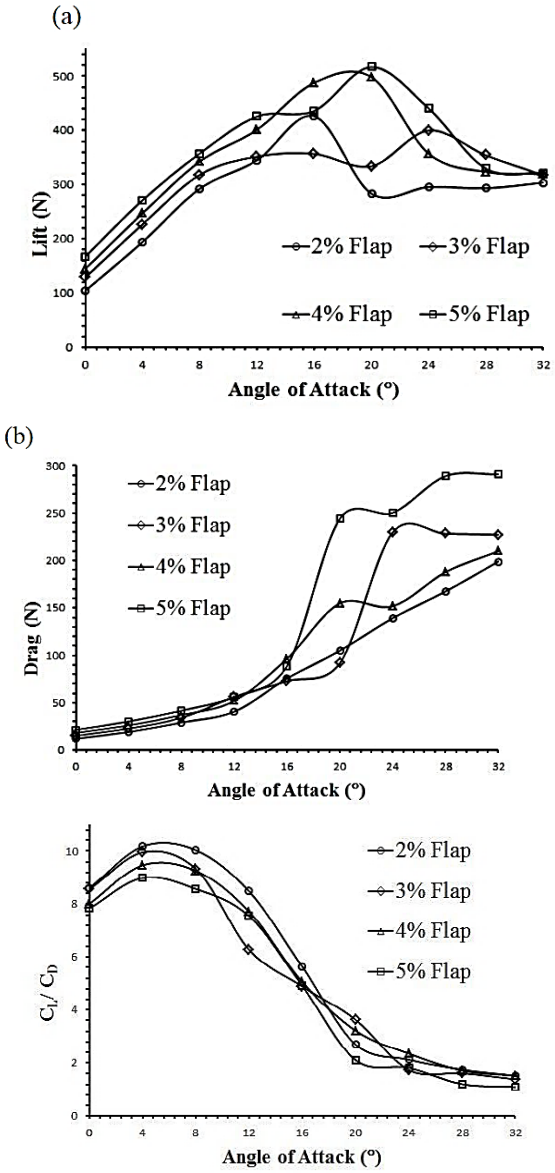


Fig. 3. Figure shows the comparison of force coefficients of different sized gurney flap with respect to angle of attack [8].
(a) Comparison between lift force: Lift is greatest for 2% chord height, but decreases steeply with angle of attacks above 16°.
(b) Comparison between drag force. Drag increases with increasing flap height at higher angle of attacks.
(c) Comparison between lift to drag ratio: 2% flap height has best performance at AoA up to 18°.

Motta et al. [11] also checked the sensitivity of airfoil to the L-tab chord wise length. A tab of double the length of chord was utilized for experimental purposes. Keeping consistency with other authors approach, it was found that a longer tab delayed the stall onset as flow re-attachment is observed. Longer tab appears to be more effective at high stall/angle of attack.

### B. *Sensitivity to Mach No*

Analysis for varying Mach Nos between 0.5-0.7 was carried out by Motta et al. [11], as the maximum lift for a rotorcraft was achieved at 0.7 M, as mentioned in helicopter textbook by Johnson. Li et al. and Yu et al. [12] have also performance the same experiments at transonic regimes. In compressible and transonic regimes, L-shaped gurney flap was found to be operating effectively. In a typical blade of

a rotor craft at low angle of attack, flap is deployed both upwards and downwards. In both configuration it was found useful as upward deflection helped in alleviating the loads whereas downward deflection increased the lift as for a typical gurney flap.

### *C. Comparison with experimental results*

Motta et al. has utilized the experimental results of Li et al. [13] on NACA 0012 airfoil calculated on clean airfoil and with gurney flap on the trailing edge at 4 deg angle of attack. Comparison between the experiments and that of Motta simulations were found quite accurate. In the linear range for a clean airfoil, the difference between the force coefficients is found very less for the experimental and numerical approaches; 3% for lift, 4% for drag force and 7% for pitching moment. For a gurney flap deflected downwards, the difference in the coefficient of life, drag and pitching moment is found to be less than 3%, 5% and 6% respectively. Same has been shown graphically in Fig. 4. Similar results were predicted for stall onset in the two comparisons.

Using PIV and pressure sensors, Motta et al. also compared the pressure distribution and velocity profile over a NACA 23012 airfoil using wind tunnel testing and numerical analysis. A very good accuracy between the two approaches was observed in 2 configurations; no flap and flap deployed. Although the results in this part maybe insignificant, it does verify the approaches used for the remaining portion of the research.

### *D. Design Modification*

Rao et al. [14] carried out numerical analysis of a NACA0012 airfoil with a trailing edge flap, deflected at 15 degrees. The TE flap was then added with a slot for better results. However, due to inconvenience of a slot at the trailing edge, an alternative approach that is the addition of a gurney flap was attached at the trailing edge. Comparison between all these approaches and the standard values for a NACA 0012 airfoil were used for validation purposes. Numerical results were found reliable as they were very close to the standard values and followed the graphical trend. In this study various modifications to airfoil and flaps were studied, in which all tend to increase the lift coefficient accompanied with drag. However, optimal results were obtained with flap at TE with a lot and a gurney flap.

From the results it was evident that the maximum lift was achieved with a flap at 15 degrees and a slot at trailing edge, with a total lift enhancement of 1.87 times. Lift enhancement from a gurney flap was found to increase by a factor of 1.78.

However, if we talk about the drag coefficient, we will see that the over CL/CD would be least for a gurney flap as it increases the drag by only a factor of 1.33 whereas the T.E flap with slot increases it by a factor of 2.22. So, to conclude, if we need maximum lift, then a flap with slot at trailing edge is preferred. However, for low drag applications as well, then the best solution would be the gurney flap.

## III. FLAPPING WING

It is no doubt that the best examples of technological solutions can be extracted from natural creations. Birds for instance, benefit greatly from their flapping wing motion, which it itself a complex aerodynamic mechanism. It however, allows the birds to maneuver quickly, produce lift necessary to stay in air, and the required thrust to move forward. With the advancement in Nano-technology, MAVs or micro aerial vehicles are becoming an upcoming topic of interest. MAVs are better designed with flapping wing motion as it has better aerodynamic efficiency and need less power to take to the air at slow speeds and small Reynolds number. Naderi et al. [15] numerically studied the influence of height, angle at which it is mounted and location of gurney flap on NACA 0012 airfoil in flapping action at Re=1000. Lagrangian-Eulerian numerical algorithm is used along with pressure-based, finite volume finite element approach. It can be employed with moving mesh and moving boundary. It also does not require dissipation/ damping function. The airfoil is oscillation in a sinusoidal fashion about one quarter of the chord. Figure 5 shows the streamlines for a clean and pitching airfoil with flap. Following conclusions can be drawn from their study;

### *A, Flap position*

The influence of changing mounting location of GF investigated by placing the flap 0,0.015,0.03c from the TE keeping the height and angle at 3%c and 90 degrees respectively. Due to the reciprocating motion of the flap, it creates a complicated unsteady, boundary layer event, As shown in Figure 6, the location of the flap has no significant effect on the CL, CD curve. However, due to highest value of $C_L$, one can say that the aerodynamic efficiency will be maximum when the gurney flap is mounted right at the trailing edge.

### *B. Influence of flap angle*

Flap was mounted at an angle of 45, 74, 95 and 135 degrees to study the effect of varying flap angle. As shown in their study, irrespective of the flap angle, the lift was found to be increasing in all cases with respect to a clean airfoil. Although the drag coefficient also increases, however, the relative increases in lift is higher which further increase the lift/ drag ratio for the flapping wing.

### *C. Influence of flap height*

To examine the effect of flap height, flap with varying heights of 1%, 3%, 6%, 8% and 12% are used. Gurney flap is taken to be mounted at TE with a fixed flap angle of 90 degrees. It is observed that in all the cases, both lift and drag increases. However, the increment in lift is relatively greater which subsequently increases the overall L/D ratio. For the case of 1-6% c of flap height, increase in drag is not drastic, however, due to drastic increase in drag for the cases of 6%c and beyond, the $C_L/C_D$ increment is relatively less. To validate their numerical approach, simulation on NACA 0015 clean airfoil in flapping action was carried out. Results were compared with those of Kinsey et al. [16] and found to be in close approximation

.

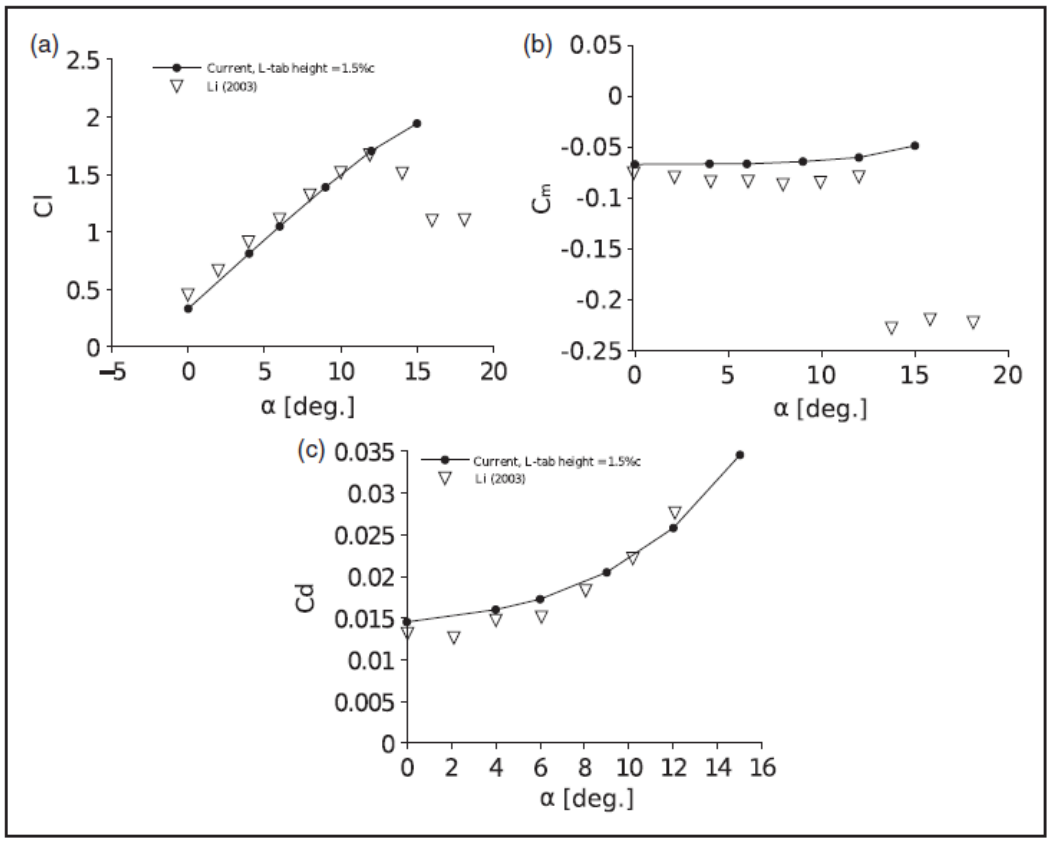


Fig. 4. Graphs show the comparison of results on a NACA0012 with its gurney flap deployed downwards as studied by Li et al. Force coefficients at steady state are computed and compared between numerical analysis and experiments with Reynolds No of $2.1 \times 10^6$ and free stream velocity of 30 m/s. [13]

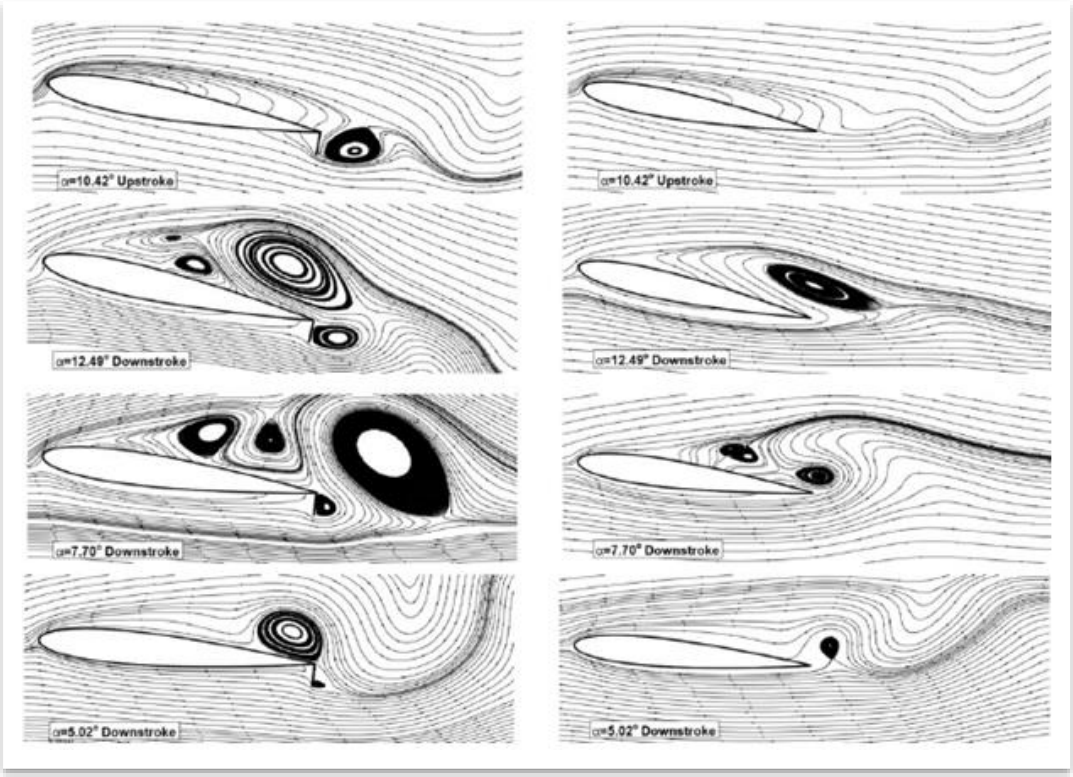


Fig. 5. Streamline of flow about the flapping airfoil shown in left and a clean airfoil, shown in right. Figure shows the vortex generation at different angle of attack during upstroke and down-stroke action of airfoil. [15]

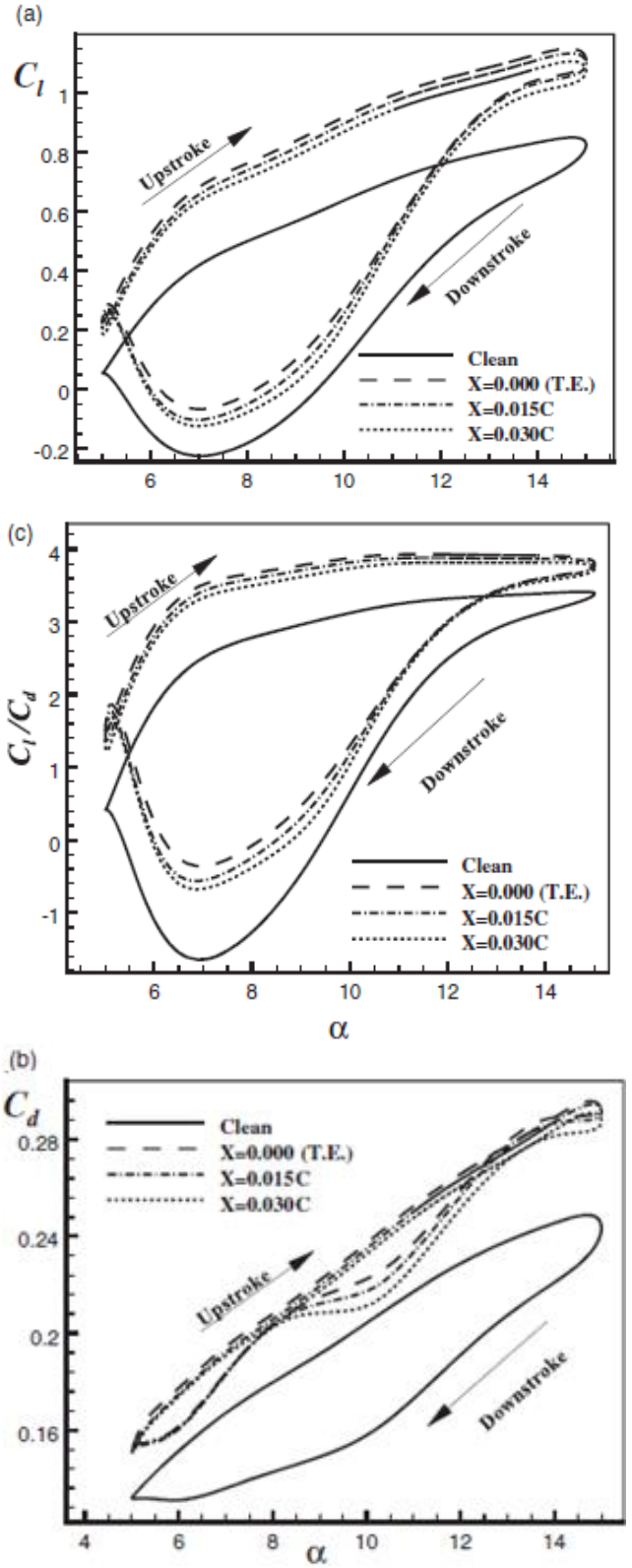


Fig. 6. The influence of Gurney flap position on force coefficients of flapping airfoil is shown on (a) $C_L$ (b) $C_D$ (c) $C_L/C_D$

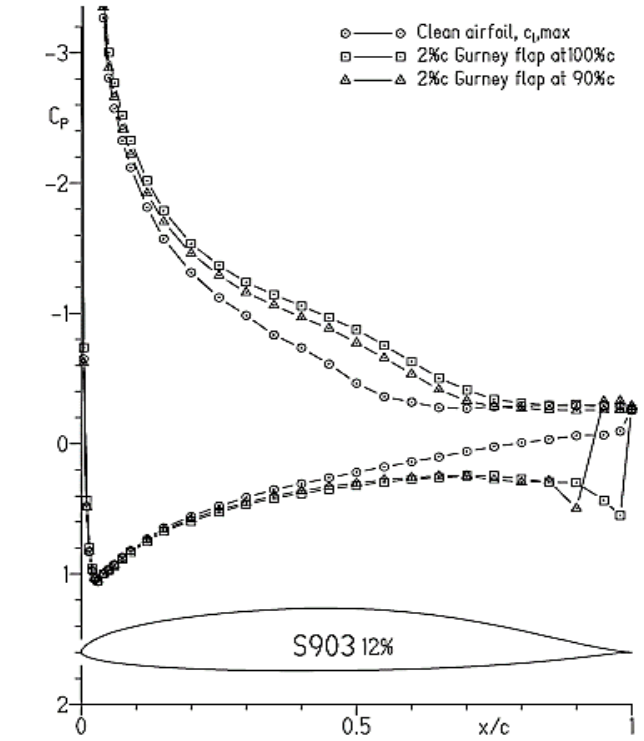


Fig. 7. Pressure distributions on S903 airfoil with and without gurney flaps at $C_{L,max}$. [17]

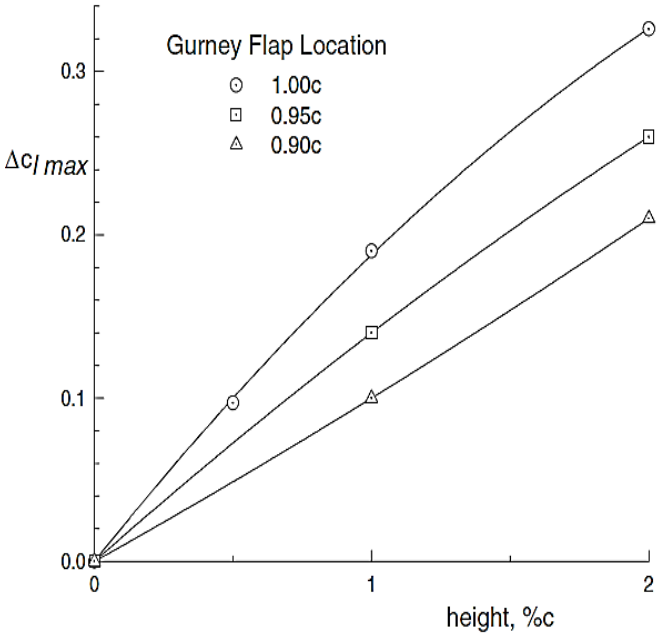


**Fig. 8.** Variation of maximum lift coefficient with changing flap heights and chord wise locations. [17]

## IV. EXPERIMENTAL RESEARCHES

Maughmer et al. in their study [17] performed wind tunnel testing of S903 airfoil at Pennsylvania State University facility to analyze steady, 2-D measurements of aerodynamic parameters in low turbulence low speed flow. Values for varying flap sizes as well as mounting locations were collected.

Figure 8 is the interpretation of wind tunnel testing results of Maughmer et al. It shows the pressure distribution along the chord of S903 airfoil with and without the gurney flap, with the gurney flap mounted at 0.9c and 1.0c.
The summary on the effect of position of the gurney flap and its height is shown in Figure 7. As can be seen, location of gurney flap is optimal at the trailing edge and linear decreases as we move towards the front in term of chord. More, the maximum lift is also achieved when height of gurney flap is take to be 0.02 times the chord length. GF of 0.02c mounted at the TE increases the maximum lift coefficient by 29%. The separation point on the airfoil is shifted upstream 0.1c-0.15c as the mounting location of flap is shifted from trailing edge to 0.9c. Drag is more sensitive to the height of flap than by its location as only 10% decrease in lift coefficient is observed by moving the gurney flap for trailing edge to 0.9c

Confidence in the obtained results of this study is achieved by comparing the results of subject wind tunnel testing with those of another facility. For this purpose, two highly reputed wind tunnel testing facilities of NASA Langley Research facility and Delft University of Technology, Netherlands were used for comparison of results. Comparison between the $C_L/C_D$ results were made with NASA Langley LTPT (Low turbulence Pressure tunnel) on Eppler 387 airfoil at $2.0x10^5$ to $4.6x10^5$. The results were found to be in a very close agreement as shown in Figure 9**.** Also, results on airfoil S805 wind-turbine airfoil at different angles of attack and Reynolds number was compared with that of Delft University. Several other comparison results are also shown in their research paper. The comparison showed excellent agreement which verifies that the approach and procedure adopted for testing purpose is correct.

## V. SIMULATION OF GURNEY FLAP USING FLUIDIC ACTUATION

Gurney flaps have found to be very useful in enhancing the aerodynamics characteristics of an airfoil, particularly in increasing the lift to drag ratio, and shifting the stall angle to higher degrees. Despite of all its advantages, there are certain drawbacks which we face with the employment of gurney flap. It is a fixed surface along the trailing edge which cannot be retracted when not required that restricts the aerodynamic ability of an airfoil. Moreover, using trailing edge flap, although provides a large increment of lift to drag ratio at small angle of attack and can be retracted, however its integration and installation requires mechanical complexities. One alternative which is under recent study is fluidic actuation, which is used to create the effects of a trailing edge flap or a gurney flap. It is achieved

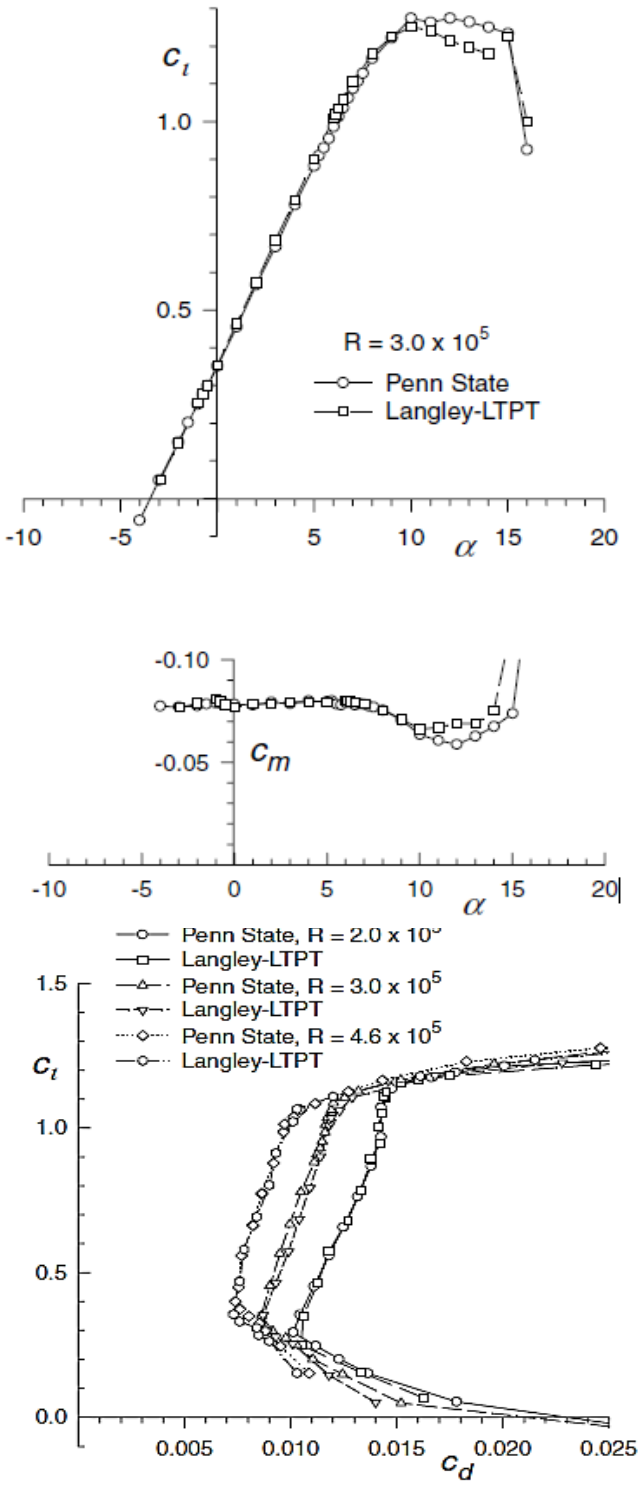


Fig. 9. The aerodynamic characteristics of Eppler387 airfoil compared with the results of NASA Langley and at Pennsylvania State University [17].

through upstream facing, high aspect ratio surface jet, which is installed both on upper and lower surface. It can be turned off when not required. Moreover, it allows for bidirectional control as it allows for individual actuation on upper and lower surface. Past investigations have shown than the fluidic actuation normal to the airfoil surface an increase the $C_{L,max}$ coefficient by 0.2 [18]. Using wind tunnel testing, Tan et al. [19] have experimentally studied the fluidic actuation effect on an airfoil. As jet actuation in the past studies (Tan et al., 2016) has rendered jet actuation

at low angle of attack to be ineffective, Tan et al. have tried to extend its operational ability in their study.

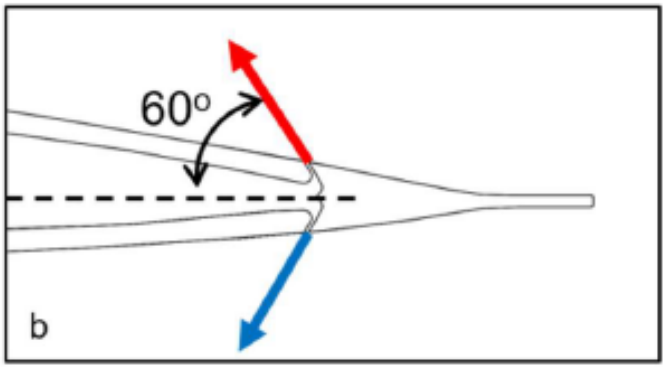


Fig. 10. Cross-sectional view of gurney flap showing the actuation jets on the lower and upper surface in proximity of the TE, at an angle of 60 degrees. [19]

Experiments on a 2-D airfoil with chord length of 0.381m in a slow-speed wind tunnel is carried out. Jets are attached at a distance of 0.88c from the LE and driven by laboratory air. The mass flow coefficients are denoted as $C_q$ and $C_u$ with orifice speed of 116 m/s.

### *D. Base flow*

At Reynolds number $5.35x10^6$, the variation of coefficients of lift drag and moment with angle of attack changing from -2 degree to 12 degrees is shown in Figure 11**.** Lift increases linearly with angle of attack, drag increases slight, while the pitching moment remains nearly same within the measurement range.

### *E. Bidirectional control*

The effect of individual actuation of upper and lower surface jets at varying momentum coefficient have been investigated by Jan et al., results of which are shown in Figure 12.

a) *Pressure surface jet actuation:* The increase in lift is linear with increasing the mass flow ratio coefficient and shows independency to angle of attack (Figure 12a). PS jet actuation leads to a decrease in the pitching moment, which is also independent of angle of attack. Drag increases with PS actuation, which is independent of α at smaller actuation level, and increases with α at higher actuation levels (Figure 12e)

b) *Suction surface jet actuation*: SS actuation gives an opposite response as compare to the PS. Lift increases linearly with increasing flow coefficient (Figure 12d) which is similar in magnitude but opposite in direction. $C_m$ increases linearly with actuation levels, but the effect fades at α greater than 2° (Figure 12d). Drag is independent of α, and is smaller in magnitude as compared to PS actuation, but increases with increase in actuation level.

To summarize, suction side appear to be in weaker control authority in terms of aerodynamic parameter variation. Hinged flap has the best L/D at AoA<=2 degrees, but quickly decreases below the values of fluidic action for higher angle of attacks. Fluidic actuation has better relative L/D as compared to hinged and gurney flap, and is also less less influenced the changes in AoA.

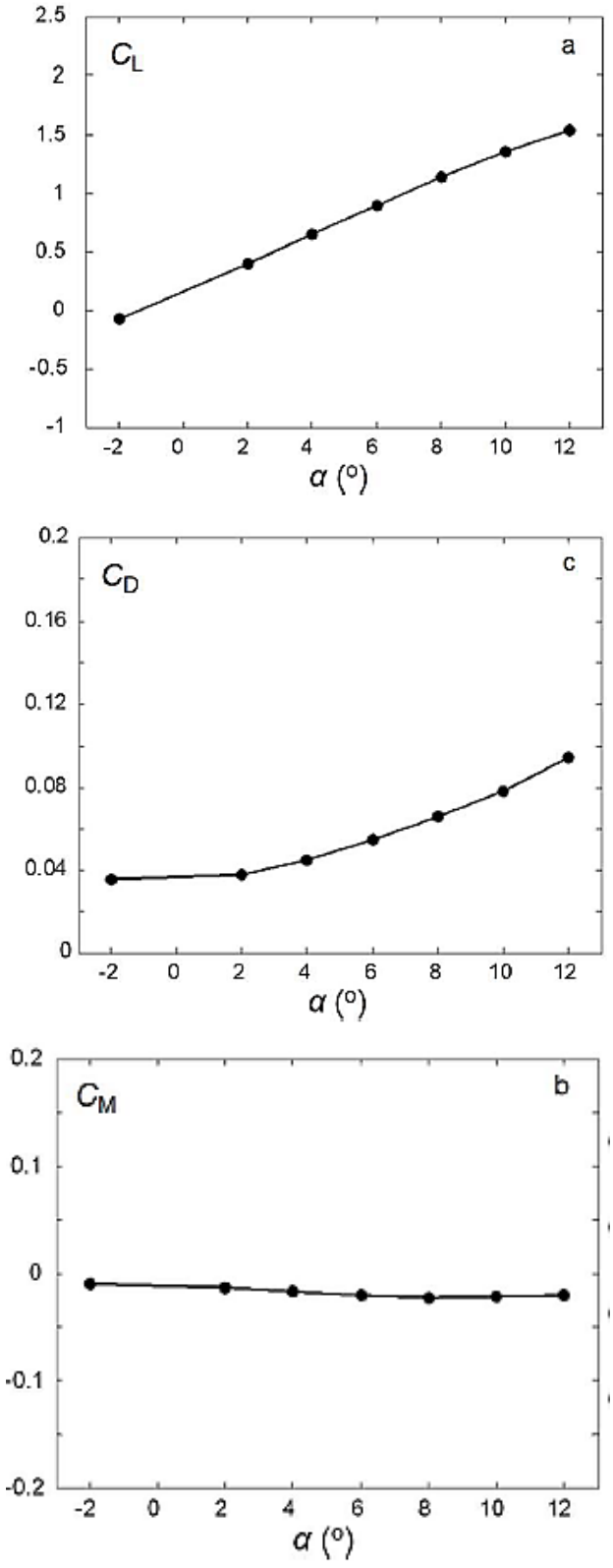


Fig. 11**.** Figure a, b and c show the sectional life, pitching moments and drag of VR-12 airfoil [19].

Jet flap has almost half the drag penalty (33% vs 65%) as compared to a drag created by hinged flap. Increase in the

maximum lift coefficient ranges from 177% (at AoA=2 degrees) to 48% (at AoA=12 degrees).

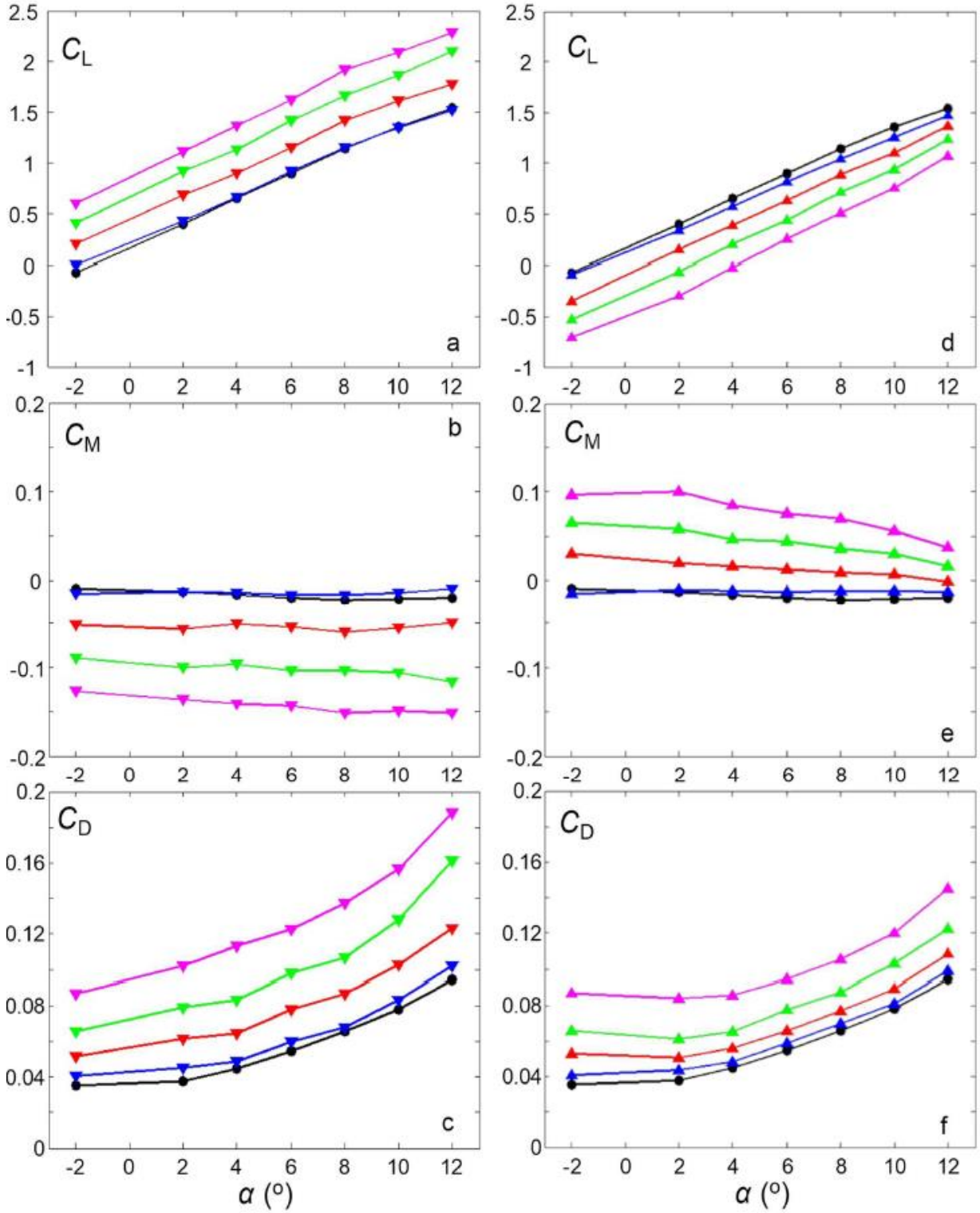


Fig. 12. Using pressure and surface actuation with Cq = (22, 44, 67, 89)e-4, or Cμ =( 3, 13, 29, 51)e-3 respectively, CL, $C_P$, $C_D$ are shown shown.

## VI. Parametric Study of Gurney Flaps in Airfoils of Wind Turbines

The electricity demand has been increasing globally and the need for more power generation systems is inevitable. A very robust and a renewable form of energy generation is wind turbine. Wind turbines can be employed with bigger rotors that improves the effectiveness, but long rotor blades become difficult to control. Moreover, rotors are also subject to severe fatigue loads, which affects the life and safety of the system. Hence, we need to come up with new materials with load control techniques. Due to their economic advantage, simple design and reliability, Gurney flaps as passive flow control device is coming up as a promising solution, which helps to slow the rate of deterioration of turbine blades . Studies in this area focuses

on increasing the lift at the rotor blades, which translates into the increase in mechanical torque applied, and hence the power generated. In a recent study by Storm et al. [20], they found that lift increased by 15% with a gurney flap of 0.5%c on NACA 4412 airfoil. Armendia et al. [21] have carried out parametric study of DU91W(2)250 airfoil to understand the effect on gurney flap on horizontal axis wind turbines. Figure 13 shows a side view of subject airfoil.

Simulations were performed on STAR CCM+ v11.2 using steady state completely turbulent model using RANS model. Menter K-Ω SST model was used, which is a combination of both K-Ω and K-ε model, with properties K-Ω near the wall and gradually changing to K-ε away form the wall. Numerical analysis at Reynolds number of $2.6x10^6$ and velocity of 30m/s was carried out and compared with Timmer et al [22].

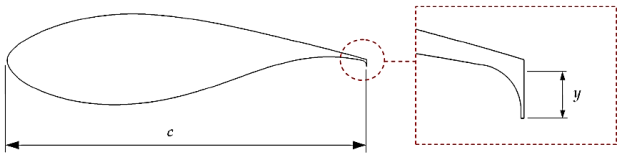


Fig. 13: View of gurney flap on DU91W(2)250 airfoil [21].

**TABLE I**. AIRFOILS DESIGNS CONSIDERED IN STUDY

| Test ID | TEST CASE | *y (% c)* |
|---|---|---|
| 0 | DU91W250 | no GF |
| 1 | DU91W(2)250GF025 | 0.25 |
| 2 | DU91W(2)250GF05 | 0.50 |
| 3 | DU91W(2)250GF075 | 0.75 |
| 4 | DU91W(2)250GF1 | 1.00 |
| 5 | DU91W(2)250GF125 | 1.25 |
| 6 | DU91W(2)250GF15 | 1.50 |
| 7 | DU91W(2)250GF175 | 1.75 |
| 8 | DU91W(2)250GF2 | 2.00 |
| 9 | DU91W(2)250GF225 | 2.25 |
| 10 | DU91W(2)250GF25 | 2.50 |
| 11 | DU91W(2)250GF275 | 2.75 |
| 12 | DU91W(2)250GF3 | 3.00 |

For all of the airfoils mentioned in Table 1**,** values for lift, and drag were noted in negative and positive angles of attacks. Comparison was made with a clean airfoil. Results are summarized as below;

### *F. Negative angle of attack*

From -6 to -4 degrees, lift to drag ratio increases as flap height increases. As we increase the AoA from -3 to -1 degrees, the maximum L/D is achieved below the maximum gurney flap height of 3%c. That is, for -3 degree, the maximum value 18.99 is attained at 2%c height, and maximum value shifts towards the smaller gurney flap size as we further increase the angle of attack to 0 degrees.

### *G. Positive angle of attack:*

A different behavior is observed in case of a positive angle of attacks. For 0 to 3 degrees angle of attack, it follows the same pattern, with the maximum values of $C_L/C_D$ being attained close to 1%c. From the result, we can see that the effect of gurney flap with heights more than 2.5%c is not favorable at angle of attacks more than 2 degrees. Gurney flap with heights more than 2%c is not favorable at angle of attacks more than 3 degrees as compared to a clean airfoil. At angle of attack ≥ 5 degrees, gurney flap of any size is not favorable as it gives smaller $C_L/C_D$ than a clean airfoil as can be seen from figure below.

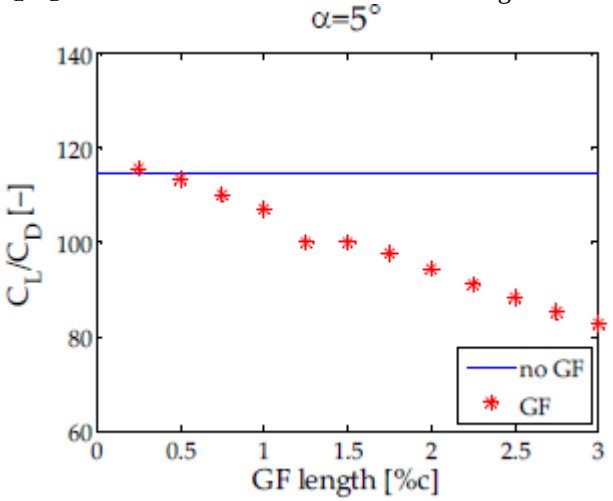


Fig. 14. $C_L/C_D$ ratio shown borderline with a clean airfoil, and decreasing with further increase in GF height. [21]

**TABLE II.** THE OPTIMUM LIFT TO DRAG RATIO OF GURNEY FLAPS AT EACH OF ATTACK WITH REFERENCE WITH NO GURNEY FLAP [24]

| AoA (°) | $C_L/C_D$ Max. | GF Length (% *c*) | $C_L/C_D$ no GF | Δ $C_L/C_D$ |
|---|---|---|---|---|
| −6 | −36.86 | 3.00 | −53.98 | 17.13 |
| −5 | −14.27 | 3.00 | −39.95 | 25.68 |
| −4 | 4.16 | 3.00 | −24.04 | 28.19 |
| −3 | 18.99 | 2.00 | −7.15 | 26.14 |
| −2 | 33.87 | 1.50 | 9.61 | 24.26 |
| −1 | 46.93 | 1.00 | 26.00 | 20.93 |
| 0 | 61.75 | 1.00 | 41.95 | 19.80 |
| 1 | 78.91 | 0.75 | 57.50 | 21.41 |
| 2 | 94.25 | 0.50 | 72.68 | 21.57 |
| 3 | 104.52 | 0.50 | 87.54 | 16.98 |
| 4 | 114.48 | 0.25 | 102.13 | 12.36 |
| 5 | 115.68 | 0.25 | 114.44 | 1.25 |
| 6 | 114.41 | 0.25 | 113.81 | 0.60 |
| 7 | 110.10 | 0.25 | 109.81 | 0.29 |
| 8 | 102.55 | 0.00 | 102.73 | 0.00 |

Summary of resutls in Table 2 shows that the maximum possible value of $C_L/C_D$ is 115.68 at 5 degree angle of attack, with a gurney flap height of 0.25%c.

### *H. ANN-based prediction model*

Artificial neural network or ANN is a powerful tool which is self-learning that can be enhanced by training algorithms and input/outputs. If an ANN is trained properly, it is capable of predicting results of a new condition with very high probability. Due to its outstanding property, ANN is being used in modelling of different systems. In their study, Armendia et al. [21] have developed an ANN for the type of airfoil being considered, which is as below along with their graphical comparison of results from ANN and CFD in Figure 15;

$$\frac{C_L}{C_D} = \sum_{i=1}^{i=Nhidden} \omega_i \cdot g_i\left(\vec{x}\right) + \theta$$

$$g_i(\vec{x}) = \frac{1}{1+e^{-h_i}} \qquad (1,2)$$

$$h_i(\vec{x}) = \sum_{j=1}^{j=Ninputs} \omega'_{i,j} \cdot x_j + \theta'_i \qquad (3)$$

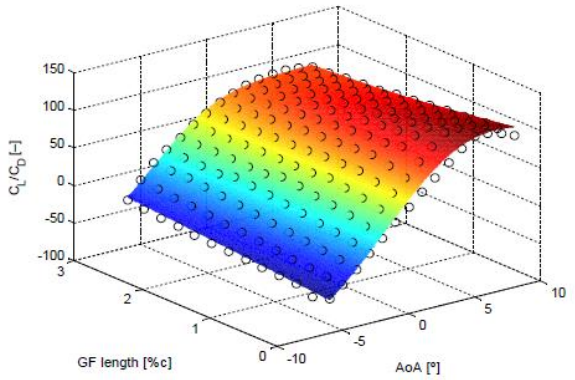


Fig. 15. Neural network results of aerodynamic performance with respect to angle of attack and GF height, compared with CFD results in black circles. Results from a well-learned ANN model shows close approximation with the numerical analysis of study [21].

## VII. PLASMA ACTUATORS AND GURNEY FLAPS

DBD or dielectric barrier discharge are the state-of-the-art devices, that can be effectively employed for flow control. It has a plain construction which just consists of two electrodes with a di-electric material in between. When current is applied, the air particles on the positive side of the electrode are ionized. The ionized air is attracted towards the charged di-electric sheet, and results in forming a jet at the wall [24]-[25]. Figure 16 shows a the most basic form of DBD plasma actuator, with the 2 electrodes and a dielectric sheet placed in between, the area of generated plasma, and direction in which the induced flow is going to move. Velocity of the flow can reach as much as 10 meter/second. Figure 17 shows that the consistency of the operation will result in a form of a jet at the wall, that resembles a flow discharge from a 2-D nozzle.

The benefits of DBD plasma actuators over a conventional gurney flap is that it does not require any moveable parts. It is electronically controlled and can be switched ON/OFF as and when required. Hence, we can take benefit from it at low speed high angle of attack for increased lift, and switch it off at higher speeds and cruise conditions. DBD plasma actuators can also be integrated with hybrid and electric vehicles. A large potential of this device is seen in the future aircraft which will have no moveable parts.

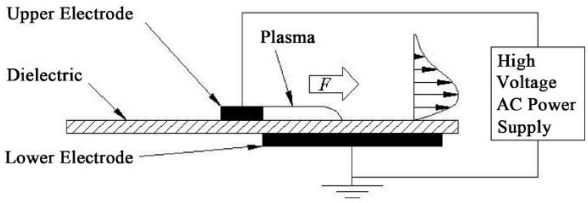


Fig. 16. Basic design of a DBD plasma actuator is shown. [35]

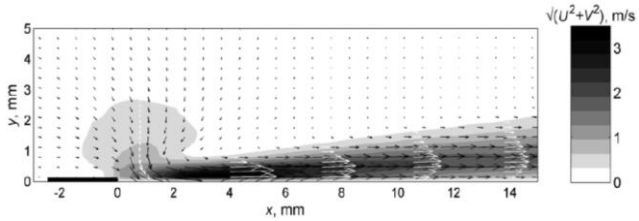


Fig. 17. Development of wall jet from a DBD plasma actuator shown in terms of velocity field. Operation of plasma can accelerate flow up to a velocity of 10m/s. [35]

### A. *Plasma equivalent of gurney flap*

Zhang et al. have studied the effect of using plasma as an alternative to create the effect created by a GF. The reason for this is that plasma gurney flap has significant benefit over the other two. Conventional gurney flap is fixed and cannot be moved during flight where it is not required. As gurney flap is deployed at the trailed edge of airfoil, it cannot be retracted as the area is too thin to include any moveable parts. As for a jet gurney flap, it overcomes the penalty of drag, however this setup requires a pneumatic pipe and an air source to blow efficiently. Plasma actuator has no moveable parts, has low mass, requires low input energy and gives a fast response. Zhang et al. have proved in their numerical study that the lift augmentation in the case of plasma actuator is the same as that for a jet or conventional flap. In addition to lift augmentation, the penalty in the case of plasma actuator is less, hence increasing the overall lift to drag ratio before stall. The flow separation is impeded as vortices downstream of airfoil are suppressed and flow is soaked in the plasma effect. The von Karman vortex street downstream of the airfoil TE in case of plasma actuator is eliminated as flow from the upper surface of the airfoil will is soaked into the plasma zone, and flow separation is inhibited. Results suggest that gurney flap created by plasma actuator is strength of $D_c$=9.15 has the equivalent effect of a conventional gurney flap with a chord height of 0.78%. jet blowing gurney flap with a momentum coefficient of $C_u$=0.01. Traub et al. concluded in their research [28] that a GF with a momentum coefficient of $C_u$=1e-2 produces equivalent effect of a conventional gurney flap with 0.78% chord. Parameter *Dc* represents the ratio of the electrical force to the inertial force.

### B. *Plasma actuator on upper surface*

Airfoils with DBD plasma actuator at the trailing edge alter the Kutta condition in a way that is analogous to that of a conventional gurney flap. This results in an evident lift enhancement. Zhang et al proved this by the placement of plasma actuator on the trailing edge of a NACA 0012 airfoil [27], which enhanced the lift of the airfoil in a way which was comparable with the same airfoil with gurney flap.

A different technique was adopted by Feng et al. They used the DBD plasma actuator in combination with gurney flap, by placing the electrodes on the downstream surface of the gurney flap. Gurney flap of different heights (3%c, 4.5%c, 7.0%c) were used, along with the variation of

plasma jet moment coefficient $C\mu$. Momentum coefficient was varied from 0.11%, 1.15% and 1.39% [30]. They wanted to investigate the extent to which the plasma jet modified or enhanced the effectiveness of the gurney flap. As anticipated, the plasma jet showed an increment in the lift coefficient at every angle of attack as tests were conducted with plasma jet activated and deactivated. Results are shown in table 18b. Results also show the lift coefficient is increased with an increase in the gurney flap height. From the results it can be inferred that the lift coefficient increment caused by an increase of 1% height of gurney flap corresponds to 1% increment of momentum coefficient, $C_\mu$.

Feng et al. presented another novel idea. They designed a gurney flap by positioning a DBD plasma actuator on the lower surface near the trailing edge of the airfoil. They presented two configurations of this design. First configuration consisted of a gurney flap created virtually by 2 pair of electrodes; a pair of 1mm-wide exposed and a pair of 44mm-wide embedded electrodes. In their second configuration, they used a single pair of electrodes of same width as first configuration. Both these configurations enhanced the $C_{L,max}$ by 10% and 5% of first and second configuration respectively. While the first configuration increased the $C_{L,\ max}$ by twice as much as second configuration, but the second configuration proved better over a larger range of angle of attacks [31]. Without the presence of plasma actuators, there exists a recirculation zone past the trailing edge at a distance of 12%c at zero angle of attack. With the presence of plasma, the recirculation zone is slightly reduced.

The interaction of freestream and the jet induced by plasma creates a high-speed zone in the vicinity of the plasma actuators. However, no difference on the suction side of the airfoil is experienced by flow. In case of the second configuration, the pressure surfaces experience a recirculation zone in the vicinity of the plasma actuator due to the interface of the freestream with the induced jet because of plasma. This way the suction on the upper surface is increased as the recirculation zone attracts air from the upper side to increase the velocity of the flow. Simultaneously, a high-pressure stagnation point is created ahead of the recirculation zone. The wake region shrinks the downstream of the airfoil which suggests plasma control increasing the effective camber of airfoil.

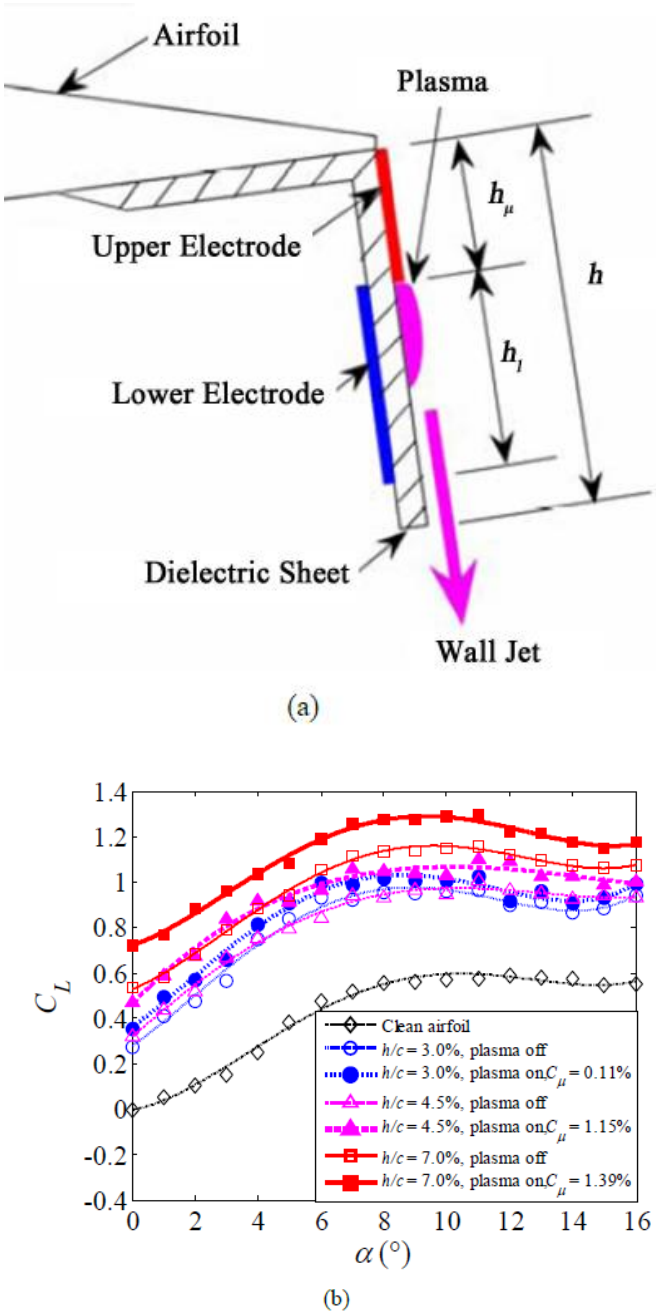


Fig. 18. (a) NACA 0012 airfoil showing plasma actuator in combination with gurney flap as researched by Feng et al.
(b) Lift enhancement characteristics on NACA 0012 airfoil. [30]

Hence, was can safely state plasma actuators enhances the lift of GF by the same principle as a conventional flap, with the added effect of not having an associated profile drag contributed due to the shape of gurney flap.

### *C. Steady and unsteady actuation of plasma*

A worker must first ready his tools to accomplish a well-done job. The extent of development and application of the plasma jet actuator is largely determined by its efficiency, working range, reliability, maintenance ease, response ability and power requirement. Synthetic jets which exhibit favorable characteristics for its application in active flow control has to be studied first. Santhanakrishnan and Jacob [32-33] conducted wind tunnel testing to investigate the flow field of PSJ. They concluded that maximum speed on

jet in unsteady PSJ was greater than that of a steady PSJ. Velocity profiles exhibited the same similarity rule in both cases. However, flow structures were not presented in details in their profile of velocities. This is where Lie et al. [34] come in with their numerical study to investigate the formation and evolution of vortexes in fields which are averaged over time. Because of their numerical study, Lie et al. came to conclude that a reasonable similarity in flow field of synthetic jets and time-averaged unsteady case if found with the steady flow field.

## VIII. CONCLUSION

This review paper has successively summarized the various methods and approaches used by many researchers to evaluate the effect of gurney flaps. GFs in various configuration have been evaluated in order to critically evaluate their aerodynamics performance.

The effect of this simple device on different type of airfoils have been discussed. The effect of changing gurney flap height, location and mounting have also been considered. Gurney flap effect can also be induced by air jet actuators positioned at the trailing edge. With all their benefits, their single most demotivating factor is their complex construction at the trailing edge, where the thickness is usually very small. DBD plasma actuators have proven their worth over conventional and jet gurney flap. DBD plasma actuators do not require any complex arrangement for their use and requires low energy input. Plasma actuators can be activated at low speed and high angle of attack, and turned off at higher speeds. Hence, the drag penalty from a conventional gurney flap is diminished completely. Plasma equivalent of a gurney flap has been reviewed, along with various novel ideas of plasma actuator principle on airfoils. It has been seen that the plasma actuators and GF enhances lift of an by the same principle. A large potential of this device is seen in the future aircraft which will have no moveable parts. Some of the significant finding of modern researches is outlined below;

- Longer tab shows higher effectiveness at high angle of attack., increase $C_L/C_D$ by almost 50%, increases stall angle by 4 deg. At low angle of attack, L-shaped gurney flap effective for both upward and downward deflection in compressible (M=0.7) regime.

- 2% height of gurney flap gave the best performance. Optimum performance achieved with flap at 90° with length equivalent to local BL thickness.

- Lift for trailing edge with slot increases by a factor of 1.87 and drag by a factor of 2.22. Gurney flap increases lift by a factor of 1.78 and drag by factor of 1.33.

- Gurney flap with 0.02c height mounted at TE shifts separation point on the airfoil upstream (0.1c-0.15c) as the mounting location of flap is shifted from trailing edge to 0.9c.

- Fluidic actuation has better relative L/D as compared to hinged flap and gurney flap. It is also less sensitive to change in angle of attack.

- Jet flap has almost half the drag penalty **(33% vs 65%)** as compared to the drag generated by a hinged flap.
A jet flap generates maximum 177% increment in lift.

## IX. RECOMMENDATION

Based on the review of many researches, the following recommendations are proposed;

- The use of DBD plasma actuator is a beneficial choice for aircraft applications because it can be turned ON/OFF as per requirement.

- The use of perforated Gurney Flap is good for formula one car applications as it always need down force.

- The use of perforated GF for wind turbine to enhance efficiency and power production would prove to be an effective solution.

- For further improvement in design, experimental analysis should be done to validate DBD plasma actuators advantages.
- Coupling of 3D simulation wind turbine testing for improvement in GF design.

## ACKNOWLEDGEMENT

I would like to acknowledge the efforts of Dr Syed Irtiza Ali Shah for imparting our class with important concepts on incompressible flows, which helped to understand the various intricacies in the research analysis. Also, all faculty members of aerospace department at CAE, Risalpur for guiding us in undertaking the research task

**TABLE III.** SUMMARY OF SIGNIFICANT RESEARCHES STUDIED IN DETAILS TO EVALUATE AERODYNAMIC PERFORMANCE OF GURNEY FLAP

| AUTHORS | APPROACH | ANALYSIS OF APPROACHES | | | | |
|---|---|---|---|---|---|---|
| | | | | | | |
| | | **COMPARISON OF SOFTWARE HARDWARE** | **COMPARISON OF GOVN EQNS** | **RESULTS** | **VERIFICATION AND VALIDATION APPROACHES** | **ADVANTAGES AND LIMITATIONS AND APPLICATIONS/ UTILITY** |
| Valentina Motta, Giuseppe Gibertini, Alex Zanotti and Giuseppe Quaranta (2016) | CFD numerical approach along with experiments on airfoil NACA 0012 model with an L-type gurney flap, in upwards and downward deployed configurations. | ROSITA numerical analysis software is used for CFD simulations. Validation through PIVs and pressure measurements | ROSITA has second order accuracy, numerically integrates RANS equations, uses SA turbulence model. Fully turbulent viscous flow is being considered. | Longer tab shows higher effectiveness at high angle of attack, increase $C_L/C_D$ by almost 50%, increases stall angle by 4 deg<br>At low angle of attack, L-shaped gurney flap effective for both upward and downward deflection in compressible (M=0.7) regime. | Numerical results compared with experiments by Li et al. for same airfoil.<br>Pressure peak at the leading edge are very well captured.<br>Differences in the lift, drag and pitching moments are less than 3,5, and 7% respectively for clean airfoil as well as for flap deployed downwards | Results computed with respect to a slot near the trailing edge, used for movement of the flap. Results effected due to its presence in high angle of attack. Study also applicable for design of rotors in rotary wing aircraft where the gurney flaps are both deployed upwards and downwards |
| Sánjoy Kumar (2018) | CFD over NACA 2412 airfoil at trailing edge. Chord height 2-5%, 0-32 deg angle of attack | Not mentioned | Two equation turbulence model K-ε model. | 2% height of gurney flap gave the best performance Optimum performance achieved with flap at 90° with length equivalent to local BL thickness | None | Low Reynolds number calculation 2.74 × 105.<br>Basic approach used with single gurney flap mounted at a fixed angle, at the trailing edge |
| Telluri Srinivasa Rao, Trilochen Mahapatra, Sei Cheitanya Mangavelli (2018) | Numerical study of NACA 0012 with design modifications compared to standard data for verification | FLUENT ANSYS | Turbulence model K-ε, momentum equation for calculation of pressure and velocity distribution in laminar flow | Lift for trailing edge with slot increases by a factor of 1.87 and drag by a factor of 2.22 Gurney flap increases lift by a factor of 1.78 and drag by factor of 1.33 | Values compared with standard values of NACA 0012 airfoil | Analysis with only varying Mach number done, with all other parameter constant. Validation done simply through the values of symmetric NACA 0012 airfoil literature |
| Mark D. Maughmer, and Gotz Bramesfeld (2008) | Wind tunnel measurements of steady, 2-D over varying chordwise locations and flap heights, Mach <0.2, | Wind tunnel sized 3.3 feet x 4.8 feet. Low turbulence, low speed (maximum speed of 250 feet/second) | Wind tunnel testing. Corrections applied to ensure the correct angle of incidence | Flap with h= 0.02c located at the TE increases the maximum lift coefficient by 29% separation point on the airfoil is shifted upstream | $C_L/C_D$ was compared with NASA Langley LTPT on Eppler 387 airfoil.<br>$C_L$, $C_m$, and $C_L/C_D$ of S805 wind-turbine airfoil at varying angles of | Analysis done on airfoils which could be used on wind-turbines as well as on rotors of rotary wing aircraft |

| | | | | | | |
|---|---|---|---|---|---|---|
| | Re=1.0x$10^6$ S903 airfoil, | | | 0.1c-0.15c as the mounting location of flap is shifted from trailing edge to 0.9c. | attack at different Reynolds number was compared with that of Delft university | |
| Alireza Naderi, Bahram Tarvirdizadeh (2018) | Numerical studies of influence of height, angle at which it is mounted and location of gurney flap using NACA-0012 airfoil in flapping action | Not mentioned | Lagrangian-Eulerian numerical algorithm, pressure-based, Finite volume finite element approach | The fixing point of the flap has no drastic effect on the $C_L$, $C_D$ curve<br>Introducing flap angle increase the $C_L$/ $C_D$ value in comparison to a clean airfoil<br>Increase of $C_L$ /$C_D$ is significant in 1-6%c flap height and decreases with a further increase in flap height | Flow around the airfoil is parametric study of power extraction airfoil in oscillating motion. Kinsey T and Dumas G. [16] | Advantage: based finite element approach is used which is based on finite volume. It can be employed with moving mesh and moving boundary.<br>It also does not require dissipation/ damping function |
| Yuehan Tan, Ari Glezer (2019) | Wind tunnel testing of VR-12 airfoil at low AoA using upstream facing jet on high AR | Wing tunnel testing,<br>Measurement of aerodynamic loads,<br>PIV for flow field 1x1 meter test section | Not mentioned | Suction side appear to be in weaker control authority<br>Hinged flap has the best L/D at AoA<=2 degrees, but quickly decreases below the values of fluidic action for higher angle of attack<br>Fluidic actuation has better relative L/D as compared to hinged flap and gurney flap, is also less sensitive to change in angle of attack.<br>Jet flap has almost half the drag penalty **(33% vs 65%)** as compared to the drag generated by a hinged flap.<br>Maximum **177%** increment in lift generator by jet flap<br><br>Verification/ Validation not done | | Simulation of gurney flaps using fluidic actuation results in comparable lift increase at that for gurney flap, but with lower drag penalties<br>Helps in vibration reduction in fixed and rotary winged aircraft<br>Allows bidirectional control using both or either jets on upper and lower side of airfoil<br>When not operated, airfoil returns to base form<br>Useless when the flow is fully attached |
| Inigo Aramendia, Ekaitz Zulueta Aitor Saenz-Aguirre, Unai Fernandez-Gamiz, Daniel Teso-Fz-Betoño (2019) | DU91W(2)250 airfoil is investigated numerically to find the optimal flap height for maximum performance | Simulations were performed on STAR CCM+ v11.2 using. | Reynolds averaged NS equations are used under steady conditions, flow is taken fully turbulent, K-Ω SST turbulence mode is used, combines K-Ω close to the wall and which gradually shifts | A maximum possible value of $C_L/C_D$ is 115.68 at 5 degree angle of attack, with a gurney flap height of 0.25%c.<br>At angle of attack ≥ 5 degrees, gurney flap of any size is not | Results were compared with the wind tunnel testing results of Timmer et al. | |

| | | | | | | |
|---|---|---|---|---|---|---|
| | | | K-ε away from body | favorable as it gives smaller $C_L/C_D$ than a clean airfoil, ANN (artificial neural network) was developed for aerodynamic efficiency prediction | | |

## REFERENCES


[1] Liebeck, R. Design of Subsonic Airfoils for High Lift. J. Aircr. 1978, 15, 547–561

[2] Jeffrey, D.; Zhang, X.; Hurst, D. Aerodynamics of Gurney flaps on a single-element high-lift wing. J. Aircr. 2000, 37, 295–301

[3] Pastrikakis, V.A.; Steijl, R.; Barakos, G.N. Effect of active Gurney flaps on overall helicopter flight envelope. Aeronaut. J. 2016, 120, 1230–1261.

[4] Tang, D.; Dowell, E.H. Aerodynamic loading for an airfoil with an oscillating gurney flap. J. Aircraft. 2007, 44, 1245–1257

[5] Lee, T.; Su, Y.Y. Lift enhancement and flow structure of airfoil with joint trailing-edge flap and Gurney flap. Exp. Fluids 2011, 50, 1671–1684

[6] Shukla, V.; Kaviti, A.K. Performance evaluation of profile modifications on straight-bladed vertical axis wind turbine by energy and Spalart Allmaras models. Energy 2017, 126, 766–795.

[7] Cole, J.A.; Vieira, B.A.O.; Coder, J.G.; Premi, A.; Maughmer, M.D. Experimental Investigation into the Effect of Gurney Flaps on Various Airfoils. J. Aircr. 2013, 50, 1287–1294.

[8] Fernandez-Gamiz, U.; Zulueta, E.; Boyano, A.; Ansoategui, I.; Uriarte, I. Five MegawattWind Turbine Power Output Improvements by Passive Flow Control Devices. Energies 2017, 10, 742

[9] Liu Chen, Haijun Xie, Jun Xu, Ren Dai and Jian Chen, "Experimental and numerical study on the performance of an axial fan with a Gurney flap," *Advances in mechanical engineering*, Vol 10, pp. 1-2, 2018

[10] Sanjoy Kumar Saha, Md. Mahbubul Alam, A. B. M. Toufique Hasan Numerical Investigation of Gurney Flap Aerodynamics over a NACA 2412 Airfoil", *International conference on Mechanical engineering, 2018*

[11] Valentina Motta, Alex Zanotti, Giuseppe Gibertini and Giuseppe Quaranta, "Numerical assessment of an L-shaped Gurney flap for load control", Journal of -Aerospace Engineering, pp. 7-25, 2016

[12] Yu T, Wang JJ and Zhang PF. Numerical simulation of Gurney flap on RAE-2822 supercritical airfoil. J Aircraft 2011; 48: 1565–1575

[13] Li Y, Wang J and Zhang P. Influences of mounting angles and locations on the effects of Gurney flaps. J Aircraft 2003, 40: 494–498

[14] Talluri Srinivasa Rao, Trilochan Mahapatraa, Sai Chaitanya Mangavellib, "Enhancement of Lift-Drag characteristics of NACA 0012", Materials today, proceeding 5, 2018

[15] Alireza Naderi, Alireza Beiki and Bahram Tarvirdizadeh, "Numerical investigation of Gurney flap influences on aerodynamic performance of a pitching airfoil in low Reynolds number flow", Journal of Aerospace Engineering, 2018

[16] Kinsey T and Dumas G. Parametric study of an oscillating airfoil in a power-extraction regime. AIAA J 2008; 46: 1318–1330.

[17] G. B. Mark D. Maughmer, "Experimental Investigation of Gurney Flaps," *Journal of Aircraft* , vol. IV, no. 5, pp. 2-6, 2008

[18] Al-Battal, Nader, David Cleaver, and Ismet Gursul. "Aerodynamic Load Control through Blowing." 54th AIAA Aerospace Sciences Meeting. 2016.

[19] Yuehan Tan, Ari Glezer, "Bi-Directional Control of Airfoil's Aerodynamic Loads at Low Angles of Attack using Fluidic Actuation", *AIAA SciTech Forum*, PP. 1-13, 2019

[20] Storms, B.L.; Jang, C.S. Lift Enhancement of an Airfoil using a Gurney Flap and Vortex Generators. J. Aircraft. 1994, 31, 542–547, *Flow Control for Practical Flows*, pp. 23–49, 2017

[21] Iñigo Aramendia, Unai Fernandez-Gamiz, Ekaitz Zulueta, Aitor Saenz-Aguirre, Daniel Teso-Fz-Betoño, "Parametric Study of a Gurney Flap Implementation in a DU91W(2)250 Airfoil,"*Energies*. 1-12, 2019

[22] Timmer,W.; van Rooij, R. Summary of the Delft University wind turbine dedicated airfoils. *J. Sol. Energy Eng. Trans*. ASME 2003, 125, 488–496

[23] Johnson, S.J.; van Dam, C.P.; Berg, D.E. Active Load Control Techniques for Wind Turbines; Sandia Report SAND 2008-4809; Sandia National Laboratories: Albuquerque, NM, USA; Livermore, CA, USA, 2008.

[24] Moreau, E. (2007) Airflow Control by Non-Thermal Plasma Actuators. *Journal of Physics D*: *Applied Physics*, 40, 605-636

[25] Corke, T.C., Enloe, C.L. and Wilkinson, S.P. (2010) Dielectric Barrier Discharge Plasma Actuators for Flow Control. *Annual Review of Fluid Mechanics*, 42, 505-529

[26] Jukes, T. and Choi, K.-S. (2013) On the Formation of Streamwise Vortices by Plasma Vortex Generators. *Journal of Fluid Mechanics*, **733**, 370-393

[27] P. F. Zhang, A. B. Liu, and J. J. Wang, "Aerodynamic Modification of a NACA 0012 Airfoil by Trailing-Edge Plasma Gurney Flap", *AIAA Journal*, vol. 47, pp. 4-6, 2010.

[28] Traub, L.W., Miller, A., and Rediniotis, O., "Comparisons of a Gurney and Jet-Flap for Hinge-Less Control," Journal of Aircraft, Vol. 41, No. 2, 2004, pp. 420–423

[29] Li, Y.C., Wang, J.J. andhang, P.F. "Effect of Gurney Flaps on a NACA 0012 Airfoil", *Flow, Turbulence Combust*, 68, 2002

[30] Feng, L.H., Jukes, T.N., Choi, K.-S. and Wang, J.J. (2012) Flow Control over a NACA 0012 Airfoil Using Dielectric-Barrier-Discharge Plasma Actuator with a Gurney Flap. *Experiments in Fluids*, 52, 1533-1546

[31] Feng, L.H., Wang, J.J. and Choi, K.-S. (2014) A Novel Concept on the Plasma Gurney Flap. *Proceedings of the* 29*th Congress of the International Council of the Aeronautical Sciences*, St. Petersburg, 7-12 September 2014, 1-7.

[32] Santhanakrishnan, A., Jacob, J. D., "On Plasma Synthetic Jet Actuators," AIAA Paper 2006–317, 2006.

[33] Santhanakrishnan, A., and Jacob, J. D., "Effect of Plasma Morphology on Flow Control Using Plasma Synthetic Jet Actuators," AIAA Paper 2007-783, 2007.

[34] B. Liu, P. F. Zhang, B. Yan, C. F. Dai, and J. J. Wang, "Flow Characteristics of Synthetic Jet Induced by Plasma Actuator", AIAA JOURNAL, Vol. 49, No. 3, pp. 1,9, 2011

[35] Jukes, T. and Choi, K.-S. (2013) On the Formation of Streamwise Vortices by Plasma Vortex Generators. *Journal of Fluid Mechanics*, 733, 370-393

# Performance Analysis of Gorlov Helical Turbine Using Numerical Techniques

M. A. Siddiqui
*Department of Mechanical & Aerospace Engineering, Institute of Avionics & Aeronautics, Air University*
Islamabad 44000, Pakistan
mohibahmadsiddiqui@gmail.com

S. D. Hasan
*Department of Mechanical & Aerospace Engineering, Institute of Avionics & Aeronautics, Air University*
Islamabad 44000, Pakistan
syedaniel@hotmail.com

F. Iqbal
*Department of Mechanical & Aerospace Engineering, Institute of Avionics & Aeronautics, Air University*
Islamabad 44000, Pakistan
furqan93@gmail.com

Bilal Mufti
*Department of Mechanical & Aerospace Engineering, Institute of Avionics & Aeronautics, Air University*
Islamabad 44000, Pakistan
bilal.mufti@mail.au.edu.pk

***Abstract*—Due to detrimental effects of using fossil fuels in generating electricity, the world is searching for alternate and renewable energy sources. The kinetic energy available in flowing water is an abundant source of energy that can act as a renewable energy source. The Gorlov helical turbine is a vertical-axis turbine with its blade swept helically to help average the unsteady torque which is inherent in other vertical axis turbines. In this research, performance analysis of a Gorlov turbine is carried out using computational fluid dynamics techniques. Performance analysis is carried out at a flow velocity of 1.2 m/s at different tips to speed ratios (TSR). The turbine operates at maximum efficiency near 2.0 TSR. A decrease in turbine efficiency is observed with increased TSR. The solution methodology and results are validated by comparing them with available experimental data at similar flow and geometric conditions. In-pipe application of Gorlov turbine is explored by installing the turbine inside a circular pipe. The flow conditions and pipe diameter were taken to match the flow conditions of water supply pipes installed in Pakistan. Coefficient of power of turbine was evaluated at different TSR values. A decrease in turbine efficiency was observed due to wall effects but the efficiency remained in acceptable limits.**

## I. INTRODUCTION

Water is the major resource responsible for sustaining life. Apart from sustenance, the flow of water serves as a vital source of energy as it moves from a higher potential to a lower one. Water turbines can be used to extract this excessive energy to generate electricity. The first practical use of turbines goes back to 70 BC when the Romans used water wheels to grind corn. The undershot waterwheel is the earliest-known ancestor of the water turbine. The first modern form of the water turbine came about in the eighteenth century by the German mathematician and naturalist Johann Andres von Segner (1704-1777); it was a water turbine enclosed in a cylindrical box with tangential openings for outflow of water.

Fresh water supply in cities is carried out by an underground water supply network. In order to meet demands at the right place at the right time, water is pressurized by pumps and elevated storage tanks (water towers). In certain areas of the supply network, pressure of the water is higher than what is required. This excess potential energy can be used to harness electrical energy by placing water turbines inside municipal pipes. The purpose of this paper is to analyze the performance of a Gorlov helical turbine inside municipal water pipes.

The Gorlov Helical turbine [1] (Fig. 1) is based on the design of a Darrieus turbine [2], but with a helical shape blade. The helical blades of the Gorlov turbine allow the mean azimuthal angle of attack of the airfoil/hydrofoil to remain constant against the flowing fluid. This characteristic reduces in magnitude, the pulses created on the turbine shaft, which occurs in the Darrieus turbine.

Performance analysis of Gorlov Helical turbine has already been carried out using experimental techniques by Bachant and Wosnik [3]. In this experiment performance of a Gorlov turbine had been evaluated in an open channel at different tip to speed ratios. The result of this study showed that the Gorlov turbine performed extremely well when installed in an open channel.

The aim of the current research is to analyze the performance of a Gorlov Helical turbine when used for in-pipe applications. Initially the validation of solution methodology is carried out by simulating the experiment of Bachant and Wosnik [3] using computational fluid dynamics technique. The Gorlov turbine is subsequently installed in a pipe and performance analysis is carried out using same solution methodology. Fluent 16.0 has been used for the analysis.

## II. TURBINE PERFORMANCE PARAMETERS

The performance of turbines is generally measured in terms of coefficient of performance or power i.e. $C_p$ [4, 5]. Coefficient of performance is defined as ratio of power extracted by turbine to total available power in flowing fluid. $C_p$ can be computed by using following equation.

$$C_p = C_m * r * \frac{\Omega}{v}$$

Where $C_m$ is the coefficient for turbine blade pitching moment, r is the radius of the turbine, $\Omega$ is the angular

velocity of the turbine and v is the linear velocity of the working fluid. Moment on the turbine occurs when the flow of the fluid tends to turn the air foil so to change its angle of attack. $C_m$ is represented by the equation;

$$C_m = \frac{M}{q*A*c}$$

Where M is the pitching moment of the turbine, q is dynamic pressure, A is the area of the blade and c is the hydrofoil chord length.

The analysis is carried out at different tip speed ratios. Tip speed ratio is the ratio between fluid velocity and turbine tangential velocity.

$$TSR = \frac{r * \Omega}{v}$$

Kinetic energy efficiency is the ratio of useful mechanical power extracted to the total amount of kinetic power removed from flowing fluid [6]. Kinetic energy efficiency is directly related to the drag and coefficient of performance of turbines and can be computed using following relationship [7].

$$\eta = \frac{C_p}{C_d - \frac{1}{4}C_d^2}$$

## III. COMPUTATIONAL SETUP

### A. *Geometry Modelling*

The Gorlov turbine used in the experiment was made in SolidWorks software in 3-D as shown in Fig. 1. Using the dimensional values used in Bachant and Wosnik experiment Table I.

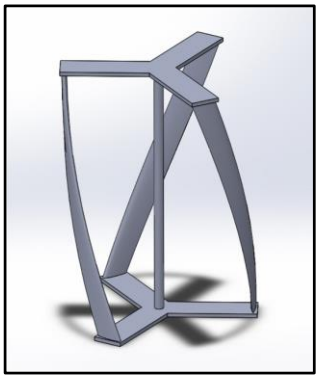

Fig. 1. Solid model of Gorlov Helical turbine previously used in open channel experiment

TABLE I. TURBINE GEOMETRIC SPECIFICATIONS

| Design Parameters | Dimensions |
|---|---|
| Diameter (m) | 1.00 |
| Height (m) | 1.32 |
| Blade Profile | NACA0020 |
| Chord Line Length (cm) | 14 |
| Camber Line Length (cm) | 14 |
| Frontal Area, $A_f$ ($m^2$) | 1.32 |
| Blade Overlap | 1/2 |

Details of municipal pipes were required to proceed further with in-pipe analysis. These pipe diameter and water flow rate data was obtained from the Water and Sanitation Agency (WASA).

### B. *Mesh Generation*

It was decided to use the multiple rotating reference frame technique to carry out the CFD analysis. Meshing of the model was done in Gambit. Hydrofoil blades of turbine were initially meshed. A sufficient mesh size was chosen to conform around the curved edges of the hydrofoil. Quad pave meshing scheme was used to generate a structured face mesh.

A growth factor was applied to generate unstructured volume mesh. Growth factor was applied in a way that mesh was kept extremely find near the hydrofoil blades and inside the rotating turbine volume Fig. 2.

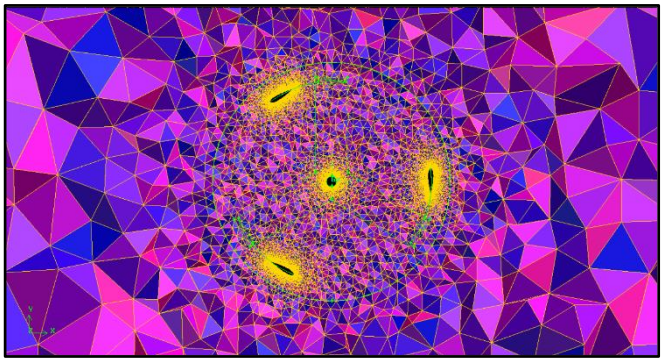

Fig. 2. Unstructured Mesh near Turbine blades.

## IV. SOLUTION STRATEGY

### A. *Mesh Independent Study*

Mesh independence study is used to ascertain whether the mesh generated is able to effectively capture the flow physics. Too coarse a mesh would give inaccurate result on the other hand an extremely fine mesh would result in high computational cost. Three different mesh sizes were generated for the open channel case. The values of $C_p$ were computed and compared with the experimental data as shown in Fig. 3. A mesh size of 3.1 M was finally selected for further analysis.

Fig. 3. Mesh independent study showing values of Cp obtained for three different mesh sizes

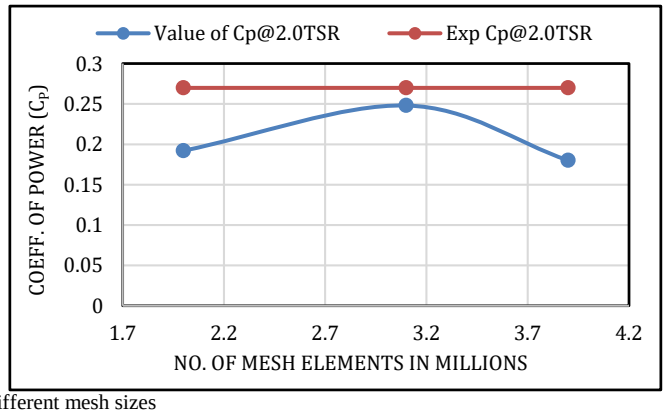


### B. *Time Independent Study*

Time independence study was carried out to determine the optimum time step size for further analysis Fig. 4. Three different time steps were initially chosen and coefficient of performance was computed for each time step. Time step corresponding to turbine rotation of 5 degrees per time step was chosen for further analysis.

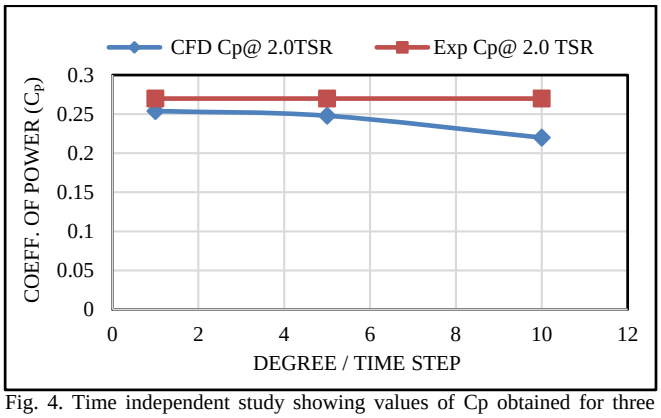


Fig. 4. Time independent study showing values of Cp obtained for three different time steps

## III. RESULTS AND DISCUSSION

### A. *CFD Validation Study of Gorlov Turbine in a Channel Flow*

Initially CFD analysis of Gorlov turbine when installed in a 3D channel similar to one used in Bachant and Wosnik experiment is carried out. An inlet flow velocity of 1.2 m/s is selected. Analysis is carried out at six different Tip to Speed Ratio (TSR). Fig. 5. shows pressure contours on a 2D plane drawn through center of turbine with flow direction shown with arrows. From the figure it can be seen clearly that turbine blade which is parallel to fluid flow direction has similar pressure field above and below the hydrofoil. The lift and moment generated by this hydrofoil would be nearly zero. The hydrofoils which are perpendicular to flow direction would feel a positive angle of attack of flow due to resultant vector of turbine rotation and flow direction. This positive angle of attack would result in positive lift and moment due to symmetric nature of hydrofoils. Due to helical nature of blades of Gorlov Turbine each cross section of helical blade is at different angle of attack but the net effect is such that the torque produced by Gorlov Turbine remains nearly constant throughout the revolution.

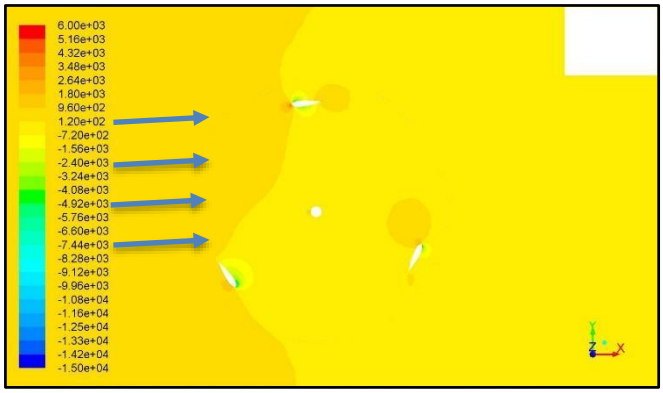


Fig. 5. Static pressure contours through horizontal cross-section of turbine. The fluid is flowing the positive X-direction. The turbine rotates in the positive Z-axis (anti-clockwise). The hydrofoil section in the extreme left is producing most lift, while the hydrofoil at the top is producing the least lift, at this time instant.

Fig. 6. shows variation of coefficient of performance with TSR. $C_p$ is computed for different TSR values. Maximum value of $C_p$ is observed at a TSR 2.0. With increase in TSR value turbine performance decreases.

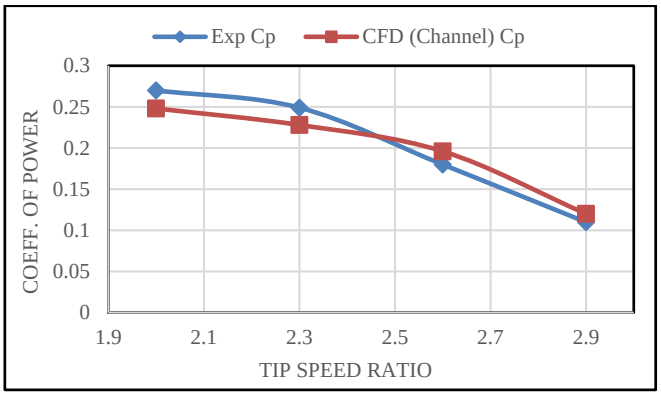


Fig. 6. Variation of $C_p$ with TSR, CFD vs Experimental results

Kinetic energy efficiency of turbine helps in measurement of its operational efficiency. High value of energy efficiency means that turbine is able to convert more of power extracted from flow into shaft power. Table. II. shows experimentally computed and CFD computed values of η for different TSRs. From table it can be seen that generally Gorlov turbine exhibits a high value of η. This efficiency decreases with increase in TSR value beyond 2.0. The values predicted by CFD analysis is in good agreement to experimental values validating the computational set up used for CFD analysis.

TABLE. II. Variation of η with TSR, CFD vs Experimental Results

| Tip Speed Ratio, TSR | Experimental Kinetic Energy Efficiency, η | CFD Kinetic Energy Efficiency, η |
|---|---|---|
| 2.0 | 0.46 | 0.412 |
| 2.3 | 0.41 | 0.372 |
| 2.6 | 0.29 | 0.244 |
| 2.9 | 0.16 | 0.148 |

### B. *CFD Analysis of In-pipe Gorlov Turbine*

The Gorlov turbine was subsequently installed inside a circular pipe. The diameter of pipe was kept equal to that of pipes used in water supplies. The dimensions of turbine and the flow inlet velocity was kept similar to that used in channel flow. CFD analysis was carried out at six different TSR values and results were compared with the channel flow results to evaluate Gorlov Turbine performance.

Fig. 7. shows velocity contours on a plane drawn at center of turbine. From the velocity contours it can be seen that the average velocity of flow inside the pipe has decreased due to wall effects present. Due to decrease in velocity the available energy in flowing fluid also decreases.

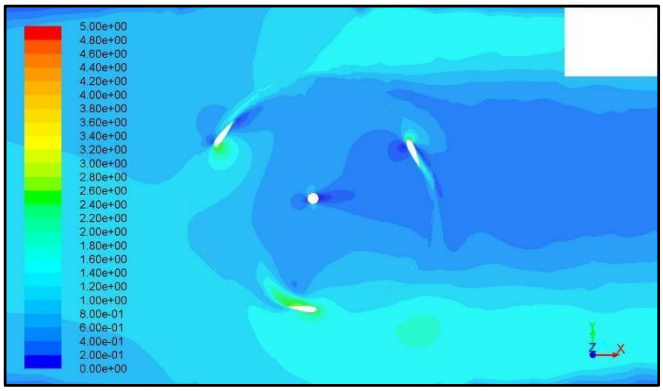


Fig. 7. Velocity magnitude contours on horizontal plane drawn through center cross-section of turbine.

Due to decrease in available flow energy the coefficient of performance of Gorlov turbine decrease when installed inside a pipe. Fig. 8. shows variation of $C_p$ with TSR for in-pipe and channel installation of turbine. As TSR value is increased $C_p$ value increases till TSR value of 2.0. As the TSR is further increased the performance of Gorlov turbine starts decreasing. The $C_p$ of in-pipe application is less than that of channel flow due to decrease in mean flow velocity available at turbine but the trend of variation of $C_p$ with TSR is quite similar.

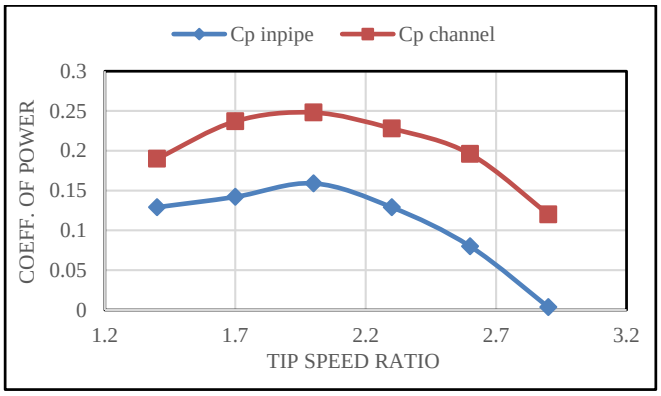


Fig. 8. Variation of $C_p$ with TSR, In-pipe vs. Channel Flow.

## V. CONCLUSION

The unsteady numerical analysis of Gorlov turbine when installed in a channel and inside a pipe has been carried out in this research. Turbine coefficient of performance and kinetic exigency efficiency was computed for both cases. Results were validated by comparing them with experimental study carried out at same conditions. Analysis was carried out at different TSR values and a prediction for most optimal TSR value was made based on this study. This study can also be used as a tool in future in carry out design optimization and changes of Gorlov Turbine for different installed and operating conditions.

## ACKNOWLEDGMENT

The authors gratefully acknowledge the use of Computer Aided Engineering Lab (CAEL) of the Institute of Avionics and Aeronautics, Air University, Islamabad, Pakistan.

## REFERENCES

[1] A. Gorlov, "Unidirectional Helical Reaction Turbine Operable Under Reversible Fluid Flow for Power Systems" U.S. Patent No. 5,451,137. 1995.

[2] Marie, D.G.J., LEBLANC VICKERS MAURICE SA, 1931. “Turbine Having Its Rotating Shaft Transverse to The Flow of The Current”. U.S. Patent 1,835,018.

[3] Bachant P. and Wosnik M., 2011, "Experimental Investigation Of Helical Cross-Flow Axis Hydrokinetic Turbines, Including Effects Of Waves And Turbulence". In ASME-JSME-KSME 2011 Joint Fluids Engineering Conference (pp. 1895-1906).

[4] Gorlov, A.M., 1998. “Helical Turbines for The Gulf Stream: Conceptual Approach to Design of a Large-Scale Floating Power Farm”. In Marine Technology and Sname News, 35(3) (p.175).

[5] Hinchey, M., 2014. “Design, Fabrication and Testing of a Water Current Energy Device”.

[6] Khan M.J., Bhuyan G., Iqbal M.T. and Quaicoe E., 2009. “Hydrokinetic Energy Conversion Systems and Assessment of Horizontal and Vertical Axis Turbines for River and Tidal Applications: A Technology Status Review”. In Applied energy, 86(10), (pp.1823-1835).

[7] Ladokun, L.L., Ajao, K.R. and Sule, B.F., 2013. “Hydrokinetic Energy Conversion Systems: Prospects and Challenges in Nigerian Hydrological Setting”. In Nigerian Journal of Technology, 32(3), (pp.538-549)

# Attitude Controller Design for ICUBE-2

Muhammad Hussan
*Department of Aeronautics and Astronautics,*
*Institute of Space Technology (IST),*
Islamabad, Pakistan.
muhammadhussan114@gmail.com

Talha Kaleem
*Department of Aeronautics and Astronautics,*
*Institute of Space Technology (IST),*
Islamabad, Pakistan.
talhakaleem7803@gmail.com

***Abstract*— ICUBE-2, the second student satellite being developed at Institute of Space Technology (IST), Islamabad is using an active attitude control system. In this paper Attitude Kinematics and Dynamics of ICUBE-2 are briefly described and atmosphere of space is modeled. Dynamics of ICUBE-2 are verified by using parameters of ZACUBE-2 satellite in the designed model and comparing the simulation results. The main features of ADCS module of ICUBE-2 which is CubeADCS is discussed. The algorithm for detumbling this satellite using an active, B-dot controller has been provided in this paper. For it, a simulator has been designed in MATLAB and Simulink in accordance with the iCube-2 mission and objectives. Performance analysis of detumbling shows that the time period required for detumbling can be lowered by using higher value of gain but it can increase overshoot and even instability. Also an attitude controller for use in normal mode is designed for ICUBE-2. A PD controller is designed for normal mode. Paper is summed up by a conclusion at the end.**

***Keywords- PD-controller, Kinematics, Dynamics, Dynamics Verification, ZACUBE-2, ICUBE-2, satellite simulator, geomagnetic field, Attitude Controller***

## I. INTRODUCTION

Launching a satellite for research and technology demonstration at university level was not possible in past due to the huge expenditures involved in the initiation. The idea of provision of cheap space research access to the university students resulted in the development of the miniaturized satellites. This led to the start of CubeSat programs under which standardized small satellites were prepared and launched for research purposes throughout various universities in the world [2]. Following the program, Institute of Space Technology (IST) has started development of the iCube-2 which will be a 3U satellite to be launched at 600 km LEO, sun synchronous orbit. It uses an active attitude determination and control system (ADCS) in which attitude is controlled using sensors and actuators through a control algorithm. This paper encompasses the design of the detumbling algorithm of iCube-2 along with a detailed literature review on the subject.

When the satellite is deployed into the orbit, its angular rates are much higher (about 0.1 rad/s) than those desired for orbital maneuvering and normal operations (below 0.03 rad/s) [5]. This high angular motion of the satellite is called tumbling and the satellite is detumbled in order to make it operable under the desired conditions with desired rates. Detumbling in CubeSats can be done with the help of various actuation schemes which can involve magnetotorquers, thrusters, reaction wheels or momentum wheels but magnetic detumbling has been employed for iCube-2.

Magnetorquers are used in the magnetic detumbling as actuators since they are lightweight and simple as compared to other actuators. The disadvantage of magnetotorquers is that the torque can only be produced if the local magnetic field is parallel to the torque rod. This means that at a given instant, only two of the three axis are controllable by this type of actuator. The complications in the magnetic field lines of the earth also limit the performance of magnetorquers.

For normal operation of a satellite it is needed by the satellite to point at different spots on earth and can also be required to do nadir pointing which can be said to be the normal mode of the satellite. And for the normal mode of operation normally a PD controller is employed which stabilizes the satellite and satellite can achieve earth pointing by using it.

The simulation of the detumbling and normal mode has been designed and run in MATLAB to test the validation of the algorithm for mission requirements. Before validation, magnetic field of earth has been modeled in the MATLAB using the International Geomagnetic Reference Frame (IGRF) Model which has been developed by International Association of Geomagnetism and Aeronomy (IAGA).

## II. CUBEADCS MODULE

CubeADCS module for ICUBE-2 has been acquired by the IST. CubeADCS module contains 3 Nano Reaction Wheels. A pair of torque rods and a magnetorquer coil. It contains deployable magnetometer, coarse sun sensor and MEMS Gyro as sensors. Total mass of the module is 502.8 grams while the power requirement of the module is 3270mW. The structural layout of the module is shown by the picture given below.

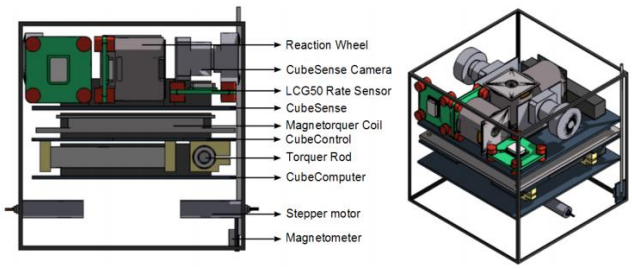


Fig 1. ADCS Module

## III. METHOGOLOGY

### A. Environment Modeling

#### 1) Model of Earth's Magnetic Field

The model of earth has been calculated in MATLAB using IGRF-15. In order to express this magnetic field in terms of the satellite's body axis, transformations of reference fields is required. The field obtained from the MATLAB model is in NED (North East Down) frame; it is converted into Earth's Inertial Frame or ECI (Earth

Centered Inertial) using the transformation matrix as follows:

$$B_{ECI} = R_{NED}^{ECI} B_{NED} \quad (1)$$

The field in ECI is then converted into satellite's body frame using transformation matrix as follows:

$$B_b = R_{ECI}^{b} B_{ECI} \quad (2)$$

Here,

$B_{ECI}$ : Earth's field in Earth Centered Inertial frame.
$R_{NED}^{ECI}$: Transformation from ECI to NED frame.
$B_{NED}$: Earth's geomagnetic field in NED frame.
$B_b$ : Earth's field in satellite body frame.
$R_{ECI}^{b}$ : Transformation matrix from ECI to body frame.
$B_{ECI}$ : Earth's geomagnetic field in ECI frame.

Applying these using SIMULINK, the magnetic field model in NED frame is generated as in fig. 1.

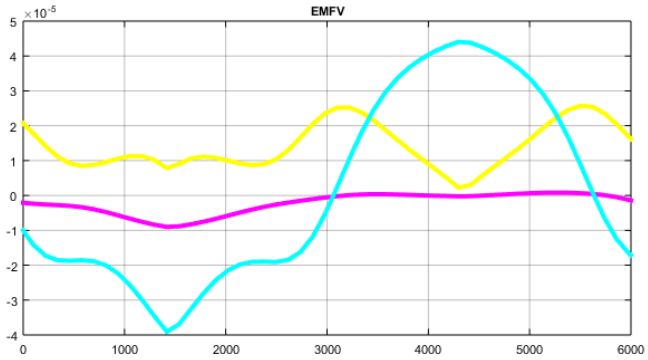


Fig 2. Earth's Geomagnetic Field in Tesla

*2) Gravity Gradient Torque*

Gravity gradient torque due to gravitational pull of earth is a very common torque in LEO orbits around earth. It depends upon the symmetry of the satellite and it's in orbit orientation as well. Mathematical relation for calculation of GG torques are as follows.

$$G_x = \frac{3\mu}{2R_0^3}(I_z - I_y)\sin(2\emptyset)cos^2(\theta) \quad (3)$$

$$G_y = \frac{3\mu}{2R_0^3}(I_z - I_x)\sin(2\theta)cos(\emptyset) \quad (4)$$

$$G_z = \frac{3\mu}{2R_0^3}(I_x - I_y)\sin(2\theta)sin(\emptyset) \quad (5)$$

Where, $G_x$, $G_y$and $G_z$ are the torques about X, Y and Z-axis respectively.

## B. Dynamics & Kinematics of ICUBE-2

*1) Moment of Inertia of ICUBE-2*

A 3D model of ICUBE-2 is shown in the figgure below.

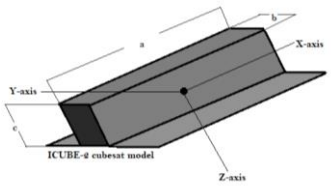


Mass of Satellite $= M_s = 3.873$ kg

Mass of Solar Panel $= M_p = 0.127$ kg

**Standard Satellite Dimensions**

a $= 0.33$meters
b $= 0.1$meters
c $= 0.1$meters

**Solar panel Dimensions**

a $= 0.325$meters
b $= 0.0826$meters
c $= 0.0022$meters

Moment of inertia of main CubeSat body and solar panels are calculated individually and then, transferred about the centroid of the body using parallel axis theorem. Moment of inertia matrix calculated about centroid is as follows.

$$I = \begin{bmatrix} 0.009746 & 0 & 0 \\ 0 & 0.041203 & 0 \\ 0 & 0 & 0.04328 \end{bmatrix} \quad (6)$$

*2) Dynaimcs*

The Euler dynamic equation explaining the dynamics of ICUBE-2 is as follows.

$$T_c + T_d + T_{mc} = \dot{h}_I = \dot{h} + w \times (Iw) \quad (7)$$

where,

$I$ = Moment of inertia of the ICUBE-2.
$\dot{w}$ = Angular acceleration of the ICUBE-2.
$T_c$= Control torque provided by the reaction wheels.
$T_{mc}$= Momentum Control torque provided by the magnetorquers.
$T_d$ = disturbance Torque.

The above equation provides angular rates w.r.t. inertial reference frame. However, for the definition of attitude we need angular rates in orbital reference frame. Equation explaining this relation is as follows.

$$w_{BI} = w_{BR} + w_{RIB} \quad (8)$$

Here,

$w_{BI} = angular\ rate\ of\ the\ satellite\ body\ frame\ w.r.t.inertial\ frame$
$w_{BR} = angular\ rate\ of\ the\ satellite\ body\ frame\ w.r.t.OR\ frame$

$$w_{RI} = \begin{bmatrix} 0 \\ -w_o \\ 0 \end{bmatrix} \quad (9)$$

$$R_{321} = \begin{bmatrix} cos\psi cos\theta & sin\psi cos\theta & -sin\theta \\ -sin\psi cos\emptyset + cos\psi sin\emptyset sin\theta & cos\psi cos\emptyset + sin\psi sin\emptyset sin\theta & sin\emptyset cos\theta \\ sin\psi sin\emptyset + cos\emptyset cos\psi sin\theta & -cos\psi sin\emptyset + cos\emptyset sin\theta sin\psi & cos\emptyset cos\theta \end{bmatrix}$$

$$w_{RIB} = R_{321} w_{RI} \quad (10)$$

*3) Kinematics*

Attitude of ICUBE-2 is defined by using 3 Euler angles Phi, Theta and Si which are the angular rotation of the satellite body about X, Y and Z-axis respectively. These Euler angles are represented in the form of equation as follows.

$$\dot{\theta} = \frac{[p\sin(\psi) + qcos(\psi)]}{\cos(\emptyset)} \quad (11)$$

$$\dot{\emptyset} = pcos(\psi) - q\sin(\psi) \quad (12)$$

$$\dot{\psi} = [p\sin(\psi) + qcos(\psi)]\tan(\emptyset) + r \quad (13)$$

Where,

$$w_{BR} = \begin{bmatrix} p \\ q \\ r \end{bmatrix} = \begin{bmatrix} sin\psi cos\emptyset\dot{\theta} + \dot{\emptyset}cos\psi \\ cos\psi cos\emptyset\dot{\theta} - \dot{\emptyset}sin\psi \\ -\dot{\theta}sin\emptyset + \dot{\psi} \end{bmatrix}$$

### C. Reaction Wheel

Reaction wheel is torque producing actuator. It consists of a motor and a wheel attached to the shaft of the motor. As, shaft rotates wheel rotate with it which as a result rotates the satellite in opposite direction.

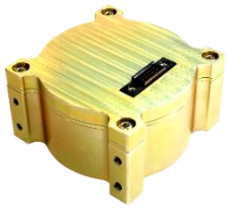

Fig 3: Reaction Wheel

The dynamics of a reaction wheel are as follows.

$$\frac{\dot{h}_w}{V} = \frac{s\left(\frac{K_M}{R_M}\right)}{s + \left(\frac{1}{I_w} + \frac{1}{I_s}\right)\left(\frac{K_v K_M}{R_M} + B\right)} \quad (14)$$

The simplified equation is as follows.

$$\frac{T_R}{T_c} = \frac{1}{1 + \frac{sR_M}{K}} \quad (15)$$

Here,

$R_M$ = Resistance of the armature of motor.

K = Reaction wheel gain constant.

The inertia of the wheel in the reaction wheel is $1.9757\text{e} - 06\text{kgm}^2$. The motor used in the reaction wheel is FAULHABER 1509 006 B BLDC Motor.

### D. Magnetorquer

Magnetorquer is a magnetic actuator. It consists of a ferromagnetic core wounded with a wire. When current is passed through the wire a magnetic field is created which upon interaction with earth's magnetic field produces a torque.

Fig 3. Magnetorquer

Mathematical equations explaining the dynamics of a magnetorquer are as follows.

$$T = m \times B \quad (16)$$

Where,

T : The torque produced

m : Magnetic moment of spacecraft

B : The Geomagnetic field in body frame

The moment generated by the magnetorquer is based on its physical properties and is given by the following relation:

$$m = \hat{n}AIN \quad (17)$$

Where,

A : Cross-sectional area of the coil

I : Current required

N : The number of the coils.

Substitution of the equations results in the following relation for torque produced:

$$T = AIBN(\hat{n} \times \hat{b}) \quad (18)$$

Where,

$\hat{n}$ : The unit vector of electro-moment dipole

$\hat{b}$ : The unit vector of local magnetic field

## IV. Verification of ICUBE-2 Dynamics

Once, the dynamics for ICUBE-2 were established they were needed to verified for their use. This verification is carried out by considering parameters of ZACUBE-2 which is a 3U CubeSat operating at altitude of about 450-500km. We catered for GG torque, momentum dumping toque for reaction wheel and reaction wheel torque itself. But atmospheric drag was not catered. Since, atmospheric drag is not prominent at altitude of 600km but is necessary to be included at altitudes close to 400km.

Inertia Tensor of ZACUBE-2 is as follows.

$$I = \begin{bmatrix} 0.0071 & 0 & 0 \\ 0 & 0.035 & 0 \\ 0 & 0 & 0.337 \end{bmatrix} kgm^2 \quad (19)$$

angular orbital velocity= $w_o = 0.0011079354\ rad/s$

The Controller of ZACUBE-2 is given below.

$$N_w = \begin{bmatrix} (0.0014)\hat{w}_{xo} + (0.000284)\hat{q}_{1e} \\ (0.007)\hat{w}_{yo} + (0.0014)\hat{q}_{2e} \\ (0.0067)\hat{w}_{zo} + (0.0013)\hat{q}_{3e} \end{bmatrix} \quad (20)$$

Simulation results for both are given below.

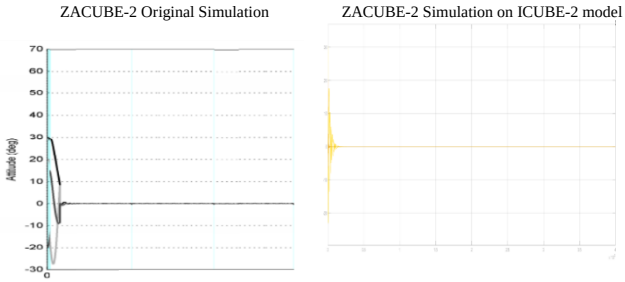


Fig 5: Comparison of Models

As, we can see from the above two figures that both of these models are showing a stable behavior. Which is ultimately proof of good dynamics.

## V. Detumbling Controller Design

In order to detumble the satellite, magnetorquer is employed through Bdot scheme, in which the angular velocity of the satellite is made equal or close to zero, using the following control torque [3]:

$$\mathrm{T_{ctrl}} = -\frac{k}{\|\vec{B}\|}(\vec{\omega} \times \vec{b}) \quad (21)$$

Where,

$$b = B/\|\vec{B}\| \quad (22)$$

And

k is a scalar positive gain.

An approximation for the value of the magnetic moment has been calculated as follows:

$$\vec{m} = -\frac{k}{\|\vec{B}\|}\dot{B} \quad (23)$$

This equation is called Bdot control law whose gain value can be approximated as follows [4]

$$k = \frac{4\pi}{T_{orb}}(1 + sini)I_{min} \quad (24)$$

This gain is not a PID or adaptive gain, but a fixed single gain. In the above expression,

$T_{orb}$ : The orbital time period in seconds.

i : The inclination angle in degrees.

$I_{min}$ : The lowest value of principal moment of inertia.

### A. *Detumbling Simulator*

The detumbling simulator has been designed in MATLAB and Simulink with a graphic user interface for better visualization. Inputs include initial angular velocity, mass and dimensions of satellite, earth's mass, disturbance torques and actuator dimensions. Outputs are in the form of graphs of angular rates of the satellite which are obtained from the dynamics of the CubeSat.

First, the magnetic field of the earth has been modeled using the IGRF-15 model put forward by the IAGA. The results obtained have already been shown in fig.1. The detumbling law requires this field to be converted into the satellite's body axis. For this various transformations have been carried out according to the relations expressed in the section II. The Simulink model of the transformations is expressed as in fig.2.

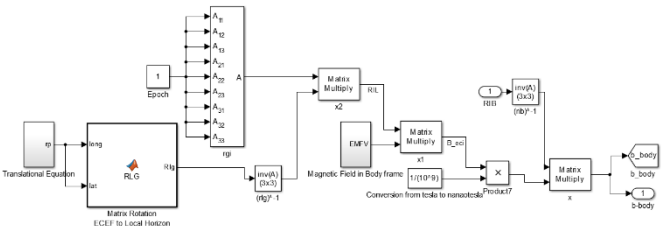


Fig 6. Rotational Transformations

Transformation equation provides the position and velocity of the satellite in meantime while epoch block provides the time at which the simulation is being run. Magnetic field of the satellite is then brought into the relation and the information of the angles of the satellite is also included. Then transformations are applied to obtain the magnetic field in the body reference frame of the satellite.

The satellite's magnetic field, angular rates, and gain are input into the Bdot algorithm and the moment required for the detumbling is obtained as shown in fig 3.

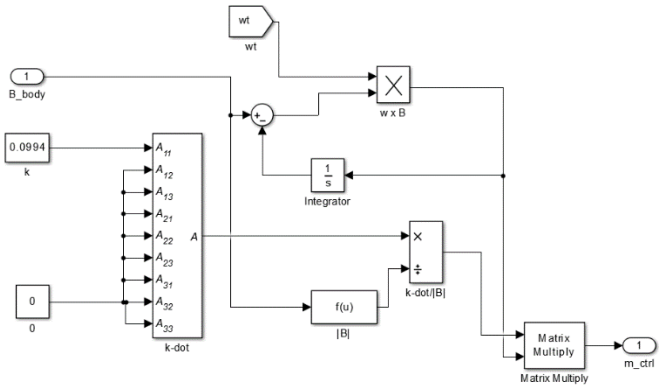


Fig 7. Bdot Algorithm

The moment obtained from the Bdot algorithm is then converted into the current so that it can be fed into the magnetometer to produce the desired moment. The relations used for this conversion included the properties of the magnetotorquer and the information of the geomagnetic field in the satellite body frame to convert it into magnetorquer torque as shown in fig 4.

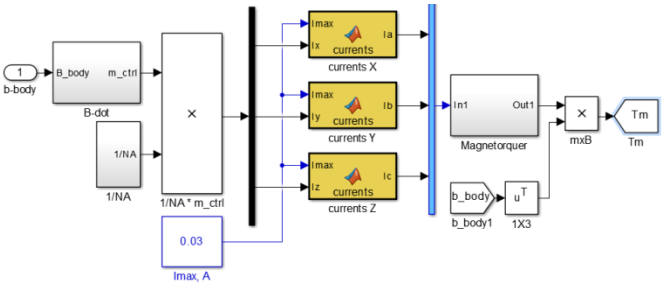


Fig 8. Generation of Magnetorquer Torque

The torque obtained is then fed into the iCube-2 dynamics block where disturbance torques and torques obtained from rotational equation are interacted to obtain the overall angular speeds of the satellite. Initial angular rates are also input at this point of the algorithm in order to account for the initial rates. The algorithm for this dynamics is illustrated in fig 5.

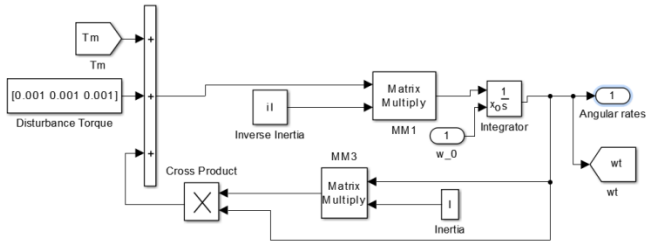


Fig 9. iCube-2 Dynamics

The angular rates are used in the kinematics relation where Euler angles of the satellite's attitude are obtained using the 313 rotational sequence of the satellite kinematics. The angles obtained are then used for the calculation of the direction cosine matrix which is used in the rotational matrix for conversion into body frame from the inertial frame of reference.

The overall Simulink diagram of the Bdot algorithm is shown in the fig 6. The initial angular velocity is taken at the start and the angular rates of the satellite are obtained from the scope ωt. These rates are then made to approach 0 rad/s in order to detumble the satellite according to the requirements. The time in which the detumbling operation

is carried out and the overshoot at the start are the factors which determine the detumbling effectiveness.

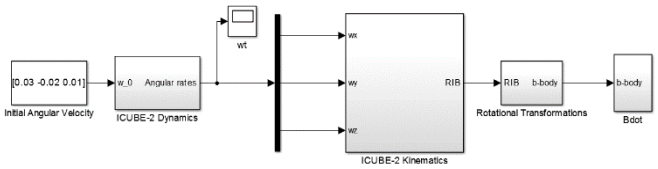


Fig 10. iCube-2 Detumbling Algorithm

## VI. Attitude Controller Design

Most of the controllers designed linear controllers for linear systems. However, generally most of the systems in nature are non-linear and are needed to be linearized. So, that linear control theory could be applied to them.

The simplest form of dynamics for ICUBE-2 can be written as follows.

$$\alpha = \frac{1}{s^2 I_i} \tag{25}$$

Where, $\alpha = \emptyset, \theta \; and \; \psi$ and $i = x, y, z$

Root locus plot of SISO system along X-axis is as follows.

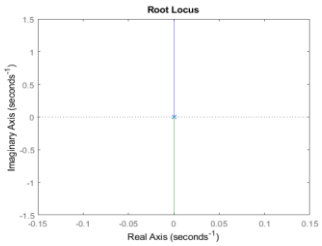


Fig 11. Rooot Locus

Step response for $\emptyset$ is given as follows.

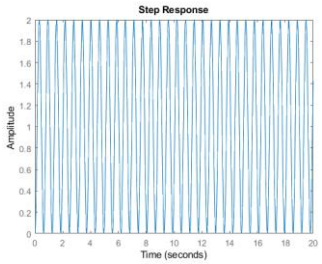


Fig 12. Step Response

For ICUBE-2 a proportional controller alone would not work. The reason is the presence of two poles at the origin which drives it marginally stable as shown in the above figure. To make it stable a derivative action is needed. Since, rate feedback of a system is stabilizing. So, Derivative action does make the system stable. But it if a steady sate error already exists in a system derivative control does not eliminates it. Steady sate error is directly related to the gain of proportional controller larger the gain smaller is the steady state error. To remove this steady state error integral part of PID control play role. For a 600km LEO orbit, disturbances are of very small value and does not lead to instability. However, a SteadyState error is generated which is very small to be considered. That's why only PD controller is implemented.

For a small spacecraft with large disturbances we would have also implemented Integral controller for removing steady state error.

A Proportional Derivative (PD) controller is defined as follows.

$$K_{PD} = k_p + k_d s \tag{26}$$

The general form of closed loop transfer function between input and output along with PD controller is defined as follows.

$$\frac{\alpha}{U} = \frac{k_{p_i} + k_{d_i} s}{I_i s^2 + k_{p_i} + k_{d_i} s} \tag{27}$$

The step response for the Phi control is as follows.

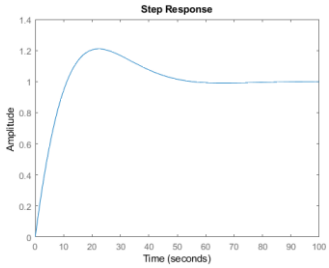


Fig 13. Step Response

A second order polynomial can be generally written in a more appropriate way as follows.

$$s^2 + 2\zeta w_n s + w_n^2 \tag{28}$$

By setting values of natural frequency to be 0.1 and that of damping ratio to be 0.7 the controller designed for each axes of the ICUBE-2 independently are as follows.

$$K_{PD_x} = 0.000097 + 0.001358s \tag{29}$$

$$K_{PD_y} = 0.000412 + 0.005768s \tag{30}$$

$$K_{PD_z} = 0.000433 + 0.006062s \tag{31}$$

## VII. Simulation Results

### A. Detumbling controller results

The simulations have been done for the detumbling mode by varying the values of the gain. The initial angular rates are $\omega_0$= [0.03 -0.02 0.01] rad/s and the Euler angles are kept to be [ψ θ ϕ] = [0 0 0] degrees, initially. Angular velocity has been plotted against time at various gains to obtain the response.

It is apparent from the plot of fig 7 that the time needed to detumble iCube-2 is nearly 1600 seconds which is less than its time period; hence it is detumbling in less than an orbit time. The effect of geomagnetic field on the y-axis is not too strong in comparison with other axes hence the full rotation has not took place at the start of the simulation. At Earth's poles, geomagnetic field is strong which causes changes in the angular velocity of the satellite. These robust changes are difficult to control, even if the gain value is large enough. Hence, near poles, there are disruptions in the satellite's attitude even after it has been detumbled properly. Similarly, the simulations were carried out at various values of gains and the plots were generated. The results illustrated are explained in the conclusions.

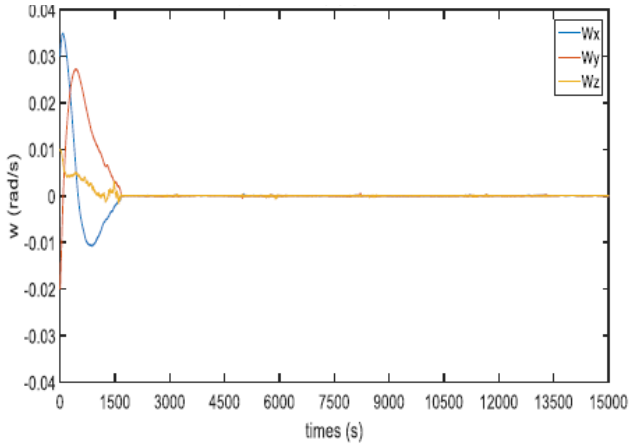


Fig 13. Angular Rates of iCube-2 for T=15000s

### *B. PD controller simulations*

The above designed SISO PD Controller is applied to complex nonlinear MIMO system with dynamic coupling present. But simulations show that the system works well and behaves in a decent way. First inputs to all the three axes is given individually and their response is observed. These responses are given below.

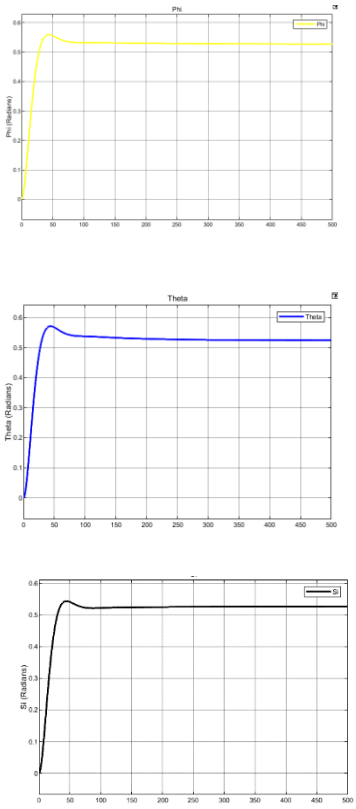

Fig 14. Responses

These simulations show that with a very small overshoot and a decent settling time satellite is able to attain its desirable reference attitude.

Now, the combined simulation is run which includes the interference and coupling of all individual axes. In this simulation a step input of 30 degrees is given to all the axes and results are plotted which are given below.

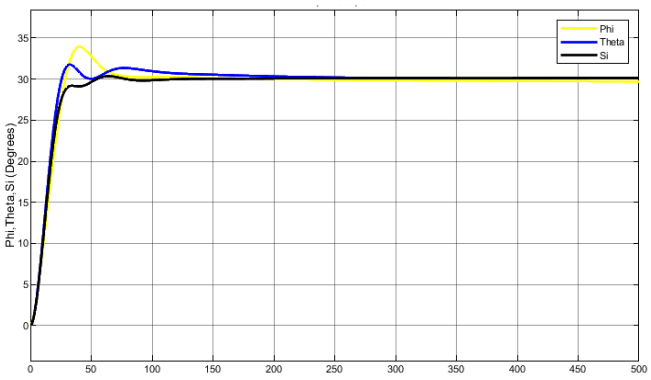


Fig 15. Combined Response

This result again shows that a good settling time and overshoot is achieved.

### *C. Conclusions*

Results show that the value of gain is a defining parameter for the sensitivity of the magnetometer model and the efficiency of the detumbling. With the increase in the value of gain, the time to achieve the detumbling is reduced and vice versa. However, too high values of gain increase the magnetic disturbances which result in high overshoot, which can have hazardous effects on the satellite's components. The best and the smooth results have been obtained in this paper using the gain value of 10. The detumbling is not achieved if the gain is increased beyond $10^5$ thus it is the maximum limit of the gain under satellite components' restraints. The system goes unstable at the gain value of 10 at time= ±1000s, regarding it to be avoidable. The value of the current has been limited to 30mA or 0.030A so that the physical limits of the actuator are not exceeded in the detumbling operation.

Another parameter which effects the satellite's detumbling is the satellite's dimensions. If moment of inertia matrix of the satellite is changed the value of gain is changed which results in the change in the satellite's detumbling time and overshoot. Thus, if the model of any other satellite is used in the detumbling simulator, the working of the simulator changes accordingly.

The designed PD controller shows very good simulation results. It shows a selling time of about 70 seconds. For individual SISO simulations an overshoot of about 10 percent can be seen which is very normal and good. With MIMO control Phi output shows an overshoot of 13 percent and settling time of 65 seconds, Theta output is showing 40 seconds of settling time and 7 percent of overshoot and the Si control is showing a 50 seconds of settling time and no overshoot at all.

### ACKNOWLEDGMENT

First, of all we would like to thank Almighty Allah for his blessing and our family for their love and support. Then, we would thank Dr. Hayat Muhammad Khan from Department of Aeronautics and Astronautics, Institute of Space Technology (IST), Islamabad as our official supervisor and Dr. Rehan Mehmood from Department of Electrical Engineering, Institute of Space Technology (IST), Islamabad, as our co-supervisor for our material and mental support in the project. We would also thank Sir, Farooq Aslam for his appreciable help and concern.

## REFERENCES


[1] Gerber, Jako. "A 3-axis attitude control system hardware design for a cubesat." PhD diss., Stellenbosch: Stellenbosch University, 2014.

[2] Mahmood, Rehan & Khurshid, Khurram & Zafar, Adnan & ul Islam, Qamar. (2011). ICUBE-1: First Step towards Developing an Experimental Pico-satellite at Institute of Space Technology. Journal of Space Technology. 1. 5-10.

[3] Makovec, Kristin Lynne. "A nonlinear magnetic controller for three-axis stability of nanosatellites." PhD diss., Virginia Tech, 2001.

[4] Muksin A, Poetro RE, Triharjanto RH. Pico-satellite detumbling simulation using magnetic atitude actuator (simulasi detumbling pada satelit piko menggunakan aktuator sikap magnetik). Jurnal Teknologi Dirgantara. 2017 Dec 14;15(1):11-20.

[5] Pignède A. Detumbling of the NTNU Test Satellite. Project thesis, Norwegian University of Science and Technology, Department of Engineering Cybernetics. 2014.

[6] Wertz, James R., ed. Spacecraft attitude determination and control. Vol. 73. Springer Science & Business Media, 2012.

[7] Sidi, Marcel J. Spacecraft dynamics and control: a practical engineering approach. Vol. 7. Cambridge university press, 1997.

[8] Auret, Jacoba. "Design of an aerodynamic attitude control system for a CubeSat." PhD diss., Stellenbosch: Stellenbosch University, 2012.

[9] Markley, F. Landis, and John L. Crassidis. Fundamentals of spacecraft attitude determination and control. Vol. 33. New York: Springer,2014

# Robotic Manipulator for Space Debris Mitigation in Low Earth Orbit

Wajih Ahmed Khan
*College of Aeronautical Engineering (CAE),*
*National University of Science and Technology (NUST) Islamabad,*
Pakistan
wajihak92@gmail.com

Dr. Ali Sarosh
*College of Aeronautical Engineering (CAE),*
*National University of Science and Technology (NUST) Islamabad,*
Pakistan
alisarosh@cae.nust.edu.pk

Usman Iqbal Ahmed
*College of Aeronautical Engineering (CAE),*
*National University of Science and Technology (NUST) Islamabad,*
Pakistan
usman.iqbal69@cae.nust.edu.pk

*Abstract*— **Natural and artificial space debris have congested the Earth orbits required by humans for spacecraft missions and it is growing day by day. Space debris remains a constant threat to all the functional satellites operating in the Low Earth Orbit (LEO). For many space agencies around the world, space debris mitigation is becoming their top priority and are performing research on various techniques that include robotic arms, net capturing, tether gripper and harpoon mechanism. In this research the design of a microsatellite (chaser) equipped with instrumentation and robot manipulator is proposed. The robotic arm satellite will be capable of performing in-orbit rendezvous with the debris (target) to capture it. Once the microsatellite comes in the vicinity of the target, Light Detection and Ranging (LIDAR) scanning and tracking will be used to locate the position of debris, thereafter an end-effector mechanism of robot manipulator will be employed to grab and dispatch space debris to either graveyard orbit or to re-enter Earth's atmosphere where the debris will burn up. Robot manipulator for space debris mitigation can assist in securing the LEO for future commercial space missions. It can allow functional satellites in LEO to operate without having to perform debris avoidance maneuvers.**

***Keywords— Space Debris Mitigation, Low Earth Orbit, In-Orbit Rendezvous, Robot Manipulator, End-Effector Mechanism, LIDAR Tracking (****key words****)***

## I. INTRODUCTION

Since the start of the space program back in 1970's, it was generally believed that NORAD was tracking all man-made artificial objects in Earth orbit and that the catalogued objects represented the serious collision threat to other operational satellites but as mentioned in the Kessler syndrome, the significant increase in the number of artificial satellites has increased the probability of in-orbit collisions which further generate more debris in the orbit [1]. Even though space debris under the influence of gravitational force of Earth suffers from atmospheric decay and burns upon re-entry to Earth's atmosphere, the amount of debris in the orbit is still on the rise.

Statistical models have estimated that there are approximately 34,000 objects present in the orbit with dimensions of more than 10 cm and around 900,000 between the sizes of 1-10 cm. Total mass of objects in the orbit is close to 8400 tons. Since 1957 there have been more than 500 incidents of collisions, explosions and break-ups of satellites adding more debris into the Earth's orbit. Table I shows the number of operational satellites and debris present in the orbit as of January, 2019.

Table I. Population of operational satellites since 1957 as of January 2019 [2]

| **Status** | **Operational Satellites** |
|---|---|
| Launched | 8950 |
| In-Orbit | 5000 |
| Still Functioning | 1950 |

The figures above determine the urgency required to develop a solution to clean the orbit for safe operations in future. Space agencies working on various methods for the removal of space debris. Tentacles mechanism requires high accuracy to operate [3]. Robotic arm (Single) have been used in space for various applications, some of the examples include ETS-7 and Canadarm-2 [4]. Multiple Robotic arms provide very effective capturing but are very complex to control and they increase the cost and mass of the system [5]. Net Capturing is a technique suitable for capturing very large debris [6]. Tether gripper Harpoon mechanism has the risk of generating more debris when come in contact with the debris [7], [8].

This research focusses on the concept of a semi-autonomous single arm robot manipulator attached to a satellite for mitigation of space debris. Equipped with high end Laser sensor to locate debris [9]. Using satellite (chaser) to perform an in-orbit rendezvous with the debris, capture it and re-direct its path to enter Earth's atmosphere or to the graveyard orbit as shown in Fig.1.

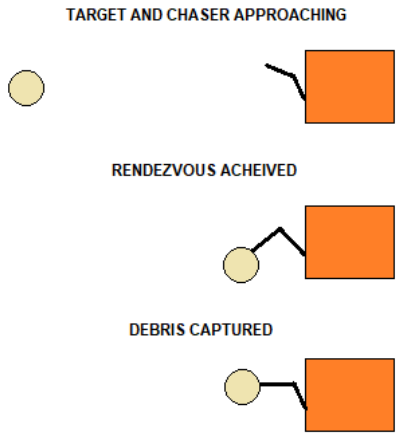


Fig. 1: Debris Capturing Concept

The paper is arranged in different sections. Section 2 comprises of the methodology applied to develop the robot manipulator. Section 3 includes the Results. Section 4 is dedicated to Analysis and section 5 consists of Conclusion.

## II. METHODOLOGY

Inverse kinematics technique was applied in capturing process since the independent variables were the joints and the process of capturing was in terms of reference coordinate frame. The robot manipulator scans the environment in front of it using LIDAR sensor. Once the debris is detected the microcontroller acquires the position of the object; ther satellite starts performing rendezvous. When the object comes in range of the manipulator, inverse kinematic solution calculates the relevant joint angles to capture the debris. The captured debris can now be dispatched away from the functional satellites using manual control of the robot arm. See Fig. 2 for flow chart.

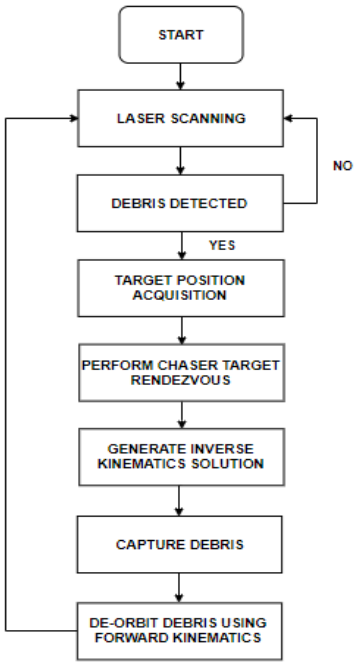


Fig. 2: Flow Chart

### A. 3D Model

Three dimensional model of the robot manipulator was designed SolidWorks software. Base of the robot attaches to the base of the satellite providing a stiff connection. U-shaped brackets form linkages of the manipulator and multi-purpose brackets hold motors at specified joints for rotation. Joints position can be seen in Fig. 3.

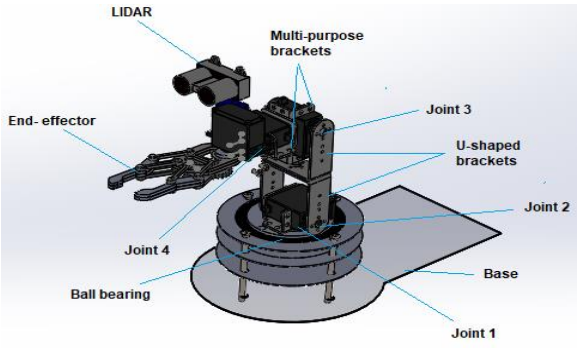


Fig. 3: 3D Model of Manipulator

### B. Denavit Hartenberg Parameters

The D-H representation results in a 4x4 homogeneous transformation matrix representing the robot arm's each link's coordinate system at the joint with respect to previous link's coordinate system [10].

Fig.4 represents the coordinate frame diagram of Debris Mitigation Robot manipulator. Every coordinate is determined and established on the basis of three rules:

- $Z_{i-1}$ axis lies along the axis of motion of the ith joint.
- $X_i$ axis is orthogonal to the $Z_{i-1}$ axis, and pointing away from it.
- $Y_i$ axis completes the coordinate system using the right hand rule.

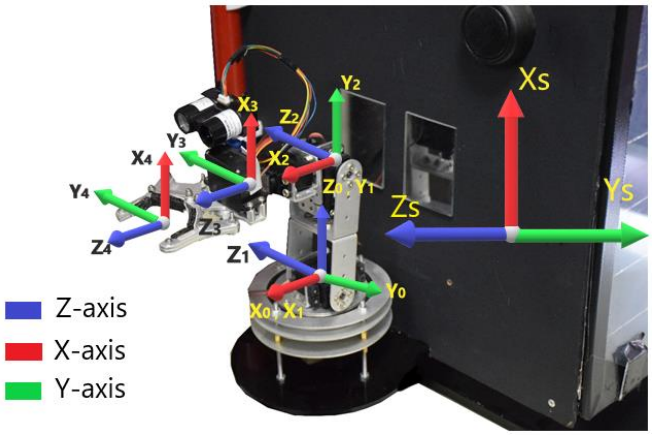


Fig. 4: Coordinate frames attached to manipulator

$\Theta_i$ is the angle of the joint from $X_{i-1}$ axis to the $X_i$ axis about $Z_{i-1}$ axis.
$d_i$ is the length between $X_{i-1}$ and Xi along $Z_{i-1}$.
$\alpha_i$ is the angle between $Z_{i-1}$ to $Z_i$ around $X_i$.
$a_i$ is the length between $Z_{i-1}$ to $Z_i$ along $X_i$.

Table II. Denavit-Hartenberg representation

| Joint | $\Theta_i$ | $d_i$ | $a_i$ | $\alpha_i$ |
|---|---|---|---|---|
| 1 | $\Theta_1$ | 0 | 0 | $\frac{\pi}{2}$ |
| 2 | $\Theta_2$ | 0 | $a_2$ | 0 |
| 3 | $\Theta_3$ | 0 | 0 | $\frac{\pi}{2}$ |
| 4 | $\Theta_4$ | $d_4$ | 0 | 0 |

### C. Transformation Matrix

Using the D-H table generated above we can find the homogeneous transformation matrix relating the ith coordinate frame to the (i-1)th coordinate frame. The forward kinematics describes the transformation from one frame to another, starting at the base and ends at the end-effector. $^{i-1}A_i$ is the transformation matrix between the coordinate frames located at ith and (i-1)th joint and $^0T_i$ is the transformation matrix from base to the end-effector.

$$^{i-1}A_i = \begin{bmatrix} \cos\theta i & -\cos\alpha i \sin\theta i & \sin\alpha i \sin\theta i & ai\cos\theta i \\ \sin\theta i & \cos\alpha i \cos\theta i & -\sin\alpha i \cos\theta i & ai\sin\theta i \\ 0 & \sin\alpha i & \cos\alpha i & di \\ 0 & 0 & 0 & 1 \end{bmatrix} \quad (1)$$

$$^0T_i = {}^0A_1\,{}^1A_2 \ldots {}^{i-1}A_i \quad (2)$$

n = Represents normal vector of the end-effector.
s = Sliding vector of the end-effector.
a = Approach vector that is always perpendicular to the palm of the end-effector.
p = It is the position vector of the end-effector.

$$T = \begin{bmatrix} n_x & s_x & a_x & p_x \\ n_y & s_y & a_y & p_y \\ n_z & s_z & a_z & p_z \\ 0 & 0 & 0 & 1 \end{bmatrix} \quad (3)$$

Elements of transformation matrix from end-effector to base of the space debris mitigation manipulator were derived as:

$$n_x = Cos\theta_1 Cos\theta_2 Cos\theta_3 Cos\theta_4 - Cos\theta_1 Sin\theta_2 Sin\theta_3 Cos\theta_4 + Sin\theta_1 Sin\theta_4 \quad (4)$$
$$n_y = Sin\theta_1 Cos\theta_2 Cos\theta_3 Cos\theta_4 - Sin\theta_1 Sin\theta_2 Sin\theta_3 Cos\theta_4 - Cos\theta_1 Sin\theta_4 \quad (5)$$
$$n_z = -Sin\theta_2 Cos\theta_3 Cos\theta_4 + Cos\theta_4 Sin\theta_3 Cos\theta_4 \quad (6)$$
$$s_x = -Cos\theta_1 Cos\theta_2 Sin\theta_4 Cos\theta_3 + Cos\theta_1 Sin\theta_2 Sin\theta_3 Sin\theta_4 + Sin\theta_1 Cos\theta_4 \quad (7)$$
$$s_y = -Sin\theta_1 Cos\theta_2 Sin\theta_4 Cos\theta_3 + Sin\theta_1 Sin\theta_2 Sin\theta_3 Sin\theta_4 - Cos\theta_1 Cos\theta_4 \quad (8)$$
$$s_z = -Sin\theta_2 Sin\theta_4 Cos\theta_3 - Cos\theta_2 Sin\theta_3 Sin\theta_4 \quad (9)$$
$$a_x = Cos\theta_1 Cos\theta_2 Sin\theta_3 + Cos\theta_1 Sin\theta_2 Cos\theta_3 \quad (10)$$
$$a_y = Sin\theta_1 Cos\theta_2 Sin\theta_3 + Sin\theta_1 Sin\theta_2 Cos\theta_3 \quad (11)$$
$$a_z = Sin\theta_2 Sin\theta_3 - Cos\theta_2 Cos\theta_3 \quad (12)$$
$$p_x = Cos\theta_1 Cos\theta_2 Sin\theta_3 d_4 + a_2 Cos\theta_1 Cos\theta_2 + Cos\theta_1 Sin\theta_2 Cos\theta_3 d_4 \quad (13)$$
$$p_y = Sin\theta_1 Cos\theta_2 Sin\theta_3 d_4 + a_2 Sin\theta_1 Cos\theta_2 + Sin\theta_1 Sin\theta_2 Cos\theta_3 d_4 \quad (14)$$
$$p_z = Sin\theta_2 Sin\theta_3 d_4 - Cos\theta_2 Cos\theta_3 d_4 + a_2 Sin\theta_2 \quad (15)$$

### D. Inverse Kinematics Solution

The inverse kinematics solution was achieved using the geometric approach to calculate the joint angles to reach the target position [11]. In Fig. 5 $\theta_1$ and $\theta_4$ remain constant during the target capturing process thus, are not included in the geometric solution of the manipulator. $l_1$ is the length of the first link and $l_2$ is the offset between joint 4 and the end-effector. *P* denotes the end-effector's position in 3D space.

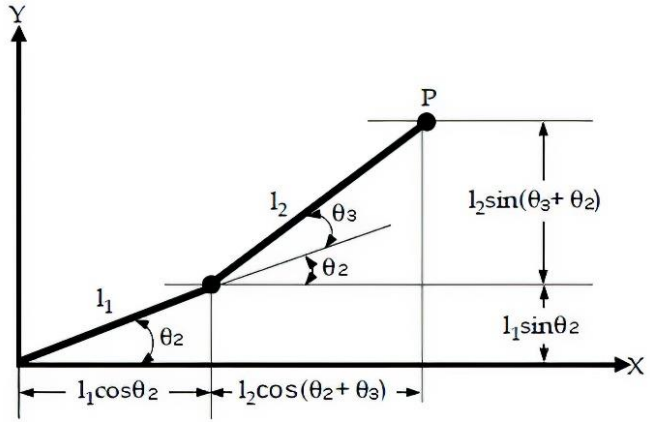


Fig. 5: Geometric Solution

$$\theta_2 = Atan2\left[\pm\sqrt{1-\left(\frac{P_x(l_1+l_2Cos\theta_3)+P_y l_2 Sin\theta_3}{P_x^2+P_y^2}\right)^2}, \left(\frac{P_x(l_1+l_2Cos\theta_3)+P_y l_2 Sin\theta_3}{P_x^2+P_y^2}\right)\right] \quad (16)$$

$$\theta_3 = Atan2\left[\pm\sqrt{1-\left(\frac{P_x^2+P_y^2-l_1^2-l_2^2}{2l_1l_2}\right)^2}, \frac{P_x^2+P_y^2-l_1^2-l_2^2}{2l_1l_2}\right] \quad (17)$$

### E. Angular Velocity of End-Effector

For a revolute joint:

$$\omega = \dot{\theta}_i \hat{u}. \quad (18)$$

$\omega$ is angular velocity of the end effector. $\dot{\theta}_i$ is the rate of change of joint variable of the $i^{th}$ joint. û is a unit vector in Z direction. Angular velocity of the end effector is given by the Jacobian in equation 19 [12]:

$$J_\omega = [\rho_1 z_0 \; \rho_2 z_1 \; \rho_3 z_2 \; \dots\dots\dots \rho_n z_{n-1}] \quad (19)$$

$\rho_i$ is 1 if the joint is revolute and is 0 if the joint is prismatic and $z_i$ is the third column of matrix ${}^0T_i$.

$$J_\omega = \begin{bmatrix} 0 & Sin\theta_1 & Sin\theta_1 & Cos\theta_1Cos\theta_2Sin\theta_3 + Cos\theta_1Cos\theta_2Cos\theta_3 \\ 0 & -Cos\theta_1 & -Cos\theta_1 & Sin\theta_1Cos\theta_2Sin\theta_3 + Sin\theta_1Sin\theta_2Cos\theta_3 \\ 1 & 0 & 0 & Cos\theta_2Cos\theta_3 - Sin\theta_2Sin\theta_3 \end{bmatrix} \quad (20)$$

### F. Linear Velocity of End-Effector

End-effector velocity moving within the base reference frame is given by the equation below.

$$\dot{O}_n^0 = \omega \, x \, r \quad (21)$$

$O_n$ = Position vector of the transformation matrix.
$O_{i-1}$ = Position vector of the (i-1)th transformation matrix.
$\dot{q}$ = Joint velocity.
$J_{v_i}$ = Linear velocity Jacobian.
$z_{i-1}$ = Axis of acceleration.

$$r = \dot{q}_i z_{i-1} \, x \, (O_n - O_{i-1}) \quad (22)$$

$$J_{v_i} = z_{i-1} \, x \, (O_n - O_{i-1}) \quad (23)$$

$$v = J_v \dot{q} \quad (24)$$

$$J_v = \begin{bmatrix} J_{v11} & J_{v12} & J_{v13} & J_{v14} \\ J_{v21} & J_{v22} & J_{v23} & J_{v24} \\ J_{v31} & J_{v32} & J_{v33} & J_{v34} \end{bmatrix} \quad (25)$$

## III. Results

Transformation matrices were calculated for three cases. In the first case transformation was done for the robot manipulator in working in scanning mode. In case two, transformation was done for the maximum robot manipulator reach in the satellite's Z-axis. In the third case, random joint angles were given to mimic the capturing process. The

calculations and validation was done using Robo Analyzer software.

*1) Case-I*

$\theta_1 = 90^\circ,\ \theta_2 = 90^\circ,\ \theta_3 = 0^\circ$ and $\theta_4 = 90^\circ$.

$$ {}^{0}T_4 = \begin{bmatrix} 1 & 0 & 0 & 0 \\ 0 & 0 & 1 & 0.16 \\ 0 & -1 & 0 & 0.12 \\ 0 & 0 & 0 & 1 \end{bmatrix} \quad (26) $$

*2) Case-II*

$\theta_1 = 90^\circ,\ \theta_2 = 0^\circ,\ \theta_3 = 90^\circ$ and $\theta_4 = 90^\circ$.

$$ {}^{0}T_4 = \begin{bmatrix} 1 & 0 & 0 & 0 \\ 0 & 0 & 1 & 0.28 \\ 0 & -1 & 0 & 0 \\ 0 & 0 & 0 & 1 \end{bmatrix} \quad (27) $$

*3) Case-III*

$\theta_1 = 135^\circ,\ \theta_2 = 62^\circ,\ \theta_3 = 35^\circ$ and $\theta_4 = 90^\circ$.

$$ {}^{0}T_4 = \begin{bmatrix} 0.707107 & -0.086175 & -0.701836 & -0.15213 \\ 0.7071070 & 0.086175 & 0.701836 & 0.15213 \\ 0 & -0.992546 & 0.121869 & 0.12453 \\ 0 & 0 & 0 & 1 \end{bmatrix} \quad (28) $$

## B. Workspace

Manipulator's workspace is depicted in Fig. 6. Joint ranges and joints' motion type are defined in Table 3.

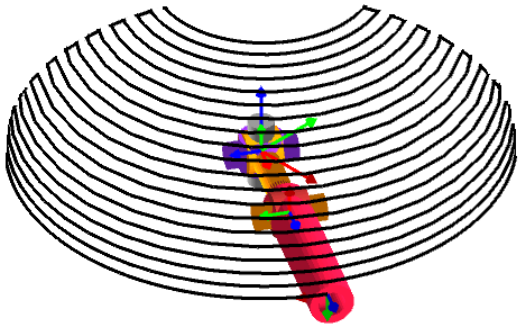

Fig. 6: Workspace of Space Debris Manipulator

Table III. Joint ranges

| Joint | Range | Motion Type |
|---|---|---|
| 01 | 180˚ | Yaw |
| 02 | 90˚ | Pitch |
| 03 | 90˚ | Pitch |
| 04 | 180˚ | Roll |

Forward Kinematics analysis was performed in the Robo Analyzer software using the cycloidal joint trajectory as input with 100 number of steps in 4 seconds. Initial joint values and final joint values are given in Table IV.

Table IV. Initial and final joint values

| Joint | Initial Value | Final Value |
|---|---|---|
| 01 | 90˚ | 120˚ |
| 02 | 90˚ | 50˚ |
| 03 | 0˚ | 45˚ |
| 04 | 90˚ | 40˚ |

Joint velocities, position and acceleration of joint 1-4 under cycloidal input are shown in Fig. 7, Fig. 8 and Fig. 9 respectively

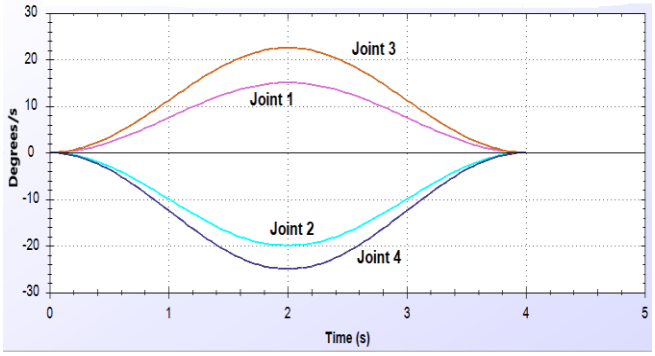


Figure 7: Joint Velocities (Degrees/s)

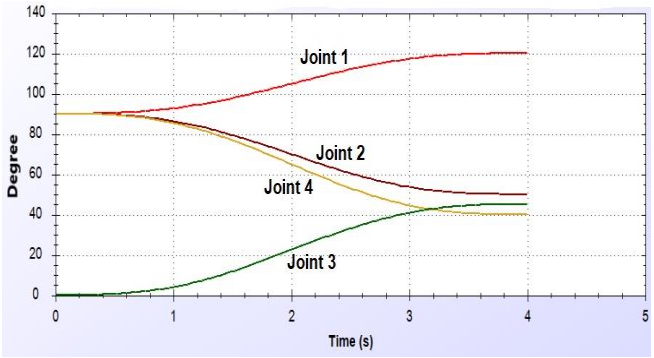


Figure 8: Joints Position (Degree)

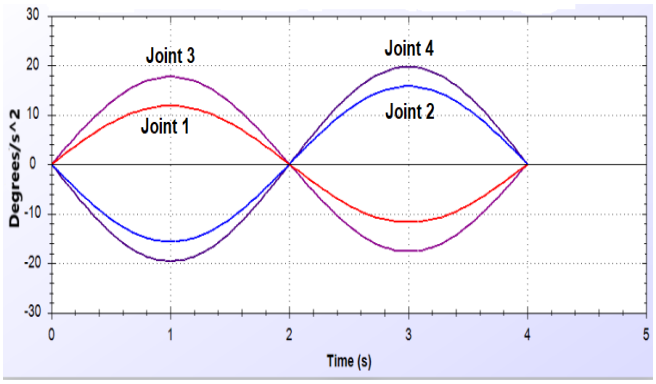


Figure 9: Joints Acceleration (Degrees/s$^{\wedge 2}$)

## C. Concept Demonstrator

The demonstrator of space debris mitigation manipulator was attached to a Micro-satellite (chaser) that was designed to operate in the Low Earth Orbit. Debris capturing and removal experiments were performed in static environment.

Robot manipulator integration with micro-satellite is shown in Fig.10.

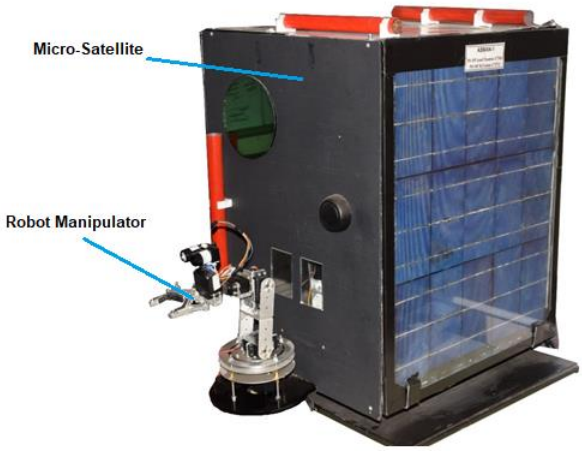


Fig. 10: Space Debris Mitigation Manipulator Assembly

## IV. Analysis

Robot manipulator for space debris mitigation can assist in future commercial and military space missions. It can allow our satellites to orbit Earth without having to perform debris avoidance maneuver that costs satellite fuel and reduces lifespan of a satellite. Other techniques such as net capturing, harpoon mechanism and tether gripper have complicated engagement methods, difficult to control and some have a risk of generating more debris while capturing large objects. On the other hand, robot manipulators are a mature technology with easy on ground handling and testing.

## V. Conclusion

In this paper we presented an efficient design and model of a 4 DoF robot manipulator for space debris mitigation. The semi-autonomous robot manipulator captures debris by using inverse kinematics technique achieved by applying geometric approach to solve for the joint angles of the manipulator. Debris removal phase is performed by the help of forward kinematics. Concept demonstrator of the debris mitigation manipulator has been tested under lab conditions and is well within the power, link and mass budget of a standard micro-satellite.

## Acknowledgment

We are thankful to Hammad Nazeer and Rayyan Azam Khan for productive discussions on inverse kinematics and robot manipulators.

## References

[1] D. a. C.-P. B. Kessler, "Collision Frequency of Artificial Satellites: The creation of a debris belt," *Journal of Geophysical Research: Space Physics*, pp. 2637-2646, 1978.

[2] "European Space Agency," 2019. [Online]. Available: https://www.esa.int/Our_Activities/Space_Safety/Space_Debris/Space_debris_by_the_numbers. [Accessed 2019].

[3] C. C. A. F. J. P. B. a. B. R. Saunders, "Results of a system feasibility study on a heavy active debris removal mission," 2014.

[4] T. O. M. a. S. T. Kasai, "Results of the ETS-7 mission-rendezvous docking and space robotics experiments," *International Symposium on Artificial Intelligence Robotics and Automation in Space*, vol. 440, p. 299, 1999.

[5] K. Yoshida, *Achievements in space robotics*, IEEE robotics and Automation Magazine, 2009.

[6] C. L. S. R. B. R. M. M. L. M. I. L. N. a. W. K. Medina A., "Validation results of satellite mock-up capturing experiment using nets," *Acta Astronautica*, no. 134, pp. 314-332, 2017.

[7] J. H. P. W. D. Cai, "Novel method of monocular real-time feature point tracking for tethered space robots," *Journal of Aerospace Engineering*, vol. XVII, no. 6, p. p.04014039, 2013.

[8] J. a. W. C. Reed J. Busquets, "Grappling system for capturing heavy space debris," *2nd European Workshop on Active Debris Removal*, vol. XXV, 2012.

[9] R. Jarvis, "A laser time of flight range scanner for robotic vision," *IEEE trans. Pattern Anal. Machine Intell.*, vol. V, no. 5, pp. 505-512, 1983.

[10] J. H. Denavit, "A kinematic notation for lower-pair mechanisms based on matrices," *Journal of applied mechanics*, vol. 77, pp. 215-221, 1955.

[11] C. Z. Lee, "A geometric approach in solving inverse kinematics of PUMA robots," *IEEE trans. Aerospace and Electronic Systems*, vol. XX, no. 6, pp. 695-706, 1984.

[12] W. W. S. David E. Orin, "Efficient computation of the jacobian for robot manipulators," *The International Journal of Robotics Research*, vol. III, no. 4, pp. 65-75, 1984.

# Prospects, Challenges and Methods based on Artificial Intelligence and Hyperspectral Remote Sensing for Precision Agriculture

Haroon Ibrahim
*WISP Lab, Department of Electrical Engineering*
*Institute of Space Technology, Islamabad*
haroon.ibrahim@mail.ist.edu.pk

Asad Abbas
*School of Electrical Engineering and Computing*
*The University of Newcastle, Australia*
asad.abbas@uon.edu.au

Muhammad Jaleed Khan
*iVision Lab, Department of Electrical Engineering*
*Institute of Space Technology, Islamabad*
mjk093@gmail.com

Khurram Khurshid
*iVision Lab, Department of Electrical Engineering*
*Institute of Space Technology, Islamabad*
khurram.khurshid@ist.edu.pk

***Abstract*—Current research has proved that rates of crop production are required to get doubled by 2050's end to fulfill the emerging demand of food of growing population. Now crop yields are not getting incremented at substantial rate to meet the requirements of future population. Current study has showed that optimization of crop yields through precision methods of agriculture, instead of enhancing land present under cultivation is the major effective and efficient path that can be used to ensure future security of food. Over the past two decades, unconventional crop monitoring methods like artificial intelligence and hyperspectral remote sensing have shown great potential in the field of precision agriculture. Deep learning has emerged with the availability of Graphical Processing Units, big data technologies and pre-trained models to provide new opportunities in precision agriculture. Current hyperspectral sensors can cover more earth surfaces with temporal resolutions, spectral and spatial resolution. Estimation of physical parameters of different complicated surfaces and identifying such materials that are similar visually having some fine spectral signatures is possible to such characteristics. Such features allows the use of hyperspectral remote sensing powered by deep learning models in precision agriculture for evaluation of crop stresses, analyzing soil and vegetation characteristics in a simple cost effective manner, thus replacing the traditional scouting methods. This paper presents a comprehensive review of research dedicated to the future prospects, state of the art methods including machine learning as well as the challenges faced in adoption of precision agriculture. The importance and applications of state of the art technologies including artificial intelligence, deep learning and hyperspectral remote sensing in precision farming are highlighted in this paper. These applications mainly include monitoring crop nutrients, water-stresses, crop diseases, insects attack and assessment of overall plant health for successful agricultural operations.**

***Keywords—artificial intelligence, precision agriculture, hyperspectral imaging, remote sensing, crop management, deep learning***

## I. INTRODUCTION

Mankind has been concerned with the rising food demands since early ages. Growing global population, use of dairy products and meat through develop developing biofuel consumption and affluence is the major factors that affect the requirements of food. Despite of the fact, that world has observed more development in the production of food in previous half century, still more of the individuals are not seen having access to appropriate energy intake and protein through diet. Number of people suffering from some form of micro-nutrient malnourishment is much larger [3]. The global population has increased from 3.7 billion in 1970 to 6.9 billion in 2010 and will continue to grow up to feedstock for biofuels and the effects of climate change are a further threat to fulfilling future food demands. Projection studies have indicated that global demand for crop protein will increase by 7 percent and global demand for crop calories will be increased by 11 percent from 2005 to 2050 [4]. However, recent studies have indicated that crop yields may no longer be increasing at sufficient rate in different regions of the world [4][5][6][7][8]. Numerous authors have indicated that most sustainable path for food security is increasing crop yield growth, rather than using more land for cultivation [2][9][10]. This can only be achieved through sustainable agriculture. Figure 1 demonstrates sustainability as a intersection of three disciplines, and can be associated with holistic effects of environmental, economic and sociological impacts of any development [11]. Thus sustainable agriculture demands fine balance between natural resources use, crop production, environmental impacts, and economics.

Fig. 1. Sustainability as a intersection of ecology, sociology and economics

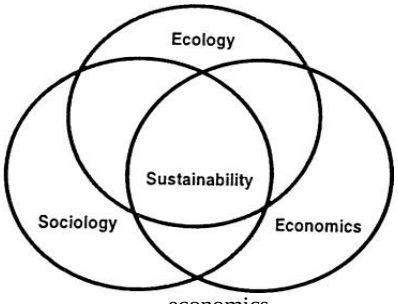


Precision agriculture (PA) stands as a promising means for attaining sustainable agriculture. PA is a crop management strategy which aims to optimize crop production while ensuring economic stability, reducing environmental effects and minimizing the waste of natural resources. It works by optimizing inputs such as nutrients and pesticides and reduces the chances of their over application as well as under application. PA has the potential to reduce hazardous impacts of over using the chemical fertilizers on cultivating land and surface water, and increases profitability for the producer. PA is being employed in many parts of the world by innovative

producers. Public sector research and educational trainers are working alongside equipment manufacturers and farm input suppliers to provide training and enough working knowledge to farmers to implement this farming strategy

Machine Learning (ML) have emerged and found applications in a vast range of related disciplines due to advent of high-performance computing (HPC) and big data making new opportunity. With these state of the art technologies, it is now possible to understand, quantify or unravel the procedures with high computational cost in the operational environments of agriculture. ML is basically described as a scientific field that provides an ability to machines to have learning without getting programmed in a stricter manner [12]. With the passage of time, ML is now applied in more of the scientific fields involving computer vision [13], satellite imaging [14], document imaging [15], [16], forensic examination [17], [18], remote sensing [19], medical imaging [20] and word spotting for data retrieval [21].

This paper focuses on the use of innovative technologies in agriculture, especially hyperspectral remote sensing and details their future prospects. It reviews hyperspectral imaging and its applications in precision agriculture in detail. It also highlights the challenges faced in the field of precision agriculture and discusses the steps that should be taken in order to overcome those challenges. The applications of ML in precision agriculture such as yield prediction, disease detection, crop quality, and species recognition are also explored

## II. Precision Agriculture Technologies

Precision agriculture technologies and strategies can be divided into three steps [22]. Step 1 comprises of conventional methods of framing with some of the exhaustive mechanization for the purpose of good quality activities and for labor saving. It is seen dependent over conventional technique of 'high-output' and 'high input'. Step 2 refers to the industrial agriculture that is basically dependent over 'low-input' and technique of 'constant-output'. However, step 3 is dependent over the usage of different intelligent technologies and it targets on 'optimized input-output solution' that is the major target of precision farming.

Precision farming comprises of set of technologies that aim to measure and identify within field variability and its root causes, identify varying crop and soil needs and accordingly prescribe input application [23]. It consists of (1) collecting information to recognize management zones within the whole field, each of these zone is more uniform in yield potential than the field taken as whole, (2) making decision about optimal input application on basis of gathered information about each management zone and (3) implementing the decisions accordingly by applying specified inputs [24]. Applications of yield monitoring, remote sensing, global positioning system (GPS), geographic information system (GIS), soil sampling and variable rate applications of fertilizer, pesticide and herbicide can be regarded as precision agriculture elements [25] Here is brief overview of precision agriculture methods:

### *A. Global Positioning System (GPS)*

- Development in GPS technology has allowed the precision agriculture to progress to its current state.
- It is responsible for linking all the corresponding layers of information acquired on the ground.

### *B. Yield Monitoring System*

- Yield monitoring sensors serves as the core of precision agriculture technology, on their bases producers can evaluate their precision agriculture management decisions.
- Proper calibration of yield monitors is the most important factor as they provide valuable data on- the-go across a field and acquire a spatial representation of yield performance.

### *C. Remote Sensing*

- Remote sensing is an emerging technology which is replacing traditional scouting methods. It provides holistic information about different stages of crop production that are critical to adjustment of plan.
- However, interpretation and evaluation of remotely sensed data remains a challenging task.

### *D. Variable-Rate Technology*

- It allows the producers to apply different rate of fertilizers at each management zones according to their specified needs.

Additional calibration and training is needed to acquire" spatial prescription" of the field zone and using fertilizer equipment capable of variable rate during operation. Earlier work in PA was focused on determination of variations in soil nutrients and applications of fertilizers by grid-sampling the fields [26]. Many important water related soil parameters were studied including texture, density, soil water holding capacity, water infiltration rate and presence of restrictive soil layer. However, these studies are time consuming and often involves a trained professional who can perform in-field characterization, followed by laboratory analysis. Due to these reasons, quantifying physical parameters of soil for precise mapping within field variations has been unfeasible. Lately, mobile sensor systems are being used to measure spatially variable soil properties. Both direct and indirect measurement sensors are available to analyze the soil and crop properties. Direct measuring sensors are able to quantify the soil strength by sensing the force on a tine [27]. Whereas, indirect measurement methods like hyperspectral remote sensing can estimate various soil parameters by measuring visible and near infrared reflectance of soil [28].

The modern models of ML have been integrated in different applications of precision agriculture involving disease detection, yield protection and crop management. The trend within different applications shows different applications that are more data intense within the higher usage of hyper-spectral images and crop. Remote sensing data is analyzed for crop management based on ML-based predictions. Deep learning is the modern form of machine learning which enables intelligent decision making in scenarios involving big data. ML and deep learning applications in precision agriculture also include livestock management, water management, and soil management. Most of the recent studies on precision agriculture include artificial neural networks (ANN) [29], convolutional neural networks (CNN) [30] and support vector machines (SVM) [31]. ANNs and CNNs are widely used for implementations in crop, water,

and soil management, while SVMs were used mostly for livestock management.

## III. Basics of Hyperspectral Imaging and Machine Learning

The fundamentals of hyperspectral imaging and machine learning are reviewed in this section. Unlike normal two-dimensional images taken by regular camera, hyperspectral imaging (HSI) is a strategy in which the photography of an object is done through different well described optical brands in wider spectral range. In HIS, a scene is seen near visible electromagnetic spectrum's portion, in mid infrared so that the images of HIS get both spatial resolution and spectral resolution. For instance, just like normal 2-D images, the geometric characteristics of image are determined through the spatial resolution. However, the spectral resolution does the measurement of different variations that are seen in the pixels as wavelength's function

Hyperspectral imaging owns important potential for the identification of material dependent on the unique signatures of spectrum [32]. Single pixel's spectrum within the hyperspectral image can basically provide more information related to the material surface as compared to some normal image. In some specified electromagnetic spectrum's range, the values of reflectance of various materials present on the surface of earth like minerals, water, forest and soil can be compared and plotted. The labeling of these plots is done as 'spectral response curves' or 'spectral signatures' [33]. Remotely, the classification of sensed images can be done through making the use of signature plots of spectrum, as each of the materials within the scene tends to own some unique signature. With more spectral resolution of an imaging sensor, more information related to classification can be attained through spectral signatures. Hyperspectral sensors tend to own higher spectral resolution as compared to different multispectral sensors and therefore it gives the capability to make distinction among more of the subtle differences within a scene.

The classification of tasks of machine learning is done into two major classes, like supervised and unsupervised learning. Within supervised learning, the presentation of data is done with some inputs and related outputs, and the major target is to develop a rule that does the mapping of inputs to different outputs. In some of the cases, like in reinforcement learning, there can be partial inputs with some missing target outputs or provided only as some kind of feedback to the actions that are taken within the dynamic environment. In supervised learning, the training is done for predict the labels of classes for the test data. However, in unsupervised learning, no distinction is seen in between test data and training data sets with unlabeled data. The learner does the processing of input data with the objective to discover some of the hidden patterns. Through integrating machine learning to some sensor data, now evolution has been made in the farm management systems and these have transformed into artificial intelligence systems giving richer insights and recommendations for actions and decisions with more scope for improvement of production. For the given scope, it is assumed that the use of models of ML will get more spread, permitting for the possibility of applicable and integrated tools. At the given time period, all approaches related to individual solutions and approaches are not connected in an appropriate way with the process of decision-making, as observed in other domains of application. This implementation of decision making, ML implementation, data analysis and automated data recording will give some of the practical tools that are seen in congruency with the knowledge-dependent agriculture for enhancing quality of bio-products and production levels.

## IV. Prospects of Precision Agriculture

Traditionally, monitoring the crops for insect attack, nutrients, water stress and disease was done through visual inspection. The methods had limitations as the visual symptoms can appear at later phases of disease, therefore making the restoration of health of plants more complicated. Advancement within ground based method of hyperspectral imaging and airborne has made the crop stress evaluation a possible task. Moreover, it also helps in doing the analysis of characteristics of vegetation and soil in cost effective way, therefore doing the replacement of traditional methods of scouting [51-53].

Different geologists have used hyperspectral imagery to map the water and land resources [34]. Moreover, these have been used for mapping heavy metals and other wastes in active and historic mining regions. Precision agriculture uses the material identification property of hyperspectral sensor for determining stress related spectral variations in crops. Farmers and crop producers can take advantage of hyperspectral imaging by monitoring and assessing vegetation status at specific critical times: Firstly HSI helps to evaluate and monitor crop condition during earlier development stages and thus enabling efficient and adequate use of fertilizer quantities [35], and second during advanced growth stages for prediction of yield and crop health monitoring. Due to such properties, hyperspectral remote sensors can play a vital role in providing valuable time-critical and time- specific information for precision farming

### *A. Nutrient Stress*

Nitrogen is considered as the major factor in crop growth and also one of the most important fertilizer for agriculture productivity. Nitrogen concentration determines the chlorophyll content in the green vegetation, which is indirectly related to one of the major physiological processes of plant like photosynthesis. More supply of nitrogen as compared to the nutritional requirements of vegetation results into eutrophication [36]. The loss of nitrogen to environment shows farmers' loss. On contrary to this, improper decrement in supply of nitrogen to nutritional requirements of vegetation outcomes into decreased yields, resulting to more loss of economy. This dilemma needs right kind of assessment of requirement of nitrogen and it variability at some critical times. Since, the condition of crop at earlier phases identifies its yields, therefore it is important to give right kind of nutrient information to farmers at the critical phases for supplying enough fertilizers to plant growth deficiencies and requirements. For this particular objective, hyperspectral

remote sensing methods are success- fully employed to study crop conditions corresponding to nutrient stress.

.

Nitrogen deficiencies were studied by foliage spectral properties [37]. Because of insufficient nitrogen content, transmittance at visible wavelength, which shows decreased chlorophyll levels in crops. Daughtry et al.[36]estimated chlorophyll levels by measuring reflected radiation from crop leaves and canopies. Deficiencies in soil contamination and nutrients result into different symptoms that can be assessed through hyperspectral imaging. Schuerger et al Dunagen et al. [39] did the analysis of levels of mercury in mustard plants and identified that spectral signatures were more associated to the levels of containment. Osborne et al. [40] identified that phosphorous and nitrogen concentrations, yield under stress and biomass can be estimated through hyperspectral imaging. Mahlein et al. [41] did a research on various phases of development of diseased sugar beet leaves making use of hyperspectral imaging. This research also identified that hyperspectral imaging tends to have more potential to analyze diseases of plant.

### *B. Drought Stress*

Drought stress is the major factor that influences the production of crop. Chances of good quality crop can be enhanced through detecting water associated stresses. Higher level stresses of water are seen more noticeable in case of variation in pigments of photosynthesis. These alterations outcome into yellowish tint into crops because of enhanced reflectance of red wavelength. Hyperspectral imaging can do the detection of these alterations at quite earlier stages. Colombo et al. [42] identified that alterations in equivalent water thickness (EWT) of water was mainly responsible for the alterations in reflectance of leaf in visible and infrared spectrum. It was identified that regression indices of hyper spectrum calculated through hyperspectral imaging were better estimation tools of content of water at leaf and at level of landscape.. Rascher et al.[27] utilized photochemical reflectance index and hyperspectral imaging system for estimating water stress within tropical tress' leaves and identified the temporal influences of dehydration on leaves of tree. Rossini et al. [43] identified that hyperspectral imaging is beneficial in doing the detection of drought stress at level of farm with corn. It was identified that deficits of irrigation can be mapped accurately before drought stress influenced the structure of canopy.

### *C. Analysis of Soil Properties*

Analysis of properties of soil can play a major part in enhancing yields of crop. Ben-Dor [28] mapped important properties of soil successfully in field scale involving soil sanity, soil organic matter and moisture. Rossel and Bratney [44] made the estimation of organic content of carbon within soil with more accuracy

## V. Challenged in Precision Agriculture

Precision agriculture method and technologies have been commercially available since early 1990s. However, its adoption has been uneven, both temporally and geographically. The economic theory of induced innovation anticipate that new technologies will be researched and adopted where they make efficient use of rare resources. Fedar and Slade [45] reviewed that "farmers actively gather information when they expect it to provide an economic return". Precision agriculture technologies are adopted at a faster rate where land and capital are cheaper but labor is costly. The uneven adoption rate is closely related to the awareness level as well as cost of replacing the expensive machinery. This section focuses on the factors affecting the adoption of precision agriculture technologies.

### *A. Educational needs of Precision Agriculture*

Beale and Bolen [46] synthesize research that suggested educational awareness was the most critical factor of the agricultural technology adoption process. Thus reluctance towards adoption and implementation of precision agriculture is primarily based upon availability of well-trained educated people, and the cost and accessibility to acquire quality education, training and equipment. Due to the rapidly changing nature of latest precision agriculture technologies, precision agricultural trainers face the challenge of providing up to date quality educational and training programs. Educational awareness leads to interest, evaluation, trial and finally to adoption stage.

The rate and extent to which precision agriculture technologies are adopted is ultimately dictated by the producers. Marketing, research and investigation strategies will be of no use if producer, as the end user is unable to realize the importance of such efforts. Thus addressing the specific barriers that the producer face should be the prime concern.

### *B. Risk Preferences*

Technological innovations are more likely to be perceived as more risky task than traditional practices. Such notion is backed up by many research studies. Feder [47]argued that the perception of increased risk in new technologies substantially reduce their adoption rate. When innovation is first introduced, the potential users are dubious of its usefulness and are hesitant to adopt it [48]. Feder and O'Mara and Hiebert [49] shows that as the learning and experience grows, the uncertainty decreases, thus persuading more risk-averse farmers to embrace a new technology, given it is profitable.

### *C. Human Capital*

Adoption decision is clearly governed by the ability to adapt new technologies for use on a farm. Fernandez- Cornejo et al. [50] measured the factors affecting adoption rate like years of farming experience, formal education or age. Likelihood of adoption is directly influenced by the formal education or experience of the producer, whereas increasing age lowers the probability due to the reasons innate in the aging process[51] On the contrary younger farmers have more tendency to adopt new technologies and are willing to innovate. so with respect to precision agriculture, human capital can take the form of awareness with innovative technologies.

### *D. Farm Size*

A fundamental hypothesis concerning technology transfer is that probability of adoption of an innovation will be greater on larger farms than smaller farms. Research studies have indicated that given the transaction and information cost, and reservations related to innovations, there exists a critical lower limit on farm size that dissuade smaller farm producer from adopting Therefore as the cost grows, the farm size limit also increases. So smaller farm producers are less likely to adopt innovative technologies that have large information costs. However, solution to such problem is the introduction of a

service sector, which can make a non-divisible technology into a divisible one [45]. Pierce and Nowak [52] pointed out that such service sector is emerging as far as precision agriculture is concerned

### *E. Dependency on Location*

Profitability of precision agriculture technologies are directly dependent on factors like climate, soil fertility and availability of water resources across different farms. Green et al. [53] and Thirkawalaetal. [54] studied that heterogeneity of the available resources greatly impact the technology adoption rate and profitability

## VI. Conclusion and Discussion

The rising food demand as a result of rapidly growing world's population calls for innovations in crop production to ensure future food security. By using site-specific information, precision agriculture technologies can help in increasing crop production by improving input efficiency, reducing environmental effects and providing economic stability. Precision agriculture technologies benefits the environment by reducing the excess application of inputs that leads to reduction of pesticide resistance development. Hyperspectral remote sensing is an emerging precision agriculture technology. Current hyperspectral remote sensors are seen capable to cover more of the earth surfaces with temporal, spectral and spatial resolutions. These characteristics permits the hyperspectral imaging's use in precision agriculture needed estimation of different physical objects of complex surfaces, along with the identification of some similar materials that have some fine signatures of spectrum. This development has made the evaluation of stresses of crop to become possible. Moreover, it has also helped in the analysis of properties of vegetation and soil and yield estimation in cost effective way, therefore doing the replacement of traditional methods of scouting.

However, there are many factors affecting the adoption rate of precision agriculture technologies. Several farm operator and farm characteristics are important determinants of precision agriculture adoption. Factors like education, awareness, farm size, farm type, farm location and human capital collectively determine its adoption. Overcoming such constraints is possible by addressing concerned issues and a sector wide public or private program to educate people about relatively new technology would enhance the probability of adoption. Over the past two decades, unconventional crop monitoring methods like artificial intelligence and hyperspectral remote sensing have shown great potential in the field of precision agriculture. Deep learning has emerged with the availability of Graphical Processing Units, big data technologies and pre-trained models to provide new opportunities in precision agriculture. The future prospects, state of the art methods including machine learning as well as the challenges faced in adoption of precision agriculture are discussed. The importance and applications of machine learning and hyperspectral remote sensing in precision farming are highlighted, which include monitoring crop nutrients, water-stresses, crop diseases, insects attack and assessment of overall plant health for successful agricultural operations.

## References


[1] P. Pingali, "Westernization of Asian diets and the transformation of food systems: Implications for research and policy," *Food Policy*, vol. 32, no. 3, pp. 281–298, Jun. 2007.

[2] H. C. J. Godfray *et al.*, "Food Security: The Challenge of Feeding 9 Billion People," *Science (80-. ).*, vol. 327, no. 5967, pp. 812–818, Feb. 2010.

[3] M. L. Finkel, *Public health in the 21st century*. Praeger, 2011.

[4] H. C. J. Godfray, "The challenge of feeding 9–10 billion people equitably and sustainably," *J. Agric. Sci.*, vol. 152, no. S1, pp. 2–8, Dec. 2014.

[5] K. G. Cassman, "Ecological intensification of cereal production systems: Yield potential, soil quality, and precision agriculture," 1999.

[6] M. Personal, R. Archive, and R. Finger, "M P RA Evidence of slowing yield growth-the example of Swiss cereal yields," 2007.

[7] P. Peltonen-Sainio, L. Jauhiainen, and I. P. Laurila, "Cereal yield trends in northern European conditions: Changes in yield potential and its realisation," *F. Crop. Res.*, vol. 110, no. 1, pp. 85–90, Jan. 2009.

[8] N. Brisson, P. Gate, D. Gouache, G. Charmet, F.-X. Oury, and F. Huard, "Why are wheat yields stagnating in Europe? A comprehensive data analysis for France," *F. Crop. Res.*, vol. 119, no. 1, pp. 201–212, Oct. 2010.

[9] J. A. Foley *et al.*, "Solutions for a cultivated planet," *Nature*, vol. 478, no. 7369, pp. 337–342, Oct. 2011.

[10] B. Phalan, A. Balmford, R. E. Green, and J. P. W. Scharlemann, "Minimising the harm to biodiversity of producing more food globally," *Food Policy*, vol. 36, no. Supplement 1, pp. 62–71, 2011.

[11] "(PDF) Resources conservation agriculture - A review." .

[12] A. L. Samuel, "Some Studies in Machine Learning Using the Game of Checkers," *IBM J. Res. Dev.*, vol. 3, no. 3, pp. 210–229, Jul. 1959.

[13] M. S. Saleem, M. J. Khan, K. Khurshid, and M. S. Hanif, "Crowd density estimation in still images using multiple local features and boosting regression ensemble," *Neural Comput. Appl.*, Jan. 2019.

[14] M. J. Khan, A. Yousaf, N. Javed, S. Nadeem, and K. Khurshid, "Automatic Target Detection in Satellite Images using Deep Learning," *J. Sp. Technol.*, vol. 7, no. 1, pp. 44–49, 2017.

[15] A. Yousaf, M. J. Khan, M. Imran, and K. Khurshid, "Benchmark dataset for offline handwritten character recognition," in *2017 13th International Conference on Emerging Technologies (ICET)*, 2017.

[16] R. Qureshi, M. Uzair, K. Khurshid, and H. Yan, "Hyperspectral document image processing: Applications, challenges and future prospects," *Pattern Recognit.*, vol. 90, pp. 12–22, Jun. 2019.

[17] M. J. Khan, A. Yousaf, A. Abbas, and K. Khurshid, "Deep learning for automated forgery detection in hyperspectral document images," *J. Electron. Imaging*, vol. 27, no. 05, p. 1, Sep. 2018.

[18] M. J. Khan, A. Yousaf, K. Khurshid, A. Abbas, and F. Shafait, "Automated Forgery Detection in Multispectral Document Images using Fuzzy Clustering," in *13th IAPR International Workshop on Document Analysis Systems*, 2018.

[19] M. J. Khan, H. S. Khan, A. Yousaf, K. Khurshid, and A. Abbas, "Modern Trends in Hyperspectral Image Analysis: A Review," *IEEE Access*, vol. 6, no. 1, pp. 14118–14129, 2018.

[20] S. Charan, M. J. Khan, and K. Khurshid, "Breast cancer detection in mammograms using convolutional neural network," in *2018 International Conference on Computing, Mathematics and Engineering Technologies (iCoMET)*, 2018, pp. 1–5.

[21] K. Khurshid, C. Faure, and N. Vincent, "Word spotting in historical printed documents using shape and sequence comparisons," *Pattern Recognit.*, vol. 45, no. 7, pp. 2598–2609, Jul. 2012.

[22] "Precision Farming Approaches to Small-Farm Agriculture." .

[23] J. Lowenberg-DeBoer, "Risk Management Potential of Precision Farming Technologies," *J. Agric. Appl. Econ.*, vol. 31, no. 02, pp. 275–285, Aug. 1999.

[24] "(PDF) Precision farming by cotton producers in fourteen Southern states: results from the 2013 Southern cotton precision farming survey." .

[25] "Information and the adoption of precision farming technologies." .

[26] R. Weisz, R. Heiniger, J. G. White, B. Knox, and L. Reed, "Long-Term Variable Rate Lime and Phosphorus Application for Piedmont No-Till Field Crops," *Precis. Agric.*, vol. 4, no. 3, pp. 311–330, 2003.

[27] U. Rascher, C. J. Nichol, C. Small, and L. Hendricks, "Monitoring Spatio-temporal Dynamics of Photosynthesis with a Portable Hyperspectral Imaging System," *Photogramm. Eng. Remote Sens.*, vol. 73, no. 1, pp. 45–56, Jan. 2007.

[28] E. Ben-Dor, K. Patkin, A. Banin, and A. Karnieli, “Mapping of several soil properties using DAIS-7915 hyperspectral scanner data - a case study over clayey soils in Israel,” *Int. J. Remote Sens.*, vol. 23, no. 6, pp. 1043–1062, Jan. 2002.

[29] A. Romero, C. Gatta, and G. Camps-Valls, “Unsupervised Deep Feature Extraction for Remote Sensing Image Classification,” *IEEE Trans. Geosci. Remote Sens.*, vol. 54, no. 3, pp. 1349–1362, Mar. 2016.

[30] Karpathy A, Toderici G, and Shetty S, “Large-scale video classification with convolutional neural networks,” in *Proceedings of the IEEE conference on Computer Vision and Pattern Recognition*, 2014, pp. 1725–1732.

[31] U. Sharif, Z. Mehmood, T. Mahmood, M. A. Javid, A. Rehman, and T. Saba, “Scene analysis and search using local features and support vector machine for effective content-based image retrieval,” *Artif. Intell. Rev.*, pp. 1–25, 2018.

[32] D. Landgrebe, “Information Extraction Principles and methods for multispectral and hyperspectral image data,” in *Information Processing For Remote Sensing*, World Scientific, 1999, pp. 3–37.

[33] T. M. Lillesand, R. W. Kiefer, and J. W. Chipman, *Remote sensing and image interpretation*. .

[34] G. A. Shaw and H. K. Burke, “Spectral Imaging for Remote Sensing,” 2003.

[35] M. S. Moran, Y. Inoue, and E. M. Barnes, “Opportunities and limitations for image-based remote sensing in precision crop management,” *Remote Sens. Environ.*, vol. 61, no. 3, pp. 319–346, Sep. 1997.

[36] C. Daughtry, “Estimating Corn Leaf Chlorophyll Concentration from Leaf and Canopy Reflectance,” *Remote Sens. Environ.*, vol. 74, no. 2, pp. 229–239, Nov. 2000.

[37] T. M. Blackmer, J. S. Schepers, G. E. Varvel, and E. A. Walter-Shea, “Nitrogen Deficiency Detection Using Reflected Shortwave Radiation from Irrigated Corn Canopies,” *Agron. J.*, vol. 88, no. 1, p. 1, 1996.

[38] “Non-Photochemical Quenching and Energy Dissipation in Plants, Algae and ... - Google Books.” .

[39] S. C. Dunagan, M. S. Gilmore, and J. C. Varekamp, “Effects of mercury on visible/near-infrared reflectance spectra of mustard spinach plants (Brassica rapa P.),” *Environ. Pollut.*, vol. 148, no. 1, pp. 301–311, Jul. 2007.

[40] S. L. Osborne, J. S. Schepers, D. D. Francis, and M. R. Schlemmer, “Detection of Phosphorus and Nitrogen Deficiencies in Corn Using Spectral Radiance Measurements,” *Agron. J.*, vol. 94, no. 6, p. 1215, 2002.

[41] A.-K. Mahlein, U. Steiner, C. Hillnhütter, H.-W. Dehne, and E.-C. Oerke, “Hyperspectral imaging for small-scale analysis of symptoms caused by different sugar beet diseases,” *Plant Methods*, vol. 8, no. 1, p. 3, Jan. 2012.

[42] R. Colombo *et al.*, “Estimation of leaf and canopy water content in poplar plantations by means of hyperspectral indices and inverse modeling,” *Remote Sens. Environ.*, vol. 112, no. 4, pp. 1820–1834, Apr. 2008.

[43] C. Cilia *et al.*, “Nitrogen Status Assessment for Variable Rate Fertilization in Maize through Hyperspectral Imagery,” *Remote Sens.*, vol. 6, no. 7, pp. 6549–6565, Jul. 2014.

[44] F. Castaldi *et al.*, “Soil Organic Carbon Estimation in Croplands by Hyperspectral Remote APEX Data Using the LUCAS Topsoil Database,” *Remote Sens.*, vol. 10, no. 2, p. 153, Jan. 2018.

[45] G. Feder and R. Slade, “The Acquisition of Information and the Adoption of New Technology,” *Am. J. Agric. Econ.*, vol. 66, no. 3, p. 312, Aug. 1984.

[46] P. A. Seck, E. Tollens, M. C. S. Wopereis, A. Diagne, and I. Bamba, “Rising trends and variability of rice prices: Threats and opportunities for sub-Saharan Africa,” *Food Policy*, vol. 35, no. 5, pp. 403–411, Oct. 2010.

[47] N. C. Rahelizatovo and J. M. Gillespie, “The Adoption of Best-Management Practices by Louisiana Dairy Producers,” *J. Agric. Appl. Econ.*, vol. 36, no. 01, pp. 229–240, Apr. 2004.

[48] M. Calderini, “Academic research, technological specialization and the innovation performance in European regions: an empirical analysis in the wireless sector,” *Ind. Corp. Chang.*, vol. 14, no. 2, pp. 279–305, Feb. 2005.

[49] L. D. Hiebert, “Risk, Learning, and the Adoption of Fertilizer Responsive Seed Varieties,” *Am. J. Agric. Econ.*, vol. 56, no. 4, p. 764, Nov. 1974.

[50] J. Fernandez-Cornejo, E. D. Beach, and W.-Y. Huang, “The Adoption of IPM Techniques By Vegetable Growers in Florida, Michigan and Texas,” *J. Agric. Appl. Econ.*, vol. 26, no. 01, pp. 158–172, Jul. 1994.

[51] P. J. Barry and L. J. Robison, “Chapter 10 Agricultural finance: Credit, credit constraints, and consequences,” *Handb. Agric. Econ.*, vol. 1, pp. 513–571, Jan. 2001.

[52] F. J. Pierce and P. Nowak, “Aspects of Precision Agriculture,” 1999, pp. 1–85.

[53] “Sustainable Irrigation Management, Technologies and Policies III - Google Books.” .

[54] S. Thrikawala, A. Weersink, G. Kachanoski, and G. Fox, “Economic Feasibility of Variable-Rate Technology for Nitrogen on Corn,” *Am. J. Agric. Econ.*, vol. 81, no. 4, p. 914, Nov. 1999.

# Modeling and Simulation of Hydrodynamic Lubrication of 1st Compression Ring of High Torque Low Speed Diesel Engine

Waleed Hussain
*Institute of Space Technology*
Islamabad, Pakistan
w.hussain9253@gmail.com

Muhammad Zubair Khan
*Institute of Space Technology*
Islamabad, Pakistan
zubair_kj@yahoo.com

Jamal Ahmed
*College of Electrical and Mechanical Engineering, NUST*
Islamabad, Pakistan
jamalahmedkhan20@gmail.com

***Abstract*— The 1st compression ring faces the maximum thrust due to high combustion pressures in piston cylinder assembly. The 1st compression ring due to an ineffective hydrodynamic lubrication causes power loss, oil consumption, low fuel efficiency and wear issues. This reduces the designed life of high torque low speed diesel engine. The presence of lubrication between ring and liner enhances the life of engine and prevents them from adhesive wear. In the present work, a numerical study is performed using matlab as a solver for a parabolic ring profile by considering elliptical bore. The hydrodynamic pressures are generated by solving Reynolds equation. The results show that hydrodynamic lubrication has reduced the friction forces and power loss significantly.**

**Keywords— Compression Ring, Diesel engine, Friction, Reynolds Equation.**

## I. INTRODUCTION

Piston ring and cylinder bore friction are an important component of the complete energy loss in a reciprocating engine. During engine running conditions, the piston's prime compression ring takes on a significant task because it avoids spillage of the combustion gas and allows heat dissemination however adds to mechanical friction. The ring-pack adds about 20% of the complete frictional losses of the engine under extreme operating circumstances [1]. The cylinder rings are therefore greased with oil, whose film thickness ends in low friction and less wear. It is very critical to lubricate an engine piston ring assembly. Researchers are always concerned with preventing ring from wearing during engine function. Efficient ring-liner lubrication mechanism, optimized film thickness and hydrodynamic lubrication avoids adhesive wear on the ring. Many researchers incorporated on the hydrodynamic, elastohydrodynamic and mixed lubrication regions considering surface roughness, dynamics of ring and temperature variations. In past some researchers worked on the hydrodynamic lubrication of 1st compression ring by solving Reynolds Equation and taking the profile of ring [2]. Castleman worked first of all on the piston ring and cylinder lubrication scheme [3]. Eilon and Saunders calculated the film thickness of piston ring and cylinder bore and computed instantaneous friction force experimentally [4]. Patir and cheng used the modified Reynolds equation by incorporating roughness factors and determined pressure flow factors to predict the film thickness and pressures [5]. Hu et al developed the lubrication model for nonaxisymmetrical piston ring [6]. G R Paul et al experimentally measured the losses of ring pack [7]. Y. Wakuri et al evaluated friction between ring pack and cylinder using hydrodynamic lubrication and concluded that losses of ring pack significantly contributes in total power loss of engine [8]. QINGMIN YANG et al developed the model for elliptical bore and evaluated that elliptical bore reduce hydrodynamic pressures significantly in circumferential direction [9]. Mohsen Esfahanian et al conducted theoretical hydrodynamic analysis of two stroke diesel engine of piston rings and computed minimum film thickness and also analyse minimum film thickness and hydrodynamic pressures at different crank angles [10].

The present paper deals with the hydrodynamic lubrication analysis of 1st compression ring of high torque low speed diesel engine. Parabolic profile of ring is considered and elliptical bore is considered. 2-d Reynolds equation is derived and Reynolds equation is discrete using finite difference technique and linear equations have been solved using successive methods of relaxation. Beside this volumetric flow rate, shear force and Power loss is also calculated. The assumptions which are used to model the whole process:

1. Flow is laminar.
2. Lubricant is incompressible.
3. Side leakage and surface roughness is ignored.
4. Viscosity of lubricant is constant in axial and circumferential direction.
5. Ring dynamics is not considered.
6. Piston tilt effect is not considered.
7. No surface roughness and asperity contact.
8. Thermal effects are neglected

## II. PISTON RING INSTANTANEOUS VELOCITY

The primary motion of piston without considering the effect of secondary motion is described by following equation *[10]*.

$$U = r\omega\sin\theta + r\omega\left(C_p + r\sin\theta\right)\cos\theta\left(l^2 - \left(C_p + r\sin\theta\right)^2\right)^{2.5} \quad (1)$$

Where

$$\omega = {2 * \pi * N}/{60} \quad (2)$$

## III. Reynolds Equation

The equation to compute hydrodynamic pressures in fluid film is called Reynolds equation.

$$\frac{\partial}{\partial x}\left(\frac{h^3}{12}\frac{\partial P}{\partial x}\right)+\frac{\partial}{\partial y}\left(\frac{h^3}{12}\frac{\partial P}{\partial y}\right)=6\left(U\mu\frac{dh}{dx}\right) \quad (3)$$

The boundary conditions to solve the above equation is

$$P(0, y) = P(b, y) = 0 \quad (4)$$

## IV. Film thickness

The shape profile of ring is parabolic type and film thickness for compression ring and non-circular bore is

$$h(x, y) = h(x) + h(y) + h_0 \quad (5)$$

$h(x)$ is along x axis in which direction piston is moving $h(y)$ is along y axis which is in circular direction and $h_0$ is minimum film thickness. The profile of parabolic faced type ring is shown in figure 1.

Film thickness of parabolic ring along x axis is given by [11]

$$h(x) = \begin{cases} S_1(x^2 - 2a_1x + {a_1}^2), & 0 \le x \le a_1 \\ 0 & a_1 < x < a_2 \\ S_1(x^2 - 2a_2x + {a_2}^2), & a_2 \le x \le b \end{cases} \quad (6)$$

The flow is due to non-circular bore is represented by following equation *[12]*

$$h(y) = R\left\{\frac{1}{\sqrt{1-\left[1-\left(\frac{R}{R+\Delta c}\right)\right]\sin\emptyset}}-1\right\} \quad (7)$$

Where

$$\emptyset = \frac{y}{R} \quad (8)$$

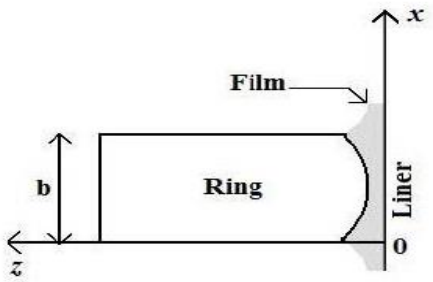


Figure1 Ring Shape Profile

## V. Equilibrum condition

Gas force acting on piston ring and hydrodynamic force due to hydrodynamic pressure are converged each other according this relation, the ring is in equilibrium condition.

$$FG - W \le \varepsilon \quad (9)$$

Where

$$W = \int_0^L \int_0^b P(x, y)\, dx\, dy \quad (10)$$

The combustion pressures profile for four strokes is shown in figure 2. The whole process is shown in Fig 7.

## VI. Numerical procedure

The Reynolds Equation is discretized according finite difference method. Then minimum film thickness $h_0$ and error criteria is initialized and pressures in fluid film are calculated. Then pressures are used to get force W. Then W is radial balanced with gas Force. When equilibrium condition is achieved, $h_0$ is updated and the entire operation for the next crank angle is repeated. If the condition of equilibrium is not met, $h_0$ will be updated according to the following reference.

$${h_0}^{(k)}{}_{approx} = \left(\frac{FG}{W}\right)^{\gamma} {h_0}^{(k)}{}_{old} \quad (11)$$

$${h_0}^{(k)}{}_{new} = {h_0}^{(k)}{}_{old} + \lambda_1\left({h_0}^{(k)}{}_{approx} - {h_0}^{(k)}{}_{old}\right) \quad (12)$$

Where $\gamma$ is empirical coefficient and $\lambda_1$ is relaxation factor which is used in successive over relaxation method and k represents the time position. If gas force and net resultant hydrodynamic load converge in given criteria then the entire process for the next crank angle is repeated if not then $h_0$ is updated according above relation.

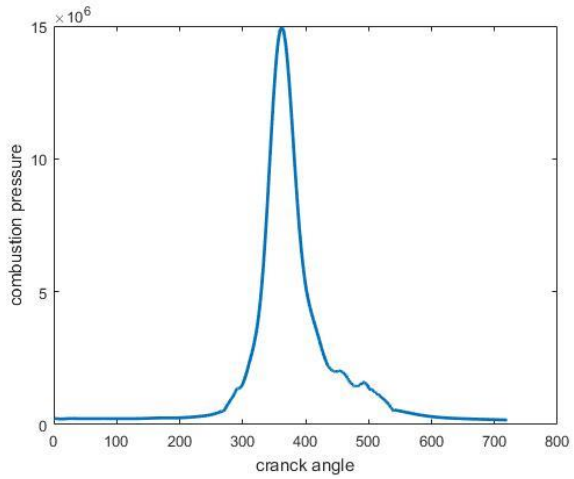


Figure 2 Combustion Pressures

## VII. Results and discussions

### A. Film thickness and Lubrication pressures

Lubrication film thickness profile for 1st compression ring of high torque low speed diesel engine is shown in figure 3 and lubricant pressures are shown in figure 4. The profile shows the different behavior during the four strokes. At the beginning of intake stroke, the film thickness starts to increase because the velocity of piston is also increasing and film thickness is in micron as shown in figure. When piston reaches the mid of intake stroke the film thickness is maximum and velocity is maximum. High velocity and high film thickness at the mid of induction generates minimum pressure which is fraction of pascals as shown in figure.

Combustion gas force effect is very low at this point as shown in figure. When piston passes the half of the intake stroke, the speed of piston or cyclic speed started to decrease and film thickness also decreases and the effect of gas pressure is minimum at the end of this stoke. At this point the pressures of fluid film has increased from fraction of pascal to few pascal. During the first half of the compression stroke, when piston is moving from bottom dead center (BDC), the effect of gas pressures started to increase and the film thickness does not rise to same extent as compare with the first half of the stroke because gas force and friction started to increase which causes the film thickness to decrease and pressure has risen till the mid of stroke as compare with the last mid of intake stroke. After passing through the mid of compression stroke the effect of gas force started to increase exponentially and sharp decrease in the film thickness and hydrodynamic pressure also increases exponentially during this half stroke. At this point the film thickness is at minimum value during whole cycle and during this region the value of gas force and hydrodynamic pressure is very high. After compression stroke, during expansion stroke when piston approaches to the mid of stroke gas force has dropped to such extent that hydrodynamic pressures has dropped from mega pascals to fraction of pascals while at this point the film thickness has increased to some extent but not as compare with the compression stroke because of the fluid film pressures. During stroke from 450 to 540 there is further reduction in pressures and film thickness also decreases as the speed of piston started to drop and at BDC the instantaneous value of film thickness is very low. During exhaust stroke, the gas force and pressure effect is so low that film thickness has generated like first stroke of the cycle.

### *B. Friction Force*

The friction force generated during the whole cycle is shown in figure. Friction force is generated because of hydrodynamic pressures, viscosity, film thickness and velocity of piston. During intake and exhaust stroke the gas force loading are low which results in less friction force. While the drastic effect in friction force can be analyzed during compression and expansion stroke. The reason is that during these strokes the combustion gas force is high, high hydrodynamic pressures and film thickness decreases. The maximum friction force can be observed round about 400 degree crank angle. During exhaust stroke low combustion force and low pressures causes low friction force.

### *C. Flow Rate*

During lubrication phenomenon it is assumed that oil is fully flooded. The oil flow is maximum during intake and exhaust stroke and generating bell shape curves. The reason is that film thickness is maximum during these strokes and gas effects and pressure effects are minimum. But during other two strokes the oil supply is not as much as compare to other two strokes because film thickness decreases during these strokes, combustion force and hydrodynamic pressures are maximum during these strokes. During the end of each strokes the flow rate decreases to zero because film thickness decreases which may damage the ring and during compression and expansion stroke the flow rate is minimum through which friction force generated.

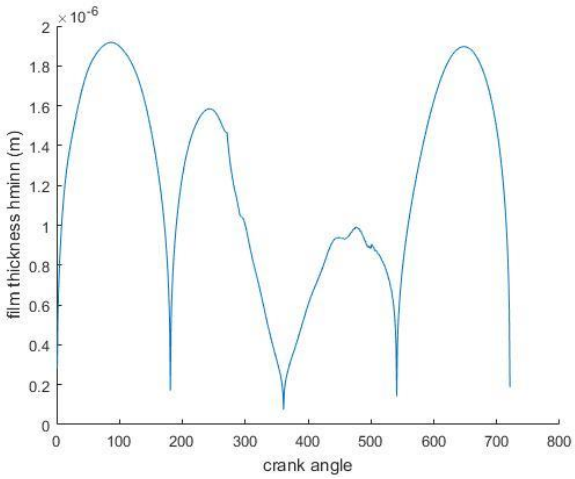

Figure 3 Hydrodynamic Film Thickness

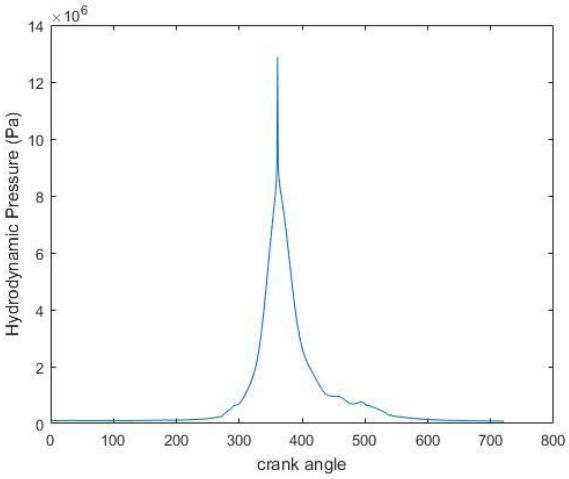

Figure 4 Hydrodynamic Pressures

## VIII. Conclusions

A 2-D hydrodynamic lubrication phenomenon is developed for parabolic type ring for high torque low speed diesel engine. During power stroke the pressure increases which causes in the reduction of film thickness and in result friction force and power loss increase, especially at the end of strokes which can damage the ring. The engine conditions must therefore be regulated during these strokes to safeguard the first compression ring from adverse effects of peak friction force, energy loss and minimal lubricant flow.

## IX. Acknowledgement

The author is indebted to his supervisor Dr. Muhammad Zubair Khan and faculty of mechanical engineering department for guidance and also Institute of Space Technology Islamabad.

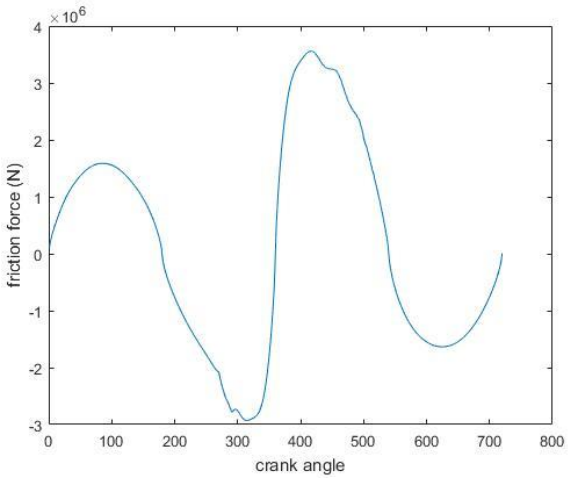


Figure 5 Friction Force

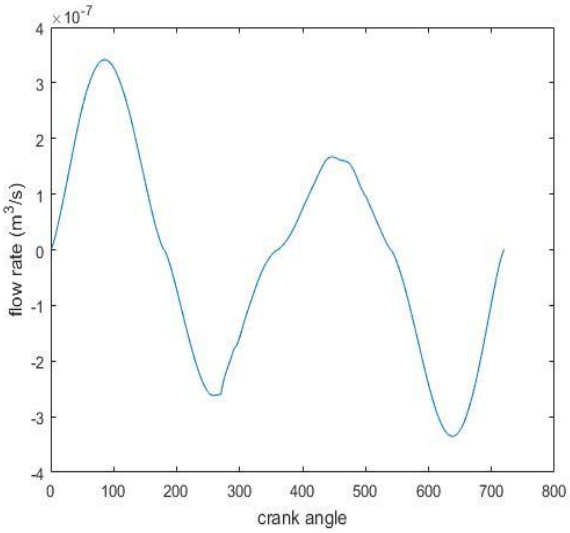


Figure 6 Flow Rate

*Table 1Engine Parameters*

| Parameters | Value |
|---|---|
| $a_1$, $a_2$ | 0.5 |
| B | 2.46 mm |
| $C_p$ | 1.04 mm |
| R | 76.105mm |
| l | 185 mm |
| r | 92.5 |
| $\Delta$c | 10 $\mu$m |

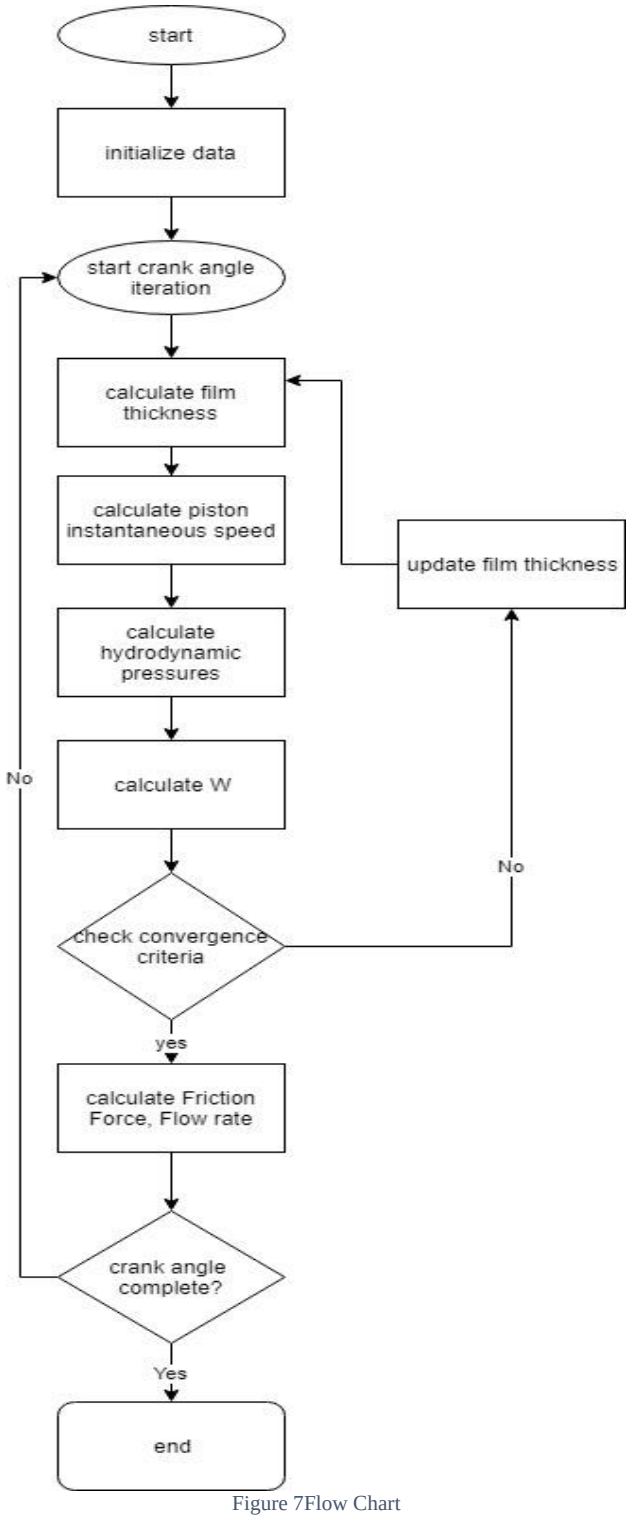


Figure 7Flow Chart

## X. REFERENCES

[1] M. S.C.Tung, "Automotive tribology overview of current advances and challenges," *Tribology International*, pp. 517-536, 2004.

[2] E. Becker, "Trends in tribological materials and engine technology," *Tribology International*, pp. 569-575, 2004.

[3] J. R. A. CASTLEMAN, "A Hydrodynamical Theory of Piston Ring Lubrication," *Journal of Applied Physics*, vol. 7, 1936.

[4] O. S.Eilon, "A study of piston-ring lubrication".

[5] H. N.Patir, "An average flow model for determining effects of three dimensional roughness on partial hydrodynamic lubrication," *Transactions of the ASME*, vol. 100, 1978.

[6] H. T. A. Y.Hu, "Numerical simulation of piston ring in mixed lubrication—a nonaxisymmetrical analysis," *Journal of Tribology*, vol. 116, 1994.

[7] I. G.R.Paul, "A new method of investigating piston ring friction under firing conditions," in *IMeche*, 1196.

[8] T. H. M. S. T. K. Y. Wakuri, "Piston ring friction in internal combustion engines," *TRIBOLOGY INTERNATIONAL*, vol. 25, 1992.

[9] T. G. K. J. Q. Yang, "Two-dimensional piston ring lubrication—part I: rigid ring and liner solution," *Tribology Transactions*, vol. 39, pp. 757-768, 1996.

[10] B. H. M. Esfahanian, "On the hydrodynamic lubrication analysis of piston rings".

[11] G. N. A.Ozgen, "Piston ring-cylinder bore friction modeling in mixed lubrication regime: part I- analytical results," *Journal of Tribology*, vol. 123, pp. 211-218, 2001.

[12] L. Z. Yong, "Two dimensional numerical analysis of piston ring lubrication of an internal combustion engine," in *SAE*, 1999.

# Plate Vibrations in Fluid having Crack at Random Angles and Locations

Ruqia Ikram
*Department of Mechanical Engineering*
*Institute of Space Technology*
Islamabad, Pakistan
ruqiaikram1993@hotmail.com

Asif Israr
*Department of Mechanical Engineering*
*Institute of Space Technology*
Islamabad, Pakistan
asif.israr@ist.edu.pk

***Abstract*— The analysis of vibrating structures such as plates is found very important in engineering structures to ensure their safety and performance. In this paper, the vibration of submerged engineering structures with a crack at random angles and locations are investigated. A series of experiments are conducted to analyze the effect of crack angle, crack location and fluid level on the plate's natural frequency for better performance of these structures. The obtained results show that natural frequency increases with crack angle and crack location. Whereas fluid acts as added mass and reduces natural frequency of the structures for evaluated case studies.**

***Keywords*— *Plate Vibrations, Fluid, Crack, Frequency and Amplitude***

## I. INTRODUCTION

Submerged plates are extensively used in engineering structures like ships, submarines, nuclear reactors etc. Vibration in engineering structures is harmful to their utility. Because when such structures come across to unwanted vibrations, there are more chances of resonance to occur that can leads to failure of structures. Therefore, it is essential to comprehend the vibration characteristics of the plates subjected to variable loadings for better and reliable designs in order to avoid the resonance condition.

The vibration phenomenon of cracked plates in air and flawless plates vibrating in a fluid medium has been investigated in literature. Due to pressure fluctuations, natural frequencies of engineering systems that sink in liquid are dissimilar to those in air. The presence of crack has a great influence on submerged structures. Some investigations have been performed over the past few years to study the vibration response of cracked plates vibrating in a fluid medium with significant contribution to the existing knowledge. However, further investigations are required to include the effect of crack position and orientation.

Most of the researchers have carried out vibration study of cracked plates without any fluid interaction. Different investigation techniques have been utilized for this ranging from analytical to Finite Element (FE) models and experimental methods. Krawczuk and Gdafisk [1] investigated the behavior of vibrating rectangular plates with crack through a FE model. This study concluded that eigen frequencies of cracked plate is a function of crack length, position and boundary conditions. Similarly, Israr [2] developed an analytical model to examine the vibrating behavior of plates with center crack. He analyzed that percentage reduction in natural frequency depends on plate dimensions and crack length. Israr et al. [3] analyzed the dynamic characteristics of a cracked plate subjected to different boundary conditions and loadings. An analytical model was formulated using Galerkin's method and Classical Plate Theory (CPT). They concluded that for CCFF boundary condition, more reduction has been seen in natural frequency of square plate as compared to plates of other aspect ratios. Israr [4] also made a comprehensive review of the methods and techniques utilized for studying the vibration response of cracked plates. Numerous experimental and theoretical studies for the vibration analysis of plates with crack have been reported but only a few of them studied the nonlinear behavior of these structures. In order to avoid catastrophic failure or damage, more studies needs to be done on nonlinear models. Joshi et al. [5] studied the vibration phenomenon in internally cracked plates and their results show that natural frequencies are more for internally cracked plates than surface cracked plates. Bose and Mohanty [6] formulated Kirchhoff's plate theory based mathematical model for the vibration of plates having crack at random angles and positions. This study shows that an incremental increase to the crack angle resulted in the reduction of natural frequencies. While an incremental increase to the distance between the center of crack and center of plate resulted in an increase to the natural frequencies. Ismail and Cartmell [7] investigated the plate vibration with the inclined surface crack at different angles by using CPT. They concluded that natural frequencies, amplitude response and nonlinear characteristics can be significantly influenced by the angular position of crack. Although, these studies provide useful information on the vibration response of vibrating plates in air. However, the vibration behavior in a fluid interaction environment has not been considered.

Over the years, many solutions have been proposed to study vibration of the flawless plates submerged in fluid.

An experimental study to the dynamic response of plates dipped at varying depths in a fluid medium with different boundary conditions was conducted by Haddara and Cao [8]. This study shows that the depth of submergence does not effect damping and modes shapes. While Muthuveerappan et al. [9] utilized an FE model for studying the behavior of an oscillating cantilever plate immersed in fluid and analyzed that the immersion depth effects the plate's natural frequencies for different aspect ratios. Ergin and Ugurlu [10] studied vibration responses of the cantilever plate interacting with the surrounding fluid. For this study, they used the method of mirror images to find differential equations of system. It is concluded that this method is preferred for submerged structures operating at high frequencies. Korosh and Farhadi [11] developed analytical model for vibrating plate partially submerged in water made from composite laminates. Their mathematical model was based on first and second-order theories of shear deformation and Classical Laminate Plate Theory (CLPT). Their results revealed that the accuracy of natural frequencies obtained by CLPT decrease with increase in thickness ratio. It is clearly observed from previous studies that the natural frequency decreases in the presence of fluid as compared to air.

A few studies based on cracked structures submerged in fluid have been founded in literature. Soni et al. [12] formulated an analytical model based on CPT and Potential Flow Theory (PFT). This model was used to study the vibration behavior of cracked plate immersed in fluid and having crack parallel to a plate side. This study revealed that combination of crack and fluid has more influenced upon vibration characteristics as compared to that when the deal separately.

A present experimental study is an extension of [12] in which we added orientation and location of crack along with the fluid is added to investigate variation in natural frequency of system.

## II. Experimental Details

A rig is designed to clamp two adjacent edges of the plate. Whereas, the other edges are unconstrained to fix the plate for CCFF boundary condition. An initial excitation is given by impulse hammer by Dytran Instruments, Inc with a range of 1000 IbF. A piezoelectric accelerometer is used to measure the response of vibrating plate. The sensitivity of this accelerometer is $100.28\ mV/g$ and range of gravitational acceleration (g's) from -50 to +50. Signal response of accelerometer is obtained on oscilloscope which is able to get signal with frequency up to 100 MHz. It can take maximum $2 \times 10^9$ sample points for one particular response.

A 1000×1000×830 mm tank is used as fluid domain to characterize the vibration response of a square plate (166×166×2) mm. Material properties are as mentioned in [12]. A part-through crack of 33×1×1.2 mm is formed to produce crack in the plate by Electric Discharge Machine. Both center and eccentric cracks are formed at different angles ranging from 0° to 90°. A series of experiments are performed for two cases (air and water) by following same method. For each experiment, accelerometer is attached at the end corner of free sides to get maximum displacement of vibrating plate. Plate is clamped in rig and bolts are fastened tightly. Initial excitation is given to plate by striking plate with hammer. Signal is captured on an oscilloscope in the form of time domain data. Fast Fourier Transform is then used to convert this data into frequency domain.

## III. Results and Discussion

Results show that natural frequency of the system has decreased due to the effect of damage or crack. This is a very important phenomenon clearly visible in the presented results and shows the importance of studying the effect of crack on the vibration characteristics of this system. The experimental model is validated with results of the recently published work [12]. The comparison is made for an intact plate (i.e., plate with no crack) and a plate cracked horizontally at the center vibrating in air and fluid. For comparison with literature, these frequencies are converted into non-dimensional frequency parameter, $F = \omega_{mn} {l_1}^2 \sqrt{\rho h / D}$

TABLE I. presents a self-explanatory quantitative comparison of the evaluated cases. It is clear that natural frequency decreases with crack. This effect is due to changes in stiffness that decreases with amount of damage produced.

TABLE I. NON-DIMENSIONAL FREQUENCY PARAMETER OF PLATE IN AIR

| **Plate Description** | **Half of Crack Length** | **Frequency Parameter** | |
|---|---|---|---|
| | | ***Present study*** | [12] |
| Intact | 0 | 4.605 | 5.118 |
| Center horizontal cracked | 0.0165 | 4.201 | 4.258 |

In fluids, Plate is suspended in fluid so that dynamic pressure of fluid is applied at the upper surface and lower surface of plate.

TABLE II. NON-DIMENSIONAL FREQUENCY PARAMETER OF PLATE IN FLUID

| **Plate Description** | **Frequency Parameter in Fluid** | |
|---|---|---|
| | ***Present study*** | [12] |
| Intact plate | 2.679 | 2.278 |

TABLE II. clearly show that natural frequency of the plate has decreased in case of vibrating in fluid compared to its vibration in air. Experimental results from the current study are agreement to the previously published results in [12]. For intact plate, natural frequency is reduced more when it submerges in fluid as compared to that obtained in air. It is due to fluid that acts as added mass.

It is also noted in [6], [7] that natural frequencies are increased with an increase in angular position of crack. Another important aspect that effects natural frequency of structure is the crack location. Effect of eccentricity along the horizontal crack on natural frequency is presented by [6]. According to this study natural frequency increases by addition of eccentricity. This is because natural frequency affects less when the crack has moved away from the fixed support or in other words damage is more critical for structure's natural frequency when it is near the fixed end. The present work also studied effect of angle and location of crack in both air and fluid.

## IV. CONCLUSION

Vibration analysis of FSI structures is very essential for under water structures like submarines, nuclear assemblies etc. The present work represents experimental study of vibration characteristics of plate in presence of fluid with crack at random angle and location. The model has been validated with literature for intact and horizontal cracked plate submerged in fluid. The results show that cracked plate vibrates at a lower natural frequency compared to an intact plate. The reduction in natural frequency for cracked plate is due to the reduction in stiffness of the plate. Fluid also effects the dynamic behavior in same manner as it acts as added mass results in reduction of frequencies. Experiments have been performed with plates having cracks at different angles and location. The results also show an increase in natural frequency of the plate with increments of angular position and this trend is similar for both vibration in air and fluid. Similarly, the crack location also increases natural frequency for the plate submerged in fluid.

## REFERENCES

[1] M.Krawczuk and Gdafisk, "Natural vibrations of rectangular plates with a through crack," Arch. Appl. Mech., vol. 63, no. 7, pp. 491–504, 1993.

[2] A. Israr, "Vibration analysis of cracked aluminium plates," University of Glasgow, 2008.

[3] A. Israr et al., "Analytical modeling and vibration analysis of partially cracked rectangular plates with different boundary conditions and loading," J. Appl. Mech., vol. 76, no. 1, p. 011005, 2009.

[4] A. Israr, "Cracked isotropic plate structures – A review," J. Sp. Technol., vol. 3, no. 1, pp. 1–12, 2013.

[5] P. V. Joshi, N. K. Jain, and G. D. Ramtekkar, "Analytical modeling and vibration analysis of internally cracked rectangular plates," J. Sound Vib., vol. 333, no. 22, pp. 5851–5864, 2014.

[6] T. Bose and A. R. Mohanty, "Vibration analysis of a rectangular thin isotropic plate with a part-through surface crack of arbitrary orientation and position," J. Sound Vib., vol. 332, no. 26, pp. 7123–7141, 2013.

[7] R. Ismail and M. P. Cartmell, "An investigation into the vibration analysis of a plate with a surface crack of variable angular orientation," J. Sound Vib., vol. 331, no. 12, pp. 2929–2948, 2012.

[8] M. R. Haddara and S. Cao, "A study of the dynamic response of submerged rectangular flat plates," no. m, 1996.

[9] G. Muthuveerappan, N. Ganesan, and M. A. Veluswami, "A note on vibration of a cantilever plate immersed in water," J. Sound Vib., vol. 63, no. 3, pp. 385–391, 1979.

[10] A. Ergin and B. Uġurlu, "Linear vibration analysis of cantilever plates partially submerged in fluid," J. Fluids Struct., vol. 17, no. 7, pp. 927–939, 2003.

[11] K. Khorshid and S. Farhadi, "Free vibration analysis of a laminated composite rectangular plate in contact with a bounded fluid," Compos. Struct., vol. 104, pp. 176–186, 2013.

[12] S. Soni, N. K. Jain, and P. V. Joshi, "Vibration analysis of partially cracked plate submerged in fluid," J. Sound Vib., vol. 412, pp. 28–57, 2018.

# Wind Turbine Turbulence And Wake Effects On Aviation Operations

Muneeb Ahsan
*Aerospace engineering department*
*Air University, Aerosace and Aviation Campus*
*Kamra, Pakistan.*
*muneebahsan@live.com*

Shuaib Salamat
*Aerospace engineering department*
*Air University, Aerosace and Aviation Campus*
*Kamra, Pakistan.*
*ssalamat@aerospace.pk*

***Abstract*—This Wind turbines have become significant contributors of energy in the recent years due to the increasing demand of energy all over the world, depletion of fossil fuels and the negative impact they impart on our environment. Despite being green and the most favorable alternative in windy areas, wind turbines pose an undue hazard on aerodromes operating in the vicinity of the wind turbine farms. These huge rotating bodies affect aviation operation in a number of ways including; electromagnetic interference and turbulent wake, which causes induced turbulence and can have adverse effects on flight and handling of the aircraft flying through it. Many military and civil airports across the world are presently operating in the close vicinity of huge wind turbine farms and their operations are being affected, especially during takeoff and landing phases. This research models the effects produced in the far wake of a wind turbine, by employing CFD techniques to analyze the wake pattern (at different velocities) behind a single wind turbine. As K-ω is known to be a good physical representation of the wake of the wind turbine, it was selected as the turbulence model in this work. Subsequently, the wake pattern generated behind the rotating blades of the wind turbine was studied as a function of free-stream wind velocity conditions to perform a thorough analysis. The analysis of the cross-wind effects of the wake on the aircraft was also studied as a function of the distance, wind speed and direction. Results from the CFD simulations provide guidelines for safe aviation operations for various categories of aircraft at aerodromes in the vicinity of wind farms.**

***Keywords— Aviation operations, wind turbine wake, CFD simulation, tip vortices, turbine wake aerodynamics. Introduction (*Heading 1*)***

## I. INTRODUCTION

Wind turbines are rapidly replacing other sources of energy throughout the world since they are cheap, renewable and an alternative source of green energy. Researches on wake produced behind rotating wind turbine blades date back to the early 1970s when the non-renewability and deteriorating effects of fossil fuels were first recognized [1].

Wind turbine types are classified into two major streams, depending upon their axis of rotation, as Horizontal Axis Wind Turbines (HAWT) and Vertical Axis Wind Turbines (VAWT). The most commonly used wind turbine type is HAWT. These wind turbines mostly have three huge blades rotating in the free-stream wind, which induces the rotational effect in the free-flowing wind. Wind turbine wake is further divided into two categories termed as near-wake and far-wake. Near-wake region of the wind turbine goes up to 1 Rotor Diameter (RD), in which flow characteristics are strongly dependent upon the geometry of the turbine blades, tip vortices and solidity-ratio of the wind turbine. The far-wake region consists of the region beyond 1 RD. Here, the wake is less dependent on the physical geometry or aerodynamic specifications of the turbine blade and more dependent upon the free-stream wind conditions. This research is based upon the study of effects produced by the rotating blades in the far-wake region. The current literature is mostly based upon the near-wake studies for the purpose of optimization of the wind turbine geometries and their power output. The rotation effect imparted on the free-flowing wind is translated into disturbances for aircraft flying in their wake; in form of cross-winds and the induced up-wash.

Wind turbine blade wake aerodynamics may seem a simple phenomenon from an observer's point of view. However, it is a complex phenomenon of 3-D flow at the hub and blade tips where the flow is in span-wise direction due to the Coriolis Effect and centrifugal forces. Furthermore, most of the previous studies conducted on the wind turbine wakes were limited only to the near-wake region for purpose of power-generation optimization. The present study utilized CFD technique in order to simulate the effects of rotating blades on the aircraft flying in the far-wake region of these wind turbines.

Wind turbines (being up-to 164m in diameter [2]) are actually the largest rotating bodies on the face of earth. Usually, a blade with its size nearly equal to the span of an Airbus A380 (79.8 m) induces rotational effects on the free-stream wind. The rotational effect produced by the wind turbines is similar to aircraft wing-tip vortices but not identical. The rotational effect in the far-wake of wind turbines causes induced cross-wind velocity and up-wash, in addition to the atmospheric turbulence present in the free-stream wind. This research studies the relationship of perturbations caused by rotating blades with respect to the wind velocities faced by the rotor of wind turbine. Cross-wind induced by these perturbations is also studied in order to draw a conclusion for safer aviation operation, especially in case of landing and take-off, on runways with wind turbine farms installed nearby.

### *A. Nomenclature*

| | |
|---|---|
| **CFD** | Computational Fluid Dynamics |
| **HAWT** | Horizontal Axis Wind Turbines |
| **RD** | Rotor Diameter |

| | |
|---|---|
| **N** | Number of blades |
| **3-D** | Three Dimensional |
| **RPM** | Rotations Per Minute |
| ***k*** | Turbulent kinetic energy |
| ***ω*** | Specific rate of dissipation |
| **u** | Free-stream wind velocity |
| **y** | Downstream velocity |
| **z** | Velocity in vertical direction |
| **CAA** | Civil Aviation Authority |
| **RANS** | Reynold-Averaged Navier Strokes equation |

## II. Wind Turbines

A wind turbine can be characterized as a mechanical device used to extract kinetic energy out of the blowing wind. This extracted energy is transformed into a useful form of energy; such as electrical energy in most of the cases. Depending upon the direction of the rotational axis of the wind turbines, they are divided into two streams; namely Vertical Axis Wind Turbines (VAWT) and Horizontal Axis Wind Turbines (HAWT). In case of HAWTs, the axis of rotation of the wind turbine rotor is parallel to the direction of flow of the wind. However, they are both orthogonal to each other in case of VAWT [3]. A wind turbine can be characterized as a mechanical device used to extract kinetic energy out of the blowing wind. This extracted energy is transformed into a useful form of energy; such as electrical energy in most of the cases. Depending upon the direction of the rotational axis of the wind turbines, they are divided into two streams; namely Vertical Axis Wind Turbines (VAWT) and Horizontal Axis Wind Turbines (HAWT). In case of HAWTs, the axis of rotation of the wind turbine rotor is parallel to the direction of flow of the wind. However, they are both orthogonal to each other in case of VAWT [3].

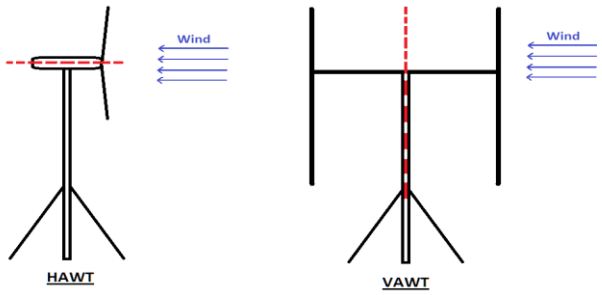


*Fig. 1. Axis of rotation for HAWT and VAWT*

## III. Horizontal Axis Wind Turbines

A Despite VAWTs being the first-ever mechanical device used to extract the energy out of blowing wind, most of the advancements and researches were carried out on the HAWTs [3]. VAWTs, being ill-famed about lower output efficiency, did not become the center of attention for a commercial alternative energy solution. Today, HAWTs enjoy the greater share of the installed wind capacity throughout the world [4].

This research is also based upon the case study of famous NORDEX N100/2500 wind turbine which is a large-sized turbine used in a number of countries all around the globe for wind power extraction. Specification of the turbine modeled in this research as given in the table below.

| **Make and Model** | **Nordex 100/2500** |
|---|---|
| **Make and Model** | 2500 kW |
| **Rated Power Output [P]** | 99.8 m |
| **Turbine Diameter** | 7822 m2 |
| **Swept Area** | IIIa |
| **Wind Turbine Class** | 80 m |
| **Hub Height** | 3 m/s |
| **Cut-In Speed** | 25 m/s |
| **Cut-Out Speed** | 129.9 m (425 ft.) |
| **Max Height** | 77 m/s |
| **Blade Tip Speed** | 14.9 RPM |

## IV. Wake Structure

A wind turbine extracts kinetic energy out of the freely blowing wind. Aerodynamic forces acting upon the blades of the wind turbine cause rotation, slowing the velocity of wind in the downstream region or the wake of the turbine. Along with slowing the free-stream wind, rotating blades of the wind turbine impart circulating effects on the wind similar to the aircraft wing-tip vortices. These circulations have a huge diameter ranging beyond 100 m depending upon the size of the wind turbine. Circulation and vorticity in the wake starts to form at two locations i.e. “tip vortices” at the tip of the blade, due to span-wise flow of air at the blade tip similar to span-wise flow at wing tip of aircraft, and “hub vortices” at the hub due the centrifugal forces acting on the wind. These vortices are distinct and dominant in the near-wake region. The farther downstream the wind goes, more will be the flow-mixing in the wake. In far-wake region, hub vortices and tip vortices produced by each blade merge into each other due to turbulent-mixing and advection in the wind. This vortex-mixing in the far wake region induces cross-wind and up-wash gusts in the wind, which can be problematic for the safe flying of aircraft depending upon the free-stream wind velocity. Wake formed behind a wind turbine can be described by the figure below [5]

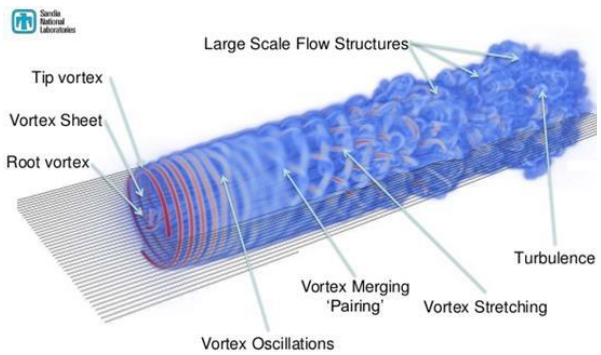


*Fig. 2. Wind turbine wake structure [5]*

## V. Single Wind Turbine Wake

### A. Flow Dynamics

Define Wake formed behind a single wind turbine has been studied extensively in past few decades. These studies are mainly focused on the large-scale exploitation of the wind energy, thus focusing on the inter-turbine distances, velocity deficit in the turbine downstream and the wake recovery. As the wind turbine extricates energy, it results in a region with decreased velocity behind the rotor blades of the wind turbine. Largest reduction in the flow speed can be observed behind the centerline at hub height [6]. Along with the occurrence of velocity deficit behind wind turbines, vorticity effects are the major concern for the safety of the aircraft. Jets and wakes are

two similarly behaving aerodynamic phenomena, but they are opposite to each other in terms of velocity gradients [7].

$$\text{Jet:} \quad u \to 0 \; as \; y \to \pm \infty \tag{1}$$

$$\text{Wake:} \quad u \to \infty \; as \; y \to \pm 0 \tag{2}$$

However, while studying wakes, we may notice that the cross-stream advection term is very small when compared to the advection term in the downstream direction. While in jets both the advection terms are comparable to each other i.e.

$$\text{Jet:} \quad u\frac{\partial u}{\partial y} \approx u\frac{\partial u}{\partial z} \tag{3}$$

$$\text{Wake:} \quad u\frac{\partial u}{\partial y} \ll u\frac{\partial u}{\partial z} \tag{4}$$

Where, y and z are the downstream and vertical components respectively. Experimental measurements behind the wind turbine's rotating blades show that both these advection terms are close to each other [6].

$$\text{Jet:} \quad u\frac{\partial u}{\partial y} \approx 0.04 - 0.05 \tag{3}$$

$$\text{Wake:} \quad u\frac{\partial u}{\partial y} \ll 0.01 - 0.04 \tag{4}$$

It is evident from the relations above and experimental measurements that flow behind rotating blades of the wind turbine is a complex 3-D mixing phenomenon; or it can be better described as a negative jet, but in terms of its aerodynamic behavior, it cannot be considered as a wake. However, wake is the most common name in literature referring to the flow behind rotating wind turbine blades and in this research it will be referred to as "wake" as well.

### B. *Modelinf for CFD Simulations*

A number of techniques and aerodynamic models have been developed for the prediction of wind turbine performance, numerically and analytically, which include the following:

- Vortex model
- Momentum model
- Cascade models

All these methods are only focused at the near-wake velocities and power extraction. This research on the other hand is focused on the far wake study therefore CFD technique is employed to simulate the vorticity effects produced in the wake of the wind turbine. $k-\omega$ is known to be a good representation of the RANS equations for the turbulence prediction. This equation solves the turbulence using two simultaneous partial differential equations, $k$ and $\omega$. Rotating CAD geometry of the Nordex 100/2500 wind turbine blade inside the stationary domain is modeled in order to predict the turbulence in far wake using $k-\omega$ model. Figure below shows the meshed CAD model of the wind turbine blades which rotate in the free-stream wind to induce the vorticity effects.

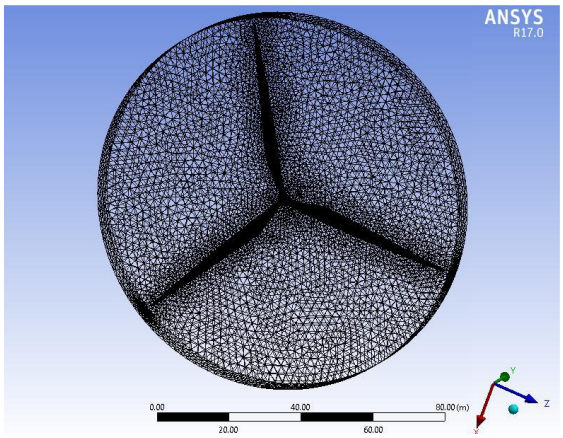


*Fig. 3. Wind turbine blade*

This wind turbine blade model is rotating at the design RPM corresponding to the free-stream speed, 80m above the ground level. It is enclosed inside a domain with a cross-section 3-RD wide in both horizontal and vertical directions. The simulation domain consists of 500m length upstream and 5 km downstream the rotor blades. Following figure shows the isometric view of the domain under study along with some boundary conditions.

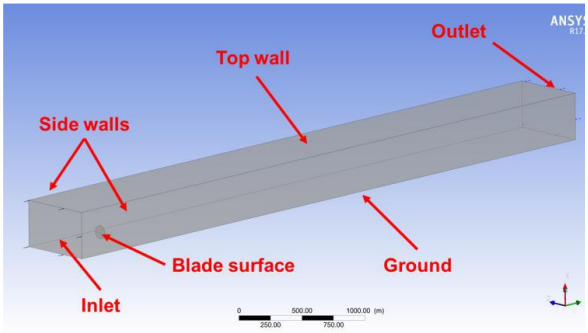


*Fig. 4. Domain under study for wind turbine wake effects*

Wind turbine wake pattern was studied on three different free-stream wind speeds:

- 3 m/s
- 5 m/s
- 16.3 m/s

Studying the wake effects produced behind the rotating blades of the wind turbines during different wind conditions enables us to draw a relation between the free-stream wind speed and the resulting perturbations along with their magnitude and distance before wake recovery.

## VI. Results

At free-stream wind velocity of 3 m/s, perturbation distance was found to be 4.2 km downstream the wind turbine rotor blades for 95% decay in the maximum vorticity produced by the wind turbine. Figure below shows top view of the vorticity contours drawn at the hub height in the modeled domain.

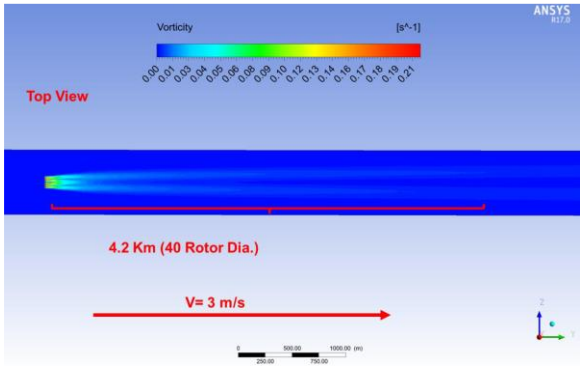


*Fig. 5. Vorticity contour for 3 m/s wind (Top view at hub height)*

Vorticity contours at various planes downstream the wind turbine show the pattern of perturbations and their mixing behavior behind the rotating blades of the wind turbine. Following figure shows the vorticity contours from the front view for 3 m/s free-stream wind velocity:

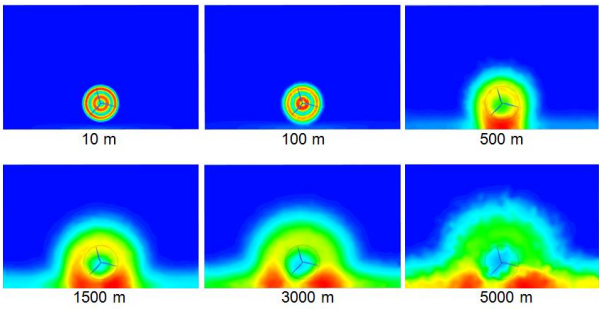


*Fig. 6.Vorticity contours for 3m/s wind (front view)*

At free-stream wind velocity of 5 m/s, the distance for 95% decay in the perturbations drops down to just 2.4km. However, the maximum magnitude of vorticity produced at the turbine blade tip and hub increases 5 times. Figure below shows the top view of the vorticity contours drawn at the hub height in the modeled domain for 5m/s free-stream wind velocity.

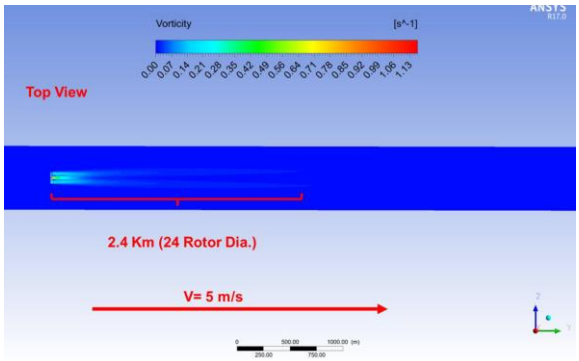


*Fig. 7. Vorticity contour for 5 m/s wind (Top view at hub height)*

Following figure shows the vorticity contours for 5m/s free-stream wind velocity at various downstream locations at planes drawn from the front view:

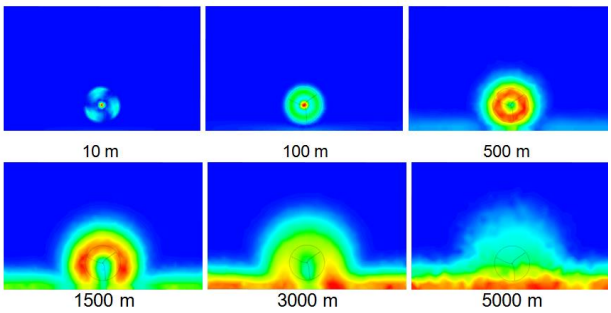


*Fig. 8. Vorticity contours for 5m/s wind (front view)*

For free-stream wind velocity of 16.3 m/s, the perturbation distance for 95% decay in vorticity further decreases to 1.8km (18- RD) and the magnitude of maximum vorticity increases to 1.52 rad/s. Figure below shows the top view of the vorticity contours drawn at the hub height in the modeled domain for 16.3sm/s free-stream wind velocity.

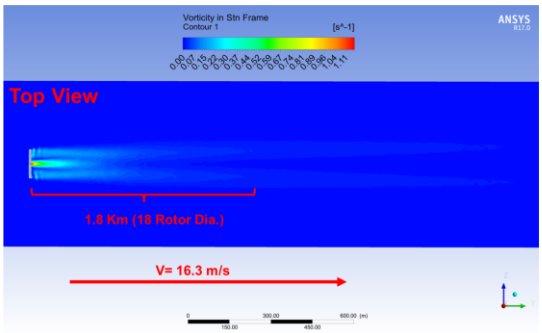


*Fig. 9. Vorticity contour for 16.3 m/s wind (Top view at hub height)*

Following figure shows the vorticity contours for 16.3 m/s free-stream wind velocity at various downstream locations at planes drawn from the front view

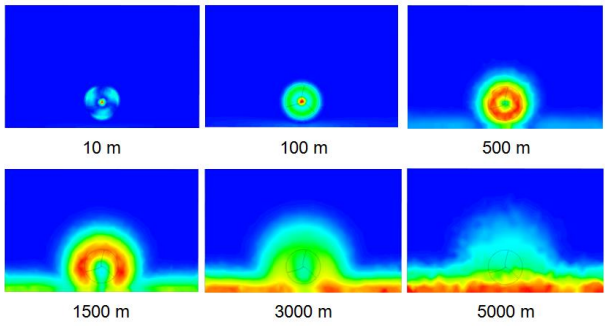


*Fig. 10. Vorticity contours for 16.3m/s wind (front view)*

These results, obtained from the CFD analysis of the rotating wind turbine blades, can be summed up in form of the following table.

| **Free-stream velocity** | **Maximum vorticity** | | **Perturbation distance** |
|---|---|---|---|
| **m/s** | **rad/sec** | **deg/sec** | **km** |
| **16.3** | 1.52 | 87 | 1.8 |
| **5** | 1.15 | 66 | 2.4 |
| **3** | 0.213 | 12.2 | 4.2 |

## VII. Analysis

From the results of vorticity contours shown above, it can be observed that perturbation distance increases with the decrease in the free-stream wind velocity. However, maximum magnitude of the perturbations produced varies directly with the free-stream wind conditions. In order to completely understand the flow characteristics behind the rotating blades of the wind turbine, it is necessary to draw some comparisons between flows at different incoming speeds.

### A. Strength Comparison

Strength of vorticity can be compared by drawing the vorticity contours behind the wind turbines at same color scale for different free-stream wind speeds. Following contours are drawn at same distances downstream the rotating rotor blades.

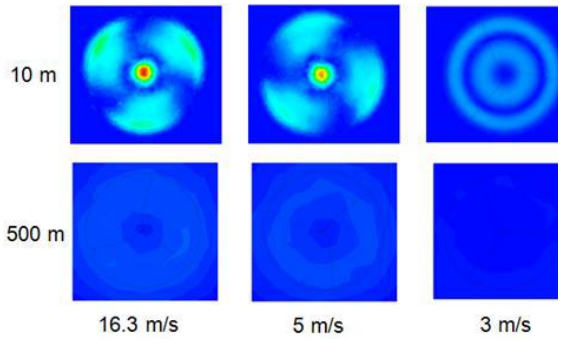


*Fig. 11. Comparison of vorticity strength at various*

From the above comparison of the strength of vorticity produced by the rotating wind turbine blades at different free-stream conditions, it can be observed that the strength of the vorticity produced is directly proportional to the increase of free-stream wind velocity. The magnitude of the resulting vorticity at lower wind speeds is nearly negligible when compared to the vorticity at higher velocity; especially, when this comparison is made at any point in far wake region. Graphically, this trend can be represented with the following graph:

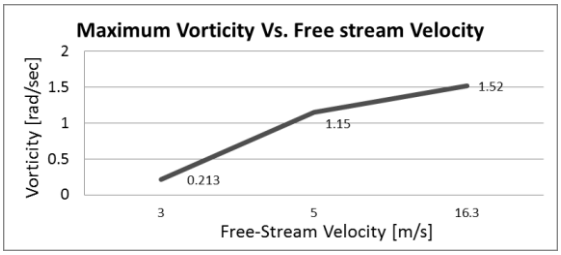


*Fig. 12. Trend of vorticity strength vs. velocity*

### B. Decay Rate and Flow-mixing Comparison

In order to understand the decay rate of perturbation and mixing of flow at various free-stream wind conditions, it is necessary to compare the pattern on vorticity downstream the wind turbine. Following contours show the comparison of the of vorticity contours, from the front view of the domain under study, at various downstream locations.

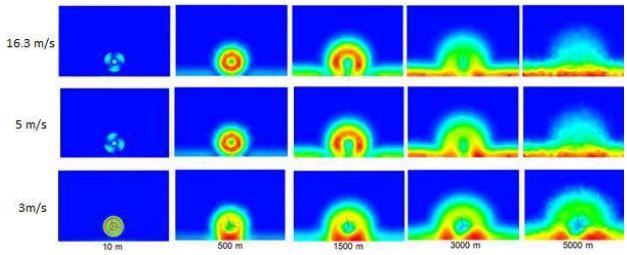


*Fig. 13. Comparison of vorticity patterns at various downstream locations*

From the comparison of the vorticity pattern at different planes downstream the wind turbines, it is evident that advective flow-mixing is lower at lower wind velocities and therefore perturbations travel a greater distance despite being less in magnitude. However, higher the wind velocity, higher will be the advection term and the flow-mixing hence perturbations will mix up in the free-stream turbulent wind at a higher rate. Vorticity contours shown from the top view of the domain under study also show this decay in distance travelled by perturbation before 95% decay in their respective strengths. These assertions can be summed up in the form of following graphs:

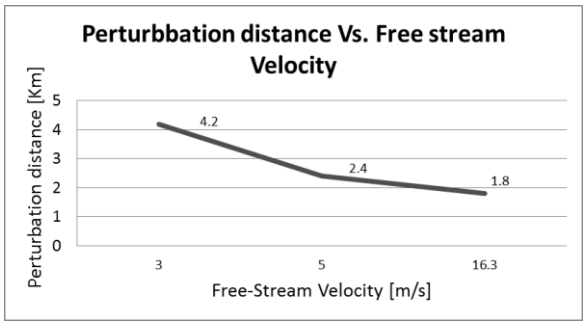


*Fig. 14. Trend of perturbation distance vs. wind velocity*

The graph below shows the comparison of the decay in vorticity at various free-stream wind velocities:

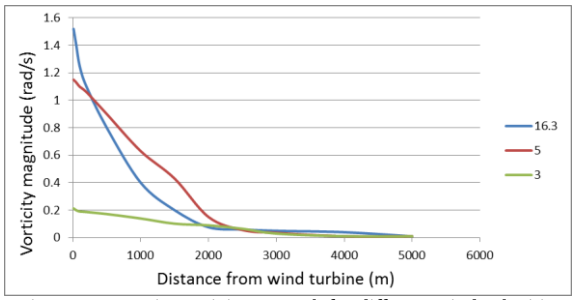


*Fig. 15. Decay in vorticity strength for different wind velocities*

From the above graph, it can be observed that the decay rate is also higher for higher wind velocities due to advection and more flow-mixing in the downstream. At lower wind velocities, flow-mixing in the wind is very less and these perturbations travel more distance for the same percentage decay in their magnitude.

### C. Cross-wind

The major concern about the wind turbine farms for safe flights of aircraft is the cross-winds induced by the rotating blades, especially in the cases when aircraft are taking-off or landing in the wake. As it is evident from the above-

mentioned analysis that strength of this vorticity is negligible at lower velocities, therefore, in this study, the cross-wind effects produced behind the wind turbines due to vortices produced at blades and hub at only the highest velocity are studied. Following figure shows the pattern for cross-wind induced by the rotating wind turbine blades. These contours are drawn from top view at the blade tip height.

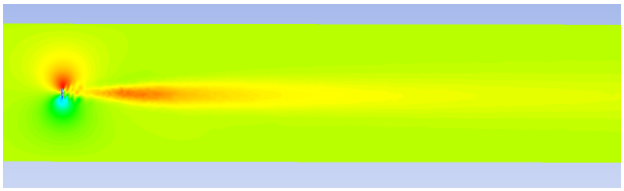

*Fig. 16. Crosswind pattern at tip height*

This figure only shows the cross-wind distribution at blade tip height however, the graph below shows the relation between the downstream distance and the magnitude of maximum cross-wind, based upon the results in the complete plane behind the wind turbine.

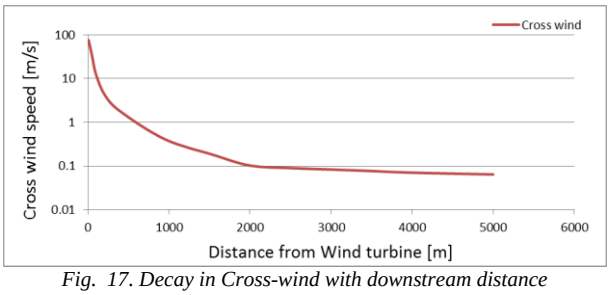


*Fig. 17. Decay in Cross-wind with downstream distance*

From the above graph of cross-wind it can be observed that the value of cross-wind beyond 2km is in range of order $10^{-2}$ rad/s which is negligible therefore aviation operation beyond this distance is considered safe regarding aerodynamic effects of the rotating blades of the wind turbine. This argument is also supported by the wind turbines policy issued by the Civil Aviation Authority (CAA) of United Kingdom which states that for non-radar equipped aerodromes, wind turbines can be installed as close as 3 km from the end of runway [8]

## VIII. Conclusion

Wind turbines impart great effect on free-stream wind and induce a rotational effect, called vorticity, in it. Although this effect and the aerodynamic stall produced at the turbine blades are not significant at lower wind speeds, they become significant when the wind speed increases. Similarly, the magnitude of the disturbances produced also increases. Also, due to higher rate of flow-mixing in the wind, decay rate of these perturbations is higher which causes a decrease in the distance travelled downstream by these perturbations. It can be observed that for a single wind turbine, cross-wind and vorticity effects are negligible beyond 20 RD or 2 Km for this case. Most of the HAWTs operating in the world are near 100m in diameter or above, therefore, area beyond 3 km distance can be considered safe for aircraft and other aviation operation considering the aerodynamic effects of a single wind turbine only. However effect produced by multiple wind turbines operating on the wake of each other needs to be explored further.

## References

[1] Vermeer, L. J., Jens Nørkær Sørensen, and A. Crespo. "Wind turbine wake aerodynamics." *Progress in aerospace sciences* 39.6 (2003): 467-510.

[2] Wittrup, Sanne. "Power from Vestas' giant turbine" (in Danish. English translation ). Ingeniøren, 28 January 2014. Retrieved 28 January 2014

[3] I. Paraschivoiu, Wind turbine design: with emphasis on Darrieus concept: Presses inter Polytechnique, 2002.

[4] W. W. E. Association, "World wind energy report 2008," *WWEA: Bonn*, 2009.

[5] Maniaci, David. "Sandia Wind Turbine Blade Workshop." 2014.

[6] Magnusson, M., and A-S. Smedman. "Air flow behind wind turbines." *Journal of Wind Engineering and Industrial Aerodynamics* 80.1 (1999): 169-189.

[7] D. Tempelmann and S. Bagheri, "Jets and Wakes", KTH Royal Institute of Technology ,Stockholm, 2008

[8] *CAA Policy and Guidelines on Wind Turbines.* Directorate of Airspace Policy, Civil Avition Authority, 2011

[9] Managing the Impact of Wind Turbines on Aviation, in Aviation Planning Considerations for Wind Turbines. Airspace & Safety Initiative Windfarm Working Group, 2013.

[10] Electromagnetic Interference, Aviation and Shadow Flicker, in Environmental *Statement.* Neuadd-goch Bank Wind Farm.

[11] *Wind Energy and Aviation Interests- Interim Guidelines.* Wind Energy, Defence & Civil Aviation Interests Working Group, UK, 2002.

[12] Stergiannis, N., et al. "CFD modelling approaches against single wind turbine wake measurements using RANS." *Journal of Physics: Conference Series*. Vol. 753. No. 3. IOP Publishing, 2016.

[13] L. Jatoi, 'Policy for Development of Renewable Energy for Power Generation', 2006. [Online]. Available: http://www.aedb.org/Documents/Policy/REpolicy.pdf. [Accessed: 3-Feb- 2017].

[14] Authority, Civil Aviation. "CAP 764." *CAA Policy and Guidelines on Wind Turbines* (2009).]

[15] Heier, Siegfried. Grid integration of wind energy: onshore and offshore conversion systems. John Wiley & Sons, 2014

[16] *Safeguarding of Aerodromes.* Airport Operators Association & General, 2006. Aviation Awareness Council.

[17] Thomas E. Mulinazzi, Z.C.Z., *Wind Farm Turbulence Impacts on General Aviation Airports in Kansas.* Kansas Department of Transportation, Kansas State University Transportation Center, and The University of Kansas The University of Kansas, 2014.

[18] E. W. E. Association, Pure Power-Wind energy targets for 2020 and 2030: Ewea, 2011.

# Development of a Small-Scale Composite Vertical-Axis Wind Turbine System

Shehan Ali
*University of Lahore*
Lahore, Pakistan
shehanali05@gmail.com

Muhammad Muneer
*University of Lahore*
Lahore, Pakistan
muneerawan17@gmail.com

Khazar Hayat
*University of Lahore*
Lahore, Pakistan
khazar.hayat@me.uol.edu.pk

***Abstract*— Energy crisis has becomes a serious matter for the country. Nature has blessed our country with numerous renewable energy resources. The basic need is to completely utilize these resources to overcome energy shortage. Pakistan has enough potential of wind to produce energy but economically it is not in the position of large scale wind power plants projects. In this research a small scale vertical axis wind turbines (VAWT) is being manufactured which is of light weight composite material, having low cost and can be installed in both urban and rural areas. The VAWT prototype is designed for 200W rated capacity. It comprises H- Darrieus configuration with three blades. NACA0021 is used which is relatively thick and symmetric air foil type and can be operated on very low air speed. To justify the research turbine blades are manufactured with fiber glass reinforced plastics (FGRPs) and polystyrene which gives stiffness with its very low weight. Generator part is also made of composite material so that mechanical losses and cogging torque would be minimized. Furthermore, the prototype testing is being carried out to evaluate its productivity as well as to identify the constraints of the model and will be shared in near future.**

***Keywords*— *Vertical axis wind turbine, fiber glass reinforced plastics, NACA0021*.**

## I. Introduction

According to the need of utilization of energy and awareness of climate circumstances humans are continuously struggling to fulfill energy demands in such a way that it would not impact the surroundings [1]. For this scenario different ways of renewable energy are getting much importance. Wind and solar energy are very common and abundant form of renewable energy resources. Resources are environment friendly and are one of the foundations of one's country economic success and its energy security [2,3]. Especially those counties in which the sun shines very bright and the wind moves moderately are focusing on utilizing these resources [4-7]. Pakistan is very fortunate by nature of having such solar and wind energy resources [8]. Pakistan can produce 300 GW power by using the wind potential but it is not being employ according to the need [9,10].

Country is facing very swear problems of energy crises. Daily energy requirement of Pakistan is 20,000MW but producing 1150MW and shortfall of 5000MW – 9000MW occurs. If we consider non-renewable energy resources it is not an economically self-sufficient country. Moreover non-renewable energy resources are continuously depleting day by day and it is impossible to overcome shortfall by them [11]. On the other hand 70% of population lives in rural areas and they are not given direct access to the main power supply of the country [12]. The need is to focus on such sources which will be reliable, low cost, and sustainable and also can be installed easily in remote areas [13-16]. For this need small scale vertical axis wind turbine is being manufactured whose installation will be easily in both remote areas and those areas which are connected to power grids which will be helpful for grids in overcoming load. Composite Material VAWT can be easily manufactured on the small scale. It should be noted that for small energy generation system, a VAWT might be a more feasible option than a horizontal-axis wind turbine (HAWT) [17-19]. As compared to the horizontal axis wind turbines these vertical axis wind turbines have simple mechanical parts and can be operated without any yawing mechanism that keeps them in specific incoming wind direction [20-22].

## II. Methodology

### A. Design of Turbine

#### 1) Aerodynamic Design of Turbine Blade

Blade energy extraction from the air is fully dependent on the aerodynamic design. In aerodynamic design two main parameters are lift force and drag force. They depends upon the angle (α) at which the air strikes the blade. Lift is a perpendicular force that is formed because of the pressure difference of the blade profile whereas drag force is due to the viscosity of air. A special type of software tool named Q blade software is a very trustworthy in the designing of airfoil blades of the turbines. This software gives us ease to generate design parameters of the blade i.e. its dimensions etc. When analysis is carried out on Q blade software it sets range for that attacking angle i.e. –26.6° to +26.6°. The values of coefficients can be seen in the following figure 1 as well.

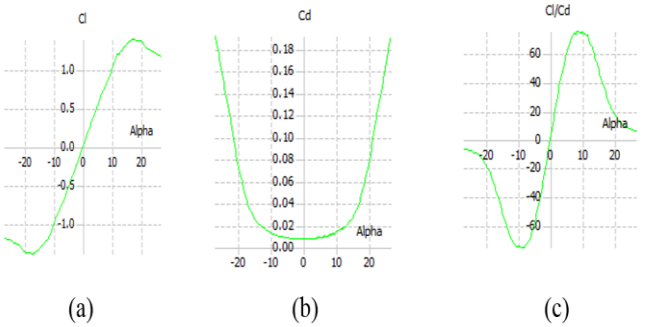


Fig. 1. Values of coefficients lift, drag and their ratio.

It can be noted that Lift is important factor and is responsible for gathering energy of wind onto the blade. Therefore its value should be as higher for the rotations of the wind turbine. On the other hand from the last graph ratio of lift to drag if increases it decreases the drag force which is also important.

The main emphasis of the exploration is about the auto startup of turbine and to create the force of lift. For this purpose NACA 0021 is taken which have favorable airfoil thickness, operates at low Reynolds number and comparatively consist of high value of lift coefficient and low value of drag coefficient. It is shown below.

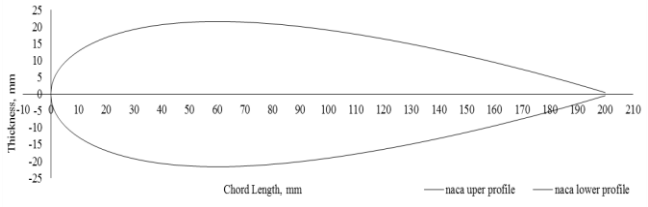


Fig. 2. Airfoil NACA 0021.

*2) Design of Generator*

Generator design parameters are router thickness 15mm, outer radius 185mm, inner radius 128mm, stator thickness 12mm, air gap 2mm, magnets 12, coils 9, rpm 200 and no load power output 200W. Two router disc are used with a single stator disc.

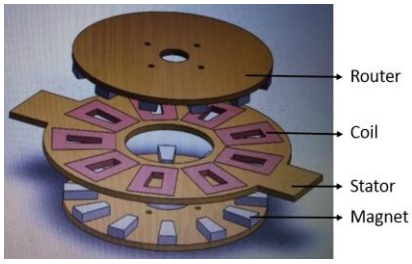


Fig. 3. Cad design of axial generator.

*B. Manufacturing of Prototype*

*1) Sandwich Construction:*

A sandwich composite construction technique is used for the development of model i.e. two layers of fiberglass with styrofoam inside. The composite material gives the relative strength to the construction and makes it in light weight. It is non-corrosive and it has thermal and electric insulation.

*2) Cutting of Airfoil:*

For the cutting of profile of blade electric hot wire cutter is used. The steel wire is kept at the voltage of 13.5 and at 4 amperes approximately which gives smooth cut without any distortion. Electricity is provided through a DC power supply.

*3) Flat Layup of Blade:*

In order to attach the airfoil, clamps of aluminum are used at the center of each airfoil with the help of epoxy. After that coated it with double layers of fiber glass and epoxy. The fibers of the fiber glass sheet must be as straight as possible. With the help of squeegee extra epoxy should be removed from the sheet as it will only increase the weight of airfoil. Make sure there are no bubbles present in the fiberglass layers and use dryer for this purpose which helps in proper wetting of fibers with epoxy. For proper cure of the mateial it takes atleast 15 hours. Similarly 2 other blades are also manufactured. Total weight of one blade is 845g i.e. 400g of fiber glass, 200g of aluminium clamp and rest is epoxy and styrofoam weight.

Fig. 4. Blade.

*4) Manufacturing of Generator:* Axial generator, also called pancake generator consist of two parts.

*a) Magnetic Disc:*

This is the rotor having 12 permanent magnets fixed in the composite material disc of fiberglas with epoxy and styrofoam as a core material. Styrofoam sheet when by cutting it in circular disc shape and cutting the pieces out at an angle 30°, where the 12 magnets are to be placed. “Neodymium magnets” are used and fix them half by half with the help of epoxy in the space cut in the styrofoam disc and a wooden ply of 2mm i.e. N-S-N pole continues with 6 magnets at a time to avoid any harm due to high strength of magnets. Then completely covered it with double coating of fiber glass with the help of epoxy which gives it strength and toughness as desired. Procedure is same like blades were build. Similarly other disc is also made. Total weight of one magnetic disc is 2.5kg i.e. 2kg of magnets and rest is epoxy, fiber glass and styrofoam weight.

Fig. 5. Magnetic disc

*b) Manufacturing of Stator:*

A wooden die was made on which coils are to be wound so that the internal space of the finished coil is of same size as that of magnets used. Stator connections are of star type with Ac output of three phase system. Connection wires were joined, soldered and are covered with sleeves for protection of short circuit. A wooden mold was used for the manufacturing of stator coils in which single ply of fiber glass is used on upper and lower side. Coils are fully dipped with epoxy and mold was tightened with nut and bolts. It takes 24 hours to cure fully. Then untightened the mold and took out the finished stator. Total weight of stator is 6.5kg i.e. 4.5 kg of copper coils and rest is epoxy.

Fig. 6. Stator

*5) Assembly of Prototype*

Finally, for its assembly all the parst are then tighted together with nut and bolts and bearing along with aluminium hub to the steel tower. Flow chart for the aseembly is shown in Fig.7.

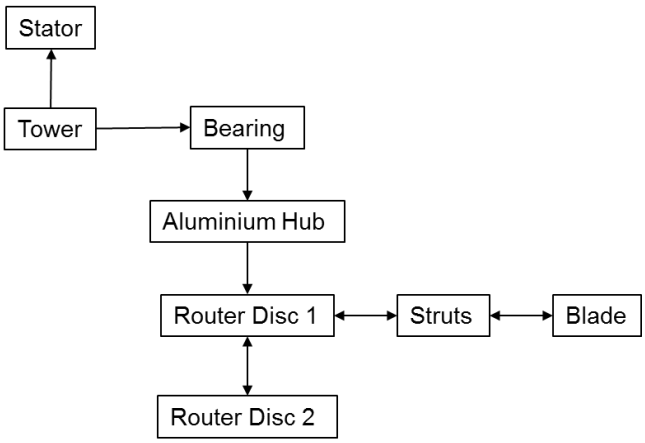


Fig. 7. Schematic assembly

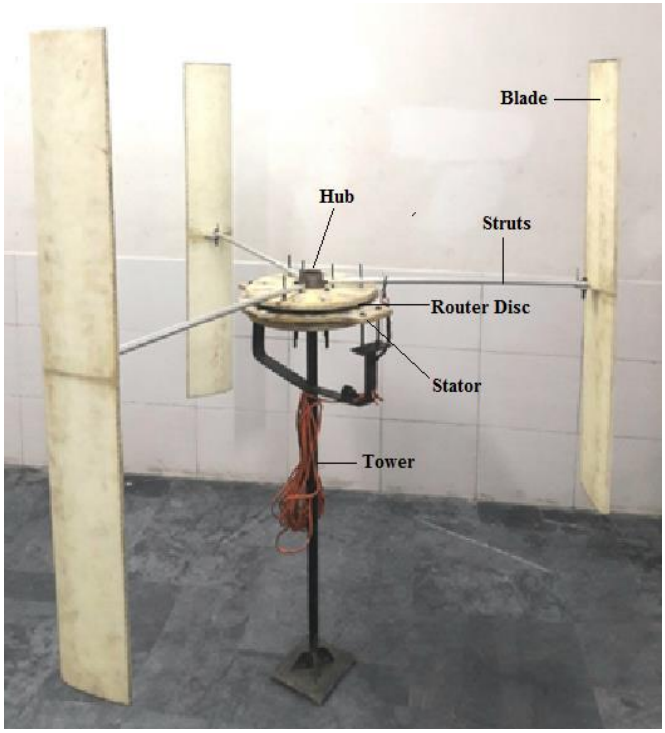


Fig. 8. Assembled model of VAWT.

*6) Cost and Weight Analysis*

Weight of the turbine rotating components is 10 Kg and total weight is 16 Kg. Cost of this turbine is PKR 26 thousands.

TABLE I. THE COST AND WEIGHT ANALYSIS OF VWAT

| Components | Cost, PKR | Weight, Kg |
|---|---|---|
| 3 Blades | -- | 2.5 |
| Stator | -- | 6.5 |
| 2 Router Discs | -- | 5.0 |
| Struts | 300 | 0.450 |
| Bearing | 450 | 0.350 |
| Aluminium Hub | 800 | 0.450 |
| Aluminium Clamps | 500 | 0.555 |
| Tower | 1500 | 4 |
| Coil | 5500 | 4.410 |
| Magnets | 12000 | 1.908 |
| Fiber Glass | 1150 | 2 |
| Thermocol | 600 | 0.40 |
| Epoxy | 3300 | 3 |
| Total | 26,100 | Miscellaneous |

15.8Kg

## III. RESULTS AND DISCUSSIONS

### A. *Judgment of Constructed Airfoil Profile of Blade with NACA*

Fig. 9 is for the judgment of constructed airfoil profile of blade of turbine with NACA used for its manufacturing and when results are compared they shows similarity in it.

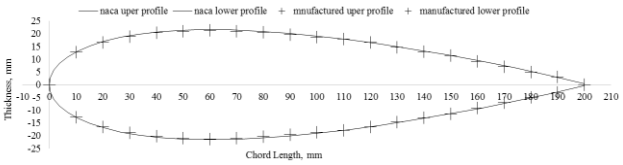


Fig. 9. Graph of constructed blade profile v/s NACA 0021.

### B. *Output Voltage by Generator*

Generator testing is carried out on the Lathe machine at its different speeds keeping the air gap of 3mm between the stator and the magnetic disc. Output voltage results are shown in following graph.

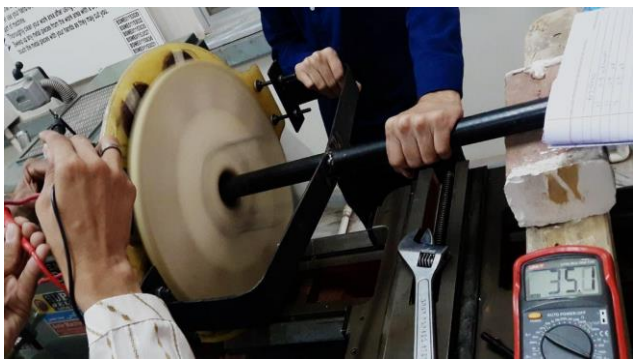

Fig. 10. Generartor testing.

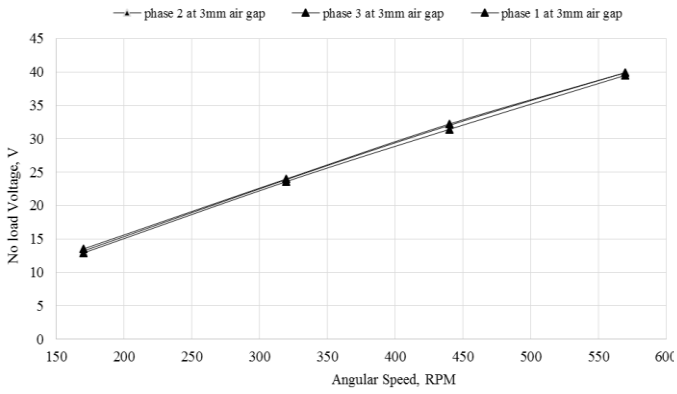


Fig. 11. Graph of output voltage by generator.

### *C. Turbine Angular speed testing*

Wind turbine is tested for angular speed against wind. For this purpose wind speed used was 2.3m/s and turbine blades were observed at different angle against the wind direction that is shown in following figure. The top angle of attack by which turbine can extract maximum energy from the wind, lies between 7° to 12°.

Fig. 12. Wind testing of VAWT.

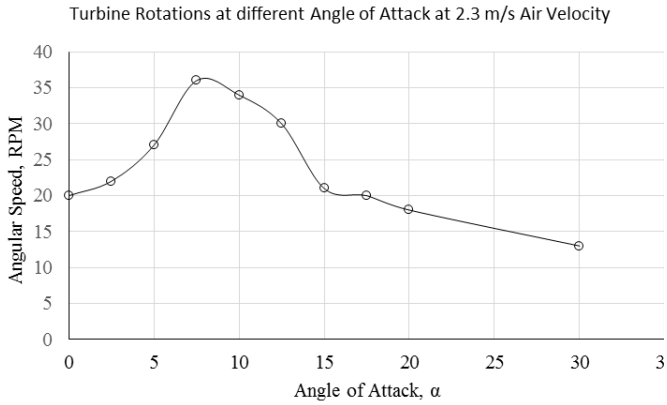


Fig. 13. Graph of turbines rotations.

## IV. Conclusion

A step towards development of a small-scale, light-weight and low cost wind energy generation system for remote areas of the country. Light weight composite construction of VAWT blades and generator reduces the mechanical losses i.e. overcoming of generator cogging problem in particular. Electric generator efficiency increases with decrease in air gap between the stator and rotor discs. Use of airfoils NACA0021 for self-startup of the VAWT at lower wind speeds. Prototype cost PKR 26000 and weight 15.8 Kg. Future, mechanical bearings can be replaced with magnetic levitation to further lower the mechanical losses and improve efficiency.

## V. References

[1] P. A. Owusu, S. A. Sarkodie, “A review of renewable energy sources, sustainability issues and climate change mitigation, Cogent Engineering, Article of Civil and Environmental Engineering, 4 April 2016.

[2] “Alternative Energy Development Board (AEDB),” Minisitry of Energy Government of Pakistan.

[3] C. Luke, Hancox, Daniel, MacKenzie and Matthew, “Whelan Design of a Vertical-Axis Wind Turbine,” MUN VAWT Design Group M11 Jonathan, Final Report, April 2014.

[4] R. Patel and N. Zhao “Pakistan’s Energy Crisis Public Interest Report, “Keeping the Lights on, Fixing Pakistan’s Energy Crisis, vol. 67 no. 2. Spring 2014.

[5] M. Katz, “The Feasibility of Renewable Energy in Pakistan,” Triple Bottom Line, 2012.

[6] M. A. Aman, S. Ahmad, M. Munir and M. Ali, “Solutions of Current Energy Crisis for Pakistan”, in International Journal of Computer Science and Information Security, June 2017.

[7] R. Ahire, S. Gawli, K. Geedh, A. Gade and S. S. Patil, ”Review on Vertical Axis Wind Turbine International Journal of Advances in Scientific Research and Engineering, ISSN, vol. 3, June 2017.

[8] Zaigham, Nayyar and Zeeshan, “Prospects of Renewable Energy Sources in Pakistan,” 2005, pp. 65-86.

[9] I. A. Mirza, S. Ahmed and M. S. Khalil, “Renewable Energy in Pakistan, Opportunities and Challenges,” vol. 16 and vol. 17, A Scientific Journal of COMSATS, Science Vision, January 2010 to December 2011.

[10] “Alternative Energy Development Board (AEDB),” Minisitry of Energy Government of Pakistan.

[11] I. A. Mirza, “Wind Data Reliability in Pakistan for Wind Generation,” 2013, pp. 22.

[12] M. Naseem, Abbas and Malik, “California Energy Crisis in Pakistan,” California, Monterey: Naval Postgraduate School, Dec 2015.

[13] M. Asif and M. Yunus, “Energy Crisis in Pakistan; Origins, Challenges, and Sustainable Solutions,” University of Oxford Press, 2011.

[14] M. A. Javaid, S. Hussain, A. Maqsood, Z. Arshad, M. A. Arshad and M. Idrees, “Electrical Energy Crisis in Pakistan and Their Possible Solutions,” in International Journal of Basic and Applied Sciences IJBAS-IJENS, vol. 11 no. 5, 2009.

[15] S. Kazmi, “CPEC and the Energy Crisis in Pakistan,” in Asia, Business, Opinion, May 2017.

[16] Mazhar, H. Baloch, G. S. Kaloi and Z. A. Memon, “Current Scenario of The Wind Energy in Pakistan Challenges and Future Perspectives,” in Energy Reports, vol. 2, November 2016, pp. 201-210.

[17] E. D. Berg, D. T. Ashwill and J. H. Sutherland, "A Retrospective of VAWT Design," Albuquerque, 2012.

[18] M. A. N. Roy and M. S. Mohiuddin, “Design and Fabrication of Vertical Axis Economical wind mill,” Int. J. Recent Innov. Trends Comput. Commun., p. 7, 2014

[19] 36. M. J. Jamanun, M. S. Misaran, M. Rahman, and W. K. Muzammil, “Performance Investigation of A Mix Wind Turbine Using A Clutch Mechanism At Low Wind Speed Condition,” IOP Conf. Ser. Mater. Sci. Eng., vol. 217, p. 012020, Jul. 2017

[20] P. Dvorak, “Vertical Axis Wind Turbine Technology Continues to Improve,” John Yan, China, sawt.com, August 2017.

[21] K. Bullis, “Will Vertical Turbines make more of the Wind?,” Technology Review, April 2013.

[22] Eriksson, S. Bernhoff and H. Leijon, “Evaluation of Different Turbine concepts for Wind Power,” Renew Sustain Energy, 2008.

# Semi Active Control of Stiffness through Permanant and Electro-magnet

Muhammad Zahid Iqbal
*Departement of Mechanical Engieering*
*Institute of Space Technology*
Islamabad, Pakistan
muhammad_zi@pieas.edu.pk

Dr. Asif Israr
*Departement of Mechanical Engieering*
*Institute of Space Technology*
*Islamabad, Pakistan*
asif.israr@ist.edu.pk

***Abstract*— The characteristic of attraction or repulsion of magnets can be used to form springs. This paper presents the basic design and experimental study of the formation of spring using permanent magnets. The magnetic field of the permanent magnets can be further changed using electromagnet. In this way a semi active control over the stiffness of the spring can be achieved. Force deflection curve is drawn to get the stiffness of the magnet which shows non-linear behavior. Non linear duffing equation is used to find the response of the spring. The change in stiffness of the magnetic spring with change of current can be used to tune the natural frequency of vibratory system. This concept can be used in many other vibration applications like active damper and actuation of many kinds of vibration.**

**Keywords— Active Spring, Electromagnet, Active damper.**

## I. INTRODUCTION

Magnetic property of various materials results in attraction or repulsion depending upon the configuration of poles. The force of attraction and repulsion depends upon the area of magnets and strength of magnetic field.

This property is controllable in electromagnet and is used for different applications to produce springs of controlled stiffness. Magnetic levitation is one of the example [1]. Many attempts have been made by different researchers to use electromagnetic stiffness and damping for variety of applications. It is important to mention here that electromagnet has a property of negative stiffness. Negative stiffness (or positive) property from electromagnet can be combined with permanent magnet stiffness to give semi active spring element. Following are some of the studies that have been carried out on this subject.

- Liu *et al.* (2006) published his work on the vibration absorber based on electromagnet [2]. The stiffness of the invented absorber can be changed according to the change in current. In this way, absorber frequency can be tuned instantaneously. This designed device was named electromagnetic vibration absorber (EMVA).
- Habel *et al.* (2010) used electromagnet and permanent magnet to develop an active spring [3]. The stiffness of the spring depends current passing through the solenoid. They used this spring in active vibration isolation systems with good isolation properties. The paper described the detailed operating principles, experimental procedure and calculation for developing the active control isolation system.
- Song *et al.* (2015) developed an actuator based on magnetic plunger and solenoid [4]. This actuator produced both rectilinear and turning motions. This plunger can be used in multi-segmented robot. Each segment is actuated by this miniature actuator producing linear and turning motion. This concept can be used in robotics as well as vibration isolation with spring of variable stiffness.
- Olaru *et al.* (2017) developed a low cost actuator to generate vibration [5]. This actuator is an active magnetic spring which was made of a permanent magnet and a solenoid. The proposed actuator can have versatile applications to vibration testing for different frequencies and amplitudes.
- Xiang *et al.* (2017) presented a damper based on two magnetic negative stiffness springs [6]. Dampers consists of number of magnets that was arranged coaxially. A conductive pipe was used that give the excellent damping characteristics. This damper does not use any energy and so is very useful in long term damping operation of vibration damping systems.
- Shin *et al.* (2015) presented a hybrid mount consisting of rubber and electromagnet [7]. This mounts was proposed for naval shipboard equipment to reduce the vibrations transferred from ship hull. Simulation presented in research shows semi active control of vibration for naval equipment.

### *A. Passive Spring Formulation:*

The magnetic spring consists of three permanent ferrite magnets. The layout is depicted in Figure 1. One magnet is fixed and is attached to a solenoid. The other two magnets are attached together with opposite poles. This combination of two magnets are aligned with third magnet with similar poles so that repulsion of the magnets is used to formulate the spring.

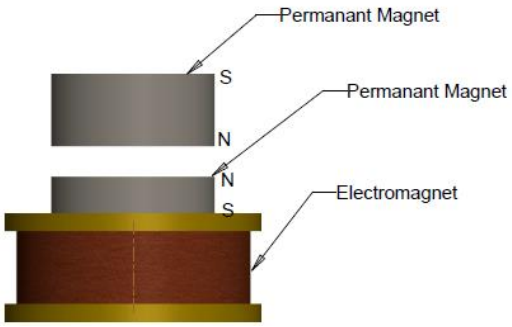


*Figure 1 Layout of Semi active spring*

### B. *Active Spring Formulation:*

The fixed Magnet is attached to the solenoid. This attachment with fixed magnet forms a spring of variable magnetic field.

### C. *Solenoid formulation*

Whenever current is passed through a conductor, it results a magnetic field. The direction and magnitude of the magnetic field produced depends upon the direction, magnitude of current and no of turns of the coil. Comparing the magnetic field on inner and outer surfaces of a solenoid. The magnetic field is negligible on outer boundaries. On the other hand, inside of solenoid, there is a strong magnetic field. A solenoid consists of a number of turns of insulated wire and is a source to generate a strong magnetic field which converts electric currents to mechanical motion and force.

In a solenoid, magnetic field can be changed in magnitude and direction by changing the direction and magnitude of the current.

The magnetic field produced due to solenoid is given by [8].

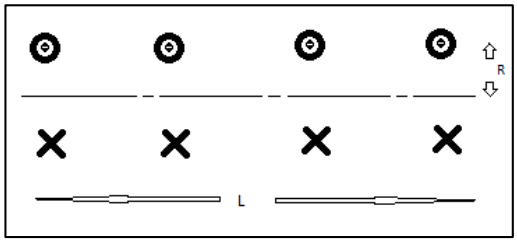


*Figure 2 Solenoid Basic Layout*

$$B = \frac{\mu_o I n}{2}\left[\frac{L}{\sqrt{L^2+R^2}}\right] \qquad (1)$$

Where

$B$ = Magnetic field generated

$I$ = Current flowing through the windings.

$L$ = The solenoid length

$R$ = The solenoid radius

$n$ = The number of turns

$\mu_o$ = The permeability of free space

And the force is given by

$$F = \frac{\Pi R^2 B^2}{2\mu_o}\left(\frac{\mu_m}{\mu_o} - 1\right) \qquad (2)$$

$\mu_m$ = Permeability of the metal producing force.

## II. Experimentation

A magnet is attached to the solenoid and is placed few millimeters away from the other magnet with similar poles as shown in Figure 1. The force of repulsion formulates the spring. The stiffness of the spring depends upon the magnetic fields strength

Due to the solenoid attached to the bottom/fixed magnet, the combined magnetic field of permanent magnet and solenoid becomes variable. The magnetic field depends upon the current in the windings. Variation of current changes the magnetic field. In this way stiffness of the spring can be changed according to amount of current produced. If the current direction is such that the magnet field due to the electromagnet have opposite poles with reference to the attached magnet, then the magnetic field will strengthen the overall field. However if current direction is in opposite direction, the magnetic field will be weaken, so the stiffness variation may be in both positive and negative direction.

## III. Results and Discussion

For carrying out the analysis the required experimental setup is developed. Figure 3 shows the developed magnetic spring is attached to a load cell. The whole arrangement undergo vertical controlled precise movement. The deflection and force noted after every 0.5 mm deflection. The load deflection curve is drawn.

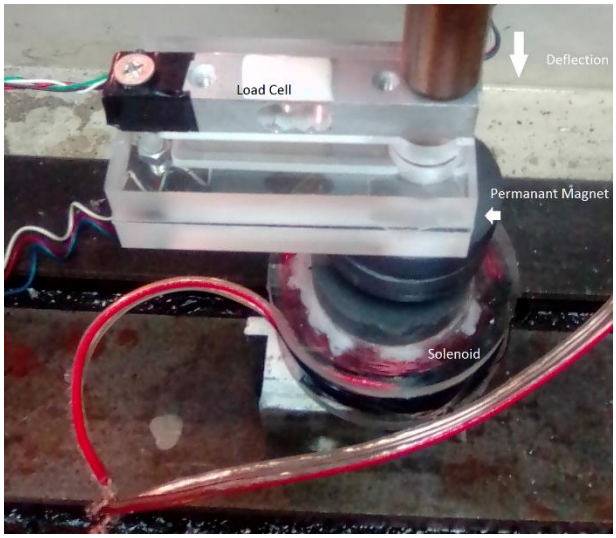


*Figure 3 Experimental Setup of Semi active spring*

Figure 4 shows three types of experimental curves. One curve is for passive spring and other two are representation of active spring. The data shows non-linear behavior. The load deflection curve is not straight line. The behavior is well represented by duffing equation [1].

$$\ddot{x} + ax + bx^3 = 0 \qquad (3)$$

The duffing equation can be modeled on the basis of experimental data. The coefficient (a and b) of duffing equation are found by fitting the data using *Curve Expert* software. Figure 4 shows 6 curves.

- Curve *(F)* is the load deflection curve when no current is in the solenoid. *(I=0)*

- Curve *(FD)* is the curve fitted to data on the basis of the duffing equation parameters. *(I=0)*
- Curve *F(A)* is the load deflection curve when solenoid is subjected to *I=2.2 A*.
- Curve *F(DA)* is the curve fitted to data on the basis of the duffing equation parameters *(I=2.2A)*
- The third graph is *F(-A)* its load deflection curve when current *-2.2 A* is applied.
- *F(-DA)* is curve fitted on the basis of duffing equation parameters when *I=-2.2A*.

Figure 4 show the stiffness changes when magnetic field due to solenoid changes. Curve *F(A)* shows change in stiffness as compared to *F* when current is applied. In a similar way graph *F(-A)* shows decrease in stiffness due to change in magnetic field. In this way a semi active control over the stiffness of the spring is presented.

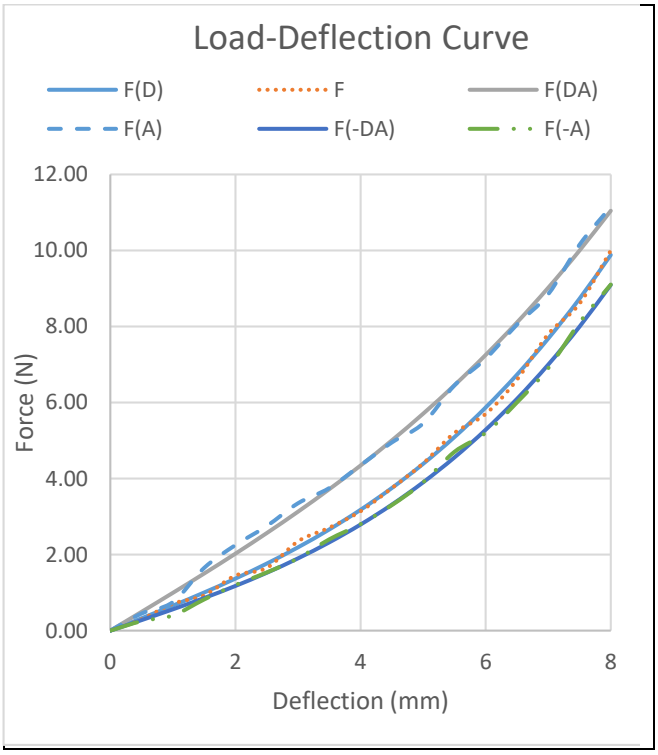


*Figure 4 Load Deflection Graphs*

| I (A) | a | b | T (sec) | ω (Hz) |
|---|---|---|---|---|
| I=0 | 0.648 | 9.18E-03 | 0.24 | 4.12 |
| I=2.2 | 0.988 | 6.14E-03 | 0.20 | 5.00 |
| I= -2.2 | 0.551 | 9.15E-03 | 0.26 | 3.84 |

*Table 1 Duffing Equation Coefficients and Solution Parameters*

Data given in Table 1 Duffing Equation Coefficients and Solution Parameters Table 1 shows the non-linear stiffness coefficients *a* and *b*. These coefficients formulates the duffing equation. The solution of this equation gives the response.

The equations formed are solved using *RK4* method and *MATLAB*. The response for the three cases are given in the Figure 5 to 7. From these responses natural frequency is calculated. The natural frequency varies from 3.84 to 4.12 Hz. Ultimately natural frequency of this semi active control spring can be controlled by controlling amount and direction of current. The variation of this natural frequency can be used to tune any vibratory system to the desired attenuation level.

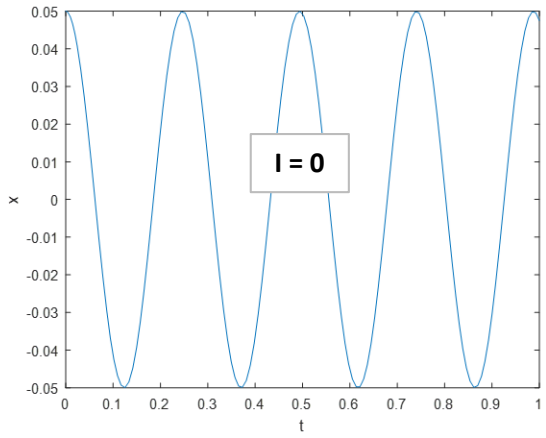


*Figure 5 Response of Duffing equation when I=0*

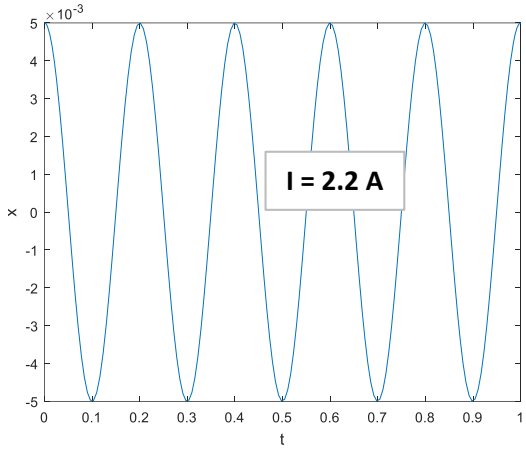


*Figure 6 Response of Duffing Equation when I-2.2 A*

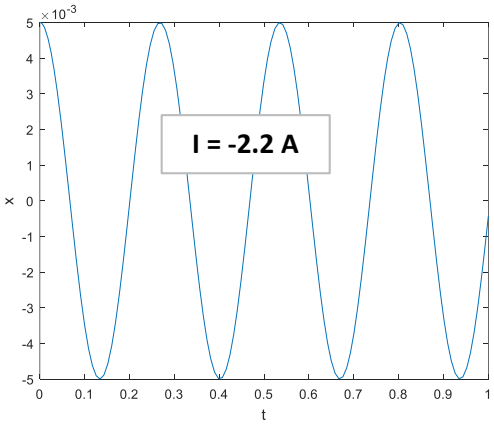


*Figure 7 Response of Duffing Equation when I=-2.2 A*

## IV. Conclusions:

A semi active spring is developed using permanent magnets and solenoid. Variation in the stiffness and natural frequency of the spring by changing the current is achieved. The idea can be used to develop semi active dampers and absorbers. These can be used for attenuation of vibration and control of natural frequencies of vibratory systems. The strength of field can be significantly increased by using strong magnets like Neodymium.

## V. References

[1] Mann, B. P., & Sims, N. D. (2009). Energy harvesting from the nonlinear oscillations of magnetic levitation. Journal of Sound and Vibration, 319(1–2), 515–530.

[2] Liu, J., & Liu, K. (2006). A tunable electromagnetic vibration absorber: Characterization and application. Journal of Sound and Vibration, 295(3–5), 708–724.

[3] Jacek, M., Control, P., & Vol, M. (2010). Magnetic Springs.(3), 40–44

[4] Song, C.-W., & Lee, S.-Y. (2015). Design of a Solenoid Actuator with a Magnetic Plunger for Miniaturized Segment Robots. Applied Sciences, 5(3), 595–607

[5] Olaru, R., Arcire, A., Petrescu, C., Mihai, M. M., & Gîrtan, B. (2017). A novel vibration actuator based on active magnetic spring. Sensors and Actuators, A: Physical, 264, 11–17.

[6] Shi, X., & Zhu, S. (2017). Simulation and optimization of magnetic negative stiffness dampers. Sensors and Actuators, A: Physical, 259, 14–33.

[7] Shin, Y. H., Moon, S. J., Kwon, J. Il, Jung, W. J., & Jeon, J. J. (2015). A new mount with moving-magnet type electromagnetic actuator for naval shipboard equipment. International Journal of Naval Architecture and Ocean Engineering, 7(1), 41–55

[8] http://spiff.rit.edu/classes/phys313/lectures/sol/sol_f01_long.html

# Backlash & Dead band Measurement of Ball-screw Drive Actuators

Naveed Riaz
*National University of Sciences& Technology*
*NUST*, Pakistan
engrnaveedriaz@gmail.com

Syed Irtiza Ali Shah
*National University of Sciences& Technology*
*NUST, Pakistan*

Faisal Rehman
*National University of Sciences& Technology*
*NUST*, Pakistan

Syed Omer Gilani
*National University of Sciences& Technology*
*NUST*, Pakistan

Emad-udin
*National University of Sciences& Technology*
*NUST*, Pakistan

***Abstract* – Ball screw drive actuators are commonly used in a wide variety of dynamic mechanical systems including robotics, CNC machinery and different aerospace applications. Ball screw drives are specifically designed on the basis of desired operational parameters like rated power, output torque, slew rate, efficiency, friction and mechanical backlash. These operating parameters significantly affect the functional performance of linear electro-mechanical actuators. Parameters like mechanical backlash and friction / dead band induces undesirable effect on the performance and functionality of overall dynamic system and disturb positioning accuracy and repeatability of entire system especially for systems under extensive loading. This paper discusses approaches for calculating mechanical backlash with and without powering up the system and friction/dead band with and without applying external loading. These parameters are calculated experimentally on a self-designed Hex Twist suspension test setup. Hex Twist setup was initially calibrated to find the deflection scale factor. Frequency response of ball screw drive actuator is also examined at ±8º desired command value and 3 Hz frequency value.**

***Keywords – Ball screw drive actuator, Mechanical backlash, Dead-band, Hex Twist Bar Suspension Test Setup, Frequency Response.***

## I. INTRODUCTION TO ACTUATOR FUNCTIONAL PARAMETERS

Ball screw drive actuators are one of the most important parts of automation and robotics and are commonly found in position and velocity control of various automated systems and machinery. These actuators should be well analyzed before putting them into the system as they affect its functionality. Performance parameters of ball screw actuators were measured using mathematical tools and then a testing setup was devised based on close simulation to actual system application. Output torque, slew rate, friction & mechanical backlash are the basic parameters which are kept in mind while designing any type of servo actuator.

A mechanical member, loaded with a moment about its longitudinal axis, is said to be in torsion, and the applied moment is then termed as torque. Torsion produced in the bar directly simulates the amount of applied torque, provided that the metallurgical properties of the bar being kept constant. This property of the bar helps to calculate the required torque along with slew rate, by measuring directly, the amount of twist produced. Twist bar jig was adjusted to calibrate the bar at required torque value for testing the actuator [1], [2].

Slew rate is the rate at which actuator achieves the desired position at rated torque value. Friction or dead band is the undesirable parameter in the design of servo actuator, and is required to be kept as minimum as possible to achieve max performance of the actuator. It is the band in the output at which the input changes but the output remains unchanged. Dead band was calculated by generating command voltage and observing the output displacement. The delay was observed that was calculated in open loop at bi-directional operation of actuator.

Backlash, another important non-linear parameter, is present inherently in the mechanical systems, and was calculated using both the power and no load condition of actuator by locking the output link and applying a step input.

## II. CALIBRATION OF HEX TWIST BAR SETUP

Consider a linear actuator as shown in figure 1 below. The actuator is driven by a prime mover (dc motor) accompanied by successive gear reduction and finally recirculation ball-screw assembly. The primary function of ball (bearing) screws is to transfer torque (rotary motion) to thrust (linear motion) and vice versa by maintaining high accuracy, reversibility and efficiency.

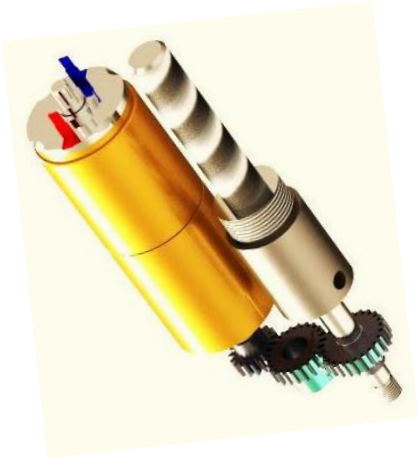

Fig.1. Ball screw drive Linear Actuator

Consider a straight hexagonal spring steel bar of length '$l$'. If we twist this steel bar around the axis resisted by the bar's torsion resistance, the effective bar spring rate can be calculated by the length, diameter and material of the bar. The bar twists about its longitudinal axis and its free end deflects through a twist angle '$\theta$'. The

The quantity $\frac{d_\theta}{d_z}$ can be written as

$$\frac{d_\theta}{d_z} = \frac{T}{GJ} \rightarrow \theta = \int_z \frac{T}{GJ} dz$$

$$\frac{d_\theta}{d_z} = constant = \frac{\theta}{L}$$

The twist $\theta$ for a circular shaft acted upon by a torque $T$ along its axis is given by:

$$\theta = \frac{Tl}{JG} \quad (1)$$

Where;

$\theta$ = Twist Angle (in radians).
$T$ = Torque applied (in Nm).
$l$ = Length of the bar (in meters).
$J$ = polar area moment of inertia of hexagonal bar.
$G$ = Rigidity Modulus.

Eq. (1) is the basis for measuring twist of actuator. The advantage of designing twist bar jig is that we don't need to calculate J and G of hex bar. These factors are calculated by calibration of twist bar. [3]

*Twist Bar Calibration Method: Theoretical calculation*

Calibration was performed on the loading jig. The loading jig comprises of a twist bar clamped with the wheel of torsion jig assembly. The other end of twist bar remains fixed. The amount of twist produced in the bar while the other end fixed simulates the loading on the steel bar. The amount of twist was measured using feedback potentiometer. When the output drive of the servo actuator was clamped with the wheel of the loading jig using link rod attachment, the twist in the bar simulates the loading on the output drive.

Hex Twist bar was calibrated in order to calculate the scale factor i.e. the amount of torque required to twist the bar to 1 degree and to check any permanent deformation produced in the bar and its spring rate. Spring rate, is the torsional resistance of the bar. The amount of twist angle '$\theta$' in twist bar was calculated by applying known weight at the end of loading arm of length 305mm clamped with the surface of testing jig. The twist bar experiences twist due to hanged weight. Measure the DC voltage generated by potentiometer due to twist produced. This was the angle '$\theta$' of torsion jig in terms of voltage at a length '$l$' of twist bar setup. From the metallurgical properties and cross section area of twist bar, the amount of twist produced at some particular required length was calculated using Eq. (1), assuming Torque = 1.5 Nm, Length of bar = 305mm and specific J and G of selected material of bar (spring steel). 'J' was calculated by dividing hexagon bar into 6 equal triangles then calculating the polar moment of inertia of each triangle and then summing it up. The polar moment of inertia of hex bar was found to be $15.75^4$ and G = 80.8 GPa where G is the modulus of rigidity of spring steel.

The twist angle '$\theta$' is;

$$\theta = \frac{1.5\ Nm\ * 0.12\ m}{1.575^{-11} * 8.08^{10}}$$

$\theta$ = 0.1414 radians = 8.10˚ (2)

Next we try to achieve that angle '$\theta$' i.e. 8.1˚ by adjusting the rear plate of the twist bar jig forward or backward (so that to change the effective twist bar length) until a reading of 0.451± 0.05V i.e. equivalent to 8.1˚ ± 0.8 is obtained. Now lock the plate at this particular position and calculate the twist bar scale factor i.e.

8.10˚ twist is generated by twist bar at = 1.5 Nm torque.
1˚ twist is generated by twist bar at = 1.5/8.1 = 0.185 Nm torque.
So, twist bar scale factor 'k'= 0.185Nm/˚

Ball screw drive actuator is operated at its maximum motor power. The amount of twist produced due to maximum force applied by the actuator is measured by potentiometer; putting it into following equation, yields the maximum torque;

$$T = k\theta$$

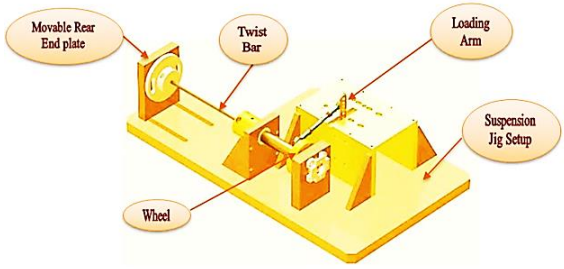


Fig.2. Hex Twist Suspension Test Setup

## III. FRICTION / DEAD BAND MEASUREMENT

Dead band or friction of linear actuator is the minimum amount of power consumed to set the output link of actuator in continuous motion. When voltage starts to rise from zero, there is no movement of output link up to certain level of input voltage. Initially when voltage begins to rise, the torque generated is used to overcome the friction of actuator, keep on increasing voltage at certain instance output link starts moving but still its motion is not uniform because there is still some dynamic friction present in the system. When

output link starts moving uniformly, at that point the friction within the system is being overcome by applied torque and the voltage is noted. This voltage range defines the dead band region of linear actuator. This value is very helpful in setting the proportional gain of controller and should be the end voltage of dead band region. Greater the dead band more is the friction so more power controller has to provide to the actuator to overcome friction.

*No Load Friction Test*

This test was performed by removing external load applied to the actuator output in the twist jig setup. Current limit of actuator variable supply was set to 3.6±0.05A and the voltage initially at 0V. Polarity switch was set to '–ve' position. The servo actuator was moved in upward direction with '-ve' polarity. Before applying the '–ve' polarity, servo actuator position was at extreme downward direction. Motor supply voltage was slowly increased until the servo fully deflected to the upward direction. Motor voltage and surface deflection was recorded. After that the actuator supply was decreased to 0V and the Polarity Switch was set to '+ve' position for downward movement of the twist jig loading bar. Motor voltage, actuator pot deflection and surface deflection were measured. Actuator no load DEAD BAND was calculated by subtracting the actuator voltage for one side deflection to the servo voltage for other side deflection.

*Full Load Friction Test*

A constant load of 65 N-m was applied on the same setup. To apply this load, load was hanged with the loading arm of actuator mechanism twist jig. Same above procedure was repeated. As the actuator started moving from downwards to upward direction, motor voltage and current were measured. Similarly measure the actuator motor voltage and current in downward direction. The actuator full load dead band was calculated by subtracting the servo actuator voltage for downward direction from the servo voltage for upward direction.

*Dead band calculation*

V1 = Measured motor supply voltage to deflect the actuator against a constant load of 65 Nm OR at No load.

V2 = Measured servo supply voltage when the servo deflects fully backward to one side with a constant load of 65 Nm OR at No load.

The dead band is:

Dead Band @ constant load/ No load = V1–V2

## IV. MECHANICAL BACKLASH MEASUREMENT

Mechanical Backlash is an undesirable play in the mechanical assembly that occurs due to looseness, manufacturing inaccuracies, unbalancing, misalignment or any other assembly integration issues in mechanical parts. In case of gearing, it is a play in meshed gear teeth due to improper tooth design, improper assembly or wear and tear of teeth. This problem cannot be eliminated but can be reduced. Backlash produces a dead band in which there is no output deflection even there is some command signal. This dead band produces oscillations in output due to unwanted delay created. When command is given to move the actuator along desired axis, the motor turns shortly before movement is initiated. This delay in movement is termed as backlash.

*Backlash Test*

Mechanical backlash was calculated by the following procedure. Output drive of the actuator was locked at zero position where feedback potentiometer shown zero deflection. Supply voltage and current was set to almost half the actual values required to drive the actuator. When system was powered the feedback potentiometer gave the deflection even the output was locked, this deflection is the backlash within the assembly. Depending upon the placement of feedback potentiometer either on output or at some intermediate position backlash can be calculated by this method.

*Backlash calculation:*

Backlash was calculated as;

$$\text{BACKLASH } (^\circ) = \frac{\text{V (Positive) - V (Negative)}}{58.8\ \text{mV}/^\circ * \text{R}} \quad (3)$$

Where,

'Positive' and 'Negative' value means maximum and minimum deviation or motion observed by the potentiometer in terms of millivolts.

'R' is the speed ratio between motor and output link.

58.8 is the factor obtained as follows;

Active electrical angle of actuator feedback potentiometer = 340˚

Total supply voltage applied to actuator feedback potentiometer = 20 Vdc.

0-340˚ electrical angle gives = 0-20 Vdc.

1˚ electrical angle gives = 20/340 = 0.0588 V/˚ = 58.8 mV/˚

By putting values in Eq. (3), we get

$$\text{BACKLASH } (^\circ) = \frac{\text{V (positive) - V (Negative)}}{0.1176}$$

This gives actuator feedback potentiometer deflection backlash.

## V. RESULTS & DISCUSSION

Based on the technique described above, the critical parameters that badly affect the functionality of linear actuator were calculated. Upon careful measurement and analysis, it was found that the experimental scheme devised in this work is highly helpful in measuring these critical parameters with this setup i.e., Hex twist bar Suspension setup along with its electronics test equipment for measuring these parameters. To confirm the repeatability of this overall system, multiple experiments can be conducted with different actuators under different loading profiles. Tables below show measurement results of test parameters including mechanical backlash, full load friction and no load friction found with this setup.

TABLE I: Zero Position & Backlash Test Result

TABLE II: Full Load Friction/Dead band Test Result

TABLE III: No Load Friction/Dead band Test Result

| Sr | TEST PARAMETER | UNIT | ↓ LIMIT | ↑ LIMIT | RESULT |
|---|---|---|---|---|---|
| 1 | Actuator Voltage (+) | mV | 18.8 | 20.2 | 20 |
| 2 | Pot Deflection | mV | 120 | 185 | 170 |
| 3 | Surface Deflection (+) | ° | 10 | 14 | 12.5 |
| 4 | Actuator Voltage (-) | V | 18.8 | 20.2 | 20.1 |
| 5 | Pot Deflection | mV | 120 | 185 | 170 |
| 6 | Surface Deflection (-) | ° | 10 | 14 | 12.6 |
| 7 | No Load Dead Band | mV | 0.1 | 0.3 | 0.1 |
| 7 | Motor voltage | V | 1.40 | 1.6 | 1.55 |
| 8 | Actuator Pot Deflection | mV | 65 | 85 | 70 |
| 9 | Motor current | mA | -210 | -190 | -205 |
| 10 | Motor voltage | V | -1.6 | -1.4 | -1.6 |
| 11 | Actuator Pot Deflection | mV | -110 | -85 | -90 |
| 12 | Actuator Backlash | ° | - | < 0.4 | 0.3 |

## VI. FREQUENCY RESPONSE RESULTS

Figure below shows results for motor with ±8° command at 3Hz frequency without any load attached to output link.

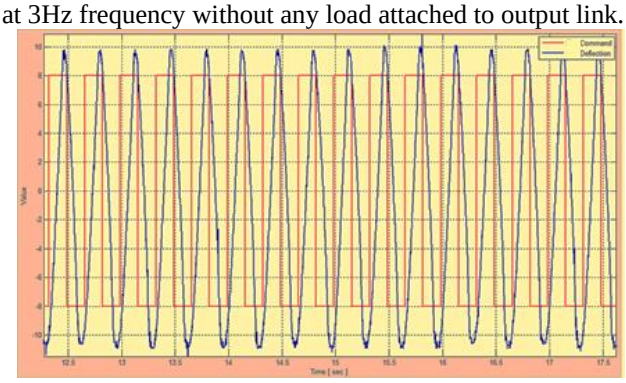

Fig.3. Response for ±8° command @ 3Hz frequency

From above figure, we calculated motor rise time, response time, and slew rate.

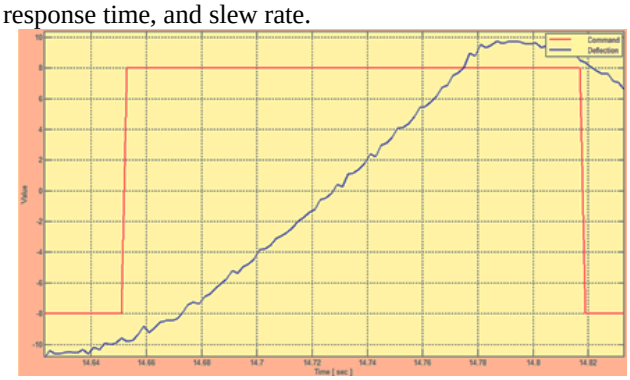

Fig.4. @ No Load, 3Hz

*Calculated Results*

Response time = 0.02558 sec
Rise Time (from 10% to 90%) = 0.09361 sec
Slew Rate (from 10% to 90%) = 157.53° per second

## VII. CONCLUSION

This paper describes an effort to test and measure critical parameters for ball-screw drive actuators. These parameters were analyzed systematically and measured using self-designed setup named as Hex Twist suspension testing setup. Precise measurement of these parameters gives the basics for the acceptance specification of actuator. The successful completion of this testing sequence verifies important functions of the assembly for use on any critical system / application. Accurate measurement of these parameters gives qualification of actuators and increase reliability to meet functional requirements of the system.

## ACKNOWLEDGMENT

The authors would like to give special thanks to their professors and colleagues for their valuable comments and suggestions in respect of this work.

## REFERENCES

[1] Torabzadeh-Tari M. Analysis of electro-meachanical actuator systems in more electric aircraft applications. PhD Dissertation, Royal Institute of Technology, Sweden, 2005

[2] Barnett S. Laboratory test set-up to evaluate electromechanical actuation system for aircraft flight control. Master Dissertation, University of Dayton, USA, 2015.

[3] Barnett SA, Lammers Z, Razidlo B, et al. Test set-up for electromechanical actuation systems for aircraft flight control. SAE paper 2012-01-2203, 2012

[4] Larry B. Li, “System and method for controlling high side slew rate in a spindle motor driver,” Texas Instruments Incorporated. USA, Patent No. US6072289 A

[5] E. M. H. Kamerbeek”On the Theoretical and Experimental Determination of the Torque in Electrical Machines", Philips *Tech. Rev.*, no. Supplement, No. 4, 1970

[6] K. Kemper , D. Koepl and J. Hurst "Optimal passive dynamics for torque/force control", *Int. Conf. Robot. Autom.*, 2010

[7] D. T. Paul Brian Hvass, Condition Based Maintenance For Intelligent Electromechanical Actuators, University of Texas, Austin, 2004

[8] S Ma, G Liu, J Zhou, R Tong 2011 Optimal design and contact analysis for Planetary Roller Screw, Applied Mechanics and Materials. 86, 361-364

[9] Varanasi, K. K. and Nayfeh, S. A, Modeling, Identification, and Control of Ballscrew Drives, American Society for Precision Engineering 16th Annual Meeting, 25: 139-142, Crystal City, Virginia, 2001.

[10] AbdElhafez A and Forsyth A. A review of more-electric aircraft. In: Thirteenth international conference on aerospace science & aviation technology (ASAT-13), 26–28 May 2009, paper no. ASAT-13-EP-01. Piscataway, NJ, USA: IEEE

[11] Erkorkmaz, K. and Kamalazadeh, A., High Bandwidth Control of Ball Screw Drives, Annals of the CIRP vol. 55/1, 2006.

[12] Antonelli MG, Bucci G, Ciancetta F, et al. Automatic test equipment for avionics Electro-Mechanical Actuators (EMAs). Measurement 2014; 57: 71–84

[13] Budinger M, Reysset A, Halabi TE, et al. Optimal preliminary design of electromechanical actuators. Proc IMechE, Part G: J Aerospace Engineering 2013; 228:1598–1616

# Design Optimization, Manufacturing And Testing of Pneumatic Catapult for UAV

Hammad ur Rahman
*Aviation Design Institute, Pakistan Aeronautical Ccomplex, Kamra*
Pakistan

Bilal A. Siddiqui
*Aviation Design Institute, Pakistan Aeronautical Ccomplex, Kamra*
Pakistan
dr.bilal.ahmed@outlook.com

Charles R. Kumar[2]
*Warmlink Pvt. Ltd., Islamabad*
Pakistan

Noman Iqbal[2]
*Warmlink Pvt. Ltd., Islamabad*
Pakistan

***Abstract* — This paper is successor of an ongoing research [1] by the authors regarding the design, simulation, manufacturing, testing and qualification of a pneumatic catapult for high speed target drones. Fixed-wing aircraft - in general – require a prepared runway surface and favorable wind direction to achieve takeoff speed. Lack of available runway facility in many practical scenarios has created the need for a powered launching mechanism. This technology serves a niche market in the aerospace and defense sector, for which there are only a handful of manufacturers globally, and none in the MENA region. This work is a step towards filling gaps in published scientific research and practical insights in this domain. A pneumatically powered UAV catapult launcher has been designed using in-house developed software tools based on physically accurate mathematical models. After thorough analysis and experimental verification, prototypes were developed for testing various mechanisms individually and collectively. Design refinement resulting from these experiments led to detailed design and manufacturing of the final product – WL7550™ – which achieved customer specified metrics. Launch speed, release attitude and maximum acceleration limits were verified through extensive sensorization by an external evaluation agency. Several successful flight tests of unmanned high speed aircraft have been carried out which showed the efficacy of design methodology.**

***Keywords—UAV, FEA, pneumatic, UAV Launcher, catapult, flight speed measurement, vibration, shock***

## I. INTRODUCTION

Drones or unmanned aerial vehicles (UAVs) can operate in inhospitable environments where it may not be possible to find prepared runway surfaces and favorable wind direction. This causes delays in flight operations, increasing the cost of operations. One way to mitigate this dependence on the whim of nature is to have vertical takeoff and landing (VTOL) mechanism in the aircraft. However, VTOL mechanisms are inefficient and result in reduced flight times and performance, as compared to conventional fixed wing aerial platforms. Another much more efficient method to overcome this impediment is to use assisted takeoff by means of rocket propulsion or rapid acceleration on a rail structure called catapult launch system. Compared to rocket assisted takeoff (RATO), catapult launch has the advantages of having less operational cost per launch, reusability, scalability while posing less hazard.

Even though steam catapults have been used on manned aircraft launched from ships since the 1950s [2], drone catapults differ in that they must be portable, have a smaller footprint and steerable into the wind, making steam infeasible as the power source. On the other hand, recently developed electromagnetic catapults [3] are too expensive in terms of power requirements and cost to be considered for launching inexpensive drones. Bungee elastic launchers are limited to low speed or low mass launches only, or require very high initial acceleration to achieve required speeds. This means that pneumatic and hydro-pneumatic methods have gained currency in reusable high speed catapult launchers.

This study presents the theoretical and practical results of research conducted by Warmlink Pvt Ltd under contract from Pakistan Aeronautical Complex for development and qualification of a pneumatically powered catapult launcher for 50 - 100 kg high speed UAV to be launched at up to 50 m/s, while respecting structural and subsystem load limit of a maximum of 12g of acceleration. This work was built on seminal results presented by the authors in [1]. The pneumatically powered catapult launcher was developed in a very short duration (8 months), starting from an in-house developed, first principles-based simulation and sizing software tool, which was tweaked to account for experimentally observed un-modelled system dynamics.

The paper is organized as follows. First, the design methodology and rationale in sizing and optimizing key components is discussed in Section II. This includes pneumatic power drive, shuttle lock and rail structure, as well as the braking mechanism. Section III details sensorization of the launcher and measurement of key parameters during each launch test. Based on preliminary testing on the prototype, the designed was refined and detailed in Section IV. Finally, some conclusions are drawn and future research areas are mentioned.

The catapult launcher, Warmlink WL-7550™ has been accepted by the customer after extensive field trials and verification by an independent testing agency. The system is mobile and easily deployable in the field, with setup time of under 25 minutes, and turnaround time of about 15 minutes.

Fig. 1. Pneumatic catapult launcher in fully extended configuration (top) for aircraft launch, and stowed configuration (bottom) for transportation.

## II. Design Methodology

Pneumatic drone catapult is sized based on the sizing software tool described in [1], based on customer provided parameters of smooth launching of 50-100kg fixed wing drone at up to 50m/s, with maximum acceleration remaining under 15g. The system has three major subsystems (a) pneumatic power pack, (b) rail and superstructure, (c) system of pulleys for speed amplification, (d) aircraft shuttle and its lock/release mechanism, (e) shuttle braking mechanism and (f) undercarriage and chassis. Co-design of these interacting subsystems was carried out in the software tool developed in-house, and manufacturing of these subsystems was carried out simultaneously with an eye on assembling and integration accuracy.

### A. *Pneumatic Power Drive*

The first system to be developed was the pneumatic power drive. All subsystems including actuator, seals and valves were manufactured and integrated indigenously. A test rig was also manufactured for verifying the following subsystems:

- Functionality of actuator seals, piston rod, pulley system
- Braking mechanism alternatives including spring and damper, pneumatic brakes, hydraulic brakes, friction pads.
- Shuttle movement
- Shuttle lock and release mechanism and interface with the UAV
- Speed measurement methods calibration.

This rudimentary test rig (Fig. 1) was instrumental in providing valuable insight, allowing a test matrix of different tank pressures, inlet valves and size/position of the vent holes to be evaluated.

Fig. 2. Test rig for verifying preliminary design parameters

### B. *Rail and Superstructure*

Structural and geometric integrity of the rail structure is imperative for correct functioning of the catapult launcher, and it is required to be lightweight while being sufficiently rigid. It is the junction of all major loads on the structure coming from the pneumatic actuator's reaction and the pulley loads. For quick prototyping and reducing cost, superstructure was constructed from hot rolled steel angle iron members arranged in the form of truses. Thickness and lengths were optimized using finite element analysis (FEA) [4]. In order to meet aggressive timelines, the superstructure and undercarriage were decided to be designed first and committed to manufacturing, while components were to be designed in parallel and consequently handed over to the manufacturing team. Design of shuttle, its lock/release mechanism and braking system were deemed to be the most challenging, and early completion of rail and undercarriage allowed it to be used as the test rig for evaluating various competing proposals of lock/release and braking mechanisms (detailed later).

The rail structure and the key components of the shuttle pulling mechanism i.e. the pulley system were designed and optimized with computational tools [4] for mass reduction and effective stress distribution throughout the structure.

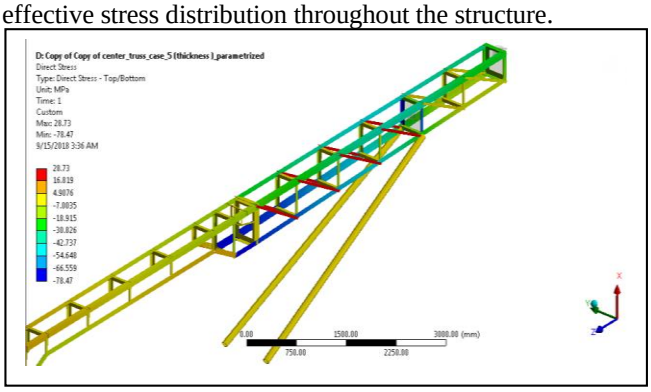

Fig. 3. Stress distribution in superstructure; all stresses within material strength limits

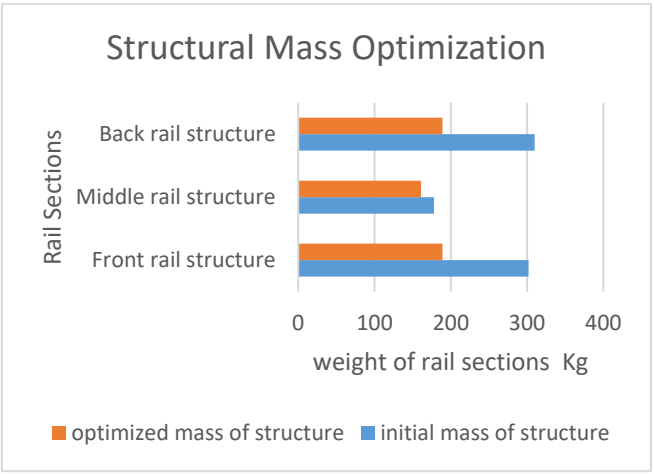


Fig. 4. Mass optimization study of the three rail segments, (front rail is the last point of contact of aircraft as it leaves the launcher)

The three segments of the rail structures are assembled on top of the undercarriage and are connected with each other by hinge joints for easy stowage during transportation.

Undercarriage design has not been shown here for lack of space.

### C. System of Pulleys and Wire-rope

Design of pulley system is crucial as they are the main components in the dynamic performance of the catapult and also bear extremely high loads for very short period of time. Significantt effort was made to design light, compact yet very rigid pulley system. There are two types of pulley in this system. One is static pulley which is fixed in the front rail segment with enough structural support to easily transfer loads of more than 10 ton during a given launch. Then, there is a moving pulley assembly which actually runs on a small track inside the front rail segment. This is put exactly in front of the static pulley to allow for smooth running of the system without rope running off the crowned pulleys. This movable pulley system is also equipped with very sturdy rope alignment guides because of the cross winding of the rope to allow for a mechanical advantage of 4 times. Therefore, it is critical for it to have sufficient strength despite weight constraints, as a heavier moveable pulley system is extra mass that needs to be accelerated during launch (thus consuming available energy). It is a critical system as failure here can cause considerable damage to pneumatic actuator system as well as superstructure. A steel wire rope was selected based on requirements of strength, flexibility and weight.

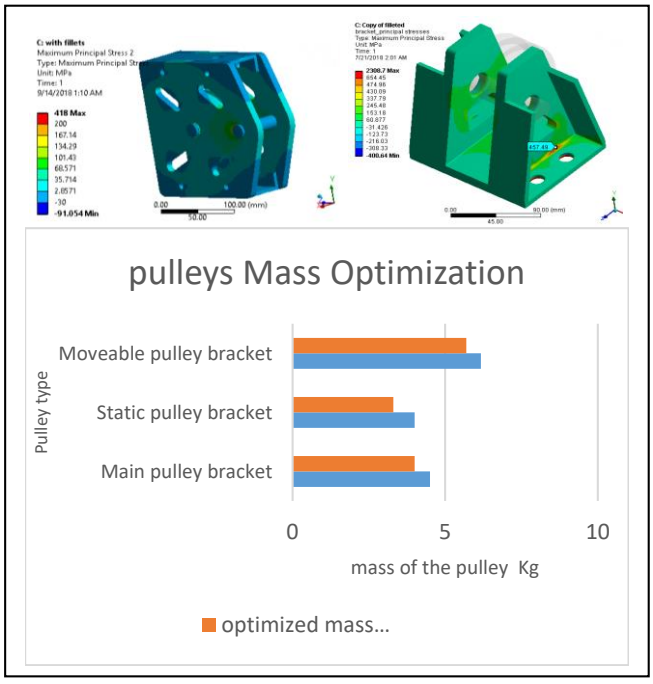


Fig. 5. Moveable pulley (top left)and and static pulley (top right). Stress is designed to be uniformly distributed to reduce weight.

### D. Aircraft Shuttle

The shuttle has to be well designed as it is the component which undergoes most fatigue (having to be accelerated suddenly and then braked in a similarly short time). It consists of an eye from which the wire-rope is attached, wheel assembly, rear fixed arms for holding rear launch pins of the aircraft, and front collapsible arms for mating with front launch pins of the aircraft. All acceleration loads due to the mass of aircraft are borne by rear arms, which are therefore designed after rigorous FEA analysis. A dynamic explicit analysis has been performed in Abaqus™ to analyse the effect of inertial loads on this part. (Abaqus™ is chosen for this study because of the better element selection and post processing tools available in it).

### E. Shuttle Lock/Release Mmechanism

Lift, weight, drag and thrust forces on aircraft needs to be supported by the shuttle, such that there is no relative motion between the shuttle and aircraft during launch acceleration on the rail. A cleverly designed special mechanism needs to exist on the shuttle for keeping the aircraft locked in position during power-stroke of the actuator, and release it smoothly at the end of the rail such that there is seamless transition between launch and climb phase of the aircraft. The front arms are collapsible towards the launch direction for disengaging the aircraft from the shuttle as brakes are applied on the shuttle. However, from just prior to the pneumatic power stroke which accelerates the aircraft till the engagement of brake, the front arms need to be locked in place to keep the aircraft in place despite thrust from the engine (on full throttle) and lift from its wings. Front and rear arms have opposite facing grooves for mating with launch pins on the aircraft.

The working principle of this lock mechanism can be understood with this schematic below. The lock arm is pivoted on the rod which provides a rigid support and free rotation to it. The lock arm is flushed with the main shaft of front arms. This arm lock is kept in its position by a spring and it is unlocked by getting in contact with a ramp built on the front portion of the rail segment, slightly ahead of the launch point. As the lock flips open the shaft of arms is now free to rotate. As soon as the shuttle hits the brake, the shuttle decelerates and the aircraft moves forward under its own inertia and thrust which flings the front arms forward (rear arms are fixed), rotating forward and falling on the shuttle base releasing aircraft to climb out due to thrust and lift. Hundreds of successful launches have proven the efficacy of this patented mechanism.

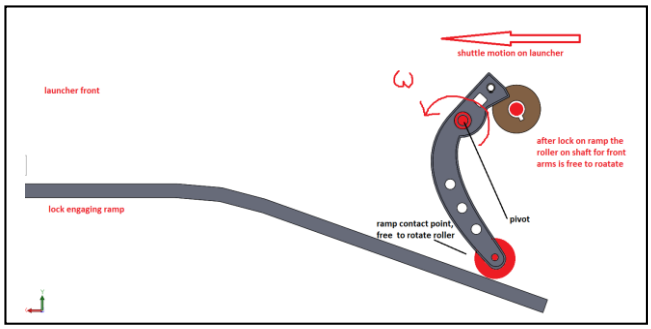


Fig. 6. The shuttle lock/release mechanism as it hits the ramp at the end of the rail. This helps it to overcome the spring force holding it back and the lock becomes free to rotate collapsing the front arms on shuttle.

### F. Braking mechanism

As the aircraft and shuttle reach launch velocity, it is necessary to affect a clean separation between them. Moreover, the shuttle needs to remain on the ramp for the next launch. Therefore, the shuttle needs to be quickly decelerated and brought to a stop without incurring unbearable stress on the shuttle or rail superstructure. Similarly, the piston inside

pneumatic cylinder needs to be brought to a quick stop and avoid hitting the end cap. Therefore, there are two different braking mechanisms, one for the shuttle and one for the piston.

The end cap of the actuator is anchored to the back segment of the rail and is solid. Slightly ahead of the end cap, two vents are provided on either side of the actuator for both releasing the pneumatic pressure behind the piston and creating an air pocket ahead of these vents thereby creating a brake for the fast moving piston. These vents were fitted with air filters and ball valves, whose opening can be adjusted to calibrate both speed of and stress distribution in the piston assembly.

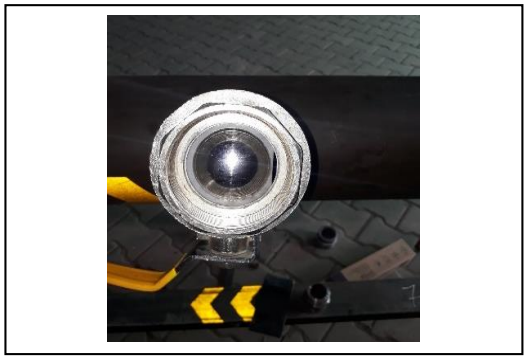

Fig. 7. Ball valves for pneumatic brake mechanism for piston

The piston stops with this air cushion, without coming in contact with the end cap (provided with a rubber damper just in case the air brake leaks). This is a unique feature that we have calibrated for this system as a passive speed control mechanism, without the need for active feedback control elements. In the future, it is planned refine the mechanism further and add active feedback control for preventing accidental launches.

For deceleration of the shuttle, several ideas were explored. The brake system was developed first in simulation using multi-body physics software packages, followed by experimental verification. The first system to be analyzed were spring oil dampers, shown below. The braking energy which needs to be provides by the spring is

$$\frac{1}{2}m_s v_{TO}^2 = \frac{1}{2}k\Delta x^2 \quad (1)$$

where $m_s$ is mass of shuttle, $v_{TO}$ is takeoff speed, $\Delta x$ is displacement of spring and k is the spring constant.

Fig. 8. Spring mounting and impact pad assembly attached on front rail segment

Many different spring coil and damper combinations were experimented with, however none of them proved satisfactory. The major problem with spring/damper braking system design is that the impact force that is transmitted to the rail by the springs is high enough to cause structural damage and weakening in the trusses. Increasing the strength of the rail will make the front rail segment quite heavy and suboptimal in stowage. Next, we investigated friction brake pads, inspired from the automotive drum brakes. This approach involved putting a pair of pads on the shuttle and a mating pair at the end of front rail section where the shuttle needs to be stopped. Shuttle is supposed to run into the rail segment pads causing friction to bring it to a gradual halt. This system also transmitted high braking force to the superstructure and was susceptible to slight misalignments.

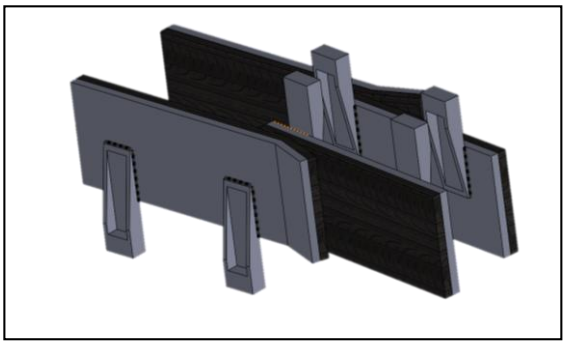

Fig. 9. Friction pad braking assembly

After these experiments, it was determined that braking stresses need to be isolated from the vulnerable superstructure. Therefore, we turned our attention towards a softer brake, albeit one which will transmitted braking force to the sturdy undercarriage instead of the superstructure. A system of arresting belt used as an elastic brake looped over guides and anchored into the undercarriage was devised. A high strength woven lifting belt was selected based on available stretch distance (spring constant). It was looped around the front rail segment in a way that it forms a flat surface for the shuttle and shuttle is modified with a curved fender that is of width slightly larger than the belt width to ensure that belt always gets trapped in it. In this way, stresses on the shuttle are also distributed more evenly.

Fig. 10. At the moment of launch, the shuttle is arrested into the belt seen as flexible elements below the rail.

## III. Speed Measurement

Several methods were used to estimate the speed of the launched aircraft. These included photogrammetry, airspeed sensor (pitot tube) and proximity sensors.

### A. Photogrammetry

Speed measurement from video is a process of counting frames that are recorded on the equally spaced points on the rail. Special software for recovering individual frames from video is utilized. The start of event frame is noted along with its timestamp and then the event end frame is noted down. Since distance between markers on the rail is known, an estimate of time (based on number of frames) between end points gives the average speed during that segment. A 2000 fps high speed monochrome camera was used to accurately measure launch speed by an independent agency. Our own camera was a GoPro 240 fps camera which produced results within 5% of the high speed camera's results.

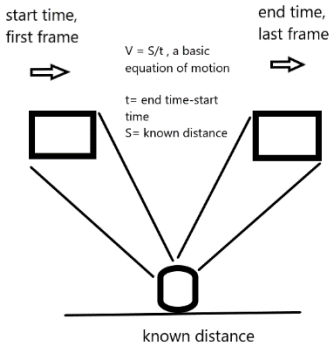


Fig. 11. Speed measurement based on video capture

### B. Proximity sensor rigs

A proximity sensor emits a beam infrared light and senses the presence of shuttle due to return signal. To measure speed with proximity sensors we have made a rig that consists of 3 proximity sensors placed on the launcher rail at known positions. As the shuttle moves across them, elapsed time between these known points is recorded by a microcontroller. The system needs careful calibration as it is susceptible to false alarms and requires high sampling rate.

Fig. 12. Proximity sensors installedat marked locations.

### C. Projectile Range

In this method the principles of projectile motion are applied on unpowered dummy loads simulating the aircraft geometry and weight. The height and launch angle of the dummy are recorded, along with distance to the touch down point. Using standard idealized projectile motion formulae (ignoring air resistance),

$$V_{TO} = \sqrt{\frac{R.g}{\sin(2\theta_r)}} \quad (1)$$

where R= range covered dummy mass and $\theta_r$ = elevation angle of the launcher rail.

### D. Time on Rail

Using linear translation under average acceleration formulae, we can express terminal velocity in terms of the time $t_r$ spent by the shuttle and aircraft in accelerating during power stroke of the piston. This distance is the rail length $L_r$.

$$V = \frac{2L_r}{t_r} \quad (2)$$

It was found that all methods produce results within 10% of each other.

## IV. Testing Based Design Upgradation

Based on speed measurements of dummy aircraft launches, it was determined that current system needs to be upgraded for fulfilling speed requirements at given payload. To increase the launch speed, an energy balance analysis of the system was carried out to determine the quickest, least costly and most effective modifications to the design. he total energy of the pressure system based on the actuator diameter and stroke is developed based on work done on piston due to polytrophic gas expansion. Equation below shows the interplay between pertinent parameters i.e. piston diameter, pressure, total accelerated mass etc.

$$K.E = W_{piston} = \int_{V_1}^{V_2} Pd\forall = \frac{P_{res}\forall_{res}}{\gamma-1}\left(1-\left(\frac{\forall_{res}+\Delta\forall}{\forall_{res}}\right)^{1-\gamma}\right) \quad (3)$$

where, $\forall_{res}$ is the total reservoir volume, γ is the ratio of specific heats and $\Delta\forall$ is the volume swept by the piston. Launch velocity can then be calculated as

$$V_{TO} = \sqrt{2\,\frac{KE-\Delta E}{m_a+m_s+\Delta m}} \quad (4)$$

Where $\Delta E$ are friction and leakage losses, $m_a$ =mass of aircraft, $\Delta m$ is equivalent of all other mobile masses referenced to the shuttle frame of reference. The prototype was severely limited by the components friction due to several points and surfaces being in sliding contact with each other. The frictional losses are estimated from test data to be around 10 kJ. This figure was halved during subsequent modifications to moving parts by making use of better seals, lubrication etc.

To propel aircraft at required speed, the chief variable to enhance the force imparted by the piston to the shuttle/aircraft. To do this we can do any or all of the following: (a) reduce the mass of moving components, (b) increase the available launch pressure and/or (c) increase the piston diameter After optimizing the cost and time taken in modifications, it was decided to simultaneously modify all the :

TABLE I. Major Modifications to the Launcher

| Parameter name | Before modification | After modification |
|---|---|---|
| Mass of shuttle | 55 Kg | 45 Kg |
| Mass of moveable pulley | 8 Kg | 6 Kg |
| Inlet diameter | 1.5 inch | 2.5 inch |
| Piston diameter | 6.5 inch | 8.5 inch |
| Max launch pressure | 15 bar | 22 bar |

High speed camera and airspeed sensors verified the following speeds achieved by the launcher for various aircraft weights after design modifications.

TABLE II. HIGH SPEED CAMERA SPEED MEASUREMENT

| Test case | Launch pressure | Speed attained |
|---|---|---|
| 60 kg aircraft | 15 bar | 50 m/s |
| 75 kg aircraft | 17 bar | 50 m/s |
| 105 kg aircraft | 16 bar | 36 m/s |
| 25 kg aircraft | 06 bar | 40 m/s |

The rail superstructure that had been designed with previous actuator of smaller size had to be modified to cater for increased reaction from the larger actuator. Moreover the middle section of the rail superstructure which houses the actuator had to be widened to accommodate the larger actuator. This included redesign of the anchor plate for the actuator and supporting points for the actuator using FEA based optimization methods [5].

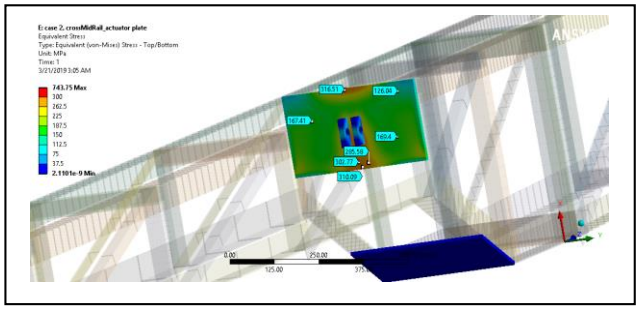

Fig. 13. Improved qnchor plate design and mounting design for modified actuator

### A. *Flight Tests:*

Actual flight tests were carried out for final verification of the aircraft catapult system. The aircraft is powered with a jet engine and provided with launch lugs which fit into c-shaped receptacles on the shuttle arms. In powered flight, the engine will try to rotate the front arms due to forward propulsive thrust. This motion is arrested by having the front arms locked, as described in Section II.C above. The shuttle is also held in place by means of cable ties, which act as weak links which break once catapulting force is applied by opening the main actuator valve. The cable ties are stronger enough to bear engine thrust (which is considerably less than tension in the steel rope connected to pneumatic actuator). Once the catapult is in motion, the rest of the journey of the aircraft on the launch rail is quite similar to dummy launch. It was observed that presence of thrust in the case of actual aircraft is helpful and adds 10% velocity to that of a similar weight dummy without thrust. Successful flight tests have been carried out with the system performing as predicted by the simulator described in [1]. All flight tests have resulted in smooth release at 50 m/s for various aircraft masses, subject to maximum acceleration constraint of 12g (aircraft structural limitations).

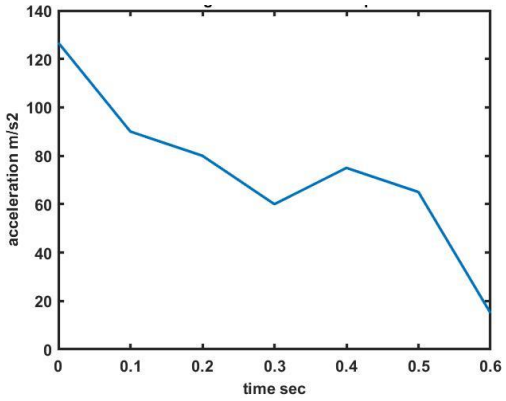


Fig. 14. Recorded acceleration of aircraft on catapult launncher.

## V. CONCLUSION

This paper described the successful development and system-level testing of the aircraft pneumatic catapult launch system. Sizing, optimization and testing results were reported. The aircraft catapult launch has reliably performed according to the predicted parameters from in-house developed simulator. Further work is being performed for optimizing transport weight and making it compatible with a bigger variety of towing vehicles. Further automation and data analytics are being added to the system. Future research directions include mechanisms of providing further vibration isolation between the shuttle and aircraft and improving system reliability.

## REFERENCES

[1] Siddiqui, B.A. et al, “Computer Aided Modelling and Simulation of Pneumatic U.A.V. Catapult Mechanism”, 7th International Mechanical Engineering Congress, Karachi, 25 Feb 2017.

[2] Zhou, Z. and Huang, J.“An optimization model of parameter matching for aircraft catapult launch”, Chin J Aeronaut, Vol 33 (1), Jan 2020.

[3] Reck, B., “First design study of an electrical catapult for unmanned air vehicles in the several hundred kilogram range”, IEEE Transactions on Magnetics, Vol 39, No 1, Jan 2003.

[4] Nelson, T. and Wang E., “Reliable FE-Modeling with ANSYS”, International Conference CADFEM, Munich, Germany, 2004.

[5] Setiawan, A.F, Sulistyo, D. and Aminullah, A., “Finite Element Method for Numerical Analysis of Post-tension Anchorage Zone”, Procedia Engineering, Vol 95, pp 272-278, 2014.

[6] “A novel automatic UAV launcher design by using Bluetooth low energy integrated electromagnetic releasing system”, IEEE Humanitarian Technology Conference, Cebu, Philippines, Dec 2015.

[7] Miller, S., “Mobile aircraft launcher”, U.S. Patent US6457673B1, 2006

[8] Anil R. Sahu, “Optimization and Finite Element Analysis of Steering Knuckle”, International Journal of Computer Applications (0975 - 8887

# Metal Detection and Bomb Disposal Robotic Vehicle

Hussain Z. Mandviwala
*Mechatroncs Department*
*PAF- Karachi Institute of Economics and Technology*
Karachi, Pakistan
hussainmandvi50@gmail.com

Fahad Khan
*Mechatroncs Department*
*PAF- Karachi Institute of Economics and Technology*
Karachi, Pakistan
fahad.mecha429@gmail.com

M. Farhan-uz-Zaman
*Mechatroncs Department*
*PAF- Karachi Institute of Economics and Technology*
Karachi, Pakistan
farhananna97@gmail.com

Mansoor Idrees Dawson
*Mechanical Engineering Department*
*DHA Suffa University*
Karachi, Pakistan
dawson_mansoor@hotmail.com

***Abstract*—This study aims to design an advance android control metal detecting and bomb disposal robot with night vision capabilities which is able to detect mines in war fields, monitor the war field using surveillance system, dispose bombs using a manipulator, design an autonomous robotic vehicle with sleek design to suit rough terrains, provide wireless controlling and monitoring device for analysis of operational area and of course reduce mortality rates. This project is divided into four sections each having its own methodologies. The robotic vehicle uses the remote control communication. Microcontroller and isolating circuits are used to counter loading effects and transmission delays. Furthermore, the central section for disposing the bomb using a robotic arm is prepared by the position controlling of servo motors through microcontroller. In addition, surveillance was attained by setting up a wireless IP network camera. Lastly, to detect metal at large expense was accomplished by using the phenomenon of proximity detection through resonant frequency. In this uncertain world, making an improvised explosive devices has never been difficult. The worth of bomb disposal and metal detection device is well known to the military people, especially in the war field. Defense and security institutions are our main target to facilitate. Many devices in the field bristle with camera feedback and microprocessors but the surplus in our account is that we can provide two major grounds (metal detection and bomb disposal) in one device.**

***Keywords— Metal detector, Bomb Disposal, Resonance frequency Oscillator, Pulse Width Modulation, Microcontroller.***

## I. INTRODUCTION

Metal detection system is a part of the bomb disposal robot, designed to serve the task of mine detecting in the war field. This will help in guiding the safest path for the robot as well as to dispose bombs. The main objective was to design a metal detection system which was cost effective, efficient and easy to use. [1]

To dispose off the bomb successfully, the robotic arm will play a vital role of picking up the bomb and disposing it to the safest location with help of the controlled circuit and electromechanical controlled motors (servo motors).[2] Other sub-objectives were transporting weapons through war field as well as to dodge various obstacles that would otherwise halt its progress. [3]

For controlling the robot out of sight, the surveillance camera allows the operator to monitor and record audio/video over a local area network or wirelessly and provide high image quality output over the user end.

Wireless transmission holds the role of controlling the robot out of sight. Various methods are used in designing wireless communication systems such as RC (Radio Control) and RF (Radio Frequency). [4]

The aim is to develop a valuable device that can become an asset in national context, to design an advance android control metal detecting and bomb disposal robot with night vision capabilities. [5] Many devices in the field bristle with camera feedback and microprocessors but the surplus in our account is that we can provide two major grounds (metal detection and bomb disposal) in one mechanism. This robot is an exceptional design of an autonomous robotic vehicle to suit rough terrains. [6] [7] It helps in detecting mines in war fields, disposes bombs using a manipulator, and monitors the war field using surveillance a system. It also provides an overall wireless controlling and monitoring device for analysis of operational area. And most importantly it will greatly help in reducing the mortality rates.

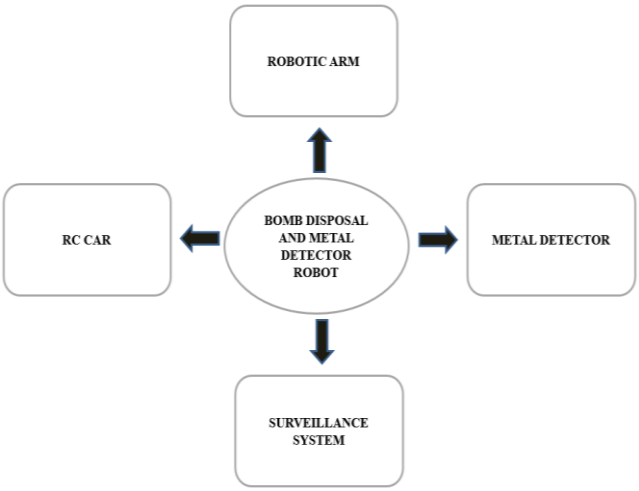


Figure 1: Overview of the Robot

## II. EXPERIMENTAL WORK

Experimental work in this study comprises in to the following processes;

A. Metal Detector
B. Hardware Structure
C. Surveillance
D. Robotic Arm

*A. Metal Detector*

In this project we have used resonant frequency oscillator method technology. [8]
Block diagram of Metal Detector:

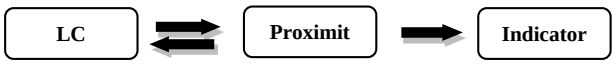


Figure 2: Metal Detection's Operational block diagram

The above block diagram in Figure 2 shows the metal detector principle operation using resonant frequency oscillator method technology.
The LC Circuit, consists of a coil and a capacitor, this is the main circuit of the metal detector. This LC Circuit, is also called as Tuned Circuit. The TDA0161 IC, is a proximity sensor IC, which acts as an oscillator and oscillates at a particular frequency.
When the LC circuit detects any resonating frequency from any metal, an electric field will be generated, and this field will induce current in to the coil and also changes in the signal flow through the coil. The, variable resistor in the circuit is used to change the proximity sensor's value equal to the LC circuit. When a metal is detected, the LC circuit will have a changed signal. The changed signal is given to the proximity detector IC (TDA 0161), which will detect the change in the signal and react accordingly.
When the output pin is high, the resistor R2 will provide positive voltage to transistor Q1. Thus, activating the indicator ON.

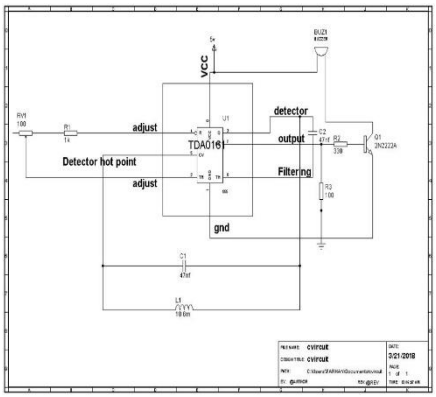


Figure 3: Metal Detection's Operational block diagram

We performed our calculations, and used two different coils for testing purpose.
Coil calculations Formula:

$$\boldsymbol{Lcoil \approx N\text{^}2 * \mu 0 * \mu r\ (D/2) *\ [ln\ (8D/d)\ -2]}$$

Where:
$L\ (coil)$ = inductance of the coil in henry (H)
$N\text{^}2$ = number of turns
$\mu 0$ = permeability of free space = $4\pi\times10^{-7}$
$\mu r$ = relative permeability
D = loop diameter
d = wire diameter
With the help of the above formula we were able to compare both the coils respect to their calculations;

Table 1: Types of coils and its parameters

| Parameters | Coil 1 | Coil 2 |
|---|---|---|
| No. of turns | 150 turns | turns |
| Loop diameter | 120mm | 60mm |
| Wire diameter | 26 AWG | AWG |
| Relative permeability | 0.99994=~ 1 | 0.99994=~ 1 |
| Inductance | 10.6mH | 4.7mH |

For resonant frequency the formula used was

$$f_{resonant} = \frac{1}{2\pi\sqrt{LC}}$$

Results:
Resonant frequency (coil1) = 7.3 KHz
Resonant frequency (coil2) = 10.7 KHz

In conclusion, coil 1 was chosen best fit as the search coil of the metal detector because its loop diameter was large enough to have a good search range, the resonant frequency of the coil is 7.3KHz which perfectly lies within the desired range of 6.5-12KHz, and since the resonant frequency of the oscillator is low, hence the search depth of the coil automatically increases up to our desired depth which was till 10cm underground, also the sensitivity of the detector decreases to large metallic objects only for examples mines.

*B. Hardware Structure*

The RC car acts as the backbone of this project. It provides a platform for the manipulator (robotic arm) and metal detector to accomplish their objective.
Our robot had to be firm and strong to bear heavy loads. The robot itself must not be overweighed. The robot should be well balanced to bear heavy loads. Links must have ability to endure high level stress. The structure must be compact.
The base was designed and constructed by the iron links joined with each other through nuts and bolts. The links were strong enough to carry more than 50kg weight in count. The structure of links in the Figure 4 is shown below;

Figure 4: Iron Links

According to our calculations, we selected the DC gear motor with 100 rpm and 15Nm, with terminal voltage of 12V. Both motors were joined on backside of the links as the driving power will be provided from backend.
The selected wheels were made up of hard composite material called polyurethane and they are usually used in skate boards, these wheels can even bear a weight of human being and provide sufficient grip to move on rough terrains. Two free wheels were joined with the front links for easy drive and balancing of structure. Whole structure is colored pitch black. A 4mm sheet of acrylic with dimensions or 1'x 1' was tighten with nut bolts over the links as for the role of base where circuits, manipulator, battery and weights were adjusted.
The upper body was also constructed by the acrylic sheet of 4mm. The complete hardware structure is shown in the Figure 5 below;

Figure 5: Hardware Structure

To get the desired outcomes through robotic arm and metal detector it is necessary that the robot's electronic controlling should be accurate eliminating the overshoots.
The flow of controlling the vehicle is provided in the Figure 13, the instruction of direction to vehicle is given by transmitter which is the remote control working on RF methodology. The signal is received by the receiver circuit installed in the car.
Initially the receiver circuit output was connected directly to the motor which causes driving of high rating current without any isolation. So we apply protection circuit by isolating the receiving circuit from motor. The output of receiving circuit was given as the input to Arduino's different I/O pins. The Arduino was programmed with such instructions that on every input we can achieve desired output through controller.
Now achieving desired output through Arduino gave us the benefit for isolating receiving signals directly to motor. The relay logic plays vital role in isolating as well as power distribution for motors.

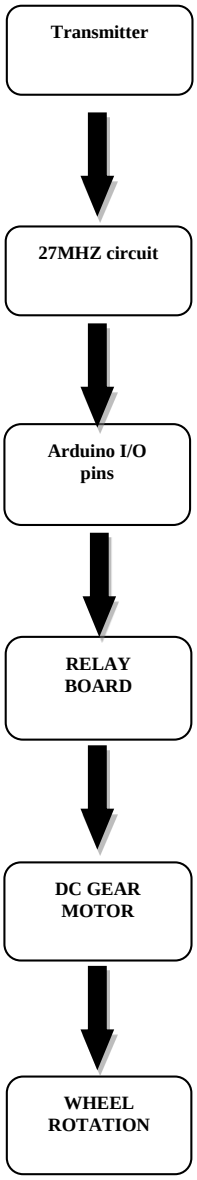


Figure 6: Robotic Vehicle's Direction Control Flow Chart

*C. Surveillance*

The newest and greatest transformation in video surveillance systems is the switching from analog cameras to the IP camera.
IP cameras may be monitored via web network via mobile. These cameras contains large storage capacity to store videos oh high definition image quality. [9]
The IP camera receives, sends and transfers the image (video signal) directly via IP networks, thus allowing the authorized user to view, record and manage the video through a proper infrastructure of IP base network. [10] The android application allows the operator to view the live video streaming.
IP network camera has greater flexibility, an easy system installation, and a better wireless reception and security.
The block diagram in Figure 2 shows the operation flow of the IP wireless camera;
The lens of the camera captures the image and passes through the optical filter. The image sensor further converts the image into electrical signals. These signals are then

converted from analog to digital signals and further then transferred over networks.
The CPU, Flash memory and DRAM memory are the computing functions of the camera and are designed for network applications. Altogether, they handle the communication with the network. With the use of Ethernet port or wireless antennae images are sent to different devices on the network.

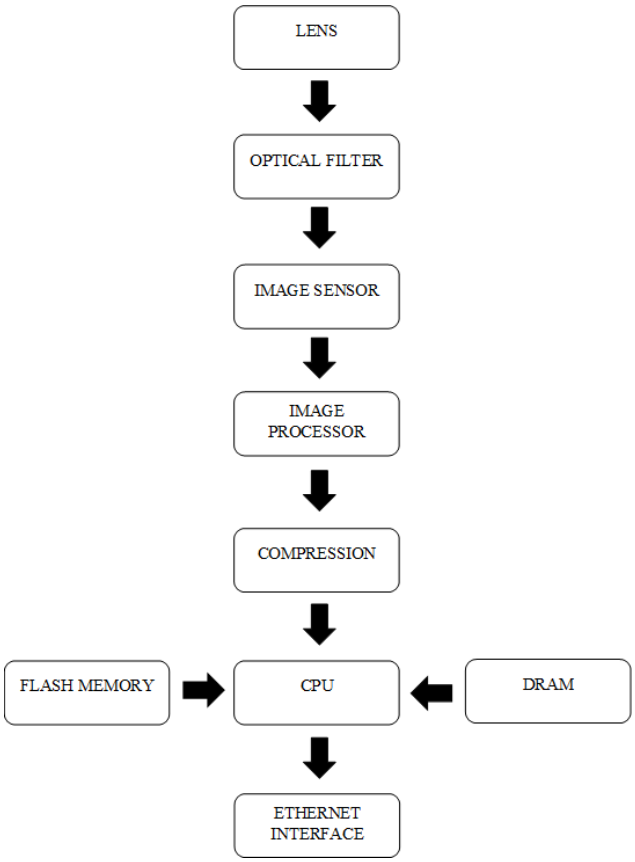


Figure 7: Surveillance System Process Flow

*D. Robotic Arm*

For disposing off the bomb with an ease of access robotic arm must be of high degree of freedom so that the operator has more option to move the manipulator in different axis, so a 4DOF(degree of freedom) was a more efficient and more economical design as shown in Figure 8;

Figure 8: 4DOF Manipulator

To meet the design objective servo motors played a vital role for lifting up the bomb, that's why metal geared servo motors were used for this project that can only be controlled by PWM (Pulse Width Modulated) signals. In our case Arduino was selected as a controller for the manipulator. The standard connection diagram of Arduino and servo motor is shown in Figure 9;

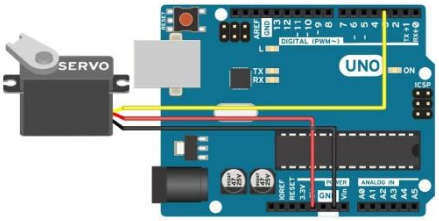


Figure 9: Servo Connections with Arduino

Controlling the manipulator wirelessly was also sub-design objective of our project, in this case we used Bluetooth wireless technology that would be more efficient and economical with the help of Arduino microcontroller and a Bluetooth module (HC-05). Figure 10 shows the wiring diagram of HC-05 and Arduino;

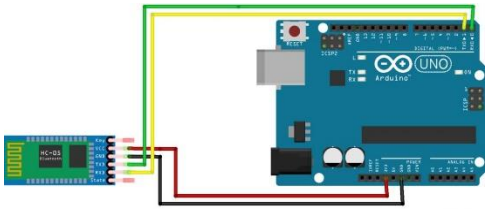

Figure 10: Bluetooth Module Connection with Arduino

A circuit was designed to give servo motors a high input current with the help of NPN high power transistors, the circuit diagram is shown in Figure 11;

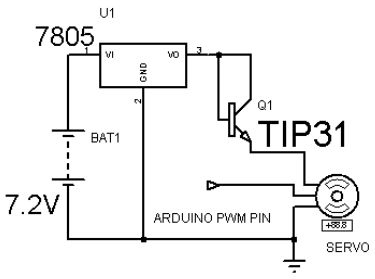


Figure11: Servo Driving Circuit using TIP31

With the help of above circuit, the motor could drive up to 3A current, which was enough for the required torque.
Since our own design had different aspects of controlling more things wirelessly including the manipulator. So, a separate android application was developed through MIT application developer, the main screen of the android application is shown in Figure 12;

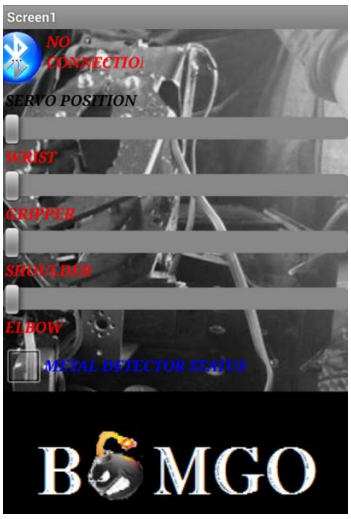


Figure 12: Android Application Screen

Through this android application, the servo positions are being controlled via Bluetooth module HC-05.

Figure 13 shows the Robotic arm control flow. The Android application sends instructions to Arduino (controller) via HC-05 Bluetooth module which controls the servo position of the servo motors in Robotic Arm through PWM signals generated from the Arduino.

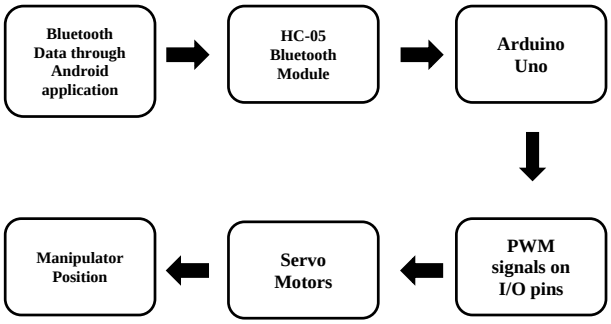


Figure 13: Robotic Arm Control Flow

## III. Results and Discussion

The achieved results are discussed

1. The metal detection circuit is able to detect the mines and indicate it by LEDs placed over the top of the end effector.
2. IP Camera is positioned on to top of the robotic arm in a certain way that we can see clear live streaming of robotic arm and vehicle position. The IP camera gives a visual image of the whole trajectory of the robotic vehicle.
3. Robotic arm is placed on the front part of the robot, which is used to pick the bomb and dispose it through android application.
4. For the operation of the robot, a wireless controlling and monitoring panel is designed. Figure 14 shows a control panel, where the IPad will be providing surveillance from the IP camera, the joysticks will be controlling the robotic vehicle motion, and through the Android application, the motion of the servo motors of the manipulator (robotic arm) will be controlled via Bluetooth.


Figure 14: Controlling & Monitoring Panel

5. The Table 2 shows the output resulted values shown on the serial monitor of each of the serial communication variables.

Table 2: Serial Communication

| S. No | Serial Communication variable | Serial monitor values |
|---|---|---|
| 1. | HC-05 baud rate | 38400 |
| 2. | Bluetooth Active | X >= 2 |
| 3. | Shoulder joint servo | 1000(min) to 1180(max) |
| 4. | Elbow joint servo | 2000(min) to 2180(max) |
| 5. | Wrist joint servo | 3000(min) to 3180(max) |
| 6. | Gripper joint servo | 4000(min) to 4180(max) |
| 7. | Metal detector servo | Turn on = 130<br>Turn off = 40 |
| 8. | Vehicle direction left | left |
| 9. | Vehicle direction right | right |
| 10. | Vehicle direction forward | forward |
| 11. | Vehicle direction backward | backward |

6. Figure 15 shows the output waveform of the LC circuit from the metal detector circuit when no metal is detected. Since there is no metallic object near the waves and there is no distortion in the signal. Resulting a proper alternating wave form of 7.6k Hertz.
(Focusing on channel 1 represented by yellow color)

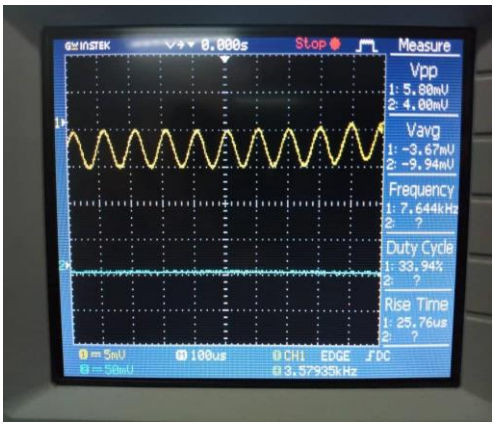


Figure 15: LC Circuit waveform

7. Figure 16 shows the voltage reading from the output of metal detector circuit when no metal is detected. Due to the built-in comparator circuit of the proximity integrated circuit TDA0161 provides around zero voltage when an undistorted field of LC circuit is compared with its own referenced resonant frequency.

   (Focusing on channel 1 represented by yellow color)

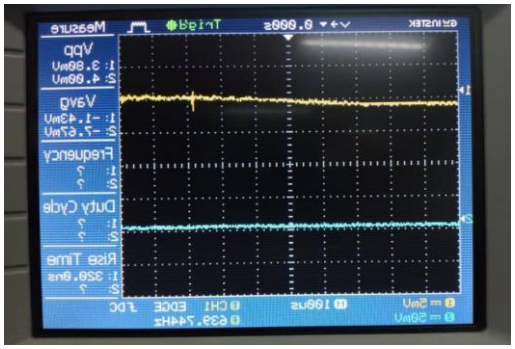

Figure 16: Metal detector output waveform

8. Figure 17 shows the voltage reading from the output of metal detector circuit when a metal is detected. Since the built-in phenomena of comparison of resonant frequency compares the resulted wave form with the referenced frequency, it generates a voltage of around 7 volts. That is the indication that a metal is detected.
   (Focusing on channel 1 represented by yellow color)


Figure 17: Metal detector output waveform

9. Figure 18 shows the output wave form of LC circuit when a metal is detected. Since the LC circuit of the detector generates a resonant frequency and when a metallic object gets near to it, it creates noise and reduces the frequency due to the phenomena of eddy current losses. Resulting a straight line on the oscilloscope.

   (Focusing on channel 1 represented by yellow color)

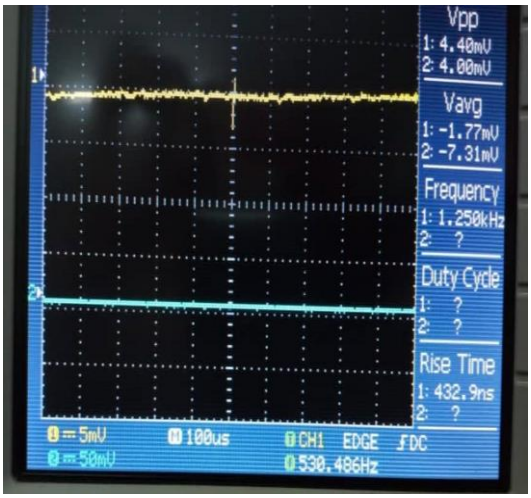


Figure 18: LC Circuit waveform

## IV. Conclusion

Metal Detection and Bomb Disposal Robotic Vehicle has been designed in such a way that it can serve to the needs of the bomb disposal squad, the armed forces, and the police. It is the minimum viable product of bomb disposal technology. This robot has innumerable applications that can be used in different scenarios. This robot can be used for detecting mines and also, provide up to date information in a hostage situation.

## References

[1] Gader, P.D., et al., Landmine detection with ground penetrating radar using hidden Markov models. 2001. **39**(6): p. 1231-1244.

[2] Okereafor, D., et al. Improving security and emergency response through the use of unmanned vehicles. in Emerging & Sustainable Technologies for Power & ICT in a Developing Society

(NIGERCON), 2013 IEEE International Conference on. 2013. IEEE.

[3] Oke, A.O. and A. Afolabi. Development of a robotic arm for dangerous object disposal. in Computer Science and Information Technology (CSIT), 2014 6th International Conference on. 2014. IEEE.

[4] Zaman, H.U., et al. Design, control & performance analysis of Muktibot. in Information Technology, Electronics and Mobile Communication Conference (IEMCON), 2016 IEEE 7th Annual. 2016. IEEE.

[5] Goldenberg, A., et al., Explosives disposal robot. 2000, Google Patents.

[6] Odedra, S., S.D. Prior, and M. Karamanoglu. Investigating the mobility of unmanned ground vehicles. in International Conference on Manufacturing and Engineering Systems. Proceedings. 2009. International Conference on Manufacturing and Engineering Systems.

[7] White, J.R., et al., All terrain mobile robot. 1990, Google Patents..

[8] OSMAN, M.T.E.M., Metal Detector. 2011, University of Khartoum.

[9] Matthews, V.O., et al., On the Implementation of IP Video Surveillance Systems. 2013. **3**(5): p. 10-16.

[10] Popovic, G., et al., Overview, characteristics and advantages of IP Camera video surveillance systems compared to systems with other kinds of camera. 2013. **2**(5): p. 356-362.

# Optimal Control Design for Smooth Level Turning Flight of an Aircraft

Muhammad Uzair Hassan
*Dept. of Electrical and Electronic Engineering*
*University of Engineering and Technology*
Rawalpindi, Pakistan
uzair11622@gmail.com

Muhammad Fawad Hussain
*Dept. of Flight Controls*
Pakistan Aeronautical Complex
Attock, Pakistan
hussain.fawad@gmail.com

Muhammad Zeeshan Babar
*Dept. of Controls*
University of Surrey
Guildford, United Kingdom
m.z.babar@surrey.ac.uk

Taha Hamid
*Dept. of Flight Controls*
Pakistan Aeronautical Complex
Attock, Pakistan
tahamid 92@hotmail.com

**Abstract-In this paper, a multi-input multi-output (MIMO) optimal state feedback control strategy is adopted for the lateral directional control of an aircraft. The aim of the proposed controller is to ensure a stable turning flight by tracking a reference roll command while keeping other inputs and states of the system in the desired physical bounds. A detailed discussion on the lateral model of the aircraft is presented. The control performance is evaluated in terms of overshoot, settling time and steady state error in the case of reference roll tracking. The effectiveness of the proposed Linear Quadratic Regulator (LQR) controller using the pre-compensation term is shown by simulation in MATLAB/Simulink.**

***Keywords—LQR, optimal control, autopilot, roll tracking, lateral control.***

## I. INTRODUCTION

Evolution of aircraft is the greatest invention of the twentieth century which has significantly reduced travel time and enabled us to reach every corner of the world [1]. Over the last century, aircraft design has evolved into advanced structures, aerodynamics, flight control surfaces and capability of high maneuverability. This makes the autopilot control an utmost requirement due to the high-performance requirements of aircraft [2, 3]. Autopilot system is basically a pilot relief mechanism that assists the pilot in case of instability, control, and navigation of the aircraft. The idea behind the autopilot system is, whenever the aircraft deviates from its actual flight path, the designed autopilot will engage and stabilize the aircraft in its orientation angles (roll, pitch, and yaw) as shown in Fig. 1 [4]. The demands for high performance modern aircraft urges engineers to adopt modern control design techniques. In 1902, Wright Brothers performed their maiden flight with an airplane equipped with automatic flight controls. In 1912, a similar approach for autopilot was proposed by Sperry brothers which was sensitive to aircraft maneuvers. In 1931, the first mechanical autopilot was licensed to fly. In 1944, electronic autopilot with improved performance was used in Northrop MX-334 rocket driven airplane. In 1978, Amerogen (Model Reference Autopilot), Ohtsu (AR Autopilot), and Kallstrom (Self Tuning Autopilot) was introduced [1].

The design of optimal feedback controllers for different dynamic aerospace systems is common yet very difficult task. Due to the requirement of high level accuracy, efficiency and reliability in terms of better control performance and system stability, the controller design is always a challenging task [5, 6]. In order to design sophisticated control algorithms for complex processes which meets the demands of better system performance and robustness, control engineers require modern design tools and better underlying theory. In addition, the information from multiple sensors and actuators play vital role in improving the performance of MIMO aerospace system [7], [8]. The LQR method emerges as one of the major success in the field of optimal control in practical control problems. It is useful for regulating the external disturbances [9] as well as it is used to track desired system performance by minimizing a quadratic cost function. The choice of LQR method is motivated by the fact that it is easily applicable to multivariate system with coupling between states [7, 10] and helps in achieving a given task with minimum control effort [5].

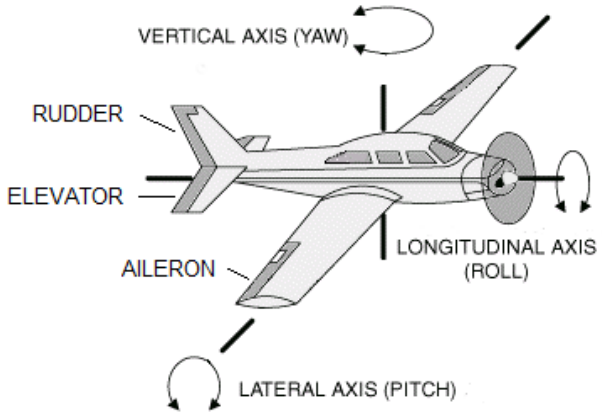


Fig. 1. Aircraft Dynamics Moments & Control Surfaces [11]

Fighter aircraft consists of highly nonlinear flight dynamics which requires adequate control during maneuvering. Statically stable aircraft has a tendency to return to its equilibrium position after being disturbed. However, in the case of statically unstable aircraft, the aircraft doesn't return to its equilibrium position, hence control of such aircraft is a challenging task [12]. Fighter aircraft are designed to be unstable in order to increase their agility, which necessitate the requirement of an efficient control strategy to maneuver and assist pilot during flight [3]. A complete aircraft model is divided into lateral and longitudinal dynamics. Longitudinal dynamics are controlled using the elevators, whereas lateral dynamics are controlled by aileron and rudder as shown in Fig. 1. Control of roll angle, sideslip angle, and heading angle

is considered as the lateral control which is discussed in this research work.

In a rolling maneuver, aileron moves asymmetrically to produce rolling movement which creates an unstable side force compelling flight path of the airplane to curve. In case of positive rolling movement, this happens when lifting force on the left wing increases whereas lift on right-wing decreases. In this study, we have considered a case where, pilot intentionally creates a side force and rolling movement with the help of rudder and aileron to achieve a tracking performance. A lateral aircraft model is considered in this work which is taken from [4]. The nonlinear model is linearized around trim flight condition. The LQR method ensure turning flight by tracking a reference roll command and reference command for sideslip angle.

Rest of the paper is organized as follow: Section II formulates problem statement in detail. Section III discusses general aircraft model followed by linearized lateral model of aircraft. Section IV discusses the LQR control method and its implementation on an aircraft system. Section V presents the simulation results and a detailed discussion on it. Section VI presents the concluding remarks.

## II. Problem Statement

Dynamic control and analysis of flight system design is a complex problem which usually deals with external disturbances and uncertainties in modeling. Most of the research in this domain is focused on the flight stability issues. Linear MIMO systems are well represented by state-space representation. The general state-space representation for linear system is given as:

$$\dot{x}(t) = Ax(t) + Bu(t) \quad (1)$$

$$y(t) = Cx(t) + Du(t) \quad (2)$$

Where x(t) is the state vector, u(t) is the input vector and y(t) is the output vector. While *A, B, C* and *D* represents the state matrix, input matrix, output matrix and direct feed-through matrix respectively.

The complete 3-DOF lateral aircraft model consists of 6 states, i.e. sideslip angle ($\beta$), roll rate ($p$), yaw rate ($r$), roll angle ($\phi$), cross range ($y$) and yaw angle ($\psi$). As the aim of this study is to design an optimal controller to achieve a smooth level turning flight, the roll angle and sideslip angle needs to be perfectly tracked. The contribution of the states '$y$' and '$\psi$' towards a smooth level flight is negligible, as it is mostly used for navigation purpose which is out of the scope of this work, hence both the states are neglected. The LQR method is a type of optimal control strategy which is used for regulation purposes. But in some scenarios, tracking with the LQR method can also be achieved by adding a pre-compensator term $\bar{N}$ to the reference input to compute an error signal [13]. For a reference value '$r$' to track, the closed loop block diagram of the LQR method is shown in Fig. 2, where $K$ is the feedback gain, $x$ represent the states, $y$ represents output, *A, B* and *C* represents plant matrix, input matrix and output matrix respectively.

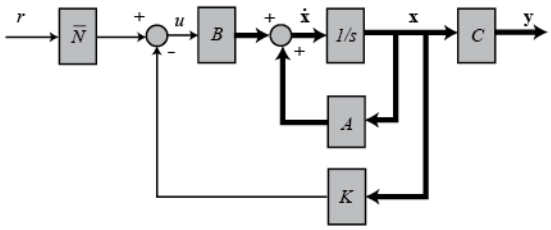


Fig. 2. Block Diagram Representation of the LQR Method [13]

The aim of this work is to achieve a smooth turning flight by designing an optimal controller which ensures the perfect tracking of reference roll angle while keeping the other states in their physical bounds. While in smooth turning flight, it is desirable to keep the sideslip angle $\beta$ to 1° in order to avoid the aircraft from stalling.

In this work, an optimal control strategy is proposed for tracking the reference roll angle ($\phi$) and sideslip angle ($\beta$) of an aircraft. It is desired that the aircraft should track the reference roll signal with an overshoot of less than 1(%), a settling time of *2sec* is required with zero steady-state error. While in the case of sideslip angle $\beta$ which has slow dynamics as compared to the roll angle $\phi$, it is desirable that the aircraft should track the reference sideslip angle within *5sec* with no overshoot and steady state error. This constraint of overshoot on the sideslip angle $\beta$ is to avoid aircraft from stalling. In order to achieve this control performance, the control efforts should also be in bound. For a lateral control of an aircraft, two control surfaces are used, the aileron $\delta_a$ and the rudder $\delta_r$. It is desirable to keep the aileron and rudder deflection within physical bounds of ±30°.

## III. A4D Aircraft Model

The McDonnell Douglas A4D (Skyhawk) is a subsonic fighter aircraft with a short-span delta wing as shown in Fig. 3 [8] which shows the 3-side view of the aircraft. The enactment of the airplane is effectively described by assuming aircraft as a point mass concentrated at the airplane's center of gravity. Forces generates moments along the center of gravity which are categorized into pitching, rolling, and yawing moment as shown in Fig. 1 [14].

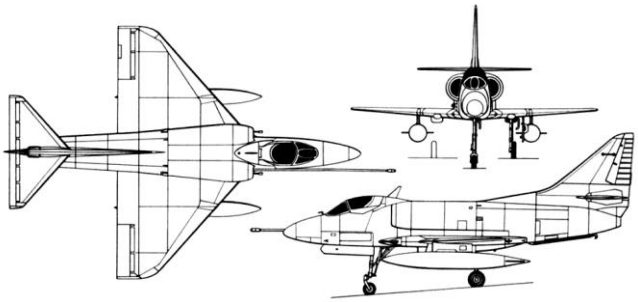

Fig. 3. McDonnell Douglas A4D (Skyhawk) 3-Side View [15]

A 6-DOF dynamic model of an aircraft is completely described by six nonlinear coupled differential equations of motion. These six equations are divided into three lateral and longitudinal dynamic equations. However, this work is focusing on the linear control system design, certain assumptions are made to decouple and linearize these

equations [16, 17]. As, in this work, we are focusing only on lateral directional control, the equations for 3-DOF lateral model considered which are given below.

$$(\frac{d}{dt} - Y_v)\Delta v - Y_p\Delta p + (u_0 - Y_r)\Delta r - gcos\theta_0\Delta\phi = Y_{\delta_r}\Delta\delta_r \quad (3)$$

$$-L_v\Delta v + (\frac{d}{dt} - L_p)\Delta p - (\frac{I_{xz}d}{I_x dt} + L_r)\Delta r = L_{\delta_a}\Delta\delta_a + L_{\delta_r}\Delta\delta_r \quad (4)$$

$$-N_v\Delta v - (\frac{I_{xz}d}{I_z dt} + N_p)\Delta p + (\frac{d}{dt} - N_r)\Delta r = N_{\delta_a}\Delta\delta_a + N_{\delta_r}\Delta\delta_r \quad (5)$$

The process of developing a complete flight dynamics model of an aircraft consists of producing state space matrices using the aerodynamic, stability, control and damping derivatives [18]. The state space model is computed at specific flight conditions which are used to calculate Eigenvalues that represent dynamic stability of the system. The 3-DOF linear model obtained from eq. (3), (4) and (5) can be written in the state space representation as below:

$$\begin{bmatrix} \Delta\dot{v} \\ \Delta\dot{p} \\ \Delta\dot{r} \\ \Delta\dot{\phi} \end{bmatrix} = \begin{bmatrix} Y_v & Y_p & -(U_0 - Y_r) & gcos\theta_0 \\ L_v & L_p & L_r & 0 \\ N_v & N_p & N_r & 0 \\ 0 & 1 & 0 & 0 \end{bmatrix} \begin{bmatrix} \Delta v \\ \Delta p \\ \Delta r \\ \Delta\phi \end{bmatrix} + \begin{bmatrix} 0 & Y_{\delta_r} \\ L_{\delta_a} & L_{\delta_r} \\ N_{\delta_a} & N_{\delta r} \\ 0 & 0 \end{bmatrix} \begin{bmatrix} \Delta\delta_a \\ \Delta\delta_r \end{bmatrix} \quad (6)$$

Sideslip angle ($\Delta\beta$) is more often used instead of side velocity ($\Delta v$). They relate in the following way [8].

$$\Delta\beta \approx tan^{-1}\frac{\Delta v}{u_0} = \frac{\Delta v}{u_0} \quad (7)$$

Putting eq. (7) into eq. (6), yields the new state space form which is given below:

$$\begin{bmatrix} \Delta\dot{\beta} \\ \Delta\dot{p} \\ \Delta\dot{r} \\ \Delta\dot{\phi} \end{bmatrix} = \begin{bmatrix} \frac{Y_\beta}{u_0} & \frac{Y_p}{u_0} & -(1 - \frac{Y_r}{u_0}) & \frac{gcos\theta_0}{u_0} \\ L_\beta & L_p & L_r & 0 \\ N_\beta & N_p & N_r & 0 \\ 0 & 1 & 0 & 0 \end{bmatrix} \begin{bmatrix} \Delta\beta \\ \Delta p \\ \Delta r \\ \Delta\phi \end{bmatrix} + \begin{bmatrix} 0 & \frac{Y_{\delta_r}}{u_0} \\ L_{\delta_a} & L_{\delta_r} \\ N_{\delta_a} & N_{\delta r} \\ 0 & 0 \end{bmatrix} \begin{bmatrix} \Delta\delta_a \\ \Delta\delta_r \end{bmatrix} \quad (8)$$

where the state vector $x^T = [\Delta\ \beta\ \Delta p\ \Delta r\ \Delta\ \phi]^T$ and the control vector $u^T = [\Delta\delta_a\ \Delta\delta_r]^T$ . The complete geometrical data along with mass, aerodynamic stability and control characteristics of McDonnell Douglas A4D (Skyhawk) are presented in TABLE I [8].

TABLE I. MCDONNELL DOUGLAS A4D (SKYHAWK) CHARACTERISTICS

| Geometric Characteristics | |
|---|---|
| Reference Area (S) | 24.2 $m^2$ |
| Reference Span (b) | 8.33 $m$ |
| Mean Aerodynamic Chord ($\bar{c}$) | 3.29 $m$ |
| **Mass Characteristics** | |
| Mass (m) | 7973.25 $kg$ |
| Center of Gravity Location | 0.25$\bar{c}$ |
| Moment of Inertia about x-axis ($I_x$) | 10968.6 $kg.m^2$ |
| Moment of Inertia about z-axis ($I_z$) | 39589.9 $kg.m^2$ |
| Moment of Inertia about xz-axis ($I_{xz}$) | 1762.6 $kg.m^2$ |
| **Aerodynamic Characteristics** | |
| $C_{Y_\beta} = -1.04$ | $C_{l_\beta} = -0.14$ |
| $C_{n_\beta} = 0.27$ | $C_{l_p} = -0.24$ |
| $C_{n_p} = 0.029$ | $C_{l_r} = 0.17$ |
| $C_{n_r} = -0.39$ | $C_{l_{\delta_a}} = 0.072$ |
| $C_{n_{\delta_a}} = 0.04$ | $C_{y_{\delta_r}} = 0.17$ |
| $C_{l_{\delta_r}} = -0.105$ | $C_{n_{\delta_r}} = 0.032$ |

The control and stability derivatives used in the state space representation of eq. (8) can be written in the form of dimensionless coefficients as shown in TABLE II [8].

TABLE II. FORCES AND MONENTS DERIVATIVES

| Y-Force Derivatives | Rolling Moment Derivatives | Yawing Moment Derivatives |
|---|---|---|
| $Y_\beta = \frac{QSC_{Y_\beta}}{m}$ | $L_\beta = \frac{QSbC_{l_\beta}}{I_x}$ | $N_\beta = \frac{QSbC_{n_\beta}}{I_z}$ |
| $Y_p = \frac{QSbC_{Y_p}}{2mu_0}$ | $L_p = \frac{QSb^2C_{l_\beta}}{2I_x u_0}$ | $N_p = \frac{QSb^2C_{n_p}}{2I_z u_0}$ |
| $Y_\beta = \frac{QSC_{Y_\beta}}{m}$ | $L_r = \frac{QSb^2C_{l_r}}{2I_x u_0}$ | $N_r = \frac{QSb^2C_{n_r}}{2I_z u_0}$ |
| $Y_{\delta_r} = \frac{QSC_{Y_{\delta_r}}}{m}$ | $L_{\delta_r} = \frac{QSbC_{l_{\delta_r}}}{I_x}$ | $N_{\delta_r} = \frac{QSbC_{n_{\delta_r}}}{I_z}$ |
| $Y_{\delta_a} = \frac{QSC_{Y_{\delta_a}}}{m}$ | $L_{\delta_a} = \frac{QSbC_{l_{\delta_a}}}{I_x}$ | $N_{\delta_a} = \frac{QSbC_{n_{\delta_a}}}{I_z}$ |

The initial flight conditions are assumed at a cruise segment with Mach 0.8 (subsonic) and altitude 35000ft. Inserting all

this data and information from TABLE I and TABLE II into eq. (8) yields the following state-space model:

$$\begin{bmatrix} \Delta\dot{\beta} \\ \Delta\dot{p} \\ \Delta\dot{r} \\ \Delta\dot{\phi} \end{bmatrix} = \begin{bmatrix} -0.1418 & 0 & -1 & 0.0414 \\ -27.4189 & -0.8250 & 0.5844 & 0 \\ 14.6505 & 0.0276 & -0.3714 & 0 \\ 0 & 1 & 0 & 0 \end{bmatrix} \begin{bmatrix} \Delta\beta \\ \Delta p \\ \Delta r \\ \Delta\phi \end{bmatrix} + \begin{bmatrix} 0 & 0 \\ 14.1011 & -20.5642 \\ 2.1704 & 1.7363 \\ 0 & 0 \end{bmatrix} \begin{bmatrix} \Delta\delta_a \\ \Delta\delta_r \end{bmatrix} \quad (9)$$

It is assumed that the sideslip angle $\beta$ and roll angle $\phi$ are measurable. The output matrix $C$ = [1 0 0 0; 0 0 0 1] is selected correspondingly.

## IV. LQR Control Design and Implementation

The LQR method is a commonly used control technique to design Stability Augmentation Systems (SAS) and autopilots. This is attained by regulating few states of the airplane and obtaining the characteristics of desirable closed-loop response. The closed-loop poles of the system are placed at desirable pole position to stabilize the aircraft. The purpose of state regulation is to ensure that the system remains in the steady state [19]. It uses cost function to describe the performance of the designed controller.

For a system represented in eq. (1) and eq. (2), the general cost function of the LQR controller is as follows:

$$J(u) = \int_0^\infty (x^T Q x + u^T R u) dt \quad (10)$$

where $x$ and $u$ represents the state and input vector respectively. The terms $Q$ and $R$ represents the weight matrix on the states and input respectively [20]. $Q$ and $R$ are design matrices which are selected to achieve desired system response and to find the optimal gain matrix. Above representation holds true for both single input single output (SISO) systems as well as multiple input multiple output (MIMO) systems [5, 6].

The choice of $Q$ and $R$ matrices has the utmost importance in the LQR control design. In eq. (10), the matrix $Q$ is usually selected as a diagonal matrix with diagonal elements used to penalize the different states deviation from steady state. The general form of matrix $Q$ is given in eq. (11), where $q_{11} > 0$; $q_{22} > 0$; $q_{33} > 0$ *and* $q_{44} > 0$ which makes it a positive definite matrix. While, the matrix $R > 0$ is a symmetric matrix usually selected as diagonal matrix as given in eq. (11). The general form of these matrices are given as:

$$Q = \begin{bmatrix} q_{11} & 0 & 0 & 0 \\ 0 & q_{22} & 0 & 0 \\ 0 & 0 & q_{33} & 0 \\ 0 & 0 & 0 & q_{44} \end{bmatrix} R = \begin{bmatrix} r_{11} & 0 \\ 0 & r_{22} \end{bmatrix} \quad (11)$$

Solving an LQR problem requires the solution of a feedback controller given as

$$u = -Kx \quad (12)$$

where $K$ is given by

$$K = R^{-1} B^T P \quad (13)$$

The solution $P$ can be found by solving the algebraic Riccati Equation which is given as

$$A^T P + PA - PBR^{-1}B^T P + Q = 0 \quad (14)$$

The LQR method can be used for tracking cases as well. When choosing the LQR method for tracking problems certain limitation are imposed especially in the case of MIMO systems. A necessary condition for the LQR implementation requires the number of inputs to be equal to the number of outputs to be tracked. Also, the method achieves perfect tracking for slow varying reference inputs. The tracking performance gets poor when the reference signal is changing rapidly.

In order to achieve desired system performance and to track the reference signal, a pre-compensator term $\bar{N}$ is augmented in the LQR model as shown in Fig. 2 which is used to compare the output signal to the reference input signal. The scaling factor $\bar{N}$is obtained by employing a user-defined MATLAB function (rscale.m). One of the limitation of this function is that it is used only for continuous single input system. However, in this study, we have adopted some changes in the code to use it for MIMO system (McDonnell Douglas A4D (Skyhawk) model).

The choice of weight matrices $Q$ and $R$ requires great knowledge of the system model as well as experience in tuning the LQR gains. The diagonal elements of $Q$ matrix $q_{11} = 10$; $q_{22} = 1$; $q_{33} = 500$; $q_{44} = 5$ are used to penalize different states deviations from steady state. Similarly weights on diagonal elements of $R$ matrix $r_{11} = 10$; $r_{22} = 10$ are used to penalize control action.

## V. Results and Discussion

The Simulink diagram of the LQR method for the lateral control of aircraft is shown in Fig. 4. The gain of the LQR controller is obtained by selecting $Q$ and $R$ weighting matrices as discussed in Section IV. The aileron $\delta_a$ and rudder $\delta_r$ are used as control inputs to track the reference sideslip angle $\beta$ and reference roll angle $\phi$.

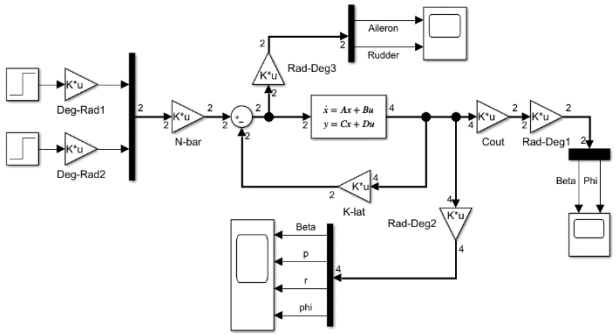


Fig. 4. Simulink Diagram for the LQR method

The desired control objective is to ensure smooth turning flight by tracking a reference roll angle $\phi$ of 20° in *2sec* with less than 1% overshoot and zero steady state error. During the smooth turning flight, the sideslip angle $\beta$ should be kept at 1°. As the dynamics of the sideslip angle $\beta$ are slow, the requirement for settling time is *5sec*. For the simulation purpose, a constant step of 20° is given as a reference roll angle $\phi$, and a step of 1° to sideslip angle $\beta$. The results for reference tracking, response of other two states and the control effort is shown in Fig. 5. It is evident from Fig. 5a that the sideslip angle $\beta$ is tracked in 5sec (step at 1sec) with no overshoot. Similarly, the Fig. 5b shows that the reference roll command is tracked in less than *2sec* (step at *1sec*). In this case, we have an overshoot of more than 2.5% which is more than the desired system requirements.

For the tracking of sideslip angle ($\beta$) and roll angle ($\phi$), a continuous deflection of aileron $\delta_a$ and rudder $\delta_r$ is required. As discussed in Section II, the control effort for both aileron and rudder should remain in bound of ±30°. It is obvious from Fig. 5e and Fig.5f that the aileron has maximum deflection of 8.7° while rudder has -13° deflection. Positive aileron deflection correspond to positive rolling movement whereas negative rudder deflection correspond to positive side force. The constant control effort is due to the continuous tracking of sideslip angle $\beta$. It is observed that all the other states of the system remain in bound as shown in Fig. 5c and Fig. 5d.

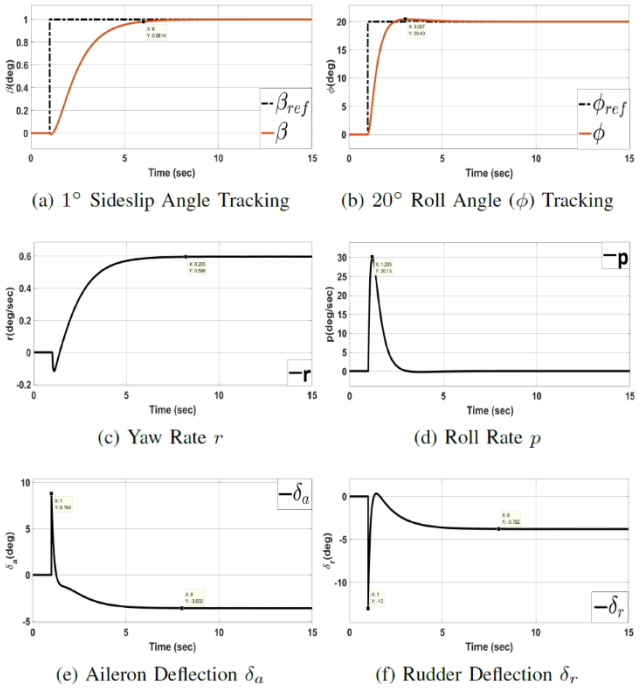


(a) 1° Sideslip Angle Tracking (b) 20° Roll Angle ($\phi$) Tracking

(c) Yaw Rate $r$ (d) Roll Rate $p$

(e) Aileron Deflection $\delta_a$ (f) Rudder Deflection $\delta_r$

Fig. 5. Simulink Diagram for the LQR method

In the simulations, it is observed that increasing the gain of $Q$ matrix helps to decrease the settling time with a cost of increasing overshoot and larger controller deflections. Simulation results shows that the controller ensures the aircraft to effectively track 1° sideslip angle $\beta$ within 5sec and 20° roll angle ($\phi$) within *2sec*. For the reference tracking of roll angle, the response is without steady-state error and has overshoot of more than 2.5%. The roll rate reaches a maximum value of 30° as shown in Fig. 5d and eventually settled to zero as the roll angle tracks the reference command.

TABLE III. ACHIEVED CONTROLLER PERFORMANCE CHARACTERISTICS

| Characteristics | Sideslip Performance | Roll Performance |
|---|---|---|
| Settling Time (sec) | 5.0 | 2.0 |
| Overshoot (%) | 0.0 | 2.5 |

In order to reduce the overshoot, weight on roll rate $p$ is increased while keeping the control weighted matrix $R$ constant. The weight on sideslip angle ($\beta$) and roll angle ($\phi$) is increased to $q_{11} = 20$ *and* $q_{44} = 7$ respectively. The weight on aileron ($\delta_a$) is also increased to $r_{11} = 50$ which has reduces the overshoot at a cost of a bigger control effort for rudder. In the above graph, with a step time of *1sec*, roll angle ($\phi$) takes approximately 2sec to track 20° with an overshoot of approximately 0.5%. Whereas, the sideslip angle ($\beta$) achieves the tracking in approximately *5sec*.

After reducing the overshoot, we observed that control efforts are still in bounds with 3.9° aileron deflection and -17.5° rudder deflection. The continuous deflection of the control effort corresponds to the constant tracking of sideslip angle ($\beta$) tracking [21].

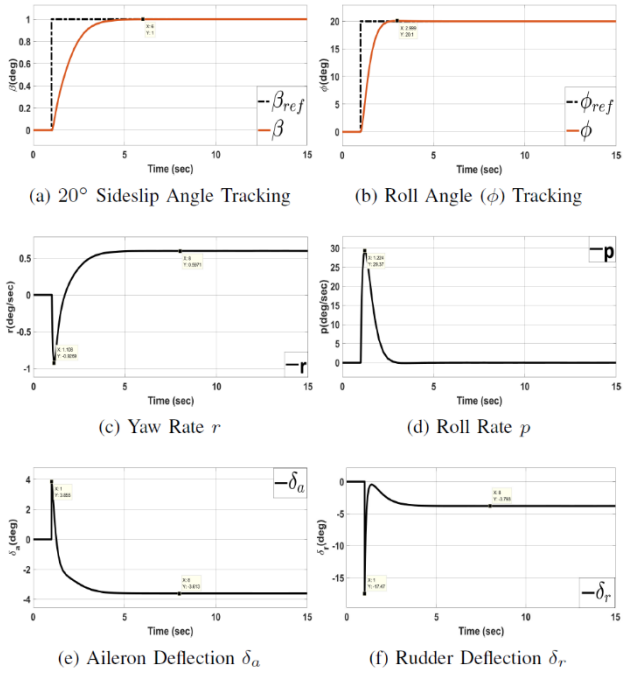


(a) 20° Sideslip Angle Tracking (b) Roll Angle ($\phi$) Tracking

(c) Yaw Rate $r$ (d) Roll Rate $p$

(e) Aileron Deflection $\delta_a$ (f) Rudder Deflection $\delta_r$

Fig. 6. McDonnell Douglas A4D (Skyhawk) System Response

Control performance characteristic with the improved LQR tuning which has resulted in the reduction of overshoot is listed below:

TABLE IV. ACHIEVED CONTROLLER PERFORMANCE CHARACTERISTICS

| Characteristics | Sideslip Performance | Roll Performance |
|---|---|---|
| Settling Time (sec) | 5.0 | 2.0 |
| Overshoot % | 0.0 | 0.5 |

We observed that change in the $Q$ matrix reduces the overshoot in roll angle with an associated cost of larger control efforts. Furthermore, it was observed that all the states are stable.

## VI. CONCLUSION

In this study, an optimal controller is designed to ensure smooth turning flight by tracking the reference roll angle ($\phi$) and the sideslip angle ($\beta$) while keeping other states of the system in their respective physical bounds. The proposed strategy is implemented on a McDonnell Douglas A4D (Skyhawk) fighter aircraft. Stability of all the states and perfect reference tracking are simultaneously achieved. In addition, the physical constraints on the control inputs are respected and the control effort remains in the specified bounds. The novelty of this work is its implementation on a MIMO system which is not directly faced in the literature.

Moreover, the effect of the elements of the weighting matrix on every particular state is discussed. The Methodology adopted in this design procedure particularly includes control of multiple inputs multiple outputs (MIMO) system. Similarly, this methodology can also be utilized for the control deign of longitudinal aircraft dynamics.

## REFERENCES


[1] H. Al-Lami, A. Aslam, T. Quigley, J. Lewis, R. Mercer, and P. Shukla, "The evolution of flight control systems," 2015.

[2] R. Lungu, M. Lungu, and L. T. Grigorie, "Automatic control of aircraft in longitudinal plane during landing," *IEEE Transactions on Aerospace and Electronic Systems*, vol. 49, no. 2, pp. 1338–1350, April 2013.

[3] T. J. Redling, "Integrated flight control systems: a new paradigm for an old art," *IEEE Aerospace and Electronic Systems Magazine*, vol. 16, no. 5, pp. 17–22, May 2001.

[4] M. A. Usta, . Akyazi, and A. S. Akpinar, "Aircraft roll control system using lqr and fuzzy logic controller," in 2011 *International Symposium on Innovations in Intelligent Systems and Applications*, June 2011, pp. 223–227.

[5] S. K. Pandey and V. Laxmi, "Optimal control of twin rotor mimo system using lqr technique," in *Computational Intelligence in Data Mining*- Volume 1. Springer, 2015, pp. 11–21.

[6] N. Gandhi, D. M. Tilbury, Y. Diao, J. Hellerstein, and S. Parekh, "Mimo control of an apache web server: Modeling and controller design," in *Proceedings of the 2002 American Control Conference (IEEE Cat. No. CH37301)*, vol. 6. IEEE, 2002, pp. 4922–4927.

[7] L. Chrif and Z. M. Kadda, "Aircraft control system using lqg and lqr controller with optimal estimation-kalman filter design," *Procedia Engineering*, vol. 80, pp. 245 – 257, 2014, 3rd *International Symposium on Aircraft Airworthiness (ISAA 2013)*. [Online]. Available: http://www.sciencedirect.com/science/article/pii/S1877705814011771

[8] R. C. Nelson et al., *Flight stability and automatic control*. WCB/McGraw Hill New York, 1998, vol. 2.

[9] E. V. Kumar, G. S. Raaja, and J. Jerome, "Adaptive pso for optimal lqr tracking control of 2 dof laboratory helicopter," *Applied Soft Computing*, vol. 41, pp. 77–90, 2016.

[10] J. Zhu, "A survey of advanced flight control theory and application," in *The Proceedings of the Multiconference on "Computational Engineering in Systems Applications"*, vol. 1, Oct 2006, pp. 655–658.

[11] "Fly by wire flight control system." [Online]. Available: http://www.havkar.com/en/blog/view/fly-by-wire-flight-controlsystem/ 104

[12] A. Ashraf, W. Mei, L. Gaoyuan, Z. Anjum, and M. M. Kamal, "Design linear feedback and lqr controller for lateral flight dynamics of f-16 aircraft," in *2018 International Conference on Control, Automation and Information Sciences (ICCAIS)*, Oct 2018, pp. 367–371.

[13] "State-space methods for controller design." [Online]. Available: http://ctms.engin.umich.edu/CTMS/index.php

[14] B. Stojiljkovic, L. Vasov, C. Mitrovic, and D. Cvetkovic, "The application of the root locus method for the design of pitch controller of an f-104a aircraft," *Journal of Mechanical Engineering*, vol. 55, 01 2009.

[15] "Mcdonnell douglas a-4 skyhawk." [Online]. Available: http://www.aviastar.org/air/usa/mcdonnel sky.php

[16] B. Aliyu, A. F.A, C. Osheku, M. Adetoro, and A. F.A, "Pitch control of an aircraft using artificial intelligence," *Journal of Scientific Research and Reports*, vol. 1, pp. 1–16, 01 2012.

[17] P. Wahi, R. Raina, and F. N. Chowdhury, "A survey of recent work in adaptive flight control," in *Proceedings of the 33rd Southeastern Symposium on System Theory (Cat. No.01EX460)*, March 2001, pp. 7–11.

[18] M. Z. Babar, R. Samar, A. I. Bhatti, and M. Baglietto, "Robust integrated lateral guidance and control of uavs," in 2015 20th *International Conference on Methods and Models in Automation and Robotics (MMAR)*. IEEE, 2015, pp. 523–528.

[19] M. Z. Babar and M. Baglietto, "Optimal feedback control for the identification of two-wheeled mobile robot," in 2017 21st *International Conference on System Theory, Control and Computing (ICSTCC)*. IEEE, 2017, pp. 112–119.

[20] N. Wahid and M. F. Rahmat, "Pitch control system using lqr and fuzzy logic controller," in *2010 IEEE Symposium on Industrial Electronics and Applications (ISIEA)*. IEEE, 2010, pp. 389–394.

M. T. Islam, M. S. Alam, M. A. R. Laskar, and A. Garg, "Modeling and simulation of longitudinal autopilot for general aviation aircraft," in *2016 5th International Conference on Informatics, Electronics and Vision (ICIEV)*. IEEE, 2016, pp. 490–495.

# Earth Ionosphere Anomalies before the 2016 Kaikoura Earthquake New Zealand from OLR and GPS-TEC

M. Arqim Adil
Institute of Space Technolgy,
Islamabad, Pakistan
arqamadil3@gmail.com

Abdur Rafeh Abbasi
Institute of Space Technolgy
Islamabad, Pakistan
abdurrafehabbasi@hotmail.com

Dr. Munawar Shah
Institute of Space Technolgy,
Islamabad, Pakistan
shahmunawar1@gmail.com

***Abstract*—Seismo ionospheric anomalies from Space and ground instruments can provide deep insights over the epicenter of future earthquake (EQ). This paper presents the variation in Total Electron Content (TEC) from Global Positioning System (GPS) and Outgoing Long wave Radiation (OLR) from GIOVANNI-AIRS prior to the November 14, 2016 Kaikoura EQ. TEC from the International GNSS services (IGS) stations of Whangaparaoa, Dunedin and MacQuarie Island within seismo-genic zone showed ionospheric variation on November 11, 2016. The variations are found on the bases on confidence interval of median and associated inter quartile range for fifteen days before and after the main shock. The bounds are calculated from continuous analysis of ten days before and after the observed day. Furthermore, we examined geomagnetic storms using Ap, Kp and Dst indices to distinguish seismo-ionospheric anomalies. After examining the TEC and OLR data, we find anomalies 3 days prior of impending EQ, which is due to the association of lithosphere and ionosphere coupling. However, TEC also showed enhancement due to geomagnetic storm on October 30, 2016 which is attributed to this huge storm.**

***Keywords—GPS-TEC, OLR, Lithosphere-Ionosphere coupling, M7.8 Earthquake***

## I. Introduction

Among the significant advancement of space based ionospheric measurements, rapid increase is observed in the study of earth atmosphere and ionosphere coupling related to large magnitude EQs[1][2][3]. Particularly forecasting of EQ via seismo-ionospheric anomalies is now getting debate among researchers. The vulnerable Kaikoura EQ of 7.8$M_w$ in New Zealand 2016 at 13-09-2016: UT: 11:02:56 and 14-09-2016: LT: 00:02:56 consider being the most complex studied EQ [4] due to the ruptures occurred on multiple faults. However, in this paper we analyze ionospheric anomalies that occurs during the EQ period. Analysis of EQ event in this paper occurred of magnitude 7.8 in Kaikoura region of New Zealand where two people died while more than a dozen were found injured. Following with EQ, tsunami warning has initiated [4]. Tsunami waves of height up to 1.5 meters reached Kaikoura within 30 minutes of the rupture taken place.

As many studies have clearly indicated that anomalies relating to EQ appear before EQs in the ionosphere. However, it is not yet confirmed, and no one culminate this topic with explicit definition. As for as the researchers concern, many theories have been introduced like comparing local TEC with global TEC and solar activity and analyzing with variations of $f_0$F2 and NmF2. They analyze statistically $f_0$F2 from F-region of earth ionosphere and compared it with EQ and solar storms. The difference between $f_o$F2 and NmF2 is that $f_o$F2 variations for the EQ can be observe in daytime while NmF2 shows discrepancies in nighttime [5]. They examine solar and various seasonal effects on characteristics of equatorial ionospheric anomaly (EIA) by inspecting GPS-TEC [6]. Yet relationship between lithosphere-ionosphere couplings is not pursued entirely and largely open for research [7]. Another parameter is outgoing long wave radiation (OLR) as it is the measures of amount of energy release from ground to outer space and atmosphere which is considered as another important source of finding anomaly in ionosphere. A study [8] discusses the identification of anomaly being visible normally 5-30 days before EQ.

This paper analyzes GPS-TEC, which is downloaded from (http://www.ionolab.org) [9][10] TEC of 30 days is acquired from IONOLAB. For the assembling of TEC, we gather the data of three different GPS stations situated near the EQ zone. Following with the TEC, we analyze Dst, Kp and Ap indices from the (http://wdc.kugi.kyoto-u.ac.jp/index.html). The geomagnetic storm indices are gathered within 30 days around the main shock. OLR data is extracted for further analysis in ionosphere from (https://giovanni.gsfc.nasa.gov/giovanni/).

## II. Data Method and Research Methodology

In this paper, TEC anomalies are studied with reference to EQ in Kaikoura, New Zealand. A powerful EQ occurred of magnitude 7.8$M_w$ in the South Island region of Kaikoura, New Zealand at 00:26:56 LT on November 14, 2016. The epicenter of the EQ was at 42.69 $^0$S, 173.02 $^0$E, just 90 km away from Christchurch. As stated by the Institute of Geological and Nuclear Sciences (GNS) New Zealand, the depth of the EQ was 15km. The EQ shock lasts up to 2 minutes. TEC is a very important constituent in EQ

forecasting studies, but earlier researchers were found to be very selective as they always associated the TEC anomalies with EQ without checking the nature of geomagnetic storms during that EQ happening [11]. Therefore, we analyze the data of geomagnetic indices, which is retrieved from (http://wdc.kugi.kyoto-u.ac.jp/index.html).

Analysis of EQ anomalies in this paper is identified through GPS-TEC and OLR, which are observed over Kaikoura region (epicenter). Data downloaded from three different International GNSS Service (IGS) stations. IGS gives full insight about the variations that occurs in the atmosphere. Whangaparaoa Peninsula (New Zealand), Dunedin (New Zealand), MacQuarie Island, Sub-Antarctic (Southern Ocean) stations are used for this purpose. Furthermore, data collected for the analysis is 20 days before the EQ and 10 days after the EQ day in corresponding with the mentioned IGS stations. Geomagnetic storms indices are also considered for the 30 days within EQ event.

Another important factor to be considered in the prediction of EQ is OLR. Because if there exists a geomagnetic storm around EQ period it is very difficult to associate TEC anomalies to the EQ as we cannot make justification of association of TEC anomalies to the EQ. The measurements of OLR are taken from top of the atmosphere, it is considered as an important source of predicting lithosphere-ionosphere anomalies as energy radiations raises from ground to atmosphere and will provide a better justification to the observed anomalies. The change in OLR data are dependable with changes in other atmospheric parameters [12]. Therefore, we analyze the OLR by collecting the data of 30 days from October 23, 2016 to November 22, 2016. We detect anomaly in OLR data beyond the limit bounds.

To analyze the anomalous TEC variations, we have chosen the operated ground stations around the epicenter within the seimogenic zone. Therefore, to measure the area size we use Dobrovolsky formula [13].

$$\rho = 10^{0.43M}\ km \qquad (1)$$

In Eq.(1), M indicates the magnitude of the EQ where ρ is radius of the region, which is in km.

To find the TEC variations, a running median upon the basis of quartile is performed. Inter-quartile range (IQR) uses the data of fifteen days before and after the main shock. Variations found on the bases of confidence interval of median$(\widetilde{X})$. Now for the limit bounds we use the following equations:

For Upper Bound (UB):

$$UB = \tilde{X} + IQR \qquad (2)$$

For Lower Bound (LB):

$$LB = \tilde{X} - IQR \qquad (3)$$

For detection of abnormality in the signal a confidence interval about 95% is declared, it is suggested that if the observed VTEC gets a higher peak than normal distribution is anomalous. Hence, we can visualize the abnormality in the signals by plotting the Eq. (2) and Eq. (3). In OLR the similar technique to construct limits bounds. Mean (μ) and Standard Deviation (σ) is used to construct limit bounds. In addition, we use Eq. (2) and Eq. (3) for OLR data to generate upper and lower bounds as well.

## III. Results and Discussion

In this paper, OLR and GPS-TEC readings are analyzed to forecast the EQ. Geomagnetic storms are also taken under consideration to check whether the variation shown by TEC from the storm or EQ. In order to avoid this controversy, we examined the OLR that will provide justification to the GPS-TEC anomalous measurements. After analyzing the data of TEC and OLR, we observe the anomaly exact 3 days prior to the EQ as shown in Fig. 1 and Fig 2. OLR measured the amount of energy released from lithosphere to upper atmosphere; therefore, it is considered an important constituent in forecasting the EQ. While

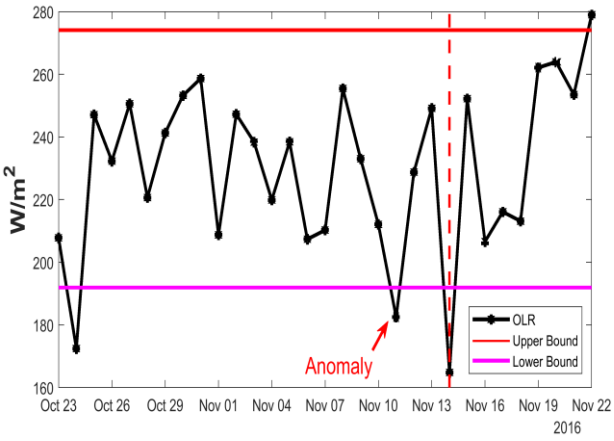


*Fig. 1. OLR readings for 7.8Mw EQ. OLR values also representing a fair anomaly 3 days before the EQ day. The solid line and a dot represent a day*

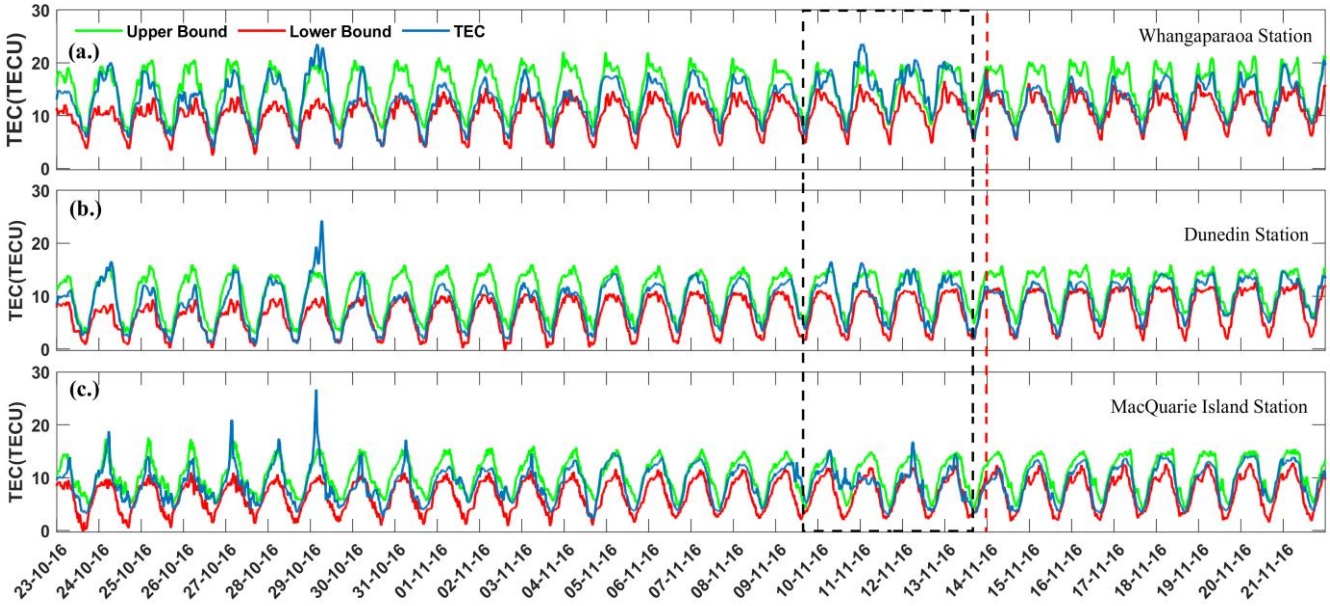


*Fig 2 Three different GPS stations are used to analyze the TEC variations. The stations are (a) Whangaparaoa Station. (b) Dunedin Station (c) MacQuarie Island Station respectively. The red dotted lines represent the EQ day and black dotted lines represents the anomalous TEC measurement measurements. blue line indicates the TEC, red line shows lower bound and green line shows upper limit bound.*

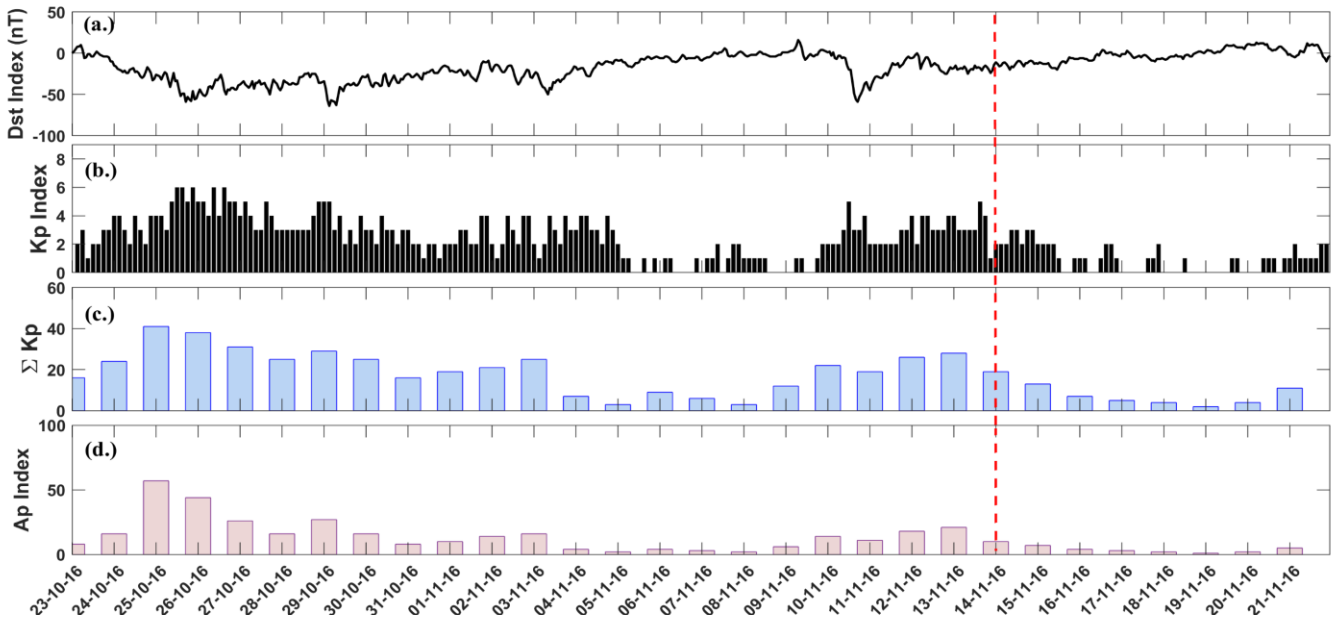


*Fig 3 (a) shows that on November 11, 2016 Dst is > -50 nT (b) shows the Kp index that is representing value <5 which is also indicates minimal signs of storm at November 11. (c) shows Σ Kp which is around 20 on November 11 which again shows minimal sign of geomagnetic storm*

observing anomalies that are related to OLR, we extracted data from (https://giovanni.gsfc.nasa.gov/giovanni/) for 30 days.

It is appropriate to measure the vulnerable ground radiations before EQ. In this case, we observed OLR Fig 2 shows clear variation occur around November 11, 2016 as TEC goes above upper bound on all three stations. Moreover, by comparing TEC with OLR readings we observe that, both shows anomalies around 3 days prior to the main shock.

readings for twenty days before and ten days after the EQ. After applying statistical methods, we detect discrepancy in OLR measurement on November 11, 2016.

Geomagnetic storms or solar storms are also causing abnormal over the global distribution TEC. As they cause temporal disturbance on the earth magnetosphere. According to (https://www.swpc.noaa.gov/phenomena/geomagnetic-storms) geomagnetic storms are changing the ionosphere

and further causing the disturbance in magnetosphere. With these geomagnetic storms, we can observe variances in TEC measurement. Moreover, while predicting EQ we to distinguish variations occurs on TEC is due to geomagnetic storms or due to EQ. Therefore, we examine Dst, Kp, Ap and Σ Kp indices. Data analyzed for the geomagnetic indices are from October 23, 2016 to November 21, 2016. If Dst index is <-50 nT or Kp > 4 we might consider the TEC anomaly due to solar storm not due to EQ. Fig 3 provides us a clear demonstration of geomagnetic storm indexes.

.

## IV. Conclusion

This study represents an ample amount of analysis on TEC and OLR measurements related to 7.8 $M_w$ EQ. Variations in TEC and OLR before the EQ signifies that the occurrence of such anomalies may be a forerunner of an impending EQ. Furthermore, the time series of OLR and GPS-TEC shows anomalies on the same day i.e., 3 days earlier to the EQ. Therefore, the observed anomalies can be a possible precursor to the Kaikoura EQ of 7.8$M_w$.

## Acknowledgment

The authors are very grateful to NASA, GIOVANNI, IONOLAB and Kyoto University for sharing the GPS-TEC, OLR and Geomagnetic Indices data.

## References

[1] U. Dogan, S. Ergintav, S.Skone, N. Arslan, and D. Oz, 2011. Monitoring of the ionosphere TEC variations during the 17th August 1999 Izmit earthquake using GPS data. Earth Planets Sp., 63 (12), 1183-1192. https://doi.org/10.5047/eps.2011.07.020

[2] D.Ouzounov et al, 2011. Atmosphere-ionosphere response to the M9 Tohoku earthquake revealed by the multi-instrument space-borne and ground observations: Preliminary results. Earthq. Sci., 24 (6), 557-564. https://doi.org/10.1007/s11589-011-0817-z

[3] M. Hasbi, M. A. Mohd Ali, and N. Misran, 2011 Ionospheric variations before some large earthquakes over Sumatra. Nat. Hazards Earth Syst. Sci., 11 (2), 597–611. https://doi.org/10.5194/nhess-11-597-2011

[4] X. Shi et al., 2017 How complex is the 2016 Mw 7.8 Kaikoura earthquake, South Island, New Zealand?, Sci. Bull., 62 (5), 309–311.https://doi.org/10.1016/j.scib.2017.01.033

[5] E. M. Ovalle, M. A. Bravo, C. U. Villalobos, and A. J. Foppiano, 2013. Maximum electron concentration and total electron content of the ionosphere over Concepción, Chile, prior to the 27 February 2010 earthquake. Adv. Sp. Res., 52(7), 1274–1288. https://doi.org/10.1016/j.asr.2013.07.005.

[6] M. A. Tariq, M. Shah, M. Hernández-Pajares, and T. Iqbal, 2019. Pre-earthquake ionospheric anomalies before three major earthquakes by GPS-TEC and GIM-TEC data during 2015–2017. Adv. Sp. Res., 63 (7), 2088–2099. https://doi.org/10.1016/j.asr.2018.12.028

[7] E. Şentürk, M. S Çepni, 2018. A statistical analysis of seismo-ionospheric TEC anomalies before 63 $M_w \geq 5.0$ earthquakes in Turkey during 2003–2016. Acta Geophysica., 66 (6), 1495–1507. https://doi.org/10.1007/s11600-018-0214-2.

[8] N. Venkatanathan, B. Kaapthick and C. Priyadharsini, 2013. OLR anomalies prior to big earthquakes (mw > 6.0) – a case study on earthquakes of India's neighboring region occurred during the year 2012. NCGT Journal, 1(3), 34-44. http://www.ncgtjournal.com/journals.html

[9] C.B. Erol, F. Arıkan, O. Arıkan, 2002. A New Technique for TEC Estimation", IGARSS 2002, IEEE International Geoscience and Remote Sensing Symposium, Toronto, Ontario, Kanada, CD. https://doi.org/10.1109/IGARSS.2002.1025915

[10] C.B. Erol, F. Arıkan, O. Arıkan, 2002. An Alternate Method for Local Vertical TEC Estimation, PIERS 2002, Progress in Electromagnetics Research Symposium, Cambridge, MA USA (ABD), 488

[11] J. Ahmed, M. Shah, W. A. Zafar, M. A. Amin, and T. Iqbal, 2018. Seismoionospheric anomalies associated with earthquakes from the analysis of the ionosonde data. J. Atmos. Solar-Terrestrial Phys., 179, 450–458. https://doi.org/10.1016/j.jastp.2018.10.004

[12] M. Shah, M. Khan, H. Ullah, S. Ali, 2017. Thermal anomalies prior to the 2015 Gorkha (Nepal) earthquake from MODIS land surface temperature and outgoing longwave radiations. Geodyn. Tectonophys., 8 (4), 923–932. https://doi.org/10.5800/GT-2018-9-1-0341

[13] Dobrovolsky, I.P., Zubkov, S.I., Miachkin, V.I., 1979. Estimation of the size of earthquake preparation zones. Pure Appl. Geophys. 117 (5), 1025–1044. https://doi.org/10.1007/BF00876083

# Detection and Parameter Estimation of Gravitational Waves

Sara Shakir
*Department of Space Science*
*Institute of Space Technology*
Islamabad 44000, Pakistan
sarashakir08@gmail.com

***Abstract*—In this research work, we discussed the detection and parameter estimation of the gravitational waves which are originated from astrophysical compact binaries such as Neutron star binaries, black hole binaries and super massive black hole captures, using Bayesian inference and Markov Chain Monte Carlo algorithms in the LISA data. We explore different gravitational wave sources and their parameters and modeling techniques used by LISA data analysis groups. We also discuss detector's operation and its response to gravitational wave sources. The waveform models used by ESA and NASA are developed using complicated Post-Newtonian approximations and numerical relativity concepts. Also, the LISA response function consists of time delay interferometry. So, working with realistic waveforms plus noise data is computationally very expensive and time consuming. Besides, the ESA data analysis group has not yet finalized the waveform models, noise sensitivity curves and detector design. Hence, a data generator, usually called LISA simulator is not yet available. Therefore, we use simple models with white and colored noises and develop a framework to extract a target signal buried in white noise and colored noise. These simple example models consist of simple sine wave signal over the background of white noise, two sine wave signals buried in the white noise and the chirping signal buried in the colored noise. We also observe the effect of parameter on the signal for example amplitude, frequency and phase.**

**When the amplitude of the signal is small then the strength of the signal is weak and when the value of amplitude is greater, the signal is more powerful as compared to the background noise. From the results we conclude that the Markov Chain Monte Carlo (MCMC) method is capable to extract the weakest signal from the noisy data accurately. This research will help us in the future study of gravitational waves. We will be able to deal with the realistic LISA data and signal models.**

***Keywords—Bayesian Inference, LISA Simulator, Chirping Signal, Post Newtonian***

## I. INTRODUCTION

In 1916, Albert Einstein predicted the existence of gravitational waves in his General theory of Relativity. The concept of space time has been established by using this theory.

When two massive accelerating objects such as super massive black holes, white dwarfs and neutron stars orbit each other about a common center of mass, they create distortions in the space time fabric and produce ripples outward (like a stone thrown into a pond and the ripples moves away from the source). These ripples are called Gravitational waves. The travelling speed of these waves is equal to the speed of light [1]. As the gravitational waves are energy carriers so they contain information regarding to sources by which these waves are generated such as neutron stars, black holes and events such as supernovae explosions. They can also help us in telling about the early universe processes.

In 1974, Russell Alan Hulse and Joseph Hooton Taylor discovered the binary pulsar PSR 1913+16. This radiating neutron star is known as PSR 1913+16 binary pulsar. This binary pulsar orbits another neutron star along their common center of mass and eventually forms the binary system. The discovery of PSR 1913+16 and the observations of its energy loss demonstrated the existence of gravitational waves [2]. This exact and straight forward measurement of gravitational radiations established the correctness of General relativity theory and opened a new window for scientists and astronomers to study the astronomical observations [3].

GWs are constantly passing from the Earth and interact with all particles coming in their way. These waves create a very tiny effect on the objects coming in its path of travelling. As the wave passes through the space time fabric, causes the stretch and squeeze into it in the direction which is perpendicular to the direction of the propagation of wave. Gravitational wave is a quadruple. It indicates that, the waveform can be divided into two orthogonal components that are offset by a rotation of 45°. Its effect can be observed by arranging the free falling particles in the form of a ring. As the wave passes through plane of the ring, the distance among the particles also changes [4].

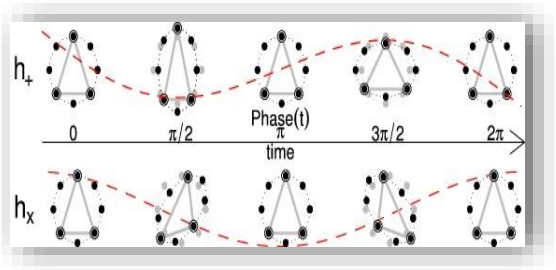


Fig 1: The effect of gravitational waves on free falling particles arranged in the ring form.

This change in the distance is known as strain amplitude. The strain amplitude is represented by (h). If the propagation direction of GWs is along the plane there will be no change in the particle motion. Gravitational waves take place in two states of polarization which are commonly known as cross (×) polarization and plus (+) polarization [5]. The upper panel in fig 1 shows the effect of plus polarization and lower panel describes the effect of

cross polarization in gravitational waves. The distortion is produced in the ring as the wave passes through it. Plus polarization changes the distance between the particles by first squeeze the ring along a horizontal direction and then along a vertical direction. The effect of polarization is same on the ring but with an inclination angle of 45°. There will be no distortion of the ring when the direction of waves is along the plane.

## I. SOURCES OF GRAVITATIONAL WAVES

At present time ground based detectors (LIGO, VIRGO) are observing signals from different gravitational waves sources. Some gravitational waves sources are given below in the following subsections.

### *A. Galactic Binaries*

Galactic binaries develop when two dense masses objects such as white dwarfs and neutron stars orbit each other [6]. Initially, both of the dense objects move in an elliptical orbit around the center of mass. With the passage of time, the two dense objects come closer to each other and at some particular point both objects rotates about center of mass at the same circular orbit. As the time increases, the orbit decays by forming a spiral. This is known as inspirals (in-spirals). As a result, the two masses emit radiations called gravitational radiation. The frequency of these radiations falls inside the LISA sensitivity band.

### *B. Mergers of Massive Binaries*

Massive binaries are identical to the galactic binaries and black hole binary systems. In this type of binary system, both objects are massive black holes having mass range of ($10^5 M_\odot$ - $10^9 M_\odot$) [7]. As the masses of these sources are very dense, still LISA detector is able to detect these sources at very large range of distances. These sources give information about the spins and the masses of both the members involved. By using information from these sources, it can be find out that how massive black hole binaries are formed and information about their merger rate.

### *C. Detectors*

The gravitational waves produced by the astrophysical objects are extremely far from the Earth and it becomes difficult for us to detect them. The change in the distance is extremely small so, it's very difficult to measure the strain amplitude. For this purpose, a very sensitive detector is required [8]. There are two types of detectors made for the detection of gravitational waves. One type is resonant mass detectors in which large masses are used [9]. They are cheaper, easy to build, contain a very narrow band width so they can only detect frequencies around the resonant frequency [10]. Another type is a laser interferometer detector which works on the principle of Michelson laser interferometer to measure the changes in the strain amplitude.

There are several detectors on Earth called ground-based detectors, which are working on the principle of Michelson interferometry for the detection of gravitational waves. There are several ground-based detectors such as GEO600 (Germany) [11], LIGO (Hanford, USA) and LIGO (Livingston, USA) [12], VIRGO (Italy) [13], and TAMA300 (Japan) [14]. These detectors are optional. Each detector consists of two long L- shaped arms which right angles to each other and 4 km from the central building [15].

Fig 2: Aerial photographs of the LIGO observatories at Hanford and Livingston, VIRGO at Italy and GEO at Germany. The lasers and optics are contained in the white and blue buildings. From the large corner building, evacuated beam tubes extend at right angles for 4Km in each direction (the full length of only one of the arms is seen in each photo); Credit: LIGO laboratory [14].

From the central station a laser beam is thrown to each arm and then the laser beam is bounced back by striking the mirrors which works as a free falling masses and suspended by a wire. A very small amount of change is occurred. This change in the distance is measured by the strain amplitude "$h = \Delta L / L$", whereas "$\Delta L$" is the change in the distance between masses and "L" is known as arm-length which is the distance between two masses. The sensitivity range of ground based detectors is 1-$10^4$ Hz [16].

A space based gravitational wave detector called the Laser Interferometer Spaced Antenna (LISA) is a joint project of NASA-ESA. It will be very sensitive detector as compared to ground based detectors because of no seismic noise. It is sensitive at frequencies between 0.03 mHZ and 0.1Hz [17]. It contains 5 million KM long arms which make an equilateral triangle which will move around the sun and 20° behind the Earth.

In future, LISA will be able to discover many astrophysical sources more clearly and accurately. The parameters such as mass, orientation of the source spin and luminosity distance can be measured more precisely.

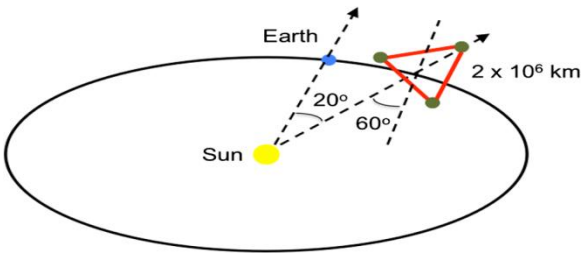


Fig 3: Constellation of LISA which is orbiting the sun. It contains 5 million KM long arms which make a triangle which will move around the sun and 20° behind the Earth. When a triangle is viewed from the sun, it rotates clock vise and inclined at an angle of 60° to the ecliptic plane [14].

## II. METHODS

### A. Bayesian Modeling

The perception of probability is the most important feature of the Bayesian methods, which characterizes the frequentist Bayesian approach and orthodox Bayesian approach.

Probability can be understood in terms of a common sense at this point. These (probabilities) are related among some type of occurrence and the calculus of probability is useful even as simplification's logic. It allows someone to progress and conclude the insufficient and deficient information state [18].

The Bayesian method therefore emerges in to the ordinary technique to bring up to date a circumstances and information's state which specifies a few observations and the data. Ultimately, it leads the way to distinctive and exceptional way to access and explain the statistical problems or complications.

The data analysis of Bayesian method begins among the description of statistical model considering the observables expressed as "y", which is based upon a few parameters of model like$\theta$. It can be accomplished through relying distribution process of sampling. Sampling distribution explains us that how observations take place by specified values of parameter, which is indicated by using the function of probability density$p(y|\theta)$. The establishment of model parameter $\theta$ then leads to the requirement of developing the information of priori regarding to parameters, once more, concerning to the probability distribution, the distribution of a prior$p(\theta)$. At this point the "probability distribution" can be penetrated like a probability distribution all over the space of parameter, affiliating the values of parameter among the probabilities.

One of the most fundamental applications of Bayesian method is the posterior distribution denoted as $p(\theta|y)$, which exhibit the more efficient and simplified information ("in the form of probability")
regarding to parameters which gives the observations y [19].

$$p(\theta|y) = \frac{p(\theta)p(y|\theta)}{p(y)} \quad (1)$$

How accurately to continue from this point and to build the way to utilize $p(\theta|y)$ relies upon the given specific problems. The posterior distribution $p(\theta|y)$ can be demonstrated graphically; either we can record a number of characterizing fundamental information. Assume that we are concern about the estimates of model parameters, at that moment the main issue is based on the nature of decision theory. The theory of decision basically desires a description of the loss function as well as a dedication for a perfect estimate $\theta$, and after that pursue through optimization above the space of a parameter [20]. If we look theoretically, the Bayesian method generally desires the posterior distribution integration which is spread through all the space of the parameter. Generally, this type of integration is difficult to perform systematically; as well as it involves functions which are as concerned to the entire data represented as "*y"*. Consequently, in order to solve required integrals, the integration which is based on Monte Carlo method is taken into account. A detailed precise requirement of the parameters of prior distribution is essential as well to obtain the beneficial conclusions. As prior distribution prior distribution desires to imitate the information of the prior regarding the parameters earlier than the data are taken into consideration. In order to collect and take the data into consideration, it is necessary for a prior distribution to reproduce the information of prior which is concerned to the parameters [21].

However, it is quite complicated to establish the prior and then provide the appropriate suggestion. Since, we can use a lot of methods to establish a prior. On the other hand, particularly in those problems in which every parameter is of a physical nature and the choices of logical options are normally very restricted. As a general rule, if there is an adequate verification regarding to the values of the parameter in the given data, then after getting the resultant posterior distribution it came to know that the prior distribution will be overweighed by the likelihood. Conversely, after the collection of data if there is not anything to be taught from it regarding to the parameters of the given model, then the state of posterior information will be approximately identical to the information about the prior, moreover as a result the specifications of the prior can be experienced astonishingly.

### B. Monte Carlo Integration

A Bayesian analysis usually needs the explanation of integrals related to the posterior distribution, which is normally characterized according to its density function denoted as$p(\theta|y)$. The density function of the posterior is generally well-known as a "normalizing constant", ever since the denominator value$p(y) = \int p(y|\theta)p(\theta)d\theta$ which does not depends upon$\theta$ and constant for the given value of *y*, is an additional mysterious integral. The basic technique to access the challenges in the given problem is originating a sample by using the posterior distribution, moreover estimates the required integrals through the averages of sample. This technique is known as Markov Chain Monte Carlo integration (MCMC) method.

### C. The Likelihood Function

As we know that gravitational waves exhibits the periodic nature, that is they repeat after a regular interval of time so they are recorded in the time domain but it is more convenient to evaluate the gravitational waves in the frequency domain as compared to analyze them in time domain because we can observe most significant characteristics in the frequency domain which we cannot observe otherwise. Some advantages of frequency domain are as follows:

- The signal can be reshaped easily
- Intensify the frequencies
- Cut off the redundant signals
- Separate the desired signal from the unrelated belongings etc.

During the analysis of Gravitational waves, when the data is in discrete form then after taking the Fourier transform of the observed data the likelihood function is given as

$$\mathcal{L}(\theta) = K \times exp\left[-2\int_0^{\infty} \frac{|\tilde{z}(f)-\tilde{s}(f,\theta)|^2}{S(f)} df\right] \quad (2)$$

When the data is in discrete form then the likelihood function will be;

$$\mathcal{L}(\theta) = K \times exp\left[-\frac{1}{v}\sum_{j=1}^{v} \frac{|\tilde{z}(f_j)-\tilde{s}(f_j,\theta)|^2}{S(f_j)}\right] \quad (3)$$

Since $v = [(N-1)/2]$, Fourier frequencies are represented as $f_j$, observables of FT are given by $\tilde{z}(f_j)$ and the model signal is denoted by $\tilde{s}(f_j, \theta)$. Whereas we assume that the one sided spectral density is known and is represented as $S_n(f_j)$ and the normalizing constant is K. In the beginning, we assume that the spectral density is not known then consider it finite. Then in this condition the alternative function of the likelihood is given as;

$$\mathcal{L}_{\omega}(\theta) = K \times exp\left[-\frac{1}{v}\sum_{j=1}^{v}\left(v \log\left(S(f_j;\theta)\right) + \frac{|\tilde{z}(f_j)-\tilde{s}(f_j,\theta)|^2}{S(f_j;\theta)}\right)\right] \quad (4)$$

The equation given above can be further simplified as

$$\mathcal{L}_{\omega}(\theta) = K \times exp\left[-\frac{1}{v}\sum_{j=1}^{v}\left(\sigma_{\epsilon}^2 v \log\left(S(f_j;\theta)\right) + \frac{|\tilde{z}(f_j)-\tilde{s}(f_j,\theta)|^2}{\sigma_{\epsilon}^2 S(f_j;\theta)}\right)\right] \quad (5)$$

This equation is known as Whittle's likelihood function [99, 100]. This Whittle likelihood function can be analyzed by maximizing $\sigma_{\epsilon}^2$.

$$\sigma_{\epsilon}^2 = -\frac{1}{v}\sum_{j=1}^{v} \frac{|\tilde{z}(f_j)-\tilde{s}(f_j,\theta)|^2}{S(f_j;\theta)} \quad (6)$$

However the value of $\sigma_{\epsilon}^2$ will results into the concentrated likelihood function

$$\mathcal{L}_{\omega c}(\theta,\sigma^2) = K \times exp\left[-\frac{1}{v}\left\{v log\left(\frac{1}{v}\sum_{j=1}^{v} \frac{|\tilde{z}(f_j)-\tilde{s}(f_j,\theta)|^2}{S(f_j;\theta)}\right) + \sum_{j=1}^{v}\left(\log\left(S(f_j;\theta)\right)\right)\right\}\right] \quad (7)$$

In this likelihood function, by utilizing the Discrete Fourier Transform properties, they suppose that the remaining fragments of DFT are generally complicated and normally distributed having zero mean value and $\sigma_{\epsilon}^2 S(f_j;\theta)$ (power spectrum). In the above equation we just maximized $\sigma_{\epsilon}^2$ and because $\hat{a}_j \sim N(0, 2/N\sigma_{\epsilon}^2)$ and $\hat{b}_j \sim N(0, 2/N\sigma_{\epsilon}^2)$ means they are normally distributed then as a result they also maximize their variances as well. Moreover, at the computation time of the likelihood function variance of noise can be successfully maximize all over the place and taking into account the squared amplitudes we do not need any further description for conditional posterior, whereas this is the advantage of the above likelihood function described in the equation written above.

However, if we think that the desired signal will be more powerful at some specific frequency range and we want to limit the computation of the likelihood function over a certain range of frequencies $[f_{j_L}, f_{j_U}]$ then the more workable and computationally well organized form of the likelihood function will be

$$\mathcal{L}_{\omega c}(\theta,\sigma^2) = K \times exp\left[-\frac{1}{v_c}\left\{v_c log\left(\frac{1}{v_c}\sum_{j=j_L}^{j_U} \frac{|\tilde{z}(f_j)-\tilde{s}(f_j,\theta)|^2}{S(f_j;\theta)}\right) - \sum_{j=j_L}^{j_U}\left(\log\left(S(f_j;\theta)\right)\right)\right\}\right] \quad (8)$$

Whereas; in the analyzed range of frequencies, the term $f_{j_L}$ represents the lower boundary and $f_{j_U}$ is expresses the upper boundary [22-23] and $v_c$ is the term that describes the total number of frequencies within certain range.

### *D. Signal to Noise Ratio*

There is a significant computation in the digital signal processing which evaluate the strength of the detected signal over the background noise which is commonly known as signal to noise ratio (SNR). It can be expressed as,

$$SNR = \sqrt{4\int_0^{\infty} \frac{|\tilde{s}(t,\theta)|^2}{S(f)} df} \quad (9)$$

For the frequencies at discrete level the SNR becomes:

$$SNR = \sqrt{\frac{4}{N}\sum_{j=1}^{v} \frac{|\tilde{s}(f_j,\theta)|^2}{S(f_j)}} \quad (10)$$

At the specific range of frequency $[f_{j_L}, f_{j_U}]$, it turn out to be

$$SNR = \sqrt{\frac{4}{N}\sum_{j=j_L}^{j_U} \frac{|\tilde{s}(f_j,\theta)|^2}{S(f_j)}} \quad (11)$$

If there are a lot of individual functions (for example K) of time series and we want to search our desired signal in its collective form then the combined signal to noise ratio will be the square root of the sum of their individual squared signal to noise ratios (SNRs) which can be expressed as;

$$SNR_K = \sqrt{\sum_{j=1}^{K} SNR_i^2} \quad (12)$$

Signal to noise ratio is very important in digital signal processing, it can give us information about the standard and condition of the observed signal and can also figure out the parameter estimation in the Markov Chain Monte Carlo method of estimation.

## III. RESULTS

As we know that data is a combination of signal and noise. In this research work, we don't have a realistic (simulated) data so we have an alternative way to generate an example by using the simplest cases. It is difficult for us to generate and process realistic LISA data because of computing hurdles and also the noise budget and LISA design is still under discussion among ESA gravitational wave groups. Therefore we will be working with simplistic examples for which we could generate data. We start from extracting a simple sinusoid buried in simple white noise and go towards more complex cases of chirping signals buried in colored noise. We will use the Bayesian and Markov Chain Monte Carlo method for the purpose.

*A. A Signal of Simple Sine Wave*

First of all we will deal with the easiest case to recover the sine wave from the background of white noise. There are three parameters which describes the features of sine wave, frequency (f), phase($\varphi$) and the amplitude (A). The model of the data will be in the form of [24].

$$y(t_i) = A\sin(2\pi f t_i + \varphi) + \varepsilon(t_i) \qquad (13)$$
$$i = 1, \ldots, N$$

Whereas, the term $A\sin(2\pi f t_i + \varphi)$ represents the signal and error is described by the term$\varepsilon(t_i)$. Since the error term is normally distributed $\varepsilon(t_i) \sim N(0, \sigma^2)$. In this simplified model the amplitude of the noise is dependent upon the value of $\sigma$ that is$A_{noise} \propto \sigma$. If the amplitude of the noise is extremely greater as compared to the amplitude of the signal i.e$A_{noise} \gg A_{signal}$, then it will be difficult for us to detect and extract the target signal. The data spectrum of the signal plus noise model is given below.

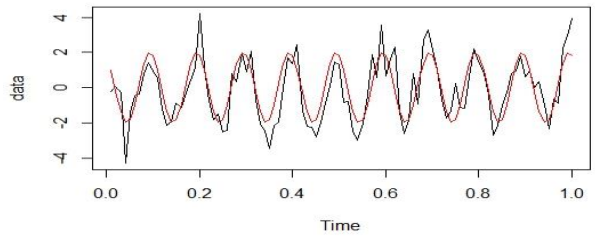


Fig 4: Data spectrum of the simple sine wave signal plus white noise

In the data spectrum we can see that the simple signal sine wave is mixed with white noise and our task is to extract the targeted signal from the data.

In our example, the value of true parameters of signal is $f = 10,\ \varphi = 2,\ A = 2.0$ moreover $\varepsilon(t_i) \sim N(0,\ 1.0)$. We can generate data by taking the time duration of one second at the discrete time points (N=100) along with the time interval $\Delta T = 0.01$. The dots represents the samples.

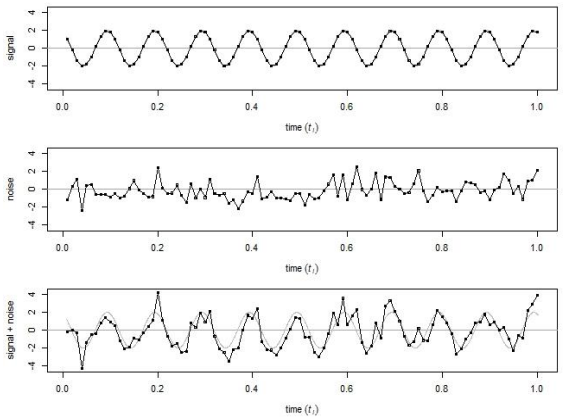


Fig 5: One sinusoidal wave, white noise and signal plus noise data

We have plotted the data of signal, noise data and signal plus noise data against time in the figure 4 for sigma (noise) 1.0. As the Bayesian and MCMC method has been used to extract the targeted signal from the noisy data with the information of prior$f \sim U[0,\ 50],\ \varphi \sim U[0,\ 2\pi]$and $A \sim U[0,\ 1500]$. Although we have used 150000 total iterations and skipped every $20^{th}$ value to get the results shown below in figure 4.3. In the consequences, we can easily observe that for all the parameters (phase, frequency and amplitude) the MCMC is moving randomly in the start until it gets the desired value or catch the true signal. The parameters of the signals are effectively spotted for the iterations which are below than 2000. So we easily reconstructed our desired signal from the noise. The trace plots of the parameters of the signal obtained for sigma 1.0 is given in fig 5. Then we will consider the nature of amplitude of the noise and discover the outcomes when the noise is extremely high. For this purpose we simply increased $\sigma$ sigma from 1.0 to 4.0 but the values of the parameters of signals remain unchanged. The results for the different values of the sigma are given below.

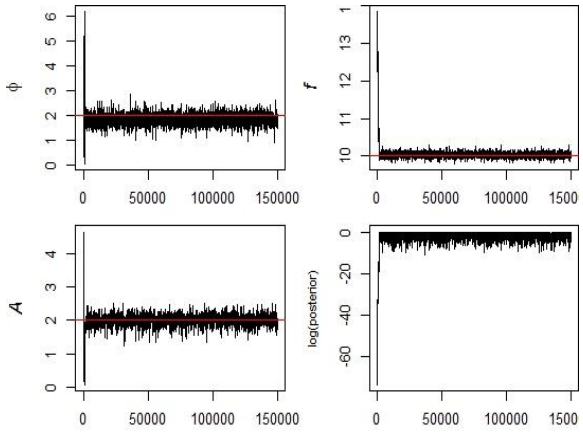


Fig 6: Trace plots for σ =1.0 and for three parameters (f, φ and A)

In figure 6, we can see that MCMC sampler quickly picked the targeted signal from the data in less than 5000 iterations because signal is more powerful as compared to noise.

- *For σ =4.0*

When the amplitude of noise is greater than amplitude of signal means the strength of noise is much greater than signal then MCMC sampler moves randomly to find out the true parameter values. The trace plots for σ =4.0 is given in the figure 7.

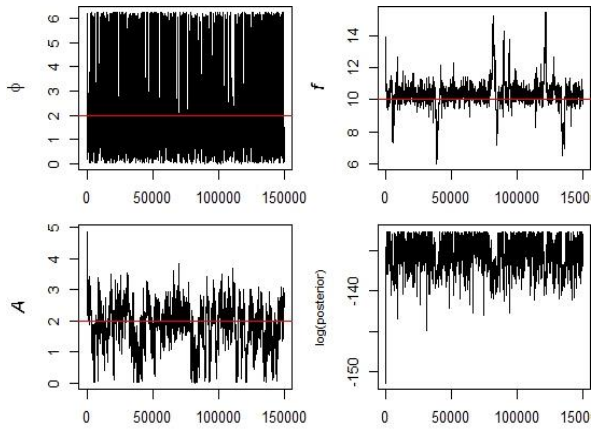


Fig 7: Trace plots for σ=4.0 and for three parameters (f, φ and A)

We can conclude that when sigma is smaller the MCMC can find out the desired signal easily and when we increased the value of noise then MCMC moves more randomly but still capable to detect the targeted signal but

with a difficulty and in the large period of time as compared to the small value of sigma.

- *Posterior density:*

Figure 8 and 9 illustrates the posterior densities of the both values of sigma (1.0 and 4.0) for the three parameters of the signal. In both posterior density graphs, we can see that the three parameters show the value of mode closer to the true parameter values. The gray line indicates the true value of the parameter. As we know that there are other parameters of the sources also like mass, spin, orientation and distance but we are only explaining the simple model of the sine wave in which no other parameters are given except amplitude, phase and frequency with some numerical values.

- *For* $\sigma = 1.0$

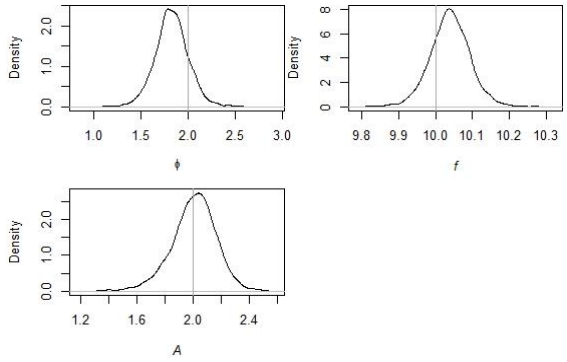


Fig 8: Posterior density plot for σ=1.0 and for three parameters (f, φ and A)

- *For* $\sigma = 4.0$

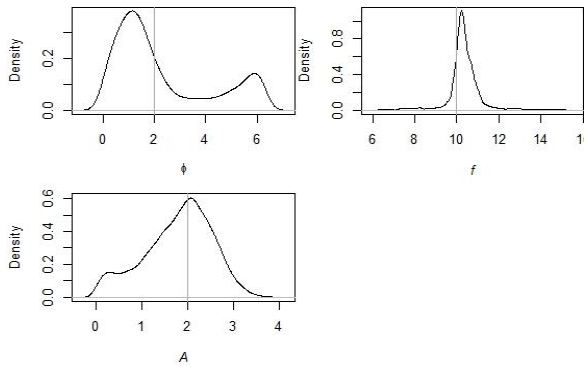


Fig 9: Posterior density plot for σ=4.0 and for three parameters (f, φ and A)

TABLE I
TRUE PARAMETER VALUES RECOVERED FROM ONE SIGNAL PLUS WHITE NOISE DATA

| Parameters | Mean | Std. Deviation | 95% BCI | True Values |
|---|---|---|---|---|
| Phase | 2.281 | 1.896 | (0.132, 6.158) | 2 |
| Amplitude | 1.793 | 0.736 | (0.191, 3.028) | 2 |
| Frequency | 10.366 | 0.905 | (8.118, 12.734) | 10 |

## *B. Two Signals of Simple Sine Wave*

The most familiar sources of gravitational waves are compact binaries, super massive black hole binaries, extreme mass ratio inspirals and a lot of other astrophysical objects. So there are millions signals which are originating at the same time from millions of sources, for example thousands of signals can be emitted from same system like CBCs. Several systems contains similar characteristics or parameter values in which masses, phases, frequencies, distances and many other parameter values are included, no matter where they are placed in the universe.

The detection, parameter estimation and the separation of two signals emitted from two systems is very challenging task. When two signals superpose each other they create confusion noise and extreme supervision is required for the extraction of signal.

In our example we will simply inject another similar signal having amplitude $A = 4$ and the rest of the values of the parameters will be same because amplitude is dependent upon the mass of the source, distance and the location of the source related to the plane of the detector. The data spectrum of two signals plus white noise has been created and given in fig 10.

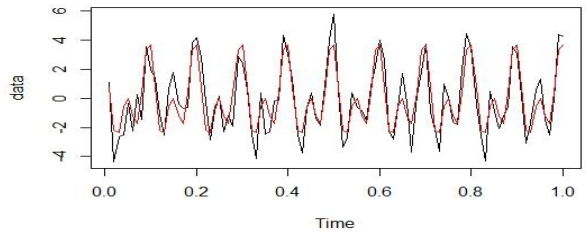


Fig 10: Data spectrum of the two simple sine waves signal plus white noise

Here the data is the combination of two simple sine wave signals and white noise. When the two signals are of same frequency and phase (parameter values) but the amplitude of both signals is different than it is extremely difficult for us to extract back our targeted signal. We have plotted data of two sinusoidal signals, data of white noise and signals plus noise data and repeated our previous MCMC strategy to extract the second signal from the noisy data.

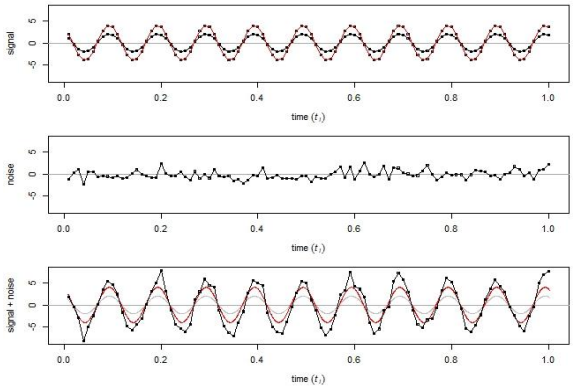


Fig 11: Two sinusoidal waves, white noise and signal plus noise data

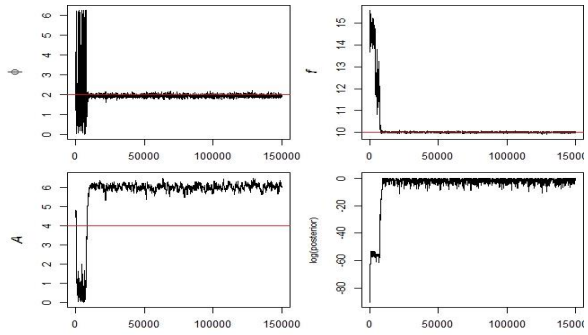


Fig 12: Trace plot for σ=1.0 and for three parameters (f, φ and A=4)

Here, the value of true parameters of the second signal is $f = 10,\ \varphi = 2,\ A = 4.0$ and the noise is normally distributed as we have done before $\varepsilon(t_i) \sim N(0,\ 1.0)$.
In the trace plots of the figure 12, there are two signals buried in white noise. We can see from the results that MCMC found its true parameter values in 10000 iterations. As the value of noise is smaller as compared to signals but still MCMC took some time to detect the signal because data consists of more than one signal plus noise.

- *For* $\sigma = 4.0$

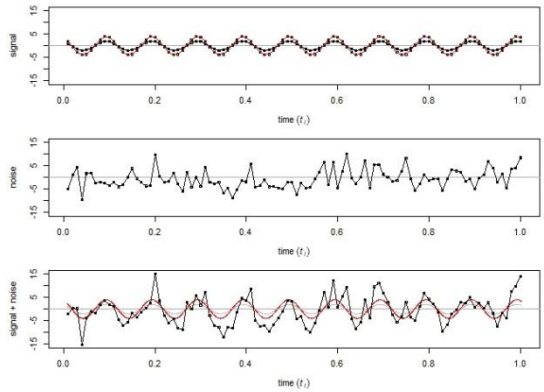


Fig 13: Two sinusoidal waves, white noise and signal plus noise data

In figure 13 it can be seen that when we increased the value of sigma (4.0) the amplitude of the noise increases and it becomes difficult for the sampler to extract the required signal which is buried in another signal plus noise.

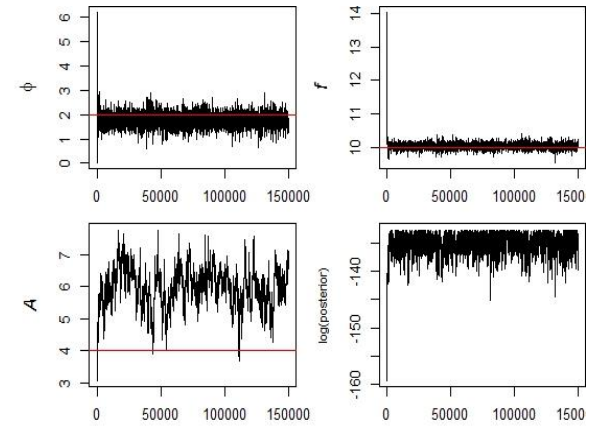


Fig 14: Trace plot for σ=4.0 and for three parameters (f, φ and A=4)

As a result it can be seen that if we have a lot of signals in a single data then MCMC can easily extract the targeted signal but it takes more number of iterations to find the true parameter values as compared to single data. In the trace plot of fig 4.10 and 14 the parameters of the signal are spotted again at less than 2000 iterations.

- *Posterior density:*

We also draw the posterior densities for both values of sigma (1.0 and 4.0). In the posterior density graph of second signal, we can see that mode is closer to real values of the parameter. For amplitude, mode is at the highest value of the both parameter that is 6. The posterior density graphs are given in figure 15 and 16. Table 2 contains the numerical results for this example.

- *For* $\sigma = 1.0$

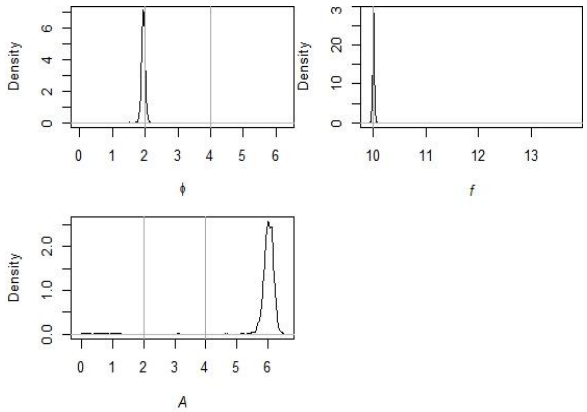


Fig 15: Posterior density plot for σ=1.0 and for three parameters (f, φ and A=4)

- *For* $\sigma = 4.0$*:*

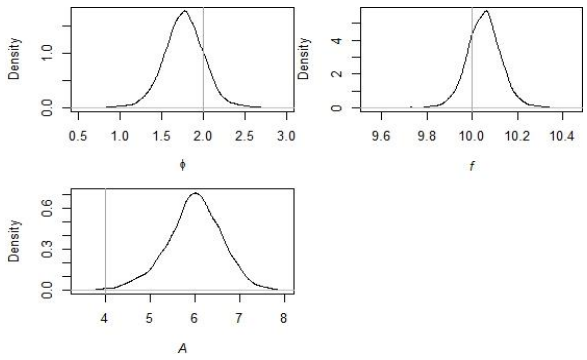


Fig 16: Posterior density plot for σ = 4.0 and for three parameters (f, φ and A = 4)

From figure 16, it is clear that when the noise level is increased the posterior densities becomes more spread out meaning that there is a greater uncertainty in the estimated values of the parameters.

TABLE II
TRUE PARAMETER VALUES RECOVERED FROM TWO SIGNALS PLUS WHITE NOISE DATA

| Parameters | Mean | Std. Deviation | 95% BCI | True Values |
|---|---|---|---|---|

| | | | | |
|---|---|---|---|---|
| Phase | 1.97692 | 0.384 | (1.815, 2.091) | 2, 2 |
| Amplitude | 5.872 | 0.846 | (3.108, 6.282) | 2, 4 |
| Frequency | 10.061 | 0.332 | (9.979, 10.179) | 10, 15 |

### *C. An Example of Chirp signal*

Now we will consider a chirp signal as an example. The frequency increases instantaneously in the chirp signal with the time. According to astrophysics, most of the binaries are known as chirping binaries. Although our example does not represents the genuine binary system. The chirping signal in our model contains the increasing frequency and increasing amplitude too with respect to time. Like our previous example of simple sine wave we generated 100 points of time series. In the chirp signal model the time series points are generated by using the deterministic component $s(t,\ \theta)$.
Whereas,

$$s(t_i, \theta) = A\sin\left(2\pi\left(f + \dot{f}t_i\right)t_i + \varphi\right) \qquad (14)$$

The parameters in the chirp signal are identical to the previous one but there exist an additional parameter known as frequency derivative and represented as$\dot{f}$. Here, the information of prior is$f \sim U[0,\ 50],\ \ \varphi \sim U[0,\ 2\pi]$ and $A \sim U[0,\ 1500]$ and we have used the colored noise model which is recognized as realistic astrophysical colored noise. Colored noise exhibits non-stationarity which in turn introduces more uncertainty into data. In our example an AR (1) noise along with uniform innovations is used denoted by $(u)$ having interval$-0.5\sqrt{12}\sigma,\ \ 0.5\sqrt{12}\sigma$. The model of the noise is given as follows [25].

$$\varepsilon(t_i) = \varphi\varepsilon(t_{i-1}) + u \qquad (15)$$

The data spectrum in which chirp signal and noise are mixed is obtained in the form given in the graph given below:

.

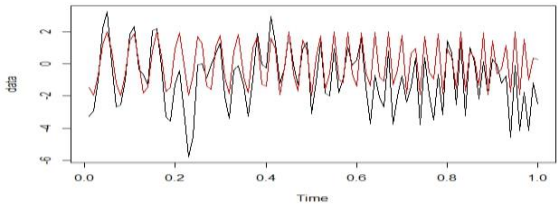


Fig 17: A chirping signal plus colored noise

In the data spectrum we can see that the chirp signal is mixed with the noise (colored) and it is difficult for us to extract the signal from this colored noise.

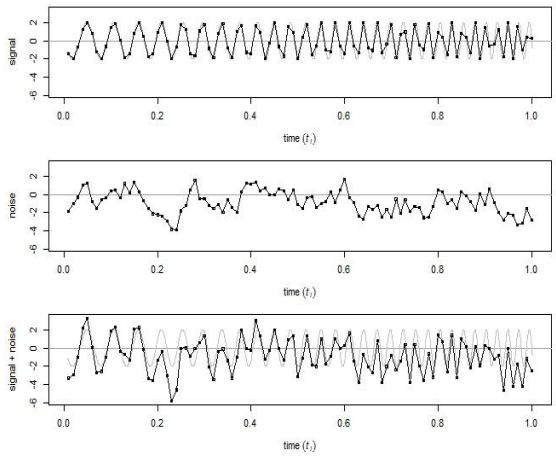


Fig 18: Chirping signal, colored noise and signal plus noise data

We have plotted the data of chirp signal, data of colored noise and the chirp signal plus noise data in the figure 18. We repeated the same procedure of MCMC method to extract back our desired signal buried in the noise. MCMC can run by taking the start at random and will give the results shown in figure 19. We see that the signal has been successfully detected after fifty thousand iterations.

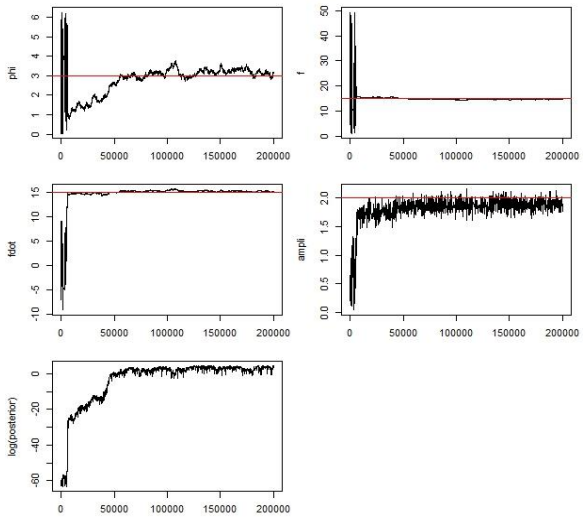


Fig 19: Trace plot for σ=1.0 and for four parameters (f, φ, A,$\dot{f}$)

In the trace plots for the chirp signal the value of true parameter is $\varphi = 3,\ f = 15,\ \dot{f} = 15$ and$A = 2$. We estimate the parameter values for 200000 iterations over sigma 1.0.

- *Posterior Density:*

In the posterior density plot over sigma 1.0 and for amplitude 2, the mode is at the highest value and the gray line shows the real value of the parameter. We see that all the parameters are well inside the kernel density range. For the numerical results please refer to table 3.

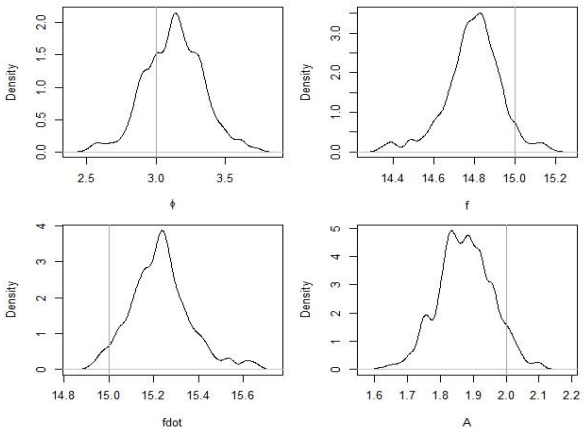


Fig 20: Posterior density plot for σ = 1.0 and for three parameters (f, φ, f˙ and A=2)

TABLE III
TRUE PARAMETER VALUES RECOVERED FROM CHIRP SIGNAL PLUS COLORED NOISE DATA

| Parameters | Mean | Std. Deviation | 95% BCI | True Values |
|---|---|---|---|---|
| Phase | 3.130 | 0.209 | (2.693, 3.556) | 3 |
| Amplitude | 1.875 | 0.082 | (1.712, 2.036) | 2 |
| Frequency | 14.794 | 0.137 | (14.467, 15.060) | 15 |
| Frequency Derivative | 15.230 | 0.133 | (14.981, 15.548) | 15 |

- *Playing with amplitude:*

When we decrease the value of signal amplitude from 2.0 to 1.0, the signal becomes weaker. The detection of this weak signal is quite difficult task as it decreases the signal to noise ratio. But still the MCMC is capable to detect the true signal but after a few thousands more iterations. The trace plots and the density plots for the signal with amplitude 1.0 are given in figure 4.19 and 4.20. The values of the true parameters are $\varphi = 3,\ f = 15,\ \dot{f} = 15$ and$A = 1$.

We estimate these parameter values for 200000 iterations. We see that for weak amplitudes some of the parameters may take long time to achieve stationarity and reach the true mode. Phase (phi) here is an example here as its chain has found its true value 130,000 iterations (see figure 21)

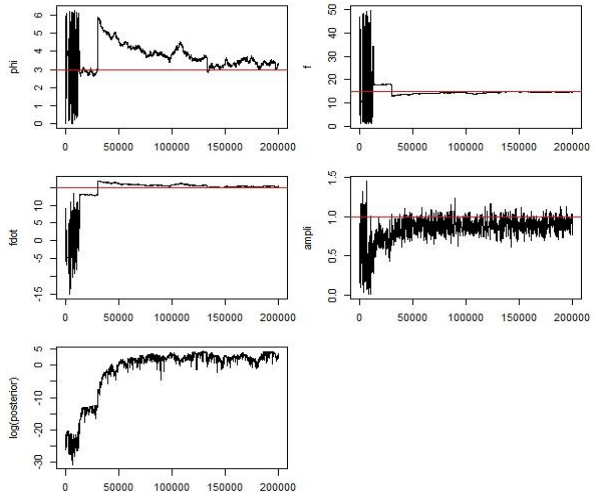


Fig 21: Trace plot for σ=1.0 and for four parameters (f, φ, f˙, A=1.0)

- *Posterior Density:*

In the posterior density plot over sigma 1.0 and for amplitude 1, there are more values of the mode because the value of amplitude is small. The posterior densities are given in fig 22. We can see the true signal parameters are still within the range of their estimated kernel densities.

These estimators can be refined by running the MCMC sampler for a little more time so that the chains reach their true convergence points.

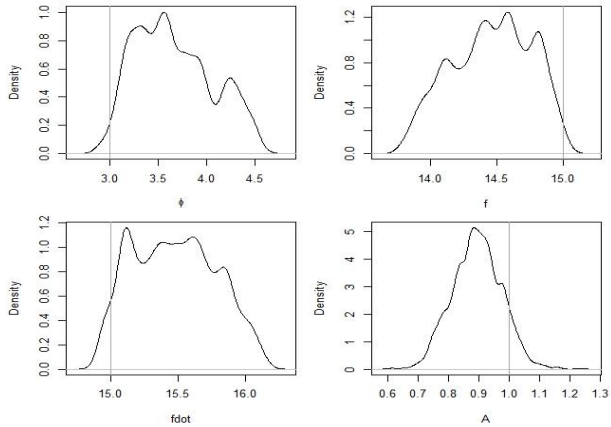


Fig 22: Posterior density plot for $\sigma$=1.0 and for three parameters (f, φ, $\dot{f}$ and A=1)

- *Signal to Noise Ratio:*

Signal to noise ratio is used to evaluate the strength of the signal over the back ground noise. When we increase the amplitude (2.0), the strength of the signal is powerful as compared to back ground noise but when we decrease the value of amplitude (1.0) the strength of the signal is weak as compared to noise. To extract the weaker signal from powerful noise background is not an easy task but we are able to find the signal by using the method of MCMC which we have explained earlier.

The signal to noise power spectrum density for different values of amplitude has been shown in the fig given below. The strength of the noise is represented by red curve and the strength of the signal is represented by green signal.

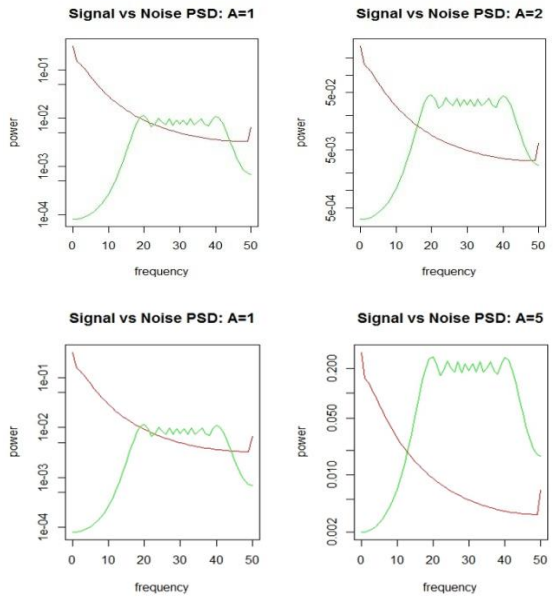


Fig 23: Signal vs. Noise PSD for amplitude 1, 2 and 5

From the figure 23, we can conclude that for the value of amplitude 2 the signal is powerful and the value of signal to noise ratio is greater. It is easy to detect this signal. For the value of amplitude 1 the signal is weaker as the signal to noise ratio is smaller and it is difficult to detect this signal.

From table 4 we can easily understand the effect of amplitude on the signal and noise. When the amplitude is smallest i.e. 1.0, the signal to noise ratio is 9.85959 which shows that the signal is weaker and for the value amplitude (5.0), the strength of the signal is much greater as compared to the background noise. This effect of amplitude has been shown in fig 23.

TABLE IV
COMPARISON OF AMPLITUDE AND SIGNAL TO NOISE RATIO

| Amplitude | SNR |
|---|---|
| 1 | 9.85959 |
| 2 | 19.71918 |
| 3 | 29.57877 |
| 4 | 39.43836 |
| 5 | 49.29795 |

## IV. CONCLUSION

We applied the Bayesian and Markov Chain Monte Carlo (MCMC) methods in order to solve the problems of signal detection and the parameter estimation of the gravitational waves. Currently we do not have realistic simulated data of the gravitational waves so we have considered some example of the signal models. These signal models are easy to examine. Although they are not similar to the real signals of the gravitational waves but we can conclude that they are fundamentally similar to each other. But a real model comprises more detailed information about the incoming waveform parameters for example, noises, response of the detector, orientation, data nature etc.

The other important thing is the noise amplitude. It affects the efficiency of MCMC and made the extraction of the signals more complicated and time consuming. However, it is easy to deal with white noise but modeling of the colored noise is still a challenging task because of unknown astronomical sources.

When there is only one signal in the data, we can easily extract it from the noisy data but we can also have more than one signal because the astrophysical objects can produce a lot of signals at the same time. So we also examined the source data with two signals with different parameter values (frequency, amplitude and phase). We also observed the effect of increasing and decreasing of amplitude upon the signal and on the noise. From the results we came to know that when the amplitude of the signal is greater than the signal to noise ratio increases and the signal is more powerful as compared to the back ground noise and when the value of amplitude is smaller the signal to noise ratio is also smaller which we have already discussed in the table .4.

At the end we can conclude that we have learned how statistics plays an important role in exploring the detection and parameter estimation of gravitational waves. Currently, we don't have realistic simulated data and models but by going through the same way we will be able to deal with the real models of the gravitational waves along with instrument and background noises in future.

## V. ACKNOWLEDGEMENT

I would like to pay my highest gratitude to my supervisor Dr. Asad Ali, whose encouragement remained a great motivational force for me.

## REFERENCES

[1] A. Królak, M. Patil. "The First Detection of Gravitational Waves".Universe, 3(3), 59. Aug. 2, 2017.
[2] B.P. Abbott, R. Abbott, T.D. Abbott, M.R. Abernathy."First Search for Gravitational Waves from Known Pulsars with Advanced LIGO." Astrophys.J.839 12. Nov. 13, 2017.
[3] B.P. Abbott. "Observation of Gravitational Waves from a Binary Black Hole Merger". 2016.
[4] [4] E. D. Feigelson. "Statistics in Astronomy". New York. 1988.
[5] A. Ali. "Bayesian Inference on EMRI Signals in LISA Data."The University of Auckland, New Zealand. 2011.

[6] D.A. Shaddock. “An overview of the Laser Interferometer Space Antenna.” Publ.Astron.Soc.Austral.26:128-132, Sep. 3, 2009.
[7] F. Viviana. “Resonant-mass detectors: status and perspectives.” Classical and Quantum Gravity, vol. 21, pp. 5, Feb. 2004.
[8] O.D. Aguiar. “The Past, Present and Future of the Resonant-Mass Gravitational Wave Detectors.” Sep. 6, 2010.
[9] S. Hild. “The LIGO Scientific Collaboration: The Status of GEO600.” Classical and Quantum Gravity, vol. 19, pp. 10, Jan. 2006.
[10] D. Sigg. “Commissioning of LIGO Detectors.” Classical and Quantum Gravity,vol. 20, pp. 9, Feb. 2007.
[11] F. Acernese. “The VIRGO Collaboration: Status of VIRGO.” Classical and Quantum Gravity, vol. 21, pp. 16, Feb. 2001.[12] R. Takahashi. “The TAMA Collaboration: Status of TAMA300. Classical and Quantum Gravity, vol. 21, pp. 20, Feb. 2004.
[12] M.V. Sluys, R. Christensen, C. Kalogera, V. Raymond, I. Mandel. “Parameter Estimation for Signals from Compact Binary Inspirals Injected into LIGO Data.”May. 2009.
[13] P.B. Lerner. “Entangled Path Interferometer Simpler, Faster than LISA.” July 5, 2011.
[14] C.J. Moore, R.H. Cole, C.P.L. Berry. “Gravitational Wave Sensitivity Curves.” Dec. 11, 2014.
[15] M.V. Sluys. “Gravitational Waves from Compact Binaries.” Aug. 5, 2011.
[16] P. Pani. “Binary Pulsars as Dark Matter Probes.” Dec. 3, 2015.
[17] Brink, S.B. Cenko, T. Jaeger, S. Kumar, T.J. Moriya, K. Nomoto, D.A. Perley, I. Shivvers, N. Smith. “A Surge of Light at the Birth of a Supernova.” Feb. 22, 2018.
[18] F. Huang, X.F. Wang, G. Hosseinzadeh, P.J. Brown, J. Mo, J.J. Zhang, K.C. Zhang.“A Type II-P Supernova with A Signature of Shock Breakout from
[19] Explosion of A Massive Red Supergiant.” Jan. 8, 2018.
[20] A. Caputo, J. Zavala, D. Blas. “Binary Pulsars as Probes of a Galactic Dark Matter Disk.”Dec. 12, 2017.
[21] D.L. Nacir, D. Blas. “Ultra Light Dark Matter Resonates with Binary Pulsars.” Dec. 20, 2016.
[22] S. Nissanke, M. Vallisneri, G. Nelemans, A.T. Prince, “Gravitational Wave Emission from Compact Galactic Binaries.” Oct. 10, 2012.
[23] B. Allen. “The stochastic gravity-wave background: sources and detection,” in Relativistic Gravitation and Gravitational Radiation: Proceedings of the Les Houches School of Physics, pp. 373-418. 1997.
[24] E. Berti, V. Cardoso, C.M. Will. “Gravitational Wave Spectroscopy of Massive Black Holes with the Space Interferometer LISA.” Phys. Rev. D, 73(6):064030. 2006.
[25] S.A. Hughes. “A Brief Survey of LISA Sources and Science.”Sep. 10, 2006.

# Delineation Of Major Urban Features Of Lahore Using Microwave Remote Sensing

Nimra Ashfaq
*Department of Space Science*
*University of the Punjab*
Lahore, Pakistan
nimraashfaq77@gmail.com

Shahid Parvez
*Department of Space Science*
*University of the Punjab*
Lahore, Pakistan
shahid.spsc@pu.edu.pk

***Abstract*—In the present study, exploitation of microwave remote sensing techniques was carried out for the identification of major urban features of the mega city Lahore (Pakistan). For this purpose, microwave images of Lahore of two dates (2015 and 2018) acquired by the Sentinel-1A satellite, were analyzed and major features of Lahore were identified. Major changes were detected in these urban features of Lahore during the study period. The results were also compared with the corresponding images of Google Earth. Changes occurred in these major urban features of Lahore were also detected using the temporal images of Sentinel-1A. The current study reveals that freely available microwave images of Sentinel-1A satellite along with SNAP software couple with optical images of Google Earth are quite useful for studies related to urban environment.**

***Keywords— Microwave Remote Sensing, Sentinel-1A, Urban features, Lahore.***

## I. INTRODUCTION

It is necessary to delineate urban features due to an increasing demand for the urban land use [1]. Due to their typically complex structures and irregular spatial arrangements of the artificial and natural land cover in urban area, it is difficult or challenging to delineate and monitor them [2]. In old times information of urban areas was taken from a very high resolution photograph on the basis of visual interpretation [3]. This method was not very efficient because of the lack of information content and widespread availability, expensive and time taking. These deficiencies open up an alternative method of getting information about the Earth through active microwave Synthetic Aperture Radar (SAR) sensor [4]. Microwave remote sensing is new technique and has stand-alone applications because microwave sensors have longer wavelengths varying from less than one centimeter to one meter [5].

Urban areas are composed of varied materials (concrete, asphalt, metal, plastic, glass, water, grass, shrubs, trees and soil) prescribed by humans in complex ways to build houses, transportation schemes, services, commercial constructions and entertaining landscapes [6]. A frequent and reliable delineation of urban footprint of Lahore is a basic requirement for the analysis and understanding of the urban dynamic of Lahore as urbanization is one of the most tenacious universal challenges[7].

### A. Study Area

The study area for this research is Lahore and is shown in Figure 1. Lahore is the megacity and the capital of the Punjab province. Average elevation of Lahore is 217 meters above mean sea level[8]. Location of Lahore is between 74˚1′1″E to 74˚38′10″E longitude and from 31˚15′ to 31˚44′2″N latitude[9]. In terms of population and urbanization Lahore is the second largest metropolitan city of Pakistan[10]. Lahore has gone through quick urbanization, infrastructure and social alterations.

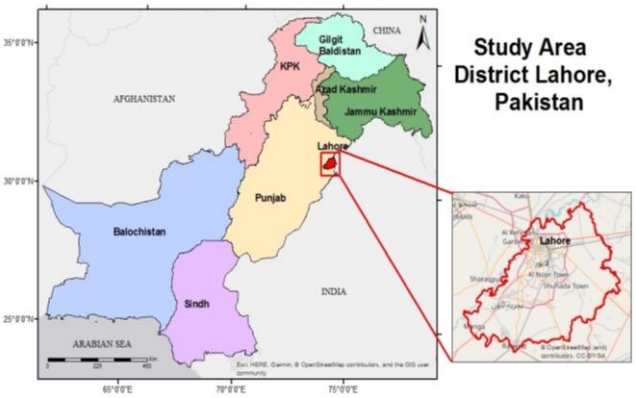


Figure 1: Location Map of study Area, Lahore

### B. Study Objectives

The main focus of the study is to identify urban features of Lahore using Sentinel-1A images [11]. Urban growth in the Lahore city is occurring very rapidly so with the help of the microwave remote sensing the important information is gathered about the urbanization in Lahore. This study helps us to know the changes occur in Lahore, Pakistan with respect to time.

Following are the main objectives of the study:

- To investigate the potential of microwave remote sensing for identifying and analyzing major urban features (airport, railway-station, major buildings, parks, canal, trees, and water bodies etc.) of mega city Lahore using level-1 products of Sentinel-1A images both in GRD and SLC modes [12].
- To detect major changes in urban footprint as well as features of Lahore using temporal images of Sentinel-1A.

- Comparing the results drawn from Sentinel-1A microwave images of Lahore with the corresponding optical images of Google Earth.
- To explore the potential of SNAP (Sentinel Application Platform) software for processing of Sentinel-1A microwave images for urban area [13].

## II. Data Analysis

Data used in this study is the level-1 SLC and GRD of Sentinel-1A images of Lahore of 2015 and 2018. These images were collected in Interferometric Wide Swath [14]. This mode allows combination of a large swath width (250 km) with a moderate geometric resolution of 10m [15].

The uncorrected images of Sentinel-1A are preprocessed by SNAP. The pre-processing flow chart is shown in Figure 2.

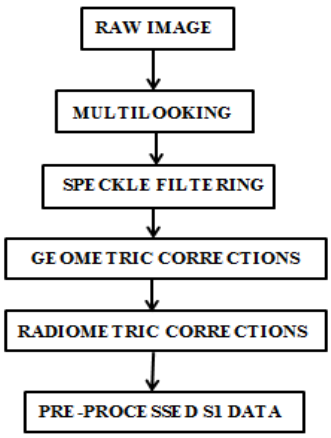


Figure 2: Flow chart for pre-processing of Sentinel-1A images

### A. *Preprocessing of GRD(VV) images*

Ground Range detected (GRD) is used, which is radiometrically corrected data and resampled to the ground range by an earth ellipsoid model this means already some preprocessing is done on it. In this data the phase information is absent. GRD (VV) data has square pixel resolutions and is good for urban footprint mapping because we do not need phase information whereas we need geo-referenced image to validate our urban information. Further processing is employed by the SNAP software to carry out the resultant major urban features of Lahore. Corrected Sentinel-1A GRD image of Lahore is shown in Figure 3.

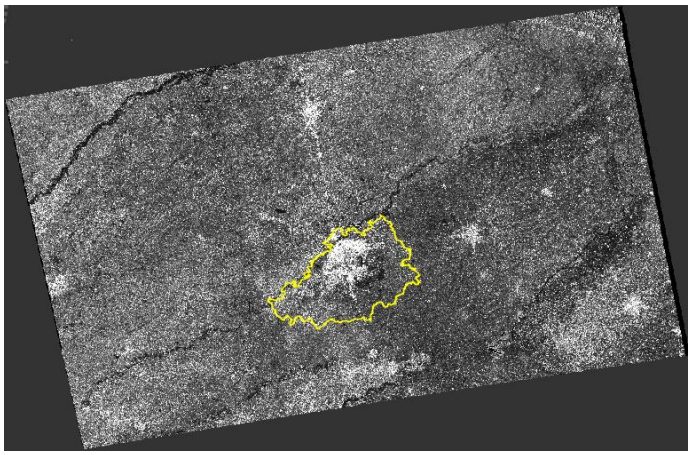

Figure 3: Terrain corrected Sentinel-1A GRD (VV) image of 24 Jan 2018 showing urban footprint of Lahore.

### B. *Preprocessing of SLC (VV) images*

Single Look complex (SLC) (VV) data is geo-referenced using attitude data from the satellite. SLC product is an image with slant range. The phase information is present in it. SLC products have single look in each dimension and are complex because of the phase information. SLC products are not so efficient for the spatial study of urban footprint mapping because we are not dealing with the heights and DEM of the features. Corrected Sentinel-1A SLC image of Lahore is shown in Figure 4.

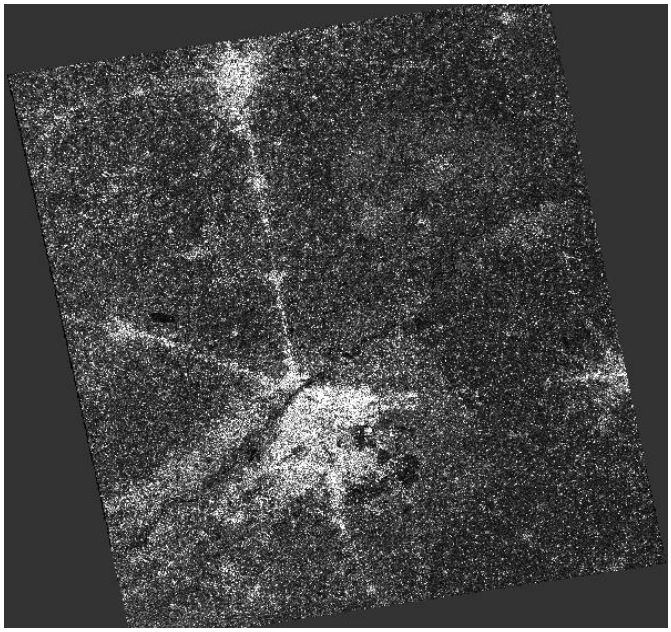

Figure 4: Terrain corrected Sentinel-1A SLC (VV) image of13 March 2018 showing urban footprint of Lahore.

### C. *Identification of Major Urban Features of Lahore in GRD (VV) images*

Identification of the major urban features in Sentinel-1A GRD image of 24 January 2018 are shown in Figure 5.

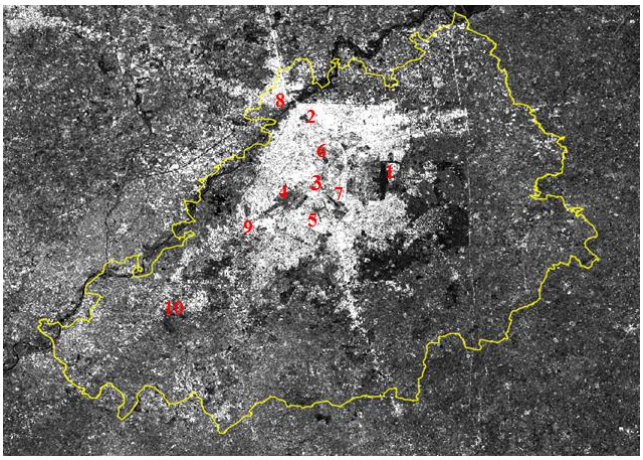


Figure 5: Urban footprint of Lahore and identification of major features

Major urban features which were delineated from the Sentinel-1A image are 1: Allama Iqbal International Airport, 2: Badshahi Mosque, 3: Gadaffi Stadium, 4: University of the Punjab, 5: Model Town, 6: Racecourse Park, 7: Walton Airport, 8: River Ravi and Bridges, 9: Emporium Mall, and 10: Bahria Town.

Figure 6 shows the comparison of Allama Iqbal International Airport in Sentinel-1A GRD (VV) image (Microwave) and the Google earth image (Optical). Airport is identified on the basis of parameters of shape and structure. Airport is also interpreted in the microwave sensed image with the help of scattering mechanism. Runway of the airport is smooth surface, which scattered the signal coming from the microwave sensor almost like a mirror and no backscattering occurred. So due to this specular reflection the energy is scattered away in forward direction. These airplane runways appear dark black in the microwave image.

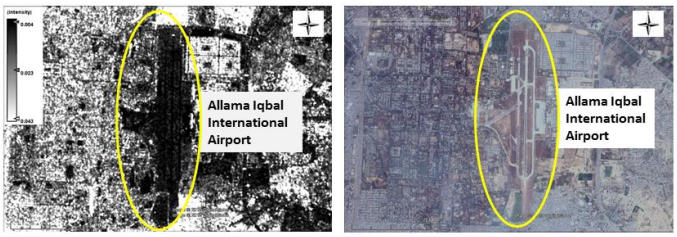


Figure 6: Airport shown in S1A GRD image of 24 Jan 2018 (Left) and Google Earth 16 Oct 2017 (Right)

Badshahi Mosque appears very dark in the image due to the specular reflection. When the signal from the microwave interacts with the smooth surface of the Badshahi Mosque, no amount of energy is backscatter from the surface. Sentinel-1A GRD image in VV polarization (Microwave) and the Google earth image is shown in Figure 7.

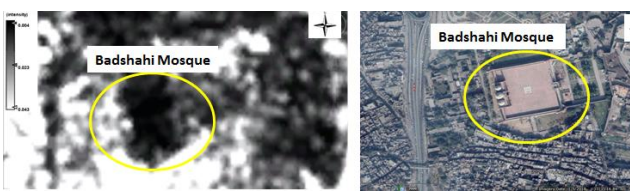


Figure 7: Badshahi Mosque shown in Sentinel-1A GRD image of 24 Jan 2018 (Left) and Google Earth 5 Jan 2018 (Right)

The size or shape of Gadaffi stadium in Sentinel-1A GRD (VV) image and optical image shown in Figure 8, suggest this is a stadium. Central dark portion in the microwave image shows the grassy smooth land, due to the smooth surface no signal is recorded in the microwave sensor so that the central part of the stadium appears black in the Sentinel-1A image whereas adjoining stands are build-up structure from where the spectators watch the match appears bright in the image due to the scattering mechanism of double bounce.

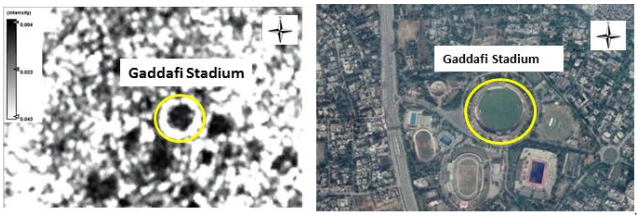


Figure 8: Gaddafi Stadium shown in Sentinel-1A GRD image 24 Jan 2018 (Left) and Google Earth 5 Jan 2018 (Right)

University of the Punjab lies in the interior of the busy city center. It is the complicated structure because it consists of building, roads and agricultural fields as visually observed in the Google earth image (Optical). Grey areas in the microwave image are mainly the agricultural fields inside the university boundary. As trees and vegetation is moderately rough and hence, they appear moderately bright grey in the Sentinel-1A image. Whereas build-up areas are very bright because these areas produce high reflectance and that is due to the double bounce effect caused by the building structures.

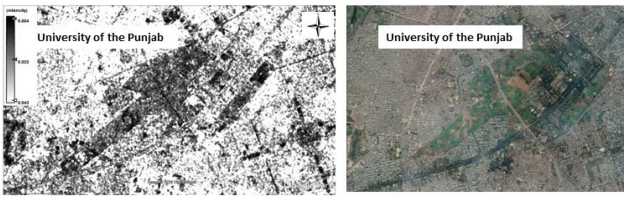


Figure 9: University of the Punjab shown in Sentinel-1A GRD image 24 Jan 2018 (Left) and Google Earth 5 Dec 2017 (Right)

Figure 10 shows the Model Town in VV band of Sentinel-1A GRD and Google earth image. Shape and the pattern are the two parameters for the identification of model town in Sentinel-1A images. Repetition of similar tones and texture due to houses laid out in the orderly manner produces a typical and recognizable pattern in the urban part of the model town and these are very bright because these structures cause the bounce off of microwave energy, both from the surface and side of the buildings.

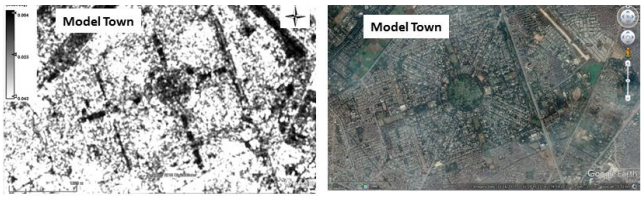


Figure 10: Model Town shown in Sentinel-1A GRD image 24 Jan 2018 (Left) and Google Earth 16 Nov 2017 (Right)

In case of the race course park, dark part in the Sentinel-1A GRD (VV) is due to the low backscatter to the sensor because of the smooth grass land in the park. In figure 11, Sentinel-1A and Google earth image of the Race Course Park is shown.

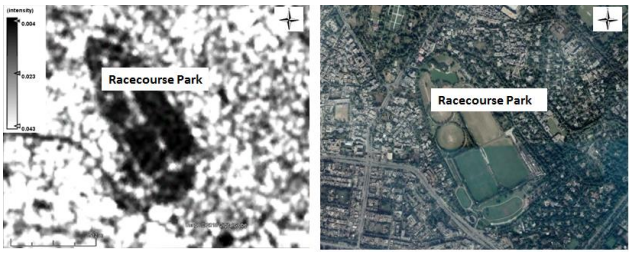


Figure 11: Race Course Park shown in Sentinel-1A GRD image 24 Jan 2018 (Left) and Google Earth 16 Nov 2017 (Right)

Runway of Walton airport is very smooth surface. So, the airport is tending to appear very dark in the VV band of Sentinel-1A image because all of the backscatter is directed away from the sensor.

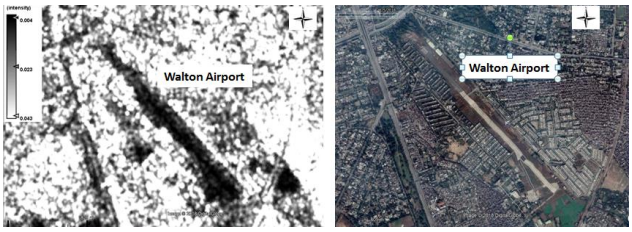


Figure 12: Walton Airport shown in Sentinel-1A GRD image 24 Jan 2018 (Left) and Google Earth 5 Jan 2018 (Right)

Ravi flows in the North of Lahore. River Ravi is a calm water body, which appears dark in the microwave imagery, because the entire backscatter is directed away from the sensor. Whereas bridges act as corner reflectors and due to high reflectance, they appear bright in the Sentinel-1A GRD (VV) image.

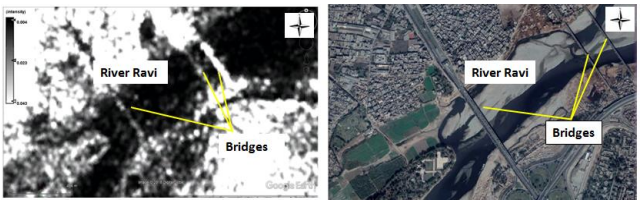


Figure 13: River Ravi and Bridges shown in Sentinel-1A GRD image 24 Jan 2018 (Left) and Google Earth 5 Jan 2018 (Right)

Emporium mall is a man-made infrastructure. Figure 14 shows Emporium Mall in the Sentinel-1A image and in the Google earth image. It behaves as a corner reflector with complex angular shapes. Because of this double bounce scattering phenomenon is enhanced and the sensor get high backscatter and so that the emporium mall appears very bright in the microwave image.


Figure 14: Emporium Mall shown in Sentinel-1A GRD image 24 Jan 2018 (Left) and Google Earth 5 Jan 2018 (Right)

Bahria is a real estate housing scheme owned by Bahria town group. It is the big urban center. So the houses or other man-made structures reflect more because of the double bounce effect by these structures. Because of this appear bright in the VV polarization band of Sentinel-1A GRD image.

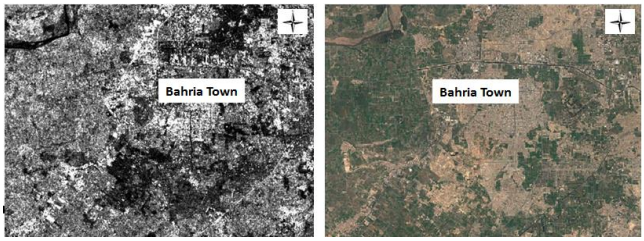


Figure 15: Bahria Town shown in Sentinel-1A GRD image 24 Jan 2018 (Left) and Google Earth 5 Jan 2018(Right)

## III. CHANGE DETECTION

Changes occurred in these major urban features of Lahore were also detected using the temporal images of Sentinel-1A in GRD mode acquired on 30 December 2015 and 24 January 2018.

The results were quite promising and comparable. Seven out of total ten features were observed to be changed significantly during past 3 years due to the construction of the new buildings in the airport's infrastructures, new departments in the university and the new houses in the town.

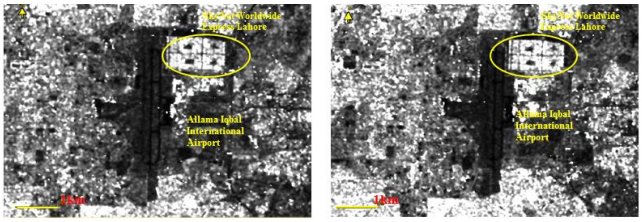


Figure 16: Change detection in Allama Iqbal International Airport shown in images of Sentinel-1A (Left: 2015, Right 2018)

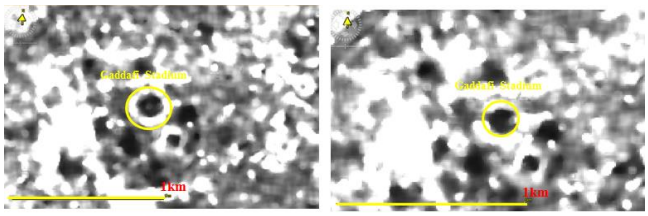


Figure 17: Change detection in Gaddafi stadium shown in images of Sentinel-1A (Left: 2015, Right 2018)

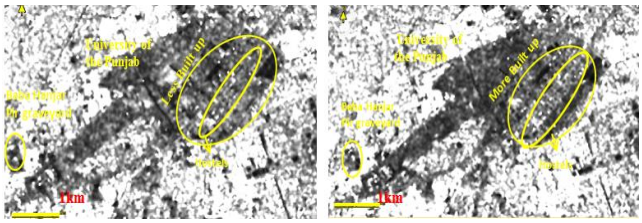


Figure 18: Change detection in University of the Punjab shown in images of Sentinel-1 A(Left: 2015, Right 2018)

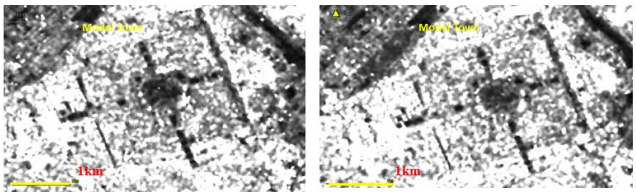


Figure 19: Change detection in Model Town shown in images of Sentinel-1A (Left: 2015, Right 2018)

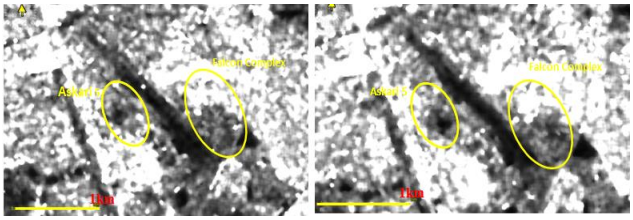


Figure 20: Change detection in Walton Airport shown in images of Sentinel-1A (Left: 2015, Right 2018)

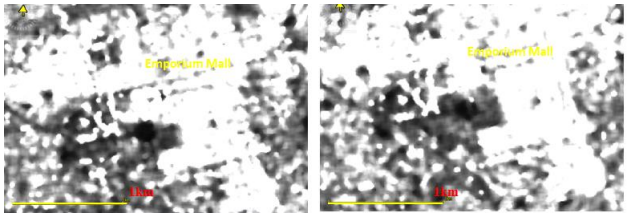


Figure 21: Change detection in Emporium Mall shown in images of Sentinel-1A (Left: 2015, Right 2018)

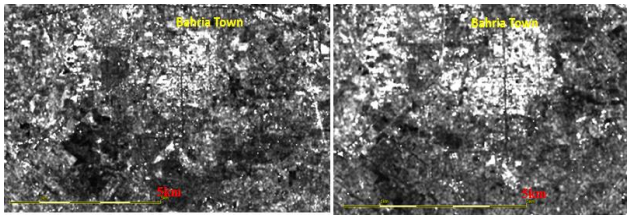


Figure 22: Change detection in Bahria Town shown in images of Sentinel-1A (Left: 2015, Right 2018)

On the other hand, Badshahi Mosque, Racecourse Park and River Ravi are the major permanent features and do not undergo any major change from 2015 to 2018.

## IV. Results and Conclusions

Based on analysis and investigations, level-1 products of Sentinel-1A images (C-band: 5.405 GHz) both in GRD and SLC modes were found to be highly useful for monitoring the urban features of mega city Lahore. It was also inferred that temporal images of Sentinel-1A in GRD mode were more useful for delineating urban features than SLC images due to flat terrain of Lahore.

Change occurred in mentioned urban features of Lahore were detected using the temporal images of Sentinel-1A in GRD mode acquired on 30 December 2015 and 24 January 2018 and in SLC mode acquired on 6 December 2015 and 13 March 2018. These changes were also compared with the corresponding Google Earth images. The results were promising and comparable. Seven out of ten features were observed to be changed significantly during past 3 years.

## Acknowledgment

The authors are thankful to Copernicus Sentinel Program Team for making freely available Sentinel-1A images and SNAP software. .

## References

[1] M. Herold, N. Goldstein, and K. Clarke, *The spatiotemporal form of urban growth: Measurement, analysis and modeling*. 2003.

[2] B. Forster, *An examination of some problems and solution in monitoring Urban Areas from Satellite Platforms*, vol. 6. 1985.

[3] X. Yang and C. P. Lo, "Using a time series of satellite imagery to detect land use and land cover changes in the Atlanta, Georgia metropolitan area," *Int. J. Remote Sens.*, vol. 23, no. 9, pp. 1775–1798, 2002.

[4] E. R. Stofan *et al.*, "Overview of results of Spaceborne Imaging Radar-C, X-Band Synthetic Aperture Radar (SIR-C/X-SAR)," *IEEE Trans. Geosci. Remote Sens.*, vol. 33, no. 4, pp. 817–828, 1995.

[5] C. Ticehurst, P. Dyce, and J. Guerschman, "Using passive microwave and optical remote sensing to monitor flood inundation in support of hydrologic modelling," *18th world IMACS Congr. modis 09 Int. Congr. Model. Simul.*, no. July, pp. 3747–3753, 2009.

[6] R. Welch, *Monitoring urban population and energy utilization patterns from satellite Data*, vol. 9. 1980.

[7] P. Kumar, H. Sajjad, R. S. Alare, C. D. Elvidge, R. Ahmed, and V. P. Mandal, "Analysis of Urban Population Dynamics Based on Residential Buildings Volume in Six Provinces of Pakistan Using Operational Linescan System Sensors," *IEEE Sens. J.*, vol. 17, no. 6, pp. 1656–1662, 2017.

[8] E. Stone, J. Schauer, T. Quraishi, and A. Mahmood, *Chemical Characterization and Source Apportionment of Fine and Coarse Particulate Matter in Lahore, Pakistan*, vol. 44. 2010.

[9] O. Riaz, "Urban Change Detection of Lahore (Pakistan) using A Time Series of Satellite Images Since 1972," *Asian J. Nat. Appl. Sci.*, vol. 2, no. 4, pp. 101–105, 2013.

[10] R. Hameed and O. Nadeem, "Challenges of Implementing Urban Master Plans: The Lahore Experience," *Int. J. Humanit. Soc. Sci.*, vol. 2, no. 12, pp. 1297–1304, 2008.

[11] A. Jacob and Y. Ban, "Sentinel-1A SAR data for global urban

mapping: Preliminary results," in *2015 IEEE International Geoscience and Remote Sensing Symposium (IGARSS)*, 2015, pp. 1179–1182.

[12] S. Abdikan, F. B. Sanli, M. Ustuner, and F. Calò, "Land cover mapping using sentinel-1 SAR data," *Int. Arch. Photogramm. Remote Sens. Spat. Inf. Sci. - ISPRS Arch.*, vol. 41, no. July, pp. 757–761, 2016.

[13] M. Foumelis *et al.*, "Esa Snap - Stamps Integrated Processing for Sentinel-1 Persistent Scatterer Interferometry," in *IGARSS 2018 - 2018 IEEE International Geoscience and Remote Sensing Symposium*, 2018, pp. 1364–1367.

[14] P. Prats-Iraola *et al.*, "Sentinel-1 assessment of the interferometric wide-swath mode," in *2015 IEEE International Geoscience and Remote Sensing Symposium (IGARSS)*, 2015, pp. 5247–5251.

[15] N. Yagüe-Martínez *et al.*, "Interferometric Processing of Sentinel-1 TOPS Data," *IEEE Trans. Geosci. Remote Sens.*, vol. 54, no. 4, pp. 2220–2234, 2016.

# Temporal Analysis of Aerosols over Mega-Cities of Lahore and Karachi

Sumayia Mehmood
*Department of Space Science*
*University of the Punjab*
Lahore, Pakistan
sumayiamehmood1@gmail.com

Aiman Nisa
*Department of Space Science*
*University of th Punjab*
Lahore, Pakistan
aimanisa786@gmail.com

***Abstract*— it is a well-known fact that aerosols affect our climate in different ways at both regional and global level. This paper is focused on the types of aerosols over the megacities of Lahore and Karachi throughout the year. Types of aerosols vary in all five seasons that is spring (FMA), summer (MJ), monsoon (JAS), autumn (ON) and winter (DJ). Data from a Ground based Aerosol Robotic Network (AERONET) is used and aerosols are classified in different types on the basis of Single Scattering Albedo (SSA) at 440nm and Fine Mode Fraction (FMF) at 500nm. AERONET data of four years (2015-2018) is used to classify aerosols in six types. From six different aerosol types, dust is most dominant in both cities throughout the year. Other types like Not Absorbing (NA) and Black Carbon (BC) aerosols are dominant in different seasons. Black Carbon (BC) is further divided in Highly Absorbing (HA), Moderate Absorbing (MA) and Slightly Absorbing (SA). Black Carbon (BC) is the major cause of climate change as it alters the radiation balance in atmosphere and its formation in atmosphere is because of incomplete combustion of different fossil fuels and soot emission. It is also the major type during winter season over study areas.***

***Keywords—Aerosols, Single Scattering Albedo (SSA), Fine Mode Fraction (FMF), Black Carbon (BC )***

## I. Introduction

For developing countries like Pakistan, air pollution has now become a critical challenge because of growing industries and road traffic causing a dramatic increase in emission of air pollutants. One the most significant air pollutants are aerosols, playing their role in climate change and effecting the seasonal variations, precipitation distribution and inconsistency of summer monsoon. Over South Asia, aerosols have gained enough attention in past years due to their influence on air quality, visibility, radiation imbalance and also health of human beings [1]. According to Intergovernmental Panel on Climate Change (IPCC), 2013, "Aerosols are important air pollutants that have adverse health impacts, lead to reductions in visibility and changes in climate". Aerosols participate as a very important character in global climate system and have a severe spatial and temporal discrepancy in their concentration [2]. The characteristics of aerosols and their effects on climate remain unpredictable because of limited knowledge about their properties and also, data availability becomes a problem during their research. However, in last few decades a number of studies have been conducted that have helped to reduce the uncertainties in the direct aerosol radiative forcing (IPCC, 2007). The major types of aerosols over Pakistan include dust, not absorbing (NA), mixtures and black carbons (BC). Dust is present almost all over the year over both sites. Dust alters radiation transfers, effects cloud nucleation and process of precipitation, and also acts as a reaction and depositional surface for reactive air pollutants [3].

When fossil fuels and biofuels are not burned completely, black carbon (BC) aerosols are produced. These black carbons have extremely variable properties including their density, morphology, absorption coefficient and their particle's size. These aerosols effect the radiation balance of the planet and are considered as the main constituent of climate change regionally and globally. This paper includes the temporal analysis of aerosols over the study sites of Lahore and Karachi. As aerosol types vary from place to place and season to season, aerosol types during all five seasons are analyzed using AERONET data. AERONET is a ground based remote sensing instrument which gives the precise measurements of aerosol optical and other properties. Level 1.5 Aerosol Inversion products are used because level 2 data was mostly unavailable for the study sites.

## II. Study Area

Pakistan is located in South Asia, sharing its eastern border with India, western border with Afghanistan and Iran and northeastern border with China. About 1046 km long coastline is present on the southern part along the Arabian Sea and Gulf of Oman [4].

Karachi is the Pakistan's leading city and is situated in the Pakistan south (24°51'N; 67° 02'E). Karachi covers an area of round 3500km$^2$ and has a residency of almost more than 15 million. Karachi's climate is moderately subtropical to arid and mild, and having yearly rainfall of 250mm. Its main industries consist of steel mill, automobiles, shipbuilding, pharmaceuticals, heavy machinery, textiles, oil refineries, chemicals and cement factories. The foremost and local cause for the aerosols in this city is industrial and vehicular exhaust and discharge of sea-salt particles from the Arabian Sea. The AERONET'S ground-based CIMEL sky radiometer has been active from August 2006, with the association of NASA at the Institute of Space Technology (IST) Karachi office [5].

Lahore (31.56°N 74.35°E), is the second most populated city of the country and has a residency of almost more than almost 7 billion. Lahore is an industrial city with the major industries including iron, thermal power plants, chemicals, textile and automobiles. Automobile emissions, road dust and biomass burning are considered to be the main cause of air pollution in Lahore [6]. AERONET instrument is placed at Space and Upper Atmosphere Research Commission (SUPARCO) in Lahore.

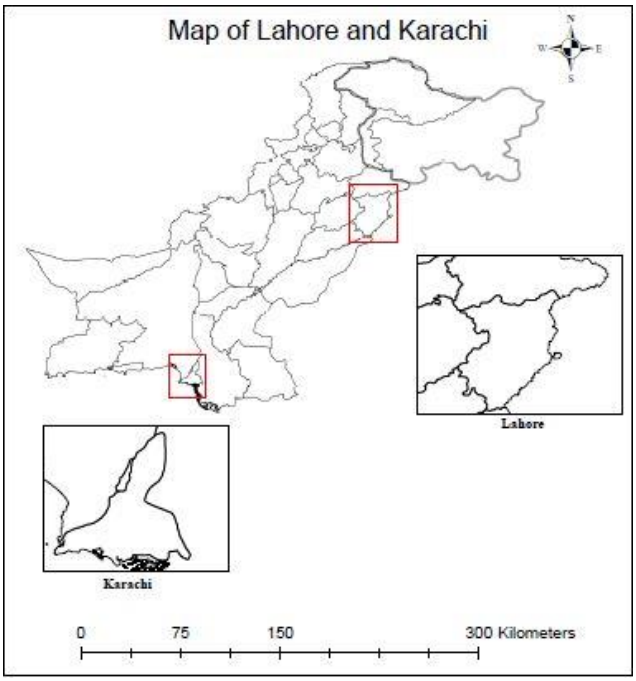


Fig 1. Study area map of Lahore and Karachi

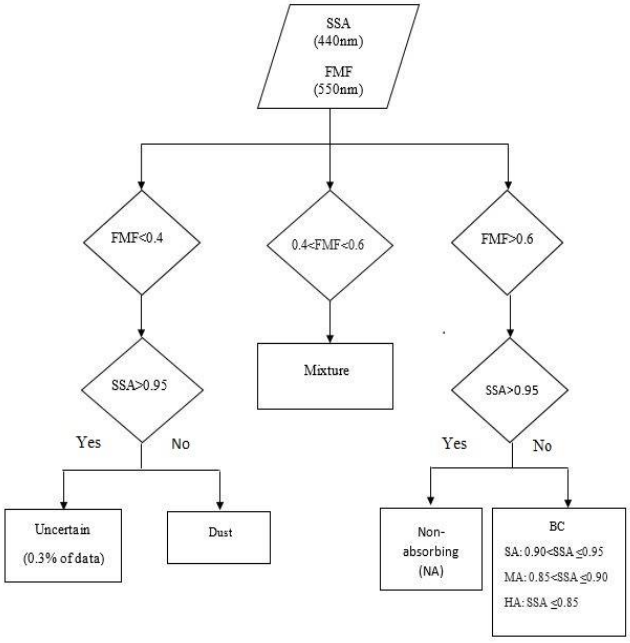


Fig 2. Methodology for classification of aerosols

## III. Methodology

AERONET is a ground-based instrument whose data is used for the precise measurements of aerosol optical properties. Daily averages data is used at level 1.5 because level 2 data is not available for the study areas. SSA from inversion products is taken at 440nm and FMF from Aerosol Optical Depth is taken at 550nm.

Aerosols can be categorized into four unique types when classified on the base of the size of particle and radiation absorptivity. These types include non-absorbing fine and non-absorbing coarse mode and also absorbing fine and absorbing coarse mode.

Classification of aerosols is done on the basis of SSA and FMF. SSA is used to differentiate between absorbing and non-absorbing. FMF is used to conclude the size of aerosol particle. FMF is used in place of AE because FMF tells the quantitative information for fine and as well as coarse-mode aerosols while AE provides qualitative information [7].

In this classification, aerosols with FMF greater than 0.6 are termed as fine-mode while those having FMF less than 0.4 are termed as coarse-mode and the particles lying between 0.6 and 0.4 are termed as Mixture of both [8]. On the basis of SSA these two modes are further categorized. If the SSA of fine mode particles is greater than 0.95 then they are classified as Not-Absorbing (NA) and if not then as Black Carbon (BC) which is further divided into Highly Absorbing (HA), Moderate Absorbing (MA) and Slightly Absorbing (SA).For the coarse-mode particles, if SSA is greater than 0.95 then they are termed as uncertain particles, which is only 0.3% of the data set, and if not then considered as Dust. For this paper we took months of February, March and April as spring, May and June as summer months, July, August, September as monsoon, October, November as autumn and December, January as winter months.

## IV. Results and Discussions

### A. SSA

The SSA (Single Scattering Albedo) is defined as "The ratio of scattering efficiency to total extinction efficiency and it provides vital information about the absorption and scattering properties of aerosols". SSA is dependent on wavelength, its values changes because of the influence of dust during summer and anthropogenic activities during winters. The value of SSA for BC and dust particles should be less than 0.9 at 440nm.Spectral variations in the SSA differ between dust and urban pollution, because SSA tends to increase as wavelength increases during summer when dust is abundant but decreases for urban pollution [9].

The value of SSA increase with wavelength over the areas where dust is dominant. This is the condition of our study site Karachi and Lahore during summer months. Also values of SSA decrease as wavelength increase for the areas where BC aerosols are abundant.

The general change in the values of SSA with wavelength over study sites is because of change in location, types of aerosols found and also meteorological conditions [10].

### B. Seasonal Analysis

Because of the presence of different aerosol types over different geographical locations, having diverse properties, and because of their temporal and spatial variation, aerosols are still not characterized properly. It is very difficult to compute the overall impact of aerosol over the entire globe due to the unavailability of reliable and detailed measurements in the majority regions over the globe.

As population is increasing rapidly over the two study areas, economic activities are also increasing causing an increase in the rate of emission of anthropogenic aerosols. These pollutants effect our climate directly and indirectly. Asia Pacific atmosphere have more organic components and

absorbing soot due to long-range transport by wind, great amount of coal and biomass burning emissions [6].

In this monthly analysis, we are intended to determine the different aerosol types during all the five seasons over the two most populated cities of Pakistan in order to characterize aerosols by their temporal analysis.

*1) Spring*

During the spring seasons of all four years, almost every aerosol type is present over each study cites. Figure (3a) shows that the majority of the concentration of aerosols during spring season includes mixture and dust and the other aerosol types are present in minorities over Karachi. Dust aerosols are present all over the years in the atmosphere of Karachi, but they become abundant during spring season. [11]. Mixture remained the most dominant aerosol types over Lahore also during the spring season shown in Figure (3b). Also, all types of BC aerosols are also present which indicates a lot of burning of fossil fuels especially in Lahore.

The process by which the atmosphere cleans itself is called deposition. The first one is dry deposition and the second is wet deposition. Dry deposition is the portion of the total deposition that is deposited in dry weather through such processes as settling, impaction, and absorption Wet deposition can be defined as a process in which atmospheric chemicals are accumulated in rain, snow, or fog droplets and are subsequently deposited onto Earth's surface. The season of spring doesn't experience either winds or heavy rainfalls. As a result, in the spring season almost all types of aerosols remain present.

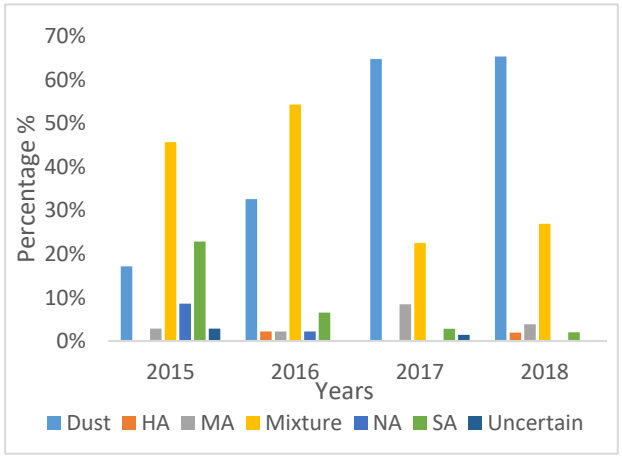


Fig 3a. Aerosol types over Karachi during spring period

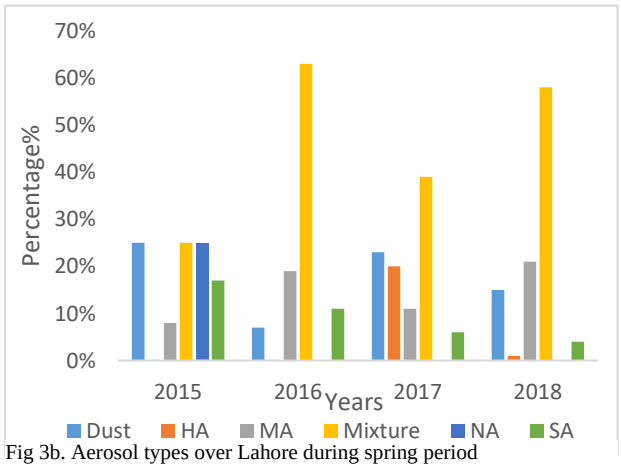


Fig 3b. Aerosol types over Lahore during spring period

*2) Summer*

Aerosol types during summer months over the two study cites of Karachi and Lahore are shown respectively in Figure (4a) and (4b). Dust is the most abundant aerosol type in summer season during all four years. More than 70% dust is present over Karachi during every summer of this data set. The other noticeable aerosol type present is Mixture. According to a research [11] it is proved that the desert dust prevails over coastal city of Karachi in the seasons of spring and summer. It was also concluded that coarse mode aerosols are present in the highest concentrations during summer months.

No data was available for the year 2015 and 2017 over the study area of Lahore. From the available data of 2016 and 2018 we can see that dust is dominant in summer over Lahore also. Mixture comes next after Dust. Unlike Karachi, some types of BC aerosols are also present over Lahore. Mixture aerosols are formed in industrial or urban regions when anthropogenic aerosols mix with the transported dust. The difference in the frequency of BC and NA is explained by the different types of burning processes being used in that region.

*3) Monsoon*

Data availability becomes one of the major problems during the spatial or temporal analysis of aerosols. No data was available during 2015 monsoon over Karachi, Figure (5a). During year 2016, almost 100% mixture aerosols are present. Whereas 50-70% dust is present during the years 2017 and 2018 followed by small quantity of mixture aerosols.

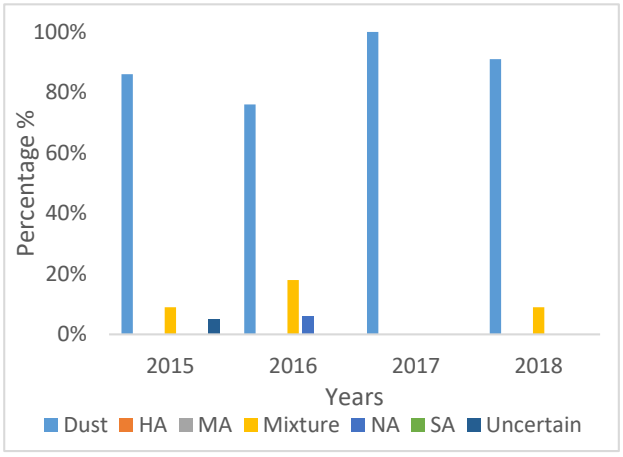


Fig 4a. Aerosol types over Karachi during summer period

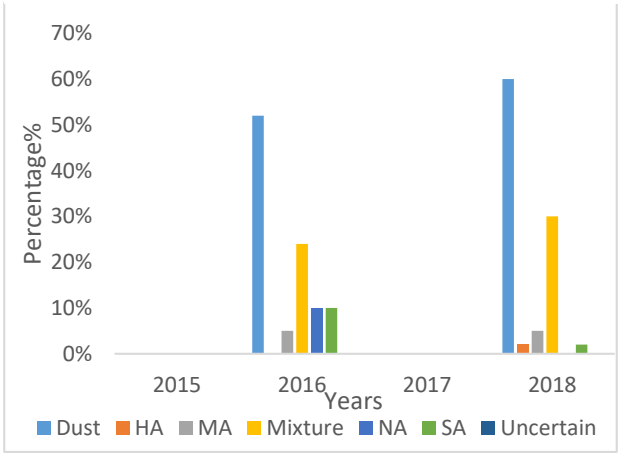


Fig 4b. Aerosol types over Lahore during summer period

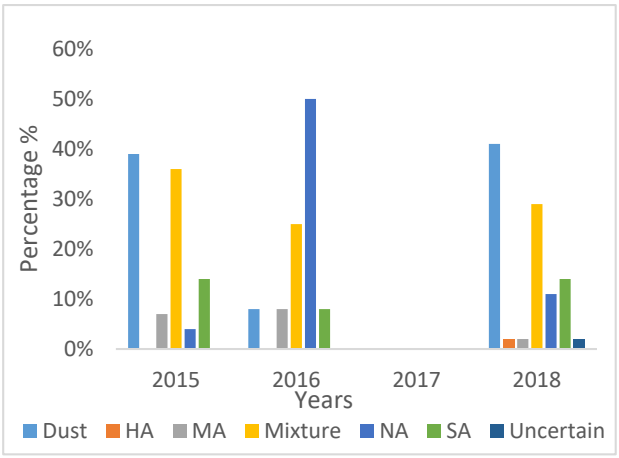


Fig 5a. Aerosol types over Karachi during monsoon period

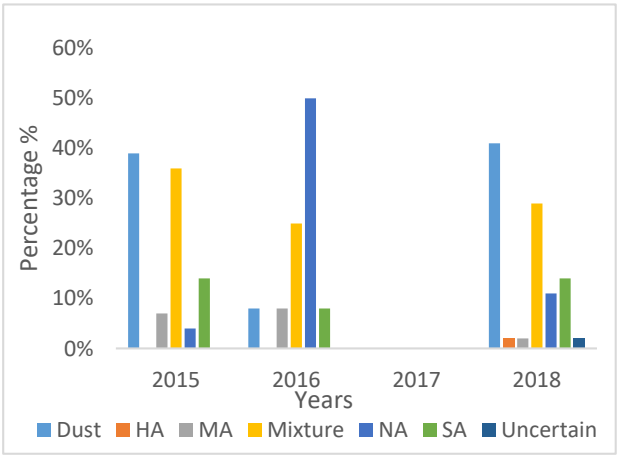


Fig 5b. Aerosol types over Lahore during monsoon period

Dust and mixture aerosols remained prominent over Lahore also, shown in Figure (5b), but other aerosol types are also present in considerable concentrations including NA and all types of BC aerosols. The presence of all these anthropogenic aerosols indicate a lot of burning processes, but the variation in the frequency of NA and BC is mainly because of aerosol source and type of burning.

*4) Autumn*

Aerosol types in autumn season are shown in figure (6a). Over Karachi, mixture remained the dominant aerosol type followed by all types of BC aerosols during autumn also. Mixture is the type of aerosol which is formed when transported dust is mixed with anthropogenic aerosols. Karachi faces a large concentration of mixture aerosols because most of the dust in the region is transported dust which the mixes with the anthropogenic aerosols produced because of automobile exhaust and partial combustion of fossil fuels. Over Lahore, figure (6b) shows the most dominant aerosol types include all classes if BC aerosols followed by mixture.NA and a small quantity of dust is also present. Unlike all other seasons, autumn is the only one in which dust is not present in considerable amount. These BC aerosols indicate massive burning of fossil fuels and emissions from the exhaust of automobiles. High aerosol deposition occurs as a result of decrease in both temperature and relative humidity which provides unfavorable conditions for the dispersion of aerosols. So, as temperature continues to

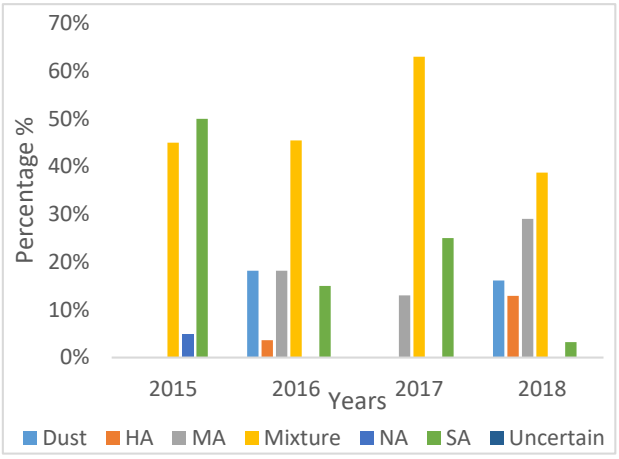


decrease during autumn, concentration of different aerosol

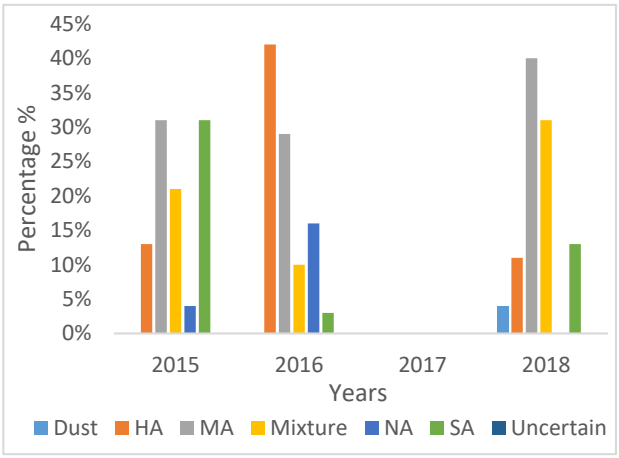


Fig 6b. Aerosol types over Lahore during autumn period

types starts to increase over the region.

*5) Winter*

The amount of coal burning increase as winters approach, and also fossil fuels, biofuels and biomass burning rates increase in both the study cites of Pakistan. As a result, the concentration of BC aerosols also increases in the atmosphere. Over the area of Karachi, Figure (7a), SA is most dominant aerosol type from the family of BC aerosols. MA, mixture and NA are also present in noticeable concentrations during these four years. But all these aerosol types are emitted into the atmosphere chiefly because of combustion.

Over the study area of Lahore, aerosols during winter season are shown in Figure (7b). MA is most dominant aerosol type from the family of BC aerosols followed by the other family members including SA and HA. Recent studies suggest that BC aerosols play a significant role in regional as

Fig 6a. Aerosol types over Karachi during autumn period

well as global climate changes.

Incoming solar radiations are scattered and absorbed by BC aerosols. Solar radiations are restricted to reach the surface of earth as they are absorbed in the atmosphere by BC. These aerosols also absorb the outgoing solar radiation reflected back from surface and reduce the amount of solar radiation reflected back to space. Therefore, the effect of black carbon aerosols opposes the cooling effect of

other aerosols at the top of the atmosphere, whereas at the surface all aerosols prevent the solar radiation. BC aerosols stay in the atmosphere from days to a few weeks. This also depends upon the geographic location and meteorological conditions over the area.

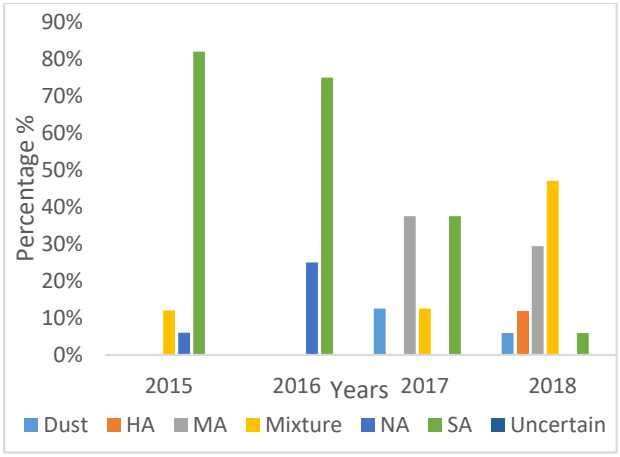


Fig 7a. Aerosol types over Karachi during winter period

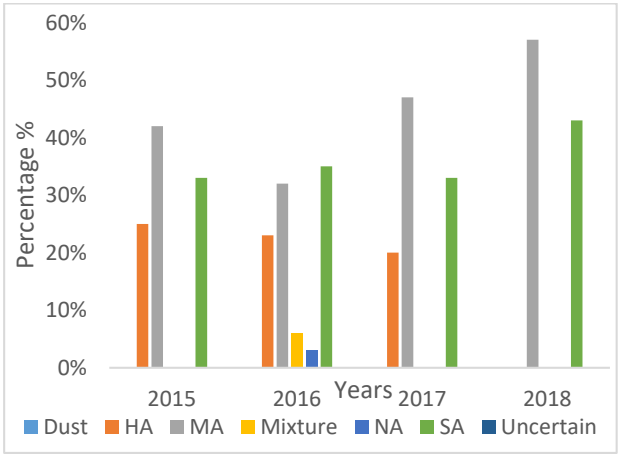


Fig 7b. Aerosol type over Lahore during winter period

## V. Conclusion

In this paper we have done a temporal analysis of aerosols over the two megacities of Karachi and Lahore. It is observed that mixture and dust remained the most abundant aerosol types in the atmosphere of Karachi all over the year. Dust and BC aerosols remained dominant in the atmosphere of Lahore all over the year. Spring is the month when desert dust prevails in Karachi. This dust gets mixed with anthropogenic aerosols and mixture is formed. Summer is the season when coarse mode aerosols are present in abundance. Almost all aerosol types were present during monsoon, this can be explained by RH and also crop burning. As the temperature starts to decrease in autumn and then in winter, burning of fossil fuels and biomass also increase so the concentration of BC and NA aerosols increases in atmosphere. Whereas the presence of BC all over the year is also because of heavy emissions from the exhausts of automobiles and chimneys of factories and industries.

## ACKNOWLEDGMENT

We are grateful to NASA and PHOTONS for establishing ground-based instrument AERONET and providing us the ground-based data. Our sincere gratitude to our supervisor Dr. Salman Tariq, Assistant Professor at Department of Space Science. University of Punjab, Lahore. I would like to thank him for his continuous support.

## References

[1] H. Bibi , K. Alam, T. Blaschke, S. Bibi and M. J. Iqbal, “Analysis of Aerosol Optical Properties over four locations in the Indo-Gangetic plains,”. Applied optics, pp 6199-6211, 2016.

[2] R. J. Charlson, S. Schwartz, J. Hales, R. D. Cess, J. J. Coakley, J. Hansen, and D. Hofmann, “Climate forcing by anthropogenic aerosols,” Science 255, pp 423–430, 1992.

[3] H. McGowan, and A. Clark, “Identification of dust transport pathways from Lake Eyre, Australia using HYSPLIT,” Atmospheric Environment, 42(29), pp 6915-6925, 2008.

[4] Muhammad Ali, Salman Tariq, Khalid Mehmood, Asim Daud, and Adila Batool, "A study of aerosol properties over Lahore (Pakistan) by using AERONET data," Asia-Pacific Journel of Atmospheric science, pp-153-162, 2014.

[5] K. Alam, T. Trautmann, T. Blaschke, and H. Majid, “Aerosol Optical and Radiative Properties during summer and winter seassons over Lahore and Karachi,” Atmospheric Environment, 50, pp- 234-245, 2012.

[6] B. N. Holben, T. F. Eck, I. Slutsker, D. Tanre, J. P. Buis, A. Setzer, and F. Lavenu, “AERONET A Federated Instrument Network and Data Archive for Aerosol Characterization,” Remote sensing of environment, 66(1), pp 1-16, 1998.

[7] G. L. Schuster, O. Dubovik, and B. N. Holben, “Angstrom exponent and bimodal aerosol size distributions,” J. Geophys, Res.111, D07207, 2006.

[8] J. Lee, J. Kim, C. H. Song, S. B. Kim, Y. Chun, B. J. Sohn, and B. N. Holben, “Characteristics of Aerosol types from AERONET Sunphotometer measurements,” Atmospheric Environment, 44(26), 2010.

[9] F. Tan, H. San Lim, K. Abdullah, T. L. Yoon, and B. Holben, “AERONET data–based determination of Aerosol types,” Atmospheric Pollution Research, 6(4), pp 682-695, 2015.

[10] K. Alam, M. J. Iqbal, T. Blaschke, S. Qureshi, and G. Khan, “Monitoring Spatio-Temporal variations in Aerosols and Aerosol–Cloud Interactions over Pakistan using MODIS data,” Advances in Space Research, 46(9), pp 1162-1176, 2010.

[11] Salman Tariq and Zia Ul-Haq, “Ground Based Remote sensing of Aerosol properties over a Coastal Megacity of Pakistan,” Advances in Meteorology, 2018.

# Assessment and Mapping of Wheat Crop in Thatta District Using Time Series Sentinel-1A

Sumbul Jabbar
*Institute of Space technology*
Karachi, Pakistan
sumbul.jabbar90@gmail.com

Rao Muhammad Zahid Khalil
*Institute of Space technology*
Karachi, Pakistan
zahidkhalil.rao@gmail.com

Dr. Ateeq Qureshi
*Institute of Space technology*
Karachi, Pakistan
atqureshi_pk@yahoo.com

***Abstract*— Agriculture sector is the main source of food and nutrition all over the world. For the food security and sustainable management of agricultural activities it is essential to monitor the crops temporally. It is a chief sector of economy which directly assists three-quarters of the population and has major share in foreign exchange earnings of Pakistan. Wheat is the significant Rabi crop and staple food of Pakistan. Pakistan is the major importer of wheat and its demand is increasing from country's population to cross border trade. The information of growing wheat crop areas and its growing condition is necessary for monitoring the agriculture programs. As a convenient and efficient instrument, remote sensing is widely playing an important role in such applications. For the assessment and monitoring of wheat crop the open access sentinel-1 C-band dense time series is used which provides the revisit schedules for agricultural monitoring and offers a new opportunity regardless of optical sensors limitations by investigating the performance of sensor backscatter image. A better understanding is expected as the data include all the wheat crop growth stages from transplanting to harvesting by studying the multi-temporal behavior of microwave backscattering characteristics from wheat crop in relation to crop growth conditions. The major aim is to assess the use of radar data for the monitoring of wheat growth and identification of wheat growth area. This study is intended on the exploration of reflective behavior of wheat crop throughout the season. The crop's backscatter is observed during the Rabi crop season of year 2017-18 (October - April) by acquiring multi-temporal C-band dual polarized (VV and VH) SAR images and to satisfy the results, ground reference data is used along with Sentinel-2 dataset.**

**The use of SAR data in agricultural applications was explored. The time-series of dual polarized backscatter was studied. The behavior of VV and VH throughout the season of Wheat crop was analyzed. The results showed that cross-polarization (VH) backscattering was useful to monitor the crop as it shows variable trend at different stages of plant growth throughout the season. The relation of NDVI with the VV and VH backscatter showed similar variability related to Wheat crop at some events such as when the crop reaches to its maturity.**
**Wheat classification was performed on Sentinel-1 data using Random forest classification which provided satisfactory results.**

***Keywords*— *Synthetic Aperture Radar (SAR), Sentinel-1, Sentinel-2, backscatter, wheat crop, crop growth monitoring, multi-temporal data.***

## I. INTRODUCTION

Pakistan is an agricultural country; major part of its economy depends on it. It is the fundamental source of income for majority of rural population. In Pakistan wheat is significant cereal crop and is consumed as a staple food. It is sown almost throughout the country. It is Rabi crop, normally starts from October to end in April. Thus, the assessment of wheat crop is essential for the development of successful strategies for the food safety measures of the country. To observe and study the agriculture for the better assessment and monitoring, remote sensing plays a vital role to provide timely and accurate depiction.

The remote sensing provides this opportunity to study, analyze and predict various factors of agriculture production and other useful information. The optical data is the major basis for most of these applications but the accessibility could diverge because of its limitation. As the optical sensors limits ability over the larger areas because of its dependency on the atmospheric conditions such as cloud cover and solar radiations; as it is depended on the solar radiations reflectance o, when the solar energy cannot reach, the information cannot be measured. This confines the ability to acquire information only during the daytime and cloud free atmosphere.

During the recent years the advancement of remote sensing opens a new epoch by providing another prospective alternative i.e. Radar remote sensing-SAR technology. The assessment of features, independency of solar radiation is its main advantage. It offers the opportunity to assess, monitor and map agriculture by penetrating the atmospheric features and allows sensing the surface irrelevant of atmospheric conditions and solar radiations.

In this context, the backscatter behavior and the potential of dual polarized Sentinel-1 data of Wheat crop is analyzed. The time series of the S-1 and S-2 is also considered to understand their relationship to the particular crop. The main aim of this work is: i) the use of SAR data for agriculture applications ii) to identify Wheat crop by using multi-temporal images.

## II. STUDY AREA

Thatta is one of the southern and border districts of Pakistan lying between 23^43' to 25^6' north and 67^05' to 68^45' east longitude. It is the district of the Sindh province following District Tharparkar and spreads over a vast area of 7,705 square kilometers. It is hot and bone-dry and gets a normal yearly precipitation of less than 125 mm. The study area is shown in figure 1.

## III. DATA COLLECTION

Sentinel-1 datasets were retrieved from ESA, through the program Copernicus. The data were acquired for Rabi season i.e. from October 2017 to April 2018. The reason behind selecting these months was to analyze the conditions of the

crop throughout the season. The used ground data were collected in the study which are used for training of classification and validation of results. The study is aimed at Rabi season. This information was collected at the start and mid of the season.

The Sentinel-1 and Sentinel-2 data that were used in this study were acquired from ESA program Copernicus. There are different other options to obtain.

The image covers southern area of the province of Sindh with geographic coordinates: 24.749731and 67.911636.

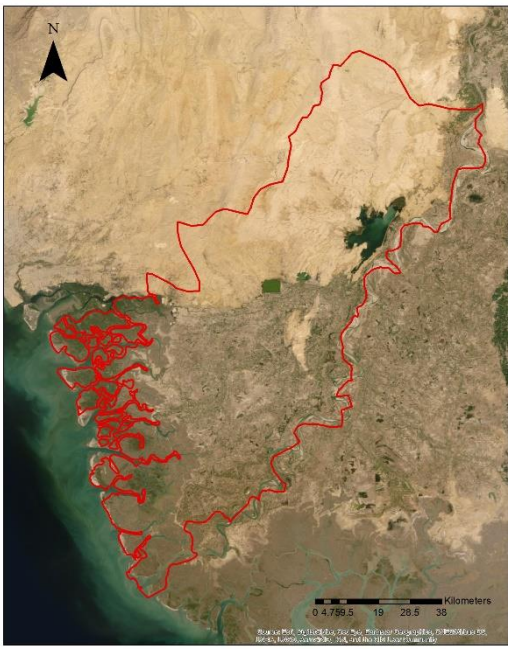


Fig. 1 Study area, Thatta, Pakistan

## IV. METHODOLOGY

The S-1A dataset processing include a number of steps to acquire geocoded intensity images starting from GRD data. To perform these operations SNAP (Sentinel Application Platform) tools were used.

Sentinel-1A data pre-processing steps includes: (i) conversion of digital pixel values of VH and VV amplitude into sigma nought (σ°) values through radiometric calibration, (ii) Lee filter 3x3 for speckle noise filtering, (iii) range doppler terrain correction, and (iv) incidence angle normalization. This study used the time-series data of VH and VV for wheat crop mapping in the study area.

To generate the VH and VV dataset time-series for the period from 01 Oct 2017 to 30 April 2018, firstly we performed the above necessary steps for every Sentinel-1 12-day scene. After, preprocessed scenes were stacked into a multi-temporal composite image. The time-series of Sentinel-1 dataset were analyzed and classification was performed using Random forest classification..

Sentinel-2 images were preprocessed using Sen2Cor processor and to identify the vegetated areas NDVI was performed. To evaluate and verify the results the time-series was generated.

## V. RESULTS AND DISCUSSION

VH and VV backscatter of wheat crop were analyzed. The signature of VH varies from -19db to -14db whereas the signature of VV varies from -7db to -9db. The highest sigma naught for VV polarization as shown in fig.3 is when the wheat plant is emerged, the same increase is visible in VH polarization pattern but the trend shows more visible change in VV backscatter.

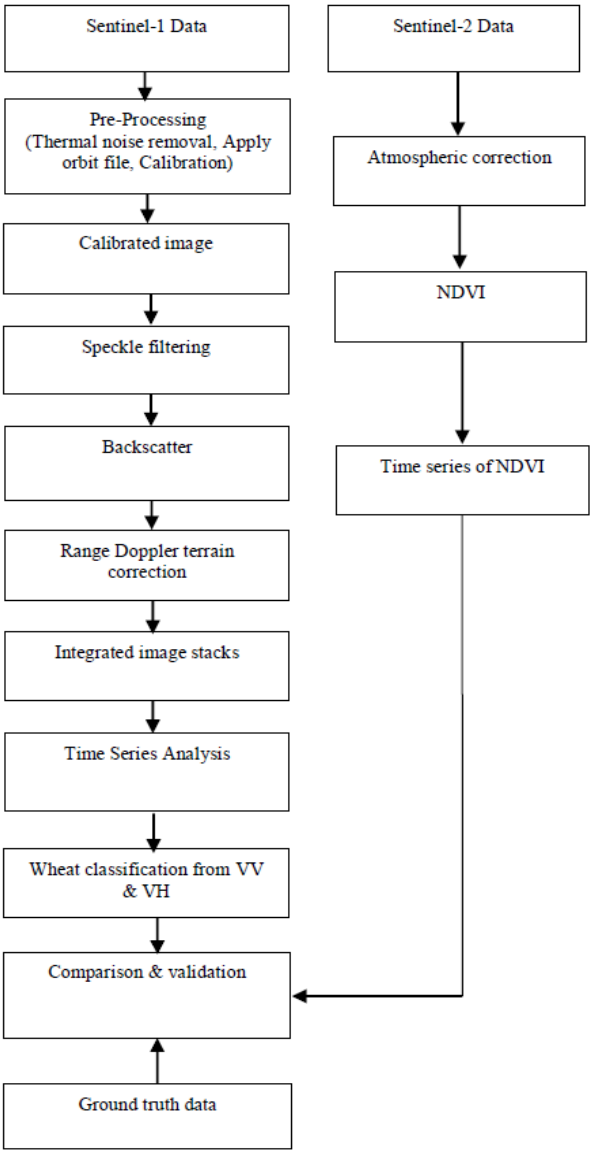


Fig. 2 Methodological workflow of the study

In figure 3, at the beginning of wheat crop growth, the backscatter co-efficient ($\sigma_{VH}$, $\sigma_{VV}$) evident that SAR scattering is more responsive to the plant height as compared to the later stage because at the early stage of plant both polarizations represent volumetric scattering than at later stage of plant growth. As the plant height increases and densely covers the area. The SAR penetration is limited and

VH and VV backscatter co-efficient is decreased due to the attenuation effect [2].
The sudden decrease in all three VV, VH and NDVI values at the mid of December may be due to the small amount of precipitation. The quantity of backscattered energy is impacted by the quantity of soil moisture or vegetation. The depth of penetration is also affected by the amount of moisture. In this situation, when moisture is present in the top layer, the reach of the energy on the top followed by the backscatter, there might be a chance of specular reflection due to availability of water. Similarly, the negative values in NDVI corresponds the availability of water by absorbing Infra-red signals and reflecting minimum red signals.
When the wheat plants are at full maturity VH shows the increase in value and VV backscatter decreases (fig.3). It is because the vertically oriented canopy features are attenuated with the vertically polarized energy. While, through the horizontal planes, horizontally polarized energy is more backscattered. The higher the volumetric scattering, the higher will be the cross-polarized VH backscatter [11].

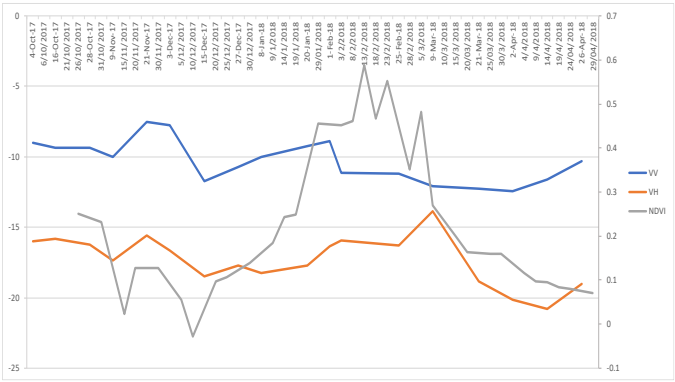

Fig. 3 VV and VH Backscatter of S-1 and NDVI of S-2

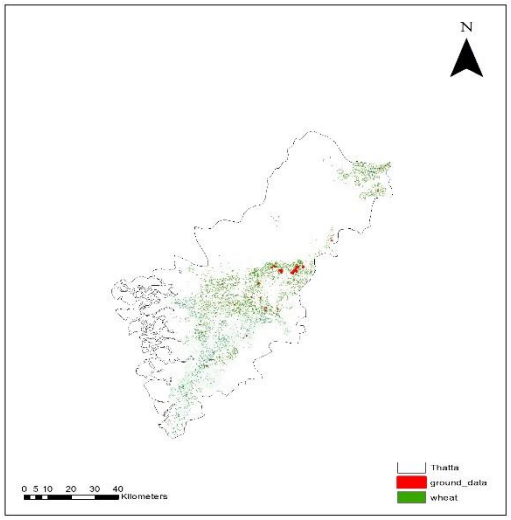

Fig. 4 Study area, Thatta Pakistan showing wheat crop

Figure 4 shows the classified image of the study area, Random forest classification method was performed to discriminate the Wheat crop from other vegetation. To extract the better results different no. of trees were applied i.e. 10, 50, 100, 150, 200, and 250. At 100 no. of trees it shows accurate result covering the area of 1818659 hectares which is in accordance with government agricultural statistical data with Thatta district i.e. 1806800 hectares. Since most of the land cover is barren and precipitation is low therefore the vegetation area is less.

## VI. CONCLUSION

In this paper, the study was focused to explore the use of Sentinel-1 data in the field of agriculture for crop identification and to analyze the behavior of backscatter of multi-temporal SAR images throughout the season of Wheat crop. The use of S-2 dataset and SAR images was to evaluate the multi-temporal SAR signal to enable the detection of wheat crop in the land cover.
Sentinel-1 time-series backscattering co-efficient were compared with NDVI obtained from Sentinel-2 data and their behavior was studied.

For the future consideration the analysis can be extended to study the different crops and different areas where ground data are available.

## REFERENCES

[1] M. Ustuner, F. B. Sanli, S. Abdikan, M. T. Esetlili, G. Bilgin, “An application of roll-invariant polarimetric features for crop Classification from multi-temporal radarsat-2 SAR data,” ISPRS TC I Mid-term Symposium “Innovative Sensing – From Sensors to Methods and Applications, Karlsruhe, Germany, Volume XLII-1, 10–12 October 2018

[2] S. Abdikan, A. Sekertekin, M. Ustunern, F. Balik Sanli, R. Nasirzadehdizaji, “Backscatter analysis using multi-temporal Sentinel-1 SAR data for crop growth of Maize in Konya basin, Turkey”, ISPRS TC III Mid-term Symposium “Developments, Technologies and Applications in Remote Sensing”, Beijing, China, Volume XLII-3, May 2018

[3] C.F. Chen*, N.T. Son, C.R. Chen, L.Y. Chang, S.H. Chiang, “Rice crop mapping using sentinel-1a phenological metrics,” 2016 XXIII ISPRS Congress, Prague, Czech Republic, Volume III-7, 12–19 July 2016

[4] D. Dimov, J. Kuhn, C. Conrad, “Assessment of cropping system diversity in the fergana valley through image fusion of landsat 8 and sentinel-1,” 2016 XXIII ISPRS Congress, Prague, Czech Republic, Volume III-7, 12–19 July 2016

[5] Nataliia Kussul, Sergii Skakun, Andrii Shelestov, Olga Kussul, “the use of satellite SAR imagery to Crop Classification in Ukraine within Jecam Project”, IEEE, 2014

[6] Chen Liu, Jiali Shang, Member, IEEE, Paris W. Vachon, Fellow, IEEE, and Heather McNairn, “Multiyear Crop Monitoring Using Polarimetric RADARSAT-2 Data”, IEEE Transactions on Geoscience and Remote Sensing, Vol. 51, NO. 4, April 2013

[7] Thuy Le Toan, Florence Ribbes, Li-Fang Wang, Nicolas Floury, Kung-Hau Ding, Jin Au Kong, Masaharu Fujita, Senior Member, IEEE, and Takashi Kurosu, “Rice Crop Mapping and Monitoring Using ERS-1 Data Based on Experiment and Modeling Results”, IEEE Transactions on Geoscience and Remote Sensing, VOL. 35, NO. 1, January 1997

[8] Meng Ji-hua, Wu Bing-fang, “Study on the crop condition monitoring methods with Remote Sensing”, The International Archives of the Photogrammetry, Remote Sensing and Spatial Information Sciences, Vol. XXXVII, Part B8. Beijing, 2008

[9] R. Kalpana, S. Natarajan, S. Mythili, D.E. Shekinah andJ. Krishnarajan, “Remote sensing for Crop monitoring - A Review”, Article.

[10] Sylvain Ferrant, Adrien Selles , Michel Le , Pierre-Alexis Herrault, Charlotte Pelletier, Ahmad Al-Bitar, Stéphane Mermoz, Simon Gascoin, Alexandre Bouvet, Mehdi Saqalli, Benoit Dewandel, Yvan Caballero, Shakeel Ahmed, Jean-Christophe Maréchal and Yann Kerr, “Detection of Irrigated Crops from Sentinel-1 and Sentinel-2 Data to Estimate Seasonal Groundwater Use in South India” , Article.

[11] C. Notarnicola, S. Asam, A. Jacob, C. Marin, M. Rossi, L. Stendardi, “Mountain crop monitoring with Multitemporal Sentinel-1 and Sentinel-2 imagery”, IEEE

# Performance Analysis of Hypersonic Scramjet Inlet using Computational Fluid Dynamics

Daniyal Ahmed Khan
*Institute of Space Technology, IST*
*Islamabad, Pakistan*
daniyalahmedkhan12@gmail.com

***Abstract*—Technological advancements in high speed propulsion continue to push the flight Mach further and thus keep expanding the flight envelope within hypersonic regime. When it comes to hypersonic air-breathing propulsion, scramjet (also known as supersonic combustion ramjet) is the only feasible option. The hypersonic free stream flow is decelerated and compressed by inlet to supersonic speeds by means of oblique shockwaves and passed downstream to combustion chamber for supersonic combustion. Complex and intriguing phenomena exhibit by the inlet such as shock-shock interaction, shock-boundary layer interaction & shock reflection make it the most significant yet critical component of scramjet to study. The main objective of this research is to conduct performance analysis of scramjet inlet using Computational Fluid Dynamics (CFD). Two dimensional coupled implicit Navier Stokes equations and k-ω SST turbulence model have been applied in ANSYS FLUENT to numerically simulate hypersonic flow field around the inlet. The scope of this research is limited to planar, variable and axisymmetric inlets. Since different inlet configurations produce different shock/flow pattern to achieve desired compression. Therefore, each inlet is modeled in CATIA and simulated in ANSYS at a particular free stream condition in order to analyze its individual performance parameters namely; total pressure recovery, kinetic energy efficiency and inlet drag coefficient. Lastly, these parameters are discussed in detail followed by simulation results to compare and evaluate best inlet design feasible for scramjet engine operation.**

***Keywords—propulsion, hypersonic, inlet, scramjet, performance, shockwaves, CFD, ANSYS***

## I. Introduction

The concept of scramjet was basically adapted from its variant known as ramjet engine. Ramjet is an air-breathing engine which rams through the high speed free stream air in order to compress the flow and has no moving components or parts. Absence of moving or rotating parts in ramjet speaks of its high efficiency at higher Mach as compare to other jet engines. This ramming effect of air decreases the flow Mach, consequentially increasing the static pressure and static temperature and decreasing the total pressure and total temperature due to the presence of shockwaves. The ramjet engine typically operates from Mach 3 ~ 5 and decelerates the flow to subsonic speed for combustion. When the speed of flow increases beyond Mach 5, decelerating flow to subsonic speed is no longer beneficial. The reasons being unsustainable extreme high pressures for the structural design of a practical combustor, substantial decrease of performance due to normal shock system, high heat transfer rates and lovery sing substantial amount of energy during combustion [1]. Thus, scramjet is an improved version of ramjet specifically designed to achieve higher Mach in hypersonic regime.

The components of scramjet inlet are different from those of turbojet and ramjet engines. The turbojet engine compresses the incoming flow by means of series of rotating and stationary blades called rotors and stators, respectively. When such engines are operated beyond Mach 3, high pressure and temperature rise across their blades cause them to melt resulting in metallurgical failure. However, the design of ramjet inlet is almost identical to scramjet ones. But characteristics of ramjet inlet such as little or no internal contraction ratio, large amount of turning and presence of terminal normal shock differentiates it from scramjet inlet. A typical scramjet inlet is comprised of a compression surface, throat, cowl and diffuser. The fundamental objective of scramjet inlet is to provide an efficient compression producing minimal drag and uniform flow entering the combustion chamber and offer these characteristics extensively throughout hypersonic flight operations [2]. Among all, sustained combustion in order to produce necessary amount of thrust to overcome enormous drag that prevails the hypersonic flight is very much essential for scramjet operation. As scramjet accelerates beyond Mach 5, the process of combustion is adversely affected because of severely low residence time for air inside the combustion chamber. While, low static pressure beyond an altitude of 20km adds further credit to the inefficient combustion. The inlet aids to cater this difficulty by decelerating the upstream air and raising the static pressure in order to make the conditions for an efficient supersonic combustion favorable. Therefore, it is beneficial to study the performance of scramjet inlet by examining certain parameters which signify them [3].

Extensive experimentation is needed to verify the performance of the designed intake. However, complex and intriguing hypersonic aero thermodynamic phenomena exhibited by scramjet and its components are difficult to achieve in ground based experimental facilities because such experiments are either very expensive or difficult to conduct with an acceptable level of accuracy [4, 5]. Hence, Computational Fluid Dynamics (CFD) is used extensively and plays a key role in studying and analyzing hypersonic engines and vehicles. Moreover, numerical simulations provide better understanding of flow physics which is critical in designing and manufacturing components/objects with higher efficiency.

## II. Scramjet Inlet Models

Various inlet designs of scramjet have been successfully tested in fulfilling different design requirements. However, the selection of an inlet is purely a compromise between the weight, performance, survivability and its integration with

other aerodynamic objects [2]. This research paper focuses on the following inlet configurations.

- Planar Inlet
- Axisymmetric Inlet
- Variable inlet

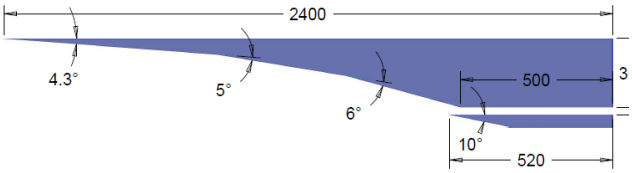


Fig. 1. Planar inlet model geometry

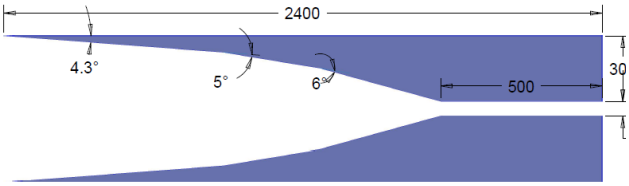


Fig. 2. Axisymmetric inlet model geometry

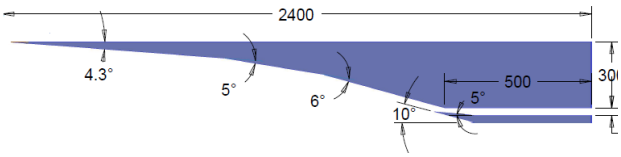


Fig. 3. Variable inlet model geometry

## III. Inlet Performance Parameters

The overall performance of scramjet depends significantly on the flow quality and energy content of the flow passed downstream of inlet in to combustion chamber and nozzle for subsequent combustion and expansion, respectively. Therefore, small intake losses may result in substantial penalty in engine thrust. Performance of scramjet inlet can be examined using various parameters but the most significant ones are total pressure recovery, kinetic energy efficiency and inlet drag coefficient.

### A. Total Pressure Recovery

The total pressure recovery, $\pi_c$ also known as total pressure ratio or total pressure efficiency, highlights unfavorable and irreversible combustion losses which occur during the presence of shockwaves. In other words, it is the ratio of the total pressure at the entrance of the combustion chamber ($p_{t_3}$)to the total pressure of the free stream ($p_{t_0}$)[1]. This is one of the most dominant performance parameters for intakes even for those operated in subsonic and supersonic regime [6, 7]. Mathematically, total pressure recovery is expressed as

$$\pi_c = \frac{p_{t_3}}{p_{t_0}} = \frac{p_3}{p_0}\left\{\frac{1+\frac{\gamma_c+1}{2}M_3^2}{1+\frac{\gamma_c+1}{2}M_0^2}\right\}^{\gamma_c/(\gamma_c-1)} \quad (1)$$

where, $\gamma_c$= ratio of specific heats, $M$ =Mach number, $p$ =static pressure and $p_t$= total pressure.

### B. Kinetic Energy Efficiency

Kinetic energy efficiency, $\eta_{KE}$ is the ratio of the kinetic energy of the flow downstream the inlet ($V_3$) to the kinetic energy of the free stream ($V_0$), assuming that the flow downstream of inlet expands isentropically to free-stream pressure [1]. This parameter is used very often in hypersonic literature because it is associated with the conservation of the most essential measure for scramjet propulsion namely, kinetic energy (velocity or momentum) which is directly linked to the amount of thrust produced. Mathematical expression for kinetic energy efficiency is

$$\eta_{KE} = \frac{V_3^2}{V_o^2} = 1 - \frac{2}{(\gamma_c - 1)M_0^2}\left(\frac{T_3}{T_0} - 1\right) \quad (2)$$

where, $\gamma_c$ =ratio of specific heats, $M$ =Mach number, $V$ =velocity and $T$= static temperature.

### C. Inlet Drag Coefficient

Inlet drag coefficient, $C_D$ is a dimensionless quantity which represents the total amount of aerodynamic drag experienced by the inlet during compression. This drag coefficient is a combination of additive drag coefficient and coefficient of other forces acting of the inlet [8]. In mathematical form, inlet drag coefficient can be written as

$$C_D = \frac{F_D}{q_\infty A_i} \quad (3)$$

where, $F_D$ =inlet drag force, $q_\infty$=dynamic pressure, $A_i$ =inlet capture area, $\rho$ =density and $q_\infty$ =free stream dynamic pressure.

## IV. Computational Analysis

The steady Navier Stokes equations together with SST k-ω turbulence model are solved in FLUENT in order to simulate flow across scramjet inlet. For spatial discretization, density-based solver is used with 2nd order spatially accurate Roe-FDS (flux difference splitting) scheme [9]. While, 2nd order implicit Euler scheme is applied for temporal discretization. In addition to this, viscous nature of the flow and shock-boundary layer interactions were also taken into account. Each simulation ran up to approximately 15,000 iterations in order to successfully converge the solution. The simulation results of each model are presented below which will be used to determine the optimal inlet configuration.

### A. Mathematical Model

The equations which govern turbulent compressible air are equations of continuity, momentum and energy [10].

#### 1) Continuity Equation

$$\frac{\partial \rho}{\partial t} + \frac{\partial (\rho u_i)}{\partial x_i} = 0 \quad (4)$$

*2) Momentum Equation*

$$\frac{\partial (\rho u_i)}{\partial t} + \frac{\partial (\rho u_i u_j)}{\partial x_j} + \frac{\partial \rho}{\partial x_i} = \frac{\partial \tau_{ij}}{\partial x_i} \quad (5)$$

*3) Energy Equation*

$$\frac{\partial (\rho E)}{\partial t} + \frac{\partial (\rho u_i H)}{\partial x_k} = -\frac{\partial (u_i \tau_{jk})}{\partial x_k} + \frac{\partial q_k}{\partial x_k} \quad (6)$$

*i, j, k= 1, 2*

Turbulent shear stress, $\tau_{jk}$ is written as

$$\tau_{jk} = \mu \left( \frac{\partial u_i}{\partial x_k} + \frac{\partial u_k}{\partial x_i} \right) \quad (7)$$

The total viscosity, μ of the fluid is defined as the sum of laminar and turbulent viscosity.

$$\mu = \mu_l + \mu_t \quad (8)$$

However, laminar viscosity, $\mu_l$ deduced from Sutherland law can be written as

$$\mu_l = \mu_{ref} \left( \frac{T}{T_{ref}} \right)^{\frac{3}{2}} \left( \frac{T_{ref} + S}{T + S} \right) \quad (9)$$

where $\mu_{ref}$, $T_{ref}$ and $S$ are known components.

The turbulent kinetic energy ($k$), turbulent dissipation rate (ε) and specific dissipation rate (ω), turbulent viscosity ($\mu_t$) and heat flux ($q_k$) are defined as

$$k = \frac{\overline{u_i' u_i'}}{2} \quad (10)$$

$$\varepsilon = \overline{v \frac{\partial u_i'}{\partial x_j} \left( \frac{\partial u_i'}{\partial x_j} + \frac{\partial u_j'}{\partial x_i} \right)} \quad (11)$$

$$\omega = \varepsilon / k \quad (12)$$

$$\mu_t = c_\mu \frac{\rho k^2}{\varepsilon} \quad (13)$$

$$q_k = -\lambda \frac{\partial T}{\partial x_k} \quad (14)$$

*4) k-ω Turbulence Model*

In this model, k and ω are expressed as a function of turbulent viscosity [11].

$$\mu_t = f \left( \frac{\rho k}{\omega} \right) \quad (15)$$

*a) Turbulent Kinetic Energy (k) Equation*

$$\frac{\partial (\rho k)}{\partial t} + \frac{\partial (\rho k u_i)}{\partial t} = \frac{\partial \left( \Gamma_k \frac{\partial k}{\partial x_j} \right)}{\partial x_j} + G_k - Y_k \quad (16)$$

*b) Specific Dissipation Rate (ω) Equation*

$$\frac{\partial (\rho \omega)}{\partial t} + \frac{\partial (\rho \omega u_i)}{\partial x_j} = \frac{\partial \left( \Gamma_\omega \frac{\partial \omega}{\partial x_j} \right)}{\partial x_j} + G_\omega - Y_\omega \quad (17)$$

*i, j = 2*

where $G_k$,$Y_k$, $\Gamma_k$ and $G_\omega$,$Y_\omega$, $\Gamma_\omega$ are the production, dissipation and diffusion terms, respectively.

*5) SST k-ω Turbulence Model*

The Menter's k-ω SST turbulence model [12, 13] is an enhanced version of k-ω turbulence model. The k-ω model can only be used for accurate prediction of flow in the near wall region while for the outer part of boundary layer, k-ε model is suitable because of its free-stream independence [14, 15]. Therefore, menter established a model by the combination of both, k-ω turbulence model and k-ε turbulence model for the sole purpose of capturing boundary layer in numerical simulations which occur due to the presence of adverse pressure gradients that other turbulence models fail to achieve. This model operates in such a way that it utilizes k-ω model in the internal area of the boundary layer and shifts to k-ε model to account for the free shear flow. In this model, k-ε model is transformed in to k-ω model by means of a blending function, $F_1$. This blending function is 1 in the inner side the boundary layer and progressively approaches to 0 near the edge of the boundary layer.

The equations corresponding to SST k-ω turbulence model are as follows [16].

*a) Turbulent Kinetic Energy (k) Equation*

$$\rho \frac{\partial k}{\partial t} + \rho u_j \frac{\partial k}{\partial x_j} = P - \beta^* \rho k \omega + \frac{\partial \left( \left[ \mu + \frac{\mu_T}{\sigma_k} \right] \frac{\partial k}{\partial x_j} \right)}{\partial x_j} \quad (18)$$

*b) Specific Dissipation Rate (ω) Equation*

$$\rho \frac{\partial \omega}{\partial t} + \rho u_j \frac{\partial \omega}{\partial x_j} = \frac{\gamma \rho}{\mu_T} P - F_4 \beta \rho \omega^2 + \frac{\partial \left( \left[ \mu + \frac{\mu_T}{\sigma_\omega} \right] \frac{\partial \omega}{\partial x_j} \right)}{\partial x_j} + 2\rho \frac{1 - F_1}{\sigma_{\omega 2} \omega} \frac{\partial k}{\partial x_j} \frac{\partial \omega}{\partial x_j} \quad (19)$$

However, the coefficient γ, production of kinetic energy turbulence, $P$ and blending function, $F_1$ are defined as

$$\gamma = \frac{\beta}{\beta^*} - \frac{\sigma_{\omega 2} \kappa^2}{\sqrt{\beta^*}}, \kappa = 0.41 \quad (20)$$

$$P = \overline{-\rho u_i'' v_i''} \frac{\partial u_i}{\partial x_j} \quad (21)$$

$$F_1 = \tanh(\Gamma^4) \tag{22}$$

where

$$\Gamma = \min\left(\max\left(\frac{\sqrt{k}}{\beta^* \omega d}; \frac{500\upsilon}{\omega d^2}\right); \frac{4\rho\sigma_{\omega 2} k}{CD_{k\omega} d^2}\right) \tag{23}$$

$$CD_{k\omega} = \max\left(\frac{2\rho}{\sigma_{\omega 2}\omega}\frac{\partial k}{\partial x_j}\frac{\partial \omega}{\partial x_j};\ CD_{k\omega\,min}\right) \tag{24}$$

$$CD_{k\omega\,min} = 10^{-20}$$

### B. *Computational Domain and Mesh Generation*

The fluid domain used for simulation is known as C-type domain in which the model is bounded by means of a semi-circle and rectangle. The radius of semi-circle is about ten times the length of the model while the rectangle is five times longer than the length of the model as shown in fig. 4.

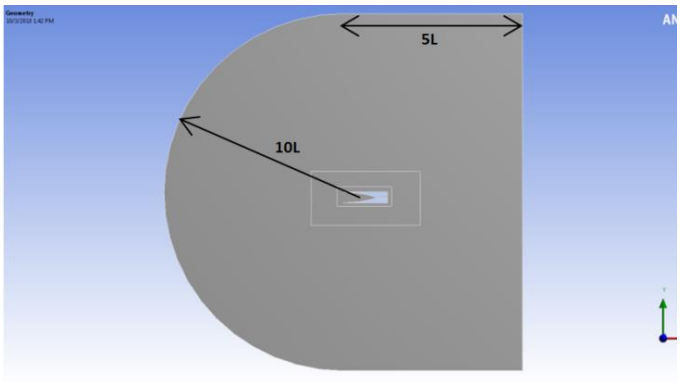


Fig. 4. Computational domain

The fluid domain is kept at a sufficient distance from the inlet model so that the boundary condition of pressure far-field could be imposed on the boundary. The domain is also distributed in to three further domains. Besides this, 20 mesh layers are developed at the boundary of the model using inflation so that the boundary layer phenomenon can be captured with better accuracy.

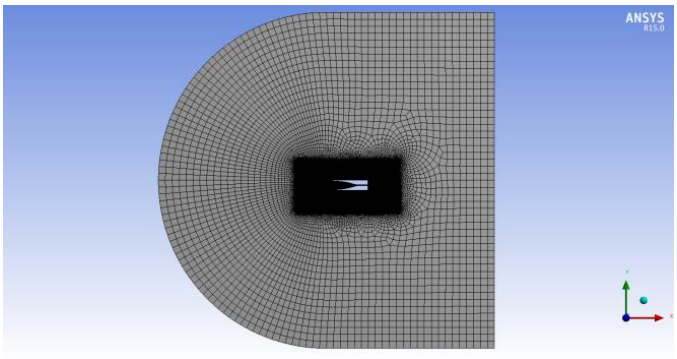


Fig. 5.Axisymmetric model mesh view – 1

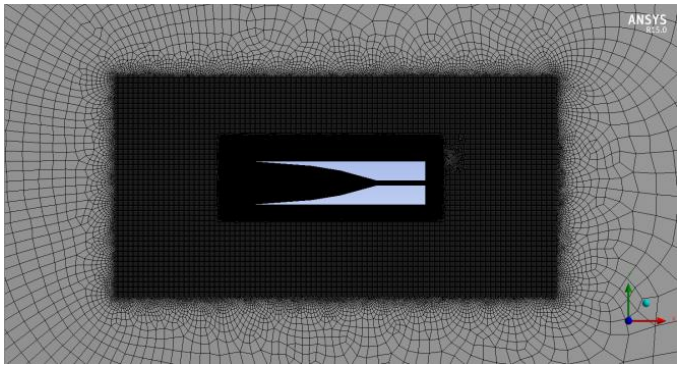


Fig. 6.Axisymmetric model mesh view – 2

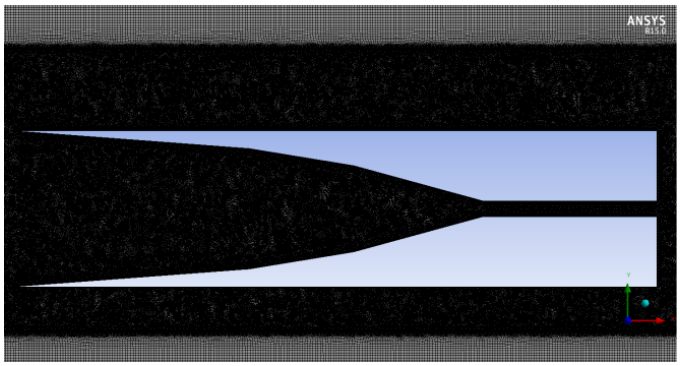


Fig. 7.Axisymmetric model mesh view – 3

For each model, three versions of mesh were constructed to conduct mesh independence study, as shown in the table below.

TABLE I. SUMMARY OF CONVERGENCE & MESH INDEPENDENCE OF AXISYMMETRIC MODEL

| | **Mesh 1** | **Mesh 2 (Final)** | **Mesh 3** |
|---|---|---|---|
| **No. of Elements** | 858895 | 1206489 | 1709849 |
| **No. of Iterations** | 7000 | 15348 | 17167 |
| **Value of $\pi_c$** | 0.6123 | 0.7138 | 0.7136 |
| **Value of $\eta_{KE}$** | 0.5987 | 0.6417 | 0.6420 |
| **Value of $C_D$** | 4.6315 | 5.0183 | 5.0186 |

The first mesh (mesh 1) is the coarser of all, which fails to capture the true results. Mesh 1 was further refined in to mesh 2 and consequently in to mesh 3 to study the improvement in simulation results. Mesh 2 predicted accurate results with less number of elements and computation time and hence, was selected as the final mesh. However, more than one million unstructured quadrilateral cells are generated in order to achieve mesh independent results.

### C. *Boundary Conditions*

Usually an aircraft operates at a dynamic pressure of 50kPa [17]. Since operation of scramjet starts in mid flight, therefore this value is considered suitable to use in this case. Two boundary conditions are used to carry out the present simulation. The boundary condition of Pressure Farfield is used for fluid domain which defines Mach, pressure and temperature of the free stream flow, as mentioned in table II. While, boundary condition for the inlet wall is selected as the wall.

TABLE II. BOUNDARY CONDITION DETAILS

| Parameter | Value |
|---|---|
| Mach | 5.00 |
| Pressure | 2.8602 kPa |
| Temperature | 220.7 K |
| Density | 0.0451 kg/m$^3$ |
| Turbulent Intensity | 5% |
| Turbulent Ratio | 10 |

## V. VALIDATION

Since no experimental data is available for the comparison of results, validation is carried out based on the mass flow balance, grid convergence and y+ values. Grid convergence was performed by using three different turbulence models on 2 grids. For the same geometry, points of first and second grid were 78000 and 330000, respectively. The contours of Mach & pressure were compared which showed the same results qualitatively. However, to ensure it, mass flow balance was applied on the wall boundaries. The variations in the mass flow values for both the grids appeared to be in between 0.2% – 0.4%. Mass flow balance was determined for each simulation and it was seen that the max difference between inflow and outflow came out to be max 1%. Hence, this ensured convergence of all simulations. While, the y+ values for all simulations were below 1.5.

## VI. RESULTS & DISCUSSIONS

### A. Planar Inlet Model

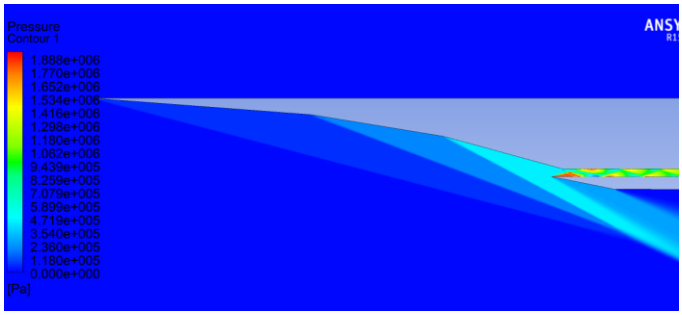


Fig. 8. Contours of pressure

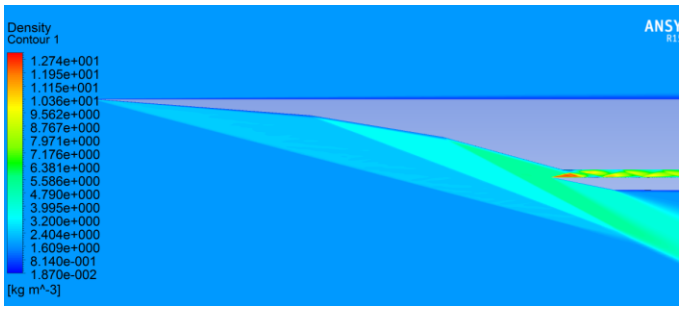


Fig. 9. Contours of density

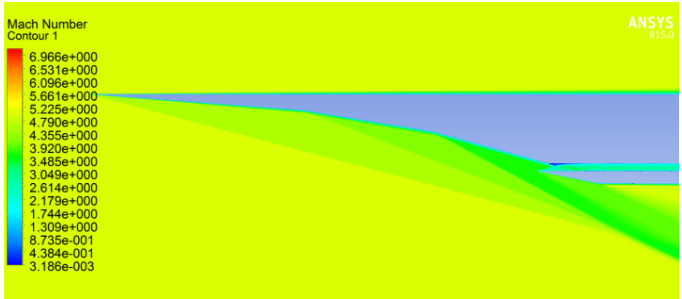


Fig. 10. Contours of Mach number

### B. Axisymmetric Inlet Model

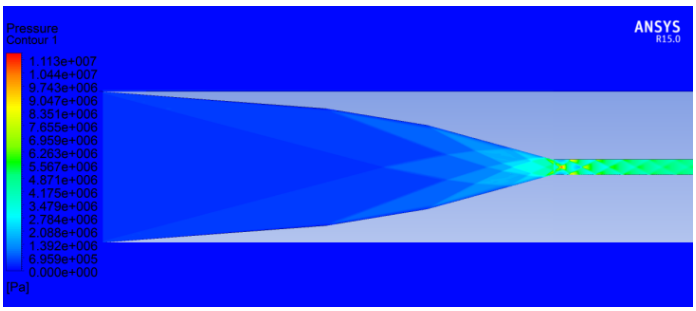


Fig. 11. Contours of pressure

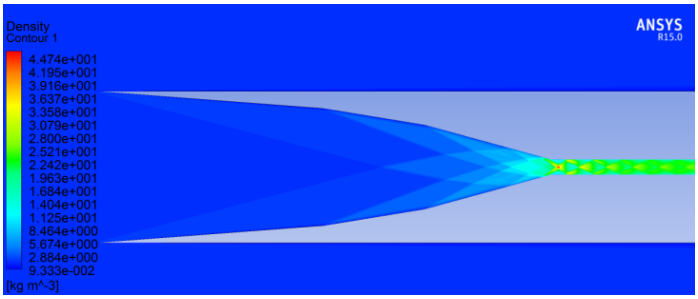


Fig. 12. Contours of density

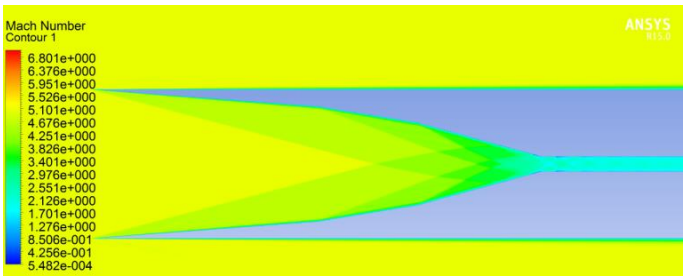


Fig. 13. Contours of Mach number

### C. Variable Inlet Model

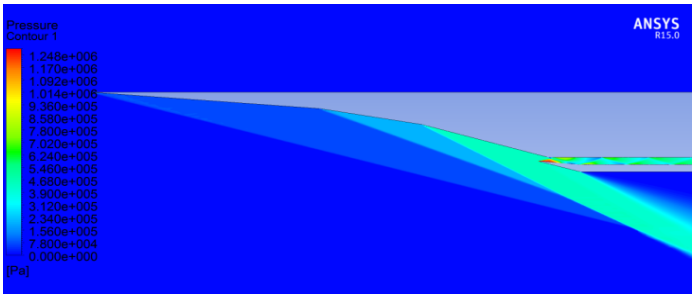


Fig. 14. Contours of pressure

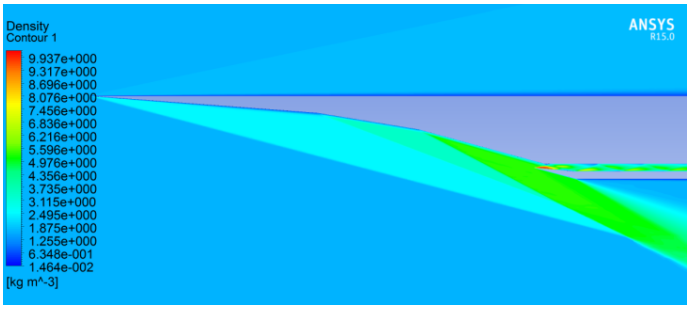


Fig. 15. Contours of density

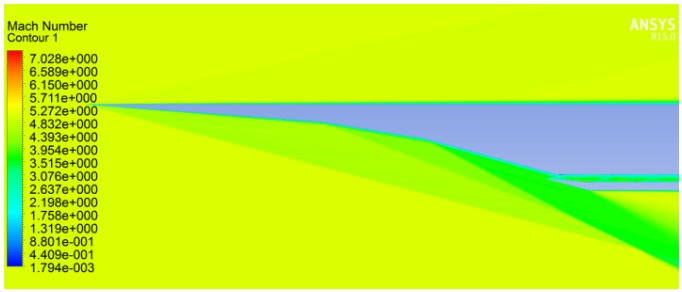


Fig. 16. Contours of Mach number

The simulation results above not only demonstrate pressure, density and Mach distribution around various inlets but also depict development of unique and significant phenomena in inlet flow field such as generation of shock train in isolator of inlet models. Moreover, shock-boundary layer reflection followed by the separation bubble at the inlet cowl is seen in fig. 10 and fig. 15. Another interesting phenomena captured by simulation is shock-shock intersection accompanied by shock reflection generated in axisymmetric inlet model as shown in fig. 11, fig.12 and fig. 13.

Apart from this, quantitative values of performance parameters as described in section III were also deduced from simulation results as shown in fig.17.

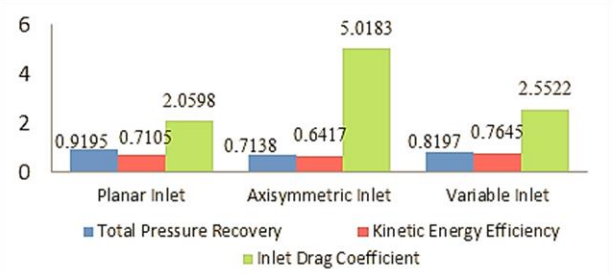


Fig. 17. Quantitative performance result of inlet models

According to the quantitative results, planar inlet model turns out to have the highest value of total pressure recovery and least value of inlet drag coefficient as contrary to axisymmetric model. While, the kinetic energy efficiency of planar and variable models are approximately the same as compared to axisymmetric model. Although, axisymmetric model prove to be beneficial in fulfilling many requirements such as it provides parallel inviscid flow to combustion chamber [18, 19] which is very much essential for an efficient combustion. But as far as, performance evaluation based on the above mentioned parameters in concerned, planar and variable models prove to be better than axisymmetric model. The primary reason for this is that axisymmetric model generates more shockwaves which results in substantial wave drag. Besides this, complex phenomena exhibit by the axisymmetric model such as shock-shock intersection further increases the drag and inefficiency of the model.

However, results of planar and variable models are fairly similar but planar model sounds more promising especially when it comes to inlet drag coefficient. Variable inlet model is actually an improved version of planar inlet model with an additional feature of movable cowl so that the inlet can be used over wide-ranging flight and engine operating conditions. Hence, variable/moving mechanism comes at a cost of increase in drag. When the inlet cowl reflects, some of the flow is lost as spillage causing spillage drag and the capture area of inlet decreases affecting the mass capture of the inlet and thus, overall performance.

The planar inlet model besides having simplistic design and configuration proves to show the best performance results. Based on the amount of required compression, planar inlet models are easily designed by distributing compression task over discrete number of ramps. These ramps are designed such that both, efficient performance and desired compression can be achieved.

## VII. Conclusion

This paper deals with the performance of scramjet inlets which has been analyzed numerically with the help of computational fluid dynamics. The simulations have been successfully carried out on three different inlet models of scramjet engine using 2D NS equations along with SST k-ω turbulence model in ANSYS. The turbulent viscosity of the flow, shock-shock interactions and shock-boundary layer interactions were catered in the computation. It was ensured that the inlet models are geometrically similar in terms of length, height, number of ramps, ramp angles, cowl position, cowl length and contraction ratio, so that appropriate comparison could be made. The C-type fluid domain was selected for the simulation and mesh independent study was successfully conducted to ensure independence of computational results from the mesh size. The computational results obtained from simulation supported the hypersonic literature and theories related to scramjet inlet and flow field associated with it. Based on the computational assessment of inlet performance, it is concluded that planar inlet model is the most suitable and optimum inlet design in contrast to axisymmetric and variable inlet models. This is because unlike variable and axisymmetric models, planar inlet model does not contain any sort of moving or rotatable part/component in its design and has less number of shocks which reduces the total drag to a minimal value. Lastly, the analysis performed and subsequent results drawn in this research are applicable to only those inlet model or geometry which is similar or congruent with the model or geometry that has been presented in this paper.

## References

[1] Heiser, W. H. and Pratt, D. T., Hypersonic Airbreathing Propulsion, AIAA Education Series, 1994.

[2] Van Wei, D. M., edited by E. T. Curran, Scramjet Propulsion, Progress in Astronautics and Aeronautics, Vol 189, AIAA, 2000.

[3] J.P. Drummond, G.S. Diskin, A.D. Cutler, Fuel–Air Mixing and Combustion in Scramjets, Technologies For Propelled Hypersonic Flight, Working Group AVT 10, Final Report, NATO Research and Technology Organization, 2001.

[4] Review of Aeronautical Wind Tunnel Facilities, Committee on Assessment of National Aeronautical Wind Tunnel Facilities, Aeronautical and Space Engineering Board, National Research Council, National Academy Press, Washington, DC, 1988.

[5] Requirements for Hypersonic Test Facilities, Report of the Ad Hoc Commitee, United States Air Force Scientific Advisory Board, Department of the Air Force, Washington, DC, May 1989.

[6] Oates, G. C., The Aerodynamics of Gas Turbine and Rocket Propulsion, Revised and Enlarged Edition, AIAA Education Series, Washington, DC, 1988.

[7] Seddon, J., and Goldsmith, E. L., Intake Aerodynamics, AIAA Education Series, New York, 1985.

[8] Michael K. Smart, Scramjet inlets, Centre for Hypersonics, The University of Queensland, Brisbane 4072, Australia, September 2010.

[9] Roe, P.L., "Characteristics based schemes for the Euler equations," Ann. Rev. Fluid Mechanics, 1986, pp 337-65.

[10] S. Saha and D. Chakraborty., "Hypersonic intake starting characteristics – a cfd validation study," Defence Science Journal, Vol. 62, No. 3, May 2012, pp. 147-152.

[11] Wilcox, D.C. "Multiscale model for turbulent lows," AIAA Journal, 1988, pp.1311-320.

[12] Menter, F., "Zonal two equation turbulence models for aerodynamic flows," 24th FluidDynamics Conference, (Orlando), AIAA paper-93-2906, July 1993.

[13] Menter, F., "Two-equation eddy-viscosity turbulence models for engineering applications," AIAA Journal, Vol. 32, August 1994, pp. 1598–1605.

[14] Wilcox, D., Turbulence modeling for CFD. La Cañada, California: DCW Industries Inc., 1993.

[15] Wilcox, D., "Reassessment of the scale-determining equation for advanced turbulence models," AIAA Journal, Vol. 26, November 1988, pp. 1299–1310.

[16] A. Hellsten., "Some improvements in menter's k-ω SST turbulence model," 29th AIAA Fluid Dynamics Conference June 15 – 18, 1997, Albuquerque, NM.

[17] L. H. Quan, N. P. Hung, Le D. Quang, Vu N. Long., "Analysis and design of a scramjet engine inlet operating from mach 5 to mach 10", International Journal of Mechanical Engineering and Applications, 2016, pp. 11-23.

[18] Molder, S., and Szpiro, E. I., "Busemann inlet for hypersonic speeds," Journal of Spacecraft,VoL 3, No. 8,1966.

[19] Van Wie, D. M., and Molder, S., "Applications of busemann inlet designs for flight at hypersonic speeds," AIAA Paper 92-1210, Feb. 1992.

# CFD Analysis of Different Bare Submarine Hulls and Finding Optimum Shape

Faran Ali
*University of Engineering & technology, Taxila*
Taxila, Pakistan
faranali@live.com

Aamir Sohail
*University of Engineering & Technology, Taxila*
Taxila, Pakistan
aamir.sohail@uettaxila.edu.pk

***Abstract*— This research is conducted to find the optimal shape of bare submarine hull. This is done by increasing the volume of submarine hull to maximum meanwhile limiting fluid resistance. Nearly 70% losses in energy of the submarine is because of wetted surface. To minimize wetted parameter different shapes of submarine hull are simulated. A synthesis model of submarine is designed consisting of parametric definition of hull geometry, using equation of ellipse and parabola. There is an aft and forward zone in submarine. By changing the parabolic equation used in forward zone, different shapes are obtained. An optimum shape is found using simulation techniques which have minimum drag resistance by the fluid. This study involves the calculation of coefficient of resistance by using Computational Fluid Dynamics (CFD). The dynamic meshing method is adopted to simulate and to get different results. Experimental calculations are also taken in order to compare them with numerical results.**

**Keywords— Wetted parameter, Dynamic Meshing, Coefficient of Resistance, Optimum Shape, Experimental calculation.**

## I. INTRODUCTION

Submarine work on batteries that are charged when it is underneath water, the Submarine utilizes power from the diesel engine when it has to come on surface of the sea. To properly work on diesel engine, the submarine has to take in air from the atmosphere since it's impossible for submarines when they are under the sea, so there should be an alternative resource. These battery banks will make submarine work effectively for some time but after a while battery will be drained. In order to use power efficiently, the submarine is made hydro dynamically plane. Also it should deliver enough space for both staff and installing machine at a time. By increasing the volume, drag force increase because the wetted area is increased. To overcome these problems an analysis of different shapes of bare submarine hulls was done. While keeping in mind the following objectives:

- To provide the sufficient volume while reducing the drag friction
- Fluid resistance minimization for submarine
- Prediction of the hydrodynamic effects of wave impact on hull structure for varying sea states (Minimization of hogging and sagging)
- Slamming of hull structure on water surface cause high stresses

## II. METHODOLOGY

First of all, three different geometries of bare hull of conventional submarine were made on SOLID WORKS with the help of ellipse and parabola equations. The aft zone of submarine hull was fixed for all i.e. it was same for all the geometries but forward zone was different for all. The value of $n_f$ was changed to vary the design. Different values were applied for $n_f$ i.e. 1.5, 2.5 and 1.35. After the completion of geometry of bare hull of submarine, an enclosure was made around the submarine whose dimensions. Enclosure was made to provide the submarine the proper conditions of sea e.g. forces acting on the hull in the enclosure are the same as they are in sea. After the enclosure, Boolean command was used to subtract the submarine geometry from the enclosure to made it single geometry which will help in the meshing process to make it simple.

After enclosing the submarine hull, the sides of the enclosure were given specific names so that there would be no difficulty in applying the boundary conditions. The side from where the fluid was entering in the enclosure was named as inlet. The side through which the fluid was leaving the enclosure was named as outlet. The other two sides of the enclosure were named as symmetry. The side above the submarine hull was named as open. The lower side of the submarine was named as wall. After that meshing was done on the given geometry with the help of meshing tools, Mesh independence was achieved by keeping on simulating one after the other by changing the type of mesh and size of element. Tetrahedron meshing and hex dominant meshing methods were applied for different sizing of elements. Tetrahedron mesh was selected as the optimum mesh after repeated iterations.

After meshing, different boundary conditions were applied on the different boundaries of the geometry to make the system as close to real as possible and because of that no difficulty was produced during the iterations. At inlet, the properties of the fluid were specified e.g. whether the flow is subsonic or sonic, speed of fluid etc. The fluid passing through inlet was subsonic and its normal speed was 15 m/s. The turbulence experienced by objects moving in sea water was of low intensity i.e. of 1% approximately. At opening pressure was taken same as that of atmosphere i.e. 1 atm. Other conditions were the same as that of inlet. Some other boundary conditions were also applied i.e. symmetry on the both sides of submarine hull's enclosure, no slip wall on the

surface of hull and on the lower wall of enclosure, speed of fluid on at outlet etc.

For the analysis, a fluid domain was made containing the useful parameters for the flow. In this domain, fluid was water and was taken as continuous fluid. Reference pressure in the domain model was one atmospheric and turbulence type was k-Epsilon. Temperature of the fluid throughout the domain was 25°C.Mesh adaption technique was also used to refine the mesh of the hull and the enclosure separately. This was necessary because the combine mesh of the assembly was not so refined to provide with the efficient results. Solution was run to get results. The convergence level was set to about $10^{-4}$ when the solution converged, the solution terminated itself.

## III. RESULTS

Results of the simulation of submarine hull have been presented. Pressure and velocity at different contours have been measured and shown. These parameters have been measured at 11 numbers of contours. Resistance to each model has been calculated in terms of drag force.

**Result of Design 01**

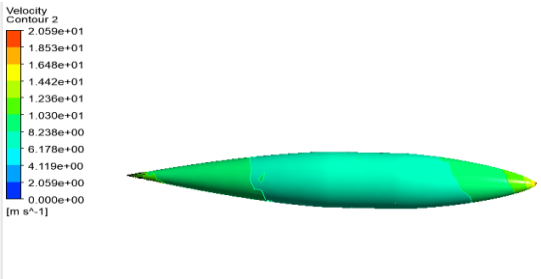


Fig. 1: Pressure contour

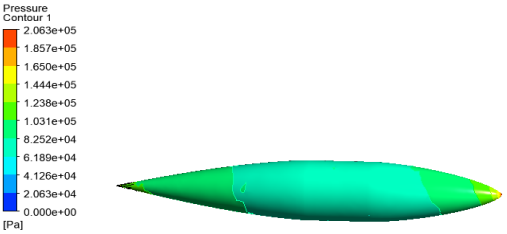


Fig. 2: Velocity contour

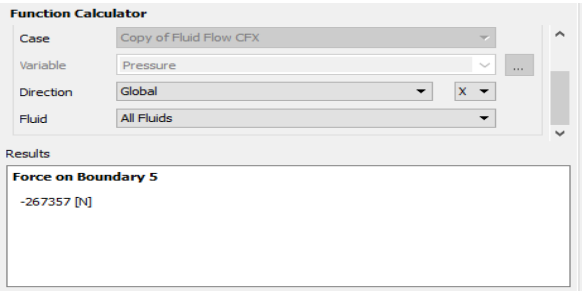


Fig. 3: Drag force

**Result of Design 02**

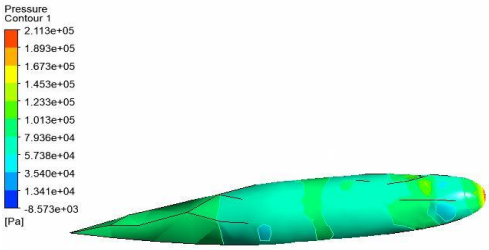


Fig. 04: Pressure contour

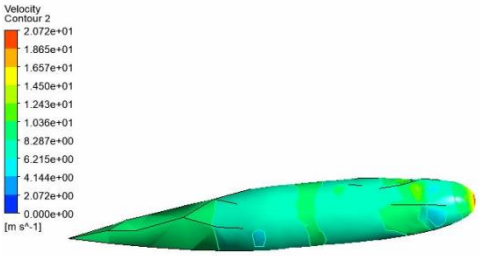


Fig. 05: Velocity contour

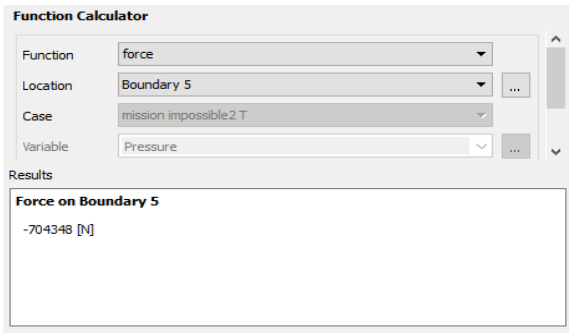


Fig. 06: Drag force

**Result of Design 03**

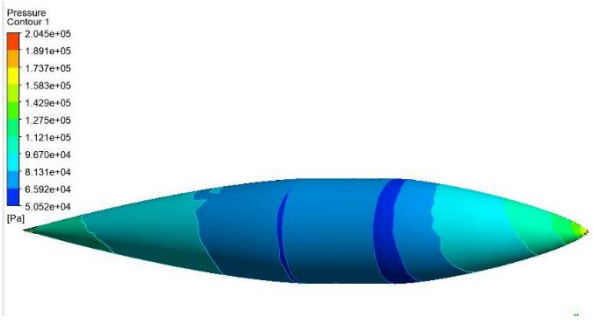


Fig. 07: Pressure contour

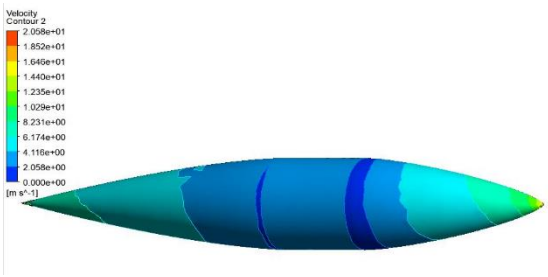


Fig. 08: Velocity contour

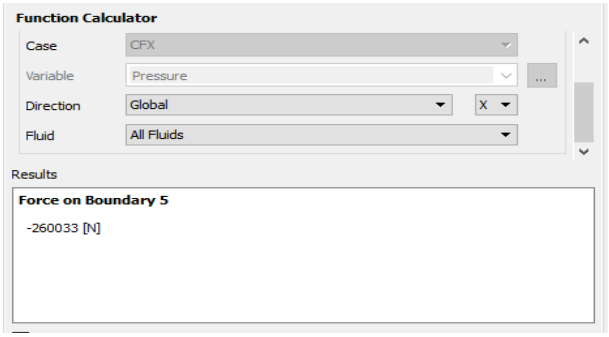


Fig. 09: Drag force

**Pressure, Velocity & Drag force comparison:**

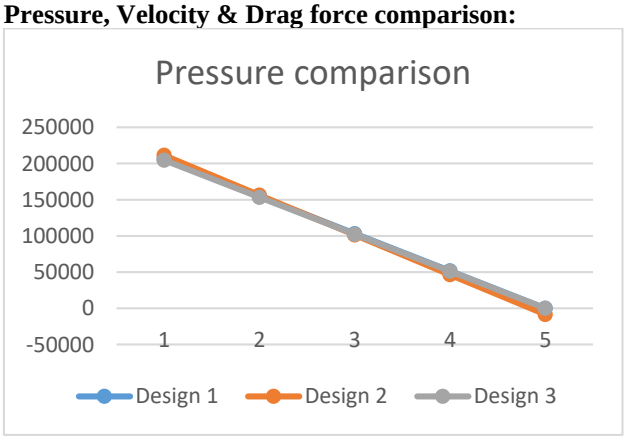


Graph 01: Pressure Comparison

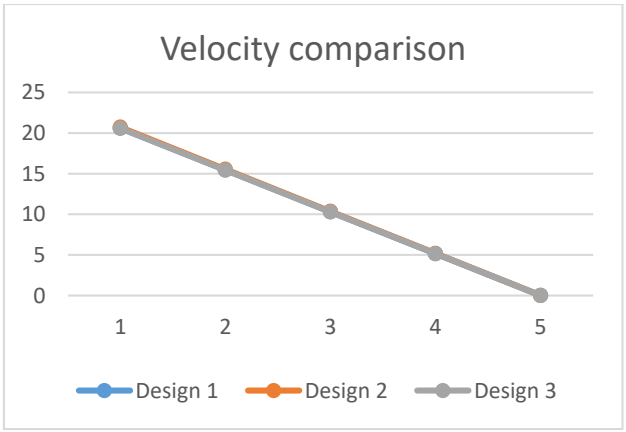


Graph 02: Velocity Comparison

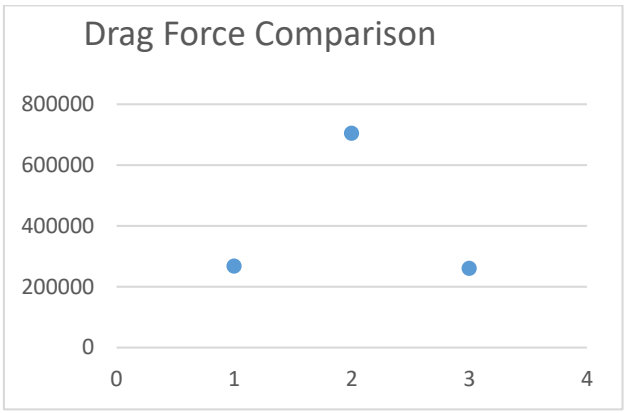


Graph 03: Drag force Comparison

From the above results, it could be seen that the third design experienced less drag resistance though it would have more pressure on its hull. So it can be said that design number 3 was the optimum design.

## CONCLUSION

The key conclusion from this work is that we were able to understand various processes take place in finding the best bare hull of submarine that is more feasible under the water which have lesser drag force and lesser fluid resistance. Project is going on and further better results are expected. Moreover, we were able to study deeply the ANSYS for fluid flow.

## REFERENCES

[1] (Pan, Zhang et al. 2012, Fureby, Anderson et al. 2016, Dong, Wang et al. 2017, Dubbioso, Broglia et al. 2017, Amiri, Esperança et al. 2018, Valentinis and Woolsey 2019)

[2] Amiri, M. M., et al. (2018). "How does the free surface affect the hydrodynamics of a shallowly submerged submarine?" Applied Ocean Research 76: 34-50.

[3] Dong, Y., et al. (2017). "Investigation of impact forces on pipeline by submarine landslide using material point method." Ocean Engineering 146: 21-28.

[4] Dubbioso, G., et al. (2017). "CFD analysis of turning abilities of a submarine model." Ocean Engineering 129: 459-479.

[5] Fureby, C., et al. (2016). "Experimental and numerical study of a generic conventional submarine at 10° yaw." Ocean Engineering 116: 1-20.

[6] Pan, Y.-c., et al. (2012). "Numerical Prediction of Submarine Hydrodynamic Coefficients using CFD Simulation." Journal of Hydrodynamics 24(6): 840-847.

[7] Valentinis, F. and C. Woolsey (2019). "Nonlinear control of a subscale submarine in emergency ascent." Ocean Engineering

# Assessing the South Asian Security Dilemma in Outer Space

Noor Ul Huda Atif
*Centre for International Peace and Stability*
*National University of Science and Technology*
Islamabad, Pakistan
nooratif96@gmail.com

**Abstract—** ***Outer space has become a global common in the 21st century that is being explored and exploited by the international community in multiple domains. South Asia is also influenced by the uniqueness of this frontier, which offers dynamic challenges. The two states of India and Pakistan have nuclearized South Asia threatening the regional security, which is now reaching to the outer space with India's growing military space ambitions. These ambitions threaten the space security in South Asia, which is explored in this paper. This paper aims to address the security dilemma that occurs in this particular region due to space militarization. The objective of this paper is to address the imbalance of civil-military capabilities between India and Pakistan in outer space. Pakistan has acquired the necessary military capabilities to counter its adversary, yet it lags behind in the strategic competition that threatens the space security. This study is based on semi-structured interviews conducted from the heads of strategic studies departments from the universities across Pakistan and includes the views and opinions of academic experts on space militarization. They have presented their point of view on space militarization in South Asia and its impact on the amateur space program of Pakistan. To understand the internal and external space security threats, it explores the features of space program of Pakistan and India, while assessing the current standing of these programs and their future ambitions. It discusses the approach that India has adopted, which pose threats towards the national security of Pakistan igniting security dilemma in the region. This paper also presents a strategy to counter the internal and external threats with formulation of a space strategy supported by a national space policy.***

***Keywords— South Asia, India, Pakistan, Outer Space, Space militarization, Security Dilemma, Space Security***

## I. INTRODUCTION

This paper is based on the analysis of the data collected through interviews addressing the security concerns that arise on South Asia. During this analysis, the available resources were overviewed, to formulate a strong policy of space program for Pakistan. It analyzed the trajectory that Pakistan must choose to strengthen the academic basis and counter the imbalance of space technology with India, in order to address the national and regional security threats due to an arms race in outer space. Regionally, the outer space dynamics revolves around the competition between China and India. However, this competition has adverse effects on Pakistan's national security as discussed previously. Considering the arms race in outer space as a national and regional security threat, the paper moves on to discuss the prospects of securing both fronts. The imbalance of outer space capabilities in this age can be challenging for a state like Pakistan. Pakistan has to not only secure its own territory but also maintain the regional peace. This paper attempts to describe the concept of security dilemma that has emerged in the South Asian astropolitcs after adversely affecting the geopolitics of the region. The threats posed towards Pakistan's security can be classifies as internal and external threats that will addressed in this paper.

## II. SECURITY DILEMMA

South Asia has been extensively studied under the lens of security dilemma due to unconventional arms race between India and Pakistan. The geopolitics of the region is compromised by conflict between these two states. They have jeopardized the regional peace and stability and are expanding the horizon of this conflict by taking it to the outer space, which gives rise to security dilemma in outer space. Security dilemma is commonly referred to the scenario where the states operate on the basis of fear and uncertainty, while the states are engaged in an anarchic environment. the proponents of security dilemma, John Herz and Robert Jervis have separately proposed the idea in different contexts. Their understanding of the concept is implied in this paper to assess the conflict between two hostile nuclear neighbours- India and Pakistan- in outer space.

*1) Robert Jervis has defined security dilemma as "the security dilemma will operate muh more strongly if statesmen do not see that their arms- sought only to secure the statusquo- may aloarm, not because they fear attack from the first state. The twofailures of empathy are linked"[1]*

*2) John Herz defines it as "a structural notion which the self help attempts of states to look after their security needs tend, regardless of intention, to lead to rising insecurityfor others as each interprets its own measures as defensive and others potentially threatening" [2]*

Based on the conceptual understanding of security dilemma that leads the two states of Pakistan and India, this paper will explore the features of space programs of both the states and analyze the military space capabilities acquired by India that has caused security dilemma in outer space.

## III. Features of Space Programs of Pakistan and India

### A. Space Program of Pakistan

Pakistan has a relatively small space program as compared to other states in the region. Despite having a head start in the space program, compared to other India, the agency and other R&D departments associated with it have not been to provide with satisfactory results. This section attempts at explaining the space program of Pakistan in multiple dimensions starting from the historical background of the program and its current standing in the international arena. It will explore the areas where Pakistan's space program (PSP) lags behind regionally and then proceed to highlight the space vision of PSP.

The world-renowned physicist and a noble laureate, Dr. Abdus Salam, was the pioneer of Pakistan's space program [3]. As [3] mentions he conceived the idea of an institution that can cater to the strategic and modern scientific needs of the state. Under the brilliance of his faculties, Pakistan became the third country in Asia to launch an ambitious space program. as He understood the strategic and scientific importance of this domain and initiated the program under the umbrella of Pakistan Atomic Energy Commission (PAEC) in 1961 [4]. According to [4] under the auspices of this parent organization, Space and Upper Atmosphere Committee that was established that was later recognized as an autonomous body in 1964. However, Space and Upper Atmosphere Commission (SUPARCO) became the successor institute of this commission that dealt with the research and development in the field of outer space [4]. Owing to the strategic significance of outer space, the status of this commission was once again changed from the autonomous body and it was placed under the direct authority of Strategic Planning Division (SPD) [5]. [5] States that since, Pakistan has lagged in the indigenous capabilities of space technology; United States that assisted in initiating the space program. US supported in the launch of sounding rockets such as Rehbar-I and Rehbar-II in 1962. In 1961, when Pakistan perceived the idea of exploring the outer space, the US president John F. Kennedy announced his ambition of landing on the moon. This mission required knowledge and information of the upper atmosphere exceeding stratosphere and Indian Ocean provided the suitable environment to collect this data. Pakistan seized this opportunity and offered to join NASA with their data collection [6]. Hence, Pakistan became the part of a historic event for humanity, the landing of man on moon. Since then, Pakistan's scientists have mastered the missile technology and have launched multiple missiles for defense purpose.

### B. Phases of space program

Establishing a strong and effective space program for Pakistan is a necessity, which cannot be ignored. The regional and international outer space hegemony has become in which the country stands nowhere [7]. Pakistan's space program is said to be a multi-stage program that in still in the development phase. Aforementioned in [7], the first phase of the research and development in the field of outer space in Pakistan comprised four main areas. It focused on the development and construction of a state of the art research facility that will assist the scientists and engineers to utilize their faculties in the best possible manner at SUPARCO. It was engaged in the production and launch of sounding rocket, and flight-testing ranges. However, SUPARCO's main focus was on the development of Badr satellite program that consisted of two satellites. This phase ended with the launch of Badr-I satellite on 16 July 1990. The second phase of the space program began with the R&D of second satellite of Badr program, named Badr-B. However, it was mostly considered a hiatus, where research and development in the field of outer space was decreased for very long time. The third phase is the on-going phase that is associated with the future of space program and space organization. The institution is working in collaboration with China under the program. The third phase of space program will launch Pakistan as an emerging space faring state in the world.

#### 1) Satellites by Pakistan

As in [6] Pakistan has managed to launch six satellites; however, the gap between the first launch of rockets and launch of satellites is very alarming. Pakistan launched the first satellite *Badr-1* in 1990, after a daunting gap of thirty years. The indigenously made satellite was launched from the Chinese Long March-2E launcher. It was an artificial satellite launched for experimental purpose, with a lifetime of fifteen years. The second satellite again took a decade to launch. *Badr-B/Badr-2* launched 2001, was a Russian Zenith-2 Rocket with only two years of shelf life. It was more sophisticated than the Badr-1 and had a CCD camera, which took pictures of the Earth. The system allowed ground stations to change the direction of satellite in space. In the same year, the *PAKSAT-1* was launched. The Turkish satellite, which was earlier used by Indonesia as well, was a communication satellites leased to Pakistan. This satellite was launched to retain the slot provided to Pakistan by the International Telecommunication Union (ITU). It took yet another decade for Pakistan to launch PAKSAT-1R, which was launched in 2011, into the geostationary orbit. Pakistan used Chinese launcher CZ-3B to launch PAKSAT-1R, which replaced PAKSAT-1 that was launched earlier. However, it took another eight years for Pakistan to launch more satellites. In July 2018, Pakistan launched PRSS-1 and PAkTES-1A. Apart from these satellites, Pakistan also owns an iCube satellite that was a project of Institute of Space Technology (IST). IST is an educational institution affiliated with the SUAPRCO. These satellites are very less in terms of quantity and quality as compared to the other states in the region that started many years after Pakistan's space program**.**

### C. Pakistan's Space Vision

Pakistan envisions space faring owing to its importance in the 21st century. The outer space has gained significance in the modern world due to technical advancement of the command, control, and communication. It broadens the horizon of capabilities for any state in the world with the dual-purpose utility, including civilian and military use. Pakistan is all set to rise as an ambitious space faring state. The space vision entails the third phase of space program that will be According to which, Pakistan launched two satellites through the Chinese Jiuquan satellite launch centre. PRSS-1 is Pakistan's' first Remote Sensing Satellite that will mainly serve the purpose of monitoring of CPEC projects. PAkTES-1A is an indigenously developed satellite by the SUPARCO [8].

Space vision was initially named the Pakistan' Space Program (PSP) -2040, approved by the then Prime Minister Yosuf Raza Gilani [9]. However, it was later renamed to *Space Vision*. The main aim of the space vision, as mentioned by [9] is that the people of Pakistan must benefit from the space technology. This can be done by utilizing outer space for socio-economic and defence purposes. Currently, Pakistan uses space technology agriculture, communication, meteorology, and aeronautics. The 'space vision' functions by an operational framework of Pakistan's Space of Program -2040. Under this framework, Pakistan has set its ambitions of developing and launch of certain quantity of satellites. This framework will provide the institution with the roadmap for development of five Geo-stationary satellites and six Low Earth Orbit (LEO) satellites. The details of the space vision have been kept confidential as Pakistan treats its space program as a national security issue with its growing utility in endangering the country's security. This space vision will prove to be a guide for Pakistan to regain its outer space autonomy and counter the threats it faces from the adversaries.

### *D.Indian Space Program*

Pakistan and India are historic rivals that have been competing, since independence, with each other in all aspects. Mentioned in [2] is that India followed Pakistan into the outer space and launched its space program in 1969. The Indian National Committee for Space Research (INCOSPAR) was established by Vikram Sarabhai, which later developed into the Indian Space Research Organization (ISRO). ISRO has been working very efficiently and effectively since its establishment. The first satellite that India launched was Aryabhata on 19 April 1975. Since then, India has launched 57 satellites in the outer space, among which 16 satellites are in use of the armed forces. India has also maintained a sub-branch of the ISRO named as the Integrated Space Cell, which is responsible for the security if space assets. On 1 April 2019, India launched a reconnaissance satellite Emisat, which is a mutual product of ISRO and DRDO. *Emisat* is an electronic intelligence satellite that will assist the military in locating hostile radars. Apart from these satellite programs, India also plans to send a mission to Mars. This is an alarming situation for Pakistan as it lacks the ability to counter the technology and protect the handful of satellites that it owns, since India is increasing its space-based military capabilities.

#### *1) India's military ambitions in space*

India has been moving abruptly with its ambitions of militarizing the outer space. It has successfully employed satellites to facilitate the ground forces and is now preparing for outer space warfare. In 2019, India successfully acquired the ASAT capability, launched Moon mission, Chandaryan-II, to the southern side and is preparing for simulation exercises of space war. India is actively involved in militarization of outer space, which is having an impact three different levels. This process of militarization has had its effect on internationally, regionally and particularly on the security of Pakistan.

##### *a) Indian Military satellites*

India has launched numerous satellites in the Low Earth Orbit and Geosynchronous orbit since it initiated its space program. While these satellites provided it with the experience of sophisticating the space technology and improving space sciences in country, it also employed technology to benefit the military forces. Apart from socio-economic benefits, it has enhanced the prospects to defence as well. India is currently engaging 16 satellites for the use by its forces [10]. As in [10] ISRO is producing these satellites in collaboration with Defence Research and Development Organization (DRDO). The Technology Experimental Satellite (TES) was launched in 22 Oct 2001. The main function of this satellite was that it demonstrated and validated technologies such as attitude and orbit control system, high-torque reaction wheels, new reaction control system. RISAT-2 and RISAT- 1 are also in the use of Indian military, launched on 20 April 2009 and 26 April 2012 is capable of radar imaging reconnaissance satellite used for border defence security. The other satellites used by the Indian military belong to the GSAT series. GSAT-7 launched on 30 August 2013 is in use of Indian Navy to enhance their blue water capabilities and communicate with ships. The GSAT-9 launched on 5 May 2017 provides navigational services to the security forces and ATC [11]. The GSAT-7A was launched on 19 Dec 2018. It is an advanced military communications satellite meant exclusively for Indian Air Force. India is heavily armed with the modern warfare equipment that provides it capabilities on all the fronts. It is capable of competing with China and Pakistan.

India has dedicated a complete series of satellites to China and Pakistan. It uses these satellites for intelligence and reconnaissance purpose. It is known as the Cartosat satellite series. As in [10] the Cartosat series are also exclusively in use of Indian Military to conduct operations against Pakistan and to monitor the developments of China-Pakistan economic corridor (CPEC). The series has been termed as Eye-in-the-Sky. CARTOSAT-1, launched on 5 May 2005 is an Observational satellite. CARTOSAT-2 that was launched on 10 Jan 2007 is capable of advanced remote sensing satellite carrying a panchromatic camera that provide scene-specific spot image. The CARTOSAT-2A that India Launched on 28 April 2008 is an Indian military satellite which carries panchromatic (PAN) camera capable of capturing black and white pictures in the visible region of electromagnetic spectrum. The CARTOSAT-2B launched on 12 July 2010 consists of panchromatic camera mounted on the satellite can be panned to 26 degrees to take photographs. The CARTOSAT-2C launched on 22 July 2016 was an Indian military satellite that it 'claims' using it for the planning of the so called 'surgical strike' across LOC in 2016. CARTOSAT-2D 15 Feb 2017 defence surveillance for military purposes similarly, the CARTOSAT-2E that India launched on 23 June 2017 has similar specifications and utilization to Cartostat-2D. Indian military ambitions have always been focused towards China and Pakistan and it has begun to employ space technology for this purpose as well.

#### *b) Acquiring ASAT capability*

Outer space weapons might not have been realized as of yet, but the concept of destroying satellites has been actualized. The powerful states that claim to have the ultimate power and hegemony in the world have acquired such tool and weapons

that are said to trigger an arms race in outer space [13]. Recently, India has also joined the domain of space power, as it tested its Anti-satellite (ASAT) capability in March 2019 [14]. Among United States, Russia, and China, India is the fourth state to achieve the status of a 'space power' by testing ASAT. India has always centred its acquisition of military stockpile towards out-growing Chinese military ambitions. However, their military aggression is always directed towards Pakistan. As in [13] after China tested its ASAT capability, India maintained a contradicting approach towards militarization of outer space. On one hand, the political leadership and civil bureaucracy maintained the stance of peaceful utility of outer space while the military hierarchy stressed upon the importance of a counter measure. Within three years, their ambitions on militarization of outer space became evidently visible. In 2010, the integrated Defence Staff of HQ stated in a policy document, "India will develop anti-satellite weapons 'for electronic and physical destruction of satellites in both LEO and GEO-synchronous orbits'. On another occasion, the chief of DRDO and the scientific advisor to the defence minister, V.K. Sarawat commented, "India has begun the development of ASAT capability". In February 2011, at the press conference after the test of Agni-III, Sarawat referred to the test as India's anti-satellite capability. He validates the simulation of anti-satellite technology on ground at the same occasion. Similarly, the president of India, APJ Abdul Kalam has also boosted about the anti-satellite technology of India. On the Golden Jubilee celebration of DRDO stating that it has the capability of intercepting and destroying any spatial object within the radius of 200km. Nine years later, after projecting its ambitions to the world, India realized its ambitions of militarizing the outer space. It conducted a successful ASAT test on 27, March 2019. India claims to be creating deterrence with China in the outer space as it prepares for Space warfare simulation exercise in July 2019.

The development of ASAT capability by India will have international and regional impacts on multiple fronts. It claims to be competing with China to counter it in outer space but this progress can have devastating effect on Pakistan in future. Pakistan should be able to foresee the threats that this aggressive advancement can have on the country and develop a multi-fold program. It is capable of countering these threats just need a proper direction. Pakistan has proven itself repeatedly at multiple occasions. Military utility and militarization of outer space is inevitable. A space program must be capable of incorporating dual-purpose utility of space assets and ground facilities as military and commercial purposes are beneficial for each other. India has attained a dual-use capability of space assets as for them it is a matter of prestige rather than the national security. This ASAT test has made India capable of challenging China but it will have tertiary impact on Pakistan.

### *c) Space Warfare Simulation Exercise*

War-gaming has always been a part of military trainings around the world. The ground forces perform training exercises to enhance their capabilities to strategically plan and analyse the situations in case of war. Until now the war-gaming exercises were performed for ground-based forces, however, India plans to take it to the next level. Recently, the western powers, including United Sates and France, have hinted towards forming space force to enhance the authority of Air force to control and secure the outer space. Evidently, the world powers are moving to equip themselves for a future galactic battle in outer space. India is also keeping pace with the changing dynamics of warfare and planning its policies accordingly and the *IndSpaceEx* is the manifestation of its new space policy [15]. The new space policy ofIndia intimates its adversaries regarding the militarization of outer space. Times of India reported that IndSpaceEx would enhance India's space warfare capabilities and counter space capabilities. The attendees of this exercise include the top officials of military and scientific community as it is perceived as a tablet-op war-game. Modi government has raised a new organization to conduct first of its nature exercise, namely Defence Space Agency (DSA). The military and civilian bureaucracy has come together to accomplish the task of preparing the ground forces for space warfare.

The significance of the IndSpaceEx has been made apparently visible by the growing importance of outer space. If the world powers raise space forces and divisions to safeguard outer space then they will need such simulation exercises in future to prepare strategically. In such case, India will prove to be an important strategic ally. The DRDO Chief G. Satheesh Reddy is of the view that outer space has become the final frontier of warfare and put the national interests at stake. He claims that through this exercise India will be capable of analysing the rudimentary space and counter space strategies. He further emphasized on the future military ambitions of India that point towards the militarization in interest of national security. Indian willingness to secure its national interest whilst militarizing the outer space is evident as it is determined to develop counter capabilities in space warfare with kinetic and non-kinetic weapons and expertise. The DRDO Chief pointed out some of the capabilities that India plan to acquire including the Directed Energy Weapons (DEWS), Lasers, Electromagnetic Pulse (EMP) weapons, and Co-orbital killers. He further adds that India is ambitious to secure its satellites from electronic and physical threats. The Indian space policy is much too ambitious to halt at the militarization of space. India is determined to follow into the footsteps of world powers to increase its hegemon by exploring and exploiting the outer space.

## IV. Available options for Pakistan

Outer space in recent times has increasingly gained popularity among the developing states pertaining to its multidimensional significance in academics, science and technology and security aspect. The global importance of the domain has become evident as defining the future. In short, world's approach towards outer space has changed altogether. The exploration has shifted to the paradigm of exploitation of outer space and its resources. This exploitation has rendered the global security vulnerable, with states like India and Pakistan becoming space faring states. The hostile nature of the two states not only jeopardizes the mutual relations but also negatively impact the regional peace and stability. If the similar scenario continues in future, the situation in outer space can lead to severe consequences. The fast-track

advancement in space technology has already created an imbalance in the capabilities of both countries, as discussed in detail previously. Owing to the assessment of the threats within these circumstances, the security of outer space in future must be sought after. The regional security dynamics of South Asia has more potential of facing direct threats as the hostile nuclear states of India and Pakistan are more capable of resorting to unconventional technological methods. India's ambitions to militarize and weaponize outer space threaten the national security of Pakistan.

### *A. Outer space as a national security emergency*

The world leaders, scholars and intellectuals regard Pakistan's location geo-strategically significant. They all acknowledge the eagerness and inclination of the Pakistani nation to achieve maximum in as little time as possible. They have been discussing Pakistan's geostrategic location and its acquisition of strategic assets for a very long time. In every era and every government setup, the pros and cons of Pakistan's political and military engagements has been discussed and analyzed at great length. The scientific community and military leadership of the country have always taken pride in becoming a nuclear power with very little resources. The hostile nature of relationship required Pakistan to ensure safety and the security of its people and territory from its adversary by initiating a nuclear program. It was a national security concern that prompted Prime Minister Zulfiqar Ali Bhutto to declare that his countrymen would even eat grass if that was required of them to make the nuclear bomb. Attaining nuclear capability was a national security emergency and it took Pakistan nearly thirty years after Bhutto's 'eating grass' statement. No stone was left unturned to achieve this strategic aim.

Today as the means of waging a war are shifting from kinetic to non-kinetic and unconventional methods, arms race in outer space is also emerging as a new security challenge. The significance of this domain in South Asia has increased in the last few years. South Asian states are using outer space like other states in any other region for militarization. Militarization is a phenomenon linked with the control of arms race in the outer space. The region is heavily militarized by India. It is quickly emerging as a space power and it should be taken into account that India's space ambitions will always be directed towards Pakistan. As mentioned in the previously the threat emanating from Indian space program should not be ignored and it should be treated as a national security emergency. Unfortunately, the weakness of Pakistan's space program lies in the inability to devise a strategy. It should be remembered that a strategy is worth nothing in the absence of a supportive policy.

### *B. National Space Policy*

This research sets out to explore the major challenges to the national and regional security due to militarization of outer space and the imbalance of civil-military space capabilities between India and Pakistan. There can be no two opinions that Pakistan needs a dynamic space program. As pointed out by many respondents from academia and Pakistan Air Force, Pakistan lacks a formal Space Policy that can be presented as a roadmap to the concerned institutions to move forward. Policies are made as a set of guidelines for an organization to help achieve its goals. The reason Pakistan's space program has lagged behind is because it lacks a formal policy. The absence of a state policy has resulted in a slow-paced progress and a lack of synergy between state institutions and military and civilian working separately in silos. It was only recently that the Minister of Science and Technology, Chaudhry Fawad Hussein, announced that Pakistan would be sending its first man into space by 2022 and this task has been given to the air force. Perhaps India's failed effort to land its first space craft on moon will give further impetus to this ambition. A space policy would provide the set of rules to our rocket scientists and planners

Countering the threats of space militarization is like a complex mathematical problem. The competition in outer space should not be zero-sum game Pakistan must play the right cards in order to win the game. The country has the potential to utilize its faculties in achieving the maximum benefit yet it lacks a proper strategic approach to solve the problem at hand. A well-planned policy should incorporate short-term and long-term goals; capacity building, enhancing the capacity and implementation of technology. It is a known fact that political and economic stability are foundational steps for a massive program to operate efficiently. However, the basic capacity building measures require realistic approach towards academic expertise in technical and social R&D. These factors will strengthen Pakistan's Space Program (PSP) and promote the peaceful utility of the program as envisioned.

### *C. Pakistan's Outer Space Strategy*

The space program has gained strategic significance over the years given the military ambitions of India, as discussed in the previously. The growing strategic significance of the outer space has prompted Pakistan to resurrect its space program and make an investment in space technology. It makes sense that space education should begin at the grass root level. The vision of Pakistan's space program should provide an institutional framework for the future. The space vision represents the state's ambitions of approaching the outer space, however, it does not provide with the operational outline. A strategically significant problem must be approached with a strategy. The state must devise a plan to counter the adversary's ambitions of threatening the country's sovereignty.

The PSP should address the military threat from outer space. The development of defensive strategies should include securing space assets, ground facilities and monitoring the space activities of adversary. The outer space strategy must be built around the national awareness of space militarization at national and educational level, incorporating the students to participate in different activities enlightening them on strategic importance of outer space. It should be prioritized at the top. Hereafter, the national strategy should be focused on Pakistan' defensive strategies that instill the counter measures in the safeguard of space assets that are of tactical importance. The adversary is capable of monitoring your activities even in the darkest of nights hence; Pakistan's priority of safeguarding your strategic assets must be treated as an urgent matter. India has developed the geo-stationary satellites that are used for monitoring and are capable of providing inter and intra communication continually.

#### *1) Development of dual-use satellites*

Space vision of Pakistan has provided with a framework of developing geo-stationary satellites that will be beneficial in the socio-economic domain. As military utilization of the outer space and its assets in inevitable in the modern age, Pakistan should invest in the development of dual-purpose satellites. The international technology has been in use of Pakistan military for ages including the space until Pakistan launched its own remote sensing satellite. Space technology offers the dimensions that can serve both civilian and military used for imagery and communication and indigenous development can address the security threat in short term. Pakistan's space program urges to promote the peaceful utilization of outer space in the longer run however; Pakistan must have strong defensive space policy and technology to counter the threat that looms in the region.

### *D.Countering External Threats in Outer Space*

The space ambitions of some advanced countries are frightening and that of India is certainly dangerous for the security of Pakistan. Strategically and militarily, India currently leads the race of militarizing outer space in South Asia. India owns the Cartosat and GSAT satellite series that has been exclusively dedicated for the use of the armed forces. These sixteen satellites are mainly used in providing intelligence, surveillance and reconnaissance (ISR) services to Indian military against Pakistan. The external threats of space militarization to Pakistan are evident from the progress of its adversary in the region. However, these external threats have emerged over the years mainly due to the inability to access the global space technology. The lead in space technology still remains with the pioneering states of Russia, Unites States and China. The nascent space faring states usually form collaborations with these advanced countries or make agreements of technology transfer. Pakistan was able avail these two available options in the initial stages, however, due to its instable political and economic conditions it could not sustain its space developments. The powerful and technologically advanced are not willing to share their information and technology besides the commercially available information is exorbitantly expensive.

## V. Conclusion

This paper has analyzed the prospects of countering national and regional security threats emerging due to the militarization of outer space by India. It has presented with the viable options of sustaining internal and external threats caused by the military ambitions of India space program. Pakistan's space program lacks a dedicated strategy, which can help in achieving the idealistic goals of Pakistan Space vision, however, a strategy must be supported by a national policy which is also absent. The unavailability of a national policy on the strategically significant issue has resulted in an incoherent approach that does not integrate various national institutions. This paper has suggested an outline for the national space policy that incorporates long term and short goals for PSP. These long term and short term goals deal with the planning of capability building measures. It starts with the basics of academic teachings to elevate the technical experts and engineers who can contribute to the uplifting of Pakistan's space program. Secondly, this paper deals with the regional security threats that have emerged due to the imbalance of military capabilities of India and Pakistan in outer space. It elaborated on the stances from the recent events where India used its satellite technology for disinformation leading to the conflicting situations between both countries that jeopardized the peace of the region.

## References


[1] Jervis, Robert, 'Cooperation Under the Security Dilemma', World Politics 30(2):186 214 (1978)

[2] Herz, John H. *Political Realism and Political Idealism*. Cambridge University Press, 1951. Print.

[3] Miqdad Mehdi and Jinyuan Su. 2019. "Pakistan Space Programme and International Cooperation: History and Prospects." Space Policy 47 (July): 175–80. https://doi.org/10.1016/j.spacepol.2018.12.002.

[4] Kingwell, Jeff. 2014. Asian Space Race: Rhetoric or Reality? Space Policy. Vol. 30. https://doi.org/10.1016/j.spacepol.2014.05.001.

[5] Salim Mehmud, 1989. "Pakistan's Space Programme," 217–26

[6] "National Space Programme." n.d.

[7] Emerging Issues, 2012. "Regulation of Space Activities," no. September.

[8] Ahsan, Ali, and Ahmad Khan. 2019. "Pakistan's Journey into Space." Astropolitics 17 (1): 38–50.

[9] Zahid, Shakeel. "An Insight into Pakistan Space Program." In *14th International Conference on Space Operations*, p. 2343. 2016

[10] Murad Shah, Regulation of Space Activities Emerging Issues & Regulatory Challenges for Pakistan's Space Program, 2012. http://suparco.gov.pk/ downloadables/nsc17.pdf. (Accessed 7 July 2018).

[11] Mian Zahid and Raja Qaiser. 2019. "Space Programs of India and Pakistan : Military and Strategic Installations in Outer Space and Precarious Regional Strategic Stability." Space Policy 47: 63–75. https://doi.org/10.1016/j.spacepol.2018.06.003.

[12] '27 Indian Satellites are currently operation, says government in Lok Sabha', http://www.dnaindia.com/india/report-27-indian- satellites-are-currently-operations-says-government-in-lok-sabha-2063999. Accessed April 12, 2017

[13] Rajeswari Pillai Rajagopalan, India's changing policy on space militarization: impact of China's ASAT test, India Rev. 10 (No. 4) (2011) 354-378. http://www.isro.gov.in/launchers/lvm3, accessed on 17 June 2019

[14] "Mission shakti and a sat missile test: all you need to know", *Times of India*, 27 March 2019, accessed 14 July 2019.

[15] Rajat Pandit, "India to hold first simulated space warfare exercise next month," *Times of India*, 8 June 2019, https://timesofindia.indiatimes.com/india/india-to-hold-first-simulated-space-warfare-exercise-next-month/articleshow/69697289.cms, accessed 16 July 2019.

# Author Index

Space Technology Education & Popularization (STEP)

# ICASE

International Conference on Aerospace Science & Engineering

## CONFERENCE SECRETARIAT


Department of Student Affairs
Institute of Space Technology
1, Islamabad Highway, Islamabad 44000 Pakistan
(+92) 51-9075454, 5476, 5578
icase2019@yahoo.com
icase.ist.edu.pk
www.facebook.com/icase.ist


PARTNERS & SPONSORS